The Radiometric Calibration of SOHO

edited by A. Pauluhn, M.C.E. Huber and R. von Steiger
International Space Science Institute
Bern, Switzerland

Contents

Foreword **vii**
A. Pauluhn, M.C.E. Huber, R. von Steiger

SOHO's Calibration Heritage **ix**

I. INTRODUCTION 1

1 Solar Variability **1**
S. K. Solanki

2 Spectroradiometry for Solar Physics in Space **21**
P. L. Smith, M.C.E. Huber

3 Spectroradiometry of Spatially-resolved Solar Plasma Structures **37**
K. Wilhelm

4 Source Standards for the Radiometric Calibration of Astronomical Instruments in the VUV Spectral Range Traceable to the Primary Standard BESSY **51**
J. Hollandt, M. Kühne, M.C.E. Huber, B. Wende

5 Calibration and Intercalibration of SOHO's Vacuum-ultraviolet Instrumentation **69**
K. Wilhelm

6 20:20 Vision and SOHO Cleanliness **91**
R. Thomas

II. INSTRUMENT RADIOMETRIC CALIBRATION 105

7 The Radiometric Calibration of the Coronal Diagnostic Spectrometer **105**
J. Lang, W. T. Thompson, C. D. Pike, B. J. Kent, C. R. Foley

8 The Radiometric Calibration of the Extreme Ultraviolet Imaging Telescope **121**
F. Clette, J.-F. Hochedez, J. S. Newmark, J. D. Moses, F. Auchère, J.-M. Defise, J.-P. Delaboudinière

9 In-flight Comparisons of Solar EUV Irradiance Measurements Provided by the CELIAS/SEM on SOHO **135**
D. R. McMullin, D. L. Judge, M. Hilchenbach, F. Ipavich, P. Bochsler, P. Wurz, A. Bürgi, W. T. Thompson, J. S. Newmark

10 Solar Vacuum-ultraviolet Radiometry with SUMER **145**
K. Wilhelm, U. Schühle, W. Curdt, I. E. Dammasch, J. Hollandt, P. Lemaire, M.C.E. Huber

11 UV Radiometric Calibration of UVCS **161**
L. D. Gardner, P. L. Smith, J. L. Kohl, N. Atkins, A. Ciaravella, M. P. Miralles, A. Panasyuk, J. C. Raymond, L. Strachan, Jr., R. M. Suleiman, M. Romoli, S. Fineschi

12 In-flight Calibration of the UVCS White Light Channel **181**
M. Romoli, R. A. Frazin, J. L. Kohl, L. D. Gardner, S. R. Cranmer, K. Reardon, S. Fineschi

13 Radiometric Calibration of the SWAN Instrument **203**
E. Quémerais, J.-L. Bertaux

III. INTERCALIBRATION **211**

14 Comparison of CDS Irradiance Measurements with SEM and EIT **211**
W. T. Thompson, D. R. McMullin, J. S. Newmark

15 Underflight Calibration of SOHO CDS by SERTS-97 **225**
R. J. Thomas

16 Intercalibration of CDS and SUMER **235**
A. Pauluhn, J. Lang, U. Schühle, S. K. Solanki, K. Wilhelm, W. T. Thompson, C. D. Pike, I. Rüedi, J. Hollandt, M.C.E. Huber

17 White Light Intercalibrations of UVCS, LASCO-C2 and Spartan 201/WLC **249**
R. A. Frazin, M. Romoli, J. L. Kohl, L. D. Gardner, D. Wang, R. A. Howard, T. A. Kucera

18 SUMER Stellar Observations to Monitor Responsivity Variations **265**
P. Lemaire

IV. ATOMIC PHYSICS **271**

19 The CHIANTI Atomic Database and Instrument Calibration: a Symbiosis **271**
H. E. Mason, G. Del Zanna, K. P. Dere, E. Landi, M. Landini, P. R. Young

20 The Use of Atomic Data for the In-flight Calibration of the CDS Spectrometers **283**
G. Del Zanna

V. WORKING GROUP REPORTS **289**

21 Cleanliness Working Group Report: Where was the SOHO Cleanliness Programme Really Effective? **289**

22 CDS and SUMER Intercalibration Working Group Report **311**

23 Irradiance Working Group Report **317**

VI. OUTLOOK **327**

24 The EUV Imaging Spectrometer and its Role in the Solar-B Mission **327**
J. L. Culhane, G. A. Doschek, T. Watanabe, J. Lang

25 The Proposed Calibration of Solar-B EIS **337**
J. Lang, B. J. Kent, J. F. Seely

26 Future Solar Irradiance Observations from the NASA TIMED and SORCE Satellites **347**
T. N. Woods, G. J. Rottman

27 The Solar Package on ISS: SOL-ACES **355**
F. G. Wienhold, J. Anders, B. Galuska, U. Klocke, M. Knothe, E. Neske, W. J. Riedel, G. Schmidtke, R. Singler, U. Ulmer, H. Wolf

28 The Solar Orbiter Mission and Design Recommendations **361**
U. Schühle, R. Thomas, J.-F. Hochedez

29 New UV Detector Concepts **371**
J.-F. Hochedez, U. Schühle, P. Lemaire

Glossary **379**

Authors' Addresses **383**

Foreword

This book reports on the radiometric calibration of the Solar and Heliospheric Observatory (SOHO) [*Fleck et al.*, 1995; *Fleck and Svestka*, 1997; *SOHO Webpage*]. Radiometric calibration and the strongly related issue of cleanliness are essential ingredients of SOHO's success as the most important solar-physics mission to date.

The complement of instruments carried by this spacecraft permits the study of the entire Sun – from its innermost core out into the heliosphere, beyond the Earth's orbit. SOHO's vantage point in a halo orbit around Lagrange point L_1 on the Earth-Sun line, 1.5×10^6 km away from the Earth towards the Sun (Figure 1), is fundamental to SOHO's capabilities. The location outside the magnetosphere in eternal sunshine and the small and gentle, accurately-known motion along the line of sight toward the Sun permit uninterrupted observing over the entire electromagnetic and particle spectrum of the day star and facilitate helioseismology studies, i.e., the analysis of solar oscillations. SOHO determines the latter with unequalled sensitivity and resolution, both in velocity and in radiance or irradiance space.

Six of SOHO's twelve instruments (Figure 2) observe in the vacuum-ultraviolet spectral region. These are: CDS, the Coronal Diagnostic Spectrometer; SUMER, the experiment for Solar Ultraviolet Measurements of Emitted Radiation; UVCS, the Ultraviolet Coronagraph Spectrometer; EIT, the Extreme-ultraviolet Imaging Telescope; SEM, the Solar Extreme-ultraviolet Monitor, which is mounted on the Charge, Element, Isotope Analysis System (CELIAS) and SWAN, which measures Solar Wind ANisotropies by observing Lyman-α fluorescence in the heliosphere. In addition, the VIRGO instrument, which measures Variability of solar IRradiance and Gravity Oscillations, determines also the total irradiance, i.e., the so-called solar constant. It thus includes the vacuum-ultraviolet part of the solar spectrum. These instruments started their observations in the first half of 1996, partly while SOHO was still on the transfer trajectory to L_1.

Vacuum-ultraviolet instrumentation on earlier solar space observatories has shown sometimes rather strong drops in responsivity after being exposed to solar radiation in space. Contamination – particularly, molecular contamination – deposited on the surfaces of mirrors and other optical components and irradiated by polymerising high-energy pho-

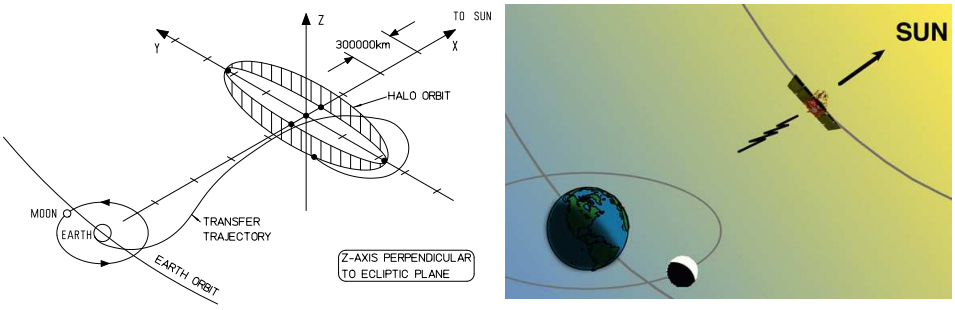

Figure 1: The halo orbit of SOHO around L_1: schematically, including the transfer trajectory (left) and in an artist's impression (right).

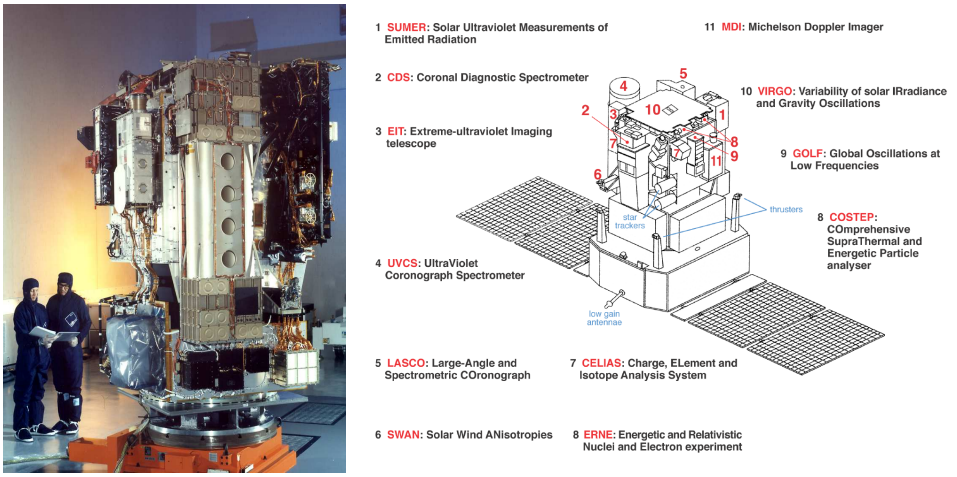

Figure 2: The SOHO spacecraft: a photograph of the payload module in the clean room (left) and a drawing of the satellite, including the service module, with the location of the instruments (right).

tons is at the root of such changes in responsivity. This means that the radiometric calibration of vacuum-ultraviolet instruments, which has been established in the laboratory, can rapidly become invalid once orbit is reached and the optics are exposed. Molecular sources of contamination – paints, potting materials, lubricants and plastics of all kinds – are widespread, and molecular sinks are not only mirrors, gratings, filters etc., but also detectors, since the latter are often cooled to achieve low noise levels.

Cleanliness, therefore, was recognised during the development of SOHO as a prime concern, and was insisted on in designing, fabricating, integrating and testing the instruments and spacecraft. A cleanliness control plan, produced in late 1989 as part of the interface documentation, spelled out the risks and gave advice on ways to minimize the effects of contamination on critical hardware. This resulted in careful design and strict material selection for instruments and spacecraft as well as a stringent observation of cleanliness procedures. The permanent monitoring of the cleanliness has been an issue right from beginning as well.

Given these extensive efforts towards cleanliness, one could hope for a stable radiometric performance of the vacuum-ultraviolet (and other) instrumentation once the spacecraft had reached orbit. And it made sense to strive toward a proper radiometric calibration – on the ground as well as in orbit.

In contrast to Earth observations, where in-orbit calibration is much advanced, but also facilitated by the possibility of using ‘ground-truth’, the inaccessibility and dynamic behaviour of the Sun makes in-orbit monitoring of instrument responsivity by use of solar radiation problematic, especially in the vacuum ultraviolet and X-ray regions.

Carrying standards into orbit for a proper end-to-end recalibration in space is still impractical. In order to compare the responsivity of different experiments and assess the stability of their radiometric calibration, one must, therefore, take recourse to co-temporal

observation of the same areas on the Sun, or to the use of an ensemble of hopefully stable stars located within the field of regard of the instruments.

The present Scientific Report on the Radiometric Calibration of SOHO is the result of two Team Workshops that have been held at the International Space Science Institute (ISSI) in Bern in February and October 2001. The participants in the workshops reviewed the entire calibration effort, that in the laboratory as well as that in orbit, and examined, and immediately used, the experience and knowledge gained by the SOHO experiments during every step of the mission. SOHO, fortunately, has carefully crafted in-orbit calibration programmes, which are designed to monitor the responsivity of its instruments. The extensive data material obtained during these in-orbit calibration programmes turned out to be particularly useful when the effects of the extreme conditions experienced during SOHO's accidental loss of attitude had to be evaluated.

This ISSI Scientific Report summarises and documents the radiometric calibration of SOHO's instruments for the first six years in orbit. Following a statement on SOHO's calibration heritage – a general message agreed to by all the workshop participants – the Report starts with an introductory part. This contains basic information, such as a description of solar variability, a general discussion of issues in spectroradiometry for solar physics from space and a digest of radiation from spatially-resolved structures. The introduction also includes a report on the development of the secondary source standards that are traceable to the primary synchrotron-radiation standard and have been developed for, and used in, the calibration of some of SOHO's telescope-spectrometer combinations. Further, the introduction also presents a précis of the actual steps taken to assure the radiometric calibration of SOHO's ultraviolet instruments as well as a summary on the subject of cleanliness.

The following two parts describe the radiometric calibration of individual instrument and their cross-calibration in orbit by use of solar or stellar radiation as 'transfer standard'. (A comparison of polarisation measurements made in the visible by the two coronagraphs on SOHO is included here, too.) A part on the use of atomic physics in radiometric calibration then follows.

The next part contains the reports and recommendations of three Working Groups that met during the workshops. The topics of the Working Groups were: (i) cleanliness, (ii) the cross-calibration between CDS and SUMER and (iii) the comparison of solar irradiance measured by SOHO and other missions.

The final part presents an outlook on space experiments and missions that address solar physics, which are either under preparation or are firmly planned. The outlook, it is hoped, will help to ensure that the experience gained with SOHO is being passed on to the benefit of future missions.

In the Workshops, the cultures of the different experiment teams coalesced into a productive, amiable atmosphere of uninhibited exchange and collaboration. Subsequently, participants showed great commitment, and invested much time and effort to write the interesting articles now being published in this ISSI Scientific Report.

The editors greatly appreciate the work of several external referees. We also want to acknowledge J.L. Kohl, C.D. Pike and K. Wilhelm, who participated in an editorial meeting that helped to improve the scientific coherence of this volume and set the rules for a consistent notation. Subsequently, K. Wilhelm, C.D. Pike and J. Lang splendidly supported the editors: they checked the final manuscripts, and without them a lot of ambiguities and

typos and many instances of improper use of the English language would have passed unnoticed. M. Böge is thanked for Unix scripts that helped in processing the manuscripts. Finally, we want to thank the SOHO Project Scientist, B. Fleck, and his team for their great support and for providing material.

Bern, August 2002

Anuschka Pauluhn, Martin C.E. Huber and Rudolf von Steiger

Bibliography

Fleck, B., Domingo, V., and Poland, A., eds., The SOHO Mission, *Sol. Phys.* **162**, Nos. 1-2, 1995.

Fleck, B., and Svestka, Z., eds., The First Results from SOHO, *Sol. Phys.* **170**, 1,**175**, 2, 1997.

SOHO Webpage, `http://sohowww.estec.esa.nl`, updated regularly, 2002.

SOHO's Calibration Heritage

The overwhelming success of the SOHO mission rests to an appreciable extent on the *stable and accurately-known radiometric response* of its extreme-ultraviolet spectroscopic solar telescopes and spectrometers.

A comprehensive *cleanliness programme* controlled both chemical and particulate contamination during fabrication and test of the SOHO spacecraft and instruments. This achieved the remarkable stability of instrument response during now over six years in orbit, in spite of the continuous exposure of some optical components to direct solar irradiation over the entire electromagnetic spectrum, to solar wind and energetic particles (and in spite of a loss of attitude with severe temperature excursions). The cleanliness measures taken for the instruments as well as for the spacecraft were adequate and there are indications that they were not excessive.

Considerable effort also went into making the *radiometric response* of the SOHO instruments directly *traceable to a primary laboratory standard*, namely synchrotron radiation produced by storage rings. This was achieved by use of both detector and source standards traceable to the primary standard. A specifically developed, transportable source standard permitted an end-to-end calibration of some of the experiments in the laboratory, where they had been assembled and tested. In some cases, direct calibration on a storage ring was performed as well.

It is stressed that a thorough end-to-end radiometric laboratory calibration is an absolute necessity for validating solar telescopes and spectrometers to be flown on spacecraft. A habitual difficulty in development programmes for such experiments is the schedule crisis that appears around the calibration phase. It is then often decided that the radiometric laboratory calibration can be abbreviated and, in part, postponed until the operations phase. Even though this pressure developed on SOHO, the Science Teams were given the opportunity to perform the most important tests in the laboratory and this has made data analysis considerably more straightforward and thus proven to be a great benefit to SOHO science. However, the short time available for these tests placed tremendous demands on the scientific and technical teams and thus increased mission risk. For future missions such risk should not be accepted.

The experience with SOHO has confirmed again that *in-flight tests by themselves can never replace a laboratory calibration with traceable radiometric standards*; on the other hand, calibration tests in flight – by use of a variety of methods, involving comparisons of instrument responsivities, but also tests by use of atomic data and astronomical standards – are essential to ensure a consistent radiometric calibration of different instruments.

Moreover, it must be recognised that, because of unavoidable detector ageing, *monitoring and maintaining the calibration in flight requires* a sustained effort over the life of the mission and beyond, and that provision for this must, in future, be made in the *planning of human resources and funding*.

We also note that the value of laboratory and in-flight calibrations now reaches further than its originally intended contribution to fundamental research; solar irradiance values measured by SOHO now flow directly into data sets used for applications, and, indeed, into operational data sets that are, for example, used for predicting the atmospheric drag which influences the decay of satellite orbits. This is a trend that further substantiates the

need for assigning *adequate priority to radiometric calibration vis-à-vis other aspects of spacecraft and experiment development*.

I. Introduction

— 1 —

Solar Variability

SAMI K. SOLANKI
Max-Planck-Institut für Aeronomie
Katlenburg-Lindau, Germany

With increasing sensitivity, wavelength coverage and photometric accuracy (including reliability in calibrations) it is becoming ever more clear that the Sun is a variable star at practically all wavelengths and timescales. A short and incomplete overview is given of the forms which this variability can take. Some of the underlying physics is also very briefly touched upon.

1.1 Introduction

The Sun is a variable star. It is variable at all observed timescales and at all wavelengths. In the visible and infrared (IR) its irradiance variations are not very large, on the order of 0.1 % or even less and require more accurate measurements than stellar astronomers generally carry out. This, and the relatively limited definition often applied to stellar variability, largely accounts for the fact that the Sun has in the past been judged to be a constant star. Thus the total radiative output of the Sun was (wrongly as it turned out) termed the 'solar constant'. The Sun is variable not just in brightness (or irradiance, which corresponds most closely to flux in stellar terminology) but in a wide variety of ways. These include variability in its particle flux (solar wind), changes in its spectrum, evolution of the morphology of surface features (i.e., the appearance and distribution of sunspots, prominences, etc.), time dependence of the magnetic flux and its surface distribution, shifts of its p-mode oscillation frequencies, etc.

In addition to the type of variability we also need to distinguish between global and (spatially) local variability, variability at different timescales, variability with different underlying physical causes and, in the case of intensity or flux variations, the wavelength of the variable radiation.

In the present overview which, by force of the extremely broad nature of the topic covered and the limited space, only picks out a few aspects of solar variability, I shall discuss the timescales of solar variability and the wavelength dependence of solar brightness variations with the help of a few examples. The physical causes are, to the extent that they are understood, briefly discussed together with the observational evidence. For a far more detailed look at solar variability see the volume edited by *Sonett et al.* [1991].

The investigation of solar variability requires stable instruments, in particular with regard to their sensitivity. The long-term stability of the radiometric calibration of radiometers and UV-sensitive instruments has become the limiting factor for many investigations of solar variability. Thus, the work presented in this volume is an important contribution to

improving our knowledge of solar variability. Conversely, the present paper may be seen as providing scientific motivation for most of the other papers in this volume.

1.2 Timescales of Solar Variability

The Sun is known to be variable on timescales ranging from fractions of seconds to its lifetime on the main sequence, i.e., over a range of 17 orders of magnitude. In the following I list some of the timescales at which the Sun exhibits, or is thought to exhibit, significant variability without, however, attempting to be complete.

- Solar evolution timescale: 10^6 to 10^{10} years [*Sackmann et al.*, 1993]
- Timescale of the evolution of solar rotation (which is also the time scale of the long-term evolution of solar magnetic activity): 10^6 to 10^{10} years
- Timescale for photons to reach the surface from the core: 10^6 years
- Timescale of heat storage in the convection zone [*Spruit*, 1982]: 10^5 years
- Timescale of 'Maunder minima', i.e., lengths of time when the Sun is almost free of spots and the 'normal' periods of cyclic magnetic activity between them: 10^2 to 10^3 years [*Eddy*, 1976, 1983; *Struiver and Brazunias*, 1989]
- Period of the Gleissberg cycle of sunspot activity: 80 to 90 years [*Gleissberg*, 1945], although the reality of this period is still under debate
- Solar magnetic cycle period: 22 years [*Hale and Nicholson*, 1925]
- Solar activity cycle period: 11 years [*Schwabe*, 1838]
- Oscillation in the rotation rate at the base of the convection zone: 1.3 years [*Howe et al.*, 2000]
- Periodicity in the occurence of gamma-ray flares: 154 to 158 days [*Rieger et al.*, 1984]
- Lifetimes of active regions: weeks to months
- Lifetimes of sunspots: hours to months
- Solar synodic rotation period: roughly 27 days at the equator, which increases to over 30 days at the poles [*Snodgrass*, 1983; *Wang et al.*, 1989]. In some cases the rotation period manifests itself in a roughly 14-day periodicity (for example when the signal is dominated by faculae).
- Lifetimes of granules, mesogranules and supergranules: minutes to days
- Timescales of flares, microflares and nanoflares, of blinkers and other forms of coronal and transition region brightenings: minutes to hours.
- Period of p-mode oscillations: approximately 5 minutes

- Period of chromospheric oscillations and waves: approximately 3 minutes
- Shortest radio spikes: 0.01 s [*Benz*, 1986]

In the following I discuss a few of these examples, without going into detail.

1.2.1 Solar Evolution

In the roughly 4.5 billion years it has spent on the main sequence the Sun has brightened (i.e., increased in luminosity) by roughly 30 %. Over the full 10^{10} years of life on the main sequence the Sun's luminosity has been calculated to change by a factor of two to three (see Figure 1.1).[1] This is dwarfed by the more than three orders of magnitude by which its brightness is expected to rise as the Sun moves up the giant branch. The various excursions up this branch, helium flashes and the final collapse of its core into a white dwarf take place on more rapid timescales of 10^4 to 10^7 years. Note that all changes on timescales longer than 10^6 years require a change in the energy production rate in the solar core, since the Sun cannot store energy for a significantly longer period of time. (This is roughly the time required by a photon to escape from the core, carrying its energy with it; neutrinos escape practically instantaneously.) The main factor determining the evolution of the energy production rate is the change in the Sun's chemical composition with time as the helium abundance in the core increases through the continuous fusion of hydrogen.

1.2.2 The Solar Cycle and Related Timescales

The best known and most clearly visible variability is that due to the activity cycle, with a period of approximately 11 years. Note that the solar cycle is not strictly periodic, with both its amplitude and period being time-dependent. The solar cycle is thought to be basically a magnetic phenomenon, whose source, a dynamo, resides at the base of the convection zone. The cyclic behaviour is produced by the repeated conversion of poloidal field (dominating during solar activity minimum) into toroidal field (dominant during activity maxima) and back again.

The number of solar phenomena varying with the solar (or Schwabe) cycle is vast. Practically every global aspect of the Sun changes to at least some degree from solar activity minimum to maximum. This includes solar total irradiance [e.g, *Fröhlich*, 2000], but also the irradiance at practically all wavelengths (for example the EUV and the 10.7 cm radio flux, see e.g., *Tapping* [1987]). In addition, the equivalent widths of particularly sensitive spectral lines (e.g., He I 1083.0 nm [*Harvey and Livingston*, 1994]), bisectors of photospheric spectral lines [*Livingston*, 1982], shapes of chromospheric lines (Mg II core-to-wing ratio), the number of and area coverage due to sunspots, the total and the interplanetary magnetic flux [e.g., *Harvey*, 1994a, b; *Lockwood et al.*, 1999], the speed of the polar solar wind [*Woch et al.*, 1997; *McComas et al.*, 2001], the spatial distribution of

[1] The figure is based on models that have the following deficiences [*A.I. Boothroyd, personal communication*]:
1.The model ignores the effect of element diffusion. This might significantly affect the total main sequence lifetime.
2. Mass loss was included via a parameterized Reimers mass loss formula, which is known to be unsatisfactory. Thus, the amount of mass loss at the tip of the red giant branch is highly uncertain. The most probable effect of the mass loss uncertainty would be that the number of helium flashes on the asymptotic giant branch could be different from that in the figure.

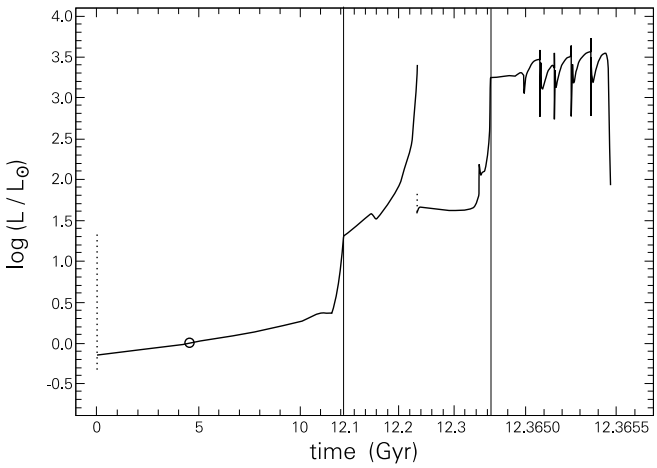

Figure 1.1: Computed luminosity of the Sun normalized to $L_\odot$, the luminosity at present, plotted as a function of time, starting from its contraction onto the main sequence (dotted line) and ending with the final contraction towards a white dwarf. Note the three different timescales, as the evolution speeds up (adapted from figure 4 of *Sackmann et al.* [1993], by permission).

prominences and coronal holes, the latitudes and shapes of coronal streamers, all change over a solar cycle, to name but a few. Not all these quantities vary by a similar amount, however. Whereas the total irradiance and *p*-mode frequencies change by far less than 1 %, the magnetic flux varies by roughly a factor of two, and the number of sunspots actually fluctuates by one to two orders of magnitude. Most of these changes occur reasonably in phase with each other, although there are some phase shifts [e.g., *Jiménez Reyes et al.*, 1998]. The evolution over the last three solar cycles of four such quantities is plotted in Figure 1.2. In general these changes can be understood in terms of the increase in magnetic flux at the solar surface and in the solar atmosphere from solar activity minimum to maximum, or in the changed distribution of this flux on the solar surface, for example into active regions harbouring sunspots and coronal loops.

One of the most intriguing results related to the solar cycle is that it also affects local properties, such as the emission from a patch of quiet Sun, or the properties of a typical sunspot. For example, the umbral brightness of sunspots is seen to change by 20 % from beginning to end of a cycle [*Albregtsen and Maltby*, 1978] and the penumbra to umbra area ratio also depends on the phase of the cycle [*Jensen et al.*, 1956]. Although proposals have been made to explain such effects [e.g., *Schüssler*, 1980] further work is definitely required.

The result found by *Schühle et al.* [2000] that the quiet Sun brightness increases towards solar activity maximum also belongs to this category. It questions the very concept of the quiet Sun as a 'standardized', time-invariant quantity. Recently, *Pauluhn and Solanki* [2002] have shown that the magnetic flux in the quiet Sun increases along with the total solar magnetic flux. In particular, the amount of magnetic flux in the regions observed in the EUV by SUMER (Solar Ultraviolet Measurements of Emitted Radiation, cf., *Wilhelm*

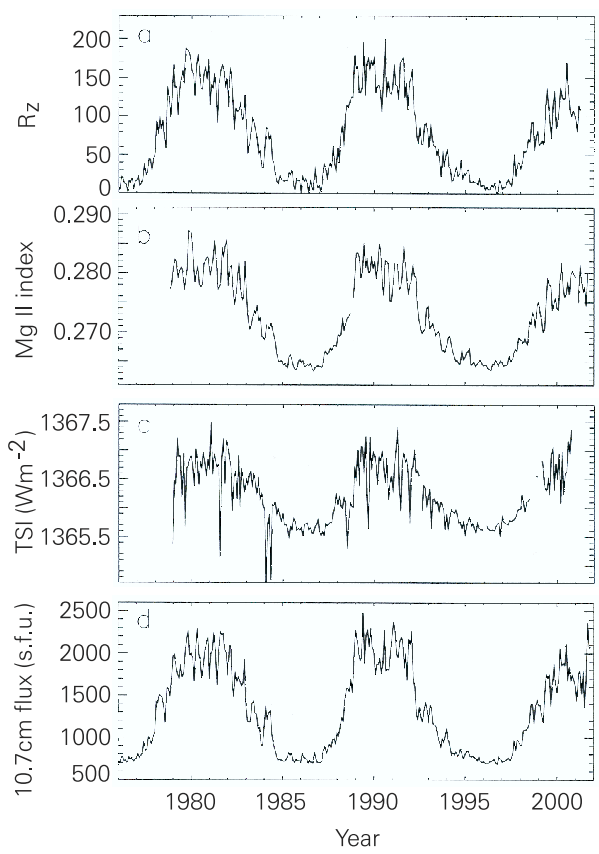

Figure 1.2: Monthly smoothed records of the following observables over sunspot cycles 21 to 23 (from top to bottom): Zürich Sunspot Relative Number, R_z, Core-to-wing ratio of the Mg II h and k lines (Mg II index), total solar irradiance (TSI) and 10.7 cm radio flux.

et al. [1995]), and CDS (Coronal Diagnostic Spectrometer), see *Harrison et al.* [1995], changes in step with the EUV brightness. It is mainly the flux in the stronger features, i.e., in the enhanced network, which is variable. This magnetic flux is directly associated with enhanced chromospheric and EUV emission [e.g., *Frazier*, 1971; *Schrijver*, 1990].

Timescales longer than 11 years are also of considerable relevance for the solar dynamo. The most obvious example is the 22-year period, which corresponds to the true periodicity of the solar magnetic field if magnetic polarity is taken into account (the so-called Hale cycle [*Hale and Nicholson*, 1925]). Systematic differences between odd and even 11-year solar cycles in sunspot numbers have also been found, and have been interpreted by *Mursula et al.* [2001] as a sign of a non-varying background field. Furthermore, both the amplitude and length of the solar activity cycle fluctuate from one cycle to the next (e.g., as manifested in the number of sunspots or other sufficiently long records of solar activity). In Figure 1.3 the yearly mean sunspot number is plotted, along with the

cycle amplitude and cycle length records deduced therefrom for the interval for which it is possible to reliably deduce these parameters from the original record.

Such fluctuations in the properties of the solar cycle can be followed on the basis of telescopic observations of sunspots for almost four centuries. The most remarkable feature in this record is that sunspots are virtually absent for a large fraction of the 17th century, during the so-called Maunder minimum [*Eddy*, 1976]. Using $^{14}C/^{12}C$ and $^{10}Be/^{9}Be$ abundance ratios (in essence measures of the open solar magnetic flux) as a proxy it is possible to follow solar activity back even further. These records reveal the presence of further Maunder minimum-like periods, in which solar activity was extremely low (and hence the cosmic-ray flux responsible for the production of the cosmogenic isotopes ^{14}C and ^{10}Be correspondingly high).

These fluctuations, including extreme cases such as Maunder minima, are finally also driven by the dynamo. What causes the dynamo to fluctuate is still being debated, and basically two proposals have been made, one being that non-linear dynamos may lead to a chaotic evolution of the field [*Rüdiger*, 2000; *Weiss and Tobias*, 2000], the other invoking stochastic influences produced by the interaction with magnetic fields in the convection zone [*Schmitt et al.*, 1996].

The concentrations of the cosmogenic isotopes indicate that the Sun's open magnetic flux also exhibits a significant secular increase since the Maunder minimum. From independent data *Lockwood et al.* [1999] deduced that the Sun's open magnetic flux has doubled in strength over the last century, in good agreement with the ^{10}Be data [*Beer*, 2000; *Solanki et al.*, 2000]. Thus, not just the active phenomena exhibit a secular trend, but also the 'quiet Sun' appears to vary on timescales longer than the solar cycle. This is also supported by observations of Sun-like stars. The intensity in the cores of the Ca II H and K lines, which is a chromospheric index of activity and of magnetic flux, is considerably lower in stars that are in a non-cyclic state (presumably similar to the Maunder minimum [*Baliunas and Jastrow*, 1990]) than in stars exhibiting a cyclic behaviour similar to the current trend. These observations have also been employed to deduce a secular variation of solar irradiance. According to quantitative estimates it has increased by at least 2 $W m^{-2}$ (or 0.17 %) since the Maunder minimum [*White et al.*, 1992; *Lean et al.*, 1992; *Zhang et al.*, 1994]. The underlying secular change of the magnetic flux is thought to be caused by overlaps between consecutive magnetic cycles in the sense that flux belonging to the new cycle starts to emerge before the old cycle has ended [*Solanki et al.*, 2002]. Such overlaps are expected within the concept of the extended solar cycle [*Wilson et al.*, 1988]. In particular *Harvey* [1992] and *Harvey* [1993] have shown that considerable magnetic flux in the form of small-scale bipolar regions, the so-called ephemeral active regions, erupts already years before the sunspots of that cycle, while the previous cycle is still in full flow.

One of the questions often addressed regarding this longer timescale is whether the modulation of the activity cycle is (roughly) periodic. The approximately 90-year Gleissberg cycle is the strongest periodicity seen in historic data (in particular in the sunspot record [*Gleissberg*, 1945]), although its reliability is much lower than that of the 11-year cycle, due to the limited length of the sunspot record and the lower reliability of earlier data.

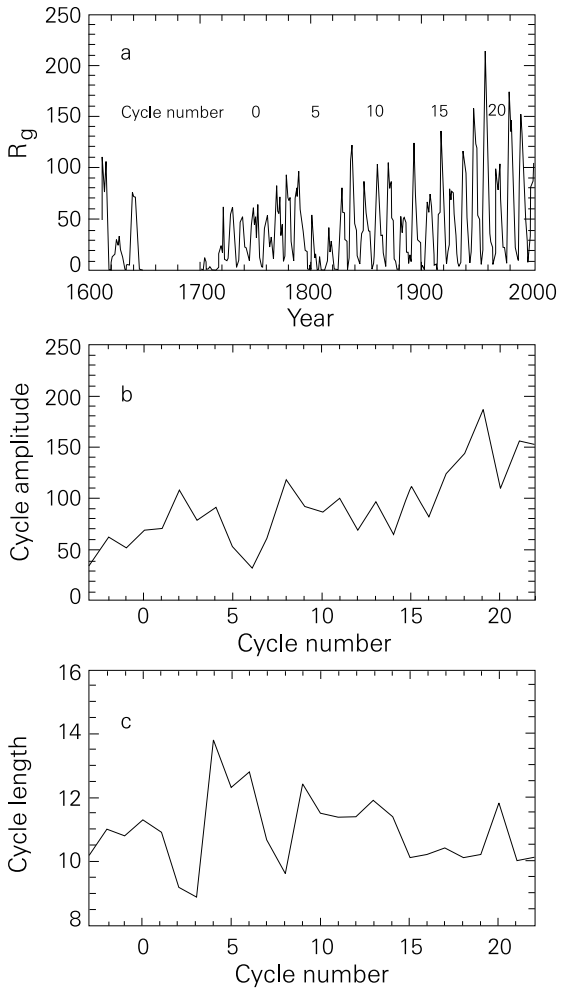

Figure 1.3: Yearly mean sunspot numbers over the last four centuries along with the cycle amplitude and cycle length records deduced from this data set. Note that these parameters can only be determined for cycles after approximately 1700.

1.2.3 Solar Rotation and Related Timescales

Periodicities at close to the Carrington rotation period of roughly 27 days and sometimes at half this period are seen in a number of records of solar observables. These periodicities are of course not due to any changes on or in the Sun, but rather to the fact that regions on the solar surface such as sunspots or active regions move in and out of view of the observer as the Sun's surface rotates past. As sunspots pass over the solar disk they

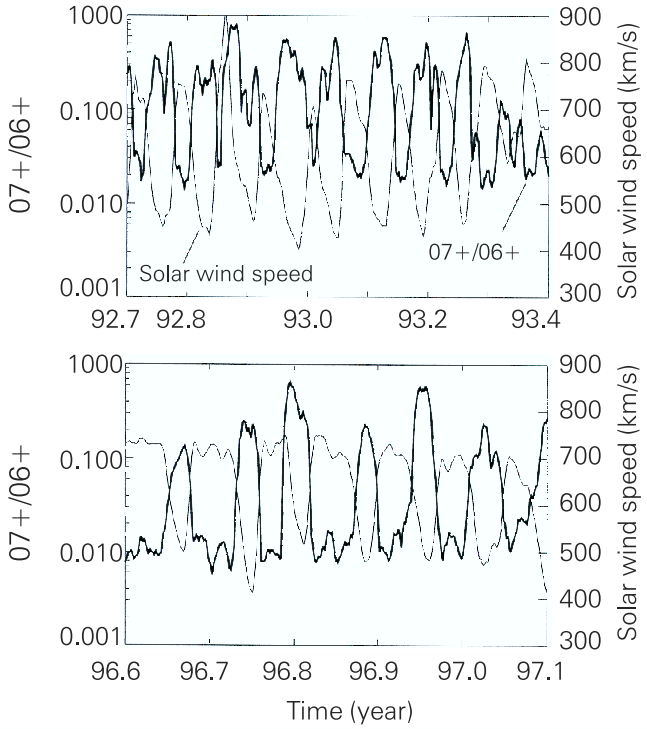

Figure 1.4: Solar wind speed (thin curves) and O^{7+}/O^{6+} ratio (thick curves) measured by the SWICS experiment on the Ulysses mission as a function of time. A low O^{7+}/O^{6+} ratio, coupled with a high wind speed is indicative of material emanating from a coronal hole.

cause solar total irradiance to decrease markedly while they are visible from Earth.[2] If the sunspots live longer than a rotation period, multiple dips in the brightness are produced with a period corresponding to the sunspot rotation period at the corresponding latitude (modulated by any proper motion that the sunspots might display). The solar wind speed often also exhibits such an (approximate) periodicity due to the repeated passage of coronal holes (mainly extensions to low latitudes of the polar holes), which can live for multiple rotations. Figure 1.4 exhibits solar wind speed and the O^{7+} / O^{6+} abundance ratio in the solar wind measured by Ulysses between 1992 and 1993 as well as a part of 1996. [cf., *von Steiger et al.*, 2000]. At these times Ulysses was at intermediate latitudes.

Solar rotation introduces a two-week period into signals that are susceptible to the passage across the solar disk of photospheric faculae, i.e., the bright parts of active regions, composed of small flux tubes. Strong faculae, i.e., those associated with spatially-averaged magnetic field strengths of a few hundred Gauss, are almost invisible at disk centre, or even slightly darker than the quiet Sun there [e.g., *Topka et al.*, 1997; *Ortiz et al.*, 2002]. They are, however, bright close to the limb. Hence the passage of a long-lived facular

[2]Here the solar total irradiance refers to the total brightness of the Sun as measured from outside the terrestrial atmosphere and at the mean distance between Sun and Earth.

structure produces two brightness peaks during a solar rotation period, namely when the structure is close to each limb. It was probably this effect which led *Claverie et al.* [1982] to misinterpret their helioseismic data in terms of a solar core rotating at twice the surface rate, as pointed out by *Durrant and Schröter* [1983], *Anderson and Maltby* [1983] and *Edmunds and Gough* [1982].

1.2.4 Lifetimes of Convection Cells and *p*-mode Periods

The hierarchy of solar convection cell sizes translates into a hierarchy of lifetimes, with larger cells living longer. Thus supergranules (average size 20 Mm to 30 Mm, lifetime 20 h) live longer than the smaller mesogranules (5 Mm, 1 to 2 h), which in turn live longer than granules (1 to 2 Mm, 5 to 10 minutes).[3] The physical processes acting during the birth and death of granules have been reviewed by *Spruit et al.* [1990], cf., *Ploner et al.* [1999]. For a first study of the physics of mesogranule evolution see *Ploner et al.* [2000]. Since most convection cells are associated with a brightness contrast, at least at some wavelengths, their evolution and in particular their birth and death produce fluctuations in the Sun's brightness. In Figure 1.5 the power spectrum of the solar irradiance time series obtained by the VIRGO (Variability of IRadiance and Gravity Oscillations) instrument on SOHO [*Fröhlich et al.*, 1995] is plotted. (For the latest update on the total solar irradiance, see *Fröhlich* [2002].) The rapid decrease of solar noise towards higher frequencies is clearly visible. This allows the group of peaks due to the solar *p*-modes to stick out above the noise at the high-frequency end. In addition to these sources, faculae and sunspots also contribute to the power. Since faculae have a high contrast and evolve slowly, they significantly raise the power at the low frequency end. The contribution of sunspots is small for the period near solar activity minimum to which these data refer.

Two parameters determine how strongly a certain type of convection cell influences the solar brightness (or the wavelength shifts of the spectral lines in the disk-integrated spectrum). One is the brightness contrast, the other is the cell size or the number of cells on the solar disk. According to the first parameter granules should have the largest influence, since they exhibit by far the largest contrast in the visible. Supergranules, on the other hand, dominate in the cores of strong lines and at shorter wavelengths, since the (magnetic) network is located at their boundaries.

Since supergranules have a 10 to 30 times larger linear dimension than granules, there are typically 100 to 1000 times more of the latter on the solar surface at any given time. Statistically the influence of a given type of convection cell on global properties decreases as $1/\sqrt{n}$, where n is the number of cells at a given time ($n \approx 10^6$ for granules).

Given this statistical factor, supergranules may have a larger effect on irradiance; however, the question is still open. The considerable uncertainty regarding the contribution of supergranules is related to the question of how strongly the magnetic network reacts to the evolution of the supergranules; do the magnetic elements flicker as supergranules evolve, or are they simply rearranged without changing brightness? This question is unanswered and may be moot, since the network magnetic flux itself evolves on the timescale of supergranule lifetimes by possibly quite independent means (for example emergence and evolution of ephemeral active regions [*Harvey and Zwaan*, 1993; *Hagenaar*, 2001]).

[3] The reality of mesogranules is still a subject of debate. Recent arguments for and against their existence have been given by *Shine et al.* [2000] and *Hathaway et al.* [2000], respectively.

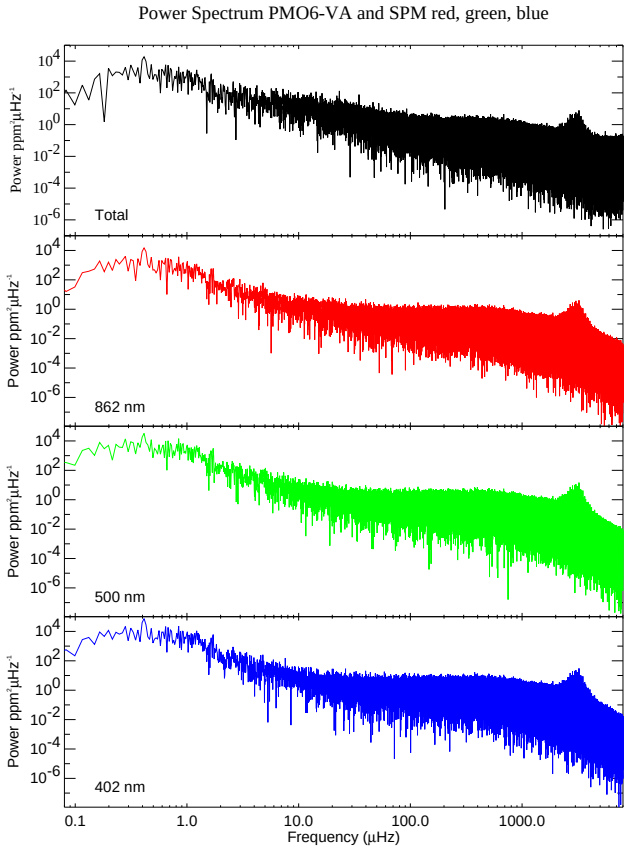

Figure 1.5: Power spectra of the total and spectral irradiance time series measured by the VIRGO instrument on SOHO. The spectral irradiance is measured in three 5 nm wide bands. The group of peaks near the right edge of the figure is produced by the *p*-mode oscillations (Figure adapted from *Fröhlich et al.* [1997]).

In a comparison of stars of different sizes *Schwarzschild* [1975] has shown that the size of granules is expected to increase faster than the stellar radius, so that the number of granules on the surface of giant and supergiant stars decreases accordingly. Hence granules could become an effective source of stellar variability for these stars. (See, however, *Gray* [2001, 2002], who does not find conclusive evidence for a granular cause of supergiant variability.)

The *p*-modes produce a distinct row of peaks in spatially unresolved (Sun-as-a-star) data (just visible in Figure 1.5) and a pattern of ridges in the $k - \omega$ diagram obtained from spatially resolved data (k is the spatial wavenumber, ω the temporal frequency). At any given point of the solar surface the overlap of all the oscillation modes present on the Sun gives rise to a seemingly chaotic signal. The regular pulse of an individual mode can be picked up by filtering out a single spatial and temporal frequency. The lowest degree ($l = 0$ to 3) modes also give a measurable signal in disk-integrated brightness and ve-

locity. Even for a given mode, the oscillation is strongly modulated on longer timescales by stochastic excitations followed by an exponential decay, with the decay time decreasing with increasing mode frequency. This combination produces complex profiles of the *p*-mode peaks in the power spectrum, which on the one hand have Lorentzian damping wings (from the finite lifetimes of the modes) and a strong χ^2-noise (from the stochastic excitations and the limited number of realisations) [*Toutain and Appourchaux*, 1994]. The former affects short-lived high-frequency modes most, while the latter is a problem mainly for the long-lived low-frequency modes.

Note that *p*-modes are solar eigenmodes resonantly excited by turbulent convection, mainly the granulation, so that any solar variability introduced by them is ultimately also due to granulation.

The granulation also excites propagating waves (i.e., those with periods shorter than the acoustic cutoff of three minutes). In the chromosphere these waves steepen into shocks, which are associated with particularly large temperature enhancements. Hence, such waves exhibit significant variations in the radiation emanating from chromospheric layers (for example the Ca II K line core *Cram and Damé* [1983]). *Carlsson and Stein* [1992, 1995, 1997] have pointed out that the variability in intensity is much smaller than the temperature variations since the hottest part of the chromosphere radiates most strongly. Thus, the bulk of the radiation in the K line core arises from the shock front as it propagates through the chromosphere in their simulations.

1.2.5 Flares, Microflares, Blinkers

One of the major discoveries of recent space missions (Yohkoh, SOHO, TRACE) has been the immense variability of the solar transition region and corona. In addition to the variability due to the sources mentioned so far there are relatively sudden brightenings in radiation sampling the chromosphere, transition region and corona of the Sun. The most energetic and spectacular of these are flares. Flares are generally detected in X-rays, coronal EUV lines, or in Hα. Flares cover a broad range of total emitted energies, peak brightnesses (for example in X-rays) and durations. See *Tandberg-Hanssen and Emslie* [1988] for an introduction to flares and an overview of their properties. The number of flares increases rapidly with decreasing amount of energy released per event [*Crosby et al.*, 1993; *Benz and Krucker*, 2002]. The very weak events are often termed microflares (or nanoflares in the case of the weakest). There are proposals by, e.g., *Parker* [1993] that these micro- and nanoflares are the main cause of coronal heating. Energy released through magnetic reconnection is thought to drive the brightening associated with a flare.

In transition-region lines similar brightenings as the microflares are seen. They have been termed blinkers [e.g., *Harrison*, 1997; *Harrison et al.* 1999; *Brković et al.*, 2001]. Examples of typical blinkers are the biggest brightenings seen in the upper right frame of Figure 1.6 (from *Brković et al.* [2002]). In CDS data plotted in the upper two frames, blinkers are significant brightenings, typically > 1.5 times the background brightness for O V 63.0 nm, which generally last between 5 and 50 minutes. A comparison with data recorded by the SUMER instrument, which are simultaneous and cospatial to the extent possible (the two lower frames in Figure 1.6), shows that SUMER exhibits over a factor of three larger variability than CDS wide-slit data. A part of the reason is that in the wide-slit mode spectral information is lost, so that the less variable nearby continuum is analyzed along with the line. Nevertheless, this still leaves over a factor of two unaccounted for, which

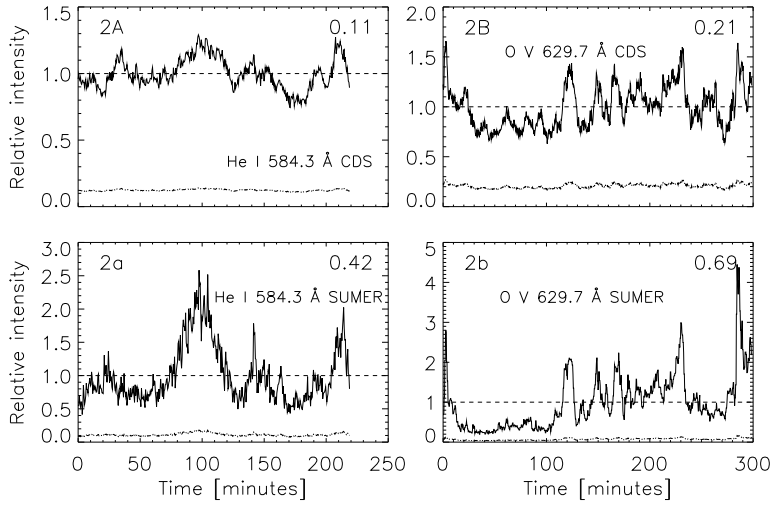

Figure 1.6: Light curves for the He I 58.4 nm and O V 63.0 nm lines observed with CDS (upper frames) and SUMER (lower frames). Plotted is the intensity relative to the time-averaged intensity (the horizontal dashed lines) for individual pixels. Note the difference in scale between the SUMER and CDS light curves. The dotted lines represent noise levels. The RMS variability is marked in the upper right of each frame (from *Brković et al.* [2002]).

Brković et al. [2002] propose is mainly due to the higher spatial resolution of SUMER. This suggests that many of the blinkers are spatially unresolved, at least by CDS.

To my knowledge still unexplained is the interesting fact that, at least, on the timescale of blinkers, the transition-region is far more variable than either the chromosphere or the corona [e.g., *Vernazza et al.*, 1975; *Brković et al.*, 2000].

1.3 Wavelength Dependence of Solar Variability

The magnitude of solar variability is strongly wavelength dependent. On the timescale of the solar-activity cycle, brightness variations have a minimum in the IR at around 1.6 μm and increase toward both shorter wavelengths, up to X-rays, and longer wavelengths to radio waves. For example, whereas the total solar irradiance (which is dominated by variations in the visible [e.g., *Solanki and Unruh*, 1998]) varies only by 0.1 % over the solar activity cycle, the EUV and X-ray flux can change by over an order of magnitude [*Acton*, 1999].

A number of causes combine to produce this wavelength dependence. In the following a few of these causes are listed.

- The temperature dependence of the Planck function increases from radio to near UV wavelengths. This means that a given change in temperature produces a larger variation in the thermal radiation at UV wavelengths than in the IR. This effect helps determine the wavelength dependence of the variability due to granulation and sunspots, but plays a minor role for, e.g., faculae or flares. For the former the

height-dependence of the temperature is more important, for the latter the radiation has a strong non-thermal component.

- Radiation formed at greater heights, i.e., lower densities (e.g., X-rays, radio), exhibits larger variations than radiation arising in deeper and denser atmospheric layers (e.g., optical radiation). In particular, the minimum in solar cycle variability at 1.6 μm is partly due to the opacity minimum located at this wavelength, so that the radiation is emitted at the greatest depth. The reason for this behaviour becomes clear when one bears in mind that the amount of energy potentially available to inject into the gas decreases more slowly with height than the gas density. Gas at a lower density is more strongly affected by the input of a given amount of energy (e.g., from the dissipation of waves or magnetic reconnection).

- Saturation effects restrict the variability of optically thick radiation, so that optically thin radiation (usually emitted from the less dense parts of the atmosphere) exhibits the largest variation.

- The structure and dynamics in the transition region and corona and the thermal energy input into them are determined by the magnetic field. Since, in the corona, gas pressure is almost negligibly small compared to magnetic pressure (but see *Gary* [2001]), large density gradients can exist stably across field lines. Similarly, since heat transport along field lines is far more efficient than across them, large cross-field thermal gradients can be built up. The hotter parts of the solar atmosphere are thus far more inhomogeneous than the cooler parts (as indicated by the very high contrast fine structures seen in data obtained by the TRACE satellite at a given wavelength). Also, magnetic heating processes (reconnection, MHD wave dissipation) tend to be very time dependent.

The wavelength dependence of the relative change in the solar irradiance between solar activity maximum and minimum of cycle 22 is plotted in Figure 1.7. Shortward of 400 nm the dashed curve corresponds to observational data from *Lean* [1997] while the solid curve results from the model calculations of *Unruh et al.* [1999]. The minimum in variability around 1.6 μm is clearly visible as is the steep increase towards the FUV and the more gentle increase towards the FIR.

Although brightenings over a large wavelength range often happen simultaneously, in extreme cases the Sun can exhibit the opposite behaviour in two different wavelengths. Perhaps the most striking example is the contrasting evolution of the solar luminosity in the visible (or integrated over all wavelengths) and in X-rays over its lifetime. Whereas the Sun has become brighter in visible light with time (see Section 1.2.1, Figure 1.1) its X-ray luminosity is expected to have decreased by between one and three orders of magnitude. This follows from the X-ray versus rotation period relationship exhibited by late-type stars. This relationship is tightest when instead of rotation period P, we use the Rossby number $R_o = P/\tau$ [e.g., *Simon*, 2001], where τ is the convective turnover time, which has remained relatively constant during the Sun's main-sequence lifetime. The rotation rate of the newborn Sun was considerably higher than the current value (like that of almost all young main sequence stars); however the Sun's exact initial rotation rate cannot be deduced from its current state [*Pinsonneault et al.*, 1989]. The X-ray luminosity of the most rapidly rotating stars is roughly three orders of magnitude larger than that

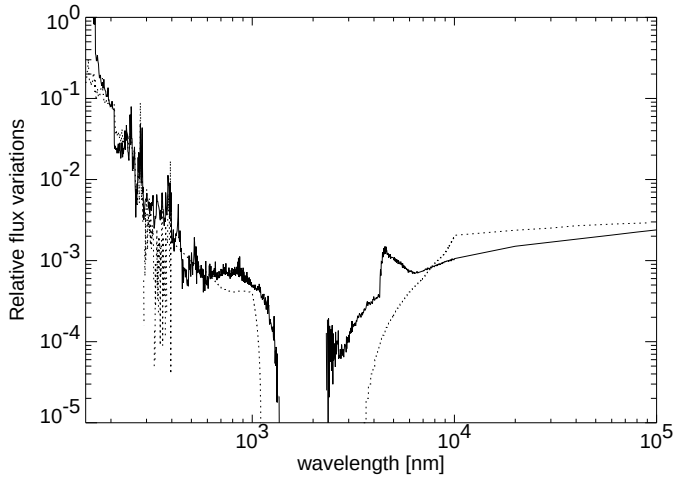

Figure 1.7: Shortward of 400 nm the dotted curve shows the observed relative irradiance variation between solar activity minimum and maximum versus wavelength, compiled by *Lean* [1997]. At longer wavelengths it is a simple extrapolation. The solid curve denotes the same quantity resulting from a 3-component model (figure from *Unruh et al.* [1999]).

of the Sun; this indicates the maximum value that the solar X-ray luminosity could have reached in the past. The intermediary connecting the stellar rotation rate to the X-ray flux is the magnetic field. The magnetic dynamo works more efficiently in a rapidly rotating star, producing more magnetic flux [*Valenti and Johns-Krull*, 2001], which in turn leads to stronger chromospheric and coronal heating.

The magnetic field also influences the rotation of the Sun by extending the Sun's moment arm and leading to an enhanced loss of angular momentum through the solar wind [e.g., *Schatzman*, 1962; *Mestel and Spruit*, 1987; *Keppens et al.*, 1995; *Solanki et al.*, 1997; *MacGregor*, 2001]. It is basically this back reaction which is responsible for the spin-down of the Sun to its current rotation rate.

1.4 Conclusion

A brief overview has been given of the variability of the Sun. The Sun varies at all timescales, although by different amounts and partly also at different wavelengths. Some of the most interesting timescales have been discussed in greater detail. The wavelength dependence of the variability has also been considered. The relative variability of the Sun increases heavily towards more extreme wavelengths. However, the absolute variation in solar irradiance or flux is largest in the visible, simply because most of the radiation is emitted in this wavelength band, so that even a small (0.1 %) relative variability leads to a large fraction of the total variability, namely 40 % [*Solanki and Unruh*, 1998].

Perhaps most intriguing is the wide range of physical processes responsible for making the Sun variable. These range from slow changes in the solar core to rapid magnetic reconnection in the solar corona. Unfortunately, the physics behind the variability has been touched upon only very rudimentarily in this overview. Another very important as-

pect which has not been considered here, but which is the subject of the other papers in this volume is the need for well-calibrated and stable instruments to reliably record solar variability. The calibration and intercalibration efforts culminating in this volume should therefore lead to a significantly improved and enhanced knowledge of solar variability.

Acknowledgements

I wish to express my thanks to A. Boothroyd, A. Brković, C. Fröhlich, N. Krivova, Y. Unruh and J. Zhang for kindly providing figures. A. Boothroyd also provided the warning in the first footnote, for which I am grateful. I am happy to acknowledge fruitful discussions with M. Schüssler.

Bibliography

Acton, L., *in Cool Stars, Stellar Systems and the Sun IX*, eds.: R. Pallavicini and A. Dupree, ASP Conf. Ser., Vol. 109, 45, 1999.

Albregtsen F., and Maltby P., New light on sunspot darkness and the solar cycle, *Nature* **274**, 41, 1978.

Anderson, B.N., and Maltby, P., Has rapid solar core rotation been observed? *Nature* **302**, 808, 1983.

Baliunas, S., and Jastrow, R., Evidence for long-term brightness changes of solar-type stars, *Nature* **348**, 520, 1990.

Beer, J., Long-term indirect indices of solar variability, *Space Sci. Rev.* **94**, 53, 2000.

Benz, A.O., Millisecond radio spikes, *Sol. Phys.* **104**, 99, 1986.

Benz, A.O., *Encyclopedia of Astronomy and Astrophysics*, Institute of Physics Press, London, 2529, 2000.

Benz, A.O., and Krucker, S., Energy distribution of microevents in the quiet solar corona, *Astrophys. J.* **568**, 413–421, 2002.

Brković, A., Rüedi, I., Solanki, S.K., Fludra, A., Harrison, R.A., Huber, M.C.E., Stenflo, J.O., and Stucki, K., EUV brightness variations in the quiet Sun, *Astron. Astrophys.* **353**, 1083–1093, 2000.

Brković, A., Solanki, S.K., and Rüedi, I., Analysis of blinkers and EUV brightenings in the quiet Sun observed with CDS, *Astron. Astrophys.* **373**, 1056–1072, 2001.

Brković, A., Solanki, S.K., and Rüedi, I., Quiet-Sun variability observed with SUMER and CDS, *Astron. Astrophys.* **385**, 257–263, 2002.

Carlsson, M., and Stein, R.F., Non-LTE radiating acoustic shocks and CA II K2V bright points, *Astrophys. J.* **397**, L59–L62, 1992.

Carlsson, M., and Stein, R.F., Does a nonmagnetic solar chromosphere exist? *Astrophys. J.* **440**, L29–L32, 1995.

Carlsson, M., and Stein, R.F., Formation of solar calcium H and K bright grains, *Astrophys. J.* **481**, 500, 1997.

Claverie, A., Isaak, G.R., McLeod, C.P., van der Raay, H.B., Palle, P.L., and Roca Cortes, T., Solar core rotation, *Nature* **299**, 704–707, 1982.

Cram, L.E., and Damé, L., High spatial and temporal resolution observations of the solar Ca II H line, *Astrophys. J.* **272**, 355–361, 1983.

Crosby, N.B., Aschwanden, M.J., and Dennis, B.R., Frequency distributions and correlations of solar X-ray flare parameters, *Sol. Phys.* **143**, 275–299, 1993.

Durrant, E.J., and Schröter, E.H., Solar global velocity oscillations and active region rotation, *Nature* **301**, 589–591, 1983.

Eddy, J.A., The Maunder Minimum, *Science* **192**, 1189–1202, 1976.

Eddy, J.A., The Maunder Minimum – A reappraisal, *Sol. Phys.* **89**, 195–207, 1983.

Edmunds, M.G., and Gough, D.O., Solar atmospheric temperature inhomogeneities induce a 13-day oscillation in full-disk Doppler measurements, *Nature* **302**, 810–812, 1983.

Frazier, E., Multi-channel magnetograph observations. III: Faculae, *Sol. Phys.* **21**, 42, 1971.

Fröhlich, C., Romero, J, Roth, H., Wehrli, C., Andersen, B.N., Appourchaux, T., Domingo, V., Telljohann, U., Berthomieu, G., Delache, P., Provost, J., Toutain, T., Crommelynck, D.A., Chevalier, A., Fichot, A., Dappen, W., Gough, D., Hoeksema, T., Jimenez, A., Gomez, M.F., Herreros, J.M., Cortes, T.R., Jones, A.R. Pap, J.M., and Willson, R.C., VIRGO: Experiment for helioseismology and solar irradiance monitoring, *Sol. Phys.* **162**, 101–128, 1995.

Fröhlich, C., Crommelynck, D.A., Wehrli, C., Anklin, M., Dewitte, S., Fichot, A., Finsterle, W., Jimenez, A., Chevalier, A., and Roth, H., In-flight performance of the Virgo solar irradiance instruments on SOHO, *Sol. Phys.* **170**, 267–286, 1997.

Fröhlich, C., Observations of irradiance variations, *Space Sci. Rev.* **94**, 15–24, 2000.

Fröhlich, C., Long-term behaviour of space radiometers, *Metrologia*, in press, 2002.

Gleissberg, W., Evidence for a long solar cycle, *Observatory* **66**, No. 827, 123–125, 1945.

Gary, G.A., Plasma beta above a solar active region: Rethinking the paradigm, *Sol. Phys.* **203**, 71–86, 2001.

Gray, D.F., Betelgeuse: Giant convection cells, *Publ. Astron. Soc. Pacific* **113**, 1378–1385, 2001.

Gray, D.F., *Astrophys. J.* in press, 2002.

Hagenaar, H.J., Ephemeral regions on a sequence of full-disk Michelson Doppler Imager magnetograms, *Astrophys. J.* **555**, 448–461, 2001.

Hale, G.E., and Nicholson, S.B., The law of sun-spot polarity, *Astrophys. J.* **62**, 270, 1925.

Harrison, R.A., Sawyer, E.C., Carter, M.K., Cruise, A.M., Cutler, R.M., Fludra, A., Hayes, R.W., Kent, B.J., Lang, J., Parker, D.J., Payne, J., Pike, C.D., Peskett, S.C., Richards, A.G., Culhane, J.L., Norman, K., Breeveld, A.A., Breeveld, E.R., Al Janabi, K.F., McCalden, A.J., Parkinson, J.H., Self, D.G., Thomas, P.D., Poland, A.I., Thomas, R.J., Thompson, W.T., Kjeldseth-Moe, O., Brekke, P., Karud, J., Maltby, P., Aschenbach, B., Bräuninger, H., Kühne, M., Hollandt, J., Siegmund, O.H.W., Huber, M.C.E., Gabriel, A.H., Mason, H.E., and Bromage, B.J.I., The Coronal Diagnostic Spectrometer for the Solar and Heliospheric Observatory, *Sol. Phys.* **162**, 233–290, 1995.

Harrison, R.A., Fludra, A., Pike, C.D., Payne, J., Thompson, W.T., Poland, A.I., Breeveld, E.R., Breeveld, A.A., Culhane, J.L., Kjeldseth-Moe, O., Huber, M.C.E., and Aschenbach, B., High-resolution observations of the extreme ultraviolet Sun, *Sol. Phys.* **175**, 467, 1997.

Harrison, R.A., Lang, J., Brooks, D.H., and Innes, D.E., A study of extreme ultraviolet blinker activity, *Astron. Astrophys.* **351**, 1115–1132, 1999.

Harvey, K.L., The cyclic behavior of solar activity, *in The Solar Cycle*, ed.: K.L. Harvey, ASP Conf. Ser. Vol. 27, 335, 1992.

Harvey, K.L., Magnetic dipoles on the Sun, PhD Thesis, University of Utrecht, 1993.

Harvey, K.L., Irradiance models based on solar magnetic fields, *in IAU Colloq. 143; The Sun as a Variable Star: Solar and Stellar Irradiance Variations*, eds.: J.M. Pap, C.

Fröhlich, H.S. Hudson, and S.K. Solanki, Cambridge Univ. Press **143**, 217, 1994a.

Harvey, K.L., *in Solar Surface Magnetism*, eds.: R.J. Rutten, and C.J. Schrijver, Kluwer, Dordrecht, 347, 1994b.

Harvey, J.W., and Livingston, W.C., Variability of the solar He I 10830 Å triplet, *in Infrared Solar Physics*, eds.: D.M. Rabin, J.T. Jefferies, and C. Lindsey, IAU Symp. No. 154, 59, 1994.

Harvey, K.L., and Zwaan, C., Properties and emergence of bipolar active regions, *Sol. Phys.* **148**, 85–118, 1993.

Hathaway, D.H., Beck, J.G., Bogart, R.S., Bachmann, K.T., Khatri, G., Petitto, J.M., Han, S., and Raymond, J., The photospheric convection spectrum, *Sol. Phys.* **193**, 313–312, 2000.

Howe, R., Christensen-Dalsgaard, J., Hill, F., Komm, R.W., Larsen, R.M., Schou, J., Thompson, M.J., and Toomre, J., Dynamic variations at the base of the solar convection zone, *Science* **287**, 2456–2460, 2000.

Jensen, E., Nordø, J., and Ringnes, T.S., Variations in the relative size of penumbra and umbra of sunspots in the Years 1878–1954, *Ann. d'Astrophys.* **19**, 165, 1956.

Jiménez-Reyes, S.J., Regulo, C., Pallé, P.L., Roca Cortés, T., Solar activity cycle frequency shifts of low-degree p-modes, *Astron. Astrophys.* **329**, 1119–1124, 1998.

Keppens, R., MacGregor, K.B., and Charbonneau, P., On the evolution of rotational velocity distributions for solar-type stars, *Astron. Astrophy.* **294**, 469–487, 1995.

Lean, J., The Sun's variable radiation and its relevance for earth, *Ann. Rev. Astron. Astrophys.* **35**, 33–67, 1997.

Lean, J., Skumanich, A., and White, O.R., Estimating the Sun's radiative output during the Maunder Minimum, *Geophys. Res. Lett.* **19**, 1591–1598, 1992.

Livingston, W.C., Magnetic fields, convection and solar luminosity variability, *Nature* **297**, 208, 1982.

Lockwood, M., Stamper, R., and Wild, M.N., A doubling of the Sun's coronal magnetic field during the past 100 years, *Nature* **399**, 437–439, 1999.

MacGregor, K.B., Spin-down of young stars: The role of magnetic fields, *in Magnetic Fields across the Hertzsprung-Russell Diagram*, eds.: G. Mathys, S.K. Solanki, and D.T. Wickramasinghe, ASP Conf. Ser., Vol. 248, 505, 2001.

McComas, D.J., Goldstein, R., Gosling, J.T., and Skoug, R.M., Ulysses' second orbit: Remarkably different solar wind, *Space Sci. Rev.* **97**, 99–103, 2001.

Mestel, L., and Spruit, H.C., On magnetic braking of late-type stars, *Monthly Notices of the RAS* **226**, 57–66, 1987.

Mursula, K., Usoskin, I.G., and Kovaltsov, G.A., Persistent 22-year cycle in sunspot activity: Evidence for a relic solar magnetic field, *Sol. Phys.* **198**, 51–56, 2001.

Ortiz, A., Solanki, S.K., Domingo, V., Fligge, M., and Sanahuja, B., *Astron. Astrophys.* **388**, 1036–1047, 2002.

Parker, E.N., Resistive dissipation and magnetic field topology in the stellar corona, *Astrophys. J.* **407**, 342–346, 1993.

Pauluhn, A., and Solanki, S.K., *Astron. Astrophys.*, to be submitted, 2002.

Pinsonneault, M.H., Kawaler, S.D., Sofia, S., and Demarque, P., Evolutionary models of the rotating Sun, *Astrophys. J.* **338**, 424–452, 1989.

Ploner, S.R.O., Solanki, S.K., and Gadun, A.S., The evolution of solar granules deduced from 2-D simulations, *Astron. Astrophys.* **352**, 679–696, 1999.

Ploner, S.R.O., Solanki, S.K., and Gadun, A.S., Is solar mesogranulation a surface phenomenon? *Astron. Astrophys.* **356**, 1050–1054, 2000.

Rieger, E., Kanbach, G., Reppin, C., Share, G.H., Forrest, D.J., and Chupp, E.L., A 154-day periodicity in the occurrence of hard solar flares? *Nature* **312**, 623–625, 1984.

Rüdiger, G., *in The Solar Cycle and Terrestrial Climate*, ed. A. Wilson, ESA SP-463, 101, 2000.

Sackmann, I.-J., Boothroyd, A.I., and Kraemer, K.W., Our Sun. III. Present and future, *Astrophys. J.* **418**, 457, 1993.

Schatzman, E., A theory of the role of magnetic activity during star formation, *Ann. Astrophys.* **25**, 18, 1962.

Schmitt, D., Schüssler, M., and Ferriz-Mas, A., Intermittent solar activity by an on-off dynamo, *Astron. Astrophys.* **311**, L1–L4, 1996.

Schrijver, C.J., Relations between the photospheric magnetic field and the emission from the outer atmospheres of cool stars. II - The C IV 1550 Å doublet, *Astron. Astrophys.* **234**, 315–322, 1990.

Schühle, U., Wilhelm, K., Hollandt, J., Lemaire, P., and Pauluhn, A., Radiance variations of the quiet Sun at far-ultraviolet wavelengths, *Astron. Astrophys.* **354**, L71–L74, 2000.

Schüssler, M., Flux tube dynamo approach to the solar cycle, *Nature* **288**, 150–152, 1980.

Schwabe, H., *Astr. Nachr.* **15**, 243, 1838.

Schwarzschild, M., On the scale of photospheric convection in red giants and supergiants, *Astrophy. J.* **195**, 137–144, 1975.

Shine, R.A., Simon, G.W., and Hurlburt, N.E., Supergranule and mesogranule evolution, *Sol. Phys.* **193**, 313–331, 2000.

Simon, T., The connection between rotation and activity, *in Cool Stars, Stellar Systems and the Sun No. 11*, eds.: R.J. García López, R. Rebolo, and M.R. Zapatero Osorio, ASP Conf. Ser. Vol. 223, 235, 2001.

Snodgrass H.B., Magnetic rotation of the solar photosphere, *Astrophys. J.* **270**, 288–299, 1983.

Solanki, S.K., Motamen S., and Keppens, R., Polar spots and stellar spindown: is dynamo saturation needed? *Astron. Astrophys.* **325**, 1039–1044, 1997.

Solanki, S.K., and Unruh, Y., A model of the wavelength dependence of solar irradiance variations, *Astron. Astrophys.* **329**, 747–753, 1998.

Solanki, S.K., Schüssler, M., and Fligge, M., Evolution of the Sun's large-scale magnetic field since the Maunder Minimum, *Nature* **408**, 445–447, 2000.

Solanki, S.K., Schüssler, M., and Fligge, M., Secular variation of the Sun's magnetic flux, *Astron. Astrophys.* **383** 706–712, 2002.

Sonett, C.P., Giampapa, M.S., and Mathews, M.W., (Eds.) *The Sun in Time*, University of Arizona Press, Tucson , 1991.

Spruit, H.C., Effect of spots on a star's radius and luminosity, *Astron. Astrophys.* **108**, 348–355, 1982.

Spruit, H.C., Nordlund, Å., and Title, A.M., Solar convection, *Ann. Rev. Astron. Astrophys.* **28**, 263–301, 1990.

Struiver, M., and Brazunias, T.F., Atmospheric ^{14}C and century-scale solar oscillations, *Nature* **338**, 405, 1989.

Tandberg-Hanssen, E., and Emslie, A.G., *The Physics of Solar Flares*, Cambridge University Press, Cambridge, 1988.

Tapping, K.F., Recent solar radio astronomy at centimeter wavelengths – The temporal variability of the 10.7-cm flux, *J. Geophys. Res.* **92**, 829–838, 1987.

Toutain, T., and Appourchaux, T., Maximum likelihood estimators: an application to the estimation of the precision of helioseismic measurements, *Astron. Astrophys.* **289**, 649–658, 1994.

Topka, K.P., Tarbell, T.D., and Title, A.M., Properties of the smallest solar magnetic elements. II. Observations versus hot wall models of faculae, *Astrophys. J.* **484**, 479, 1997.

Unruh, Y., Solanki, S.K., and Fligge, M., The spectral dependence of facular contrast and solar irradiance variations, *Astron. Astrophys.* **345**, 635–642, 1999.

Valenti, J.A., and Johns-Krull, C., Magnetic field measurements for cool stars, in *Magnetic Fields across the Hertzsprung-Russell Diagram*, eds.: G. Mathys, S.K. Solanki, and D.T. Wickramasinghe, ASP Conf. Ser. **248**, 179, 2001.

Vernazza, J.E., Foukal, P.V., Noyes, R.W., Reeves, E.M., Schmahl, E.J., Timothy, J.G., Withbroe, G.L., and Huber, M.C.E., Time variations in extreme-ultraviolet emission lines and the problem of coronal heating, *Astrophys. J.* **199**, L123–L126, 1975.

von Steiger, R., Schwadron, N.A., Fisk, L.A., Geiss, J., Gloeckler, G., Hefti, S., Wilken, B., Wimmer-Schweingruber, R.F., and Zurbuchen, T.H., Composition of quasi-stationary solar wind flows from Ulysses/Solar Wind Ion Composition Spectrometer, *J. Geophys. Res.* **105**, 27217–27238, 2000.

Wang, Y.-M., Nash, A.G., and Sheeley, N.R., Jr., Magnetic flux transport on the sun, *Science* **245**, 712–718, 1989.

Weiss, N.O., and Tobias, S.M., Physical causes of solar activity, *Space Sci. Rev.* **94**, 99–112, 2000.

White, O.R., Skumanich, A., Lean, J., Livingston, W.C., and Keil, S.L., The sun in a noncycling state, *Publ. Astron. Soc. Pacific* **104**, 1139–1143, 1992.

Wilhelm, K., Curdt, W., Marsch, E., Schühle, U., Lemaire, P., Gabriel, A., Vial, J.-C., Grewing, M., Huber, M.C.E., Jordan, S.D., Poland, A.I., Thomas, R.J., Kühne, M., Timothy, J.G., Hassler, D.M., and Siegmund, O.H.W., SUMER–Solar Ultraviolet Measurements of Emitted Radiation, *Sol. Phys.* **162**, 189–231, 1995.

Wilson, P.R., Altrock, R.C., Harvey, K.L., Martin, S.F., and Snodgrass, H.B., The extended solar activity cycle, *Nature* **333**, 748, 1988.

Woch, J., Axford, W.I., Mall, U., Wilken, B., Livi, S., Geiss, J., Gloeckler, G., and Forsyth, R.-J., SWICS/Ulysses observations: The three-dimensional structure of the heliosphere in the declining/minimum phase of the solar cycle, *Geophys. Res. Lett.* **24**, 2885, 1997.

Zhang, Q., Soon, W., Baliunas, S.L., Lockwood, G.W., Skiff, B.A., and Radick, R.R., A method of determining possible brightness variations of the Sun in past centuries from observations of solar-type stars, *Astrophys. J.* **427**, L111–L114, 1994.

— 2 —

Spectroradiometry for Solar Physics in Space

PETER L. SMITH
Harvard-Smithsonian Center for Astrophysics
Cambridge, MA, USA

MARTIN C. E. HUBER
International Space Science Institute
Bern, Switzerland

Realistic physical and chemical descriptions of the Sun require observations that have been made with spectroradiometrically calibrated telescopes and spectrometers, i.e., with instruments that have a known spectral responsivity. Such calibrations assure that a measured spectral radiance or irradiance is determined on a scale that is defined by the radiometric standards realised and used in laboratories.

For ground-based observations of the Sun in the visible or near-infrared spectral regions, comparisons with laboratory standards of radiance or irradiance are relatively straightforward. However, measurements at shorter or longer wavelengths, or measurements of the total solar irradiance with a radiometric accuracy to within one part in 1000 which is indispensable for climatology today, require observations outside the atmosphere. For these the spectral responsivity of the instrumentation must be known.

However, calibrating telescope-spectrometer combinations for the wide wavelength range of space observations is a complex and problematic task, particularly for extended space missions. Satellite telescope-spectrometer combinations can be calibrated before launch in the laboratory by use of appropriate primary or secondary source or detector standards. We review such standards and their use in the context of the SOHO instrument calibrations and we note limitations in accuracy and coverage of parameter space.

Environmental influences, such as contamination on the ground and the influence of radiation in space, may, however, cause the spectral responsivity of satellite instruments to change between laboratory calibration and initial operation in space and during the subsequent long period of orbital operations. In-orbit monitoring and validation of the responsivity of a satellite instrument is, therefore, necessary. This has been achieved for SOHO by intercomparisons of the responses of the various instruments when a common source is viewed, by observations of stars and by under-flights.

In the past, solar physics has often broken new ground and introduced and refined astronomical techniques. The efforts to calibrate solar observations as they are reported in this book should, therefore, be of interest for astronomy as a whole.

2.1 Introduction

The advent of spectroscopy in solar physics led, about 100 years ago, to the development of astrophysics. Today, our knowledge of the Universe is, in part, based on spectroradiometric[1] observations, i.e., on the determination of the spectral irradiance or spectral radiance[2] of a variety of objects and over a wide range of wavelengths. Such measurements require determination of the number, the spectral and, in the case of radiance, also the spatial distribution of photons from an object that arrive in the focal plane of an observer's telescope. When combined with atomic and molecular data, spectroradiometrically accurate observations provide evidence for deriving temperatures, densities, elemental abundances, ionisation stages, and flow and turbulent velocities in objects that are in the gaseous or plasma state. In this way, we elucidate the physical structure and chemical composition of astronomical objects, as well as the processes that cause them to emit and evolve. Such observations also provide similar insight into the properties of plasma, gas and dust in interplanetary, interstellar and intergalactic space.

Because rigorous science requires accurate data, solar physicists should insist that their spectroradiometric observations are traceable to laboratory standards through sufficiently frequent and thorough spectroradiometric calibration. This implies determination of the spectral responsivity, i.e., the effective area of a telescope-spectrometer combination as a function of energy or wavelength.[3]

In Section 2.2, we consider the laboratory basis for radiometric calibration, and discuss, with explicit attention to solar physics, the transfer of the calibration to satellite instruments. In Section 2.3, we discuss specific cases of solar satellite instrument calibrations and introduce the calibration of telescope-spectrometer combinations on the Solar and Heliospheric Observatory (SOHO).

The radiometric inter-calibration of SOHO is an example of an effort to reconcile the responsivities of all the spectroradiometric instruments on a spacecraft under real-time operations and without recourse to stellar atmosphere modelling, such as that used for the radiometric calibration of the Hubble Space Telescope [*Colina and Bohlin*, 1994].

The effort described in this book originally had a purely scientific aim, namely to assure a correct physical interpretation of the SOHO observations. In the meantime, this effort has also attained a practical use: irradiance measurements by SOHO instruments are today directly flowing into data sets that are made available for operational purposes [cf., *McMullin et al.*, 2002b].

---

[1] In astronomy, the term *photometry* is often used when dealing with broadband intensity measurements; those with higher spectral resolution are called *spectrophotometry*. However, in the terminology of physics, photometry refers to intensity determinations that are relevant to human vision. Therefore, we have chosen to use the terms *radiometry* or *spectroradiometry* in this paper.

[2] If an object is not spatially resolved, irradiance, I, the power detected per unit area (i.e., W m^{-2}; often, loosely, called flux) is measured. *Spectral* irradiance refers to the irradiance per energy (or wavelength) interval at a given energy (or wavelength), i.e., W m^{-2} eV^{-1} (or W m^{-2} nm^{-1}). Radiance, R, is the power emitted per unit area per unit solid angle, i.e., W m^{-2} sr^{-1} [*Grum and Becherer*, 1979]. *Spectral* radiance refers to the radiance per energy (or wavelength) interval at a given energy (or wavelength), i.e., W m^{-2} sr^{-1} eV^{-1} (or W m^{-2} sr^{-1} nm^{-1}). If the distance, d, to a uniformly emitting object of area, S, is known, then the irradiance is related to the radiance by $I = R(S/d^2)$.

[3] The effective area of an instrument is the equivalent collecting area of an ideal instrument, i.e., of an instrument that detects incident radiant energy with a responsivity of 100 %.

2.2 The Laboratory Basis for Spectroradiometry and its Transfer to Orbit

Any spectroradiometric measurements that are performed on the Sun or other astronomical object with the aim of deriving physical properties must be traceable to (ultimately based on a comparison with) primary laboratory standards. Such standards are absolute radiation sources or detectors that can be realised in the laboratory [*Cook*, 1994]. [4] In this Section we discuss the primary standards for laboratory radiometry and general ways of applying them to the spectroradiometric calibration of solar spectrometric space telescopes. We also consider calibration changes during an instrument's orbital lifetime and how one can determine changes from the laboratory calibration once an instrument is in orbit.

2.2.1 Primary Radiometric Standards

Ideally, there would be one primary standard for absolute spectroradiometry. However, because of the large range of radiance and irradiance as well as energy (or wavelength) of electromagnetic radiation studied in science and its applications, practical considerations and current technology have resulted in four. There are two emission, or source, standards – black bodies and electron (or positron) storage rings – and two detector standards – double-ionisation chambers and cryogenic electric substitution radiometers (ESRs).

Black bodies [cf., *Kaase et al.*, 1984] are emission standards based on thermodynamics: the radiation from a black body is related to its temperature by the Planck law. To optimise the accuracy of these standards, they are normally operated at the melting temperature of an appropriate metal.

Electron or positron storage rings [cf., *Madden et al.*, 1992] are standards based on electrodynamics. Here, the *Schwinger* [1949] formula is used to calculate the synchrotron radiation emitted by accelerated, relativistic charged particles. Inputs required for the calculation are the energy and current of the stored beam, as well as the magnetic induction at the point where the radiation is emitted; small corrections are required to account for the finite vertical extent and divergence of the particle beam.

Rare-gas double-ionisation chambers are detector standards based on the fact that the photo-ionisation yield of various rare gases, present in an optically thick column, is unity from 22.8 nm (the second ionisation threshold for He) to 101.2 nm (the first ionisation threshold for Xe) [*Samson*, 1964; *West*, 1998].

Cryogenic ESRs [cf., *Möstl*, 1991] are detector standards that are based on accurate current and voltage measurements. The temperature increase of an irradiated cavity cooled to liquid helium temperature is compared by a null method with the temperature increase caused by deposition of accurately measured electrical power into an equivalent cavity. Although corrections for reflections, scattering, and diffraction must be made, cryogenic ESRs are accepted as the most accurate radiometric standards [*Fox and Martin*, 1990].

[4] The criterion for a primary standard is that it can give a result directly without the need for any calibration relative to the quantity being measured. One must be able to write down its operating equation in full without any unknown (or empirically determined) constants or functions that are a function of the quantity being measured [*Quinn*, 2001]. By international convention, namely through the International Committee for Weights and Measures (CIPM), standards are given in terms of the units defined by the Système International (SI).

The accuracy with which the radiometric scales are realised by synchrotron radiation, black bodies (at $\lambda > 650$ nm) and cryogenic substitution radiometers has been evaluated by *Stock et al.* [1993]. Their uncertainty analysis, carried out for visible radiation, indicated that synchrotron radiation, black bodies and cryogenic ESRs produced and detected spectral radiant intensity[5] with uncertainties of 0.1 %, 0.07 % and 0.007 %, respectively.[6] *Thornagel et al.* [1996] measured emission from an electron storage ring with a cryogenic radiometer and found agreement between the two primary standards within 0.3 % at a photon energy of 15 keV and 0.08 % for visible radiation; in the latter case confirming the analysis by *Stock et al.* [1993].

For the vacuum ultraviolet (VUV) spectral domain, which is of prime interest in this paper, black bodies are not suitable, since their VUV spectral radiance is very low (cf., figure 1 of *Hollandt et al.* [1996b; 2002]). Similarly, for practical reasons, rare-gas double-ionisation chambers are infrequently used in laboratory calibrations.[7] Thus, the primary standards used in laboratory calibrations of the VUV radiometric responsivity of spectrometric space telescopes are storage rings and cryogenic radiometers.

2.2.2 Secondary Standards

Storage rings are large, complex and expensive; cryogenic radiometers are less so, but still inconvenient for routine laboratory applications. Therefore, it is often more practical to use simpler, stable sources or detectors, known as transfer standards, that are themselves calibrated by comparison with a primary standard. Examples for use in the VUV include D_2 lamps [*Saunders et al.*, 1978], hollow-cathode [*Hollandt et al.*, 1994] and Penning [*Heise et al.*, 1994] discharges, as well as silicon photodiodes [*Canfield et al.*, 1998a; *Gullikson et al.*, 1996], trap detectors [*Fox*, 1991], and metal photo-emissive diodes [*Bass*, 1995; *Canfield*, 1998b].

2.2.3 Radiometric Calibration of Spectral Irradiance Detectors and Telescope-Spectrometer Combinations for Use in Space

In modern solar astronomy from space, an assortment of four methods is used to calibrate irradiance detectors as well as telescope-spectrometer combinations:

- Calibration by use of a primary or secondary standard that is operated in orbit as part of the scientific payload. Standards carried into orbit can seldom be used to assure a calibration "end-to-end", i.e., from entrance aperture to detector output, of a telescope-spectrometer system. However, they have been employed for monitoring the stability of irradiance detectors.

- Pre-flight calibration in the laboratory by end-to-end, component, and/or subsystem level tests, with radiometric standards being employed where required.

- Calibration of an orbiting telescope-spectrometer combination by comparing simultaneous observations of the same source made by both the telescope-spectrometer

[5] *radiant intensity* is a radiometric quantity whose SI unit is W sr^{-1}.

[6] Unless otherwise indicated, all uncertainties in this paper are given in terms of one relative standard uncertainty, i.e., with a 68 % confidence limit.

[7] See, however, *Wienhold et al.* [2002], for an application as an in-orbit standard.

combination to be calibrated and a similar instrument flown on a sub-orbital rocket or the Space Shuttle. Such measurements, sometimes referred to as "underflights", use instruments that are calibrated with a radiometric standard in the laboratory before and after use in space.

- Calibration in orbit by what are called "celestial standards", i.e., by stars or other astronomical objects whose spectral irradiances are stable and have been determined earlier.

Use has also been made of the physical principles underlying the optical characteristics of given components in predicting the performance of instruments [*Rosa*, 1997]. Given a few benchmark measurements, such predictions can be used to interpolate from responsivity measurements for a few values of instrument parameters into a continuous calibration space.

2.2.4 Monitoring the Stability of Spectral Responsivity

Unless extreme care is exercised, the consequences of contamination of optical surfaces can be dramatic for a solar telescope in space. Surface layers that originate from exposure to pre-launch environments or from "outgassing" from the spacecraft bus and payload itself cause changes in performance when exposed to the harsh electromagnetic and particle emission from the Sun.[8] The variability of the VUV radiation of the Sun [*Solanki*, 2002] compounds the problem: disentangling solar variations from changes in calibration is often not trivial. Underflights are, therefore, usually required.

Unless on-board radiometric standards that calibrate the overall system from end to end, or reliable celestial standards that are confirmed to be stable and can be compared easily with solar radiation, are available, it is particularly difficult to detect whether a change in the spectroradiometric responsivity has occurred between laboratory calibrations and measurements in orbit.

2.3 Absolute Calibration of Solar Instruments on board Spacecraft

2.3.1 Solar Total Irradiance Monitors

In order to demonstrate connections between laboratory primary standards and radiometrically accurate observations of the Sun, we start with a discussion of total solar irradiance monitors. A number of these are directly traceable to primary laboratory standards.

The most accurate radiometric instruments operated in space are electric substitution radiometers (ESRs), such as the Active Cavity Irradiance Monitors (ACRIM) [*Willson*, 1999] on the Solar Maximum Mission (SMM) [*Bohlin et al.*, 1980; *Chipman*, 1981] and the Upper Atmosphere Research Satellite (UARS) [*Reber et al.*, 1993], and the Differential Absolute Radiometers (DIARAD) and PMO6-V instruments that are part of the Variability of Solar Irradiance and Gravity Oscillations (VIRGO) [*Fröhlich et al.*, 1995] package on

[8] How such contamination has been minimised for SOHO is summarised in this volume by *Thomas* [2002].

SOHO. These ESRs operate at about 300 K and, in principle, have measurement uncertainties at the 0.2 % level [*Fröhlich and Lean*, 1998]. Nevertheless, significant adjustments of the data from given instruments – adjustments that are justified by apparent degradations and changes in observing parameters – have been required [*Fröhlich*, 2002]. Moreover, in order to make a plausible time series out of data sets that cover different periods and were obtained by different instruments, the absolute scale of some measurements had to be shifted by up to 0.5 % to make them fit onto the Space Absolute Radiometric Reference Scale [*Crommelynck et al.*, 1995]. The need for such data reconciliation, which exceeds the expected instrument uncertainties, demonstrates the problematic nature of absolute radiometry from space platforms and the need for improvements in instrumentation.

The variations in the total solar irradiance over time scales beyond an 11-year activity cycle – variations that are relevant to understanding the influence of the Sun on the climate of the Earth – are thought to be at the 0.1 % level. *Quinn and Fröhlich* [1999] suggest that the next generation of instruments for such measurements should employ a primary standard, namely a cryogenic ESR whose measurement uncertainty is 0.05 % or better.

2.3.2 A Solar EUV Broadband Radiometer

The SOHO spacecraft carries a Solar Extreme-ultraviolet Monitor (SEM) that has been described as "highly stable" [*Hovestadt et al.*, 1995]. SEM comprises a freestanding 5000 l/mm transmission grating, aluminium-coated silicon photodiodes, and aluminium filters that define the bandpass. SEM was designed to measure the He II 30.4 nm irradiance from the Sun as well as the integrated flux between 17 nm and 70 nm.

Although originally assumed to be insensitive to in-flight degradation, the responsivity of SEM is now believed to have decreased by about 15 % over a period of 400 d at 30.4 nm [*McMullin et al.*, 2002a]. This change in performance was discovered as a result of a series of pre-planned, dedicated underflights – an experience that points to the need for such measurements for all space experiments that require radiometric accuracy.

2.3.3 Solar Spectral Irradiance Measurements

The only satellite spectrometers with true, on-board, *spectral* irradiance calibration capabilities that permit efficiency changes to be tracked from the time of laboratory calibration through integration, launch, and years of use in orbit are the Solar Ultraviolet Spectral Irradiance Monitors (SUSIM) [*VanHoosier et al.*, 1988; *Brueckner et al.*, 1993]. These have modest spectral resolving power and no telescope, but monitor the full-disk VUV and UV solar spectral irradiance in the wavelength band that drives the photochemistry of the Earth's ozone layer. The SUSIMs, which have observed the Sun several times from the Space Shuttle and from UARS, comprise several spectrometers and four D_2-lamp transfer standards, which have significantly different duty cycles. The initial spectrometer calibrations were established in the laboratory by direct comparison with synchrotron radiation. During orbital operations, one of the spectrometers is not used to view the Sun, since this could contribute to degradation in performance, but only to monitor relative changes in the output of the D_2 lamps.

The Solar Stellar Irradiance Comparison Experiment (SOLSTICE) [*Rottman and Woods*, 1994] is also part of the UARS instrument complement and monitors the solar spectral irradiance with approximately the same resolution and spectral range as SUSIM.

SOLSTICE was calibrated using synchrotron radiation before launch, but has no on-board calibration lamp per se. Instead, SOLSTICE tracks changes in its responsivity by comparing solar irradiances to those of hot stars that are thought to have negligible variability. The set of stars is large enough that changes in the instrument can be disentangled from unexpected stellar variability by comparing each star to the ensemble average. Moreover, excessive variability was not expected, since the stars in question had earlier been observed by IUE and HST. Two potential difficulties with SOLSTICE measurements are: (i) possible undetected change in the instrument responsivity between pre-launch calibration and in-orbit observations, and (ii) the large dynamic range, about 10^8, over which accurate radiometry is required. Different exposure times and a wide range of spectrometer entrance and exit apertures accommodate this range. However, the aperture differences mean that the solar and stellar observations use different fractions of the spectrometer optics, which may be non-uniform in performance. Careful instrument design and weekly monitoring of relevant non-uniformities indicated that their influence remained within a few percent over the ten-year UARS mission.

The UARS SUSIM and SOLSTICE instruments have monitored the VUV solar irradiance regularly and simultaneously since 1992. *Woods et al.* [1996] compared the results and those of several other VUV solar irradiance monitors. The difficulties in making spectral irradiance measurements are demonstrated, in part, by the delay between the launch of UARS and the publishing of this comparison: despite the emphasis on careful pre-flight calibrations, protection of the instruments from contamination, and on-board calibration (SUSIM) and efficiency tracking (SOLSTICE), early results did not agree. Extended observations gave the observing teams additional insight into their instruments, especially scattered light properties, and now there is confidence that the two instruments agree and both provide regular, accurate measurements of the VUV solar spectral irradiance within the uncertainty limits.

The next generation of solar spectral irradiance instruments is represented by the Solar EUV Experiment (SEE) on the TIMED spacecraft [*Woods et al.*, 1998] and the Spectral Irradiance Monitor (SIM) [*Rottman et al.*, 1998; *Lawrence et al.*, 1998]. The latter is particularly interesting because it incorporates a very sensitive ESR as a detector in its focal plane and a dual spectrometer arrangement that allows degradation in orbit to be tracked.

2.3.4 Telescope-Spectrometer Combinations for Solar Spectral Radiometry

Solar physicists have attempted spectroradiometric measurements of the solar radiance from space since the 1960s. The telescope mirrors and spectrometers on the Orbiting Solar Observatories OSO-4 and OSO-6 were separately calibrated before launch with transfer standard photodiodes [*Reeves and Parkinson*, 1970; *Huber et al.*, 1973]. However, it was shown during these calibrations that spatial non-uniformities in the diffraction efficiency of a concave grating, which was used in the calibration facility to produce a monochromatic test beam, introduced an inherent uncertainty of at least 10 % [*Huber et al.*, 1973] into the radiometric pre-launch calibration. Such optical non-uniformities have also affected the responsivity of the CDS [*Lang et al.*, 2000] and UVCS [*Gardner et al.*, 2000] instruments on SOHO. The calibration of the S-055 spectrometer on Skylab [*Reeves et al.*, 1977a] was similar to that of the OSO-6 instrument [*Reeves et al.*, 1977b] and performance was monitored during the mission by means of underflights [*Timothy et al.*, 1975]. Nevertheless,

the ultimate S-055 radiometric accuracy was insufficient to disentangle possible changes in the instrument sensitivity from variations in the VUV output of the Sun.

The radiometric calibration of the spectroheliometer flown on OSO-8 was also established in the laboratory [*Arztner et al.*, 1977; *Bonnet et al.*, 1978]. This instrument had a Cassegrain telescope and suffered a large loss of responsivity in orbit. A similar instrument, also first flown on OSO-8 [*Bruner*, 1977], was part of the payload of the Solar Maximum Mission (SMM). This instrument, in its second version, had a Gregorian telescope and featured a polarimetric capability. Data on the responsivity of the SMM-spectroheliometer were published [*Woodgate et al.*, 1980], albeit without an assessment of uncertainties.

2.3.5 Solar Spectroradiometric Telescopes on SOHO

This book reports on spectroradiometric calibrations for the SOHO mission [*Fleck et al.*, 1995] and covers the most comprehensive effort to date to achieve accurate solar spectroradiometric measurements from space. The SOHO mission required extreme cleanliness in construction, integration and launch operations so that changes in performance in orbit would be minimised [*Thomas*, 2002]. The spacecraft builders worked with a cleanliness requirement of a few hundred nanogram of condensable and particulate contamination per square centimetre, while the instrument teams aimed for even less. The minimal deterioration in the responsivity of these instruments over the course of the SOHO mission [*Pauluhn et al.*, 1999; 2001; *Schühle et al.*, 2002; *Gardner et al.*, 2002] is attributable to the cleanliness achieved.[9]

2.3.5.1 UVCS

The spectroradiometric efficiency of the Ultraviolet Coronagraph Spectrometer on SOHO (UVCS) [*Kohl et al.*, 1995] was determined before launch at selected wavelengths by use of transfer-standard photodiodes that had been calibrated at the U.S. National Institute of Standards and Technology (NIST). A one-meter spectrometer selected a narrow wavelength band from an external light source and a large collimating mirror produced a simulated solar beam [*Gardner et al.*, 1996]. The results, which had an estimated uncertainty of 16 %, have been confirmed [cf., *Gardner et al.*, 2002] by underflights with the Spartan 201 Shuttle-deployed coronal spectrometer.

Annual observations of stars that pass through the field of view of UVCS have shown changes in responsivity that are functions of aperture, i.e., of the position of the UVCS internal occulter. At the standard aperture width[10] of 11 mm, the decrease in responsivity appears to be 7.5 % per year [*Gardner et al.*, 2002]. This decrease has been confirmed by *Valcu et al.* [2002], who compared spectra of ζ Tau obtained with the two UV channels of UVCS in the 117 nm to 125 nm region with spectra obtained by IUE.

[9] However, it is worth mentioning that some of the detectors flown on SOHO were not those originally foreseen. The replacements required a gain that was too high for solar applications and, as a consequence, lost gain prematurely in regions of the detector where the total number of detected counts was large. The high voltage on the replacement detectors therefore had (and still has) to be increased periodically, so that their responsivity could be maintained over the mission.

[10] UVCS is a coronagraph with external and internal occulters. Adjustment of the latter, which is done to reduce the level of scattered light, changes the aperture.

Because of limited resources and instrument constraints, it was not possible to calibrate UVCS before launch over the full range of instrument apertures used in science observations. In-orbit studies and laboratory tests using replicas of the flight gratings have shown that, because the diffraction efficiency of the gratings is not uniform across their surface, the effective areas of the UVCS O VI and Ly-α channels are slightly non-linear functions of the width of the apertures [*Gardner et al.*, 2000; 2002].

The performance of the UVCS gratings and detectors is instructive to those who attempt to model the performance of complex instruments from first principles [*Rosa*, 1997; *Ballester and Rosa*, 1997]: it is often difficult to predict the behaviour of state-of-the-art optical components, including detectors, and coatings – and the inevitable contaminants – over the complete range of physical dimensions, optical angles, wavelengths and accumulated signal expected in use. Thus, performance models should be verified with benchmark measurements over as much parameter space as possible.

2.3.5.2 SUMER

The spectroradiometric efficiency of SUMER, the Solar Ultraviolet Measurements of Emitted Radiation instrument on SOHO [*Wilhelm et al.*, 1995], was measured prior to launch [*Hollandt et al.*, 1996a] by using a source standard that was calibrated by comparing it with synchrotron radiation [*Hollandt et al.*, 1996b]. [11] The source standard consisted of a hollow cathode, which emitted a line spectrum, and a spherical normal-incidence collimating mirror. The collimated beam had a diameter and divergence of (10 ± 1) mm and $\pm\, 1'$, respectively. In the laboratory calibration of SUMER, the image of the flux-limiting aperture of the hollow cathode underfilled the aperture in the focal plane of the telescope, which is, at the same time, the entrance slit plane of the spectrometer. An unobstructed observation of the entire source radiation was thus achieved and spectroradiometric responsivities that included the reflectivities of all optical surfaces, the grating efficiencies, as well as the detector performance could be established. Indeed, appropriate adjustments of the source and telescope mirror also permitted mapping of the responsivity of the instrument as a function of the position of the light beam within the entrance pupil. The pre-launch calibrations have subsequently been further refined under operational conditions [*Wilhelm et al.*, 1997; *Schühle et al.*, 2000].

2.3.5.3 CDS

The spectroradiometric responsivity of CDS, the Coronal Diagnostic Spectrometer [*Harrison et al.*, 1995], was measured prior to launch in a manner similar to that used for SUMER, i.e., by using a source standard that had been calibrated by comparing it to synchrotron radiation. But, in this instance, a Wolter type-II telescope served as the collimator [*Hollandt et al.*, 1996b] and the collimated beam was limited to 5 mm diameter when it left the telescope. The nominal divergence was $\pm 30''$. Inside its vacuum tank,

[11] The calibration of the transfer source standard was performed by the Physikalisch-Technische Bundesanstalt (PTB) Berlin by use of the BESSY (Berliner Speicherring-Gesellschaft für Synchrotronstrahlung m.b.H.) storage ring. It was verified in the course of this calibration that the radiometric scale of the source standard agreed with that of a NIST photodiode: a NIST photodiode generated the signal expected from the photon flux in the helium lines, when it was illuminated by the collimated beam of the source standard, run with helium gas (cf. [*Hollandt et al.*, 2002]). Although this was not a high-quality metrological comparison of the NIST and PTB scales, the test provided an important reassurance within the accuracy aimed for.

the CDS instrument could be moved perpendicularly to the beam while the optical axis was maintained, so that the instrument apertures that illuminated the grazing- and normal-incidence gratings could be mapped. The laboratory calibration of CDS [*Lang et al.*, 2000] turned out to be a much more complex undertaking than that of SUMER. Several reasons contributed to this, for example, the collimated beam was not uniform, i.e., showed structure in its cross section, and exhibited an angular divergence exceeding its nominal value by nearly a factor of four.

2.3.5.4 In-orbit Comparisons with Stellar Spectra

It is of interest to compare the calibrations of instruments designed for observations of the Sun, such as those on SOHO, with those designed for observing night-sky objects. Such a comparison informs us about whether the radiometric scales realised for solar and stellar ultraviolet observations agree with each other within the expected uncertainty limits. The comparison is more than a check on the correct application and transfer of the laboratory standards, because in a pragmatic but debatable course of action, observers using some of the space telescopes for night-sky objects, such as IUE, Voyager, and, most importantly, the Hubble Space Telescope, made use of stellar models rather than laboratory standards to establish the ultraviolet responsivity.[12] Other space telescopes, the Hopkins Ultraviolet Telescope (HUT) [*Kruk et al.*, 1999], for example, are traceable to primary standards and have pre- and post-flight calibration or are validated by underflights.

UVCS observations early in the SOHO mission show that its radiometric scale agreed with that of IUE to within the measurement uncertainties [*Valcu et al.*, 2002; *Gardner et al.*, 2002]. Other intercomparisons with stellar observations are in progress [*Lemaire*, 2002; *Wilhelm et al.*, 2002].

2.4 Conclusions and Outlook

The ISSI Team Workshop on the Radiometric Inter-Calibration of SOHO and this volume are testimony to the fact that the calibration of SOHO was performed with foresight, care and regard for an approach that involved traceability to primary radiometric standards. Such laboratory standards provide a basis for obtaining accurate physical information from radiometric observations.

The Team Workshop dealt with radiometric calibration only. However, the overall calibration of telescope-spectrometer combinations requires that a number of additional quantities be determined: the pointing accuracy and stability, plate-scale, on- and off-axis point-spread functions, the spacecraft reference frame, flat-field maps, straylight and the occurrence of ghost images, counting non-linearities, dark counts and lengths of observation intervals. We enumerate these measurement parameters here for the sake of completeness, and note that some of them must be known for a proper spectroradiometric calibration, too.

[12] The accuracy of 3 % claimed for the responsivity of HST in the ultraviolet, which is better than our knowledge of the solar ultraviolet radiometric spectrum, may, in fact, be correct, and an intercomparison with solar radiometric scales may seem superfluous. Yet, the reader is reminded that exquisite accuracy for the mirror shape of HST was claimed before the presence of spherical aberration was discovered. Unexpected discrepancies are always possible before an experimental check has been made.

The SOHO concern for all aspects of calibration has not been common for satellite missions. In the past, many astronomical findings have been made in spite of what may be considered a cavalier attitude toward spectroradiometric instrument calibration. Given time pressures in a competitive environment, some might argue that timely launch of many astronomical missions was achieved as a result of such neglect and that suppression of in-orbit calibration runs gained more, albeit uncalibrated, observing time. However, we note that it is the data quality and not the data quantity that enables scientific discovery: long observations that result in a statistical accuracy significantly greater than the radiometric accuracy are often unnecessary.

A growing tendency towards more accuracy in solar astronomy will make reliable calibration of observing instruments more and more of a necessity. And as many calibrated quantities are susceptible to change during orbital operations, or as consequence of particular events such as spacecraft eclipses or large solar flares, frequent in-orbit monitoring of the various parameters is necessary as well.

Acknowledgements

The authors sincerely thank J. Hollandt, L. D. Gardner, M. Kühne, W. H. Parkinson, A. Pauluhn and H. Stock for illuminating discussions, reference material, both published and unpublished, and other assistance. J. L. Kohl made particularly constructive comments on the manuscript. Part of this paper was written while MCEH was a Research Scholar at the Smithsonian Astrophysical Observatory. PLS was supported in part by NASA Grant NAG5-11420; he also thanks the Space Science Department of ESA for travel support.

A broader view of radiometric calibration of space instruments by the authors is in preparation.

Bibliography

Artzner, G., Bonnet, R.M., Lemaire, P., Vial, J.C., Jouchoux, A., Leibacher, J.W., Vidal-Madjar, A., and Vite, M., The LPSP instrument on OSO-8. I. Instrumentation, description of operations, laboratory calibrations, and pre-launch performance, *Space Sci. Instrum.* **3**, 131–161, 1977.

Ballester, P., and Rosa, M.R., Modeling echelle spectrographs, *Astron. Astrophys. Suppl.* **126**, 563–571, 1997.

Bass, M. (ed.), Handbook of Optics, Opt. Soc. Am, 2nd ed. (New York: McGraw-Hill), 1995.

Bohlin, J.D., Frost, K.U., Burr, P.T., Guha, A.K., and Withbroe, G.L., Solar Maximum Mission, *Sol. Phys.* **65**, 5–14, 1980.

Bonnet, R.M., Lemaire, P., Vial, J.C., Artzner, G., Gouttebroze, P., Jouchoux, A., Vidal-Madjar, A., Leibacher, J.W., and Skumanich, A., The LPSP instrument on OSO 8. II – In-flight performance and preliminary results, *Astrophys. J.* **221**, 1032–1061, 1978.

Brueckner, G.E., Edlow, K.L., Floyd, L.E., IV, Lean, J.L., and VanHoosier, M.E., The solar ultraviolet spectral irradiance monitor (SUSIM) experiment on board the Upper Atmosphere Research Satellite (UARS), *J. Geophys. Res.* **98**, 10695–10711, 1993.

Bruner, E.C., Jr., The University of Colorado OSO-8 spectrometer experiment. I - Introduction and optical design considerations, *Space Sci. Instrum.* **3**, 369–387, 1977.

Canfield, L.R., Vest, R.E., Korde, R., Schmidtke, H., and Desor, R., Absolute silicon photodiodes for 160 nm to 254 nm photons, *Metrologia* **35**, 329–334, 1998a.

Canfield, L.R., Photodiode Detectors in Vacuum Ultraviolet Spectroscopy II, eds. J.A.R. Samson and D.L. Ederer, Academic Press, San Diego, 117–138, 1998b.

Chipman, E.G., The Solar Maximum Mission, *Astrophys. J.* **244**, L113–L115, 1981.

Colina, L., and Bohlin, R.C., Absolute flux calibration of optical spectrophotometric standard stars, *Astron. J.* **108**, 1931–1935, 1994.

Cook, A.H., The observational foundations of physics, Cambridge University Press: New York, 1994.

Crommelynck, D., Fichot, A., Lee, R.B., III, and Romero, J., First realisation of the Space Absolute Radiometric Reference (SARR) during the ATLAS 2 flight period, *Adv. Space Res.* **16**, 17–23, 1995.

Fleck, B., Domingo, V., and Poland, A.I., The SOHO mission, *Sol. Phys.* **162**, 1995.

Fox, N.P., Trap detectors and their properties, *Metrologia* **28**, 197, 1991.

Fox, N.P., and Martin, J.E., Comparison of two cryogenic radiometers by determining the absolute spectral responsivity of silicon photodiodes with an uncertainty of 0.02 %. *Appl. Opt.* **29**, 4686–4693, 1990.

Fröhlich, C., and Lean, J.L., The Sun's total irradiance: Cycles, trends, and related climate change uncertainties since 1976, *Geophys. Res. Lett.* **25**, 4377–4380, 1988.

Fröhlich, C., Romero, J., Roth, H., Wehrli, C., Andersen, B.N., Appourchaux, T., Domingo, V., Telljohann, U., Berthomieu, G., Delache, P., Provost, J., Toutain, T., Crommelynck, D.A., Chevalier, A., Fichot, A., Däppen, W., Gough, D., Hoeksema, T., Jiménez, A., Gómez, M.F., Herreros, J.M., Cortés, T.R., Jones, A.R., Pap, J.M., and Willson, R.C., VIRGO: experiment for helioseismology and solar irradiance monitoring, *Sol. Phys.* **162**, 101–128, 1995.

Fröhlich, C., Long-term behaviour of space radiometers, *Metrologia*, in press, 2002.

Gardner, L.D., Kohl, J.L., Daigneau, P.S., Dennis, E.F., Fineschi, S., Michels, J., Nystrom, G.U., Panasyuk, A., Raymond, J.C., Reisenfeld, D.J., Smith, P.L., Strachan, L., Suleiman, R., Noci, G.C., Romoli, M., Ciaravella, A., Modigliani, A., Huber, M.C.E., Antonucci, E., Benna, C., Giordano, S., Tondello, G., Nicolosi, P., Naletto, G., Pernechele, C., Spadaro, D., Siegmund, O.H.W., Allegra, A., Carosso, P.A., and Jhabvala, M.D., Stray light, radiometric, and spectral characterization of UVCS/SOHO: laboratory calibration and flight performance, *Proc. SPIE* **2831**, 2–24, 1996.

Gardner, L.D., Atkins, N., Fineschi, S., Smith, P.L., Kohl, J.L., Maccari, L., and Romoli, M., Efficiency variations of UVCS/SOHO based on laboratory measurements of replica gratings, *Proc. SPIE* **4139**, 362–369, 2000.

Gardner, L.D., Smith, P.L., Kohl, J.L., Atkins, N., Ciaravella, A., Miralles, M.-P., Panasyuk, A., Raymond, J.C., Strachan, Jr., L., and Suleiman, R., UV radiometric calibration of UVCS/SOHO, this volume, 2002.

Grum, F., and Becherer, R.J., Optical Radiation Measurements, Vol. I: Radiometry, Plenum: New York, 1979.

Gullikson, E.M., Korde, R., Canfield, L.R., and Vest, R.E., Stable silicon photodiodes for absolute intensity measurements in the VUV and soft X-ray regions, *J. Electron Spectrosc. and Related Phenomena* **80**, 313–316, 1996.

Harrison, R.A., Sawyer, E.C., Carter, M.K., Cruise, A.M., Cutler, R.M., Fludra, A., Hayes, R.W., Kent, B.J., Lang, J., Parker, D.J., Payne, J., Pike, C.D., Peskett, S.C., Richards, A.G., Culhane, J.L., Norman, K., Breeveld, A.A., Breeveld, E.B.R., Janabi, K.F., McCalden, A.J., Parkinson, J.H., Self, C.D.G., Thomas, P.D., Poland, A.I., Thomas, R.J., Thompson, D.W.T., Kjeldseth-Moe, O., Brekke, P., Karud, J., Maltby, E.P., Aschen-

bach, B., Bräuninger, H., Kühne, M., Hollandt, J., Siegmund, O.H.W., Huber, M.C.E., Gabriel, A.H., Mason, H.E., and Bromage, B.J.I., The Coronal Diagnostic Spectrometer for the Solar and Heliospheric Observatory, *Sol. Phys.* **162**, 233–290, 1995.

Heise, C., Kling, R., Kock, M., Hollandt, J., and Kühne, M., Radiometric characterization of a Penning discharge in the vacuum ultraviolet, *Appl. Opt.* **33**, 5111–5117, 1994.

Hollandt, J., Kühne, M., and Wende, B., High-current hollow-cathode source as a radiant intensity standard in the 40-125-nm wavelength range, *Appl. Opt.* **33**, 68–74, 1994.

Hollandt, J., Kühne, M., Huber, M.C.E., and Wende, B., Source standards for the radiometric calibration of astronomical telescopes in the VUV spectral range traceable to the primary standard BESSY, this volume, 2002.

Hollandt, J., Schühle, U., Paustian, W., Curdt, W., Kühne, M., Wende, B., and Wilhelm, K., Radiometric calibration of the telescope and ultraviolet spectrometer SUMER on SOHO, *Appl. Opt.* **35**, 5125–5133, 1996a.

Hollandt, J., Kühne, M., Huber, M.C.E., and Wende, B., Source standards for the radiometric calibration of astronomical telescopes in the VUV spectral range , *Astron. Astrophys.* **115**, 561–572, 1996b.

Hovestadt, D., Hilchenbach, M., Bürgi, A., Klecker, B., Laeverenz, P., Scholer, M., Grunwaldt, H., Axford, W.I., Livi, S., Marsch, E., Wilken, B., Winterhoff, H.P., Ipavich, F.M., Bedini, P., Coplan, M.A., Galvin, A.B., Gloeckler, G., Bochsler, P., Balsiger, H., Fischer, J., Geiss, J., Kallenbach, R., Wurz, P., Reiche, K.-U., Gliem, F., Judge, D.L., Ogawa, H.S., Hsieh, K.C., Möbius, E., Lee, M.A., Managadze, G.G., Verigin, M.I., and Neugebauer, M., CELIAS - Charge, Element and Isotope Analysis System for SOHO, *Sol. Phys.* **162**, 441–481, 1995.

Huber, M.C.E., Dupree, A.K., Goldberg, L., Noyes, R.W., Parkinson, W.H., and Reeves, E.M., Withbroe, G.L., The Harvard Experiment on OSO-6: Instrumentation, Calibration, Operation, and Description of Observations, *Astrophys. J.* **183**, 291–312, 1973.

Kaase, H., Bischoff, K., and Metzdorf, J., *Licht-Forschung* 6, 29, 1984.

Kohl, J.L., Esser, R., Gardner, L.D., Habbal, S., Daigneau, P.S., Dennis, E.F., Nystrom, G.U., Panasyuk, A., Raymond, J., Smith, P.L., Strachan, L., van Ballegooijen, A.A., Noci, G., Fineschi, S., Romoli, M., Ciaravella, A., Modigliani, A., Huber, M.C.E., Antonucci, E., Benna, C., Giordano, S., Tondello, G., Nicolosi, P., Naletto, G., Pernechele, C., Spadaro, D., Poletto, G., Livi, S., von der Lühe, O., Geiss, J., Timothy, J.G., Gloeckler, G., Allegra, A., Basile, G., Brusa, R., Wood, B., Siegmund, O.H.W., Fowler, W., Fisher, R., and Jhabvala, M., Ultraviolet Coronagraph Spectrometer for the Solar and Heliospheric Observatory: instrument description and calibration overview, *Sol. Phys.* **162**, 313–356, 1995.

Kruk, J.W., Brown, T.M., Davidsen, A.F., Espey, B.R., Finley, D.S., and Kriss, G.A., Final Astro-2 Calibration of the Hopkins Ultraviolet Telescope, *Astrophys. J. Suppl.* **122**, 299–329, 1999.

Lang, J., Kent, B.J., Breeveld, A.A., Breeveld, E.R., Bromage, B.J.I., Hollandt, J., Payne, J., Pike, C.D., and Thompson, W.T., The laboratory calibration of the SOHO Coronal Diagnostic Spectrometer, *J. Opt. A: Pure Appl. Opt.* **2**, 88–106, 2000.

Lawrence, G.M., Harder, J.W., Rottman, G.J., Woods, T.N., Richardson, J., and Mount, G., Stability considerations for a solar spectral intensity monitor (SIM), *Proc. SPIE* **3427**, 477–485, 1998.

Lemaire, P., SUMER Stellar Observations to monitor responsivity variations, this volume, 2002.

Madden, R.P., Canfield, L.R., Furst, M., Hamilton, A., and Hughey, L., SURF II: characteristics, facilities, and plans, *Rev. Sci. Instrum.* **63**, 1594–1595, 1992.

McMullin, D.R., Judge, D.L., Hilchenbach, M., Ipavich, F., Bochsler, P., Wurz, P., Bürgi, A., Thompson W.T., and Newmark, J.S., In-flight comparison of Solar EUV Irradiance Measurements Provided by the CELIAS/SEM on SOHO, this volume, 2002a.

McMullin, D.R., Woods, T., Dammasch, I.E., Wilhelm, K., Judge, D.L., Lemaire, P., Newark, J.S., Thompson, W.T., and Tobiska, W.K., Irradiance Working Group Report, this volume, 2002b.

Miralles, M.P., et al., in preparation, 2002.

Möstl, K., in Landolt-Börnstein (New Series), Units and Fundamental Constants in Physics and Chemistry, Subvol. a, ed. J. Bortfield and B. Kramer (Berlin: Springer-Verlag), p. 2.348, 1991.

Pauluhn, A., Rüedi, I., Solanki, S.K., Lang, J., Pike, C.D., Schühle, U., Thompson, W.T., Hollandt, J., and Huber, M.C.E., Intercalibration of SUMER and CDS on SOHO. I. SUMER detector A and CDS NIS , *Appl. Opt.* **38**, 7035–7046, 1999.

Pauluhn, A., Rüedi, I., Solanki, S.K., Schühle, U., Wilhelm, K., Lang, J., Thompson, W.T., Hollandt, J., and Huber, M.C.E., Intercalibration of SUMER and CDS on SOHO. II. SUMER Detectors A and B and CDS NIS, *Appl. Opt.* **40**, 6292–6300, 2001.

Quinn, T.J., and Fröhlich, C., Accurate radiometers should measure the output of the Sun, *Nature* **401**, 841, 1999.

Quinn, T.J., personal communication, 2001.

Reber, C.A., Trevathan, C.E., McNeal, R.J., and Luther, M.R., The Upper Atmosphere Research Satellite (UARS) mission, *J. Geophys. Res.* **98,** 10643–10647, 1993.

Reeves, E.M., and Parkinson, W.H., An Atlas of Extreme-Ultraviolet Spectroheliograms from OSO-IV, *Astrophys. J. Suppl.* **21**, 1–30, 1970.

Reeves, E.M., Timothy, J.G., and Huber, M.C.E., Extreme UV spectroheliometer on the Apollo Telescope Mount, *Appl. Opt.* **16**, 837–848, 1977a.

Reeves, E.M., Timothy, J.G., Withbroe, G.L., and Huber, M.C.E., Photometric calibration of the EUV spectroheliometer on ATM, *Appl. Opt.* **16**, 849–857, 1977b.

Rosa, M.R., Physical Modeling of Scientific Instruments, *ASP Conf. Ser.* **125**, 411–414, 1997.

Rottman, G.J., Woods, T.N., and Sparn, T.P., Solar Stellar Irradiance Comparison Experiment I. 1 Instrument Design and Operation, J. Geophys. Res. **98**, 10 667–10 677, 1993.

Rottman, G.J., and Woods, T.N., UARS Solar Stellar Irradiance Comparison Experiment (SOLSTICE), *Proc. SPIE* **2266**, 317–329, 1994.

Rottman, G.J., Mount, G.H., Lawrence, G.M., Woods, T.N., Harder, J., and Tournois, S., Solar spectral irradiance measurements: Visible to near-infrared regions, *Metrologia* **35**, 707–712, 1998.

Samson, J.A.R., Absolute intensity measurements in the vacuum ultraviolet, *J. Opt. Soc. Am.* **54**, 6–15, 1964.

Saunders, R.D., Ott, W.R., and Bridges, J.M., Spectral irradiance standard for the ultraviolet: the deuterium lamp, *Appl. Opt.* **17**, 593–600, 1978.

Schühle, U., Thomas, R., Kent, B.J., Clette, F., Defise, J.M., Delaboudinière, J.P., Fröhlich, C., Gardner, L.D., Hochedez, J.F., Kohl, J.L., and Moses, D.J., Summary of Cleanliness Discussion: Where was the SOHO Cleanliness Programme Really Effective?, this volume, 2002.

Schühle, U., Curdt, W., Hollandt, J., Feldman, U., Lemaire, P., and Wilhelm, K., Radiometric Calibration of the Vacuum-Ultraviolet Spectrograph SUMER on SOHO with the B detector, *Appl. Opt.* **39**, 418–425, 2000.

Schwinger, J., On the classical radiation of accelerated electrons, *Phys. Rev.* **75**, 1912–1925, 1949.

Solanki, S.K., Solar Variability, this volume, 2002.

Stock, M., Fischer, J., Friedrich, R., Jung, H.J., Thornagel, R., Ulm, G., and Wende, B., Present state of the comparison between radiometric scales based on three primary standards, *Metrologia* **30**, 439–449, 1993.

Thomas, R., 20:20 vision; SOHO Cleanliness, this volume, 2002.

Thornagel, R., Fischer, J., Friedrich, R., Stock, M., Ulm, G., and Wende, B., The electron storage ring BESSY as a primary standard source – a radiometric comparison with a cryogenic electrical substitution radiometer in the visible, *Metrologia* **32**, 459–462, 1996.

Timothy, J.G., Chambers, R.M., D'Entremont, A.M., Lanham, N.W., and Reeves, E.M., A sounding rocket spectroheliometer for photometric studies at extreme ultraviolet wavelengths, *Space Sci. Instrum.* **1**, 23–49, 1975.

Valcu, B., Smith, P.L., Kohl, J.L., and Gardner, L.D., In-flight Radiometric Calibration of UVCS/SOHO: Comparison with IUE and Copernicus Spectra of ζ Tauri, in preparation, 2002.

VanHoosier, M.E., Bartoe, J.D., Brueckner, G.E., and Prinz, D.K., Absolute solar spectral irradiance 120 nm-400 nm (Results from the Solar Ultraviolet Spectral Irradiance Monitor-SUSIM-Experiment on board Spacelab 2), *Astrophys. Lett. Commun.* **27**, 163–168, 1988.

West, J.B., Gas Detectors, in Vacuum Ultraviolet Spectroscopy II, eds. J.A.R. Samson and D.L. Ederer, Academic Press: San Diego, 107–115, 1998.

Wienhold, F.G., Anders, J., Galuska, B., Klocke, U., Knothe, M., Neske, E., Riedel, W.J., Schmidtke, G., Singler, R., Ulmer, U., and Wolf, H., The Solar Package on ISS: SOLACES, this volume, 2002.

Wilhelm, K., Curdt, W., Marsch, E., Schühle, U., Lemaire, P., Gabriel, A., Vial, J.-C., Grewing, M., Huber, M.C.E., Jordan, S.D., Poland, A.I., Thomas, R.J., Kühne, M., Timothy, J.G., Hassler, D.M., and Siegmund, O.H.W., SUMER – Solar Ultraviolet Measurements of Emitted Radiation , *Sol. Phys.* **162**, 189–231, 1995.

Wilhelm, K., Lemaire, P., Feldman, U., Hollandt, J., Schühle, U., and Curdt, W., Radiometric calibration of SUMER: refinement of the laboratory results under operational conditions on SOHO , *Appl. Opt.* **36**, 6416–6422, 1997.

Wilhelm, K., Schühle, U., Curdt, W., Dammasch, I.E., Hollandt, J., Lemaire, P., and Huber, M.C.E, Solar vacuum-ultraviolet radiometry with SUMER, this volume, 2002.

Willson, R.C., Solar irradiance variations, in The many faces of the Sun: a summary of the results from NASA's Solar Maximum Mission, eds. K.T. Strong, J.L.R. Saba, M. Haisch and J.T. Schmelz, Springer: New York, 19, 1999.

Woodgate, B.E., Brandt, J.C., Kalet, M.W., Kenny, P.J., Tandberg-Hanssen, E.A., Bruner, E.C., Beckers, J.M., Henze, W., Knox, E.D., and Hyder, C.L., The Ultraviolet Spectrometer and Polarimeter on the Solar Maximum Mission, *Sol. Phys.* **65**, 73–90, 1980.

Woods, T.N., Prinz, D.K., Rottman, G.J., London, J., Crane, P.C., Cebula, R.P., Hilsenrath, E., Brueckner, G.E., Andrews, M.D., White, O.R., VanHoosier, M.E., Floyd, L.E., Herring, L.C., Knapp, B.G., and Pankratz, C.K., Validation of the UARS solar ultraviolet

irradiances: Comparison with the ATLAS 1 and 2 measurements, *J. Geophys. Res.* **101**, 9541–9570, 1996.

Woods, T.N., Bailey, S.M., Eparvier, F.G., Lawrence, G.M., Lean, J., McClintock, W.E., Roble, R.G., Rottman, G.J., Solomon, S.C., Tobiska, W.K., Ucker, G.J., and White, O.R., TIMED solar EUV experiment, *Proc. SPIE* **3442**, 180–191, 1998.

— 3 —

Spectroradiometry of Spatially-resolved Solar Plasma Structures

KLAUS WILHELM
Max-Planck-Institut für Aeronomie, Katlenburg-Lindau, Germany

Denn eben wo Begriffe fehlen,
da stellt ein Wort zur rechten Zeit sich ein.
J.W. v. Goethe, Faust I, Mephistopheles

The investigation of spatially-resolved solar plasma features in terms of radiometric measurements requires concepts different from those useful for full-Sun observations. After a definition of the relevant physical quantities, formulae are derived for studies of optically-thick and optically-thin plasmas observed with both spectral and spatial resolution. Simple examples of their applications to the determination of electron densities and electron temperatures as well as to studies of emission measures and elemental abundances are discussed.

3.1 Introduction

The Sun, a very close main-sequence star of spectral class G2 V, allows us to study its atmosphere in great detail, and, in particular, perform spatially-resolved observations. In these studies, not only the morphology is of importance, but also the dynamical processes in the solar plasma. Spectral information is required to disentangle this complex system. Moreover, after the atomic processes leading to the emission of radiation have been understood, the observed radiation has to be interpreted in terms of the generation processes. This calls for a quantitative investigation of the solar radiation emitted by small structures.

Since the middle of the last century, space technology has made it possible to observe the Sun in the vacuum-ultraviolet (VUV) radiation, and thus to exploit the rich information contained in the spectral emission lines and continua in this wavelength regime. The radiation is formed at temperatures corresponding to those prevailing in the solar chromosphere, transition region and corona. Early instruments had very limited or no spatial resolution at all, and, consequently, obtained Sun-as-a-star observations. Assuming specific distributions of the radiating plasmas, even then sub-resolution inferences could be drawn [cf., *Pottasch*, 1963]. However, some of the evaluation procedures established at that time have never been thoroughly adjusted so as to take into account the high spatial and spectral resolution measurements available now.

The purpose of this article is to discuss the radiometric aspects of such an adjustment in line with the standard usage of SI (The International System of Units [*BIPM*, 1998]), which explicitly lists the following quantities with special names which are relevant in this context: “power” (“radiant flux”) in units of watt (W), “irradiance” in watt per

square metre (W m^{-2}), "radiant intensity" in watt per steradian (W sr^{-1}), and "radiance" in watt per square metre steradian (W $m^{-2}sr^{-1}$). They will be supplemented by the corresponding spectrally-resolved quantities, which are usually given per nanometre (nm $^{-1}$), although many solar physicists still use per ångström ($Å^{-1}$) as the wavelength interval (1 Å = 0.1 nm).

3.2 Elementary Radiation Theory

For most solar applications, the electromagnetic VUV radiation can be thought of as emitted during transitions of electrons between different energy levels of atoms or ions. This is the case that will be considered here. Let

$$\Delta\varepsilon_{ij} = \frac{hc_0}{\lambda_{ji}} \tag{3.1}$$

be the energy difference between two levels and thus the resulting photon energy, where h is the Planck constant and c_0 is the speed of light in vacuum, then radiation with a wavelength of λ_{ji} will be emitted during the transition from the upper level j to the lower level i. For various reasons (atomic physics, thermal and non-thermal speeds of the emitters), the wavelength, λ, will exhibit a certain spread around its nominal value, λ_{ji}, generating a spectral profile of the emission line, which will be assumed here to be resolved by a spectrometer.

3.2.1 Radiation from Optically-thick Plasmas

The assumption of an optically-thick plasma is made in this section in order to establish a radiating surface. We will not discuss the radiation transfer processes inside a plasma volume. On its surface, with total area S_T, we assume in Figure 3.1 a surface element with the area dS and a normal $\boldsymbol{n}$. We then specify a solid angle $\mathbf{d}\boldsymbol{\omega}$ by

$$|\,\mathbf{d}\boldsymbol{\omega}\,| = \mathrm{d}\omega = \mathrm{d}\vartheta\,\sin\vartheta\,\mathrm{d}\psi \tag{3.2}$$

in a direction of the co-elevation angle ϑ and the azimuthal angle ψ. The spectral radiance, L_λ, is then defined by

$$\mathrm{d}Q = L_\lambda(\vartheta,\psi)\cos\vartheta\;\mathrm{d}S\,\mathrm{d}\omega\,\mathrm{d}t\,\mathrm{d}\lambda \tag{3.3}$$

where dQ is the differential radiant energy emitted from d$S\cos\vartheta$, the projected area normal to $\mathbf{d}\boldsymbol{\omega}$, at the position P_0 on the radiant surface into the solid angle $\mathbf{d}\boldsymbol{\omega}$ during the time interval $(t,\, t+\mathrm{d}t)$ and in the wavelength interval $(\lambda,\ \lambda+\mathrm{d}\lambda)$.

As indicated in Equation (3.3), L_λ is a function of λ, ϑ, and ψ (and, in general, of P_0 and t). Since the wavelength, λ, is specified, the energy, dQ, can be expressed by the number of photons, dN_λ, according to Equation (3.1) as

$$\mathrm{d}Q = \frac{hc_0}{\lambda}\,\mathrm{d}N_\lambda \tag{3.4}$$

If L_λ and all other energy-related quantities were then reckoned in photon units, one could drop the photon energy, $\Delta\varepsilon_{ij}$, from the equations. Although these photon units are

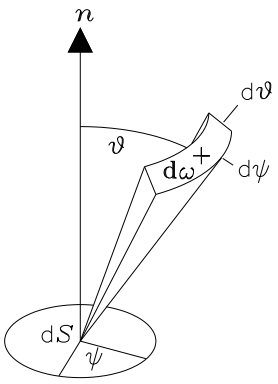

Figure 3.1: Geometrical relation of the solid angle, $\mathbf{d}\boldsymbol{\omega}$, to the surface element with an area of dS and its normal, $\boldsymbol{n}$. The co-elevation is given by the angle ϑ and the azimuth by ψ. The surface element is part of the total surface with area S_T of a plasma volume.

quite popular in the solar physics literature, we will not apply them here, because we want to follow SI definitions as much as possible. In any case, it is very important to establish for a radiometric study whether it is performed in photon or energy units.

By integrating the spectral radiance over all ψ and ϑ from 0 to $\pi/2$, we obtain the outward spectral radiant flux density

$$M_\lambda^+ \;=\; \int_{\psi=0}^{2\pi} \int_{\vartheta=0}^{\pi/2} L_\lambda(\vartheta, \psi) \cos\vartheta \sin\vartheta \, \mathrm{d}\vartheta \, \mathrm{d}\psi \tag{3.5}$$

as a function of P_0, t, and λ.

The radiant flux density is sometimes called "emittance". It corresponds to the irradiance at the source[1], i.e., a power divided by an area.

Integration of the spectral radiance over the projected surface area of the source, S', visible from the direction (ϑ, ψ) gives the spectral radiant intensity

$$I_\lambda(\vartheta, \psi) \;=\; \int_{S'} L_\lambda(\vartheta, \psi) \cos\vartheta \, \mathrm{d}S \;=\; \langle\, L_\lambda(\vartheta, \psi) \,\rangle\, S' \tag{3.6}$$

which depends on ϑ, ψ, t, and λ. The spectral intensity can be obtained by multiplying the spatially-averaged spectral radiance by the projected area, S'. Note, in particular, that the intensity is related to the total projected area of a source, and thus is helpful in characterizing a radiation field, but is not very useful in studying the structure of an extended source. For point sources ($S' = 0$), on the other hand, the *intensity* is the best choice as the quantity *radiance* cannot be defined for such an unphysical case.

[1] In the official French text of SI: "flux density" is named "flux surfacique" and "irradiance" corresponds to "éclairement énergétique" [*BIPM*, 1998].

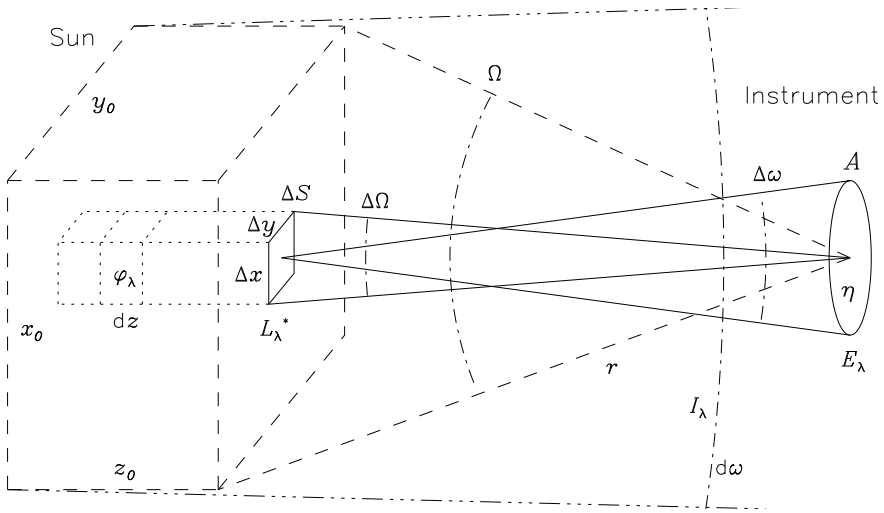

Figure 3.2: Observing geometry (schematic and not to scale) showing the principles of a radiance measurement for an optically-thick plasma (solid lines), and a generalization to the optically-thin case (dotted lines). Also sketched is an irradiance measurement (dashed lines). The solid angles are only marked by some of the extreme rays to keep the drawing simple. The spectral intensity, I_λ, is indicated in the solid angle $d\omega$ (dashed-dotted lines).

Both integration of the spectral intensity over the full sphere and integration of the spectral flux density over the total surface area yield the spectral radiant power

$$\Phi_\lambda \;=\; \int\limits_{4\pi} I_\lambda(\vartheta,\psi)\mathrm{d}\omega \;=\; \int\limits_{S_T} M_\lambda^+ \mathrm{d}S \tag{3.7}$$

Not much more can be learnt from this discussion unless specific assumptions are made that are appropriate for solar observations. As will become clear later on, very little loss of generality, as far as spatially-resolved observations are concerned, will result from assuming the following: a rectangular coordinate system ($\boldsymbol{x}$, $\boldsymbol{y}$, $\boldsymbol{z}$) with the $\boldsymbol{z}$ coordinate parallel to the viewing direction, the line of sight (LOS), of an instrument observing from a distance, r, which is much larger than all other dimensions. The radiating plasma is contained in the volume $x_0 y_0 z_0$. We now define the area, ΔS, of a surface element in accordance with the spatial resolution desired. Specifically we write

$$\Delta S \;=\; \Delta x\,\Delta y \tag{3.8}$$

with increments Δx and Δy corresponding to the linear resolution elements of the instrument. ΔS will then be perpendicular to the LOS. Since, in this case, only observations near $\vartheta \;=\; 0$ are relevant, the dependence of the radiance on the azimuth, ψ, vanishes and

$$L_\lambda^* \;=\; L_\lambda(0,\psi) \tag{3.9}$$

can be considered representing the spectral radiance within a small solid angle, $\Delta\omega$. This geometry is sketched with solid lines in Figure 3.2, where, in addition, an aperture of the

observing instrument – a telescope followed by a spectrometer – with an area, A, is shown. We then choose the size of a solid angle, $\Delta\omega$, so as to fill the aperture at a distance r from the source. Hence

$$\Delta\omega = \frac{A}{r^2} \tag{3.10}$$

and define another small solid angle centred at the position of the aperture by

$$\Delta\Omega = \frac{\Delta S}{r^2} = \frac{\Delta x\, \Delta y}{r^2} \tag{3.11}$$

This equation relates the angular resolution of the instrument to its spatial resolution at a distance r (for a technical realization see Section 3.2.2 below).

The consequences of assuming $\hat{L}_\lambda = L_\lambda(\vartheta)$ instead of Equation (3.9), i.e., $\hat{L}_\lambda$ is only dependent on ϑ, but not on ψ, are treated by *Wilhelm et al.* [1998a] and *Fontenla et al.* [1999] in the context of VUV irradiance measurements.

From Equation (3.3), applied to $\Delta\omega$ and ΔS, and with Equations (3.8 to 3.11), it follows that the radiant energy collected by the spectrometer during the sampling time Δt and in a spectral resolution element, $\Delta\lambda$, on its effective detector section is

$$\Delta Q = \overline{L^*_\lambda}\, \Delta S\, \Delta\omega\, \Delta t\, \Delta\lambda = \overline{L^*_\lambda}\, A\, \Delta\Omega\, \Delta t\, \Delta\lambda \tag{3.12}$$

where the spectral radiance is approximated by its average value in the resolution elements selected. Equation (3.12) elucidates the transition from a solid angle centred at the Sun to an instrumental geometry.

There will be a certain responsivity, η, of the detector to radiation at λ, which relates the energy, ΔQ, entering the sensitive area of the instrument to the number of output counts, ΔN_c. We define the responsivity by

$$\eta(\lambda) = \frac{\Delta N_c}{\Delta Q} \tag{3.13}$$

In realistic cases, the responsivity is a strong function of the wavelength of the radiation. In order to obtain radiometric measurements, the responsivity has to be determined by a calibration procedure, in which the radiant energy, ΔQ, must be traceable to a primary radiometric standard [cf., e.g., *Hollandt et al.*, 1996, 2002]. All the other quantities in Equations (3.12 and 3.13) require length and time measurements, which can be performed with calibrated laboratory instrumentation.

This provides the basis for a measurement of the average spectral radiance of the surface area ΔS:

$$\overline{L^*_\lambda} = \frac{\Delta N_c}{\eta\, A\, \Delta\Omega\, \Delta t\, \Delta\lambda} \tag{3.14}$$

Note that the result obtained for $\overline{L^*_\lambda}$ depends not only on the plasma conditions, but also on the choice of $\Delta\Omega$ (ΔS), Δt, and $\Delta\lambda$. Conversely, we can predict the output counts of the detector for certain observational conditions

$$\Delta N_c = \eta\, \overline{L^*_\lambda}\, A\, \Delta\Omega\, \Delta t\, \Delta\lambda = \eta\, \overline{L^*_\lambda}\, A\, \frac{\Delta S}{r^2}\, \Delta t\, \Delta\lambda \tag{3.15}$$

With given instrumental parameters η, A, $\Delta\Omega$, Δt, and $\Delta\lambda$, the number of counts is linearly related to the radiance. In particular, it is not dependent on the distance of the observing instrument from the source of the radiation. If, on the other hand, the area of the spatial resolution element, ΔS, is held constant at different distances by varying $\Delta\Omega$ according to Equation (3.11), then the number of counts is proportional to the inverse square of the distance, r, to the source for constant $\overline{L_\lambda^*}$.

3.2.2 Conceptual Optical Design

The determination of the spectral radiance according to Equation (3.14) is rather straightforward with the exception of the experimental realization of $\Delta\Omega$. In Figure 3.3 an optical design of a model instrument is drawn to demonstrate its essential features. The surface element with area ΔS is imaged through an optical system with focal length f on a detector pixel, P. The aperture stop of the design has an area of A. The field stop is represented by the pixel, P, of size $\Delta x'\,\Delta y'$. We then have from the central rays (not all are shown in the figure)

$$\Delta\Omega \;=\; \Delta\Omega' \;=\; \frac{\Delta x'\,\Delta y'}{f^2} \tag{3.16}$$

defining $\Delta\Omega$ by the pixel size and the focal length. We also find

$$\frac{\Delta x}{r} \;=\; \frac{\Delta x'}{f} \tag{3.17}$$

and

$$\frac{\Delta y}{r} \;=\; \frac{\Delta y'}{f} \tag{3.18}$$

With fixed f, $\Delta x'$, and $\Delta y'$, the linear spatial resolution elements, Δx and Δy, are proportional to the distance, r, while, of course, $\Delta\Omega$ is not dependent on r and, with reference to Equation (3.15), the output count number, ΔN_c, is constant for different r.

3.2.3 Radiation from Optically-thin Plasmas

Most of the solar upper atmosphere can be assumed to be optically thin for VUV radiation, and, consequently, these conditions have attracted quite some attention in the literature. For a discussion of principles, reference is made again to Figure 3.2, especially to the portion drawn in dotted lines and the volume element $\Delta x\,\Delta y\,\mathrm{d}z$, from which radiation is isotropically emitted (seen from a great distance). Its contribution to the spectral radiant power can be expressed as

$$\mathrm{d}\Phi_\lambda \;=\; \varphi_\lambda\,\Delta x\,\Delta y\,\mathrm{d}z \tag{3.19}$$

where φ_λ is defined as the spectral radiant power density[2], i.e., as power divided by volume. As will be outlined in the next section, φ_λ may be directly linked to the generation

[2]Compare with footnote in Section 3.2.1 and note that “power density” is “puissance volumique” [*BIPM*, 1998].

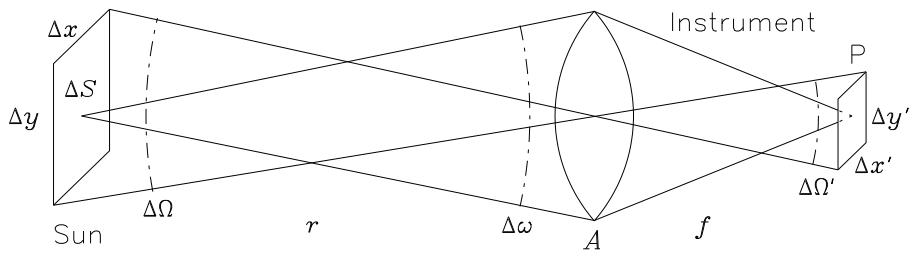

Figure 3.3: An imaging element (a lens in this model design, but a concave mirror for VUV applications) with focal length f and an aperture stop with area A projects the radiant surface element, $\Delta x\,\Delta y$, at a distance $r \gg f$ on the photon-sensitive area, $\Delta x'\,\Delta y'$, defined by the field stop, P, which usually is a detector pixel. The spectrometer portion has been omitted.

process of the radiation through the "emission measure", and thus its observational determination is one of our prime objectives.

First we calculate the contribution of the volume $\Delta x\,\Delta y\,z_0$ to the spectral irradiance, E_λ, which is incident on the surface of a sphere with radius $r \gg x_0, y_0, z_0$ centred around the total emitting volume, $x_0 y_0 z_0$. We obtain with Equation (3.11)

$$\Delta E_\lambda \;=\; \frac{\langle\varphi_\lambda\rangle\, z_0\,\Delta x\,\Delta y}{4\pi r^2} \;=\; \frac{\langle\varphi_\lambda\rangle\, z_0\,\Delta\Omega}{4\pi} \tag{3.20}$$

where

$$\langle\varphi_\lambda\rangle \;=\; \frac{1}{z_0}\int\limits_{z_0} \varphi_\lambda\,\mathrm{d}z \tag{3.21}$$

is the average spectral power density along z_0.

By considering the radiance of the surface element ΔS, we find, with the help of the definition in Equation (3.9) and Equations (3.8, 3.10, and 3.11), the irradiance at the aperture stop of the instrument as

$$\Delta E^*_\lambda \;=\; \overline{L^*_\lambda}\,\Delta x\,\Delta y\,\frac{\Delta\omega}{A} \;=\; \overline{L^*_\lambda}\Delta\Omega \tag{3.22}$$

We have used here that $\Delta\omega$ and $\Delta\Omega$ are constant to a very good approximation for positions of $\Delta x\Delta y$ along $z_0 \ll r$. We then note that ΔE_λ is uniform on the surface of the sphere under the conditions assumed. Thus

$$\Delta E_\lambda \;=\; \Delta E^*_\lambda \tag{3.23}$$

and hence, by comparing Equations (3.20 and 3.22),

$$\overline{L^*_\lambda} \;=\; \frac{\langle\varphi_\lambda\rangle\, z_0}{4\pi} \tag{3.24}$$

It should also be noted that, from summing Equation (3.22) over $x_0\, y_0$ and with Equation (3.23), it follows

$$E_\lambda \;=\; \langle L^*_\lambda \rangle\, \Omega \tag{3.25}$$

with $\Omega = x_0\, y_0 / r^2$ (Figure 5.2, dashed lines) and the average spectral radiance $\langle L^*_\lambda \rangle$ of the surface area $x_0 y_0$.

The irradiance, E_λ, can be obtained through observations either by opening up the angular acceptance cone of the instrument so as to encompass the complete radiant volume, or by covering Ω by a raster with $\Delta\Omega$, if temporal variations are slow with respect to the scan duration. The solar irradiance is often given for $r = 1$ AU if used for terrestrial applications.[3]

By combining Equations (3.14 and 3.24) the final result of this section is

$$\langle \varphi_\lambda \rangle \;=\; \frac{4\pi\, \Delta N_c}{\eta\, z_0\, A\, \Delta\Omega\, \Delta\lambda\, \Delta t} \tag{3.26}$$

which is directly applicable if z_0, the length of the LOS in the radiating plasma volume, is small compared to the structures under study. In this case we can use the approximation

$$\varphi_\lambda \;\approx\; \langle \varphi_\lambda \rangle \tag{3.27}$$

Otherwise, Equation (3.21) describes the well-known LOS problem, and $\langle \varphi_\lambda \rangle$ along z_0 is all that can be determined without additional observations or assumptions. It is, however, evident that the exact orientation of the plasma boundary near the surface is not of critical importance, because of the integration along the LOS. This justifies the assumptions of a surface element $\Delta x\, \Delta y$ perpendicular to the LOS and of L^*_λ, at least for optically-thin conditions. It might be appropriate to mention in this context that stereoscopic measurements, i.e., observations from two or more different directions, would be extremely useful in resolving such a LOS problem.

3.3 Emission Measures

The purpose of observing the Sun in the VUV is not to study radiation theory, but to extract information on the physical conditions in and the composition of the solar atmosphere. This requires an interpretation of the observed radiation in terms of processes responsible for the VUV emission. Even a summary presentation of the available literature would be far beyond the scope of this discussion. The reader is referred to the research and review articles on this topic [e.g., *Mariska*, 1980; *Raymond and Doyle*, 1981; *Mariska*, 1992; *Mason and Monsignori Fossi*, 1994; *Dwivedi*, 1994; *Dere et al.*, 1997; *Mason et al.*, 1997; *Landi et al.*, 1997]. Without further specific reference to earlier work, concepts and results obtained in the past will be re-formulated here in accordance with Section 3.2. This will first of all affect, on a formal level, the nomenclature: L_λ the spectral radiance, I_λ the spectral intensity, Φ_λ the spectral radiant power, M^+_λ the outward spectral radiant flux density, φ_λ the spectral radiant power density, and E_λ the spectral irradiance. However, it should be noted that, in most cases, the *radiance* was called *intensity* in the past, and it

[3] In *BIPM* [1998], the official unit symbol for the astronomical unit is (ua).

is not always clear whether a change is merely a formal one or not. Even the quantities *irradiance* and *radiance* have not always been unambiguously defined, which can lead to significant confusion: the irradiance is decreasing with the inverse square of the observing distance (cf., Equation (3.25)), whereas the radiance does not depend on this distance (cf., Equation (3.14)).

The quantities $\langle\varphi_\lambda\rangle$ and φ_λ in Equations (3.20, 3.24, 3.26, and 3.27) contain information on the plasma conditions. All other quantities are related to the instrumental configuration and/or the observing geometry. In order to formulate ideas, and in line with many earlier treatments, we will assume here an optically-thin solar plasma with a certain elemental abundance and ionization stages according to equilibrium conditions characterized by an electron temperature, T_e. Furthermore, only discrete states of atoms and ions excited by electron collisions from the ground state are considered, restricting the following discussion to certain classes of emission lines, but a generalization to other cases would, of course, be possible in the framework of the concepts outlined in Section 3.2. Once excited, the atoms and ions spontaneously emit photons as the main depopulation process. The probability for a transition from state j to state i is given by the Einstein coefficient, A_{ji}. This produces a radiant power density[4] in the spectral line at λ_{ji} of

$$\varphi(\lambda_{ji}) \;=\; \Delta\varepsilon_{ij}\, A_{ji}\, n_j \tag{3.28}$$

where n_j is the number density of the radiating atoms or ions in state j. The quantity $\varphi(\lambda_{ji})$ follows from φ_λ in Equation (3.19), if a wavelength range, $\delta\lambda$, can be selected in such a way that only the complete profile of the spectral line at λ_{ji} is included and if the background, b_λ, is taken out. Hence we get

$$\varphi(\lambda_{ji}) \;=\; \int\limits_{\lambda_{ji}-\delta\lambda/2}^{\lambda_{ji}+\delta\lambda/2} (\varphi_\lambda - b_\lambda)\,\mathrm{d}\lambda \tag{3.29}$$

Equations (3.26 and 3.27) provide the means of measuring φ_λ under favourable conditions or provide at least an estimate. The background has to be determined from the shape of the spectrum near the spectral line. This requires adequate spectral resolution in the measurements.

To maintain the spectral radiant power density in Equation (3.28), an excitation rate from the ground state is necessary according to

$$A_{ji}\, n_j \;=\; n_g\, n_\mathrm{e}\, C^\mathrm{e}_{gj} \tag{3.30}$$

with n_g the number density of the particles in the ground state, n_e the electron density, and C^e_{gj} the collisional excitation rate coefficient. For a Maxwellian electron velocity distribution with temperature, T_e, this coefficient is

$$C^\mathrm{e}_{gj} \;=\; \gamma\,\frac{1}{\sqrt{T_\mathrm{e}}}\,\exp\left(\frac{-\Delta\varepsilon_{gj}}{kT_\mathrm{e}}\right) \tag{3.31}$$

[4]Often called "emissivity" in the solar physics literature, whereas in Symbols, Units and Nomenclature in Physics (see Doc. U.I.P. 20, 1978) "emissivity" is defined as ratio of the emission of a surface to the corresponding black-body radiation.

where $\Delta\varepsilon_{gj}$ is the energy difference between the states g and j, and k is the Boltzmann constant. The number density, n_g, can be expressed by the ionic fraction, n_g/n_X [*Arnaud and Rothenflug*, 1985; *Arnaud and Raymond*, 1992; *Mazzotta et al.*, 1998]; the elemental abundance of X with respect to hydrogen, n_X/n_H; the number density of hydrogen relative to the electron density, n_H/n_e; and the electron density, n_e, as

$$n_g \;=\; \frac{n_g}{n_X}\,\frac{n_X}{n_H}\,\frac{n_H}{n_e}\,n_e \tag{3.32}$$

In this conceptual presentation, we will thus assume that most of the atoms or ions are in the ground state, and, in particular, n_i is small – a condition which may be violated for metastable levels. The unspecified factor γ in Equation (3.31) is of no importance here and will not be discussed any further, but will be assumed to be constant as long as a specific spectral line is being considered. From Equations (3.28 and 3.30 to 3.32), we find

$$\gamma\,\Delta\varepsilon_{ij}\,\frac{n_X}{n_H}\,\frac{n_H}{n_e}\,n_e^2\,\frac{n_g}{n_X}\,\frac{1}{\sqrt{T_e}}\exp\left(\frac{-\Delta\varepsilon_{gj}}{kT_e}\right) \;=\; \varphi(\lambda_{ji}) \tag{3.33}$$

With the definition of a contribution function

$$G(T_e) \;=\; \frac{n_g}{n_X}\,\frac{1}{\sqrt{T_e}}\exp\left(\frac{-\Delta\varepsilon_{gj}}{kT_e}\right) \tag{3.34}$$

the Equation (3.33) becomes

$$\gamma\,\Delta\varepsilon_{ij}\,\frac{n_X}{n_H}\,\frac{n_H}{n_e}\,n_e^2\,G(T_e) \;=\; \varphi(\lambda_{ji}) \tag{3.35}$$

The quantity on the right-hand side can be measured for structures with small extensions along the LOS, as we have seen in Section 3.2.3 and in Equation (3.29). In this case, some of the concepts of separating the influences of the abundance, the electron density and the temperature will be mentioned below, but they are not the main topic of this communication. For long LOS paths, z_0, we can only measure $\langle\varphi_\lambda\rangle$ and thus obtain $\langle\varphi(\lambda_{ji})\rangle$. Therefore the integral over z_0

$$\gamma\,\frac{n_H}{n_e}\,\frac{n_X}{n_H}\,\frac{\Delta\varepsilon_{ij}}{z_0}\int\limits_{z_0} n_e^2\,G(T_e)\,\mathrm{d}z \;=\; \langle\varphi(\lambda_{ji})\rangle \tag{3.36}$$

has to be considered, where the elemental abundance, which is of great importance in solar physics studies, is removed from the integral in view of the fact that, in general, the gradients of the abundance variations in the solar atmosphere are much smaller than those of the electron density and temperature. The temperature-dependent function $G(T_e)$, which is strongly peaked for most ions at the so-called "formation temperature", can also be removed from the integral, if, for instance, it can be assumed that T_e has also no gradient along z_0 (which, of course, is not generally true, but see *Feldman et al.* [1999] and *Mason et al.* [2002] for such cases). The resulting integral along z_0

$$\int\limits_{z_0} n_e^2\,\mathrm{d}z \;=\; \langle n_e^2\rangle\,z_0 \;=\; \frac{\langle\varphi(\lambda_{ji})\rangle\,z_0}{\gamma\,\Delta\varepsilon_{ij}\,G(T_e)}\,\frac{n_H}{n_X}\,\frac{n_e}{n_H} \;=\; \frac{4\pi\,L^*(\lambda_{ji})}{\gamma\,\Delta\varepsilon_{ij}\,G(T_e)}\,\frac{n_H}{n_X}\,\frac{n_e}{n_H} \tag{3.37}$$

is called "emission measure".

The radiance of the spectral line, $L^*(\lambda_{ji})$, is determined from the spectral radiance, $\overline{L^*_\lambda}$, obtained in Equation (3.14) in analogy to Equation (3.29) by integrating the background-corrected spectral radiance over the line width

$$L^*(\lambda_{ji}) = \int_{\lambda_{ji}-\delta_{\lambda/2}}^{\lambda_{ji}+\delta_{\lambda/2}} (\overline{L^*_\lambda} - B_\lambda)\,\mathrm{d}\lambda \tag{3.38}$$

Provided the spectral line can be isolated from other lines, the line radiance, $L^*(\lambda_{ji})$, does not depend on the spectral resolution of the measurement in contrast to $\overline{L^*_\lambda}$, but will still be influenced by the spatial and temporal resolution (see Section 3.2.1).

Other definitions of the emission measure, in particular the volume emission measure, are not really relevant in the context of spatially-resolved observations, but are useful in interpreting full-disk irradiance measurements [*Pottasch*, 1963; *Athay*, 1966]. The differential emission measure should only be mentioned here, but will not be discussed any further. For more information on this topic see, for example, *Mariska* [1992].

3.4 Line-ratio Measurements

3.4.1 Density-sensitive Line Ratios

For detailed treatments of the theory of density-sensitive emission see the appropriate articles cited below. Here we note that collisionally-excited states may also be depopulated by non-radiative processes, in particular, if they are metastable and if the electron density, n_e, is high. The radiant power density in Equation (3.28) is thus reduced for emission lines from such states as a function of n_e. The ratio

$$R_{12} = \frac{\varphi(\lambda_1)}{\varphi(\lambda_2)} \tag{3.39}$$

of an allowed emission line at λ_1 and a line at λ_2 emitted from a metastable level, for instance, is consequently changing with n_e, and can be calculated from atomic physics principles. If the ratio can be measured in a plasma of the solar atmosphere, the electron density can then be estimated. From Equations (3.24 or 3.37), we may conclude that this can be accomplished by measuring the ratio of the line radiances

$$R_{12} = \frac{L^*(\lambda_1)}{L^*(\lambda_2)} \tag{3.40}$$

This method is especially useful if both spectral lines are emitted by atomic particles of the same species and ionization stage, because abundance and ionization variations will then have no effect. It has been used extensively in the literature [cf., *Gabriel and Jordan*, 1969; *Feldman et al.*, 1978; *Laming et al.*, 1997; *Doschek et al.*, 1997; *Wilhelm et al.*, 1998b].

Under favourable conditions the electron density so determined can be compared with the mean electron density obtained from the emission measure analysis in Equation (3.37). Any discrepancy points to the fact that the so-called "filling factor" is not unity [*Feldman et al.*, 1979; *Dere et al.*, 1987], because the line-ratio method provides an estimate of the electron density at the source of the radiation, whereas the emission measure depends on the distribution of the electrons within the unresolved emitting volume.

3.4.2 Temperature-sensitive Line Ratios

If two excited states, j_1 and j_2, from which emission lines originate, have very different energy levels, their relative collisional excitation becomes a function of the electron temperature, T_e. As in Section 3.4.1, a ratio R_{12} can be obtained from atomic physics calculations. The measured ratio of the line radiances in Equation (3.40) then provides a handle on the determination of the electron temperature. For examples see *Heroux et al.* [1972], *Doschek and Feldman* [1987], and *David et al.* [1998].

3.5 Abundance Measurements

If, in Equation (3.35), we consider two emission lines at λ_1 and λ_2 from different species, but with very similar contribution functions, emitted from the same location in the solar atmosphere, and thus at the same electron density, then the ratio of the radiant power densities, $\varphi(\lambda_1)$ and $\varphi(\lambda_2)$, or, from Equation (3.37), the ratio of the corresponding line radiances (adjusted for any variations of $\Delta\varepsilon_{ij}$ and γ), can be used to obtain the elemental abundance ratio. The spectral lines of Mg VI and Ne VI may serve as examples, as well as those of Mg VII and Ne VII, which have been treated by *Young and Mason* [1997], *Laming et al.* [1999], and *Dwivedi et al.* [1999] as typical species with low and high first-ionization potentials.

3.6 Concluding Remarks

The spectral radiance and the radiance of emission lines in the VUV wavelength range are described as the basic physical quantities for characterizing spatially-resolved radiant sources, such as the Sun or features in the solar atmosphere. The relationship to other radiometric quantities, in particular to radiant power (flux), emittance, power density, irradiance, and intensity is discussed in detail, as well as the observational determination of these quantities in optically-thick or optically-thin plasma regimes. Some methods of interpreting the observations in terms of the plasma conditions in the source regions are mentioned with reference to a selection of the relevant literature.

Acknowledgements

I thank A. Pauluhn, C.D. Pike, and B. Inhester for many valuable comments and suggestions.

Bibliography

Arnaud, M., and Rothenflug, R., An updated evaluation of recombination and ionization rates, *Astron. Astrophys. Suppl. Ser.* **60**, 425–457, 1985.

Arnaud, M., and Raymond, J., Iron ionization and recombination rates and ionization equilibrium, *Astrophys. J.* **398**, 394–406, 1992.

Athay, R.G., Radiative energy loss from the solar chromosphere and corona, *Astrophys. J.* **146**, 223–240, 1966.

BIPM (Bureau International des Poids et Mesures), Le Système International d'Unités (SI) and The International System of Units, 7th ed., Sèvres, France, 1998.

David, C., Gabriel, A.H., Bely-Dubau, F., Fludra, A., Lemaire, P., and Wilhelm, K., Measurement of the electron temperature gradient in a solar coronal hole, *Astron. Astrophys.* **336**, L90–L94, 1998.

Dere, K.P., Bartoe, J.-D.F., Brueckner, G.E., Cook, J.W., and Socker, D.G., Discrete subresolution structures in the solar transition zone, *Sol. Phys.* **114**, 223–237, 1987.

Dere, K.P., Landi. E., Mason, H.E., Monsignori Fossi, B.C., and Young, P.R., CHIANTI – an atomic database for emission lines. I. Wavelengths greater than 50 Å, *Astron. Astrophys. Suppl. Ser.* **125**, 149–173, 1997.

Doschek, G.A., and Feldman, U., Ultraviolet Al III emission lines and the physics of the solar transition region, *Astrophys. J.* **315**, L67–L70, 1987.

Doschek, G.A., Warren, H.P., Laming, J.M., Mariska, J.T., Wilhelm, K., Lemaire, P., Schühle, U., and Moran, T.G., Electron densities in the solar polar coronal holes from density-sensitive line ratios of Si VIII and S X, *Astrophys. J.* **482**, L109–L112, 1997.

Dwivedi, B.N., EUV spectroscopy as a plasma diagnostic, *Space Sci. Rev.* **65**, 289–316, 1994.

Dwivedi, B.N., Curdt, W., and Wilhelm, K., Analysis of extreme-ultraviolet off-limb spectra obtained with SUMER/SOHO: Ne VI/Mg VI emission lines, *Astrophys. J.* **517**, 516–525, 1999.

Feldman, U., Doschek, G.A., Mariska, J.T., Bhatia, A.K., and Mason, H.E., Electron densities in the corona from density-sensitive line ratios in the N I isoelectronic sequence, *Astrophys. J.* **226**, 674–678, 1978.

Feldman, U., Doschek, G.A., and Mariska, J.T., On the structure of the solar transition zone and lower corona, *Astrophys. J.* **229**, 369–374, 1979.

Feldman, U., Doschek, G.A., Schühle, U., and Wilhelm, K., Properties of quiet-Sun coronal plasmas at distances of $1.04 \leq R_{\odot} \leq 1.50$ along the solar equatorial plane, *Astrophys. J.* **518**, 500–507, 1999.

Fontenla, J., White, O.R., Fox, P.A., Avrett, E.H., and Kurucz, R.L., Calculation of solar irradiances. I. Synthesis of the solar spectrum, *Astrophys. J.* **518**, 480–499, 1999.

Gabriel, A.H., and Jordan, C., Interpretation of solar helium-like ion line intensities, *Mon. Not. R. Astr. Soc.* **145**, 241–248, 1969.

Heroux, L., Cohen, M., and Malinovsky, M., The interpretation of XUV rocket measurements of intensity ratios of solar spectral lines of the lithiumlike ions O VI, Ne VIII, and Mg X, *Sol. Phys.* **23**, 369–393, 1972.

Hollandt, J., Schühle, U., Paustian, W., Curdt, W., Kühne, M., Wende, B., and Wilhelm, K., Radiometric calibration of the telescope and ultraviolet spectrometer SUMER on SOHO, *Appl. Opt.* **35**, 5125–5133, 1996.

Hollandt, J., Kühne, M., Huber, M.C.E., and Wende, B., Source standards for the radiometric calibration of astronomical telescopes in the VUV spectral range traceable to the primary standard BESSY, this volume, 2002.

Laming, J.M., Feldman, U., Schühle, U., Lemaire, P., Curdt, W., and Wilhelm, K., Electron density diagnostics for the solar upper atmosphere from spectra obtained by SUMER/SOHO, *Astrophys. J.* **485**, 911–919, 1997.

Laming, J.M., Feldman, U., Drake, J.J., and Lemaire, P., The off-limb behavior of the first ionization potential effect in $T > 5 \times 10^5$ K solar plasmas, *Astrophys. J.* **518**, 926–936, 1999.

Landi, E., Landini, M., Pike, C.D., and Mason, H.E., SOHO CDS-NIS in-flight intensity calibration using a plasma diagnostic method, *Sol. Phys.* **175**, 553–570, 1997.

Mariska, J.T., Relative chemical abundances in different solar regions, *Astrophys. J.* **235**, 268–273, 1980.

Mariska, J.T., The solar transition region, *Cambridge Astrophysics Series*, **23**, University Press, Cambridge, 1992.

Mason, H.E., and Monsignori Fossi, B.C., Spectroscopic diagnostics in the VUV for solar and stellar plasmas, *Astron. Astrophys. Rev.* **6**, 123–179, 1994.

Mason, H.E., Young, P.R., Pike, C.D., Harrison, R.A., Fludra, A., Bromage, B.J.I., and Del Zanna, G., Application of spectroscopic diagnostics to early observations with the SOHO Coronal Diagnostic Spectrometer, *Sol. Phys.* **170**, 143–161, 1997.

Mason, H.E., Del Zanna, G., Dere, K.P., Landi, E., Landini, M., and Young, P.R., Evaluating CHIANTI and atomic data: Cases of SOHO (CDS, SUMER, EIT) and SERTS, this volume, 2002.

Mazzotta, P., Mazzitelli, G., Colafrancesco, S., and Vittorio, N., Ionization balance for optically thin plasmas: Rate coefficients for all atoms and ions of the elements H to Ni, *Astron. Astrophys. Suppl. Ser.* **133**, 403–409, 1998.

Pottasch, S.R., The lower solar corona: Interpretation of the ultraviolet spectrum, *Astrophys. J.* **137**, 945–966, 1963.

Raymond, J.C., and Doyle, J.G., Emissivities of strong ultraviolet lines, *Astrophys. J.* **245**, 1141–1144, 1981.

Young, P.R., and Mason, H.E., The Mg/Ne abundance ratio in a recently emerged flux region observed by CDS, *Sol. Phys.* **175**, 523–539, 1997.

Wilhelm, K., Lemaire, P., Dammasch, I.E., Hollandt, J., Schühle, U., Curdt, W., Kucera, T., Hassler, D.M., and Huber, M.C.E., Solar irradiances and radiances of UV and EUV lines during the minimum of the sunspot activity in 1996, *Astron. Astrophys.* **334**, 685–702, 1998a.

Wilhelm, K., Marsch, E., Dwivedi, B.N., Hassler, D.M., Lemaire, P., Gabriel, A.H., and Huber, M.C.E., The solar corona above polar coronal holes as seen by SUMER on SOHO, *Astrophys. J.* **500**, 1023–1038, 1998b.

— 4 —

Source Standards for the Radiometric Calibration of Astronomical Instruments in the VUV Spectral Range Traceable to the Primary Standard BESSY[1]

JÖRG HOLLANDT
Physikalisch-Technische Bundesanstalt
Berlin, Germany

MICHAEL KÜHNE
Physikalisch-Technische Bundesanstalt
Berlin, Germany

MARTIN C.E. HUBER
International Space Science Institute
Bern, Switzerland

BURKHARD WENDE
Physikalisch-Technische Bundesanstalt
Berlin, Germany

On the basis of a high-current hollow-cathode discharge we have developed two transfer source standards suitable for the radiometric calibration of vacuum-ultraviolet (VUV) telescopes. The source standards are transportable and (in their current design) produce collimated beams of 5 mm (grazing-incidence region) and 2.5 mm, 5 mm, 10 mm and 15 mm (normal-incidence region) diameter. By irradiating the entrance aperture of the telescope with this beam, the overall spectral response of the instrument can be determined and spectral-responsivity variations over the entrance aperture can be directly evaluated. The transfer standards described in this paper have been calibrated in the radiometry laboratory of the Physikalisch-Technische Bundesanstalt (PTB) by use of the calculable spectral photon flux of the Berlin electron storage ring for synchrotron radiation BESSY I: a primary radiometric VUV source standard. The output of the source standards has been determined at 57 emission lines covering the wavelength range 15 nm to 150 nm. The photon flux in these emission lines ranges from 10^4 s^{-1} to 10^9 s^{-1} and the overall relative standard uncertainty of the photon flux in any given line is found to be not more than 8 %.

4.1 Introduction

The radiometric calibration of instruments is based on either source or detector standards. Since in the vacuum-ultraviolet (VUV) spectral domain reliable celestial standards are still being established, the radiometric calibration of space-borne VUV instruments must be based on laboratory standards.

In the past, calibrations in the vacuum-ultraviolet have been made almost exclusively by use of detector standards rather than source standards. The detector standard was used

[1]This paper is an updated version of Hollandt, J., Kühne, M., Huber, M.C.E., and Wende, B., *Astron. Astrophys. Suppl.* **115**, 561–572, 1996.

to determine the photon flux entering the telescope when the complete instrument was illuminated with a monochromatic photon beam. The ratio of the instrument detector response and the measured monochromatic flux entering the telescope then represented the spectral responsivity of the complete instrument at this particular wavelength. This procedure was repeated at different wavelengths in order to establish the wavelength-dependent spectral responsivity of the instrument. For practical reasons, in many cases the overall calibration was made in two (or more) steps: the transmission of the telescope and the responsivity of the spectrometer-detector system had to be measured separately [*Reeves et al.*, 1977].

A wide variety of VUV detector standards is available in the form of photoemission diodes [*Canfield and Swanson*, 1987], sodium-salicilate-based detectors [*Philips*, 1984], proportional counters [*Henke and Tester*, 1975; *Kroth et al.*, 1990] or photoelectric ionization chambers [*Samson*, 1964; *Samson and Haddad*, 1974]. The relative uncertainties of these detector standards are of the order of 10 % (1σ), and, particularly for photoemission diodes and sodium-salicilate-based detectors, long-term stability is a problem. The possibilities offered by the significantly lower uncertainties that have been achieved using electrical substitution radiometers operating at liquid-helium temperature as the primary detector standard [*Rabus et al.*, 1997; *Shaw et al.*, 1999] will be briefly addressed in Section 4.5 of this paper.

In contrast to the rather complex procedures that are required to accommodate the use of detector standards, a radiometric instrument calibration based on source standards is straightforward. If the radiation of the source is well-matched to the demands of the calibration and a level of uncertainty of a few percent is sufficient, the instrument to be calibrated is illuminated with the source of known spectral emission and the spectral response of the detector is measured. This classical approach to radiometric calibration could not, however, be used in the VUV until about two decades ago, since such sources were not available.

During the last two decades, VUV source standards – in particular, dedicated electron storage rings (in fact, the primary radiometric VUV standard) – have become available and several instruments have been calibrated with the SURF-II storage ring at the U.S. National Institute of Standards and Technology (NIST) [*Furst et al.*, 1995]. Similar activities took place at the positron storage ring SUPER-ACO at the Institut d'Astronomie Spatiale (IAS) at Orsay [*Besson et al.*, 1989].

The spectral distribution of radiation at most synchrotron sources (see Figure 4.1 for BESSY I) is usually not well matched to the VUV emission of the Sun or other stars. The increase of photon flux with decreasing wavelength of the typical synchrotron source can cause extremely high contributions from high orders of the spectrometer grating, especially for grazing-incidence optics. In order to overcome some of the major difficulties that occur when space instruments are calibrated by direct use of synchrotron radiation, we have developed transfer source standards. Being based on a conventional emission-line source (a hollow-cathode discharge source) with a collimated output beam, our transfer standards avoid the problems associated with the uncollimated, spectrally-continuous, synchrotron radiation, whose polarization, moreover, varies with the viewing angle. The hollow-cathode discharge source we describe here emits well-separated emission lines and thus avoids the often severe problem of high-order contributions that occur in grating instruments. It also provides a wavelength calibration as a matter of course. The transfer standards in question are transportable and can, accordingly, be mounted on the test tank in the laboratory, where the instrument to be calibrated has been developed. Thus there is

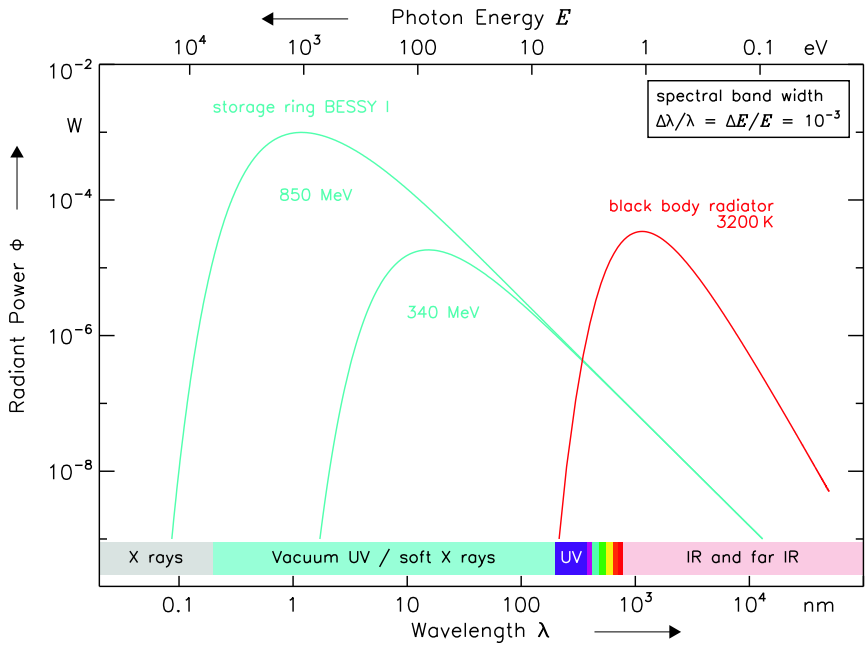

Figure 4.1: Comparison of a black-body radiator at a temperature of 3200 K and the synchrotron-radiation spectrum of the electron storage ring BESSY I at an electron energy of 340 MeV and 850 MeV.

no need for a special calibration tank nor is there a need to transport the instrument for calibration. This also removes schedule incompatibilities as they are bound to occur with the inflexible beam-scheduling that is mandatory for multi-purpose storage ring facilities. A given transfer standard can, in principle, also be brought to different instruments so that an intercalibration by use of the same standard can be achieved. A further interesting property of our transfer source standards is that they produce detector count-rates in the telescope systems under calibration which are comparable with those expected for the instruments when in flight.

4.2 Transfer Source Standards

4.2.1 Hollow-cathode Source

The source standards for the measurement of the spectral responsivity of astronomical instruments are based on a high-current, hollow-cathode, glow-discharge source (Figure 4.2). This source emits intense, unpolarized, line-radiation from the buffer gas and the cathode material (99.5 % aluminium) at wavelengths above 15 nm (Figure 4.3). Equipped with a compact, two-stage, differential pumping system, the source allows windowless observation of its VUV radiation under ultrahigh-vacuum conditions. The flux-limiting aperture stop with a diameter of 0.6 mm is part of the differential pumping system.

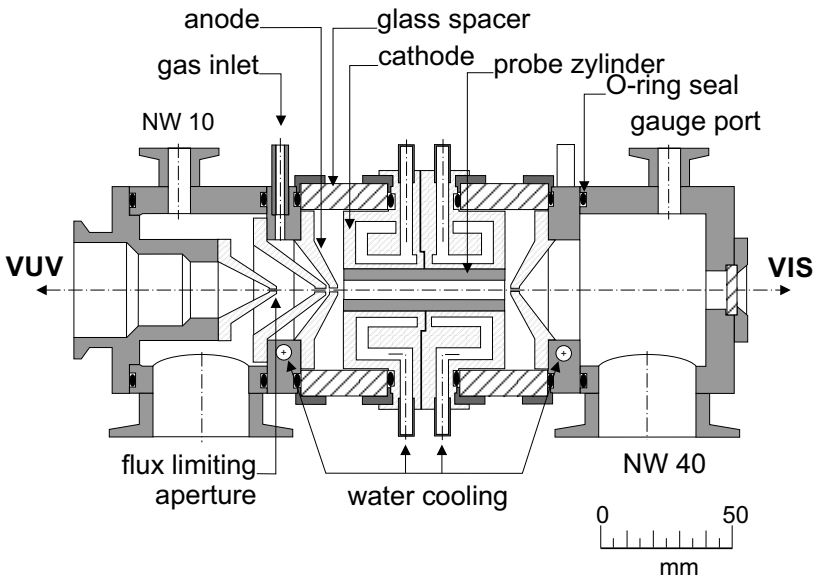

Figure 4.2: Longitudinal section of the hollow-cathode source with an integrated two-stage, differential pumping system.

As a radiometric transfer standard the source is operated with a fixed current (e.g., 1 A) with a current stability better than 1 mA. The voltage drop over the hollow-cathode discharge (e.g., 500 V) is sensitive to buffer-gas pressure (typically 1 mbar). It can be stabilized (to better than $\pm$ 1 V) by regulating the buffer-gas flow with an automatic needle-valve (Balzers RME 010) and a self-regulating voltage control unit. In this mode of operation, the radiant intensity of the VUV emission lines is reproducible within $\pm$ 5 % over a period of 40 operating hours.

In order to provide a large number of calibration lines within the spectral range from 15 nm to 150 nm, the hollow-cathode source is alternately operated with various rare gases serving as the buffer gas. Changing the buffer gas does not affect the reproducibility of the emission values, if measures are taken to fully drive out the preceding buffer gas from the discharge tube. After 40 hours of operation the source has to be cleaned of sputtered cathode material and the aluminium cathode cylinder has to be replaced. To reproduce the old photon-flux after cleaning the source, the oxide layer from the fresh aluminium cathode has to be removed, otherwise this layer severely limits the sputtering coefficient of aluminium atoms from the cathode. This can be accomplished by discharge-cleaning when the source is operated with argon for one to two hours with a current of at least 1 A. Over a period of three years the hollow-cathode discharge has been operated for more than 1000 hours without any detectable systematic changes in its radiant intensity. Detailed descriptions of its operation and radiometric characterization as a standard of radiant intensity are given in *Danzmann et al.* [1988] and *Hollandt et al.* [1994].

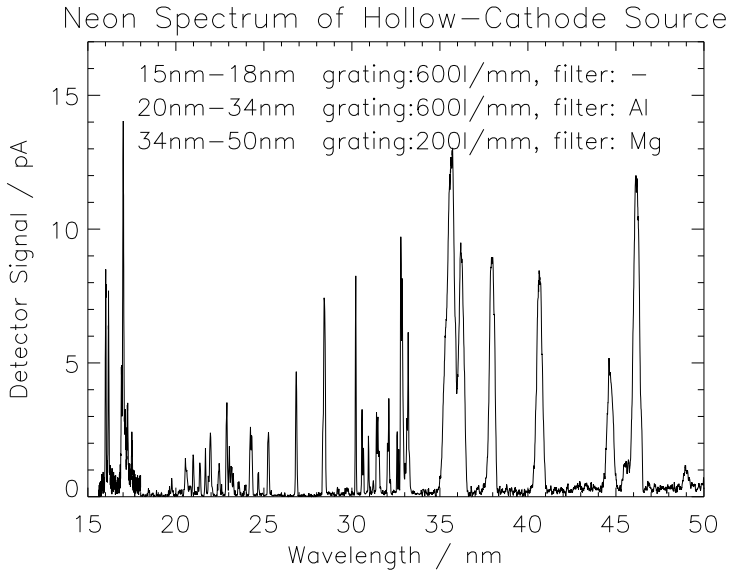

Figure 4.3: Spectrum of the hollow-cathode discharge, showing line emission from multiply-ionized aluminium and neon ions. The spectrum was measured with three different configurations of the toric-grating monochromator beam line.

4.2.2 Source Standards

To serve as a transfer standard for the radiometric calibration of astronomical instruments, the hollow-cathode source has to be combined with adequate optics to convert the diverging radiation of the source into a collimated beam. To cover the spectral range from 15 nm to 150 nm with suitable, collimated, spectral photon flux, two telescope-calibration standards, one working in grazing incidence the other in normal incidence, have been developed [*Hollandt et al.*, 1993].

Grazing-incidence Source Standard:
In the grazing-incidence spectral range, a Wolter type-II telescope with an effective focal length of 2.120 m is used to provide a collimated beam (Figure 4.4). The aperture stop of the hollow-cathode source is placed at the focus of the Wolter telescope. The diameter of the collimated beam is limited to 5 mm when it leaves the telescope. The complete transfer standard is mounted on a platform that can be moved up and down ($\pm$150 mm) to allow a precise vertical mapping of the primary telescope mirror of the instrument for calibration with the collimated radiation.

Normal-incidence Source Standard:
To provide collimated VUV radiation above 50 nm, the flux-limiting aperture stop of the hollow-cathode source is placed at the focus of a gold-coated, concave mirror with a focal length of 1.090 m (Figure 4.5). The angle of incidence between the mirror normal and the incoming radiation is 3°. The diameter of the collimated radiation is limited to 10 mm (standard diameter) on the mirror surface. (Since the limiting aperture is mounted on a precisely moveable linear feedthrough, apertures resulting in diameters of the beam of

Table 4.1: Radiant power of the grazing-incidence source standard in the He I resonance line at 58.43 nm over a period of thirteen months.

Emission line	Radiant Power April '92	Radiant Power August '92	Radiant Power November '92	Radiant Power May '93
58.43 nm He I	605 pW	608 pW	591 pW	630 pW

2.5 mm, 5 mm, and 15 mm are also available.) The spherical collimating mirror can be tilted about two perpendicular axes (±20 mrad). In the case that the instrument to be calibrated also posseses the ability to tilt its primary mirror this allows a two-dimensional mapping of the primary telescope mirror with the collimated radiation.

The hollow-cathode discharge of the grazing-incidence source standard is operated at a fixed working point of 2 A and 400 V. Since the emission lines of highly-ionized ions typically show a pronounced superlinear current dependence of their radiant intensity, the 2-A/400-V working point provides sufficient photon flux in the 15 nm to 50 nm spectral range, where the spectrum of the source is dominated by doubly- and triply-ionized neon and aluminium emission lines. For the normal-incidence source standard a working point of 1 A and 500 V has been chosen. Under these conditions, the neutral and singly-ionized buffer-gas emission lines that predominate in the spectrum of the source above 50 nm appear with adequate flux.

As an example of the radiometric, long-term stability of the hollow-cathode source the radiant power of the grazing-incidence source standard in the He I resonance line at 58.43 nm is given in Table 4.1 for a period of thirteen months. During this period, the aluminium cathode was replaced 22 times and the source was transported three times between the storage ring BESSY in Berlin and the Rutherford Appleton Laboratory near Oxford, UK, to enable the ground-based calibration of CDS (Coronal Diagnostic Spectrometer).

The vacuum systems of both source standards are made of stainless steel and built according to ultrahigh-vacuum standards. Hollow-cathode sources and mirror chambers are pumped by turbomolecular pumps. Typical pressures in the mirror chambers are in the lower 10^{-8} mbar range when the hollow-cathode source is not in operation. Pressures in the mirror chambers go up into the 10^{-6} mbar range when the discharge is operated with rare gases.

4.3 Calibration Procedure of the Transfer Source Standards

In order to perform the spectral-responsivity calibration of astronomical instrumentation, the photon flux in the emission lines of the collimated radiation of the transfer source standards must be known. The spectral radiant flux for a given collection geometry of synchrotron radiation from an electron storage ring is calculable according to Schwinger's formula [*Schwinger*, 1949] from three storage ring parameters: electron energy, magnetic field in the bending magnet, and the current represented by the electrons in the ring. Thus, well-characterized electron storage rings are primary radiometric source standards for radiation which extends from the far-infrared to the X-ray region. PTB had set up a radiometric laboratory at the Berlin electron storage ring BESSY I, which was a storage ring

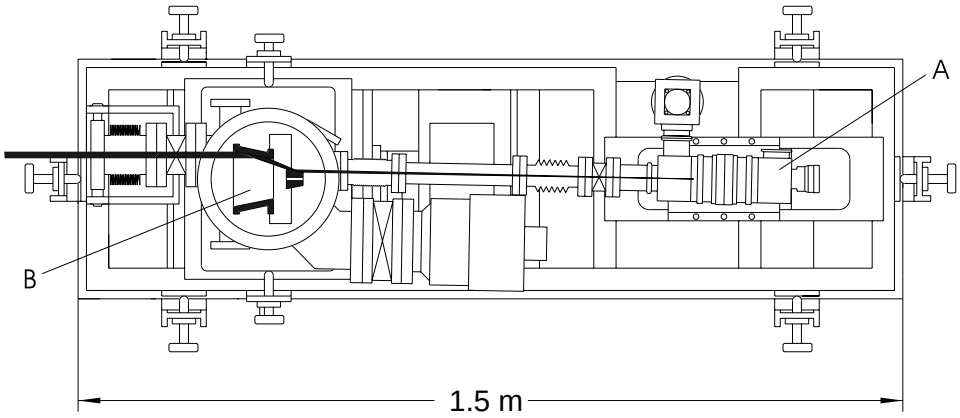

Figure 4.4: Schematic drawing of the grazing-incidence source standard. The diverging radiation from the hollow-cathode source (A) is collimated by a Wolter type-II telescope (B).

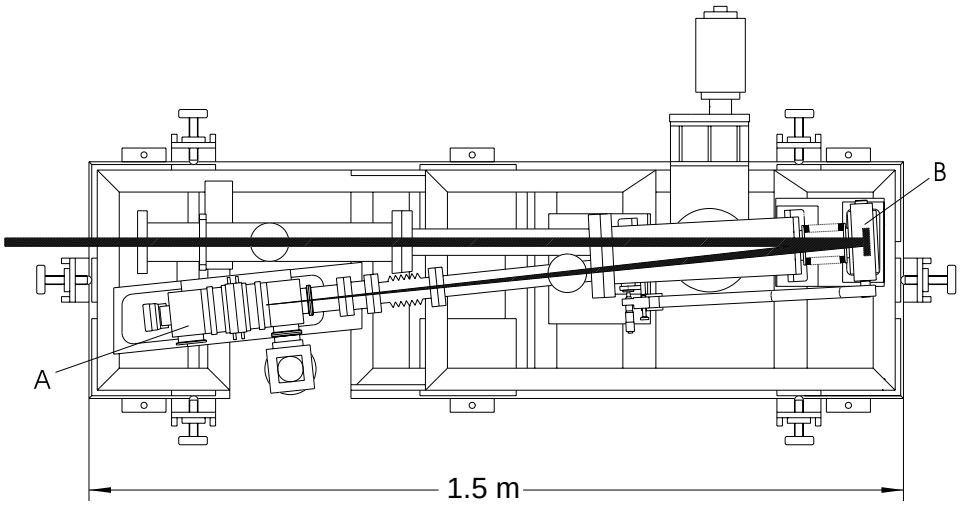

Figure 4.5: Schematic drawing of the normal-incidence source standard. The diverging radiation from the hollow-cathode source (A) is collimated by a concave, gold-coated mirror (B).

dedicated, among other things, to VUV radiometry. In this laboratory, special beam-lines have been developed for the radiometric characterization of VUV sources. (Note: BESSY I closed down in November 1999 and the radiometry laboratory of PTB was transfered to BESSY II. All the work described in this paper has been performed at BESSY I.) The radiometric calibration is performed on these beam lines by comparing the unknown radiation of transfer standards with the calculable synchrotron radiation of the primary standard BESSY I. The photon flux in the emission line of a transfer standard Φ^{TS} is determined

by comparing the detected photocurrent $i^{TS}(\lambda)$ of the transfer standard with the detected photocurrent $i^{SR}(\lambda)$ of the calculable spectral photon flux of the synchrotron radiation $\Phi_\lambda^{SR}(\lambda)$ (for details see *Fischer et al.* [1986] and *Hollandt et al.* [1992]):

$$\Phi^{TS} = \int \Phi_\lambda^{TS}(\lambda)\,\mathrm{d}\lambda = \int \left[i_0^{TS}(\lambda)/i_0^{SR}(\lambda) \right] \Phi_\lambda^{SR}(\lambda) F_0(\lambda)\,\mathrm{d}\lambda \tag{4.1}$$

$$\Phi^{TS} = \int \Phi_\lambda^{TS}(\lambda)\,\mathrm{d}\lambda = \int \left[i_{90}^{TS}(\lambda)/i_{90}^{SR}(\lambda) \right] \Phi_\lambda^{SR}(\lambda) F_{90}(\lambda)\,\mathrm{d}\lambda \tag{4.2}$$

The subscripts 0 and 90 indicate the orientation of the optical plane of the instrumentation used for the flux comparison with respect to the electron orbit plane. The term $F(\lambda)$ describes the different degrees of polarization of the two sources and the polarizing property of the instrumentation used for the flux comparison.

4.3.1 Grazing-incidence Monochromator Beam Line

In the 15 nm to 60 nm spectral range the calibration has been performed with a grazing-incidence, toric-grating, monochromator (TGM) beam line [*Fischer et al.*, 1986]. For the radiometric comparison, an ellipsoidal focusing-mirror can image either the tangent point of the storage ring or the aperture stop of the hollow-cathode source into the entrance slit of the monochromator in such a way that, for both sources, the image of the source is not limited in width or height by the size of the entrance slit (Figure 4.6). The monochromator is moved along its optical axis to compensate for the different image distances of the two sources. Measurements have been performed with a grating of 600 lines/mm (15 nm to 32 nm) and of 200 lines/mm (22 nm to 60 nm). To allow for corrections caused by the different degrees of polarization of the transfer standard and the synchrotron radiation, the monochromator can be rotated by 90 ° around its optical axis, which is defined by the center of the entrance slit and the center of the grating. This allows measurements with the optical plane of the instrument parallel and perpendicular to the plane of the electron orbit. The polarizing property of the monochromator-detector system $M^{MD}(\lambda)$ is determined from measurements of the completely polarized synchrotron radiation in both orientations of the monochromator,

$$M^{MD}(\lambda) = \frac{1 + P^{SR}(\lambda)\, M^E(\lambda)}{P^{SR}(\lambda) + M^E(\lambda)} \cdot \frac{i_0^{SR}(\lambda) - i_{90}^{SR}(\lambda)}{i_0^{SR}(\lambda) + i_{90}^{SR}(\lambda)} \tag{4.3}$$

The polarizing property of the ellipsoidal focusing mirror $M^E(\lambda)$ is calculated by use of the Fresnel formulae. The degree of linear polarization is defined as

$$P(\lambda) = \frac{\Phi_\lambda^{\parallel}(\lambda) - \Phi_\lambda^{\perp}(\lambda)}{\Phi_\lambda^{\parallel}(\lambda) + \Phi_\lambda^{\perp}(\lambda)} \tag{4.4}$$

$\Phi_\lambda^{\parallel}(\lambda)$ and $\Phi_\lambda^{\perp}(\lambda)$ are the components of the spectral radiant power with the electric-field vector oscillating parallel and perpendicular to the plane of the electron orbit. With Equations (4.3) and (4.4) the wavelength-dependent functions $F_0(\lambda)$ and $F_{90}(\lambda)$ in Equations (4.1) and (4.2) are given by

$$F_{0/90}(\lambda) = \frac{1 \pm P^{SR} M^{MD} + M^E \cdot (P^{SR} + M^{MD})}{1 \pm P^{TS} M^{MD} + M^E \cdot (P^{TS} + M^{MD})} \tag{4.5}$$

For the radiometric calibration, knowledge of the percentage of radiation diffracted into the higher orders of the synchrotron radiation spectrum is essential. Therefore, the high-order performance of the gratings has been measured [*Kühne and Müller*, 1989]. Additionally, in specific wavelength ranges, absorption-edge filters (Al: 20 nm – 32 nm, Mg: 25 nm – 41 nm, Sn: 53 nm – 59 nm) have been used behind the exit slit to suppress the influence of synchrotron radiation diffracted in higher order, and the storage ring has been operated with a reduced electron-beam energy of 340 MeV (vs. the standard energy of 800 MeV), which reduced the photon flux on the short-wavelength side of the synchrotron radiation spectrum significantly.

4.3.2 Normal-incidence Monochromator Beam Line

Complementary to the grazing-incidence beam line, a normal-incidence monochromator (NIM) beam line has been used for the calibration of selected emission lines above 40 nm (Figure 4.7). This beam line consisted of an aperture stop (defining the solid angle of the accepted synchrotron radiation), a spherical imaging mirror, a 15° McPherson-type monochromator and a photomultiplier detector. Again, the instrumentation is built for the comparison of a transfer standard with the primary standard BESSY. For that purpose, the entire instrumentation can be rotated around a vertical axis, which permits the spherical mirror to form alternately an image of the tangent point of the storage ring or the aperture stop of the hollow-cathode source in the entrance slit of the monochromator. As in the case of the toric-grating monochromator, the size of the entrance slit does not limit the radiant flux of either source. The different distances of the two sources under comparison require that the normal-incidence monochromator can be moved along its optical axis. In contrast to the TGM beam line, the complete normal-incidence instrumentation (including the imaging mirror) can be rotated by 90° about its horizontal axis, which coincides with the optical entrance axis. By measuring the synchrotron radiation with the optical plane of the instrumentation both parallel and perpendicular to the plane of the electron orbit, the polarizing property of the mirror-monochromator-detector system $M(\lambda)$ is determined by

$$M(\lambda) = \frac{1}{P^{SR}(\lambda)} \cdot \frac{i_0^{SR}(\lambda) - i_{90}^{SR}(\lambda)}{i_0^{SR}(\lambda) + i_{90}^{SR}(\lambda)} \tag{4.6}$$

With Equations (4.4) and (4.6) the functions $F_0(\lambda)$ and $F_{90}(\lambda)$ in Equations (4.1) and (4.2) are given by

$$F_{0/90}(\lambda) = \frac{1 \pm P^{SR}(\lambda)\ M(\lambda)}{1 \pm P^{TS}(\lambda)\ M(\lambda)} \tag{4.7}$$

To optimize the instrumentation for the calibration of the transfer source standards in a specific wavelength range, particular combinations of imaging mirror, grating and detector system have been used. Calibrations have been performed with two gratings, differing in line spacing and blaze angle, with two differently-coated, spherical mirrors and with two different photomultiplier detectors. For the source comparison the high-order performance of the gratings has been determined and its influence on the synchrotron radiation spectrum has been considered. Additionally, above 105 nm, LiF-filters have been used to suppress high-order contributions in the dispersed synchrotron radiation spectrum. For details on the NIM beam line see *Hollandt et al.* [1992] and *Hollandt et al.* [1994].

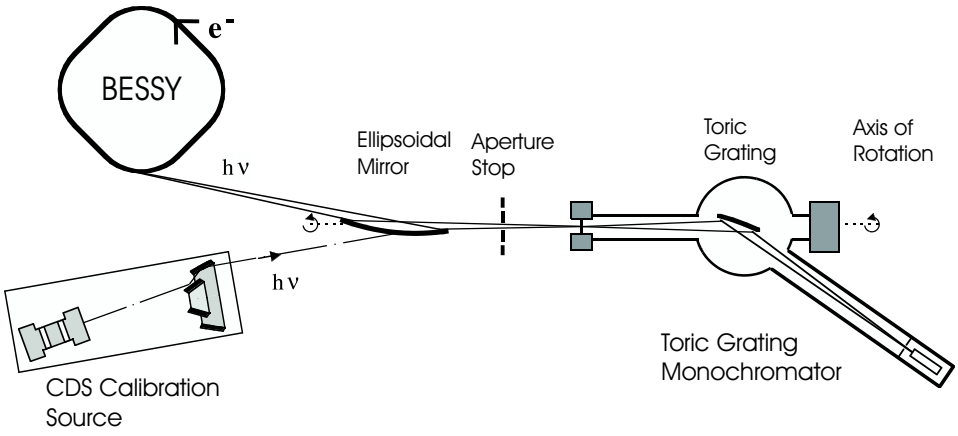

Figure 4.6: Schematic drawing of the grazing-incidence monochromator beam line for the radiometric calibration of transfer source standards in the 15 nm to 60 nm spectral range.

Due to the spectral range of the grazing-incidence source standard, it has been characterized from 15 nm to 60 nm with the TGM beam line and from 40 nm to 80 nm with the NIM beam line. From these measurements, twenty-five aluminium and rare-gas emission lines have been chosen for calibration. All these emission lines have been successively calibrated with adequate combinations of the optical elements, filters and detectors. Whenever possible the emission lines have been calibrated with at least two different configurations of the instrumentation to check for systematic uncertainties caused by inhomogeneity of the efficiency of the grating and high-order contributions in the dispersed synchrotron radiation spectrum.

The normal-incidence source standard could be characterized completely between 50 nm and 150 nm by use of the NIM beam line. In this spectral range, 32 rare-gas emission lines have been selected for calibration. Again, all emission lines have been calibrated with at least two different configurations of imaging mirror, grating and detector to check for systematic uncertainties. Additionally, a coarse cross-calibration with the VUV spectral responsivity scale, which is traceable to NIST, has been performed. For this purpose a NIST-calibrated Al_2O_3 photoemission diode has been brought into the collimated radiation of the normal-incidence source standard when the source has been operated with helium. The measured signal of the diode agreed well, within the combined uncertainty of the comparison (15 % at 1 σ level), with the calibrated photon flux of the source.

4.4 Results and Uncertainties

4.4.1 Photon Flux

The photon flux in the 25 selected emission lines of the grazing-incidence source standard is shown in Table 4.2. It ranges from 5×10^4 s^{-1} for the Al IV emission-line doublet (16.01 nm to 16.17 nm) to 2×10^8 s^{-1} for the He I resonance line at 58.43 nm. While the emitted radiation of the hollow-cathode source itself is unpolarized, the collimated

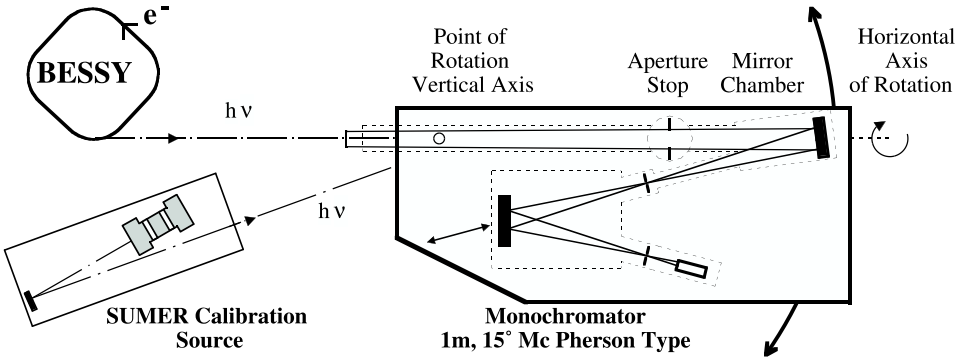

Figure 4.7: Schematic drawing of the normal-incidence monochromator beam line for the radiometric calibration of the transfer source standards in the 40 nm to 150 nm spectral range.

radiation of the grazing-incidence source standard is partly polarized owing to the two grazing-incidence reflections in the Wolter telescope. Below 50 nm the polarization of the collimated radiation is less than 20 %. In the spectral range from 50 nm to 80 nm the polarization goes up to 50 %. Especially when calibrating an instrument with grazing-incidence optics at longer wavelengths, the significant polarization of the grazing-incidence source standard must be considered. Ideally, either the instrument or the source should be rotated by 90° around the axis of the collimated beam to correct for the polarization of the instrument.

The photon flux in the 32 selected emission lines of the normal-incidence source standard is shown in Table 4.3. It ranges from 4×10^6 s^{-1} for the Ar II emission line at 58.34 nm to 7×10^8 s^{-1} for the He I line at 58.43 nm. After only one reflection with an angle of incidence between the mirror normal and the incoming radiation of 3° the degree of polarization of the collimated radiation is less than 1 % for all emission lines.

4.4.2 Uncertainties

The overall uncertainty of the photon flux in the calibrated emission lines of Tables 4.2 and 4.3 originates from the uncertainty of the spectral photon flux of the primary standard BESSY, the uncertainties inherent in the comparison procedure of the transfer source standards with the primary standard and the long-term stability of the radiation emission of the transfer standards.

The spectral photon flux of the synchrotron radiation through the flux-limiting aperture stop of a source calibration beam line $\Phi_\lambda^{SR}(\lambda)$ is calculated according to Schwinger's formula. $\Phi_\lambda^{SR}(\lambda)$ is a function of six parameters $\Phi_\lambda^{SR}(\lambda) = \Phi_\lambda^{SR}(\lambda, W, B, I, a, d, \Psi_0)$. W is the energy of the stored electrons in the ring, B the magnetic induction in the bending magnet at the point of observation, and I is the current represented by the stored electrons.

PTB measured the standard electron energy of 800 MeV at BESSY I by means of resonant spin depolarization of the electrons [*Derbenev et al.*, 1980]. Since the characteristic polarization time of the electrons is proportional to W^{-5}, this method is not feasible for energies below 700 MeV, when the polarization time becomes longer than the life-time of

Table 4.2: Radiant power and photon flux of selected emission lines of the grazing-incidence source standard – working point: 2 A, 400 V.

Wavelength / nm	Spectrum/buffer gas	Radiant Power / pW	Photon Flux / s^{-1}	Rel. standard uncertainty (1σ)
16.01 / 16.17	Al IV / Ne	0.67	5.43×10^4	8 %
16.95 – 17.56	Al III / Ne	1.41	1.22×10^5	8 %
16.01 / 16.17	Al IV / Ar	0.60	4.86×10^4	8 %
16.95 – 17.56	Al III / Ar	1.01	8.77×10^4	8 %
20.43 – 20.89	Ne IV	3.3	3.43×10^5	8 %
21.26	Ne IV	1.15	1.23×10^5	8 %
21.54 – 21.88	Ne IV	4.4	4.81×10^5	8 %
22.26 – 22.36	Ne IV	1.81	2.03×10^5	8 %
26.71 – 26.77	Ne III	7.5	1.01×10^6	8 %
28.25 – 28.39	Ne III	18.3	2.61×10^6	7 %
30.11	Ne III	10.2	1.55×10^6	7 %
30.38	He II	320	4.89×10^7	7 %
30.86	Ne III	4.0	6.21×10^5	7 %
31.31 – 31.39	Ne III	12.4	1.96×10^6	7 %
37.93	Ne III	57	1.09×10^7	7 %
40.59 / 40.71	Ne II	98	2.01×10^7	7 %
44.50 – 44.78	Ne III	173	3.89×10^7	7 %
46.07 – 46.24	Ne II	676	1.57×10^8	7 %
48.81 – 49.11	Ne III	71	1.75×10^7	7 %
53.70	He I	26.5	7.16×10^6	7 %
58.43	He I	609	1.79×10^8	7 %
71.81 – 74.53	Ar II	69	2.54×10^7	7 %
73.59	Ne I	271	1.00×10^8	7 %
74.37	Ne I	157	5.88×10^7	7 %
76.92	Ar III	5.8	2.25×10^6	7 %

the electrons stored in the ring. The flux comparison with the TGM beam line has been performed with the low electron-energy operation of BESSY of 340 MeV to reduce the synchrotron radiation diffracted in higher order in the spectrum. In the low-energy mode of BESSY the electron energy has been determined from an absolute measurement of the synchrotron radiation spectrum measured with a calibrated, energy-dispersive, Si(Li) detector [*Tegeler and Ulm*, 1988].

The magnetic induction was measured by a nuclear magnetic resonance probe in the center of the dipole magnet. Since the tangent points of both source calibration beam lines are not in the center of the dipole magnet, the uncertainty of B is dominated by the field inhomogeneity along the electron path, which has been measured relatively with a Hall probe.

To measure the electron current over the full range from 0.8 pA (one stored electron in the ring) up to 1 A, PTB is using three different methods [*Ulm et al.*, 1989]. While small currents up to 1000 stored electrons are accurately measured by single-electron counting [*Riehle et al.*, 1988], a current above 0.5 mA is measured, with an uncertainty of 5 μA,

Table 4.3: Radiant power and photon flux of selected emission lines of the normal-incidence source standard – working point: 1 A, 500 V.

Wavelength / nm	Spectrum	Radiant Power / pW	Photon Flux / s^{-1}	Rel. standard uncertainty (1σ)
53.70	He I	55.3	1.49×10^7	6 %
54.29 / 54.32	Ar II	50.9	1.39×10^7	6 %
54.75	Ar II	67.9	1.87×10^7	6 %
58.34	Ar II	14.3	4.20×10^6	6 %
58.43	He I	2394	7.04×10^8	6 %
60.29 / 60.42	Ar II / Ar III	19.8	6.02×10^6	6 %
61.24	Ar II	13.6	4.19×10^6	6 %
67.09 – 67.29	Ar II	66.9	2.26×10^7	6 %
71.81	Ar II	18.8	6.80×10^6	7 %
72.20	Kr III	33.5	1.22×10^7	7 %
72.34 / 72.55	Ar II	68.1	2.48×10^7	7 %
73.09	Ar II	23.0	8.47×10^6	7 %
73.59	Ne I	955	3.54×10^8	7 %
74.03	Ar II	55.7	2.08×10^7	7 %
74.37	Ne I	526	1.97×10^8	7 %
74.49 / 74.53	Ar II	42.5	1.59×10^7	7 %
76.92	Ar III	24.7	9.56×10^6	7 %
88.41 / 88.63	Kr II	212	9.45×10^7	7 %
89.10	Kr II	75.8	3.40×10^7	7 %
91.74	Kr II	382	1.77×10^8	7 %
91.98	Ar II	812	3.76×10^8	7 %
93.21	Ar II	486	2.28×10^8	7 %
96.50	Kr II	455	2.21×10^8	7 %
104.82	Ar I	508	2.68×10^8	7 %
106.67	Ar I	406	2.18×10^8	7 %
110.04	Xe II	108	5.98×10^7	7 %
115.85	Xe II	47.6	2.78×10^7	7 %
116.49	Kr I	136	7.98×10^7	6 %
118.31	Xe II	95.0	5.66×10^7	6 %
123.58	Kr I	421	2.62×10^8	6 %
124.48	Xe II	22.5	1.41×10^7	6 %
146.96	Xe I	200	1.48×10^8	6 %

by two identical dc-beam-current transformers. For the calibration of the transfer source standards the storage ring has been operated with an electron current of typically 100 μA to adjust the accepted photon flux of the synchrotron radiation to the photon flux of the transfer standards. In this intermediate current range (0.8 nA $<$ I $<$ 1.5 mA) the current is measured by means of different photodiodes, which have to be calibrated against the current transformer at typically 1 mA. The uncertainty of the current measurement is therefore dominated by the calibration uncertainty and the linearity of the photodiodes.

The angle Ψ_0 of the center of the flux-limiting aperture with respect to the electron orbit plane was determined from the measured vertical angular distribution of the syn-

chrotron radiation. Additionally, the size of the aperture stop a and its distance d from the tangent point of observation had to be measured. A description of the measurement procedure is given in *Thornagel et al.* [1996].

In Table 4.4 the influence of the uncertainties of the storage ring parameters and the geometrical quantities on the uncertainty of the spectral photon flux of BESSY I is shown for typical wavelengths of the two source-calibration beam lines. For all measurements with the two source standards, the relative standard uncertainty of the spectral photon flux of the synchrotron radiation has been below 2.5 %. It should be mentioned that, for precision experiments, a significantly smaller uncertainty of the spectral photon flux of the synchrotron radiation was achieved at BESSY I [*Arnold and Ulm*, 1992; *Thornagel et al.*, 1996].

In the overall uncertainty of the photon flux of the transfer standards, the main contributions of the comparison procedure stem from spatial variations of the grating efficiency and the detector responsivity. Therefore, it has been of crucial importance for the flux comparison to illuminate, as far as possible, identical areas on the grating and on the detector by both the transfer and primary standards. The uncertainties resulting from the inhomogeneities of the optical components and the detectors were determined from measurements of the synchrotron radiation with aperture stops of different sizes, which resulted in slightly different responsivities of the instrumentation used in the flux comparison.

Additionally, in general, the synchrotron radiation signal $i^{SR}(\lambda)$ contains radiation diffracted in higher order. With the TGM beam line, the contribution of high-order diffraction to the uncertainty of the flux comparison is reduced to 1 % by the use of filters and a reduced electron energy (340 MeV). With the NIM beam-line no filters have been applied below 105 nm and the influence of second-order diffracted radiation could be corrected from the knowledge of the high-order performance of the gratings employed. The uncertainty of this correction strongly depends on the observed wavelength and the imaging mirror used. As mentioned earlier, LiF filters were used to suppress radiation diffracted in higher order above 105 nm.

In Table 4.5 the contributions of the primary standard BESSY I, of the comparison procedure and of the stability of the hollow-cathode source to the uncertainty of the photon flux of the transfer standards are given for two different wavelengths and two different optical configurations of the NIM beam-line. The overall relative uncertainty of the photon flux in the calibrated emission lines results from the sum, in quadrature, of these contributions and is listed in Table 4.2 and Table 4.3.

4.5 Summary

We describe transfer source standards based on hollow-cathode, glow discharges which can be used for the overall radiometric calibration of VUV astronomical instrumentation. Our standards have a photon flux that is traceable to the electron storage ring BESSY I, a primary radiometric standard, and produce a collimated beam that can directly irradiate the telescope entrance aperture. The source standards are transportable, and their differential pumping system permits windowless operation in connection with an ultrahigh-vacuum system.

Calibration can thus take place in the tank that is used for instrument development and testing; the instrument need not be transported to a special calibration facility. Scheduling

Table 4.4: Contributions to the relative uncertainty (1σ) of the spectral photon flux of the synchrotron radiation.

Source of uncertainty	Value for TGM beam line	Rel. standard uncertainty[a] at 40 nm	Value for NIM beam line	Rel. standard uncertainty[a] at 90 nm
Electron energy	W = (337 ±2) MeV	0.99 %	W = (798 ± 1) MeV	0.09 %
Magnetic induction	B = (0.631±0.005) T	0.13 %	B = (1.482± 0.005) T	0.23 %
Electron current: Diode calibration at Linearity of diode	I = (1500± 5) μA ± 0.5 %	0.60 %	I = (1500 ±5) μA ± 0.5 %	0.60 %
Diameter of aperture stop	a = (5.286 ± 0.010) mm	0.38 %	a = (10.00 ± 0.02) mm	0.40 %
Distance of aperture stop	d = (15050 ± 15) mm	0.20 %	d = (23745 ± 50) mm	0.42 %
Emission angle	Ψ_0 = (0.04 ± 0.02) mrad	0.01 %	Ψ_0 = (0.50 ± 0.05) mrad	0.93 %
Beam emittance: vertical beam divergence vertical beam size	 ± 30 μrad ± 500 μm	 } 0.03 %	 ± 30 μrad ± 500 μm	 } 0.01 %
Total sum in quadrature $\Delta\Phi\lambda^{SR}/\Phi\lambda^{SR}$		**1.2 %**		**1.3 %**

[a] The relative standard uncertainty is given by $\Delta\Phi\lambda^{SR}/\Phi\lambda^{SR}$.

problems, as they are bound to occur with the primary synchrotron source standards, are also avoided. The transfer source standards produce a line spectrum so that they can be used for both radiometric and wavelength calibration; order-sorting is straightforward.

The diameters of the collimated beams (5 mm and 10 mm) are small compared to those of a typical (solar or non-solar) space-telescope entrance-aperture (100 mm to several meters). This permits a mapping of local spectral-responsivity variations over the telescope aperture. At the same time, the small, collimated input beams generate instrument count-rates typical of those expected in flight, since their photon flux corresponds to that typically collected in flight by the entire telescope aperture.

Accordingly, these transportable source standards are suitable for the calibration not only of solar VUV instruments (for which they were originally developed), but also for astronomical space instrumentation in general. Two of the instruments flown on SOHO, CDS (Coronal Diagnostic Spectrometer, *Harrison et al.* [1995]) and SUMER (Solar Ultraviolet Measurements of Emitted Radiation, *Wilhelm et al.* [1995]), have been calibrated by use of the systems described in this paper [*Hollandt et al.*, 1996; *Lang et al.*, 2000].

The photon flux of the source standards is known to better than 8 % (1σ value). This is clearly adequate for the current requirement for quantitative solar spectroscopy, particularly in the extreme-ultraviolet spectral domain, where accuracy is limited by the larger

Table 4.5: Overall relative uncertainty (1σ) of the photon flux of the normal-incidence source standard.

Source of uncertainty	at 55 nm		at 90 nm	
	Imaging mirror:			
	Au	SiC	Au	SiC
Spectral photon flux of synchrotron radiation	1.4 %	1.4 %	1.3 %	1.3 %
Synchrotron radiation diffracted in high-order	–	–	2.5 %	0.6 %
Inhomogeneity of optical components and detector	3.0 %	3.5 %	3.0 %	3.5 %
Linearity of detector	0.6 %	0.6 %	0.6 %	0.6 %
Wavelength calibration	0.4 %	0.9 %	0.1 %	0.1 %
Stability of hollow cathode source	5 %	5 %	5 %	5 %
Total sum in quadrature $\Delta\Phi\lambda^{SR}/\Phi\lambda^{SR}$	**6.0 %**	**6.4 %**	**6.5 %**	**6.3 %**

uncertainties in the atomic data used in diagnostic investigations of solar plasma [*Mason and Monsignori Fossi*, 1994].

We maintain that the existence of a reliable laboratory standard is a prerequisite for verifying the radiometric stability of an instrument, as long as it is on the ground. Particularly, collimated source standards, such as those described here, provide a precise means of testing the radiometric stability of the entire, assembled system, rather than only of its individual optical components.

As indicated in the introduction, at the radiometry laboratory of PTB at BESSY, an improved primary detector standard – an electrical substitution radiometer operating at liquid-helium temperature [*Rabus et al.*, 1997] – has achieved significantly lower uncertainties. In the spectral range between 40 nm and 400 nm, the spectral responsivity of photodiodes has been determined with a relative uncertainty better than 1 %, the results being in good agreement with a calibration against the laser-operated cryogenic radiometer of PTB Berlin [*Rabus et al.*, 1997]. Similar progress has also been made in the determination of the spectral responsivity of photodiodes with this method in the soft X-ray range (0.1 nm to 25 nm) [*Krumrey et al.*, 2000]. Such well-characterized transfer detector standards, in combination with collimated monochromatized radiation, offer the potential to calibrate complete astronomical telescopes at special synchrotron radiation beam lines with smaller uncertainties than those realized in the past. A beam line of this kind is planned at the radiometry laboratory of PTB at the electron storage ring BESSY II.

Acknowledgements

We thank E. Tegeler and G. Ulm for many helpful discussions. We also thank M. Bock, P. Klein, and W. Paustian for their valuable technical support. This work was financially supported by the European Space Agency (Contract No.9419/91/F/BZ) and the Max-Planck-Institut für Aeronomie.

Bibliography

Arnold, D., and Ulm, G., Electron storage ring BESSY as a source of calculable spectral photon flux in the X-ray region, *Rev. Sci. Instrum.* **63**, 1539, 1992.

Besson, J.C., Certain, P., Dael, A. et al., Super-ACO: Results on a positron low emittance ring, *Rev. Sci. Instrum.* **60**, 1373, 1989.

Canfield, L.R., and Swanson, N., Far ultraviolet detector standards, *Journal of Research of the National Bureau of Standards* **92**, 97, 1987.

Danzmann, K., Günther, M., Fischer, J., Kock, M., and Kühne, M., High current hollow cathode as a radiometric transfer standard source for the extreme vacuum ultraviolet, *Appl. Opt.* **27**, 4947, 1988.

Derbenev, Y.S., Kondratenko, A.M., Serednyakov, S.I., Skrinsky, A.N., Tumaikin, G.M., and Shatunov, Y.M., Accurate calibration of the beam energy in a storage ring based on measurement of spin precession frequency of polarized particles, *Particle Accel.* **10**, 177, 1980.

Fischer, J., Kühne, M., and Wende, B., Instrumentation for spectral radiant power measurements of sources in the wavelength range from 5 to 150 nm using the electron storage ring BESSY as a radiometric standard source, *Nucl. Instrum. Methods A* **246**, 404, 1986.

Furst, M.L., Graves, R.M., Canfield, L.R., and Vest, R.E., Radiometry at the NIST SURF II storage ring facility, *Rev. Sci. Instrum.* **66**, 2257, 1995.

Harrison, R.A., Sawyer, E.C., Carter, M.K., Cruise, A.M., Cutler, R.M., Fludra, A., Haynes, R.W., Kent, B.J., Lang, J., Parker, D.J., Payne, J., Pike, C.D., Peskett, S.C., Richards, A.G., Culhane, J.L., Norman, K., Breeveld, A.A. Breeveld, E.R., Al Janabi, K.F., McCalden, A.J., Parkinson, J.H., Self, D.G., Thomas, P.D., Poland, A.I., Thomas, R.J., Thompson, W.T., Kjeldseth-Moe, O., Brekke, P., Karud, J., Maltby, P., Aschenbach, B., Bräuninger, H., Kühne, M., Hollandt, J., Siegmund, O.H.W., Huber, M.C.E., Gabriel, A.H., Mason, H.E., and Bromage, B.J.I., The Coronal Diagnostic Spectrometer for the Solar and Heliospheric Observatory, *Sol. Phys.* **162**, 233, 1995.

Henke, B.L., and Tester, M.A., Techniques of low energy X-ray spectroscopy, *Adv. X-Ray Anal.* **18**, 76, 1975.

Hollandt, J., Jans, W., Kühne, M., Lindenlauf, F., and Wende, B., A beam line for radiant power measurements of vacuum ultraviolet and ultraviolet sources in the wavelength range 40 – 400 nm, *Rev. Sci. Instrum.* **63**, 1278, 1992.

Hollandt, J., Huber, M.C.E., and Kühne, M., Hollow cathode transfer standards for the radiometric calibration of VUV telescopes of the Solar and Heliospheric Observatory, *Metrologia* **30**, 381, 1993.

Hollandt, J., Kühne, M., and Wende, B., High-current hollow-cathode source as a radiant intensity standard in the 40 – 125 nm wavelength range, *Appl. Opt.* **33**, 68, 1994.

Hollandt, J., Schühle, U., Paustian, W., Curdt, W., Kühne, M., Wende, B., and Wilhelm, K., Radiometric calibration of the telescope and ultraviolet spectrometer SUMER on SOHO, *Appl. Opt.* **35**, 5125, 1996.

Kroth, U., Saito, T., and Tegeler, E., Quantum efficiency of a semiconductor photodiode in the VUV determined by comparison with a proportional counter in monochromatized synchrotron radiation, *Appl. Opt.* **29**, 18, 1990.

Krumrey, M., Herrmann, C., Müller, P., and Ulm, G., Synchrotron-radiation-based cryogenic radiometry in the X-ray range, *Metrologia* **37**, 361, 2000.

Kühne, M., and Müller, P., Higher order contributions in the synchrotron radiation spectrum of a toroidal grating monochromator determined by the use of a transmission grating, *Rev. Sci. Instrum.* **60**, 2101, 1989.

Lang, J., Kent, B.J., Breeveld, A.A., Breeveld, E.R, Bromage, B.J.I., Hollandt, J., Payne, J., Pike, C.D., and Thompson, W.T., The laboratory calibration of the SOHO Coronal Diagnostic Spectrometer, *J. Opt. A* **2**, 88, 2000.

Lemaire, P., Sensitivity changes in the CNRS ultraviolet spectrometer aboard OSO-8, *ESA J.* **15**, 237, 1991.

Mason, H.E., and Monsignori Fossi, B., Spectroscopic diagnostics in the VUV for solar and stellar plasmas, *Astron. Astrophys. Rev.* **6**, 123, 1994.

Philips, R., Sources and applications of ultraviolet radiation, Academic Press, London, p. 138 and citations therein, 1984.

Rabus, H., Scholze, F., Thornagel, R., and Ulm, G., Detector calibration at the PTB radiometry laboratory at BESSY, *Nucl. Instrum. Methods A* **377**, 209, 1996.

Rabus, H., Persch, V., and Ulm, G., Synchrotron-radiation-operated cryogenic electrical substitution radiometer as the high-accuracy primary detector standard in the ultraviolet, vacuum-ultraviolet, and soft-X-ray spectral ranges, *Appl. Opt.* **36**, 5421, 1997.

Reeves, E.M., Timothy, J.G., Huber, M.C.E., and Withbroe, G.L., Photometric calibration of the EUV spectroheliometer on ATM, *Appl. Opt.* **16**, 849, 1977.

Riehle, F., Bernstorff, S., Fröhling, R., and Wolf, F.P., Determination of electron currents below 1 nA in the storage ring BESSY by measurement of the synchrotron radiation of single electrons, *Nucl. Instrum. Methods A* **268**, 262, 1988.

Samson, J.A.R., Absolute intensity measurement in the vacuum ultraviolet, *J. Opt. Soc. Am.* **54**, 6, 1964.

Samson, J.A.R., and Haddad, G.N., Absolute photon flux measurement in the vacuum ultraviolet, *J. Opt. Soc. Am.* **64**, 47, 1974.

Schwinger, J., On the classical radiation of accelerated electrons, *Phys. Rev.* **75**, 1912, 1949.

Shaw, P.-S., Lykke, K.R., Gupta, R., O'Brien, T.R., Arp, U., White, H.H., Lucatorto, T.B., Dehmer, J.L., and Parr, A.C., Ultraviolet radiometry with synchrotron radiation and cryogenic radiometry, *Appl. Opt.* **38**, 18, 1999.

Tegeler, E., and Ulm, G., Determination of the beam energy of an electron storage ring by using calibrated energy dispersive Si(Li)-detectors, *Nucl. Instr. and Meth. A* **266**, 185, 1988.

Thornagel, R., Fischer, J., Friedrich, R., Stock, M., Ulm, G., and Wende, B., The electron storage ring BESSY as a primary standard source – a radiometric comparison with a cryogenic electrical substitution radiometer in the visible, *Metrologia* **32**, 459, 1996.

Ulm, G., Hänsel-Ziegler, W., Bernstorff, S., and Wolf, F.P., Measuring devices at BESSY for stored beam currents ranging from 0.8 pA to 1 A, *Rev. Sci. Instrum.* **60**, 1752, 1989.

Wilhelm, K., Curdt, W., Marsch, E., Schühle, U., Lemaire, P., Gabriel, A., Vial, J.-C., Grewing, M., Huber, M.C.E., Jordan, S.D., Poland, A.I., Thomas, R.J., Kühne, M., Timothy, J.G., Hassler, D.M., and Siegmund, O.H.W., SUMER-Solar Ultraviolet Measurements of Emitted Radiation, *Sol. Phys.* **162**, 189, 1995.

— 5 —

Calibration and Inter-calibration of SOHO's Vacuum-ultraviolet Instrumentation

KLAUS WILHELM
Max-Planck-Institut für Aeronomie, Katlenburg-Lindau, Germany

The SOlar and Heliospheric Observatory (SOHO) is equipped with a suite of instruments capable of observing the Sun from the core to the outer corona. Several of these instruments observe radiation in the vacuum-ultraviolet (VUV) wavelength range, where precise and accurate radiometric measurements are of extreme significance for solar and terrestrial investigations, but, at the same time, are very difficult to obtain due to degradation effects of most optical systems under solar ultraviolet irradiation. Radiometric-calibration and cross-calibration matters have consequently been important topics from the initial planning phase of the mission to the operational implementation. An attempt will be made here to summarize the early requirements and goals as well as the achievements of SOHO in this context. Although not all plans could be carried out, the general picture is very encouraging. SOHO allowed us to make a major step forward in solar radiometry, in particular of spatially-resolved structures.

5.1 Introduction

Solar electromagnetic radiation in the VUV (10 nm to 200 nm) is strongly absorbed in the Earth's atmosphere [cf., *Rees*, 1989]. The direct consequence is that observations at these wavelengths are only possible from rockets or spacecraft. Both for many fields of solar research (for example, elemental abundance studies and plasma diagnostics) and for an understanding of the processes in the Earth's atmosphere, it is of vital importance that the radiation be measured quantitatively. Spatially-resolved spectral radiance measurements have to be obtained for most of the solar studies, whereas spectral irradiance data are needed for terrestrial applications.

The early history of solar VUV radiometry, in particular from instruments on the Orbiting Solar Observatories (OSO) and the Skylab mission, is characterized by significant progress in obtaining radiance and irradiance data with better and better accuracy [e.g., *Dupree and Reeves*, 1971; *Huber et al.*, 1973; *Reeves et al.*, 1977; *Hinteregger*, 1977; *Heroux and Higgins*, 1977; *Schmidtke et al.*, 1992]. However, it also became evident [e.g., *Reeves and Parkinson*, 1970] that some long-term observations in this range were plagued with severe responsivity deterioration, which at least in one case [*Bruner*, 1977; *Woodgate et al.*, 1980] amounted to losses of factors of ten within days. To cope with this difficulty, two complementary strategies were developed: (1) one devises sophisticated methods of monitoring the degradation and thus maintaining an established radiometric-calibration

status, and (2) one discovers and understands the processes that lead to the degradation, and then employs appropriate procedures and design concepts to eliminate them.

At the beginning of the development phase of SOHO, after the final instrument selection in 1988, the time was ripe to follow the route of the second strategy, while, at the same time, performing careful calibration tracking. The degradation problem had been clearly identified on many occasions, not only for spacecraft, but also for synchrotron applications. The processes responsible for it had been described as a combination of contamination of optical surfaces with hydrocarbons and other outgassing products from structural elements, followed by photo-activated polymerization under UV irradiation [cf., *Austin*, 1982; *Boller et al.*, 1983; *Kent et al.*, 1993, 1994; *Schühle*, 1993]. Thus a promising strategy was to eliminate sources of contamination and outgassing wherever possible and to monitor quantitatively and continuously any that may unavoidably be present. This approach was adopted for SOHO and is fully described in the contributions covering the cleanliness aspects of the spacecraft [*Thomas*, 2002] and the instruments [*Lang et al.*, 2002; *Schühle et al.*, 2002]. The cleanliness requirements were, however, not part of the SOHO Assessment Study dated September 1983, and were only briefly mentioned in the joint ESA/NASA SOHO Announcement of Opportunity (AO) of March 1987. They had to be defined in detail by the instrument and spacecraft teams. As we will see in the following sections, these endeavours were extremely successful. With a few exceptions, which will be mentioned below, the SOHO VUV instruments did not show any long-term degradation of their radiometric responsivities under nominal operational conditions.

We will discuss only the solar VUV instruments on the SOHO spacecraft, namely, CDS (Coronal Diagnostic Spectrometer), EIT (Extreme-ultraviolet Imaging Telescope), SEM (Solar Extreme-ultraviolet Monitor), SUMER (Solar Ultraviolet Measurements of Emitted Radiation), and UVCS (UltraViolet Coronagraph Spectrometer). SWAN (Solar Wind ANisotropies), although an H I Ly-α instrument, looks away from the Sun and is not included in this report. For a review of the history of the SOHO mission in general see *Huber et al.* [1996].

5.2 Scientific Requirements

5.2.1 Proposal Phase

The scientific requirements as far as VUV radiometry was concerned were discussed during this phase in a series of meetings starting in 1986 – before the SOHO AO in March 1987 – and continuing until the end of 1987, shortly before the submission deadline for the revised proposals on 8 January 1988. Some of the meetings were quite eventful as, for instance, the session in January 1987, when many potential participants were stranded somewhere in snow-hit Paris, and those actually present in Verrières could not take off their coats without freezing to death in the old Vauban castle.

It was realized early on in these discussions that the radiometric calibration was not the only calibration task at hand. Wavelength measurements, telescope and spectrometer spatial and spectral resolutions, as well as pointing performance were intimately related to the absolute calibration. This was summarized by Peter McWhirter in notes taken at the meeting held in Paris on 23 and 24 April 1987. For the radiometric work itself, it was suggested to consider a typical relative standard uncertainty of atomic data of $\approx$ 10 % as

a guide, and aim for relative uncertainties of the observations between 25 % and 30 % at the short-wavelength range and rather better performance at longer wavelengths. All uncertainties are given here as relative standard uncertainties, unless specified otherwise.

Based on past experience, severe degradation of the responsivity was expected in flight, in particular for normal-incidence instruments. Monitoring of the calibration status was suggested to be performed against well-calibrated spacecraft instruments (e.g., SUSIM, the Solar Ultraviolet Spectral Irradiance Monitor on UARS, the Upper Atmosphere Research Satellite) and calibration rockets. In addition, internal checks and cross-calibration might be possible using atomic physics data on branching ratios and other line ratios not very sensitive to the source plasma conditions.

Synchrotron radiation was identified as the primary radiometric standard, in particular from the Super-ACO positron storage ring at the Laboratoire pour l'Utilisation du Rayonnement Electromagnétique (L.U.R.E.) in Orsay, the Synchrotron Ultraviolet Radiation Facility (SURF-II) at the National Institute of Standards and Technology (NIST), and the Berlin Electron Storage ring for SYnchrotron radiation (BESSY I), but the need for transfer standards was also recognized. It was thought that both individual components and the fully-assembled instruments had to be radiometrically calibrated. These requirements formed the basis of the VUV calibration plans in the SOHO proposals of January 1988. In addition, the desirability of a re-calibration opportunity between instrument deliveries and launch was stressed. A direct radiometric in-flight calibration using transfer standards was also considered, but it was felt that it could not reliably be implemented within the project constraints (see, however, Section 5.5 for details on the in-flight calibration).

5.2.2 Definition and Design Phases

In some of the SOHO proposals, theoretical support groups were identified as Associate Scientist (AS) teams. These groups played an important rôle in the detailed definition of the scientific requirements. The SUMER AS team met in Paris in June 1988 for the first time, followed by a CDS/SUMER science workshop in Oxford in September. Since many of the participants were involved in both the CDS and the SUMER investigations, and, moreover, a close coordination of the CDS and SUMER science planning was highly desirable, the following meetings were held as Joint CDS/SUMER Science Meetings. On many occasions, radiometric-calibration topics were on the agenda and those meetings are included in Table 5.1, which lists all meetings relevant in this context held after the SOHO AO had been issued. A special calibration panel chaired by P. McWhirter (at the first JMAS meeting in February 1989) came up with a report, concluding that relative standard uncertainties should ideally be less than 20 %. A realistic aim appeared to be 35 %, and 50 % would be the lowest level worth attempting for solar radiometry. It should be noted, however, that for planetary applications uncertainties of the irradiance of less than 5 % were required. Notice also that, in narrow wavelength ranges, line ratios can be determined with smaller uncertainties without involving absolute radiometry. The required or anticipated, and later achieved, radiometric uncertainties as documented in meeting reports or the open literature are summarized in Table 5.2. The ways suggested to obtain the required accuracies were:
(1) extensive laboratory calibration with secondary standards traceable to primary standards; (2) cross-calibration (called here also "inter-calibration") on SOHO and with in-

Table 5.1: Meetings Related to SOHO Calibration and Inter-calibration Activities.

Date	Place	Meeting[a,b] and Remarks
23/24 Apr 1987	Paris	Proposal preparation; atomic data $\approx$ 10 %[c]
21/22 Jun 1988	Paris	1st SUMER AS Meeting; requirements
29/30 Sep 1988	Oxford	CDS/SUMER Science Meeting; requirements
7/8 Feb 1989	Lindau	JMAS-1; calibration panel report
11/12 Jul 1989	Berlin	WSVUV-1; HCL and mirror chambers
5/6 Oct 1989	Abingdon	JMAS-2; uncertainty 20 % envisaged
5/6 Nov 1989	Noordwijk	SICWG-1; irradiance for terrestrial use 5 %
14/17 May 1990	Noordwijk	SICWG-2; cleanliness important
22/23 Oct 1990	Berlin	WSVUV-2; SUSIM irradiance comparison
25/26 Oct 1990	Lindau	JMAS-3; uncertainties 20 % to 30 %
27+30 Nov 1990	Noordwijk	SICWG-3; stars; SEM recommendation
3 Jun 1991	Noordwijk	SICWG-4; HCL: uncertainty $<$ 20 %
18 Nov 1991	Noordwijk	SICWG-5; report on SUSIM degradation
15–18 Jun 1992	Killarney	SOHO/Cluster; CDS/SUMER calibration
21–23 Oct 1992	Orsay	JMAS-5; absolute wavelengths: 20 pm
25/26 Jan 1993	Noordwijk	SICWG-6; calibration rehearsals
22–24 Nov 1993	Abingdon	JMAS-6; purge directly to instruments
24/25 Jan 1994	Noordwijk	SICWG-7; uncertainties considered
13 Jun 1994	Portsmouth	SICWG-8; report on some anomalies
3–5 Oct 1994	Greenbelt	JMAS-7; calibration rockets; UARS/SOLSTICE[d]
11+13 Jan 1996	Greenbelt	SICWG-9; inter-calibration JOPs; Spartan
9 Feb 1996	Greenbelt	SICWG-10; Intercal-1, Intercal-9
17 May 1996	Greenbelt	SICWG-11; Intercal-2: No He II full disks
31 Oct/1 Nov 1996	Berlin	WSVUV-3; first results presented
5–7 Nov 1996	Orsay	JMAS-9; last meeting of this series
13/14 Nov 1997	Orsay	WSVUV-4; continue Intercal-1 and rockets
29/30 Mar 1999	Berlin	WSVUV-5; inauguration of BESSY II
12/16 Feb 2001	Bern	WSVUV-6; review SOHO calibration tasks
8/12 Oct 2001	Bern	WSVUV-7; continuation of WSVUV-6

[a] JMAS: Joint Meeting of Associate Scientists (CDS/SUMER);
WSVUV: WorkShop on VUV radiometry and inter-calibration;
SICWG: SOHO Inter-Calibration Working Group.
[b] JMAS-4 (2 to 4 October 1991, Nice) and JMAS-8 (19 to 21 September 1995, Oslo) did not cover calibration aspects.
[c] This relative standard uncertainty was originally related to branching ratios, which may even be known to 5 %. Doublets should be accurate within relative deviations of 10 % and density/temperature insensitive ratios for each ion within $\approx$ 20 %; ratios, in general, can be expected to have relative uncertainties of as much as 30 % [*H.E. Mason, personal communication*, 2001].
[d] SOLSTICE: SOLar-STellar Irradiance Comparison Experiment.

Table 5.2: Relative Standard Radiometric Uncertainties in Percent [%][a,b].

Phase/Document/Channel	HCL	CDS	SUMER	UVCS	EIT	SEM[c]
1987 pre-proposal	20	25...30	< 25	20	-	-
1988 rev. 1 of proposals	25	25...30	30...50	20	-	-
1989 early development	**13**	< 20 ... 35 ... 50		≈ 10	≈ 100	-
1988/90 early Coloured Books	15...20	< 20	< 20	20	-	-
1991/92 calibration plans	10	< 20	15...30	12...15	-	< 10
1994/95 final Coloured Books	**6...8**	-	< 20	-	-	-
1993/95 laboratory calibration	**6...7**	$\approx$ **30**	**15**	**16**	**60...150**	**10**
unvignetted	-	-	**11**	-	-	-
1996/98 in-flight calibration	-	-	-	-	**15**(He)	**10**
CDS – NIS	-	**15...29**	-	-	-	-
– GIS	-	**45**	-	-	-	-
SUMER – Detector A	-	-	**15**	-	-	-
– Detector B	-	-	**20**	-	-	-
UVCS – H I α and O VI	-	-	-	**20**	-	-
1998/2001 in-flight calibration	-	-	-	-	$\approx$ **20**	**10**
CDS – NIS	-	**20...30**	-	-	-	-
– GIS	-	**45** (TBC)	-	-	-	-
SUMER – Detector A	-	-	**33**	-	-	-
– Detector B	-	-	**36**	-	-	-
UVCS – H I Ly α and O VI	-	-	-	**20**	-	-

[a] Radiometric uncertainties are given for the prime wavelength ranges (for further details see text and/or the corresponding instrument contributions). Bold face: values achieved as published.
[b] Solar irradiance instruments on UARS report relative uncertainties of 2 % to 5 %. For a comparison with stellar astronomy: the EUV Explorer (EUVE) calibration plan specifies a relative uncertainty of 25 % (3 σ), which corresponds to a coverage factor of $k = 3$, the Far-Ultraviolet Spectroscopic Explorer (FUSE) achieved an in-flight performance of $\approx$ 10 % relative uncertainty [*Sahnow et al.*, 2000], but experienced a change of the effective area by a factor of about 0.95 over a period of four months [*Moos et al.*, 2000]; the International Ultraviolet Explorer (IUE) relative radiometric uncertainties are $\approx$ 10 % with final adjustments of 4 % to 10 % [*Nichols and Linsky*, 1996].
[c] SEM was added to the SOHO payload in 1990/91 [*McMullin et al.*, 2002b].

struments on other spacecraft; (3) calibration rockets, and (4) comparisons with stellar sources.

It was also noted that good co-alignment, knowledge of the polarization properties, cleanliness standards, and wavelength stability were of great importance in achieving the radiometric-calibration goals. These requirements were eventually adopted in the CDS "Blue Book", the UVCS "Yellow Book", and the SUMER "Red Book" (first draft editions by *Harrison* [1988], *Kohl and Noci* [1989], and *Wilhelm* [1990]). The Blue and Red Books were subsequently revised quite often, mostly as a consequence of the deliberations at the Joint Science Meetings, but the radiometric requirements did not significantly change until the launch of SOHO on 2 December 1995. In general, the Blue, Yellow, and Red Books provided a wide exchange of information about the instruments in non-technical

formats and helped during the preparation of the observations. They will be referred to as "Coloured Books" here.

Radiometric-calibration issues of SOHO instruments were specifically taken up by: (1) an inter-calibration working group chaired by John Kohl, and (2) workshops on spectroradiometry.

The SICWG was set up by the SOHO Science Working Team (SWT) of the SOHO principal investigators and the workshops were organized on an ad hoc basis (see Table 5.1). The SICWG prepared the SOHO inter-calibration activities by defining several inter-calibration JOPs (Joint Observing Programme) and monitoring the flight schedule of calibration rockets (Table 5.3), which were carried out in support of SOHO, but managed independently, and, in many cases, with additional scientific objectives. The panel repeatedly emphasized the need for stringent spacecraft and instrument cleanliness requirements. Reports that the responsivity of the operational channel of SUSIM decreased by a factor of 1.3 within days demonstrated the urgency of such measures. The workshops on spectroradiometry discussed the instrument calibration and inter-calibration aspects on a broader scope, and also covered the particulate and molecular cleanliness requirements of the mission. The first workshop took place in Berlin on 11 and 12 July 1989, where the participants outlined the calibration concepts of CDS and SUMER based on transfer standard sources [*Hollandt et al.*, 1993] consisting of Hollow-Cathode Lamps (HCL) [*Danzmann et al.*, 1988] and collimating mirror chambers.

5.3 Radiometric Calibration before Launch

In this section, no attempt will be made to cover all aspects related to the calibration effort of the VUV instruments on SOHO. Rather some events or facts directly relevant to this review will be presented. For further details the instrument-related publications should be consulted [*Clette et al.*, 2002; *Gardner et al.*, 2002; *Lang et al.*, 2002; *McMullin et al.*, 2002a; *Wilhelm et al.*, 2002]. *Hollandt et al.* [2002] discuss VUV radiometric-calibration matters in general. Some introductory remarks referring to more than one instrument are related to the cleanliness concepts.

Before the beginning of the instrument development phase, it was common wisdom that radiometric-responsivity degradation was unavoidable in the VUV range, as was mentioned above. Even after the SOHO cleanliness procedures had been defined, there was no proof that they would eliminate the problem or at least improve the situation. It was thus felt that, in order to maintain the laboratory calibration from instrument delivery to operation in space, a re-calibration just before launch was required as well as purging directly to the instruments on the spacecraft until lift-off. The purging was implemented [cf., *Thomas, 2002*]. However, when in August 1993 ESA announced that there would be no re-calibration slots for the VUV instruments before launch, it was thought that this would have an adverse effect on their calibration status in flight. Only in the case of UVCS did the final calibration occur six months before launch. Fortunately, for all the VUV instruments the pre-flight calibrations by and large nevertheless remained valid after launch.

Table 5.3: Payloads Launched[a] to Verify SOHO Calibrations.

Date	Time[b]	Payload[c,d]	Remarks[e]
26 Jun 1996	19:00	Cal-SO-2	(30.4 ± 4.0) nm: uncertainty 8 %; monitor spectral responsivity of SEM
15 May 1997	19:15	EGS, XPS	uncertainty 6 % to 10 %; CDS update;
		MXUVI	Fe IX/X (17.1 nm); EIT, TRACE
11 Aug 1997	18:18	Cal-SO-3	calibration update for SEM/SOHO
16 Oct 1997	19:00	EIT CalRoc	EIT degradation correction and flat fielding
18 Nov 1997	19:35	SERTS-97	uncertainty < 25 %; with EM (0.1 to 50) nm used for CDS-NIS and EIT updates
31 Jan 1998	04:30	XDT[f]	Fe XIV (21.13 nm) images; Dopplergrams
1 Nov 1998	21:49	UVCS	calibration update for UVCS;
– 3 Nov 1998	12:45	Spartan 201[g]	uncertainty 25 %
2 Nov 1998	18:20	EGS, XPS	validated SNOE SXP calibration;
		MXUVI	Fe IX/X (17.1 nm) images
24 Jun 1999	17:00	SERTS-99	uncertainty 25 %; with EM
18 Aug 1999	18:05	Cal-SO-4	calibration update for SEM/SOHO
26 Jul 2000	18:00	SERTS-00	uncertainty 25 %; with EM

[a] XDT launched from Kagoshima, all other rocket payloads launched from White Sands.
[b] In Coordinated Universal Time (UTC).
[c] Payload names:

Cal-SO	Rocket underflights for SOHO cross-calibration
EGS	EUV Grating Spectrograph
EM	EUV monitor (simplified SEM) to update SEM/SOHO channel 2
HRTS	High Resolution Telescope and Spectrograph
MXUVI	Multiple XUV Imager
SERTS	Solar EUV Research Telescope and Spectrograph
SNOE	Student Nitric Oxide Explorer
SXP	Solar X-ray Photometer
XDT	XUV Doppler Telescope
XPS	XUV Photometer System

[d] The SERTS-96 flight on 13 November 1996 at 18:30 UTC and the HRTS-10 flight on 30 September 1997 20:10 UTC are not listed, because no radiometric calibrations were available.
[e] Accuracies, a, are indicated here by their relative standard uncertainties, u_r, and not by $a = 1 - u_r$.
[f] Details on XDT have been published by *Sakao et al.* [1999] and *Hara et al.* [1999]. The instrument was calibrated at component level. An initial comparison with EIT showed a factor of two less in emission measure.
[g] Launched on the Space Shuttle.

5.3.1 CDS

The CDS team concluded that the only viable method for pre-launch radiometric calibration was a transfer standard traceable to a synchrotron radiation facility as primary

source standard. At the first WSVUV in July 1989, this concept was outlined and a coordination with the SUMER calibration was agreed. The HCLs later employed for the SOHO instrument calibrations performed even better than anticipated at that time: a typical relative stability of 2.5 % was achieved over 40 h with one gas and 5 % after a change of gas. The grazing-incidence telescope of CDS required a collimating mirror different from the collimator for SUMER, but the HCLs and the general schemes were the same.

In total, twenty-nine emission lines were selected covering the spectral range of the instrument. The transfer source was calibrated against BESSY I in these spectral lines. After an end-to-end calibration of CDS, the source was returned to BESSY for a post-calibration. For the NIS-2 waveband, the comparison of the pre-launch estimates of the efficiencies of the components with measured responsivities of the instrument were close, whereas for NIS-1 and NIS-2 in second order the deficiencies were a factor of ten. They are attributed to problems with the measured detector quantum efficiencies used in the estimate. For the four GIS channels the comparison yields about a factor of twenty, noting that the estimates for the pre-launch sensitivities of the components were much poorer. The relative uncertainties in the laboratory measurements of the responsivities for both GIS and NIS were estimated at around 30 % [see *Lang et al.*, 2000, 2002].

5.3.2 EIT

The ground-based programme provided a complete calibration of the EIT system [*Defise et al.*, 1995], but time constraints during the integration schedule and difficulties in combining it with the priority scheme of a large synchrotron facility, as well as the substitution of a new detector (Tektronix, thinned back-side, back-illuminated, CCD sensor) after the end-to-end test (using silicon diodes calibrated at NIST) reduced the validity of the pre-flight characterization [*Defise et al.*, 1998; *Clette et al.*, 2002]. Consequently, *Dere et al.* [2000] suggested, for instance, formal relative combined standard uncertainties at the end of the laboratory calibration of (60, 70, and 75) % for the (19.5, 28.4, and 30.4) nm channels, respectively.

5.3.3 SEM

The main purpose of the SEM instrument [*Judge et al.*, 1998] is to measure with high precision and accuracy the solar irradiance near the prominent He II emission line in the wavelength range (30.4 ± 4.0) nm (Channel 1), but it also monitors the wavelength band between 0.1 nm and 50 nm (Channel 2). It has been calibrated with Beamlines 2 and 9 at SURF-II with typical relative uncertainties of 5 % for the 30.4 nm channel providing solar irradiances, after the convolution needed, with an uncertainty of 10 % [*McMullin et al.*, 2002a]. A typical value for the broad-band channel is also 10 % [*Judge et al.*, 1999].

5.3.4 SUMER

The re-calibration idea, which had to be abandoned in 1993, had been suggested for SUMER by ESA in a status review in October 1991 and had been the agreed scenario since November 1991. The original plan to calibrate the assembled instrument at the Super-ACO facility was also not carried out, because it was felt that cleanliness and schedule

constraints would lead to severe difficulties. The controlled attenuation of the intense synchrotron radiation was another problem area. The method finally adopted at WSVUV-1, in cooperation with CDS, used a transfer standard source consisting of a lamp (HCL) attached to a chamber with a spherical concave scan mirror. A total number of thirty-two emission lines was calibrated in the wavelength range from 53.7 nm to 147.0 nm at BESSY I. The source was also successfully compared with a diode calibrated at NIST [cf., *Hollandt et al.*, 2002]. The responsivities of both detectors of the SUMER instrument were very similar, but that of detector B, when operated at nominal gain, generally was a factor of $\approx$ 1.2 higher than detector A. The actual responsivities found were between 0.65 and 1.35 of the prediction based on sub-system measurements [*Wilhelm et al.*, 1995]. The relative uncertainty of the SUMER laboratory radiometric calibration was 11 % [*Hollandt et al.*, 1996].

A specific feature of this calibration was that the calibrated beam was not vignetted inside SUMER (cf., Table 5.2). Apertures and stops therefore had to be taken into account separately in evaluating the throughput of the instrument [*Wilhelm et al.*, 2000]. To verify the imaging properties of the telescope, it was necessary to fill the whole aperture of SUMER with a collimated, even if uncalibrated, beam. This was generated with the help of the Spectral and Angular Resolution UV Tube (SARUVT). It should be mentioned that the end-to-end calibration was performed under extreme time pressure, which had been caused, at least partially, by a late change of the detector system.

The sensitivity to the state of polarization of the incident radiation could not be determined for the assembled instrument. An engineering model of the plane mirror and the holographic grating was used to determine the effects of these polarization-sensitive items at the Super-ACO facility [*Hassler et al.*, 1997].

5.3.5 UVCS

The development programme of UVCS relied on component calibrations and an end-to-end calibration as well as a rigorous contamination control programme to limit optical degradation. UVCS was delivered to ESA for spacecraft integration with its end-to-end behaviour uncharacterized (and without flight detectors). While at ESA, the flight detectors were installed, the diffraction gratings were replaced, the H I Ly-α channel telescope mirror was replaced, and the O VI-channel mirror cleaned. In June and July 1995, UVCS was returned after spacecraft-level testing to laboratories at the Smithsonian Astrophysical Observatory. There, over a period of about 32 d, the UVCS was radiometrically calibrated end-to-end and its stray-light rejection measured.

The UVCS radiometric response was measured against secondary photodiode (cesium telluride and aluminium oxide) standards from NIST [*Gardner et al.*, 1996]. Radiation from a gas-discharge radiation source was pre-dispersed using a monochromator. A single bright spectral line was focused onto the exit slits. The radiation passing through the slits (and through insertable filters of known attenuation) was collimated by a 4.6 m focal-length mirror and directed through the UVCS instrument aperture and onto its telescope mirrors completely filling the portion not covered by the launch-locked internal occulter [*Gardner et al.*, 2002]. That portion, which is the one used for observations at 2.7 solar radii from Sun centre, was the only part of the aperture that could be calibrated during the end-to-end measurements. The radiance was found to be uniform with relative variations of less than 10 %. The UVCS entrance slits were opened sufficiently to pass all of the

radiation in that image towards the gratings where it was dispersed and focused onto a detector. The counting rates registered on the detectors were compared directly to the output of the NIST photodiodes, thereby giving the system responsivity. Measurements were made for both UV channels at several wavelengths near the centres of their intended operating ranges. The relative standard uncertainty for each of the radiometric measurements was 16 %.

Laboratory measurements on gratings replicated from the same masters as the flight gratings, together with in-flight data (see Section 5.5) have allowed extension of the results from the laboratory calibration to all telescope apertures available to UVCS [*Gardner et al.*, 2000, 2002].

5.4 Inter-calibration Plans and Achievements

Whereas laboratory calibrations were to a large extent the tasks of the various instrument teams, inter-calibration could only be attempted as a cooperative effort. Most of the meetings listed in Table 5.1 therefore had inter-calibration items on their agendas. The discussions led to the definition of SOHO inter-calibration JOPs, named ICAL, which will be summarized here (all procedures can be found on the SOHO operations pages at `http://soho.nascom.nasa.gov`). Some of them have been widely used. Others were just defined for a special occasion and were either successfully executed or abandoned. Additionally, various other inter-calibration activities have been performed that are not under the formal ICAL listings and form the basis for some of the results reported in this volume. It is worth noting that data taken at regular intervals with standardized observing sequences, such as reference spectra, full-Sun rasters, etc. (not necessarily designed for radiometric purposes), turned out to be very useful in many cases.

5.4.1 ICAL 01

The roots of this JOP go back to the SOHO Assessment Study, ESA SCI (83) 3, of September 1983, where a wavelength overlap between the normal-incidence spectrometer (NIS) and the grazing-incidence spectrometer (GIS) of the model payload was recommended. Such an overlap was indeed suggested by the original CDS and SUMER proposals in July 1987, but it disappeared after the selection in 1988 according to the first published list of SOHO investigations in EOS, 69, No. 13, of 29 March 1988. Fortunately, however, the final wavelength choice of CDS in December 1988 again introduced common wavelength bands with SUMER. This made comparisons between the instruments possible in the bands: 65.6 nm to 78.5 nm CDS GIS-4 (first order) with SUMER detector A (second order) and detector B (first order); 51.3 nm to 63.3 nm CDS NIS-2 (first order) with SUMER detectors A and B (second order). (The GIS and NIS instruments of the SOHO model payload should not be confused with the GIS and NIS channels of CDS.)

In the common ranges, the bright spectral lines He I 58.4 nm, Mg X (60.9, 62.5) nm, and Ne VIII 77.0 nm are available for CDS/SUMER cross-calibrations. In 1994 the details of the wavelength selection and the procedure for ICAL 01 were discussed by the SICWG, before the agreement was reached that ICAL 01 should be an on-disk comparison of quiet-Sun regions aimed at good counting statistics. CDS, SUMER, EIT, and later the Transition Region and Coronal Explorer (TRACE) participated in most of the runs, whilst UVCS per-

formed on-disk observations only a few times. In 1996 and 1997, UVCS/SUMER cross-calibrations at N V 123.8 nm were well within the uncertainty margins, with UVCS indicating radiances about a factor of 1.18 less than SUMER. Since August 1999, the O V 63.0 nm line has been included in the ICAL 01 sequence.

Data obtained on a regular basis with ICAL 01 were analysed to investigate in detail the CDS/SUMER cross-calibration aspects [*Pauluhn et al.*, 1999, 2001a, b]. The agreement was, in general, within the combined uncertainties. An important result was that the variations of the radiances measured by both instruments were highly correlated and, consequently, must have been of solar origin. The SUMER observations were also used to study the calibration changes during the loss of attitude control in 1998 [*Wilhelm et al.*, 2000; *Schühle et al.*, 2000a], and the long-term variability of quiet-Sun radiances [*Schühle et al.*, 2000b]. No published radiometric comparison with TRACE is known.

5.4.2 ICAL 02

The plan was to transfer SEM irradiance data of the He II 30.4 nm channel with the help of EIT images to small regions on the Sun for CDS updates. In addition, the EIT responsivity should be mapped by a full CDS raster. It was also hoped that the results could be transferred to longer wavelengths (SUMER and UVCS). ICAL 02 did not produce the expected results, because the large bandpass of SEM (cf., Section 5.3.3), with the accompanying variety of spectral lines other than He II 30.4 nm, limits a direct comparison of the SEM irradiance with the single-line radiance measurements of CDS. The CDS full-Sun rasters have not proven very useful in providing flat-field information to EIT due to the differing plate scales, the undersampling by CDS, and the timing difference ($\approx$ 12 h for a full-Sun scan as opposed to 30 s for an EIT image).

CDS/SUMER irradiance comparisons had been performed in 1996 and agreed well within the combined uncertainty estimates for He I 58.4 nm and Mg X 62.4 nm [*McMullin et al.*, 2002b]. For O V 63.0 nm, however, CDS observed irradiances were lower by about a factor of 1.35 than SUMER. Both instrument evaluations agreed on the centre-to-limb variation in this line ($\approx$ 4). These O V observations are just compatible within the combined uncertainty margins.

5.4.3 ICAL 03

This JOP was also meant to compare full-Sun data of SEM, EIT and CDS at 30.4 nm. It was not executed, because the load on the CDS detector would have been too high. *Thompson et al.* [2002] present comparisons of irradiance measurements by CDS – tied to EGS 1997 (cf., Table 5.3) – with SEM and EIT, which appear to achieve the goals of ICAL 03, albeit with a different method involving a differential emission measure analysis of the CDS and EIT data. For CDS, differential emission measures were used only to fill in the SEM bandpass below 30 nm. CDS irradiances are lower by 1.05 to 1.15 than SEM values (using a fixed spectrum) and factors of 1.05 to 1.3 lower than those of EIT. CDS and EIT give consistent results on the sum of the He II and Si XI contributions to the SEM 30.4 nm channel [*Thompson et al.*, 2002; *McMullin et al.*, 2002b].

5.4.4 ICAL 04 and ICAL 05

These JOPs were aimed at CDS/SUMER/EIT/MDI alignment and responsivity cross-calibrations. Both goals are now incorporated in the final ICAL 01 sequence. Without specific pointing adjustments, typical misalignments of the instruments were found, in line with expectations, to be less than 10″. This could be improved by an order of magnitude by correlating images with solar disk structures or the limb.

Brynildsen et al. [1998] performed an early CDS/SUMER radiance comparison in the O V 63.0 nm line and found a factor of 1.5 to 2 more with CDS. *Pauluhn et al.* [2001b] studied the O V 63.0 nm line in more detail and found agreement within relative deviations of 15 %. Variations of the solar radiance dominate over instrumental effects in this spectral line as well as in the other lines observed during ICAL 01. However, in later comparisons, CDS radiances appear to be lower by 1.31 [*Pauluhn et al.*, 2002]. These findings are thus consistent with the irradiance results in Section 5.4.2.

5.4.5 ICAL 06

Three SERTS payloads [*Neupert et al.*, 1992] were launched in the years 1997 to 2000, which also carried an SEM-type instrument for observations in the wavelength band from 0.1 nm to 50 nm (see Table 5.3). These flights span the period of the attitude loss of SOHO and can be used to study the changes of the spacecraft instrument responsivities. SERTS covers a bandpass from 29.9 nm to 35.3 nm. A radiometric calibration was performed between flights with the re-calibrated CDS transfer source standard and provided a relative uncertainty of 25 % for the instrument responsivity, confirmed by density- and temperature-insensitive line ratios. The SERTS-97 rocket underflight formed (together with EGS, see Section 5.4.10) the basis for the most recent CDS NIS-1 responsivity determination in first order and for NIS-2 in second order. Since SERTS as well as CDS can clearly resolve the strong Si XI and He II lines at 30.4 nm, this also gives information on the spectral composition of the EIT and SEM 30.4 nm channels, in addition to the results reported in Section 5.4.3. Comparisons of SERTS-97 observations with EIT are presently ongoing.

5.4.6 ICAL 07

Since 1996 SUMER and, in particular, UVCS have carried out many observations of bright, hot stars close to the ecliptic plane. The SUMER measurements of α and ρ Leo near 125 nm agreed very well with the corresponding laboratory calibration and can be taken as verification that no responsivity loss occurred during the spacecraft integration and the launch activities. At longer wavelengths the stellar calibration based on IUE (cf., Table 5.2) was adopted for SUMER, because no reliable ground calibrations were available. In this range, stellar observations also provided information on the responsivity changes in 1998 [*Lemaire*, 2002].

UVCS has observed approximately fifteen stars as well as the planet Jupiter. Included are the stars α and ρ Leo also observed by SUMER. Inter-comparison of the two instrument calibrations using those stars is progressing [*Gardner et al.*, 2002; *Lemaire*, 2002]. Several of the other stars have been observed by instruments aboard other spacecraft (e.g., IUE, Voyager, and FUSE). In general, the relative variations of irradiances measured by

UVCS and IUE are less than 10 %. A comparison of the UVCS O VI channel response to that of Voyager, observing the star τ Tau at wavelengths shorter than was possible with IUE, shows relative agreement to within 20 %. The irradiance of Feige 110, a white dwarf star measured by UVCS in February 2001 near 100 nm, has been compared to measurements made by FUSE. Relative agreement is found to within 15 %. Yearly observations of the bright star δ Sco have been carried out with nearly identical instrument configurations. They show irradiance measurements without trends and relative variations of no more than 5 % over the elapsed SOHO mission time.

5.4.7 ICAL 08

This procedure was not defined.

5.4.8 ICAL 09

The ICAL 09 procedure attempted to inter-calibrate UVCS and SUMER with a coronal streamer near the east or west limb. It was performed several times in 1996 with the participation of both instruments. This inter-calibration was not successful because of the strong radial gradient of the radiance which, for a reliable comparison, required a very good spatial coalignment of the field of view. This could not be ascertained in the featureless coronal streamer.

5.4.9 ICAL 10

The radiometric cross-calibration of SOHO instruments with the HIgh-RESolution EUV spectroheliometer (HIRES) could not be carried out, because the rocket payload has not been launched yet.

5.4.10 ICAL 11

This JOP describes a rocket payload with the instruments EGS, XPS and MXUVI and the radiometric comparisons with SOHO and TRACE. EGS [*Woods and Rottman*, 1990] was calibrated using Beamline 2 of SURF-II. The relative uncertainty in the wavelength band 25 nm to 120 nm was 6 % to 10 %. Five XUV photometers (XPS) (radiometers) in the range 1 nm to 40 nm were calibrated with 10 % to 20 % uncertainty. The EGS data were used to update the CDS calibration (see Section 5.5.1).

During the flight on 15 May 1997, SUMER observed spectra along the central meridian, but was not operating on 2 November 1998, when the rocket payload was launched again. MXUVI obtained Fe IX/X (17.1 nm) images for comparison with EIT and TRACE [*Auchère et al.*, 2001].

5.4.11 ICAL 12

This inter-calibration JOP specifies the rocket underflights in support of SEM and other EUV instrumentation aboard SOHO. The Cal-SO rockets [*Judge et al.*, 1999] are equipped with a solar EUV monitor representative of SEM. It has been calibrated using SURF-II, and transmits bands near He II 30.4 nm and from 0.1 nm to 50 nm. The first flight on

26 June 1996 obtained an irradiance in photons at 1 AU (astronomical unit) of 1.18×10^{14} m^{-2} s^{-1} with a relative uncertainty of 11 % in the band (26 to 34) nm. A comparison of this and the following flights with SEM identified a modest amount of degradation in the spacecraft instrument, probably because of a deposition of carbon (contained in hydrocarbon layers) on the optical surfaces. At SICWG-4, it was reported that there was an average relative degradation of 5.5 % between pre- and post-flight rocket calibrations of a silicon diode with aluminium filter.

SUMER observed full-Sun images in the He I 58.4 nm line on 26 June 1996 and obtained a photon line irradiance of 1.02×10^{13} m^{-2} s^{-1} with a relative uncertainty of ≈ 16 %.

5.4.12 ICAL 13

The first launch of the EIT CalRoc produced 512×512 pixel images in all four EIT wavebands. They have been used for deriving SOHO EIT flat-field information [*Defise et al.*, 1998]. In preparing this rocket underflight, tests showed that there was an EUV-dose dependence to the electric potential distribution in the CCD charge-collection region. The rocket flight provided input for the degradation correction, and indicated changes of the multi-layer coatings. A second launch of the EIT CalRoc is planned for 2002 with improved multi-layer sealing.

5.5 Radiometric Calibration in Flight

Inter-calibration activities play an important rôle in most of the in-flight calibrations, and consequently the inter-calibration chapter was presented first. There are, however, some aspects, which could not be adequately treated in that context. One of them is the change in responsivity of the instruments during the attitude loss of SOHO in the year 1998.

5.5.1 CDS

Three sounding rocket payloads (EGS, SERTS, Cal-SO; see Table 5.3) on several flights provided relevant measurements for the CDS in-flight calibration. A comparison with the NIS-2 band of CDS led to a relative uncertainty of 15 % at He I 58.4 nm and 25 % at either end of the band [*Brekke et al.*, 2000]. Consideration of the wide-slit burn-in correction later led to 18 % and 29 %, respectively [*Lang et al.*, 2002]. The comparison with NIS-1 at Mg IX 36.8 nm uncovered a severe discrepancy of a factor of 2.75, which is interpreted as an effect of an undetected misalignment during ground calibration. After adoption of the Mg IX point and a further refinement with the help of a SERTS-97 flight, a relative uncertainty of 15 % (in the SERTS wavelength range) to 25 % (close to 36.8 nm) was assigned to the NIS-1 band in first order. It should be noted that the SERTS-97 instrument was calibrated using the CDS HCL and its calibration is thus traceable to BESSY I (see Section 5.4.5). The ICAL 1 observations (CDS/SUMER) are being used to check the laboratory calibration of the GIS-4 band (longest wavelength) [*Pauluhn et al.*, 2002]. The results of *Landi et al.* [1999] show that there are no gross deviations between the laboratory and in-flight relative calibrations of the GIS detectors. *Del Zanna et*

al. [2001] and *Del Zanna* [2002] applied spectroscopic methods to achieve a relative calibration of all CDS channels. The incorporation of the results into the CDS calibration is still in progress.

The SOHO attitude loss affected the CDS channels as follows: the NIS-2 band appears to be unchanged, but a slight increase is applied to the relevant uncertainty; the NIS-1 band may have changed by a factor of 1.5. Its responsivity is still under study [*Lang et al.*, 2002]. The calibration of the CDS GIS appears unaffected by the loss of attitude control. CDS was very warm during most of the time without attitude control. This is estimated to have led to a relative reduction of $\approx$ 20 % of the burn-in pattern. This also caused the spectral lines to change position on the detector, altering the burn-in characteristics [*Thompson et al.*, 2002]. Further information, including references to in-flight measurements of line ratios which are independent of solar plasma conditions, is given in *Lang et al.* [2002].

5.5.2 EIT

In-flight calibration results are presented by *Clette et al.* [2002] including grid corrections, point-spread function and stray-light determinations. Also covered is the degradation of the responsivity caused by contamination and EUV-induced reduction of the CCD charge-collection efficiency. The latter effect is responsible for most of the degradation observed. Inter-calibration of EIT with SEM indicates a relative uncertainty close to 20 % after appropriate corrections have been carried out. The on-board, visible-light calibration lamp and SOHO off-point manœuvres were used to derive flat-field images and correction procedures, which also benefit from the EIT CalRoc data (see Table 5.3 and Section 5.4.12). During the attitude loss of SOHO, EIT was very warm and the responsivities of all channels recovered by a factor of about two.

5.5.3 SEM

The in-flight calibration of SEM is closely related to the Cal-SO rocket underflights (see Table 5.3 and Section 5.4.11). With their help, it could be determined that a carbon deposition of $\approx$ 16 nm thickness had accumulated after five years in orbit, for which correction functions have been established as far as the degradation of the EUV responsivities is concerned. After this correction, the relative SEM uncertainties in both channels are $\approx$ 10 %. During the SOHO attitude loss, SEM was warmer than nominal, but no change in responsivity was reported.

5.5.4 SUMER

As for all space instruments, the most critical task was to verify that the SUMER laboratory radiometric calibration did not degrade during spacecraft integration and launch. As a relative measure it could be confirmed that the ratios of the responsivities of the photocathodes (KBr and bare microchannel plate) for both detectors were not affected over the entire wavelength range. With invariant line ratios the relative shape of the responsivity curves has successfully been checked and, finally, stellar observations allowed a comparison with IUE data near 120 nm, for which an agreement within a few percent of the individual observations was found [*Wilhelm et al.*, 1997; *Schühle et al.*, 2000c]. A cross-calibration with SOLSTICE on UARS (calibrated at NIST before launch and with

early-type stars in flight) gave consistent irradiance results with relative deviations of 10 % to 14 % in the range from 123.8 nm to 155.0 nm [*Wilhelm et al.*, 1999], and, with the latest SUMER calibration, even 4 % for C IV at 154.8 nm [*Wilhelm et al.*, 2002]. The ICAL 01 data and the H I Lyman continuum measurements acquired during flat-field exposures were used to perform calibration tracking [*Schühle et al.*, 1998]. No loss of responsivity has been found, but rather a slight increase is seen in most of the emission lines, which is considered to be of solar origin. It should be noted that the gain of the microchannel plates is a function of the counting rate and the total counts. Correction procedures for high counting rates are available. In order to maintain the radiometric calibration after the accumulation of a large number of total counts requires an increase of the operating voltage. This option is available until the maximal voltage levels of the power supplies are reached for both detectors.

After the SOHO recovery late in 1998, the SUMER responsivity had decreased by a factor of ≈ 1.31 for both detectors, and the relative uncertainty estimates had to be raised to above 30 %. A final result is not yet available [*Wilhelm et al.*, 2002]. One of the difficulties is that the ICAL 01 spectral lines are optimized for comparisons with other instruments, but not for an internal tracking of a potentially wavelength-dependent loss of responsivity. SUMER was very cold during the period when SOHO's attitude was lost.

5.5.5 UVCS

The radiometric calibration of the two UVCS ultraviolet channels has been confirmed by several methods. The successful inter-calibrations to IUE, Voyager, FUSE, and SUMER using stars have been outlined in Section 5.4.6, and the favourable on-disk inter-comparison with SUMER at N V 123.8 nm was mentioned in Section 5.4.1. Comparisons of UVCS on SOHO to UVCS/Spartan at H I Ly α were carried out in November 1998 (cf., Table 5.3). Spartan was calibrated in the laboratory before and after its flight. Agreement with UVCS/SOHO was found within 15 % of each other, well within the uncertainty of 25 % [*Frazin et al.*, 2002]. UVCS/SOHO has also made measurements of the interplanetary H I Ly-α emission, and found a radiance consistent with the accepted value.

A number of other radiometrically-important instrument functions has been determined in flight. For example, field uniformities have been measured. A major effort has been to track the degradation of field uniformity resulting from changes in detector gain, and make periodic increases in the high voltage to keep the local detector responses within 5 % of the nominal values. These measurements use a combination of star observations and grating scans of bright coronal emission lines. Details of these measurements can be found in *Gardner et al.* [2002] and references therein. The response of the H I Ly-α redundant path in the O VI channel is dependent on the irradiation of the redundant path mirror, which is a function of the grating angle as well as the unvignetted telescope mirror area. These functions have also been evaluated in flight. Such observations were also used to ensure radiometric consistency for observations common to both ultraviolet channels.

The yearly observations of several stars by UVCS indicate that there were no changes in its responsivities as a consequence of the SOHO attitude loss, during which UVCS experienced moderate temperature excursions. Indeed these same observations indicate that there have been no significant changes to date at all. This is likely to be due to the strict cleanliness programme and to the fact that UVCS has a telescope with occulter. Its mirrors thus are not routinely exposed to direct solar irradiation.

5.6 Conclusions

A reliable and consistent radiometric calibration of the SOHO VUV instrumentation on the ground and in flight is a major undertaking, which is still in progress as the mission continues. It has been closely related to the corresponding cleanliness programmes of the spacecraft and the instruments. Together with the coordinated calibration rocket flights, the calibration and inter-calibration activities (not restricted to SOHO instruments) have been very successful and have led to a large database of solar VUV radiation measurements with high accuracy from the sunspot minimum in 1996 to the sunspot maximum in 2000 and beyond. The accuracy achieved must be considered as the minimum standard for future solar missions, which will have the advantage of building on these experiences and results.

Acknowledgements

This history of the SOHO calibration and inter-calibration work was compiled after reading the relevant documents starting in 1983. In the first years of the instrument and spacecraft definition period, a group of people actively pursued the VUV calibration and cleanliness aspects that eventually led to the success of SOHO in this area. I want to list those involved here in alphabetical order: J. Austin, C. Becker, J.-P. Delaboudinière, R.A. Harrison, J. Hollandt, M.C.E. Huber, B.J. Kent, J.L. Kohl, M. Kühne, J. Lang, P. Lemaire, R.W.P. McWhirter, B.E. Patchett, U. Schühle, R. Thomas, J.G. Timothy, and O. von der Lühe. I wish to thank F. Clette, K.P. Dere, B. Fleck, L.D. Gardner, H. Hara, R.A. Harrison, D.M. Hassler, J.L. Kohl, J. Lang, D.R. McMullin, J.D. Moses, J.S. Newmark, W.H. Parkinson, A. Pauluhn, C.D. Pike, J.C. Raymond, U. Schühle, R.J. Thomas, W.T. Thompson, and T.N. Woods for many suggestions and for providing information on details of some of the instrument performance characteristics or the data obtained.

Bibliography

Auchère, F., Hassler, D.M., Slater, D.C., and Woods, T.N., SWRI/LASP sounding rocket inter-calibration with the EIT instrument on board SOHO, *Sol. Phys.* **202**, 269–280, 2001.

Austin, J.D., Contamination control plan for prelaunch operations, *Proc. SPIE* **338**, 42, 1982.

Boller, K., Haelbich, R.-P., Hogrefe, H., Jark, W., and Kunz, C., Investigation of carbon contamination of mirror surfaces exposed to synchrotron radiation, *Nucl. Instr. and Methods* **208**, 273–279, 1983.

Brekke, P., Thompson, W.T., Woods, T.N., and Eparvier, F.G., The extreme-ultraviolet solar irradiance spectrum observed with the Coronal Diagnostic Spectrometer (CDS) on SOHO, *Astrophys. J.* **536**, 959–970, 2000.

Bruner, Jr., E.C., The University of Colorado OSO-8 experiment. I – Introduction and optical design considerations, *Space Sci. Instrum.* **3**, 369–387, 1977.

Brynildsen, N., Brekke, P., Fredvik, T., Haugan, S.V.H., Kjeldseth-Moe, O., Maltby, P., Harrison, R.A., Pike, C.D., Rimmele, T., Thompson, W.T., and Wilhelm, K., EUV spectroscopy of the sunspot region NOAA 7981 using SOHO. I. Line emission and time dependence, *Sol. Phys.* **179**, 43–74, 1998.

Clette, F., Hochedez, J.-F., Newmark, J., Moses, D., Auchère, F., Defise, J.-M., and Delaboudinière, J.-P., The Radiometric Calibration of the Extreme Ultraviolet Imaging Telescope, this volume, 2002.

Danzmann, K., Günther, M., Fischer, J., Kühne, M., and Kock, M., High current hollow cathode as a radiometric transfer standard source for the extreme vacuum ultraviolet, *Appl. Opt.* **27**, 4947–4951, 1988.

Defise, J.-M., Song, X., Delaboudinière, J.-P., Artzner, G.E., Carabetian, C., Hochedez, J.-F., Brunaud, J., Moses, J.D., Catura, R.C., Clette, F., and Maucherat, A.J., Calibration of the EIT instrument for the SOHO mission, *Proc. SPIE* **2517**, 29–39, 1995.

Defise, J.M., Moses, J.D., Clette, F., and the EIT Consortium, In-orbit performances of the EIT instrument on-board SOHO and intercalibration with the EIT CalRoc sounding rocket program, *Proc. SPIE* **3442**, 126–139, 1998.

Del Zanna, G., Bromage, B.J.I., Landi, E., and Landini, M., Solar EUV spectroscopic observations with SOHO/CDS. I. An in-flight calibration study, *Astron. Astrophys.* **379**, 708–734, 2001.

Del Zanna, G., The use of atomic data for the in-flight calibration of the CDS spectrometers, this volume, 2002.

Dere, K.P., Moses, J.D., Delaboudinière, J.-P., Brunaud, J., Carabetian, C., Hochedez, J.-F., Song, X.Y., Catura, R.C., Clette, F., and Defise, J.-M., The pre-flight photometric calibration of the Extreme-ultraviolet Imaging Telescope EIT, *Sol. Phys.* **195**, 13–44, 2000.

Dupree, A.K., and Reeves, E.M., The extreme-ultraviolet spectrum of the quiet Sun, *Astrophys. J.* **165**, 599–613, 1971.

Frazin, R.A., Romoli, M., Kohl, J.L., Gardner, L.D., Wang, D., Howard, R.A., and Kucera, T.A., White light inter-calibrations of UVCS, LASCO and Spartan 201/WLC, this volume, 2002.

Gardner, L.D., Kohl, J.L., Daigneau, P.S., Dennis, E.F., Fineschi, S., Michels, J., Nystrom, G.U., Panasyuk, A., Raymond, J.C., Reisenfeld, D.J., Smith, P.L., Strachan, L., Suleiman, R., Noci, G.C., Romoli, M., Ciaravella, A., Modigliani, A., Huber, M.C.E., Antonucci, E., Benna, C., Giordano, S., Tondello, G., Nicolosi, P., Naletto, G., Pernechele, C., Spadaro, D., Siegmund, O.H.W., Allegra, A., Carosso, P.A., and Jhabvala, M.D., Stray light, radiometric, and spectral characterization of UVCS/SOHO: Laboratory calibration and flight performance, *Proc. SPIE* **2831**, 2–24, 1996.

Gardner, L.D., Atkins, N., Fineschi, S., Smith, P.L., Kohl, J.L., Maccari, L., and Romoli, M., Efficiency variations of UVCS/SOHO based on laboratory measurements of replica gratings, *Proc. SPIE* **4139**, 362–369, 2000.

Gardner, L.D., Smith, P.L., Kohl, J.L., Atkins, N., Ciaravella, A., Miralles, M.-P., Panasyuk, A., Raymond, J.C., Strachan, Jr., L., and Suleiman, R., UV radiometric calibration of UVCS/SOHO, this volume, 2002.

Hara, H., Nagata, S., Kano, R., Kumagai, K., Sakao, T., Shimizu, T., Tsuneta, S., Yoshida, T., Ishiyama, W., Oshino, T., and Murakami, K., Narrow-band multilayer mirrors for an extreme-ultraviolet Doppler telescope, *Appl. Opt.* **38**, 6617–6627, 1999.

Harrison, R.A., The Coronal Diagnostic Spectrometer for SOHO: Scientific report (The Blue Book), 1988, attn.: later revisions until 1995.

Hassler, D.M., Lemaire, P., and Longval, Y., Polarization sensitivity of the SUMER instrument on SOHO, *Appl. Opt.* **36**, 353–359, 1997.

Heroux, L., and Higgins, J.E., Summary of full-disk solar fluxes between 250 and 1940 Å, *J. Geophys. Res.* **82**, 3307–3310, 1977.

Hinteregger, H.E., EUV flux variation during end of solar cycle 20 and beginning cycle 21, observed from AE-C satellite, *Geophys. Res. Lett.* **4**, 231–234, 1977.

Hollandt, J., Huber, M.C.E., and Kühne, M., Hollow cathode transfer standards for the radiometric calibration of VUV telescopes of the Solar and Heliospheric Observatory (SOHO), *Metrologia* **30**, 381–388, 1993.

Hollandt, J., Schühle, U., Paustian, W., Curdt, W., Kühne, M., Wende, B., and Wilhelm, K., Radiometric calibration of the telescope and ultraviolet spectrometer SUMER on SOHO, *Appl. Opt.* **35**, 5125–5133, 1996.

Hollandt, J., Kühne, M., Huber, M.C.E., and Wende, B., Source standards for the radiometric calibration of astronomical telescopes in the VUV spectral range traceable to the primary standard BESSY, this volume, 2002.

Huber, M.C.E., Dupree, A.K., Goldberg, L., Noyes, R.W., Parkinson, W.H., Reeves, E.M., and Withbroe, G.L., The Harvard Experiment on OSO-6: Instrumentation, calibration, operation, and description of observations, *Astrophys. J.* **183**, 291–312, 1973.

Huber, M.C.E., Bonnet, R.M., Dale, D.C., Arduini, M., Fröhlich, C., Domingo, V., and Whitcomb, G., The history of the SOHO mission, *ESA Bulletin* **86**, 25–35, 1996.

Judge, D.L., McMullin, D.R., Ogawa, H.S., Hovestadt, D., Klecker, B., Hilchenbach, M., Möbius, E., Canfield, L.R., Vest, R.E., Watts, R., Tarrio, C., Kühne, M., and Wurz, P., First solar EUV irradiances obtained from SOHO by the CELIAS/SEM, *Sol. Phys.* **177**, 161–173, 1998.

Judge, D.L., McMullin, D.R., and Ogawa, H.S., Absolute solar 30.4 nm flux from sounding rocket observations during the solar cycle 23 minimum, *J. Geophys. Res.* **104**, 28321–28324, 1999.

Kent, B.J., Swinyard, B.M., and Hicks, D., Contamination effects on EUV optics in the space environment, *Proc. SPIE* **1945**, 348–360, 1993.

Kent, B.J., Swinyard, B.M., and Martin, E.L., Contamination control and material screening for the extreme ultraviolet Coronal Diagnostic Spectrometer on SOHO, *Proc. SPIE* **2210**, 474–484, 1994.

Kohl, J.L., and Noci, G., Ultraviolet coronagraph spectrometer (The Yellow Book), 1989, attn.: later revision 1994.

Landi, E., Del Zanna, G., Breeveld, E.R., Landini, M., Bromage, B.J.I., and Pike C.D., Relative intensity calibration of CDS-GIS detectors on SOHO using a plasma diagnostic technique, *Astron. Astrophys. Suppl. Ser.* **135**, 171–185, 1999.

Lang, J., Kent, B.J., Breeveld, A.A., Breeveld, E.R., Bromage, B.J.I., Hollandt, J., Payne, J., Pike, C.D., and Thompson, W.T., The laboratory calibration of the SOHO Coronal Diagnostic Spectrometer, *J. Opt. A: Pure Appl. Opt.* **2**, 88–106, 2000.

Lang, J., Thompson, W.T., Pike, C.D., Kent, B.J., and Foley, C.R., The radiometric calibration of the Coronal Diagnostic Spectrometer, this volume, 2002.

Lemaire, P., SUMER stellar observations to monitor responsivity variations, this volume, 2002.

McMullin, D.R., Judge, D.L., Hilchenbach, M., Ipavich, F., Bochsler, P., Wurz, P., Bürgi, A., Thompson, W.T., and Newmark, J.S., In-flight comparisons of solar EUV irradiance measurements provided by the CELIAS/SEM on SOHO, this volume, 2002a.

McMullin, D.R., Woods, T.N., Dammasch, I.E., Judge, D.L., Lemaire, P., Newmark, J.S., Thompson, W.T., Tobiska, W.K., and Wilhelm, K., Irradiance working group report for

the SOHO inter-calibration workshop, this volume, 2002b.

Moos, H.W., Cash, W.C., Cowie, L.L., Davidsen, A.F., Dupree, A.K., Feldman, P.D., Friedman, S.D., Green, J.C., Green, R.F., Gry, C., Hutchings, J.B., Jenkins, E.B., Linsky, J.L., Malina, R.F., Michalitsianos, A.G., Savage, B.D., Shull, J.M., Siegmund, O.H.W., Snow, T.P., Sonneborn, G., Vidal-Madjar, A., Willis, A.J., Woodgate, B.E., York, D.G., Ake, T.B., Andersson, B.-G., Andrews, J.P., Barkhouser, R.H., Bianchi, L., Blair, W.P., Brownsberger, K.R., Cha, A.N., Chayer, P., Conard, S.J., Fullerton, A.W., Gaines, G.A., Grange, R., Gummin, M.A., Hebrard, G., Kriss, G.A., Kruk, J.W., Mark, D., McCarthy, D.K., Morbey, C.L., Murowinski, R., Murphy, E.M., Oegerle, W.R., Ohl, R.G., Oliveira, C., Osterman, S.N., Sahnow, D.J., Saisse, M., Sembach, K.R., Weaver, H.A., Welsh, B.Y., Wilkinson, E., and Zheng, W., Overview of the Far Ultraviolet Spectroscopic Explorer mission, *Astrophys. J.* **538**, L1–L6, 2000.

Neupert, W.M., Epstein, G.L., Thomas, R.J., and Thompson, W.T., An EUV imaging spectrograph for high-resolution observations of the solar corona, *Sol. Phys.* **137**, 87–104, 1992.

Nichols, J.S., and Linsky, J.L., The final archive and recalibration of the International Ultraviolet Explorer (IUE) satellite, *Astron. J.* **111**, 517–536, 1996.

Pauluhn, A., Rüedi, I., Solanki, S.K., Lang, J., Pike, C.D., Schühle, U., Thompson, W.T., Hollandt, J., and Huber, M.C.E., Intercalibration of SUMER and CDS on SOHO. I. SUMER detector A and CDS NIS, *Appl. Opt.* **38**, 7035–7046, 1999.

Pauluhn, A., Rüedi, I., Solanki, S.K., Schühle, U., Wilhelm, K., Lang, J., Thompson, W.T., Rüedi, I., Hollandt, J., and Huber, M.C.E., Comparison of quiet-Sun radiances measured by SUMER and CDS on SOHO, *Space Sci. Rev.* **97**, 63–66, 2001a.

Pauluhn, A., Rüedi, I., Solanki, S.K., Schühle, U., Wilhelm, K., Lang, J., Thompson, W.T., Hollandt, J., and Huber, M.C.E., Intercalibration of SUMER and CDS on SOHO. II. SUMER detectors A and B and CDS NIS, *Appl. Opt.* **40**, 6292–6300, 2001b.

Pauluhn, A., Lang, J., Schühle, U., Solanki, S.K., Wilhelm, K., Thompson, W.T., Pike, C.D., Rüedi, I., Hollandt, J., and Huber, M.C.E., Intercalibration of CDS and SUMER, this volume, 2002.

Rees, M.H., Physics and chemistry of the upper atmosphere. Cambridge University Press, Cambridge 1989.

Reeves, E.M., and Parkinson, W.H., Calibration changes in EUV solar satellite instruments, *Appl. Opt.* **9**, 1201–1208, 1970.

Reeves, E.M., Timothy, J.G., Withbroe, G.L., and Huber, M.C.E., Photometric calibration of the EUV spectroheliometer on ATM, *Appl. Opt.* **16**, 849–857, 1977.

Sahnow, D.J., Moos, H.W., Ake, T.B., Andersen, J., Andersson, B.-G., Andre, M., Artis, D., Berman, A.F., Blair, W.P., Brownsberger, K.R., Calvani, H.M., Chayer, P., Conard, S.J., Feldman, P.D., Friedman, S.D., Fullerton, A.W., Gaines, G.A., Gawne, W.C., Green, J.C., Gummin, M.A., Jennings, T.B., Joyce, J.B., Kaiser, M.E., Kruk, J.W., Lindler, D.J., Massa, D., Murphy, E.M., Oegerle, W.R., Ohl, R.G., Roberts, B.A., Romelfanger, M.L., Roth, K.C., Sankrit, R., Sembach, K.R., Shelton, R.L., Siegmund, O.H.W., Silva, C.J., Sonneborn, G., Vaclavik, S.R., Weaver, H.A., and Wilkinson, E., On-orbit performance of the Far Ultraviolet Spectroscopic Explorer satellite, *Astrophys. J.* **538**, L7–L11, 2000.

Sakao, T., Tsuneta, S., Hara, H., Shimizu, T., Kano, R., Kumagai, K., Yoshida, T., Nagata, S., and Kobayashi, K., The XUV Doppler Telescope (XDT), *Sol. Phys.* **187**, 303–333, 1999.

Schmidtke, G., Woods, T.N., Worden, J., Rottman, G.J., Doll, H., Wita, C., and Solomon, S.C., Solar EUV irradiance from the San Marco ASSI – A reference spectrum, *Geophys. Res. Lett.* **19**, 2175–2178, 1992.

Schühle, U., The cleanliness control program for SUMER/SOHO, in: UV and X-Ray Spectroscopy of Astrophysical and Laboratory Plasmas, *Proc. 10th International Colloquium*, (eds. E.H. Silver and S.M. Kahn), Cambridge University Press, 373–382, 1993.

Schühle, U., Thomas, R., Kent, B.J., Clette, F., Defise, J.-M., Delaboudinière, J.-P., Fröhlich, C., Gardner, L.D., Hochedez, J.-F., Kohl, J.L., and Moses, J.D., Summary of cleanliness discussion: Where was the SOHO cleanliness programme really effective? this volume, 2002.

Schühle, U., Brekke, P., Curdt, W., Hollandt, J., Lemaire, P., and Wilhelm, K., Radiometric calibration tracking of the vacuum-ultraviolet spectrometer SUMER during the first year of the SOHO mission, *Appl. Opt.* **37**, 2646–2652, 1998.

Schühle, U., Hollandt, J., Pauluhn, A., and Wilhelm, K., Mid-term radiance variation of far-ultraviolet emission lines from quiet-Sun areas, *ESA SP*-**463**, 427–430, 2000a.

Schühle, U., Wilhelm, K., Hollandt, J., Lemaire, P., and Pauluhn, A., Radiance variations of the quiet Sun at far-ultraviolet wavelengths, *Astron. Astrophys.* **354**, L71–L74, 2000b.

Schühle, U., Curdt, W., Hollandt, J., Feldman, U., Lemaire, P., and Wilhelm, K., Radiometric calibration of the vacuum-ultraviolet spectrograph SUMER on the SOHO spacecraft with the B detector, *Appl. Opt.* **39**, 418–425, 2000c.

Thomas, R., 20:20 vision; SOHO cleanliness, this volume, 2002.

Thompson, W.T., McMullin, D.R., and Newmark, J., Comparison of CDS irradiance measurements with SEM and EIT, this volume, 2002.

Wilhelm, K., The SUMER spectrometer for SOHO (The Red Book), 1990, attn.: later revisions until 1995.

Wilhelm, K., Curdt, W., Marsch, E., Schühle, U., Lemaire, P., Gabriel, A.H., Vial, J.-C., Grewing, M., Huber, M.C.E., Jordan, S.D., Poland, A.I., Thomas, R.J., Kühne, M., Timothy, J.G., Hassler, D.M., and Siegmund, O.H.W., SUMER – Solar Ultraviolet Measurements of Emitted Radiation, *Sol. Phys.* **162**, 189–231, 1995.

Wilhelm, K., Lemaire, P., Curdt, W., Schühle, U., Marsch, E., Poland, A.I., Jordan, S.D., Thomas, R.J., Hassler, D.M., Huber, M.C.E., Vial, J.-C., Kühne, M., Siegmund, O.H.W., Gabriel, A., Timothy, J.G., Grewing, M., Feldman, U., Hollandt, J., and Brekke, P., First results of the SUMER telescope and spectrometer – Solar Ultraviolet Measurements of Emitted Radiation – on SOHO. I. Spectra and spectroradiometry, *Sol. Phys.* **170**, 75–104, 1997.

Wilhelm, K., Woods, T.N., Schühle, U., Curdt, W., Lemaire, P., and Rottman, G.J., The solar ultraviolet spectrum from 1200 Å to 1560 Å: A radiometric comparison between SUMER/SOHO and SOLSTICE/UARS, *Astron. Astrophys.* **352**, 321–326, 1999.

Wilhelm, K., Schühle, U., Curdt, W., Dammasch, I.E., Hollandt, J., Lemaire, P., and Huber, M.C.E., Solar spectroradiometry with the telescope and spectrograph SUMER on the Solar and Heliospheric Observatory SOHO, *Metrologia* **37**, 393–398, 2000.

Wilhelm, K,. Schühle, U., Curdt, W., Dammasch, I.E., Hollandt, J., Lemaire, P., and Huber, M.C.E., Solar vacuum-ultraviolet radiometry with SUMER, this volume, 2002.

Woodgate, B.E., Tandberg-Hanssen, E.A., Bruner, E.C., Beckers, J.M., Brandt, J.C., Henze, W., Hyder, C.L., Kalet, M.W., Kenny, P.J., Knox, E.D, Michalitsianos, A.G., Rehse, R., Shine, R.A., and Tinsley, H.D., The Ultraviolet Spectrometer and Polarimeter on the Solar Maximum Mission, *Sol. Phys.* **65**, 73–90, 1980.

Woods, T.N., and Rottman, G.J., Solar EUV irradiance derived from a sounding rocket experiment on November 10, 1988, *J. Geophys. Res.* **95**, 6227–6236, 1990.

— 6 —

20:20 Vision and SOHO Cleanliness

RON THOMAS
former ESA/ESTEC, Noordwijk, The Netherlands
private Whiteoaks, Monkmead Lane, West Chiltington, UK

A summary of the SOHO cleanliness efforts, from spacecraft design to in-flight actions, is given. The measures taken to ensure an as stringent as possible cleanliness programme and their outcomes are critically reviewed.

6.1 Introduction

Firstly, I am greatly honoured to have been invited to give this paper especially as I retired from ESA in 1998. However, my present status means that I have not had full access to the records from the project time so I must apologize if many of the statements I make are without substantive references. I hope to point out many of the areas of cleanliness control which are based on opinions rather than cold scientific data, but which, with the benefit of 20:20 hindsight, appear to have been justified by the results each instrument has returned in the past five years, double the minimum contractual life. I must also qualify my statements as being personal, from one inside the ESA project team: a rather blinkered view of the sum of the activities leading to SOHO.

The 20:20 vision of the title is also linked to the concept of perfection, implying here that the performance of the instrument optics and detectors would not be compromised by the degrading effects of contamination, whether by dust particles or by molecular deposition. I propose to discuss these effects briefly, reviewing the controls applicable sequentially from instrument design through spacecraft integration and test, launch and post-launch activities. I shall also discuss possible molecular contamination modeling as could have been applied to instruments and as was applied at spacecraft levels.

6.2 Planning Phase

6.2.1 Cleanliness Guidelines

One of the first tasks I undertook on joining the SOHO Project team in late 1989 was to produce a Cleanliness Control Plan (see *ESA SOHO EID-C* [1990], especially Section 5), somewhat misnamed, but spelling out for those instrument teams with low sensitivity to cleanliness hazards advice of the greater risks and ways to minimize their effects on more critical hardware. This plan was written specifically for SOHO already knowing which instruments were planned and how the spacecraft was to be built even if the final layout of ‘black boxes’ was still fluid. I am quite sure that the teams for the critical instruments

were familiar with the recommendations, but no criticisms were raised even if some of the ESA contractors were reluctant to acknowledge the implications. A series of workshops supported by Jim Austin of Ball Bros. reinforced the message among the instrument teams, leading to beneficial changes in at least one VUV test area.

Design advice given was to ensure that optical boxes were arranged to eliminate sources of contamination, both particulate and molecular and to facilitate cleaning to remove dust trapped in assembly. I use the electronic concept of sources and sinks for cleanliness, with examples of dust sources being mechanisms, sliding surfaces and, in rare cases, paint-films degraded by poor processing. Molecular sources are more widespread: paints, potting materials, lubricants and plastics of all kinds being typical. The sinks for dust are the slits, mirrors and detectors of the optics, though in most instruments dust particles will not collect preferentially in any one area. Molecular sinks are all too often the detectors since these are usually cooled for low noise and the residence time for molecular species increases by a factor of ten for a 25 °C reduction. For SOHO, the fascination of staring at the Sun in the ultraviolet, brought the danger, for several instruments, of polymerisation of the contaminating species, leading to permanent degradation. Here the danger is greatest at the input window, if present, as the illumination is there most intense, while the risks are greater at shorter wavelengths. Taking MDI as an example, its input window, while in full sunlight, passed only red light, with a bandwidth of only 5 nm and so, within the instrument, became almost immune from polymerisation.

6.2.2 Early Flight

One early recommendation was that instruments should be slow to open doors to maximize time for outgassing, particularly since science was only planned for the halo orbit, which was expected to be reached some five months after launch. An unstated reason was that time would be required for the attitude-control capabilities to be demonstrated and mis-pointing with an open optics path might lead to overheating of black paint at the instrument ‘front ends’ or polymerisation of early outgassed products.

6.2.3 Assessment of Needs

Roughly at the end of phase B, I was asked to assess each instrument from the point of view of cleanliness to verify that all were capable of success. Dry-gas purging was considered essential for the majority of instruments while the practicality of using individual purge carts was poor. Hence I advocated the fitting of a common purge system for the payload module (PLM) and a shared purge cart. Since the purge gas could be a common mode failure for all the instruments concerned, that implied a cart with high quality molecular, particulate and humidity filters, with two bottles and a spectrograph to enable monitoring of the molecular cleanliness of the gas. This became expensive in both capital and manpower terms, but autonomy allowed intervention to be at one week intervals.

6.2.4 Spacecraft Layout

The design of SOHO lent itself rather well to cleanliness of the payload though improvements in certain areas were adopted. The division into service and payload modules was the most important feature, for almost all of the electronics units could be housed

within the service module (SVM) and it was feasible to arrange a collective venting of outgassed products via the $-X$ end, as remote as possible from the 'business ends' of the instruments. (X, Y and Z refer to spacecraft coordinates.) The instrument electronics and a relatively low number of service units could be fitted to the outside of the PLM box structure, mainly at the $-X$ end. These units were to be covered with thermal blankets which could have the secondary function of collecting unit outgassing and redirecting it away from the $+X$ surface of the spacecraft. A very few electronic boxes had to be housed close to the $+X$ surface, with several mounted on a floor just below that. In the first designs, the volume between these planes would have vented around the VIRGO sensor, directly into full-intensity sunlight and close to several instrument apertures. That was avoided by increasing the gas flow impedance around VIRGO and arranging a low impedance vent, facing $-X$, adjacent to UVCS.

6.2.5 Assessment

Almost all instruments chose to enclose their optical systems to allow close thermal control and stray-light protection with the benefit that contamination from external sources was thereby minimized. Their optical surfaces were susceptible to contamination from particulates and chemical deposition, the latter most likely where the detectors were operated at cold temperatures for low noise. With the additional adoption of shutters, which would be closed throughout virtually all of ground testing, the risks of instrument contamination of either type became controllable, with the possible exception of thermal vacuum (TV) exposure. This isolation of instruments from the spacecraft and from each other also had political benefits; any contaminated instrument was likely to be self-contaminated and therefore each instrument team had to do what was practical to eliminate dust generators and to control outgassing, while the spacecraft level risks were almost confined to guaranteeing the cleanliness of the purge and the TV exposure.

Assembly and test activities at spacecraft level remained a concern since the contractors had offered a standard class 100 000 cleanroom for both activities, with some test work in less clean conditions. At length, Matra Marconi Space (MMS, Toulouse) accepted to complete the PLM in class 1000 conditions and a 'clean tent' was erected over the spacecraft in much of its time at Intespace for test preparation and mechanical testing. The PLM was assembled first at MMS (Portsmouth) and, in spite of the care taken to limit particle deposition, witness-plates under the hardware sometimes showed high levels of deposits. Given the complexities of the mechanical integration with the electrical harnesses (including test hardware for vibration and thermal testing) I rather doubt that those levels could have been improved by practical measures. The solution was, and is, to vacuum clean all surfaces at reasonable intervals, certainly before closing volumes by the addition of other boxes or installing thermal blankets.

That philosophy broke down later in two ways. Firstly, multilayer insulation (MLI) using indium titanium oxide (ITO) as an external coating can carry enough charge to attract and retain particles while attempts to remove them often release new particles from the operator's clothing. Secondly, the MLI internal to the Atlas fairing was not cleaned to that standard, while time and contractual difficulties prevented further cleaning operations. The thermal lining of the inner shroud had been cleaned in a class 100 000 facility before delivery, but was non-conductive and attracted charged particles after unpacking. Admittedly the particles probably remained attached to the shroud during launch and separated

with it. By design, the spacecraft and instruments were effectively closed throughout the pre-launch and launch activities.

6.3 Implementation Phase

6.3.1 Verification

One deficiency was the verification of the cleanliness inside each instrument. Dust can be measured in several ways. We are familiar with the definition of cleanrooms or benches as class 100 000 or 100, which refers to the number of half-micron particles[1] present in a cubic foot of air downstream of the cleanroom filter (there are also as many as 700 particles of >5 microns size in the class 100 000 air stream). That quantity can be measured by meters which sample the air, but that is a poor guide to the number of particles that may become trapped in hardware (more details see *ESA PSS-01-201*). Please note that at the recommended air flow for a cleanroom of 90 ft min^{-1}, 1.3×10^{10} half-micron particles pass over the hardware per day in a flow cross-section of 1 ft^2 (1 ft = 30.48 cm = 0.3048 m). Given the box-like forms of instruments and spacecraft, turbulent flow will lead to some fallout, at least of the larger particles. It is possible to use witness-plates to trap some of these particles and the fallout can be quantified in classes of size or summed as 'obscuration' factors: meaningful if optical transmission rather than scattering is the prime concern. However, the real problem is that there is no way that witness-plates can be placed in the critical areas of an instrument and still less is it practical to allow removal of the plates at regular intervals for counting particles; in fact the intervention is likely to introduce more particles than were collected in the passive intervals.

In principle, verification of molecular cleanliness could use the instrument optics but not usefully in the ultraviolet. More practically it depends on quartz-crystal monitors (QCMs), usually temperature-controlled, and several of these were used in the system-level thermal vacuum test phase for SOHO. Such QCMs could be fitted inside instruments, though complexity is added by the desirability of cooling them to at least 25 °C below that of the coldest optical element. Again, the QCM cannot be located at the most optically-critical location. This latter disadvantage is reduced if the box is virtually closed since outgassed molecules will find, and be retained by, the coldest surfaces within the box. Again, witness-plates could be fitted inside the box for periodic removal and measurement, but no more conveniently than for particle verification.

6.3.2 Particles

These fall into two classes, with the larger and denser being of mechanical origin caused by machining swarf either trapped in crevices of the assembly or perhaps generated while screws are being tightened or when moving mechanisms are operated. Such particles may be visible to the naked eye, particularly if a strong, grazing-incidence light is used as an aid to inspection. Lower density particles are generated by people and include hairs, skin particles, lint from clothing and paper debris. The largest of these can be seen most easily if illuminated by 'black' light, as they often fluoresce, but the finer particles may be overlooked. There are plastic tapes (with clean adhesives) that may be used to lift particles

[1] 1 micron = 1 μm = 10^{-6}m

too small to see without optical aids. These are most often used for verification that a surface is clean, either by manually counting the number of particles within certain size-classes in a given area, or by using camera-scanning of optically-enlarged views of the tape to automate counting. Reasonably efficient cleaning may be achieved by the use of a vacuum-hose, possibly with either a (bottled) gas jet or an artist's brush, but a few large lint-fibres often appear in the course of even careful cleaning.

To minimize the number of particles within an assembly it is recommended to:

1. Design the inner surfaces of the optical enclosure to be as smooth as possible, even polished if that is optically acceptable.

2. Use generously radiused corners between inner surface planes.

3. Avoid blind holes drilled from the inside, and preferably fit screws from the inside.

4. If screw mechanisms are needed (for focusing), try to fit shields (bellows or telescopic) over the screws to avoid wear- or lubricant-debris escaping to the optics. If this is impossible, try to shield the motors, gears and bearings of mechanisms from a direct view of optical elements.

5. Take special care with harnesses; the insulation can attract charged particles and the bundling of cables makes cleaning difficult. The use of an overall sleeve is one way to retain particles within it, but note that a shrink-sleeve stiffens the harness and may increase the quantity of outgassing; a better solution may be to use a flat cable.

6.3.3 Molecular Cleanliness

Some of the above recommendations apply also for molecular cleanliness but additionally:

1. Only use materials known to be clean in the application (no plasticisers).

2. As item (1) is too idealistic, at least minimize the quantities, in volume and exposed areas (the larger and more deleterious molecules have to diffuse their way through the bulk) and that may reduce the outgassing rate to acceptable values. Overcoating the exposed areas with materials to still further reduce diffusion rates may be worthwhile.

3. Accelerate the outgassing by vacuum baking before the critical optics are installed or apply dry-gas purging.

4. Consider adding cold surfaces to preferentially trap outgassed material and so protect critical optics.

5. Note that anodised aluminium has a much higher surface area at molecular level than is apparent; polish or paint to block the pores.

6. Honeycomb structures should use perforated cores and the outer skin of the structure should be vented (1 mm diameter holes at 100 mm spacing for example).

7. Note that lubricants used in the conductor drawing process for cables may be trapped under the insulation and may exude in vacuum; a sensible precaution might be to seal the ends with a potting compound, combined with the sleeve as suggested for particle control of cables.

8. Remember that an Electronical Ground Support Equipment (EGSE), used near optics in assembly or test, does not use space-clean materials and becomes warm or hot in use and so will outgas; at least direct fan-assisted exhausts away from the optics.

9. Where a detector is the coldest item in an optics enclosure, have recourse to local, intermittent heating to drive off any condensed material; try to ensure that the emitted material does not return to the detector on recooling.

6.4 System Test Phase

6.4.1 Mechanical Testing at System Level

Acceptance testing of large spacecraft involves much handling in buildings that are difficult to clean and it is rare for facilities to do more than meet the general particle cleanliness level of a 100 000 cleanroom given the need for overhead cranes, acoustic chambers, vibration and mass properties test equipment. Under this classification I would also add electromagnetic test facilities, partly because of the need for cranes but also recalling the fact that the walls and ceilings are covered with conductive foams, impractical to clean and liable to release carbon-loaded dust with age.

At equipment and instrument level, it may be practical to wrap the hardware in clean plastic but at spacecraft level complete coverage is impossible. For SOHO's tests a combination of clean tents and bags open only at their bases provided some protection as far as particulates were concerned, but transfers between these and the test hardware briefly expose the spacecraft to the basic test-hall cleanliness, much below that used in spacecraft assembly.

6.4.2 Thermal Vacuum Testing at System Level

As foreseen in EID-C, the system-level thermal balance test was a high contamination-risk operation and extraordinary measures were taken to minimize this risk. The most valuable measure was to insist on an in-chamber instrument purge system, used both in the first part of pumpdown and, more importantly, during recovery. Ideally, the latter operation would have relied solely on the instrument purge to refill the chamber before warming the shrouds, which, having been at 80 K throughout the tests, collected all the material outgassed from the spacecraft and otherwise might have been returned contamination to the latter's external surfaces. However, the duration of such a recovery phase would have exceeded a week and would have been very expensive. As a result a compromise was reached. The chamber was actually repressurised through the instruments to 1 mbar, at which pressure the molecular free path is ≈ 1 m, after which the shrouds could be warmed and the chamber repressurised via its normal system. Measurements of the material deposited on witness-plates attached to the outer surface of the spacecraft showed acceptable

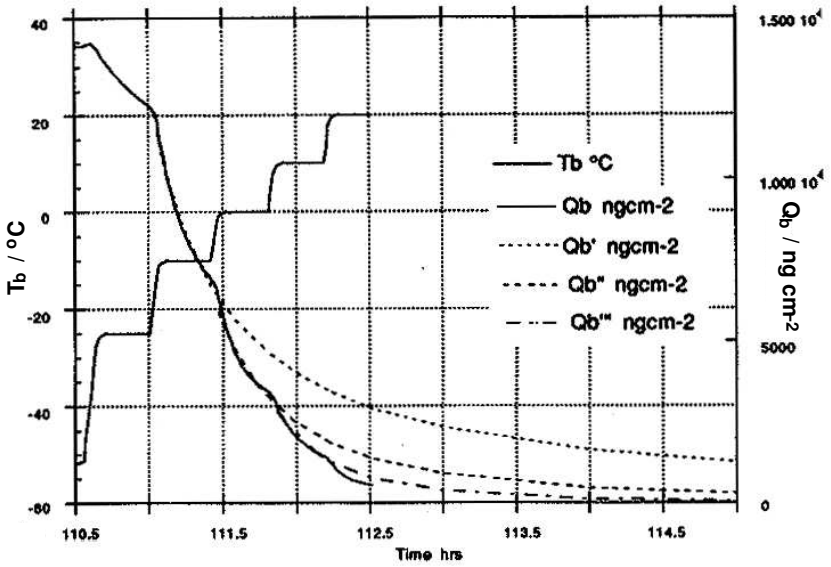

Figure 6.1: Quartz-crystal monitor QCM B warming at 110 hrs.

cleanliness after test, proving the recovery was effectively clean (but admittedly not proving it was necessary). Incidentally, one witness-plate showed anomalous deposition, which subsequent analysis indicated was associated with the local use of a non-flight-approved tape to support test instrumentation. Fortunately it was used in small quantities and in non-critical areas.

Giving more confidence in the cleanliness of the spacecraft during this test was the use of thermally-controlled QCMs located beside the PLM and looking at it. These were normally operated at -50 °C and sampled the outgassing, most of which was trapped on the shrouds behind the QCMs and at -190 °C. At various intervals these QCMs were heated in steps of 10 °C until $+30$ °C, the step durations being thirty minutes. These warming-cycles showed that 82 % of the deposits vanished at temperatures of $+10$ °C: below the expected faceplate temperatures of the instruments and of the $+X$ panel. Figure 6.1 shows one such warming cycle for QCM B at 110 hours into the thermal balance (TB) test. The dotted lines indicate extrapolation of the reducing mass deposits on the QCM as its temperature is varied; these indicate that if the temperature plateau of 0 °C had been held for some hours then the clean up would have been achieved without further warming. From these observations it was concluded that the $+X$ cleanliness-critical areas were not at risk from spacecraft outgassing.

6.5 Cleanliness Modeling

6.5.1 Background

Much of my cleanliness experience came from the Hubble Space Telescope (HST) programme when I was involved with ESA's Faint Object Camera (FOC) instrument (flying on HST until March 2002). This was designed to count photons in the range 121 nm to 800 nm at very low levels of illumination. To minimize molecular deposits on the optics, an extensive test programme was performed on most of the materials used within its optical enclosure and this was used to identify cleaner materials or a need for either 'space-conditioning' or shielding with metal foils. The tests applied were termed Vacuum Balance and Quartz Crystal (VBQC) tests and involved heating a small sample of the subject material in vacuum and measuring, continuously over several days, sample mass-loss and the mass gained by a QCM; for the FOC, a standard QCM temperature of -25 °C was used while the sample was heated to $+50$ °C. An early extension of the test increased the sample temperature to 80 °C or more for a short time to represent 'space conditioning', a process that could be applied to instrument hardware to drive off contaminants before sensitive detectors or optics were fitted. Some years later this VBQC test was further modified to progressively heat the samples to (+50, +75, +100 and +125) °C, with step durations of 24 hours [*van Eesbeek and Zwaal*, 1985]. I have reservations about the utility of the higher source-temperature tests (except as guidance for space conditioning) as the outgassed molecules may include thermal-degradation products.

The general observation was that the condensed material tended to be only about 1 % of the mass emitted while much of the material loss occurred in the first ten hours of pumpdown, being water vapour and adsorbed gases. Curve-fitting techniques were used to predict the outgassing over longer periods. For example, data taken at $+50$ °C were used to model the FOC contamination for the required five-year lifetime. Given that this temperature was some 33 °C above the FOC's controlled condition while the QCM was 42 °C cooler, it is clear that the predictions would be pessimistic, but narrower test-ranges would have required tests of much longer duration.

The model applied to the FOC is described here since, in principle, similar models could be applied to any nearly closed box. The FOC had a volume of 1 m^3 and an internal surface area of 8 m^2 which was coated with black paint. Ignoring the mirrors and filters of the optical path, the critical area of the detector faceplates was about 13 cm^2. From the VBQC test data for the paint in question (Figure 6.2), extrapolation of the curve fitting indicated that 0.003 % of the paint-film mass would be deposited on the optics after five years. The test showed that heating the paint to 80 °C for 24 hours eliminated much of the outgassing and a lower deposition rate would apply in the real case. Accordingly, the structure of the enclosure was vacuum-baked under those conditions before assembly. The temperature used was the highest acceptable to the structural engineers in view of the materials involved. With an applied paint mass of 10 mg cm^{-2}, the contamination expected would then be 300 μg cm^{-2}. This assumes that the sticking coefficient for the molecules concerned would be identical for quartz and the actual MgF_2 faceplates. The fact that much of the painted area was not in direct view of the faceplates is unimportant since the volume was effectively closed, hence any given molecule would find its way to the detector at some time after many collisions with other molecules or the enclosure

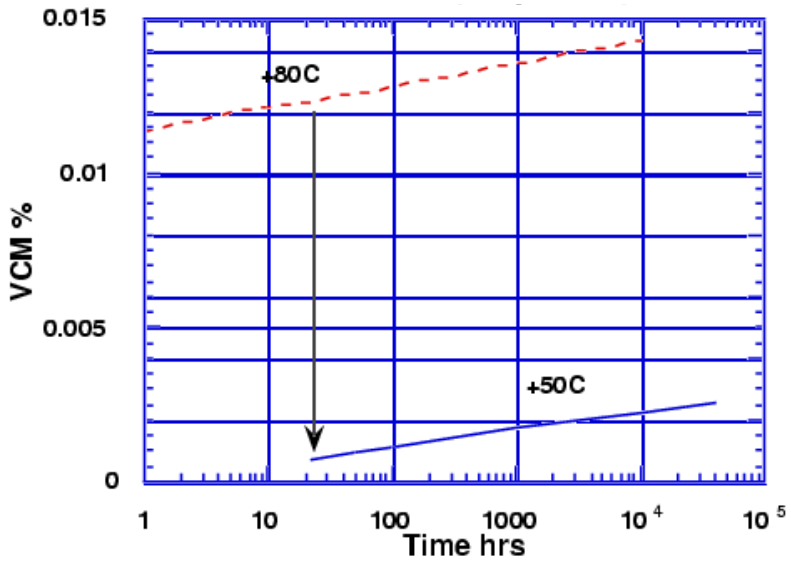

Figure 6.2: Vacuum Balance Quartz Crystal (VBQC) test, Chemglaze Z306 Paint. Upper curve shows measured Volatile Condensable Materials (VCM) data over 22 hours at +80 °C, then at +50 °C for a further 24 hours, indicating a saving of 85 % of that outgassing without vacuum baking.

walls. Similar calculations were performed for the deposition of molecules from the other materials used within the enclosure.

Naturally, if the FOC had had a large vent to space then corrections would have been required to allow for its pumping capacity, but light-tightness did not allow this and a large vent would have facilitated ingress of contamination from external sources.

Not mentioned so far is the fact that all these surfaces were at the same temperature (+17 °C). Had the detector-faceplate been at a substantially lower temperature then contamination residence times would have been much longer and the thickness of the deposit greater. In the absence of measured data it would be reasonable to use the Arrhenius factor: as a rough rule the residence-time and deposit-mass are extended by an order of magnitude per 25 °C cooling. This simple approach is invalid for temperature differences greater than about 25 °C. In such cases modelling following *van Eesbeek and Zwaal* [1985] is more realistic. Likewise the FOC never saw high levels of UV radiation since it was designed to count photons received from $m_V = 28$ stars. Residence times could otherwise have become infinite. Chemical effects between the surfaces and the deposited molecules were neglected.

Another material was used in significant quantity and had a less acceptable outgassing rate as measured in the VBQC test. The (potting) material choice was imposed by other considerations but was accepted for cleanliness since the exposed surface was in fact rather small. Thus the outgassing rate reduced to a much more reasonable figure. Ideally, the diffusion rate for molecules through the material should have been measured to justify this reduction, but tests to determine this failed to produce reliable data. For still another

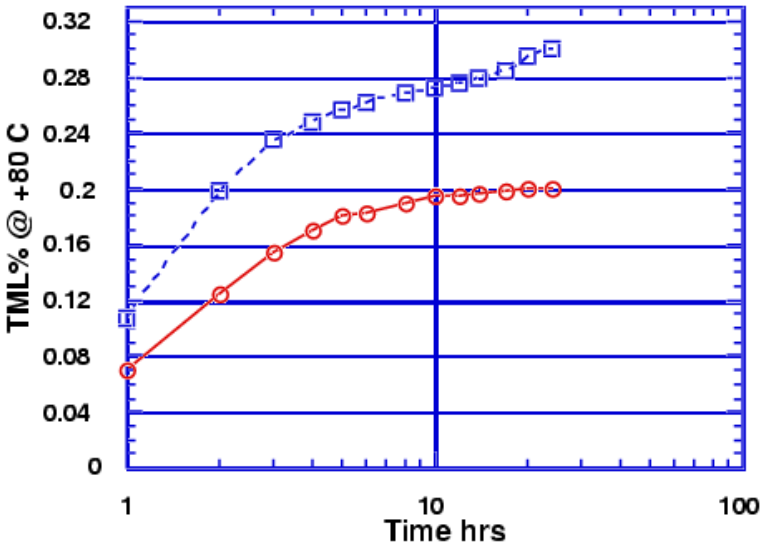

Figure 6.3: Total mass loss (TML) of Solithane at +80 °C. Upper curve in vacuum, lower at ambient pressure.

imposed material with a high outgassing-rate, a solution was found by glueing aluminium foil to the exposed surface of the material wherever possible, so reducing the exposed area from which molecules might be emitted.

6.5.2 Cleaning by Purging

One other technique is worth mentioning. Most of the other instruments of HST used gaseous N_2 purging once their structural enclosures were complete. The main reason for that was to reduce the moisture content of the carbon fiber reinforced polymer (CFRP) materials of their optical benches to a figure close to the orbital operational values, with the added benefits of reducing the volatile material content of the internal components. Such dry-gas purging is nearly as effective in removing potential outgassing as vacuum baking, which is rarely possible at elevated temperatures at instrument level. Figure 6.3 shows the results of one experiment with Solithane, heated at +80 °C, with the upper curve showing weight-loss versus time for a sample in high vacuum while the lower was heated at ambient pressure. Clearly the latter is less efficient at driving off volatiles, but it is much cheaper and easier to arrange [*Zwaal, unpublished data*].

6.5.3 Modeling External Cleanliness

Described above is one method of modeling contamination quantities within an instrument, but this needs extension to contamination from external sources. In flight these are contained in or on other instruments, the spacecraft “service” hardware and thrusters, while for the brief period of the launch, the environment produced by the launcher needs con-

sideration. This would have been difficult and expensive to completely model for SOHO and it was agreed to merely calculate the deposit on MDI's window since its size and location were well-known to Matra Marconi Space. For other instruments, a calculation of the deposit on a notional window at the instrument's aperture would have been possible, but the probability of a molecule entering that aperture would depend on its velocity, on the molecular-flow impedance of the aperture and on the probable gas-flow from the instrument. Note that a high flow-impedance also leads to a positive out-flow in early flight so reducing the probability of ingress. In general any attempt to calculate this probability is likely to be unreliable.

Even to calculate the contamination on an entrance window is difficult. The method adopted for SOHO was to estimate the outgassing from the spacecraft by summing all the rates from the materials of all the sources, knowing their masses, assuming the material reached, and uniformly coated, a sphere of 10 m diameter around SOHO and then that 1 % was reflected, not radially, back to the spacecraft. For simplification, no re-emission was considered, which is reasonable for the $-X$, Y and Z surfaces since their skin (thermal blanket) temperatures were extremely low.

Unfortunately, the VBQC test data were limited to total mass-loss (TML) rate data, which I do not consider really appropriate, especially for external modeling. Taking Kapton as an example, 99 % of its TML is water, or equally volatile material, lost within a few hours of entry to vacuum and does not condense on surfaces warmer than -25 °C. That loss of material is of little consequence given that the instrument apertures were closed for much longer.

The assumed isotropic distribution of outgassing was also false since the thermal blankets and boxes were generally vented towards the $-X$ direction (or outboard where this was not possible). The assumption was made as a simplification since the actual vent forms and locations were not well-known while in some cases a vent-flow to the $-X$ direction might be redirected by impinging on other hardware. The conclusion was that deposits would be about double the specified values, but would be mainly deposited prior to opening the instrument-sensor doors. It could well be the case that this modeling was an unnecessary luxury but the actions taken to control the outgassing direction I consider to be fully justified by the experience from NASA's *LDEF* (Long Duration Exposure Facility, 1984/90) and ESA's *EURECA* (EUropean REtrievable CArrier mission, 1992/93), where thick, brown deposits were associated with gaps or overlaps of thermal blankets. External modelling could be necessary for other spacecraft designs such as those where instruments cannot be closed or are scattered over the structure.

Modeling of likely contamination within a thermal vacuum chamber might have been more useful, though the practical experience reported above indicates that it was not necessary. The greatest risk comes in the repressurisation phase. As the chamber is brought back to room temperature, material may be released from the shrouds since they will have acquired almost all the spacecraft material outgassed throughout the test.

Contamination modeling of the plumes from the on-board thrusters was more useful in my opinion. Those firing towards the $+X$ direction (approximately) could have contaminated several instruments (mainly their radiators, where fitted), but, after considering the local surface temperatures, the residence times of the plume products was shown to be unimportant. Similar modeling of the launcher upper-stage, post-separation thruster operations showed acceptable deposits, even with unacceptable spacecraft attitudes (failed tip off springs, etc.).

6.6 Flight Experience

6.6.1 Long Term Results

After approximately five years of operation, none of the cleanliness-critical instruments has reported unacceptable degradation due to contamination. Two have reported some effects. EIT had been maintained under a moderate vacuum throughout ground-build and test but the pressure was limited to about 1 mbar. Launch brought a rapid improvement believed to be due to loss of water adsorbed during storage on the ground. However, the cold CCD tends to build up contamination and requires heating at intervals of one or now two months to restore performance. (See also next paragraph.) CELIAS/SEM has noticed a gradual deterioration consistent with an exponential accumulation of 15 nm of carbon over 1300 days. This sensor was a late addition to the payload and was fitted in a non-optimum location behind the $+X$ plane and close to thermal insulation.

6.6.2 Loss of Attitude Control

About thirty months after launch and just four months after the expiry of the contractually-required life, attitude control was lost by a combination of human error and wear of the gyros, and SOHO entered a flat spin with Sun on the spacecraft sides. This was highly undesirable from a contamination point of view because until then the sides had been cold-sinks for outgassing and the $+X$ end had been warm and, therefore, relatively free of contamination. In the flat spin this plate became very cold and the sides in turn became hot so releasing molecular contamination and risking some deposition on the $+X$ plate. After the near-miraculous recovery, there was a chance that some of this contamination might enter the instrument apertures. Examination of the temperature plots for the $+X$ plate does show a gradual increase with time, consistent with darkening of the reflector surface caused by polymerisation of outgassed and deposited material. The rate of temperature-increase fell with time, as expected, since outgassing rates gradually fall. Figure 6.4 (courtesy of J. Candé of ESTEC) shows the mean temperature (data points) of the Optical Surface Reflector (OSR) plate with a curve showing the predictions based on expected changes of absorption. The discontinuity at about 1060 days represents a reduction of heater power applied to the plate. Careful inspection of the plot does show a small step increase (≈ 0.5 °C) following the interruption of operations, but not one of any real concern. The danger of degrading the instruments was minimized anyhow since doors remained closed until two days or so after attitude recovery. There are no other indications on the spacecraft of any contamination which resulted from the loss of attitude.

Fortunately, the loss of control occurred after preparations for a planned manoeuvre and instruments with doors had closed them beforehand. EIT and SEM did not have closable doors and so were exposed to any release of contamination from the previously-cold MLI. The event resulted in long exposures to abnormal temperatures in the absence of spacecraft power and the varying attitude. SEM, EIT and CDS were hot and SUMER, VIRGO and LASCO were cold while UVCS was probably a little colder than usual. SEM did not see any adverse effects as a result of the eighty-day shutdown while EIT experienced a considerable gain in response, thought to be due to CCD temperatures of $+50$ °C, some 30° higher than the usual bake-out temperature. CDS detected no change in the GIS and NIS-2 responses, but significant loss was seen in NIS-1. The detector of NIS-1 is

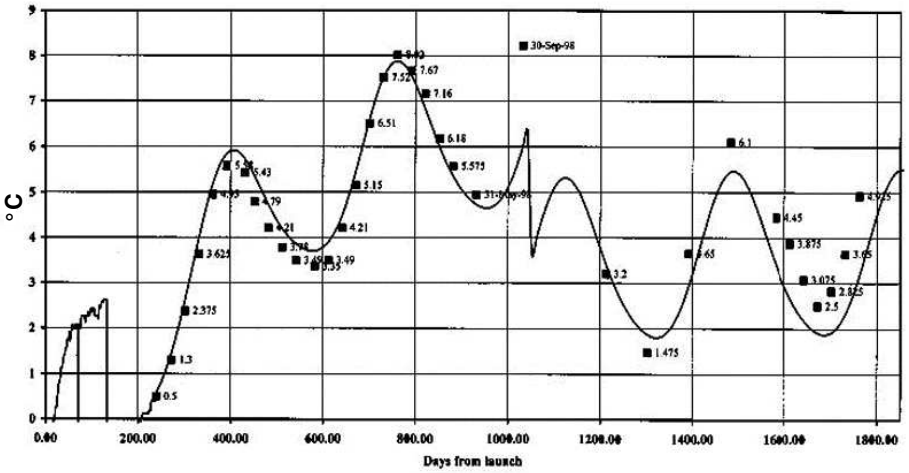

Figure 6.4: Mean Optical Surface Reflector (OSR) temperature versus flight days.

the same as that of NIS-2 so it is possible that some thermo-mechanical distortion of the grating may explain the change, noting that CDS may have reached $+80$ °C. SUMER experienced a 31 % loss of responsivity which is believed to be associated with the cooling of its primary mirror from the normal $+80$ ($+40$ if the door is closed) to -80 °C. The responsivity has not subsequently recovered so it is assumed that some of the material which condensed on the mirror has now been polymerised by unfiltered sunlight. VIRGO also experienced changed responses of 300 ppm in PMO6V-A and 70 ppm in DIARAD-L, but not in the redundant sensors. The explanation for that is unclear. Neither LASCO nor UVCS reported any performance degradation due to contamination in this phase. No reports of changes were available for the particle instruments CEPAC and CELIAS or for GOLF, MDI and SWAN. All of those instruments are less sensitive to molecular contamination than the others discussed above. From these results it is clear that SOHO's instruments have been remarkably successful in avoiding contamination-related degradation.

6.7 Conclusions

I believe SOHO has proved to be a clean spacecraft and more than met its ambitious requirements for performance. Less certain is whether a reduced programme of cleanliness-control would have achieved the same ends. The costs of the modeling analysis could have been saved, and maybe some of the anti-dust precautions at Intespace could have been dropped with more attention being paid to surface cleaning on completion of the test phases, but the risks could not be justified at the time.

I hope the date of the next ESA Sun-staring spacecraft will be earlier than 2020, but wish the experiments success equal to that of SOHO and, finally, that SOHO may continue to be of scientific value for years to come.

Acknowledgements

While I take responsibility for the views here expressed I must acknowledge the debt I owe to members of ESTEC's Materials Division, chiefly Arie Zwaal (now retired), M. van Eesbeek and J. Guyt. Thanks are also due to the personnel of MMS (now Astrium) responsible for the design, build and test of SOHO and in particular to Daniel Herbin for his help in producing a clean spacecraft.

Bibliography

van Eesbeek, M., and Zwaal, A., Outgassing and contamination model based on residence time, in the Third European Symposium on Spacecraft Materials in Space Environment, ESA SP-232, 1985.

ESA SOHO EID-C, part 5 in particular, delivered to each PI in 1990.

ESA PSS-01-201, Contamination and Cleanliness Control.

EURECA, EUropean REtrievable CArrier mission 1992/93, see e.g., ESA BR-16, ESA, 1983.
See also `http://www.estec.esa.nl/xrmwww/pubs/cat/prog/eureca.htm` and `http://heasarc.gsfc.nasa.gov/docs/heasarc/missions/eureca.html`.

LDEF, Long Duration Exposure Facility 1984/90, see e.g., `http://setas-www.larc.nasa.gov/LDEF/index.html` at NASA's Langley Research Center, Hampton, VA, USA.

II. Instrument Radiometric Calibration

— 7 —

The Radiometric Calibration of the Coronal Diagnostic Spectrometer

JAMES LANG
Rutherford Appleton Laboratory
Chilton, Didcot, Oxfordshire, UK

WILLIAM T. THOMPSON
L3 Communications Analytics Corporation
NASA Goddard Space Flight Center
Greenbelt, MD, USA

C. DAVID PIKE
Rutherford Appleton Laboratory
Chilton, Didcot, Oxfordshire, UK

BARRY J. KENT
Rutherford Appleton Laboratory
Chilton, Didcot, Oxfordshire, UK

CARL R. FOLEY
Mullard Space Science Laboratory, University College London
Holmbury St Mary, Surrey, UK

The radiometric calibration of the Coronal Diagnostic Spectrometer (CDS) on SOHO is discussed. Following a brief overview of CDS, its laboratory calibration, cleanliness programme, application of the calibration and in-flight calibration are described. The status of the calibration of the instrument five and a half years into a mission with a nominal lifetime of two years is given. Overall, the radiometric calibration is well-understood and continues to be satisfactory as the SOHO mission continues.

7.1 Introduction

The Coronal Diagnostic Spectrometer (CDS) on the SOHO spacecraft observes the Sun in the 15.0 nm to 78.5 nm wavelength range. Measurements of the intensities of spectral lines and line profiles allow the derivation of electron temperature, electron density, flow and abundance measurements for the plasma constituting the outer solar atmosphere. The international team building CDS recognised that to maximise the return from their investment it was necessary to have the best-available radiometric calibration. In addition, it was noted that previous vacuum-ultraviolet (VUV) and extreme-ultraviolet (EUV) experiments had problems whereby the responsivity of the instrument deteriorated while in space, curtailing the observing programme. This was attributed to contamination migrating to the optical surfaces and being irreversibly polymerised by the solar radiation. Thus, in common with the other SOHO experiments and the spacecraft team, a stringent cleanliness programme was introduced. In addition, the CDS team allowed a long, post-launch, out-gassing period of three months. This paper reports the status of the radiometric calibration of CDS five and a half years into a mission with a nominal lifetime of two years. The next section gives a brief overview of CDS, while the following three sections describe

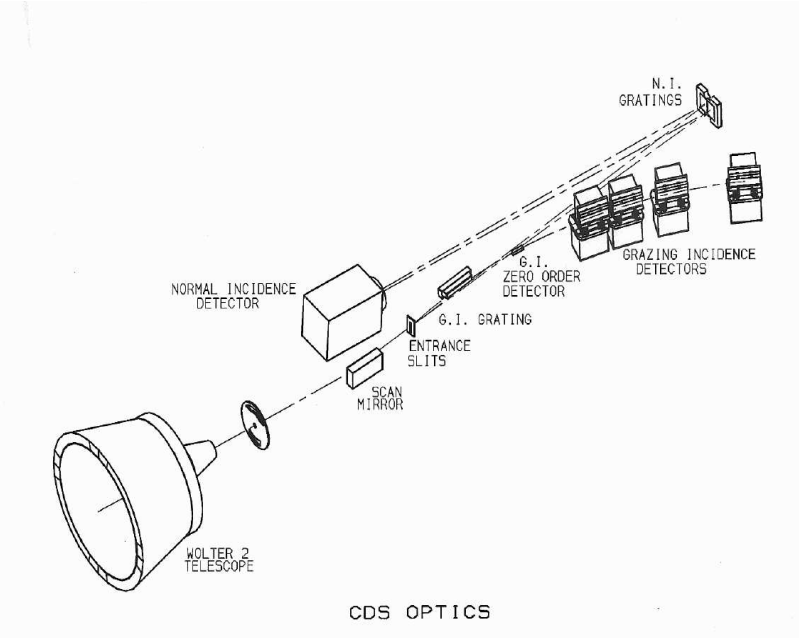

Figure 7.1: The CDS optical layout. The overall dimensions of CDS are 1.7 m by 0.50 m by 0.46 m. The distance from the entrance aperture to the entrance slits is 0.83 m and from the slits to the normal-incidence grating is 0.74 m.

the cleanliness programme, the laboratory calibration and the application of the calibration. Then the in-flight calibration situation is outlined. The penultimate section contains details of the status of the calibration and is followed by the conclusions.

7.2 Overview of CDS

CDS is a combined telescope and dual-spectrometer, and a full description has been given by *Harrison et al.* [1995]. The optical layout is shown in Figure 7.1. A grazing-incidence telescope in a Wolter-Schwarzschild II configuration is focused at the common entrance-slit of a pair of spectrometers via a scan mirror. Only two parts of the full figure of revolution are used. Two apertures immediately in front of the telescope and lightstops behind define two different optical paths, which illuminate the two spectrometers through the slit assembly. The field of view is $4'$ by $4'$ and full-Sun coverage is obtained by moving the whole instrument on its legs.

In the stigmatic Normal Incidence Spectrometer (NIS), a pair of toroidal gratings is used to give diffracted images of the entrance slit on the detector. The gratings are slightly tilted with respect to each other, allowing the two spectra to be imaged simultaneously on the two-dimensional detector, a micro-channel plate (MCP) intensified CCD [*Thompson et al.*, 1992]. The scan mirror is used to build up images by rastering the solar image across the slit. The wavelength ranges are for NIS-1 from 30.8 nm to 38.1 nm and for NIS-2 from 51.3 nm to 63.3 nm. In the astigmatic Grazing Incidence Spectrometer (GIS),

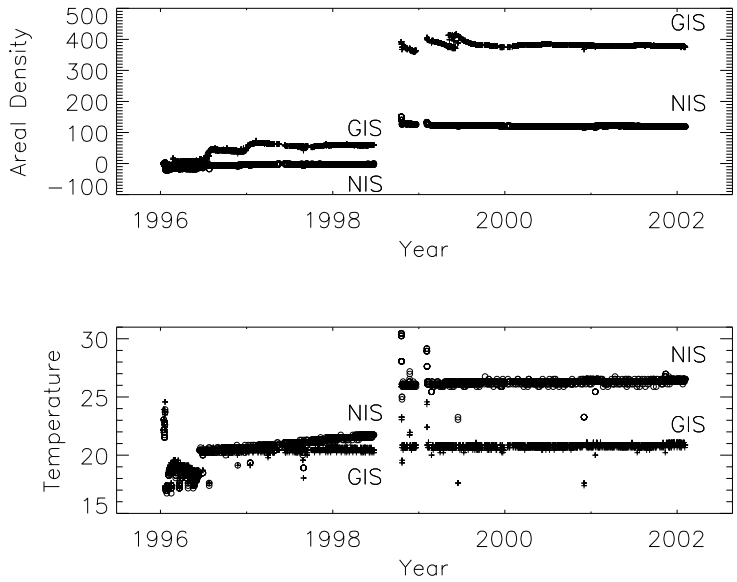

Figure 7.2: The QCM readings since the launch of SOHO. The NIS and GIS data are plotted as ∘ and + respectively. The temperature is in degrees Celsius. The areal density is in nanogram per square centimetre which is equivalent to a layer thickness of 0.01 nm cm $^{-2}$ for a material density of 1 g cm^{-3}. The areal densities measured are well below the allocated end-of-life density of 2 μg cm^{-2}.

radiation diffracted by a spherical grating at grazing incidence is dispersed on to four one-dimensional, windowless, triple Z-stack, MCP detectors with spiral anode (SPAN) readouts [*Breeveld et al.*, 1992; *Breeveld*, 1995]. Images are built up by moving both the scan mirror and slit. The wavelength ranges are for GIS-1 from 15.1 nm to 22.1 nm, for GIS-2 from 25.6 nm to 33.8 nm, for GIS-3 from 39.3 nm to 49.3 nm and for GIS-4 from 65.6 nm to 78.5 nm.

7.3 Cleanliness

The use of normal-incidence diffraction gratings and grazing-incidence optical components drove the contamination control requirements. The design of CDS to minimise contamination, the component cleaning procedures and screening programme, and the monitoring of the contamination in the instrument and its environment are described by *Kent et al.* [1993], *Kent et al.* [1994] and *Harrison et al.* [1995]. For in-flight contamination monitoring two quartz-crystal microbalances (QCMs) are used; one is mounted close to the NIS gratings and the other close to the GIS detectors.

The QCM readings since the launch of SOHO are given in Figure 7.2. The areal density plots are given in units of nanogram per square centimetre which, assuming a material density of 1 g cm^{-3}, equates to a layer thickness of 0.01 nm cm^{-2}. The figures show a relationship between areal density and temperature. This is due to two effects. Firstly, the

temperature of materials directly influences their out-gassing rates and, secondly, in spite of the QCM operating at the beat-frequency of the matched crystals, there is still a residual temperature-dependent frequency effect. The loss of attitude-control of SOHO (four months from loss to complete recovery) is clearly seen in the large temperature and areal-density steps in 1998. During the loss and much of the recovery, CDS was at a temperature of around 100 °C, well above the 0 °C to 40 °C range over which it had been tested in the laboratory. However, despite this, the deposited thickness on the quartz crystals, and hence on the optics, is still significantly less than 10 nm (the budget was 20 nm) after more than five years of operation. CDS is still significantly warmer after recovery and this probably relates to degradation in the performance of the multi-layer insulation which occurred during the loss-of-attitude.

7.4 The Laboratory Calibration of CDS

The laboratory calibration of CDS was achieved using a secondary standard which was radiometrically calibrated by PTB in Berlin using a primary standard of radiation, the BESSY I electron storage ring. A high-current, hollow-cathode discharge lamp provided the EUV radiation. It is very stable and reproducible (with a relative standard uncertainty of 7 or 8 %). The output from the 1 cm diameter hollow cathode is stopped down by a 0.6 mm diameter pinhole, which is at the focus of a Wolter II telescope used to provide a collimated output beam 5 mm in diameter. The calibration of the source (lamp and telescope) and its use for calibration is discussed by *Hollandt et al.* [2002]. A report on the calibration of CDS carried out at the Rutherford Appleton Laboratory (RAL) was prepared by *Bromage et al.* [1996]. This has been superseded by the work of *Lang et al.* [2000]. The former contained an error in the interpretation of the GIS line-widths; a factor of 1.6 (GIS-4) to 1.02 (GIS–1) instead of unity was mistakenly introduced to allow for the grating illumination during the calibration. In addition, the latter work included the effects of polarisation on the interpretation of the results, gave the responsivity as a function of wavelength for the NIS, a responsivity for NIS-2 in second order and a re-analysis of the GIS data. The relative standard uncertainty in the radiometric calibration was estimated at around 30 %. Considering the responsivity measurements for NIS-2, there was good agreement between the calibration and the predicted response, which was based on some measurements, for example, grating response and quantum efficiency (QE) of the detector. For NIS-2 2nd order and NIS-1 there was a factor of ten difference compared to the model and this is attributed to the QE used in the model. For the GIS there was about a factor of twenty compared to the model, but the model was much poorer than in the NIS case. Note that the relative uncertainties on the calibration are less than previous EUV satellite instrumentation, e.g., Skylab S055 35 % above 45 nm and a factor of two below 45 nm and over most of the range covered in second order [*Reeves et al.*, 1977], Skylab S082A 40 % for a line intensity ratio [*Dere et al.*, 1979] and a factor of two for a line intensity [*Dere*, 1982].

7.5 Application of the Calibration

The application of the calibration, including information on obtaining the necessary software and its documentation, is described by *Lang et al.* [2000]. The uncertainty budgets for various observations such as individual line intensities in NIS and GIS, line ratios between NIS-1 and NIS-2 and pairs of GIS channels, and line ratios within a single channel are also presented. The values and uncertainties given for the responsivities should be updated as detailed later in this paper. In addition, the burn-in correction uncertainties (as discussed later) should be included.

7.6 The In-flight Calibration Situation

Following the laboratory calibration there were eighteen months before launch and then four months (three months out-gassing and one for the commissioning) before CDS operations started in March 1996. There is a need to check if any changes took place during this period. In-flight measurements are necessary to monitor for burn-in at the fixed positions of strong lines on the detectors and for total dose for the GIS detectors. Also, observations of line ratios (for example, lines from a common upper level and density- and temperature-insensitive ratios) and analysis using the differential emission measure (DEM) method are used to check the calibration.

7.6.1 Rocket Underflight Calibrations

A direct check on the calibration can be obtained using rocket underflights. The rocket payloads are calibrated before and after the flights. As far as practicable, the same area of the Sun is observed simultaneously by the payload and CDS.

The EUV Grating Spectrometer (EGS) [*Woods et al.*, 1994, 1998b], which flew on a NASA-LASP rocket, gave joint observations of the full Sun on 15 May 1997. EGS was calibrated at the SURF synchrotron facility at NIST. The calibration had 21 % and 12 % relative uncertainties in the NIS-1 and NIS-2 bands, respectively. Comparison of the observations was used to refine the CDS NIS responsivities. A version of EGS is on board the TIMED satellite [*Woods et al.*, 1998a], and will be used to check the current CDS NIS calibration.

The NASA-GSFC-SERTS rocket has flown four times since the launch of SOHO: 1996, 1997, 1999 and 2000. It operates in the 30 nm to 36 nm wavelength range and is used for cross-calibration with NIS-1. The efficiencies of the individual optical elements are measured at the NIST synchrotron. For the last three flights, the whole payload has also been calibrated at RAL using the same equipment as for SOHO CDS [*Thomas*, 2002].

7.6.2 Intercalibration with SOHO SUMER

The SOHO Intercal_01 Joint Observing Programme (JOP) is run regularly. The CDS and SUMER elements of this allow comparison of measurements of the same area of the Sun with a) SUMER and NIS-2 at 58.4 nm (He I), 60.9 nm and 62.4 nm (Mg X) and, since August 1999, 63.0 nm (O V), and b) SUMER and GIS-4 at 77.0 nm (Ne VIII).

Note that SUMER was calibrated using a similar hollow cathode with a normal-incidence telescope, the combination also being calibrated using the BESSY I storage ring [*Hollandt et al.*, 2002]. It has its own in-flight calibration programme [*Wilhelm et al.*, 2002].

7.7 Status of the Calibration

7.7.1 NIS

When analysing NIS observations, corrections have to be made to the data. The detector data need skew-line correction, debias correction, cosmic-ray cleaning and, in rare instances, corrections for non-linearity in response. To allow for the pixel-to-pixel variation in responsivity of the detector (a few percent) a flat-field correction is necessary. This correction was determined before launch. However, as a slight shift in alignment was found after launch, the correction was modified but some small inaccuracies persist. For brighter lines this can be improved by making observations with the largest slit (90″ by 240″) while moving CDS using its adjustable legs.

Corrections for burn-in must also be made. The detector MCP suffers from degradation when exposed to radiation. As expected, its responsivity declines with photons detected (or effectively time) in a process called scrubbing. As the NIS optical elements are fixed, the emission lines fall more or less in the same area of the MCP. The effect is greatest for the strongest lines and they are said to be burnt into the detector. Most NIS observations are made using the two narrowest slits (2″ or 4″ by 240″) with another 5 % or so made using the largest (90″ by 240″) slit with a few isolated cases using other slits. The burn-in correction for the narrow-slit pair is determined using observations with the widest slit. Regular observations, suitably averaged to 'wash out' the effect of solar spatial emission variation, are used. The largest slit itself also causes burn-in and this is allowed for, although it is not straightforward. The combined narrow- and wide-slit burn-in correction for the strongest line in the NIS spectrum, He I 58.4 nm, is shown in Figure 7.3. The cores of the lines will burn in faster than the wings, and as the burn-in slows down after a depth of 30 % is reached (following an initial, rapid fall) the line profile will deviate from Gaussian. The correction does not entirely replicate the burn-in behaviour and additional corrections are applied. Some movement of the centre of the burn-in profiles with time has been identified. For example the lines at 58.4 nm and 63.0 nm appear to have shifted by 0.3 pixels between September 1996 and May 1998. From the start of CDS operations to the loss-of-attitude of SOHO (June 1998), the average width of the He I 58.4 nm line decreased by 10 %. A correction is available for those lines which show appreciable line-width variations. For the same period, the relative uncertainty of the burn-in correction appears to be 10 %.

During the early CDS operations, the wide slit was used to observe active regions. The He I 58.4 nm line is more intense in active regions than in the quiet Sun and the burn-in from active regions will be greater than that from the quiet Sun. The software is able to track this extra wide-slit burn-in from active regions. However, if another line brightens up significantly faster in active regions than He I 58.4 nm, then it will burn in even more and this extra burn-in will not be accommodated by the software. In fact, the Fe XVI 33.5 nm and 36.1 nm lines in NIS-1 only appear in plasma hotter than the quiet Sun. Their wide-slit burn-in is thus not known and is thought to be greater than any of

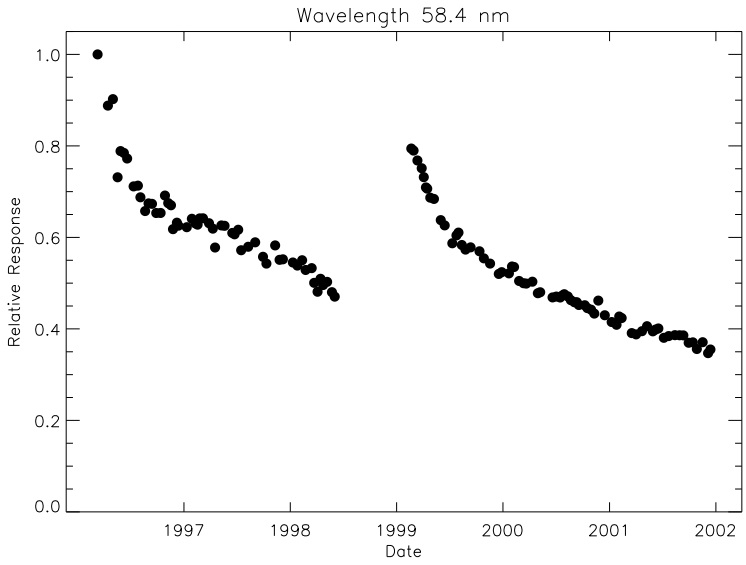

Figure 7.3: The correction for the burn-in of the He I 58.4 nm line as a function of time. As the brightest line observed by NIS, the 58.4 nm line requires the largest correction. Such corrections to the flat-field for all data are tracked and handled by the CDS analysis software.

the other lines in the NIS-1 waveband, except perhaps for the Mg IX line at 36.8 nm. Accordingly, for areas of the detector at these wavelengths there is some uncorrected loss of responsivity. Although the 33.5 nm line is twice as intense as the 36.1 nm line, the ratio of the instrument responsivity is almost the opposite, so both affect the detector by the same amount and their intensity ratio is as expected.

As noted earlier, during the loss and recovery of the attitude of SOHO, CDS was at a temperature well above the range over which it had been tested pre-launch. This baking caused an irreversible distortion in the instrument. The line-profiles changed, those for NIS-1 now exhibit broader wings while those for NIS-2 are asymmetrical showing a broadened long-wavelength wing. The location of the spectra on the MCP also changed, necessitating the development of a new burn-in procedure. Immediately after the recovery of SOHO, relatively high intensities were measured. This is attributed to the baking causing volatiles to migrate from the instrument to the detector, a process which reversed the scrubbing. The software now corrects for this partial reversal of the scrubbing. Subsequent exposure to radiation again removes the volatiles. Changes to the flat-field caused by exposure to radiation and baking are tracked and handled by the CDS analysis software. The post-recovery burn-in correction introduces an additional 10 % relative uncertainty.

The responsivity of the NIS as applied by the CDS software has been updated at various stages during the SOHO mission. Table 7.1 gives the version numbers, the dates when the versions were introduced and the basis for the update, for both NIS and GIS.

Table 7.1: CDS calibration versions, dates of introduction and the reason for the update.

Version	Date	Comment
1	16-09-1996	Points from *Bromage et al.* [1996] and shape from *Landi et al.* [1997].
1.1	22-11-1996	Corrected mistake in NIS-2 curve.
2	23-12-1998	NIS-1 and NIS-2 based on EGS results.
3	28-02-2000	NIS-1 based on EGS and SERTS.
4	21-05-2002	Re-analysis of EGS results to include wide-slit burn-in correction and NIS-2 2nd order responsivity introduced. GIS calibration updated from Version 1.

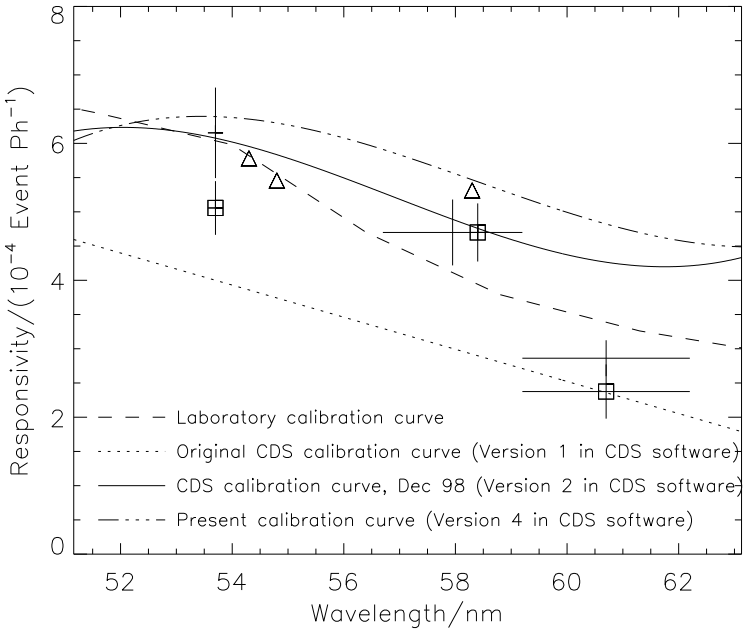

Figure 7.4: The CDS NIS-2 responsivity as a function of wavelength.

7.7.1.1 The NIS-2 Calibration

The original NIS-2 responsivity, as shown in Figure 7.4, was obtained from the preliminary report on the CDS laboratory calibration by *Bromage et al.* [1996] (the data point on the Version 1 curve) and the curve from the DEM analysis of NIS observations by *Landi et al.* [1997].

The laboratory responsivity curve comes from the laboratory measurements [*Lang et al.*, 2000] where the results at He I 53.7 nm and 58.4 nm were taken to define the calibration (mean of results at their mean wavelength). The lines were obtained simultaneously, with high intensity (minimising uncertainties due to poor statistics and background sub-

traction), and the source-spot image could be observed to check the optical alignment of the equipment. The slope of the curve was taken as that of the predicted response.

The next update to the calibration (Version 2) was that of *Brekke et al.* [2000] who compared simultaneous observations using NIS and the NASA-LASP EGS experiment. The estimated relative uncertainty in the responsivity varied from 15 % at 58.4 nm to 25 % at the ends of the NIS-2 waveband. *Del Zanna et al.* [2001] and *Del Zanna* [2002] published a relative calibration based mainly on the comparison of predicted and measured line-ratios. This was based on the work of *Del Zanna* [1999] which was finished and published before the wide-slit burn-in correction was adopted as the default. Thus the wide-slit burn-in correction was not taken into account. The resulting responsivity has bumps, which, qualitatively at least, match the wavelength regions where the correction is largest. Otherwise, the shape of their responsivity (normalised to *Brekke et al.* [2000] at He I 58.4 nm) agrees with that of the Version 2 calibration when the uncertainties are considered.

However, a re-analysis of the *Brekke et al.* [2000] responsivity has been undertaken to include the wide-slit burn-in correction, which was not available when the original analysis was done. This is the presently adopted calibration and is designated Version 4 in Figure 7.4. Its relative uncertainty varies from 18 % at 58.4 nm to 29 % at the ends of the NIS-2 waveband. In applying the calibration it should be remembered that the appropriate uncertainty of the burn-in should be added for the line being calibrated.

Note that the event-to-photon factor in the laboratory calibration is given with a relative uncertainty of 23 % but in fact at 58.4 nm is 9 % i.e., $(4.70 \pm 0.42) \times 10^{-4}$ events/photon. The re-analysed results of *Brekke et al.* [2000] yield $(5.44 \pm 0.98) \times 10^{-4}$ events/photon which is in good agreement, within the uncertainties, with the laboratory calibration.

The NIS-2 calibration appears the same before and after the accidental loss-of-attitude of SOHO. The calibration is confirmed by the results of ICAL01 JOP with SUMER [*Pauluhn et al.*, 1999, 2001, 2002b] where measurements of common areas of the Sun for the same lines by CDS NIS-2 and SUMER agree within their uncertainties.

7.7.1.2 The NIS-1 Calibration

The NIS-1 responsivity is shown in Figure 7.5. The original NIS-1 calibration (Version 1) was obtained from the preliminary report on the CDS laboratory calibration by *Bromage et al.* [1996] (the data point) and the curve from the DEM analysis of NIS observations by *Landi et al.* [1997].

The Version 2 calibration was taken from *Brekke et al.* [2000] who compared simultaneous observations using NIS and the NASA-LASP EGS experiment. This gave one point in the NIS-1 spectra, the Mg IX line at 36.8 nm. The responsivity was extended to other wavelengths by adopting the slope of the laboratory calibration. The relative uncertainty in the responsivity was estimated as 25 % near 36.8 nm, otherwise 45 % was assigned. The difference between the laboratory and rocket measurements is consistent with, and is attributed to, undetected misalignment during the laboratory work. Unlike the NIS-2 case, no single line was bright enough to allow the alignment to be checked.

Version 3 of the calibration was obtained by refining Version 2 using the analysis of coordinated measurements with the 1997 SERTS rocket flight [*Thomas*, 2002]. A re-analysis of the calibration has been undertaken to include the wide-slit burn-in correction, which was not available when the original analysis was done. The corrections at the times of

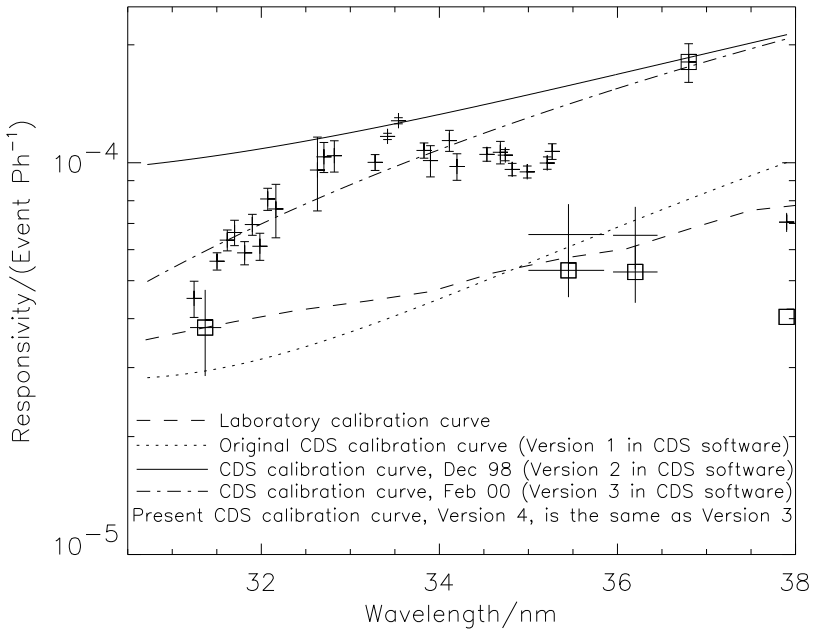

Figure 7.5: The CDS NIS-1 responsivity as a function of wavelength.

the 1997 EGS and SERTS flights are too small to affect the Version 3 calibration. Thus Version 3 and Version 4 of the NIS-1 calibration are identical.

As described in the NIS-2 section above, the *Del Zanna et al.* [2001] and *Del Zanna* [2002] relative calibration did not take the wide-slit burn-in correction into account and included the Fe XVI lines where there is uncorrected loss of responsivity. Their resulting responsivity has bumps which, qualitatively at least, match the regions where correction is needed. Allowing for this, the shape of their normalised responsivity agrees with that of the calibration when the uncertainties are considered.

The SERTS data, in conjunction with the EGS result, give a slope closer to that of Version 1. The relative uncertainty in the responsivity is taken as 15 % in the SERTS wavelength range and 25 % close to 36.8 nm. Again, in applying the calibration it should be remembered that the appropriate uncertainty of the burn-in should be added for the line being calibrated.

After the attitude-loss of SOHO, indications are that the NIS-1 lost responsivity, by about a factor 1.5 at around 36.8 nm. The situation at other wavelengths is unclear. Further analysis, using the line-ratios calibration technique and data from SERTS, EGS and TIMED will investigate this.

7.7.1.3 The NIS-2 Second-order Calibration

The laboratory measurement was made using He II 30.4 nm radiation, one of the measurements providing well-aligned data. The responsivity, as shown in Figure 7.6, was extended to other wavelengths using the model.

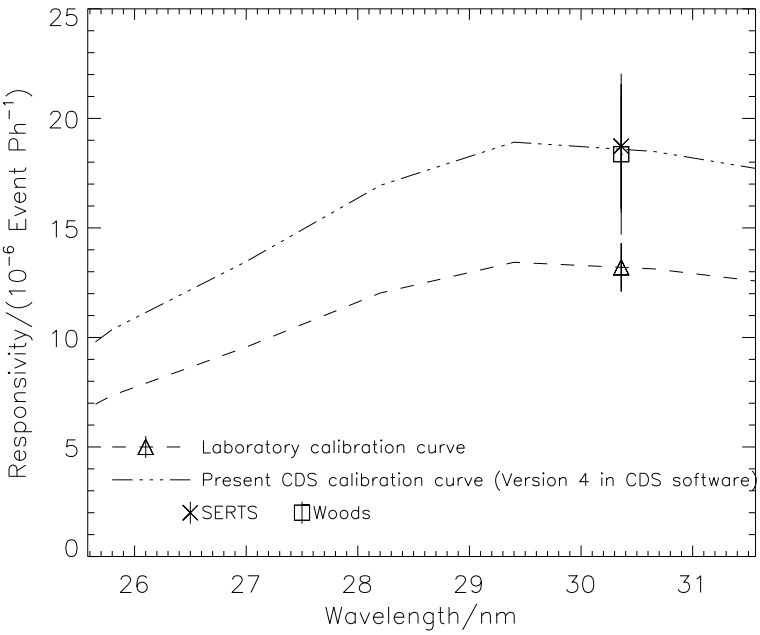

Figure 7.6: The CDS NIS-2 second-order responsivity as a function of wavelength.

The sounding-rocket data (EGS and SERTS 97) gave results for the He II 30.4 nm line, but no values were implemented in the software. The data have been re-analysed to include the correction for the wide-slit burn-in, and are shown in Figure 7.6. The rocket data do not agree within the uncertainties with the well-aligned laboratory data. It is interesting to note that *Lang et al.* [2000] present laboratory results whose alignment could not be confirmed, but which agree with the revised rocket measurements within the uncertainties. The weighted average of the rocket measurements is taken to define the calibration at 30.4 nm with a relative uncertainty of 12 %. The values given by *Lang et al.* [2000] are taken for the wavelength dependence of the responsivity and its relative uncertainty (25 %). In evaluating the calibration, as for the first orders, the uncertainty of the burn-in should be added for the line being calibrated.

Del Zanna et al. [2001] and *Del Zanna* [2002] give 1.36×10^{-5} events/photon for the responsivity at 30.4 nm and this updates the value in *Del Zanna* [1999]. As their results were normalised to that at 58.4 nm in Version 3 of the CDS calibration, this becomes 1.56×10^{-5} events/photon on re-normalising to the Version-4 value. As noted previously in the discussion of NIS-1 and NIS-2, these three papers did not include the wide-slit burn-in correction. The re-normalised value is in agreement within the uncertainties with the rocket measurements.

The NIS-2 second-order calibration appears to be the same (within 20 %) before and after the loss-of-attitude of the SOHO spacecraft. Further analysis will be done to confirm this.

7.7.2 The GIS Calibration

The GIS detector data need correcting for fixed-patterning and ghosting, electronics dead-time, and flat-field. Fixed patterning arises with many position-sensitive detectors where the measured quantities, in this case the collected charge, are digitised before being divided [*Geesmann et al.*, 1992]. This gives an excess of events in some bins with a corresponding decrease in others. To overcome this, the data are smoothed with a Hanning function which preserves the total events in the lines with a small increase in the width. About 40 % to 50 % of the spectrum in each detector is affected by ghosts. Data from the detector come as coordinate pairs which, when plotted, form a spiral with the spectral dimension along the length of the spiral and intensity given by the number of events at each position along the spiral. Electronic noise in the integrated flight equipment causes offsets in the analogue electronics which gives errors in the analogue-to-digital converters and hence positional uncertainty in the spiral. This causes the spiral to broaden, and, in regions of overlap of the spiral arm, there is movement of events from one wavelength to another. This produces the ghosts. Special software is used to correct the ghosting with a consequent increase in the uncertainty of the events in the spectral line. Three dead-times are allowed for; the net result is that event rates above 5×10^4 s^{-1} are ambiguous. The flat-field is checked routinely using electron-emitting filaments without solar radiation.

The main cause of change in responsivity across the detector is gain depression in the MCP. There are two forms, one long-term and the other short-term. The long-term form has two parts, global decay across the whole detector caused by out-gassing and ageing and differential decay caused by strong irradiation of the same pores of the MCP (burn-in). The He II 30.4 nm line observed in GIS-2 is affected by burn-in, but the detector is tuned to observe the other lines in its wavelength range and the He II line data are ignored. Burn-in has been found in other strong lines in the GIS detectors. Measurements made periodically using the electron-emitting filaments allow the burn-in to be tracked and correction factors can be applied using the CDS software. The other form of gain-depression is short-term and is count-rate dependent. If the count-rate is high enough, the MCP pores cannot recharge fast enough and the gain falls, causing loss of events. Pre-launch data are used to test for this and, if the correction exceeds 4 %, the pixel is marked as not calibratable.

Note that the GIS-2 detector was not operational between 26 April 1999 and 20 June 2001. High background levels were measured and these were ascribed to out-gassing. Once the out-gassing had finished, as tested by turning the detector on, the detector could again be used.

The Version 1 calibration of the GIS, shown in Figure 7.7, is based on the laboratory measurements. A polynomial has been fitted to the measured points to give the responsivity at all wavelengths. The laboratory responsivities had relative uncertainties of 30 %. However, noting that for the GIS it was not possible to check the alignment during the calibration, it could be anticipated that the laboratory responsivity may be too low.

Del Zanna et al. [2001] and *Del Zanna* [2002] found a responsivity at 73.2 nm which was a factor 1.9 higher than the laboratory results by measuring line-ratios between NIS and GIS. Re-normalising their result to allow for the change from Version 3 to Version 4 of the NIS calibration changes the factor to 2.2. However, the correction factor will need to be updated to allow for burn-in in the GIS and wide-slit burn-in in the NIS. The Intercal 01 JOP with SUMER and CDS allows the calibration of CDS GIS-4 relative to SUMER to

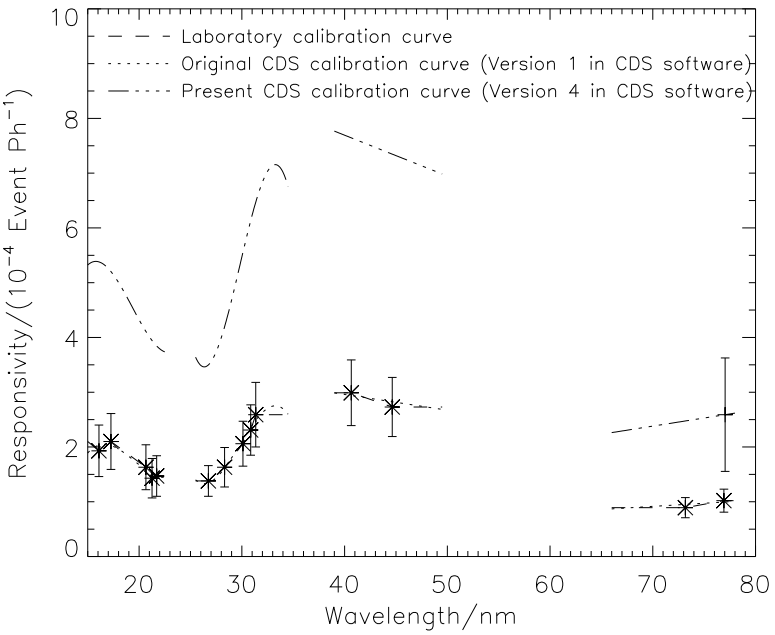

Figure 7.7: The CDS GIS responsivity as a function of wavelength. The version numbers are chosen to be consistent with those used for the NIS.

be evaluated. The results of *Pauluhn et al.* [2002a], with allowance for the GIS and NIS wide-slit burn-in, gave a responsivity a factor of 2.6±0.9 higher than the laboratory calibration, before the loss-of-attitude of SOHO. Following the recommendation of *Pauluhn et al.* [2002a], their result was used to define the Version 4 GIS-4 calibration at 77.0 nm. This is higher than the result of *Del Zanna et al.* [2001] and *Del Zanna* [2002] (uncorrected for burn-in) but consistent with it within the measurement uncertainties. The calibration at other wavelengths is extrapolated from the value at 77.0 nm using the laboratory calibration. The results from *Landi et al.* [1999], *Del Zanna et al.* [2001] and *Del Zanna* [2002] are compatible with the adopted Version 4 calibration noting that neither the NIS wide-slit nor GIS burn-in corrections were available when the work was done and were thus not applied. *Landi et al.* [1999] found no gross deviations from the laboratory responsivities in the relative calibrations for the GIS channels. *Del Zanna et al.* [2001] gave correction factors at a specified wavelength for each of the GIS channels and derived a wavelength dependence of the responsivity. These correction factors, when their uncertainties are considered, are consistent with the Version 4 calibration and with the results of *Landi et al.* [1999]. The uncertainty of the Version 4 calibration at 77.0 nm is estimated at 40 %, and at other wavelengths as 45 %. To this should be added the uncertainty in the burn-in for the line.

Del Zanna et al. [2001] and *Del Zanna* [2002] give responsivities without uncertainties for second order lines observed in GIS-3 and GIS-4. As for the second order responsivity of NIS-2, these values update the values in *Del Zanna* [1999]. A reasonable estimate of the relative uncertainty in the GIS second order responsivities is probably a factor of two.

The results of *Pauluhn et al.* [2002a] give a factor of 2.1±0.7 after the loss-of-attitude of SOHO, consistent with their result from before the loss-of-attitude. As discussed by them, the difference could be a statistical effect, or the SUMER post-recovery responsivity correction factor could be too high or the GIS responsivity could be different before and after the accident to SOHO, or even a combination of all three. Changes in the responsivity of GIS-4 at 77.0 nm are hard to detect because of the strong variability of the line.

7.8 Conclusions

The pre-launch calibration of CDS gave the baseline data for the calibration. The use of underflight calibration rockets has allowed the measured laboratory responsivities to be checked. For NIS-2 the responsivity adopted is based on a calibration obtained by a rocket flight. It agrees closely with the laboratory responsivity measured at 58.4 nm. In addition it has been confirmed by comparison with SUMER. For NIS-1, the laboratory measurements have been superseded by results from comparisons with coordinated measurements made using sounding rockets. The attitude loss of SOHO caused the calibration to change and this is still being investigated. For NIS-2 second order, the laboratory and rocket results almost agree within the combined uncertainties. For the GIS the laboratory calibration has been updated using results from the SOHO IntercalL01 JOP with SUMER.

All-in-all, noting the differences between the pre-launch and in-flight calibrations and the uncertainties added by applying the necessary flat-fielding, particularly the burn-in correction, the uncertainties in the calibration of CDS are still less than those for previous EUV satellite instrumentation in the CDS wavelength range.

The radiometric calibration of CDS is well understood and evolves as operations continue.

Acknowledgements

CDS was built and is operated by a consortium led by the Rutherford Appleton Laboratory and including the Mullard Space Science Laboratory, the NASA Goddard Space Flight Center, the Max-Planck-Institute for Extraterrestrial Physics, Garching and Oslo University. SOHO is a mission of international cooperation between ESA and NASA.

Bibliography

Breeveld, A.A., Ultraviolet detectors for solar observations on the SOHO spacecraft, PhD Thesis, University of London, 1995.

Breeveld, A.A., Edgar, M.L., Smith, A., Lapington, J.S., and Thomas, P.D., A SPAN MCP detector for the Coronal Diagnostic Spectrometer, *Rev. Sci. Instrum.* **63**, 673–676, 1992.

Brekke, P., Thompson, W.T., Woods T.N., and Eparvier, F.G., The extreme-ultraviolet solar irradiance spectrum observed with the Coronal Diagnostic Spectrometer (CDS) on SOHO, *Astrophys. J.* **536**, 959–970, 2000.

Bromage, B.J.I., Breeveld, A.A., Kent, B.J., Pike, C.D., and Harrison, R.A., Report of the pre-launch calibration of CDS, *University of Central Lancashire Report*, CFA/96/09, 1996.

Del Zanna, G., Extreme ultraviolet spectroscopy of the solar corona, PhD Thesis, University of Central Lancashire, 1999.

Del Zanna, G., Bromage, B.J.I., Landi, E., and Landini, M., Solar EUV spectroscopic observations with SOHO/CDS I. An in-flight calibration study, *Astron. Astrophys.* **379**, 708–734, 2001.

Del Zanna, G., The use of atomic data for the in-flight calibration of the CDS spectrometers, this volume, 2002.

Dere, K.P., Extreme ultraviolet spectra of solar active regions and their analysis, *Sol. Phys.* **77**, 77-93, 1982.

Dere, K.P., Mason, H.E., Widing, K.G., and Bhatia, A.K., XUV electron density diagnostics for solar flares, *Astrophys. J. Suppl. Ser.* **40**, 341–364, 1979.

Geesmann, H., Hanne, G.F., Stauffer, A.D., and Stauffer, J.A., The dangers of digitisation. An analysis of digitised position sensitive detectors, *Nucl. Instr. and Methods* **A307**, 413–419, 1992.

Harrison, R.A., Sawyer, E.C., Carter, M.K., Cruise, A.M., Cutler, R.M., Fludra, A., Hayes, R.W., Kent, B.J., Lang, J., Parker, D.J., Payne, J., Pike, C.D., Peskett, S.C., Richards, A.G., Culhane, J.L., Norman, K., Breeveld, A.A., Breeveld, E.R., Al Janabi, K.F., McCalden, A.J., Parkinson, J.H., Self, D.G., Thomas, P.D., Poland, A.I., Thomas, R.J., Thompson, W.T., Kjeldseth-Moe, O., Brekke, P., Karud, J., Maltby, P., Aschenbach, B., Bräuninger, H., Kühne, M., Hollandt, J., Siegmund, O.H.W., Huber, M.C.E., Gabriel, A.H., Mason, H.E., and Bromage, B.J.I., The Coronal Diagnostic Spectrometer for the Solar and Heliospheric Observatory, *Sol. Phys.* **162**, 233–290, 1995.

Hollandt, J., Kühne, M., Huber, M.C.E., and Wende, B., Source standards for radiometric calibration of astronomical instruments in the VUV spectral range traceable to the primary standard BESSY, this volume, 2002.

Kent, B.J., Swinyard, B.M., and Hicks, D.H., Contamination effects on EUV optics in the space environment, *Proc. SPIE* **1945**, 348–360, 1993.

Kent, B.J., Swinyard, B.M., and Martin, E.L., Contamination control and material screening for the extreme ultraviolet Coronal Diagnostic Spectrometer on SOHO, *Proc. SPIE* **2210**, 474–484, 1994.

Landi, E., Landini, M., Pike, C.D., and Mason, H.E., SOHO CDS-NIS in-flight intensity calibration using a plasma diagnostic method, *Sol. Phys.* **175**, 553–570, 1997.

Landi, E., Del Zanna, G., Breeveld, E.R., Landini, M., Bromage, B.J.I., and Pike C.D., Relative intensity calibration of CDS-GIS detectors on SOHO using a plasma diagnostic technique, *Astron. Astrophys. Suppl. Ser.* **135**, 171–185, 1999.

Lang, J., Kent, B.J., Breeveld, A.A., Breeveld, E.R., Bromage, B.J.I., Hollandt, J., Payne, J., Pike, C.D., and Thompson, W.T., The laboratory calibration of the SOHO Coronal Diagnostic Spectrometer, *J. Opt. A: Pure Appl. Opt.* **2**, 88–106, 2000.

Pauluhn, A., Rüedi, I., Solanki, S.K., Lang, J., Pike, C.D., Schühle, U., Thompson, W.T., Hollandt, J., and Huber, M.C.E., Intercalibration of SUMER and CDS on SOHO. I. SUMER detector A and CDS NIS, *Appl. Opt.* **38**, 7035–7046, 1999.

Pauluhn, A., Rüedi, I., Solanki, S.K., Schühle, U., Wilhelm K., Lang, J.,Thompson, W.T., Hollandt, J., and Huber, M.C.E., Intercalibration of SUMER and CDS on SOHO. II. SUMER A and B detectors and CDS NIS, *Appl. Opt.* **40**, 6292–6300, 2001.

Pauluhn, A., Lang, J., Breeveld, E.R., Solanki, S.K., and Schühle, U., Intercalibration of SUMER and CDS on SOHO. III. SUMER and CDS GIS, *Appl. Opt.*, in press, 2002a.

Pauluhn, A., Lang, J., Schühle, U., Solanki, S.K., Wilhelm K., Thompson, W.T., Pike, C.D., Rüedi, I., Hollandt, J., and Huber, M.C.E., Intercalibration of CDS and SUMER, this volume, 2002b.

Reeves, E.M., Timothy, J.G., Huber, M.C.E., and Withbroe, G.L., Photometric calibration of the EUV spectroheliometer on ATM, *Appl. Opt.* **16**, 849–857, 1977.

Thompson, W.T., Poland, A.I., Siegmund, O.H.W., Swartz, M., Levition, D.B., and Payne, L.J., Measurements of an intensified CCD detector for the Solar and Heliospheric Observatory, *Proc. SPIE* **1743**, 464–474, 1992.

Thomas, R.J., Underflight Calibration of SOHO CDS by SERTS-97, this volume, 2002.

Wilhelm, K., Schühle, U., Curdt, W., Dammasch, I.E., Hollandt, J., Lemaire, P., and Huber, M.C.E., Solar vacuum-ultraviolet radiometry with SUMER, this volume, 2002.

Woods, T.N., Rottman, G.J., Bailey, S. M., and Solomon, S.C., Vacuum-ultraviolet instrumentation for solar irradiance and thermospheric airglow, *Opt. Eng.* **33**, 438–444, 1994.

Woods, T.N., Bailey, S.M., Eparvier, F.G., Lawrence, G.M., Lean, J., McClintock, W.E., Roble, R.G., Rottman, G.J., Solomon, S.C., Tobiska, W.K., Ucker, G.J., and White, O.R., TIMED solar EUV experiment, *Proc. SPIE* **3442**, 180–191, 1998a.

Woods, T.N., Rottman, G.J., Bailey, S.M., Solomon, S.C., and Worden, J.R., Solar extreme ultraviolet irradiance measurements during solar cycle 22, *Sol. Phys.* **177**, 133–146, 1998b.

— 8 —

The Radiometric Calibration of the Extreme Ultraviolet Imaging Telescope

FRÉDÉRIC CLETTE, JEAN-FRANÇOIS HOCHEDEZ
Observatoire Royal de Belgique
Bruxelles, Belgium

JEFFREY S. NEWMARK, J. DANIEL MOSES
Naval Research Laboratory
Washington, DC, USA

FRÉDÉRIC AUCHÈRE
Universities Space Research Association/NASA GSFC
Greenbelt, MD, USA

JEAN-MARC DEFISE
Centre Spatial de Liège
Angleur-Liège, Belgium

JEAN-PIERRE DELABOUDINIÈRE
Institut d'Astrophysique Spatiale
Orsay, France

After a five-year effort, the analysis of the pre-flight and in-flight calibrations of EIT is finally yielding firm results. In this introductory overview, we will summarize what we learned "internally" from EIT itself. This includes the interpretation of the pre-flight calibrations, the original flat-field components (CCD, grid), the in-flight determination of the point-spread function and straylight and the compensation of the in-orbit response degradation. Based on this experience, we conclude with some suggestions of possible improvements to future calibrations, on SOHO and other planned missions.

8.1 Instrument Description

EIT, the Extreme ultraviolet Imaging Telescope experiment was designed to provide whole-disk images of the lower corona in four extreme-ultraviolet (EUV) bandpasses [*Delaboudinière et al.*, 1995; *Moses et al.*, 1997]. It consists of a normal-incidence Ritchey-Chrétien telescope using multilayer optics, with a back-side illuminated, thinned CCD sensor at the primary focus.

As illustrated in Figure 8.1, the components contributing to the EIT response are the visible-light rejection filters (transmittances of entrance-aperture filters, filter-wheel and straylight filters), the mirrors (reflectances and bandpasses), the CCD sensor (quantum efficiency), as well as some vignetting due to internal light-baffles. A large effort has been put forth into understanding the spectral response, the absolute calibration and the instrument

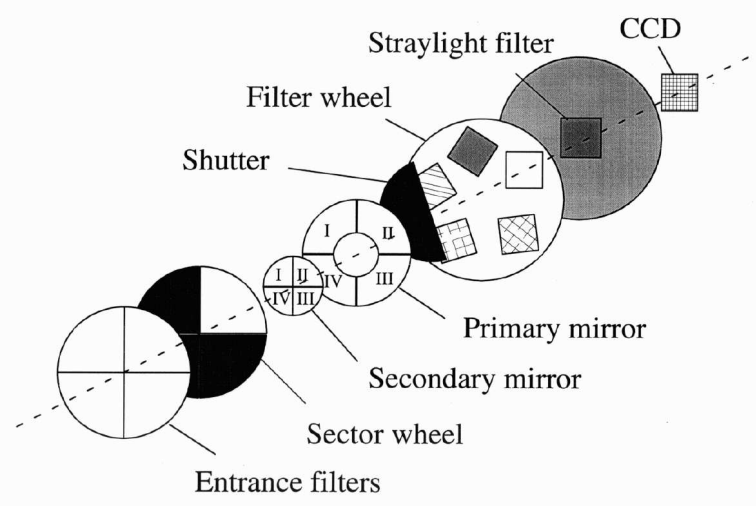

Figure 8.1: Optical components of EIT.

responsivity changes. This happened in two mains steps: the pre-launch laboratory characterization of a limited set of instrument properties and a comprehensive time-dependent radiometric calibration. This calibration was only achieved recently, several years into the SOHO mission, in part because this required data accumulation over a long time interval.

As EIT was among the very first EUV instruments based on normal-incidence multilayer optics, its initial calibration requirements were conservative ($\approx$ 100 %). However, the in-flight experience showed that much better accuracies were achievable and also essential for many scientific applications which emerged in the course of the SOHO mission. For instance, long-term solar cycle studies, made possible by SOHO's extended lifetime, require the compensation of slow instrumental trends. At the other extreme, short-term solar dynamics studies suffer from uncorrected sensor non-uniformities, as the solar rotation translates such spatial variations into fast random or periodic modulations. Therefore, the improved EIT calibration opens new fields of investigation, which were not considered among EIT's prime goals, but for which this EUV imager proved to be a unique source of information.

8.2 Pre-flight Calibration

The pre-launch calibration allowed the determination of component efficiencies (filters, mirrors, CCD) and the global instrumental efficiency as a function of wavelength: the absolute spectral response over the four EIT bandpasses. It also led to the determination of the initial CCD flat-field.

8.2.1 Spectral Response

The calibration measurements were carried out at the Institut d'Astrophysique Spatiale (IAS), in Orsay, France in 1993 to 1994 using synchrotron radiation from the Super-ACO

Table 8.1: Chronological table of instrumental configurations used for the EIT calibration. In Nov. 1993 and Sept. 1994, EIT was tested with its flight mirrors and filters and two different CCD cameras. The flight camera configuration uses the FM1 head with CCD3 and was thoroughly characterized in Dec. 1994. No end-to-end calibration of EIT could be done with the flight camera.

Date	Camera head	CCD sensor	Setup
Nov. 1993	FM1	CCD1 “Techno”	EIT telescope
July 1994	FM1	CCD1 “Techno”	camera only
July 1994	FM2	CCD2 “Flight”	camera only
Sept. 1994	FM2	CCD2 “Flight”	EIT telescope
Dec. 1994	FM1	CCD3 “Realflight”	camera only

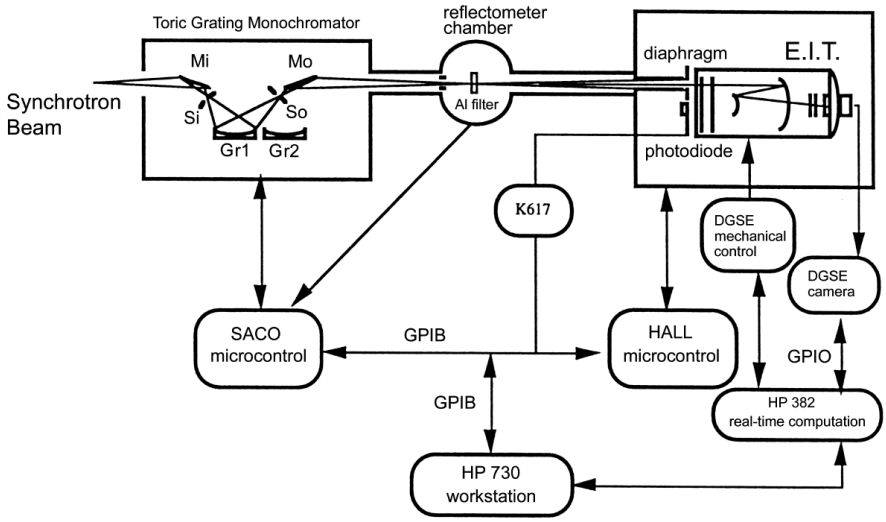

Figure 8.2: EIT calibration system at IAS.

positron storage ring [*Dhez et al.*, 1997]. A toroidal-grating monochromator allowed us to scan the whole EUV wavelength range observed by EIT. The standard of reference for all measurements was an IRD#925 Si photodiode calibrated by the National Institute of Standards and Technology (NIST, October 1993). This photodiode was placed in the incoming beam just in front of the EIT entrance pupil and alternately replaced by a square aperture of the same size. Three different CCD chips and two different camera heads were used in different configurations, which are summarized in Table 8.1. The calibration setup (Figure 8.2) and procedure are described in detail by *Song* [1995].

The analysis of these laboratory data has now been largely completed [*Dere et al.*, 2000; *Newmark et al.*, 2000a, b] and the results have been integrated in the EIT tools of the SolarSoftWare (SSW) library: for example `eit_prep`, `eit_parms`, `eit_flux`, `eit_temp`. Figure 8.3 shows the resulting EIT spectral response over the four EIT bandpasses.

The uncertainty budget published by Dere (Table V in *Dere et al.* [2000]) shows fairly high uncertainties, from 60 % to 150 % depending on the mirror quadrant, but is based on the discrepancies between a small number of spectral scans (geometrical averages). These conservative values can be considered as worst-case estimates and have subsequently been lowered, based on the in-flight calibrations (for example, see *Auchère* [2000]: 15 % instead of 75 % uncertainty at 30.4 nm).

8.2.2 CCD Flat-field Determination

Given the non-uniformity of the entrance synchrotron radiation beam, sequences of spatially displaced images were produced and each image set was processed using the Kuhn, Lin and Loranz algorithm (KLL; *Kuhn et al.* [1991]) to extract detector blemishes. Good flat-fields were obtained at two wavelengths: 17.1 nm and 28.4 nm (Figure 8.4, left). Those relative-correction maps were normalized to unity and have a relative standard uncertainty of 4 % (variable across the field-of-view). This correction is part of the SSW `eit_prep` tool. However, once in space, the CCD flat-field has been substantially modified, in particular in the strongest blemishes corresponding to sensor surface defects. The actual uncertainties are thus larger. Although no direct proof could be derived so far, this initial flat-field change may have been caused by chemical interactions with surface contaminants. Indeed, the existence of a thin water-ice deposit, which formed soon after launch, was firmly established through the initial changes in the EUV instrument responsivity and the presence of ice crystal patterns in the first EUV flat-fields, before the first detector bakeout of May 1996, which eliminated this ice.

8.3 In-flight Calibration: Flat-field and Other Diagnostics

Several components of the calibration could not be measured accurately on the ground and were extracted indirectly after launch from the solar images themselves.

8.3.1 Focal-filter Grid Correction

Several aluminium filters are located just in front of the focal plane: the fixed CCD straylight filter and the redundant filters on the filter wheel. To improve their mechanical strength, those filters are supported by a tungsten grid which casts an unsharp shadow-pattern on the CCD sensor (diffraction effects are negligible). This pattern is purely periodic (P = $\pm$21 pixels) and uniform over the field-of-view, but with a slight tilt angle relative to the edges of the CCD. It was extracted from smoothed solar images (8-day rotational averaging), by a Fourier transform and digital filtering (more than 40 harmonics).

An accurate correction pattern was derived out to the corners in the four quadrants and in the two main filter-wheel positions: Clear aperture and Al+1 redundant filter (Fig-

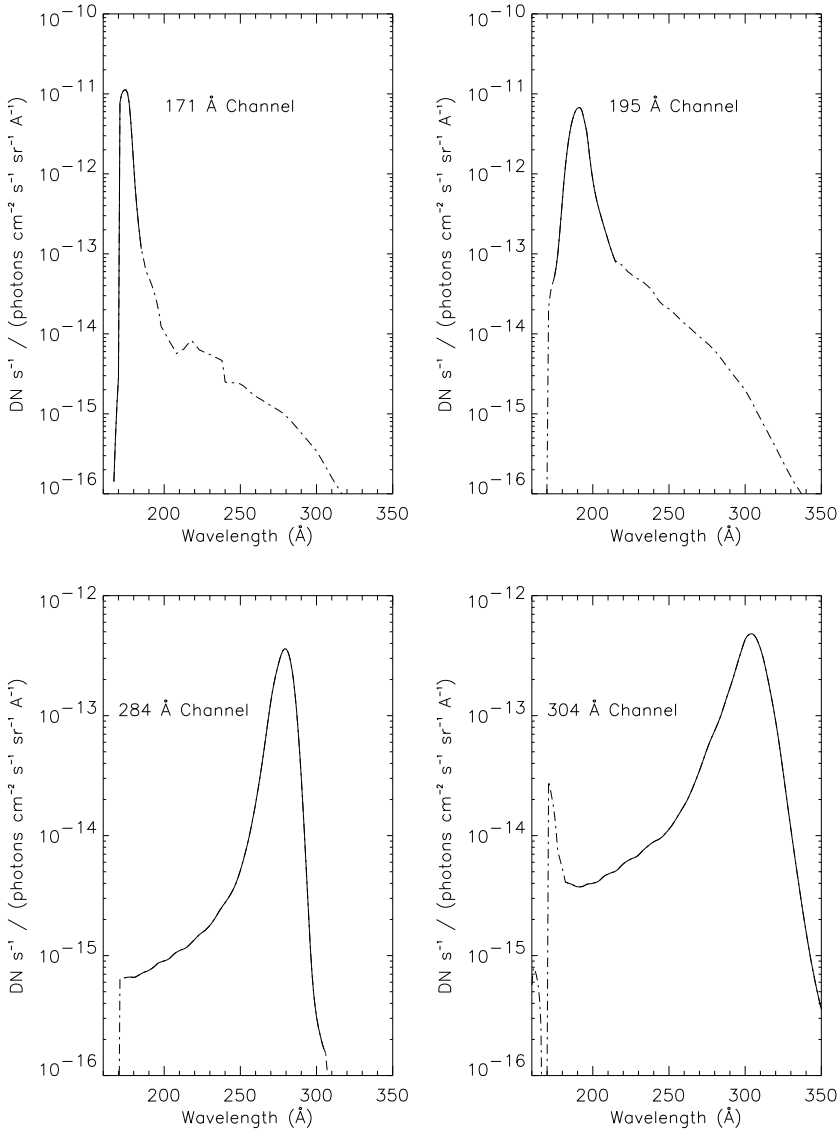

Figure 8.3: Instrument efficiencies for the four EIT bandpasses.

ure 8.4). The extracted patterns were normalized to unity and multiplied by the geometrical obstruction factor of the grid mesh. Those grid corrections are now part of the `eit_prep` tool, but too few images were made in the Al+2, Block-East and Block-West filter wheel positions to allow the extraction of a good correction-pattern for those filters. The amplitude of the grid modulation is large, amounting to 20 % peak-to-peak (5 % rms) in the

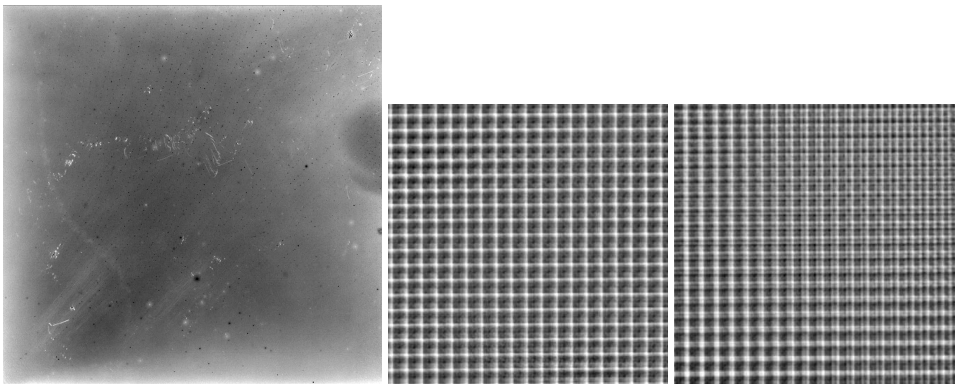

Figure 8.4: Pre-flight CCD flat-field (left) and the extracted grid pattern in the Clear (center) and Al+1 (right) filter-wheel positions, i.e., with the fixed focal Al filter alone or superimposed with the redundant Al filter on the filter wheel (only middle portions of the grids spanning 1/4 of the field-of-view are shown).

Clear position and 17 % peak-to-peak (3 % rms) in the Al+1 position. Furthermore, all grid patterns are modulating the radiation-induced ageing effects which are described below.

8.3.2 EIT Optical Properties

The core part of the EIT optical point-spread function (PSF) was determined by interferometry (wavelength: 633 nm) and wave-front error analysis [*Defise*, 1999]. In flight, the exact focus setting of the instrument has been established by using the sub-pixel decentering of the optical PSF associated with the asymmetrical entrance pupil of each mirror sector. The default thermal-focus setting, which has been maintained throughout the mission, has in fact a 253 μm defocus (0.33 pix decenter): the optical PSF core is 10 μm wider, causing a 50 % increase of the effective PSF width [*Defise et al.*, 1999].

Finally, using simultaneous EIT and MDI images taken during the SOHO offpoint of 3 to 4 April 1996, the plate scale was measured to be $(2.629 \pm 0.001)''$ per pixel [*Auchère et al.*, 2000].

8.3.3 In-flight PSF Wings and Straylight

The straylight and far-wings of the PSF were determined by combining different and independent pieces of evidence: occasional flare images (only in the 19.5 nm quadrant), relative off-limb straylight profiles from a SOHO controlled roll sequence (date: 20 March 1997; 12 positions; 30° steps, KLL extraction algorithm) and the absolute calibration provided over a few locations during the Mercury transit of 15 to 16 November 1999. The various data showed a good consistency and allowed us to derive an extended PSF profile (Figure 8.5), which is elongated along one diagonal and reaches a peak response of 60 %. This means that 40 % of the light at any position is diffused into the far wings. As the brightest sources are on the solar disk, the resulting straylight background is large off the

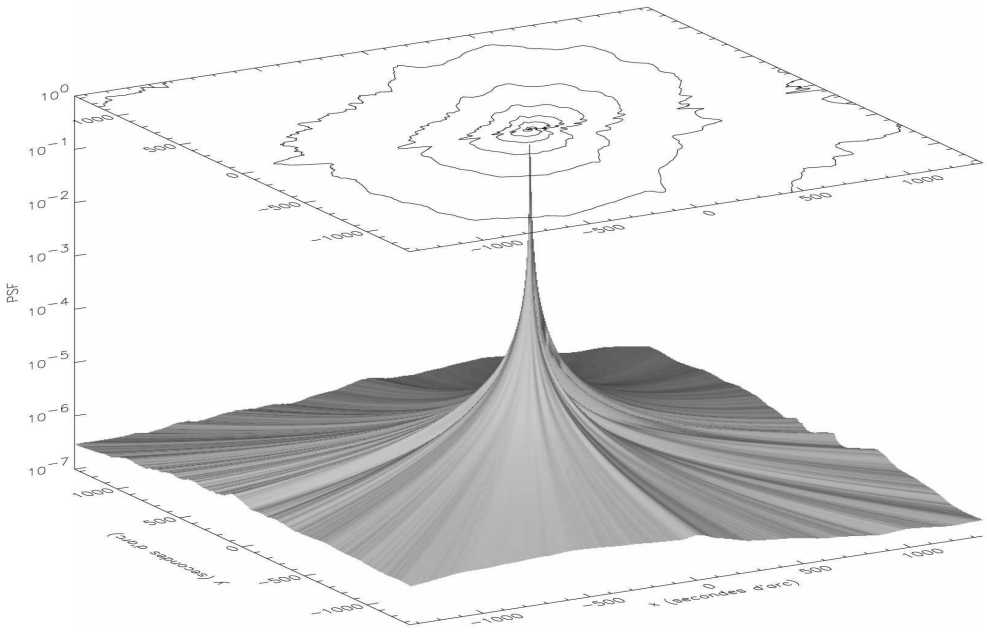

Figure 8.5: PSF extended wings as determined from flare images over a 2630″ square area (equivalent to the full EIT field-of-view), showing the asymmetry along a diagonal which can be attributed to the asymmetric pupil and baffling for each mirror quadrant.

limb: in 30.4 nm images, it reaches 40 % of the average local intensity at 1.2 $R_\odot$, 70 % at 1.4 $R_\odot$ and 80 % at 1.6 $R_\odot$(corners of the field-of-view) [*Auchère*, 2000; *Auchère et al.*, 2001]. As no straylight correction has been implemented in the software yet, radiometric measurements can thus be strongly biased in off-limb regions far from the limb.

8.3.4 Other Factors Affecting the Radiometric Calibration

For completeness, let us also mention the presence of light leaks due to tiny pinholes in the Al filters, which allow some visible light to reach the focal plane. One leak was present right after launch in 28.4 nm images at the North edge of the field-of-view (Clear filter position). In February 1998, new pinholes formed and severely affected all four bandpasses. Since then, all images have been taken with the Al+1 redundant filter, which has no detectable visible-light leak. The optical vignetting of the telescope was modelled by ray tracing and consists only of a small, smooth correction reaching a maximum of 6 % in one corner of the field-of-view [*Defise et al.*, 1999].

Finally, we found recently (2001) that the CCD sensor had a photometric offset between images taken at full resolution and those taken in the two-by-two binned mode (the difference is 5 DN[1]).

[1]DN = Digital Number; raw units of the analogue-to-digital converter in the CCD camera. 1 DN corresponds to 17 electrons in the case of EIT, which has a 14-bit converter, providing a 14 000 DN dynamic range.

This offset and a small, long-term drift of the offset are now corrected in the `eit_prep` routine.

8.4 In-flight Calibration of the Response Degradation

Early in the SOHO mission, it was recognized that the instrument response is undergoing a time-varying degradation. This radiation-induced loss of instrument efficiency has now become the largest correction factor in the EIT calibration. Details concerning the degradation and initial investigations have been discussed by *Moses et al.* [1997], *Defise et al.* [1997, 1998] and *Defise* [1999]. These papers have discussed the case for two sources of degradation, a condensate on the CCD and an EUV-induced spatially-localized decrease in charge collection efficiency (CCE). Complete details of the in-flight calibration of EIT are given in *Newmark et al.* [2002].

8.4.1 Degradation

The degradation process consists of several components which are difficult to separate. The two basic processes contributing to the degradation are the absorption by a surface contaminant of the EUV light, before it interacts with the CCD, and the reduction of CCE in the CCD due to EUV-induced device damage. The first component was significant during the first 2.5 years of the mission, until February to April 1998. During this latter period, most of the contaminant was apparently driven off (possibly related to the increase in pinholes in the front filter). Subsequently, the loss of spacecraft attitude control during the mission interruption (June to October 1998) resulted in significant heating ($> 30\,^{\circ}\mathrm{C}$) for the EIT CCD and annealed part of the electronic damage. The second component has continued to be significant throughout the mission. As the average EUV intensity in the coronal and transition-region images is highly non-uniform, the resulting burned-in flat-field pattern contains strong residuals of local solar-activity features.

The condensation of contaminant on the CCD is expected, since the detector is one of the coldest surfaces in the instrument. In anticipation of in-flight contamination, a cleanliness program was maintained in the construction of the instrument and heaters for the CCD were included in the design. Accumulation of contamination at a constant rate will result in an exponential decline in response. If no polymerization of an organic component is involved, then the condensate will evaporate rapidly during temperature cycling. The straylight baffling around the CCD unfortunately reduces the vacuum conductance out of the vicinity of the CCD, so that further outgassing during a temperature cycle is not feasible.

One can distinguish between the effect of an absorbing surface contaminant and the loss of CCE in the device. Since each interacting EUV photon generates more than one electron, the CCE can be determined by the comparison of the observed signal to the photon shot noise. However, the practical limitations of the CCE analysis from signal-to-noise measurements are significant. Since there is no EUV flat-field illumination capability on EIT, the signal-to-noise ratio must be determined from the solar illumination. The application of this technique to determine the portion of the cumulative degradation from ordinary operations which can be attributed to CCE degradation is discussed in *Defise et al.* [1997], based upon analysis of the Naval Research Laboratory (NRL) EIT Calibration Rocket

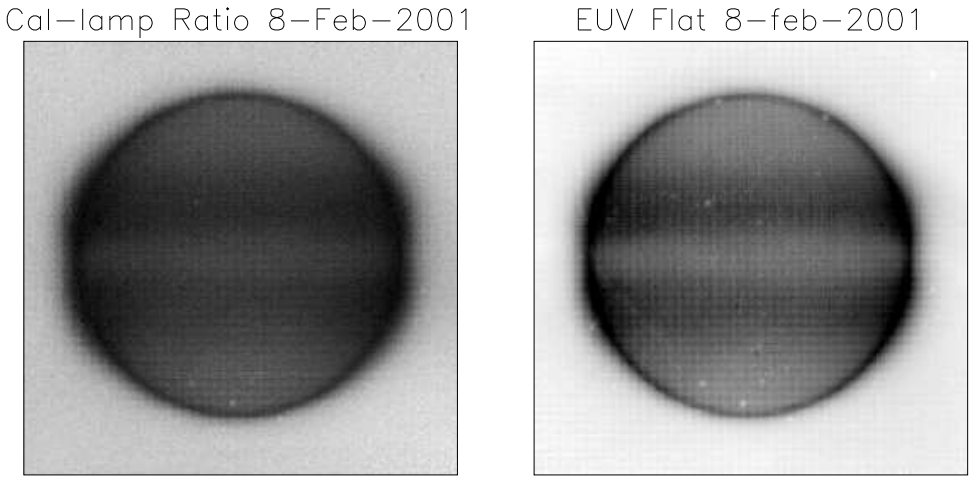

Figure 8.6: EUV flat-field derived from the SOHO offpoint manœuvre of 8 February 2001 (right) and the corresponding calibration lamp ratio (left).

(CalRoc) flown on 16 October 1997. However, the CCE analysis allowed us, for instance, to demonstrate that the degradation of the device for the 29 July 1996 shutter-hang event was totally due to CCE degradation.

8.4.2 Flat-fields

Additional information concerning the CCE decrease can be obtained by examining the visible-light calibration lamp (cal-lamp) images. Most thin condensate layers are transparent to visible photons, so these images should provide information only on the pattern of CCE loss. Indeed, although cal-lamp images do not give direct information in the EUV wavelength range, it was recognized by *Clette* [1998] using NRL CalRoc data that a monotonic relationship exists between the observed CCE loss, as determined above, and the loss of response observed in the cal-lamp images. This work has now been extended using EUV flat-fields derived from a series of offpoints of the SOHO spacecraft, using the KLL method.

Figure 8.6 (right) represents the EUV flat-field determined by *Auchère* [2000] using offpoints generated by spacecraft manœuvres on 8 February 2001. It is compared with an equivalent visible-light flat-field (left) obtained by taking the ratio of a cal-lamp image for that day with the first cal-lamp image taken before any EUV dose accumulated on the detector. Solar features are clearly visible in the flat-field in the form of a negative imprint of an average solar disk, plus limb brightening and plus active-region belts. However, as the Kuhn algorithm only gives relative gain variations, the absolute scale factor must be fixed separately. As the corners of the CCD (1.5 $R_{\odot}$) receive very little EUV radiation, we have assumed that the CCE loss is negligible here and we have thus rescaled the whole map to adjust the corners to unit gain.

Figure 8.7 is a scatter plot showing the relationship between the cal-lamp ratio (Cal-lamp at time t / Initial cal-lamp) and the EUV flat-field for two different days. Clearly,

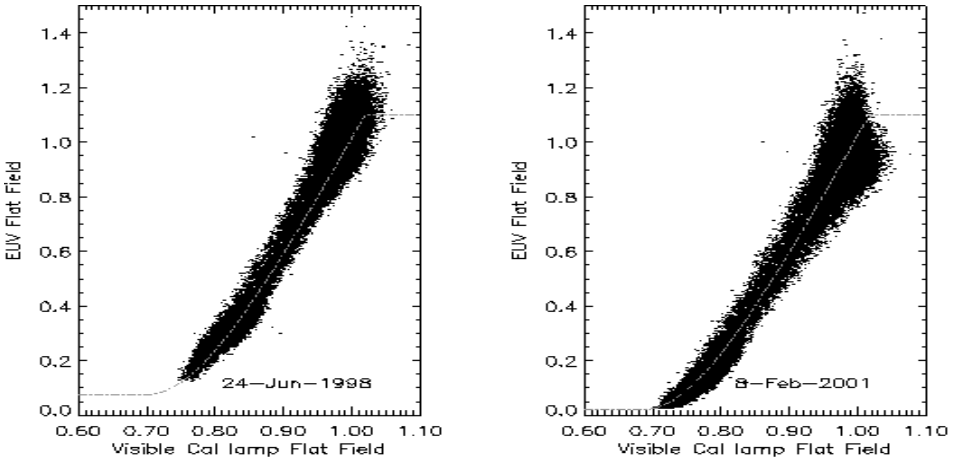

Figure 8.7: Visible to EUV relationship for the June 1998 accidental SOHO attitude loss (left) and for the February 2001 SOHO controlled offpoint (right). Dashed lines show the fitted conversion curves used in the ageing-correction software.

there is a tight relationship and also some time-variability which depends upon the depth of the degradation. We use these data, plus those from two other days, to define our functional relationship between EUV and visible, which is dependent upon the level of visible degradation (dashed lines overplotted on each day). We have taken cal-lamps regularly throughout most of the mission. Therefore, given the above relationship, we can construct, by interpolation, a daily EUV flat-field correction for each pixel.

8.4.3 Corrected Images

The above correction accounts for the CCE effects which dominate the degradation. One way to look at the magnitude and accuracy of the correction is to examine the summed flux (irradiance) of the corrected daily images for each bandpass. The magnitude of the irradiance correction is a factor of ten by early 2001. We find that this correction is within ± 30 % of the total correction. The contaminant portion of the degradation has not yet been accounted for and there are systematic local deviations in the flat-fields due to a number of factors. These include lack of good time-coverage of cal-lamps early in the mission, difficulty in understanding the time period between February and April 1998, and any long-term trends due to slight changes in the filter transmittances or mirror reflectances.

In order to correct for the contaminant and minimize the other systematic errors, we perform a correlation between the CCE-corrected EIT irradiance and a solar index. In this procedure, we assume that this correction is uniform over the CCD. We need to find the coefficients K_1, K_2, K_3, K_4 that optimize the relation: $F/(K_1 \times e^{(K_2 \times time)}) = (K_3 + K_4 \times Index)$, where F is the CCE-corrected irradiance and $Index$ is our chosen solar-activity index. The left side of this equation is then our final corrected irradiance and therefore, the corrected pixel-by-pixel flux. This correlation is performed for each time period between CCD bakeouts. We have investigated the use of various solar indices (for example the SOHO Solar EUV Monitor (SEM, 26.0 nm to 34.0 nm, *Judge et al.* [1998]),

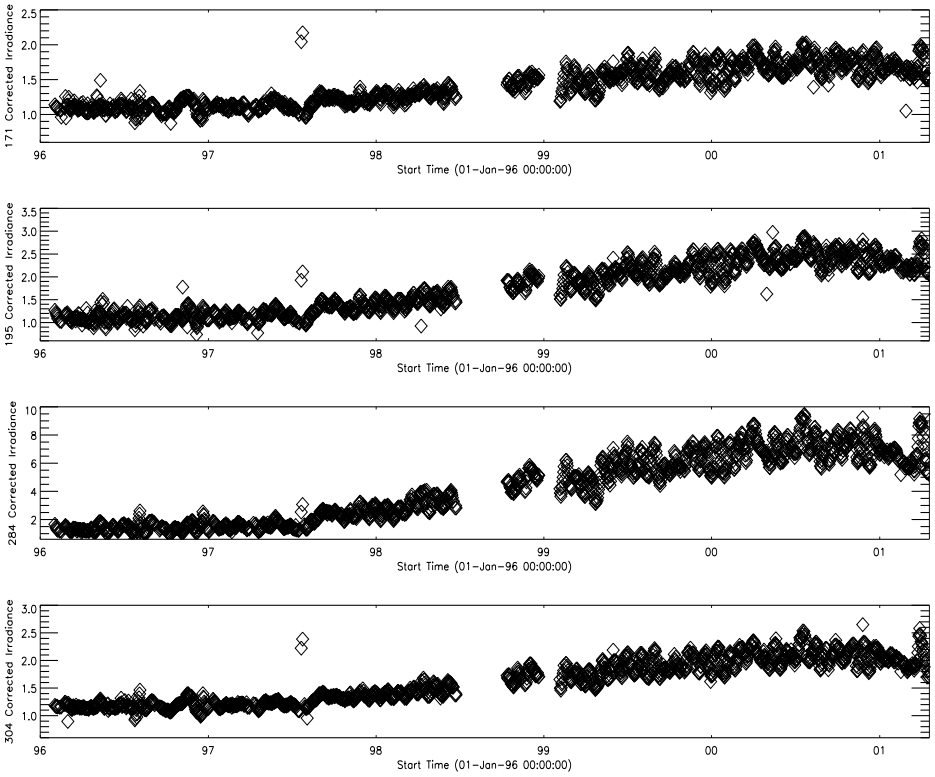

Figure 8.8: Corrected EIT irradiances over the whole mission (normalized to 1 February 1996) in the four EIT bandpasses.

the F10.7 cm radio flux, and the SUSIM Mg II index), and we find almost identical results with each choice. We use the SUSIM Mg II index in our final correlation. This choice and comparisons to other indices are discussed in detail in *Newmark et al.* [2002].

It is important to stress that, in performing this correlation, we are not insisting the EIT data match the chosen solar index, only that there is a linear relationship between the two. The magnitude of this correction is ± 20 % in any time period.

The final relative irradiance over the entire SOHO mission is shown in Figure 8.8. The corrected irradiance shown here has been normalized to 1 February 1996 (shortly after EIT first-light and initial outgassing). This correction can be obtained through the `eit_prep` software tool in the SSW package.

8.5 Conclusions

Table 8.2 provides an overview of all calibration components of EIT, distinguishing the constant and time-dependent corrections and indicating those which are implemented in the SSW EIT routines. EIT being an imager, radiometric calibration and flat-field extrac-

Table 8.2: Constant versus time-varying corrections. "**[SSW]**" indicates the corrections which are embedded in the software. *Italics* highlight the corrections still requiring further analysis.

Constant components	**Variable components**
– Bandpasses, plasma response **[SSW]**	*– Radiometric calibration (ageing), line ratio (absolute)*
– CCD flat-field (initial, local) **[SSW]**	– CCD radiation-induced aging **[SSW]**
– Grid corrections **[SSW]**	*– Light leaks (focal filter pinholes)*
– Straylight (PSF far wings)	– PSF core and focus
– Optical vignetting	– CCD offset value **[SSW]**

tion are intimately related, although those corrections were generally obtained separately and by independent methods. Thanks to its wide field-of-view, EIT can play a special role by providing a connection between absolute global indices (whole-Sun irradiance monitors) and local absolute intercalibrations (subfields, spectrometers). Now that a good integrated calibration has been achieved, EIT can act as a pivot point in the global context of the SOHO intercalibration: a role that was not considered earlier in the mission.

Regarding the future, the continuous monitoring of various classes of solar features, like active-region, bright-point or network brightness distributions, has now been undertaken and could provide standard candles against which long-term instrumental trends could then be validated and better interpreted. For future intercalibration runs, our past experience has shown the extreme importance of two requirements to make intercomparisons more accurate or in some cases even simply valid. These are a knowledge of the spectral irradiance across the broad EIT passbands (spectral scans, DEM modelling) and the accurate timing and close simultaneity (solar variability effects) of observations.

Finally, given the difficulties that we faced when calibrating EIT, we would make the following suggestions in the perspective of future EUV imagers. On-board, multiple LED sources (blue-green LED) or an internal EUV diffusor would greatly help in the interpretation and correction of instrument ageing. The calibration would also be simplified and improved by the introduction of new visible-blind radiation-hard sensors (no cooling, single visible-blocking filter). Even with the present technology, we have learned that significant improvements could be obtained by a more accurate exposure control (shutter mechanism, electronic shuttering), by the mandatory completion of a pre-flight end-to-end calibration of the integrated experiment, by a pre-flight bakeout strategy evaluation (higher temperature, duration) and also by laboratory characterizations of ageing properties (multilayer coatings, sensor CCE).

Acknowledgements

The authors would like to thank K. Wilhelm and E. Verwichte for their useful comments and corrections. Authors JSN and JDM received support from NRL, the Office of Naval Research and NASA grant NDPRS-92385.

Bibliography

Auchère, F., DeForest, C.E., and Artzner, G., In-flight determination of the plate scale of the Extreme-ultraviolet Imaging Telescope, *Astrophys. J.* **529**, L115–L117, 2000.

Auchère, F., *Contribution à l'étude de l'hélium dans la couronne solaire: Observations du télescope EIT*, PhD Thesis, Univ. Paris 6, IAS, Orsay, 2000.

Auchère, F., Hassler, D.M., Slater, D.C., and Woods, T.N., SWRI/LASP Sounding rocket inter-calibration with the EIT instrument on board SOHO, *Sol. Phys.* **202**, 269–280, 2001.

Clette, F., *LASCO/EIT Consortium meeting*, Coolfont WV, 1998.

Defise, J.-M., Clette, F., Moses, J.D., and Hochedez, J.-F., In-orbit diagnostics of EIT EUV CCD radiation-induced ageing, *Proc. SPIE* **3114**, 598–607, 1997.

Defise, J.-M., Moses, J.D., and Clette, F., In-orbit performances of the EIT instrument on board SOHO and intercalibration with the EIT Calroc Sounding Rocket program, *Proc. SPIE* **3442**, 126–139, 1998.

Defise, J.-M., Clette, F., and Auchère, F., In-flight characterization and compensation of the optical properties of the EIT instrument, *Proc. SPIE* **3765**, 341–350, 1999.

Defise, J.-M., *Analyse des performances instrumentales du télescope spatial EIT*, PhD Thesis, Univ. de Liège, 1999.

Delaboudinière, J.-P., Artzner, G.E., Brunaud, J., Gabriel, A.H., Hochedez, J.F., Millier, F., Song, X.Y., Au, B., Dere, K.P., Howard, R.A., Kreplin, R., Michels, D.J., Moses, J.D., Defise, J.M., Jamar, C., Rochus, P., Chauvineau, J.P., Marioge, J.P., Catura, R.C., Lemen, J.R., Shing, L., Stern, R.A., Gurman, J.B., Neupert, W.M., Maucherat, A., Clette, F., Cugnon, P., and van Dessel, E.L., EIT: Extreme-Ultraviolet Imaging Telescope for the SOHO Mission, *Sol. Phys.* **162**, 291–312, 1995.

Dere, K.P., Moses, J.D., Delaboudinière, J.-P., Brunaud, J., Carabetian, C., Hochedez, J.-F., Song, X.Y., Catura, R.C., Clette, F., and Defise, J.-M., The preflight photometric calibration of the Extreme-ultraviolet Imaging Telescope EIT, *Sol. Phys.* **195**, 13–44, 2000.

Dhez, P., Jourdain, E., Hainaut, O., Hochedez, J.-F., Labeque, A., Salvetat, P., and Song, X.Y., Institut d'Astrophysique Spatiale (IAS) 0.1- to 15-keV synchrotron radiation facility beam lines, *Proc. SPIE* **3114**, 134–142, 1997.

Judge, D.L., McMullin, D.R., Ogawa, H.S., Hovestadt, D., Klecker, B., Hilchenbach, M., Möbius, E., Canfield, L.R., Vest, R.E., Watts, R., Tarrio, C., Kühne, M., and Wurz, P., First solar EUV irradiances obtained from SOHO by the CELIAS/SEM, *Sol. Phys.* **177**, 161–173, 1998.

Kuhn, J.R., Lin, H., and Loranz, D., Gain calibrating nonuniform image-array data using only the image data, *Publ. Astron. Soc. Pac.* **103**, 1097–1108, 1991.

Moses, D., Clette, F., Delaboudiniere, J.-P., Artzner, G.E., Bougnet, M., Brunaud, J., Carabetian, C., Gabriel, A.H., Hochedez, J.F., Millier, F., Song, X.Y., Au, B., Dere, K.P., Howard, R.A., Kreplin, R., Michels, D.J., Defise, J.M., Jamar, C., Rochus, P., Chauvineau, J.P., Marioge, J.P., Catura, R.C., Lemen, J.R., Shing, L., Stern, R.A., Gurman, J.B., Neupert, W.M., Newmark, J., Thompson, B., Maucherat, A., Portier-Fozzani, F., Berghmans, D., Cugnon, P., van Dessel, E.L., and Gabryl, J.R., EIT observations of the extreme ultraviolet Sun, *Sol. Phys.* **175**, 571–599, 1997.

Newmark, J.S., Moses, J.D., Cook, J.W., Delaboudinière, J.-P., Song, X.Y., Carabetian, C., Bougnet, M., Brunaud, J., Defise, J.-M., Clette, F., and Hochedez, J.-F., Calibration and

flight of the NRL EIT CalRoc, *Proc. SPIE* **4139**, 328–339, 2000.

Newmark, J.S., SOHO - EIT User's Guide, Chapter 6: EIT Calibration, `http://umbra.nascom.nasa.gov/eit/eit_guide/guide.html`, 2000.

Newmark, J.S., Cook, J.W., Auchère, F., Moses, J.D., and Clette, F., In-Flight Calibration of SOHO EIT, in preparation, 2002.

Song, X.Y., Caractérisation et étalonnage radiométrique du télescope solaire EIT à l'aide du rayonnement synchrotron (entre 10 et 100 nm), PhD Thesis, Univ. Paris-Sud, IAS, Orsay, 1995.

— 9 —

In-flight Comparisons of Solar EUV Irradiance Measurements Provided by the CELIAS/SEM on SOHO

DONALD R. MCMULLIN, DARRELL L. JUDGE
University of Southern California, Space Sciences Center
Los Angeles, California, USA

MARTIN HILCHENBACH
Max-Planck-Institut für Aeronomie
Katlenburg-Lindau, Germany

FRED IPAVICH
Department of Physics and Astronomy and IPST
University of Maryland, College Park, MD, USA

PETER BOCHSLER, PETER WURZ, ALFRED BÜRGI
Physikalisches Institut der Universität Bern
Bern, Switzerland

WILLIAM T. THOMPSON
L3 Communications Analytics Corporation
NASA GSFC, Greenbelt, MD, USA

JEFFREY S. NEWMARK
Naval Research Laboratory
Washington, DC, USA

Since 1 January 1996, the Solar EUV Monitor (SEM) on the Solar and Heliospheric Observatory (SOHO) has continuously measured the solar EUV irradiance. The SEM monitors the full-disk irradiance from 0.1 nm to 50 nm in a broadband channel and also within an 8 nm wide bandpass centered at 30.4 nm. SEM irradiance measurements have been monitored periodically during the SOHO mission using sounding rockets. Through this in-flight calibration program, modest instrument degradation has been identified and corrected for in the published datasets. The relative standard uncertainty (1 σ) of SEM irradiance measurements is $\approx$ 10 %. The 81-d average of the calibrated SEM dataset shows an increase in EUV irradiance of a factor of three during the rise phase of solar cycle 23. The absolute value of the solar irradiance in the two SEM bands is also in agreement with measurements of the solar irradiance determined by ionization cells. The calibrated SEM irradiance values have been compared with irradiance values derived independently from SOHO/CDS and SOHO/EIT observations. The CDS and EIT irradiance values agree with the SEM within the combined uncertainties of the measurements.

9.1 Introduction

The Solar EUV Monitor (SEM) on the Solar and Heliospheric Observatory (SOHO) is integrated as part of the Charge, Element, and Isotope Analysis System (CELIAS). The CELIAS instrument on SOHO is designed to study the composition of the solar wind and of solar and interplanetary energetic particles [*Hovestadt et al.*, 1995]. One of the specific science objectives of CELIAS was to study the composition and dynamics of interplanetary pick-up ions, which originate from neutral particles (inflowing interstellar neutral atoms) that are ionized either through solar photons or by charge exchange with solar-wind ions. The production of pick-up ions through photoionization required measurement of the absolute photoionizing solar flux. The SEM was accordingly included to provide such data.

9.2 Instrument Description

The SEM is a simple transmission-grating spectrometer that makes use of state-of-the-art technology in the EUV wavelength region [*Hovestadt et al.*, 1995; *Judge et al.*, 1998]. Briefly, it is a lightweight (0.480 kg) instrument that consists of a high-density transmission grating (5000 bars / mm) and a free-standing aluminum filter positioned immediately behind the 2 mm $\times$ 10 mm entrance aperture. The aluminum film reduces the heat load on the grating and limits the wavelength range to the aluminum transmission region. The dispersed light is detected by three highly efficient, aluminum-coated, silicon photodiodes located 200 mm behind the grating at the zero-order and two first-order positions at 30.4 nm. The zero-order detector (channel 2) primarily measures the solar irradiance shortward of 50 nm. Due to the high sensitivity of silicon photodiodes and the relatively high transmission of aluminum at short wavelengths, the zero-order channel is quite sensitive to solar X-rays shortward of approximately 5 nm. The first-order detectors (channels 1 and 3) measure the irradiance within an 8 nm bandpass centered at the 30.4 nm solar He II resonance line emission, and are nominally insensitive to soft X-rays (see *Judge et al.* [1998]).

9.3 Cleanliness

Cleanliness of the optical components was a consideration in the design of the SEM housing. Potential degradation of the aluminum filter due to solar-wind particles is minimized by solar-wind deflector plates placed in front of the SEM entrance aperture. Material selection was considered to minimize the possible outgassing of organic material within the optics chamber. The SEM electronics reside below the optical bench, and are separated by the two-chamber design. The single electronics board is mounted below the optical housing. The optics chamber of the SEM is allowed to vent out separately through the entrance aperture at the front of the instrument. Conversely, the electronics chamber is vented out through a sintered, stainless steel, porous plug at the bottom of the instrument.

Table 9.1: Uncertainty Summary.

Item	Description	Uncertainty (%)
1	Calibration	5.0
2	Solar Spectral Distribution	9.0
3	Entrance Aperture	1.0
4	Statistical	0.5
Net Uncertainty		10.4

9.4 Pre-launch Calibration Standards Used and Calibration Methods

The SEM was calibrated at the Synchrotron Ultraviolet Radiation Facility (SURF II) [*Furst et al.*, 1995; *Canfield*, 1987] at the National Institute of Standards and Technology (NIST) in Gaithersburg, Maryland, USA. The individual components of the SEM (filter, gratings, and detectors) were first calibrated separately. Then the instrument as a whole was calibrated using both monochromatic radiation (on beamline 9) and undispersed synchrotron radiation (on beamline 2). The calibration constant of the current-to-frequency conversion electronics, the transmission of the grating (at 25.5 nm, 30.4 nm, and 33.5 nm), the quantum yield of the aluminum coated photodiodes (from 5 nm to 80 nm), and the transmission of the free-standing aluminum filter (from 5 nm to 80 nm) were measured independently. The zero-order quantum sensitivity has been extended shortward of the measured calibration (5 nm to 80.0 nm) to 0.1 nm by theoretical modeling. Each of the three detectors was modeled based on the physical parameters of the materials used in the detector design. Using the thickness and transmission properties of silicon, silicon dioxide, aluminum, and aluminum oxide between 0.1 nm and 50 nm [*Henke et al.*, 1993] the quantum efficiency was calculated as a function of wavelength. Modeling over the entire wavelength range for the end-to-end instrument in-flight configuration established the instrument responsivity at all wavelengths that were not directly calibrated.

9.5 Uncertainty Analysis

To convert the SEM count rates into absolute solar EUV flux, a convolution of the relative solar EUV spectral distribution and instrument efficiency is necessary. In order to determine the absolute solar flux it is necessary to adopt a nominal solar EUV spectrum in order to weight the wavelength-dependent instrument quantum efficiencies, Q_λ (counts/photon), of the SEM spectrometer. In the present analysis, we have used the SOLERS22 composite spectral distribution [*Woods et al.*, 1998] divided into 1 nm bins. In addition to knowledge of the instrument response as a function of wavelength (λ) and the relative spectral distribution (β_λ), the accuracy of SEM irradiance values is also dependent on the uncertainty in the measurement of the entrance aperture (A) and the statistical uncertainty of the measured instrument output (count rate). The absolute value of the pre-flight calibration flux is provided by NIST. The total uncertainty is made up of the independent uncertainties listed in Table 9.1, summed in quadrature, and yields a total SOHO/SEM relative standard uncertainty of ≈ 10 % (1σ).

The convolution of β_λ and Q_λ yields an irradiance conversion factor K, given below (Equation 9.1), that, when multiplied by the net count rate (CR), represents the measured absolute solar EUV irradiance in the wavelength band of interest, Φ_{total} (Equation 9.2).

$$\mathrm{K} = \frac{1}{A\Sigma\beta_\lambda Q_\lambda} \tag{9.1}$$

where

$$\Phi_{\text{total}} = \mathrm{CRK} \tag{9.2}$$

It should be noted and emphasized here that the resultant total solar flux value reported is dependent on the relative spectral distribution (β_λ) used to determine the absolute flux measured by both the SOHO/SEM and the rocket calibration SEM. As can be seen in the equations above, any changes in instrument responsivity observed by comparing the results from the rocket SEM with the SOHO/SEM can be attributed to changes in Q_λ on SOHO. In this calculation the solar spectral distribution must be considered. For the analysis of SEM data, we have chosen a fixed relative spectral distribution for consistency. Since it is widely known and available in the literature, we have completed the final analysis of the flight data using the SOLERS22 composite spectral distribution. Given the sensitivity of the SEM irradiance values to different reference spectra, we have assigned a 9 % relative standard uncertainty to our data (see also Table 9.1). However, to check the uncertainty of the absolute flux values reported using the method described above, the SOHO/SEM results have also been re-evaluated using spectra derived from both SOHO/CDS and SOHO/EIT observations, and the irradiance results for all three instruments have been compared. This second analysis has shown that when adjusting for the changes in the solar spectrum, as observed by CDS or EIT, the SEM results remain within the original instrument uncertainty of 10 %. Details of the SEM inter-comparisons using the CDS and EIT spectral distributions are described in *Thompson et al.* [2002].

After converting the observed count rates to solar irradiances measured at L_1 (the SOHO spacecraft location), the irradiances are normalized to a distance of 1 AU for comparison with other such normalized data.

9.6 In-flight Calibration

From the beginning, monitoring the in-flight stability of the instrument responsivity over time was an integral part of the SEM program. A calibration rocket payload that carries an identical SEM instrument provides a direct check of the absolute flux observed from the SOHO/SEM. The rocket SEM instrument is calibrated both before and after flight to monitor any responsivity changes, which may have occurred. The rocket SEM was calibrated using the NIST SURF II beamline 9. From just before the launch of SOHO in December 1995 until August 1999, six calibration series at NIST and three calibration rocket flights of the CELIAS/SEM spectrometer have been completed. Over this period of time, the responsivity of the rocket SEM has been verified as unchanged [*Judge et al.*, 1999].

9.7 Changes in Responsivity

Changes in responsivity on SOHO are determined by comparing the SOHO/SEM measurements with the calibrated rocket SEM, and are checked independently through simultaneous, absolute solar-flux measurements using ionization cells (see Section 9.9). From these measurement points, we derive a function that describes the change in responsivity for the SOHO/SEM for each channel. Based on the calibration rocket flight results [*Judge et al.*, 1999], a modest decrease in responsivity has been observed in all three SOHO/SEM channels. In direct comparison with the calibrated rocket flight instrument, the SOHO/SEM channels 1 and 3 (first-order position) both show the same amount of responsivity loss while channel 2 (central order) shows a smaller loss in responsivity, as expected, based on the degradation model discussed below. This model was developed to provide a method to adjust and correct the irradiance values between calibration rocket flights. The corrected dataset has since been used in extensive comparisons with CDS and EIT results. A detailed description of these comparisons can be found in *Thompson et al.* [2002].

9.8 Degradation Analysis

Analysis of the loss of responsivity observed in the SOHO/SEM channels indicates a common source for the observed degradation. That is, channel 1 and channel 3 both show the same amount of loss of responsivity, yet they are both independent channels, from the detectors through the electronics. However, all three channels share a common aluminum filter placed directly behind the entrance aperture. The observed differences in loss of responsivity have been modeled assuming carbon deposition on the aluminum filter as the cause of loss of responsivity. That is, hydrocarbon molecules that come into contact with the forward aluminum film are polymerized by EUV radiation and thus deposited onto the surface. Since the hydrogen absorption cross section is negligible, the deposition onto the filter can be modeled as a carbon film. Considering the transmission of carbon as a function of wavelength, the smaller loss in responsivity (measured as loss of signal) observed in the central image channel is consistent with the differences in efficiency between the central channel (channel 2) and first-order channels (channels 1 and 3) since the absorption cross-section of carbon is wavelength dependent. This difference is clearly seen when looking at the loss in signal between the first two calibration rocket flights. Over a period of 400 d, when compared with the observations from the rocket clone instrument, the SOHO/SEM reported a loss in signal of 15 % in both channel 1 and channel 3, and only a 5 percent loss in channel 2. This ratio of loss between the first-order and central-order channels is consistent with the addition of hydrocarbon deposition on the forward aluminum filter. In this case, the equivalent of 5 nm of carbon can explain the degradation of responsivity, using the transmission of carbon modeled as a function of wavelength [*Henke et al.*, 1993]. The smaller loss of signal observed in channel 2, the central image, is due to the relatively higher percentage of signal in channel 2 due to short wavelength photons, where the transmission of carbon is much less than the transmission at 30 nm (where channels 1 and 3 are most sensitive). In a similar manner, by including the results from the third calibration rocket flight, an exponential curve can be fit to the deposition rate of carbon on the forward aluminum film. The exponential curve is a logical assumption since it is be-

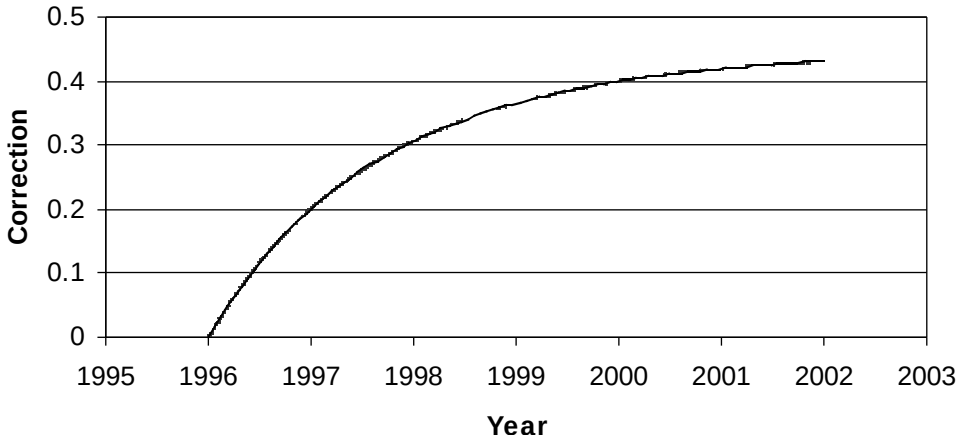

Figure 9.1: Correction to SEM results since 1 January 1996, based on sounding rocket calibration flight data.

lieved that the source of carbon contamination would be spacecraft outgassing. Using the initial pre-launch calibration as a starting point, and the subsequent three rocket flight data points to establish the carbon deposition rate, a simple model of loss of responsivity due to carbon deposition is used to correct the absolute value of the reported SEM irradiance. The time dependent correction derived from the three calibration points for the SEM is shown in Figure 9.1.

9.9 Comparisons

SEM irradiance values have been extensively compared with CDS and EIT irradiance results throughout the SOHO mission. A summary of these results can be found in *McMullin et al.* [2002a], with further details available in *Thompson et al.* [2002] and *Newmark et al.* [2002]. Briefly, the solar irradiance inter-comparisons of CDS and EIT to SEM, in the 26 nm to 34 nm band, are consistent within the instrument calibration uncertainties. These results are consistent when comparing the absolute value as well as the relative changes in solar irradiance over the solar cycle observed thus far (see Figure 9.2).

Additionally, the SEM results have been compared with simultaneous irradiance measurements provided by a Rare Gas Ionization Cell (RGIC) flown with the rocket calibration instrument. A detailed description of the ionization cell flown and the analysis method can be found in *Carlson* [1984]. A paper on the results from the ionization cell observations reported here is currently in preparation [*McMullin et al.*, 2002b]. The ionization cell flown for these measurements used neon gas, which provides the integral solar flux shortward of the ionization limit of neon. Correspondingly, the solar irradiance derived from the neon ionization cell is between $\approx$ 5 nm and 57.5 nm. The neon ionization cell yields measurements with an uncertainty of approximately 7 % [*Carlson*, 1984; *McMullin et al.*, 2002b]. This bandpass is very close to the SEM central-order bandpass of 0.1 nm to 50 nm. The results from the neon ionization cell are plotted with the SEM irradiance in Figure 9.3. The

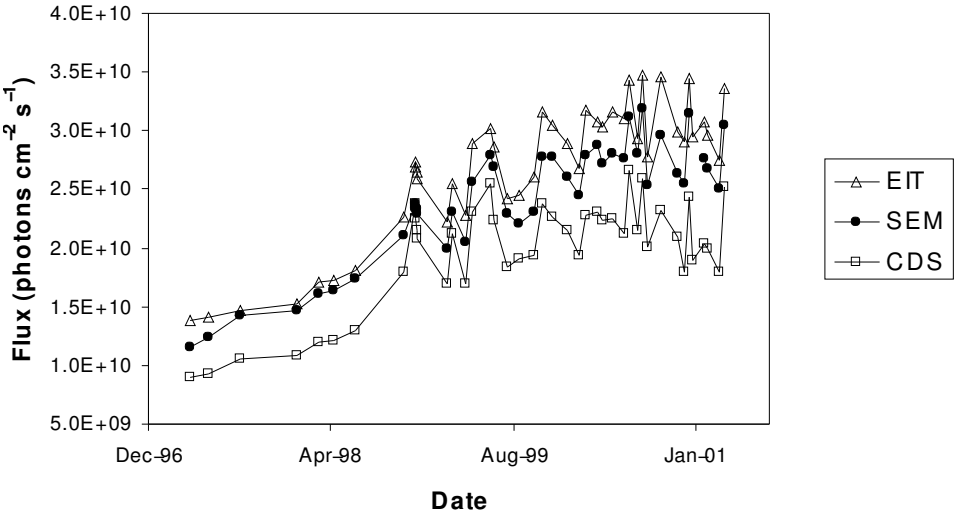

Figure 9.2: Absolute solar EUV irradiance from 26 nm to 34 nm from SEM, CDS, and EIT. All three measurements show similar trends in irradiance variability. Absolute values are within combined instrument calibration uncertainties.

inclusion of the neon absolute ionization detector in the calibration rocket payload provides independent in-flight verification of the absolute flux observed by the rocket SEM instrument in an overlapping wavelength range. As can be seen from the comparison, both instruments measured a similar increase in solar flux over the same time period, and agree within the respective measurement uncertainties. It is also interesting to note that for all three flights, the flux reported by the SEM 26 nm to 34 nm channel is approximately 50 % of the flux measured by the RGIC. These results indicate that the changes observed in the narrow band (26 nm to 34 nm) and the much wider band (5 nm to 57.5 nm) increase and decrease similarly, perhaps within a few percent, for a quasi-quiet Sun. That is, during the simultaneous measurements, there were no eruptive events producing a more than proportional increase of EUV flux in the short-wavelength band. This is also observed from the SEM central-order channel, which is very sensitive to changes in the soft X-ray flux during solar events [*Judge et al.*, 1998]. For quiet-Sun conditions, these two instruments have observed similar changes in the full-disk solar flux throughout the current solar cycle.

9.10 Helium Photoionization Rates

Using atomic cross-section data and the SEM-measured solar flux, the photoionization rate of helium is calculated. The ionization rate determined by this method using the SEM absolute flux is then compared against direct measurements as an independent verification of the absolute flux value reported. The SEM helium photoionization rates are determined by multiplying the measured wavelength dependent EUV irradiance by the helium pho-

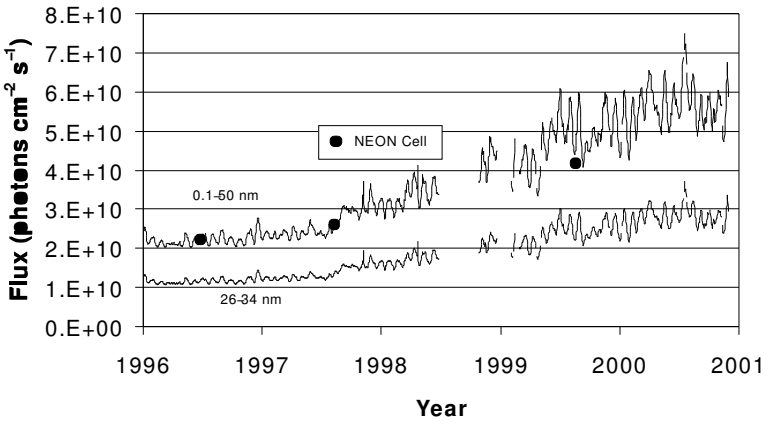

Figure 9.3: The absolute solar EUV irradiance at 1 AU from CELIAS/SEM 26 nm to 34 nm first-order and 0.1 nm to 50 nm central-order channels and the neon ionization cell flown at the same time.

toionization cross-section (in barn[1]) and then integrating the product over the ionizing wavelength range. The defining rate equation is

$$\nu = \int \Phi(\lambda)\sigma(\lambda)\mathrm{d}\lambda \tag{9.3}$$

In Equation (9.3), ν is the photoionization rate of helium in s^{-1}, $\Phi(\lambda)$ is the solar flux at wavelength λ in photons cm^{-2} s^{-1}, and $\sigma(\lambda)$ is the photoionization cross-section in barn, as a function of wavelength λ. This method has been used by *Banks and Kockarts* [1973], *Torr et al.* [1979] and *Torr and Torr* [1985]. The wavelength distribution of the integrated irradiance measured by the SEM is determined by using the relative solar spectrum given in *Woods et al.* [1998]. The absolute helium photoionization cross-section over the spectral region of interest is given by *Samson et al.* [1994]. The SEM-derived ionization results have been compared with direct measurements of the solar photoionization rate of helium by using a double-ionization helium gas cell [*Ogawa et al.*, 1997] to simultaneously measure the photoionization rate of helium. For these measurements, the helium ionization cell was flown on the Space Shuttle and simultaneous observations were coordinated with SOHO ICAL_12. The results of these measurements are described in detail by *McMullin et al.* [2002c]. This direct measurement of the helium ionization rate is in excellent agreement with the indirect results obtained by using the SEM flux data. Both results are shown in Figure 9.4.

9.11 Conclusions

The CELIAS/SEM on SOHO has provided the first continuous dataset of solar EUV irradiance measurements from solar minimum through solar maximum. The complete SEM dataset has shown good agreement with the limited full-disk observations available from

[1] 1 barn = 10^{-28} m^2

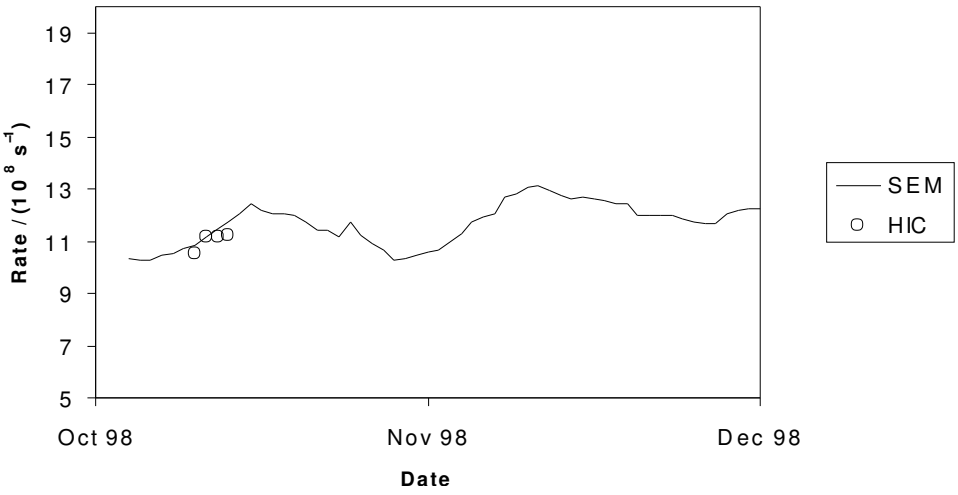

Figure 9.4: Helium photoionization rate derived from CELIAS/SEM irradiance data plotted with direct measurements for four days from the Helium Ionization Cell (HIC) flown on the Space Shuttle.

the SOHO CDS and EIT instruments in this same wavelength region in terms of the trend over the solar cycle, the variability throughout the cycle and the absolute value. On an absolute scale, the SEM irradiance values have been monitored throughout the SOHO mission by periodic rocket flights. These simultaneous rocket measurements have maintained the relative standard uncertainty of the SOHO/SEM dataset calibration at 10 %. Additionally, the absolute value is in good agreement with independent measurements from a rare-gas ionization cell flown simultaneously and with independent observations of the photoionization rate of helium.

Acknowledgements

This work has been supported by the National Aeronautics and Space Administration under grant No. NAG-5333 issued through the Office of Space Science, the Swiss National Science Foundation, and the PRODEX programme of ESA. Author JSN received support from NRL, the Office of Naval Research and NASA grant NDPRS-92385.

Bibliography

Banks, P.M., and Kockarts, G., Aeronomy, part A, Academic, San Diego, Calif., 1973.

Canfield, L.R., New far UV detector calibration facility at the National Bureau of Standards, *Appl. Opt.* **26**, 3831, 1987.

Carlson, R.W., Ogawa, H.S., Phillips, E., and Judge, D.L., Absolute measurement of the extreme UV solar flux, *Appl. Opt.* **23**, 2327–2332, 1984.

Furst, M.L., Graves, R.M., Canfield, L.R., and Vest, R.E., Radiometry at the NIST SURF II storage ring facility, *Rev. Sci. Instrum.* **66**, 2257, 1995.

Henke, B.L., Gullikson, E.M., and Davis, J.C., X-ray interactions: photoabsorption, scattering, transmission, and reflection at E=50–30000 eV, Z=1–92, *Atomic Data and Nuclear Data Tables* **54** (no. 2), 181, 1993.

Hovestadt, D., Hilchenbach, M., Bürgi, A., Klecker, B., Laeverenz, P., Scholer, M., Grünwaldt, H., Axford, W.I., Livi, S., Marsch, E., Wilken, B., Winterhoff, H.P., Ipavich, F.M., Bedini, P., Coplan, M.A., Galvin, A.B., Gloeckler, G., Bochsler, P., Balsiger, H., Fischer, J., Geiss, J., Kallenbach, R., Wurz, P., Reiche, K.U., Gliem, F., Judge, D.L., Ogawa, H.S., Hsieh, K.C., Möbius, E., Lee, M.A., Managadze, G.G., Verigin, M.I., and Neugebauer, M., CELIAS – Charge, element, and isotope analysis system for SOHO, *Sol. Phys.* **162**, 441–481, 1995.

Judge, D.L., McMullin, D.R., Ogawa, H.S., Hovestadt, D., Klecker, B., Hilchenbach, M., Möbius, E., Canfield, L.R., Vest, R.E., Watts, R., Tarrio, C., Kühne, M., and Wurz, P., First solar EUV irradiances obtained from SOHO by the CELIAS/SEM, *Sol. Phys.* **177**, 161, 1998.

Judge, D.L., McMullin, D.R., and Ogawa, H.S., Absolute Solar 30.4 nm flux from sounding rocket observations during the solar cycle 23 minimum, *J. Geophys. Res.* **104** A12, 28321–28324, 1999.

McMullin, D.R., Woods, T.N., Dammasch, I.E., Judge, D.L., Lemaire, P., Newmark, J.S., Thompson, W.T., Tobiska, W.K., and Wilhelm, K., Irradiance working group report for the SOHO Inter-Calibration Workshop, this volume, 2002.

McMullin, D.R., Phillips, E., Judge, D.L., Rogers, N., and Ogawa, H.S., Absolute measurements of the solar EUV flux using a rare gas ionization cell, to be submitted, 2002.

McMullin, D.R., Judge, D.L., Phillips, E., Hilchenbach, M., Hovestadt, D., Klecker, B., Ipavich, F., Bochsler, P., Wurz, P., Möbius, E., Galvin, A., and Gliem, F., Helium photoionization rates determined from the CELIAS/SEM instrument on SOHO, to be submitted, 2002.

Newmark, J.S., Cook, J.W., and McMullin, D.R., Solar model EUV and He II irradiances from SOHO EIT derived DEM maps, *Astrophys. J.*, in preparation, 2002.

Ogawa, H.S., Phillips, E., and Judge, D.L., Direct measurements of the helium photoionization rate from sounding rockets, *J. Geophys. Res.* **102**, 11557, 1997.

Samson, J.A.R., He, Z.X., Yin, L., and Haddad, G.N., Precision measurements of the absolute photoionization cross-sections of He, *J. Phys. B* **27**, 887, 1994.

Thompson, W.T., McMullin, D.R., and Newmark, J.S., Comparison of CDS irradiance measurements with SEM and EIT, this volume, 2002.

Torr, M.R., and Torr, D.G., Ionization frequencies for solar cycle 21: Revised, *J. Geophys. Res.* **90**, 6675, 1985.

Torr, M.R., Torr, D.G., Ong, R.A., and Hinteregger, H.E., Ionization frequencies for major thermospheric constituents as a function of solar cycle 21, *Geophys. Res. Lett.* **6**, 771, 1979.

Woods, T., Ogawa, H.S., Tobiska, W.K., and Farnil, F., SOLERS22 WG-4 and WG-5 report, *Sol. Phys.* **177**, 511, 1998.

— 10 —

Solar Vacuum-ultraviolet Radiometry with SUMER

KLAUS WILHELM, UDO SCHÜHLE, WERNER CURDT, INGOLF E. DAMMASCH
Max-Planck-Institut für Aeronomie, Katlenburg-Lindau, Germany

JÖRG HOLLANDT
Physikalisch-Technische Bundesanstalt, Berlin, Germany

PHILIPPE LEMAIRE
Institut d'Astrophysique Spatiale, Unité Mixte, CNRS-Université Paris XI, Orsay, France

MARTIN C.E. HUBER
ESA, Space Science Department, Noordwijk, The Netherlands currently at: International Space Science Institute, Bern, Switzerland

Since the beginning of 1996, the space-based telescope and spectrograph SUMER (Solar Ultraviolet Measurements of Emitted Radiation) on the SOlar and Heliospheric Observatory (SOHO) of ESA and NASA has obtained spectra of many features of the quiescent and active Sun with high spectral and spatial resolution. In addition, irradiance and radiance measurements of line and continuum emission have been performed in the wavelength range 46.5 nm to 161.0 nm. The instrument was radiometrically calibrated against the Berlin Electron Storage ring for SYnchrotron radiation (BESSY I), a primary source standard, with the help of a transfer source standard based on a hollow-cathode discharge lamp. A thorough cleanliness programme, specifically aimed at chemical contamination control, resulted in an excellent radiometric stability of the normal-incidence optical system as well as of the detectors. This has been verified under operational conditions by various techniques employed during the SOHO mission, such as line-ratio studies, observations of stars, and comparisons with other instruments. The observations provide vacuum-ultraviolet (VUV) radiometry of the Sun in many emission lines and continua of atoms and ions with relative standard uncertainties of 15 % (detector A) and 20 % (detector B) for the wavelength range 53 nm to 124 nm, with larger uncertainties outside this interval and after the SOHO recovery in 1998. We report on the present state of the SUMER radiometric calibration and provide a full bibliography related to this topic.

10.1 Introduction

A quantitative investigation of the solar VUV radiation is of great interest because its variation is closely related to solar magnetic activity. The VUV radiation incident on

the Earth is completely absorbed by the high-altitude atmosphere. Consequently, it controls many processes in the upper atmosphere; this is the reason why knowledge of the irradiance in this wavelength range is of importance. Shortward of 102.6 nm, the O_2 photoionization limit, the VUV is responsible for the daytime ionosphere and its heating. This absorption also leads to other important processes in the Earth's ionosphere, including photoionization of N_2, O and NO at wavelengths shorter than (79.6, 91.1, and 134.0) nm, respectively, as well as photodissociation of N_2 shortward of 127.0 nm and O_2 shortward of 242.2 nm. The solar VUV spectrum is highly variable on all time scales. It varies, for instance, with the Sun's rotation period and the solar sunspot cycle. The variability during a solar rotation is to a large extent controlled by the contributions of active regions.

The emission lines in this wavelength range are formed at electron temperatures between 10 000 K and several million kelvin allowing us to probe the solar atmosphere from the chromosphere through the transition region to the corona. The continuum radiation near 150 nm is emitted close to the temperature minimum at the top of the photosphere.

The aim of this contribution is to present the radiometric status of SUMER on SOHO after more than five years of successful solar observations. SOHO [*Domingo et al.*, 1995] was launched on 2 December 1995 and has been observing the Sun from the inner Sun-Earth Lagrange point (L1, about 1.5×10^6 km sunwards from the Earth) since early 1996. During the first years of operation, the solar activity was near its minimum between sunspot cycles 22 and 23 and reached the next maximum in 2000. The observations were interrupted from June until October 1998. A loss of the spacecraft attitude led to totally-uncontrolled thermal conditions. The SUMER subsystems, for instance, experienced severe temperature excursions from the design values: in the case of the telescope mirror a decrease of more than 100 °C has been estimated for this radiometrically-critical item.

10.2 Instrument Description

SUMER and its calibration concept have been described elsewhere [*Schühle*, 1994; *Wilhelm et al.*, 1995], and its performance characteristics, after several months of space-based operation, have been summarized by *Wilhelm et al.* [1997a] and *Lemaire et al.* [1997]. Both SUMER detectors A and B have photocathode areas with different responsivities: the central part of its microchannel plate (MCP) has a coating of potassium bromide (KBr) and the other parts use the bare plate. The angular pixel size in the direction along the slit is approximately $1''$ ($\approx 4.85 \times 10^{-6}$ rad), corresponding to about 715 km on the Sun. The spectral resolution element in first order is about 4.4 pm, and 2.2 pm in second order. The instrument can perform spectral scans in the wavelength range 66 nm to 161 nm (in first order) and from 46.5 nm to 80.5 nm (in second order: the lower limit is determined by the low reflectivity of the normal-incidence optics at short wavelengths). The first-order and the second-order spectra are superimposed (some lines are seen even in third order) and can be recorded at pointing positions selected on the disk or above the limb in the low corona. With the slits oriented in the north-south direction, raster images of the full solar disk (or parts of it) and of the inner corona have been obtained by scanning the telescope mirror. Scans were performed in angular step sizes of multiples of $0.375''$ across the disk and in eight swaths for most of the full-Sun images.

10.3 Radiometric Calibration

The radiometric calibration and the long-term responsivity tracking of an instrument designed to take measurements on spacecraft pose specific difficulties. The laboratory calibration of SUMER was performed with the help of a transfer source standard [*Hollandt et al.*, 1992, 1993, 1996a, b] traceable to BESSY I as a primary source standard. It was completed in early 1995. Extreme particulate and chemical cleanliness requirements [*Schühle*, 1993] had to be fulfilled during this operation and during the spacecraft integration activities [*Thomas*, 2002]. An instrument door and an electrostatic solar-wind deflector in front of the primary telescope mirror are specific features incorporated in the design in order to maintain the radiometric responsivity during the launch and operational phases. First VUV observations of the Sun were performed with SUMER in January 1996.

10.3.1 Initial Characterization

The laboratory calibration was primarily intended to measure the radiometric response of the system, as far as mirror reflectivities and detector responsivities were concerned. This was achieved without internal vignetting of the incident calibrated beam. An assessment of the relative standard uncertainties of the SUMER system and its subsystems for measurements in the spectral range from 53.7 nm to 123.6 nm, which could be reliably calibrated in the laboratory, has been presented in table 1 of *Wilhelm et al.* [2000a]. It resulted in relative uncertainties of 11 % using a 2 mm hole in place of the slit, and 12 % with slit # 2 ($1'' \times 300''$), where some vignetting by the slit had to be accepted in order to increase the spectral resolution and to reduce the detector counting rates [*Hollandt et al.*, 1996a]. We find a relative uncertainty of approximately 18 % for the smallest slit ($0.3'' \times 120''$). When applying the spectral responsivity curves shown in Figure 10.1(b), (c), (d), which are based on the most recent assessment of the performance of the instrument (discussed below), to solar measurements, it is therefore necessary to take into account the vignetting effects of field stops as well as the diffraction at the slit. This can be accomplished by applying the SUMER calibration programme `radiometry.pro`. This programme can be found in the software tree of Solarsoft at `http://soho.nascom.nasa.gov/solarsoft/soho/sumer/idl/contrib/wilhelm/rad/`. It is under configuration control. Although the responsivities and, later on, the irradiance measurements are shown here in photon units, the programme is also designed to perform all calculations in energy units in accordance with the International System of Units (SI) [*BIPM*, 1998].

Note that the uncertainties given in panels (c) and (d) include the contributions of optical stops and diffraction effects. They can be considered as system characteristics of the SUMER configuration, but the uncertainty of the pixel size has to be treated separately. The relative uncertainty for detector B in the central wavelength range is larger, because this device is, in the interest of longevity, operated at a lower gain than during the ground calibration [*Schühle et al.*, 2000a]. This reduced the responsivity by a factor of 1.17. As detector B had a relative responsivity approximately 20 % higher than detector A during the laboratory calibration (cf., figure 7 of *Wilhelm et al.* [1995]), both detectors were expected to have the same responsivity in flight.

In order to obtain a radiometric characterization in the spectral ranges at shorter and longer wavelengths, we compared line-radiance ratios measured on the solar disk with the results of atomic physics calculations. We also evaluated SUMER stellar observations and

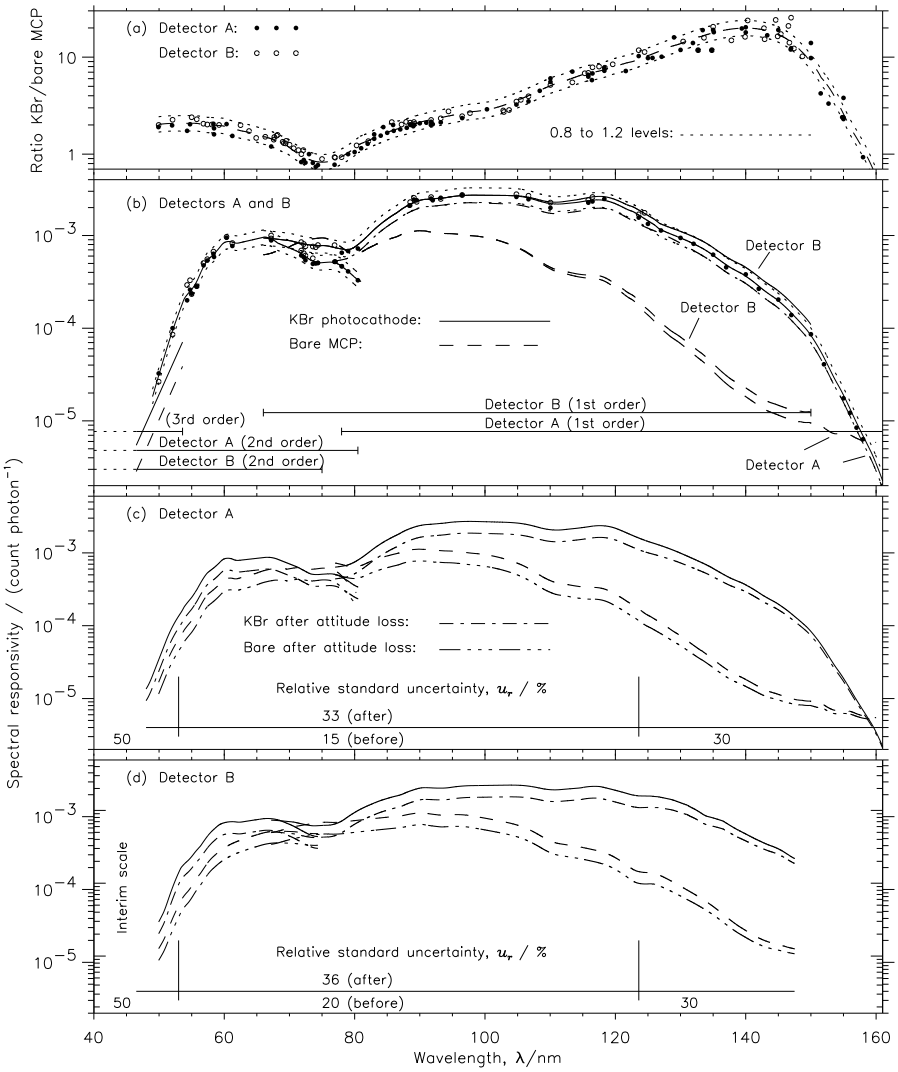

Figure 10.1: Spectral responsivities of the SUMER instrument with its detectors A and B, and the corresponding relative uncertainties for the $1'' \times 300''$ slit. (a) In the upper panel the responsivity ratio of the photocathodes is shown. (b) First-order and second-order KBr responsivities evaluated jointly for detectors A and B. The long-wavelength deviation of detector B is treated in the text as well as the bare MCP responsivities and the third-order calibration of detector A. The bars in the lower portion of this panel indicate the order of diffraction. (c) Independent detector A assessment, and (d) corresponding results for detector B. The relative uncertainties in the central wavelength range (indicated by vertical bars at 53 nm and 124 nm) are derived from the laboratory calibration and are smaller than those of the in-flight calibration extensions. The changes after the attitude loss of SOHO are indicated for both detectors. On the long-wavelength side, the relative uncertainty refers to the KBr photocathode only. The "Interim scale" of detector B is explained in the text.

obtained radiometric information with the help of the International Ultraviolet Explorer (IUE) and Hubble Space Telescope standard stars [*Bohlin et al.*, 1990; *Nichols and Linsky*, 1996; *Wilhelm et al.*, 1997b; *Hollandt et al.*, 1998; *Schühle et al.*, 2000a]. The responsivity ratios of the KBr and bare photocathodes in panel (a) have been measured in the laboratory and, in a wider wavelength range, during the mission operations. A very consistent and stable spectral dependence has been found employing various methods [*Wilhelm et al.*, 2000a].

In the past, both detectors were treated independently. This type of evaluation is continued here, and the latest results are shown in panels (c) and (d). The main change compared to earlier evaluations is related to the post-loss responsivity (cf., Section 10.3.3).

Up to now responsivity functions were only available in first and second order. A deep-exposure reference spectrum obtained with detector A in a stable coronal streamer on 13 and 14 June 2000 showed the Si XII pair at 49.94 nm and 52.07 nm in second and third order of diffraction. This allows us to establish responsivity curves in third order for both photocathodes. As the technical parameters of SUMER restrict observations of spectral lines in third order to the narrow range of 46.5 nm to 53.6 nm, the Si XII results were, with some confidence, extrapolated over this range as shown in Figure 10.1(b).

10.3.2 Calibration Tracking

Unless a space-borne instrument can be recovered after flight and re-calibrated, its calibration stability is a major concern during the launch phase and the mission duration. Comparison with other instruments offers a solution that we have used extensively. In addition to the IUE data mentioned above, which agreed with SUMER observations near 120 nm, where both instruments overlap in their wavelength ranges, comparisons with the Coronal Diagnostic Spectrometer (CDS) on SOHO [*Harrison et al.*, 1995] and with the SOLar-STellar Irradiance Comparison Experiment (SOLSTICE) on the Upper Atmosphere Research Satellite (UARS) [*Rottman et al.*, 1993] have been considered in this context. The CDS indicated higher radiance values of quiet-Sun regions than SUMER, but the relative deviations of about 30 % for He I at 58.4 nm and 9 % to 17 % for Mg X at (60.9 and 62.5) nm are within the combined uncertainty margins [*Pauluhn et al.*, 1999]. An important aspect is that the ratio of the radiances derived from both instruments remained rather constant over several months, although relative variations in radiance of ± 20 % occurred. Consequently, we can conclude that the variations are of solar origin [*Pauluhn et al.*, 2001a, b]. SOLSTICE solar irradiance measurements in N V at 123.8 nm resulted in values a factor of 1.14 higher than those obtained from SUMER full-disk rasters and only by 1.11 higher in C IV at 154.8 nm [*Wilhelm et al.*, 1999a]. Given the good radiometric calibration and stability of SOLSTICE this seemed to indicate that the SUMER response was too small by a factor just over 1.1 on the long-wavelength side at that time.

In a comparison between a coronal spectrum obtained by SUMER and the CHIANTI database, *Landi et al.* [2002] found that the observed ratio of the Si XII lines at 49.9 nm and 52.0 nm agrees very well with the theoretical predictions. Moreover, there is no evidence for any other gross inaccuracy in the full SUMER wavelength range. *Doschek et al.* [1999] also compared theoretically-calculated line ratios of several ions with SUMER observations. In many cases, excellent agreement was found, but also significant discrepancies, even for ratios in narrow wavelength intervals. Consequently, the main conclusion

was that improvements in atomic data calculations are required, in particular, for sulfur ions.

A stable radiometric calibration is also supported by the results of the SUMER flat-field exposures performed in the H I Lyman continuum near 88 nm. Quiet-Sun conditions have been selected by pointing to appropriate areas. No significant change of the responsivity of detector A has been found over 200 d, nor was there any decrease in detector B over 350 d, but a relative increase of less than 20 % could not be ruled out [*Schühle et al.*, 1998]. In addition, the stable flat-field counting rates, in particular in the case of detector A, indicate that the radiometric characterization could be maintained, although the high voltage applied for the operation of the MCPs had to be raised by more than 500 V to achieve a constant gain.

However, the recent detection of two slight inconsistencies has led to an update of the SUMER radiometric calibration in two areas: (1) a comparison of the full-Sun data of detector A with those of detector B in S VI at 93.3 nm and H I at 93.7 nm showed that a test period had to be introduced in `radiometry.pro` at the end of September 1996 (see Section 10.4); (2) stellar observations [see *Lemaire*, 2002] and recent reference spectra of quiet-Sun regions taken on both detectors indicate that the responsivity of detector B is higher than detector A longward of 104 nm. However, the slope of the increase is different, in that the stellar observations show a factor of nearly two at 147 nm, whereas the reference spectra give only 1.31 at 150 nm. Work is ongoing to resolve this discrepancy. At this stage we provide both options in the SUMER radiometry evaluation. Firstly, we assume the reference spectrum result and re-scale detector B accordingly. It then transpires that the data points available for both detectors are not systematically different within the relative uncertainty margin of 20 %. It has thus been possible to determine joint KBr responsivity functions for detectors A and B in Figure 10.1(b). The detector B excess longward of 104 nm has, of course, to be taken into account again later. Finally, with the help of the KBr-to-bare ratio, responsivities can be obtained for the bare MCP. Secondly, we adopt the ratio obtained with the star α Leo which was the basis for the previous, separately-evaluated responsivities of both detectors. See Section 10.5 for the actual implementation in `radiometry.pro`.

10.3.3 Other Aspects Relating to Radiometry

The radiometric characterization of SUMER has been performed in such a way that averages over many detector pixels have been used to determine the responsivity [*Wilhelm et al.*, 1995; *Hollandt et al.*, 1996a]. Because of relative variations of the pixel size (2 % in the spectral dimension and 1.5 % in the spatial dimension), and a varying flat-field response [*Dammasch et al.*, 1999a; *Schühle et al.*, 2000a], the single-pixel data have to be treated with great care.

The spectral responsivity curves displayed in Figure 10.1(b), (c), (d) refer to situations with low counting rates both for the total detector and for single pixels. Whenever the total counting rate exceeds about 5×10^4 s^{-1}, a deadtime correction is required and with a single-pixel rate above about 3 s^{-1}, a gain-depression correction is called for (cf., Section 10.5).

The responsivity curves are the best functions available to date for the period from January 1996 to June 1998 and from November 1998 to December 2001, but they have undergone modifications in the past and might do so again in the future. There are two

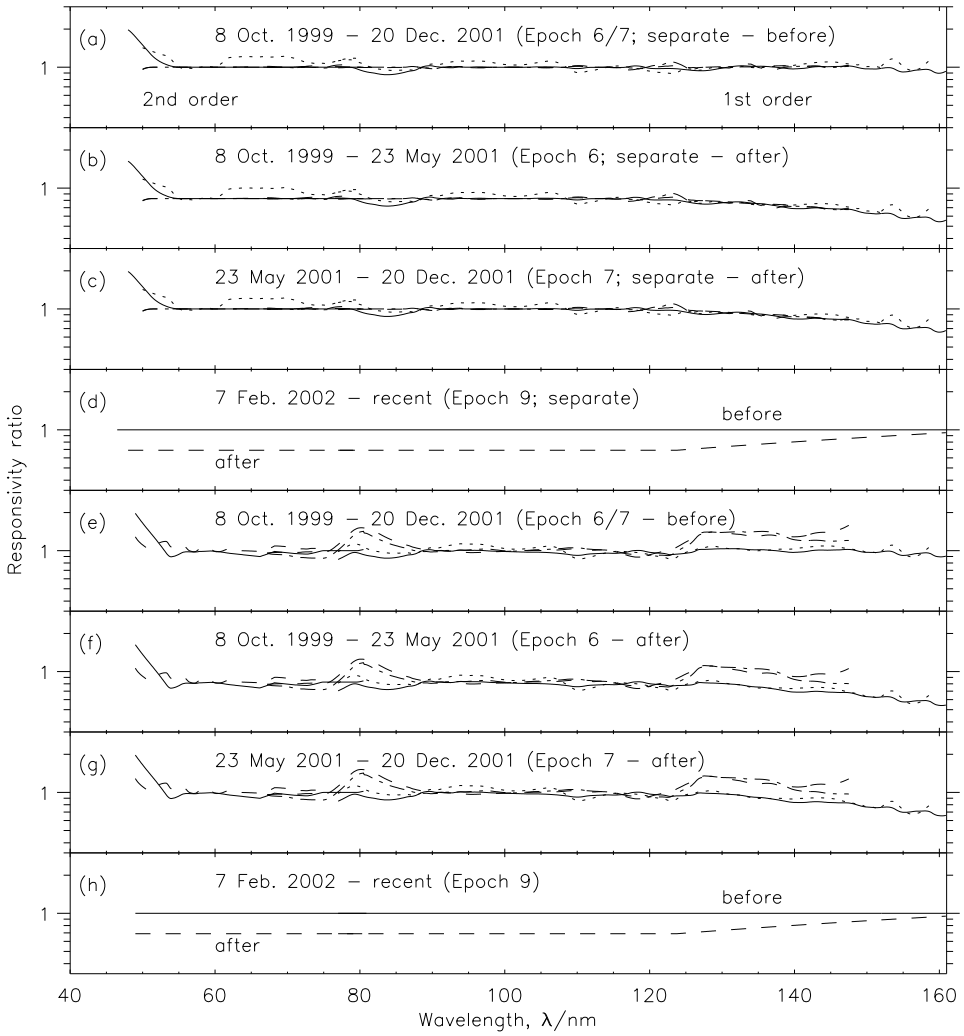

Figure 10.2: Continuation of the history of the SUMER radiometric calibration revisions during the SOHO mission until 7 February 2002. The period from December 2001 to 7 February 2002 (Epoch 8) is not shown as it deviates from the recent one only by a slight modification of the interpolation method between 70 nm and 80 nm on the bare MCP. The calibration status before October 1999 is documented in Figure 4 of *Wilhelm et al.* [2000a]. The ratios (shown on a scale between 0.33 and 3) of the responsivity functions to the most recent functions are shown for both detector A (KBr: solid lines; bare: dotted lines) and detector B (KBr: dashed lines; bare: dashed-dotted lines) in both orders of diffraction. The epochs applied are given in each panel. The best calibrations available now are represented by unity in panel (d) for the separate evaluation in panels (a) to (c) and in (h) for the joint one in panels (e) to (g). In panels (d) and (h), the reduction of responsivity caused by the attitude loss is also indicated. The test phase of detector B in 1996 could not be documented in the format of this diagram.

reasons for such modifications: an improved understanding of the performance of the instrument including its calibration, and changes of the status of the instrument with time. Figure 10.2 summarizes the modifications since October 1999 continuing the history documented in figure 4 of *Wilhelm et al.* [2000a]. The plots demonstrate that the calibration status in the central wavelength range is very consistent over time for both detectors. The changes apparent at long wavelengths in panels (e) to (g) for detector B are related to the inconsistencies of the star data mentioned above. We recommend the use of the joint evaluation in this range. Most of the other small changes present stem from modifications of the interpolation method.

The bulge near 80 nm for detector B seems to indicate that in this interval both detectors cannot be treated jointly. It might be advisable to use the separate responsivity of detector B here. At short wavelengths, the deep exposure in the corona furnished, in addition to the third-order measurements of the Si XII line pair, precise second-order data that led to a modification for detector A. The deep exposure also proved that the Ne VII line at 46.52 nm in second order cannot be separated from H I 93.08 nm and H II 93.03 nm in first order. It was, therefore, eliminated from the data set. Before an adequate low-gain level of detector B was found, a test configuration was used between 24 September and 6 October 1996, which will be considered below. The revisions shown in Figure 10.2(a) to (c) and (e) to (g) resulted from a better understanding of the calibration status. However, a major change of the responsivity happened during the attitude loss of SOHO.

After the recovery of SOHO, a responsivity decrease was found over a wide spectral range as shown in panels (d) and (h) by the dashed curves. We attribute this change to the deposition of contaminants and subsequent polymerization on the optical surfaces of the instrument, because both detectors were equally affected. The telescope mirror is considered to be the prime candidate. This critical item was held at an elevated temperature of about 40 °C (non-operational) or about 80 °C (operational) compared with 23 °C of the optical bench structure at all times of the nominal mission. This was done in order to avoid any condensation on the mirror. During the interval of SOHO's uncontrolled attitude, however, the temperature estimate for this mirror was near −80 °C, whereas other parts of the spacecraft reached very high temperatures. A first assessment led to a decrease in relative responsivity of 43 % [*Wilhelm et al.*, 2000a]. *Schühle et al.* [2000b], in a second study, included only observations which could not have been influenced by active-region contributions. Relative losses of 26 % for He I 58.4 nm, 28 % for Mg X (60.9 and 62.4) nm, 34 % for Ne VIII 77.0 nm, 39 % for N V 123.8 nm, and 29 % for the H I Lyman continuum were obtained, resulting in an average relative loss of 31 %. It should be noted that star observations of α Leo before and after the attitude loss provide strong evidence that the responsivity decrease is wavelength dependent with a tendency to become rather small at the longest wavelengths. Additional observations were performed in August 2001 [*Lemaire*, 2002]. Reference spectra taken in quiet-Sun regions furnish yet another means of determining the wavelength dependence of instrumental changes. The small solar areas covered by the slit during the observation of reference spectra and the relatively short integration times lead, together with significant variations of the solar radiance even of the quiet-Sun chromospheric network, to considerable scatter and uncertainties. However, these observations confirm that the longer wavelengths of the SUMER range are less affected by the attitude loss. Consequently, we adopted a relative loss in the responsivities of 31 % for wavelengths shorter than 123.8 nm (N V) (as before), which linearly decreases to 5 % at 161 nm.

Quiet-Sun reference spectra obtained with both detectors also provide consistency checks on the responsivity functions of detectors A and B, which have been established independently, as well as on the KBr-to-bare photocathode ratio. No significant change of this ratio could be detected over the operational period since the laboratory measurements (cf., Figure 10.1(a)).

10.4 Radiances and Irradiances

A first-order solar radiance spectrum obtained on 12 August 1996 and treated with the most recent calibration software is displayed in Figure 10.3. In addition to the emission lines, several continua are very prominent. Some black-body radiation levels have been plotted by adjusting the temperature in Planck's law. The temperature required to produce an adequate fit at long wavelengths is close to the values expected near the temperature minimum in the solar atmosphere [cf., *Brekke and Kjeldseth-Moe*, 1994; *Samain et al.*, 1975], thus supporting the responsivity curves applied. By studying the line radiance measurements of quiet-Sun areas performed by the Joint Observing Programme (JOP) named ICAL 01, which was designed for the inter-calibration of SOHO instruments, a significant increase in all emission lines has been found from 1996 onwards [*Schühle et al.*, 2000b, c, d; *Wilhelm et al.*, 2000a].

In evaluating spectra of the type shown in Figure 10.3, the overlapping first and second orders of diffraction cause some difficulties. For emission lines the separation is relatively straightforward (provided their orders have been established). The second-order lines have in fact been manually removed from the spectrum in Figure 10.3. However for continua the task is not so trivial. In principle, observations on both photocathodes could be used to separate the diffraction orders, but at long wavelengths, where the second-order contribution is most significant, the KBr-to-bare ratios are close to one in both orders (cf., Figure 10.1(a)), and the results are rather uncertain. A complete quiet-Sun reference spectrum observed on detector A (78 to 160) nm on 12 November 2001 and another one on detector B (67 to 149) nm shortly afterwards, allowed us to separate the continua between 134 nm and 160 nm, where second-order contributions are of importance. The first-to-second-order responsivity ratio of the grating had been found to be 1.66 at 79.0 nm (O IV) for detector A [*Wilhelm et al.*, 1997a]. This ratio could be confirmed with the recent B spectrum for this line, but the lines Ne VIII 77.0 nm and N V 76.5 nm indicate a decrease of the ratio with decreasing wavelength. At 70.4 nm (O III), we find 1.16. Under the assumption of a linear decrease of the ratio with wavelength, we can then use the spectra obtained to find the contribution of the second-order continuum to the first-order observations at long wavelengths. The results are plotted in Figure 10.4 for both photocathodes.

Solar irradiances of emission lines can be derived from SUMER measurements without assumptions only when a raster scan of the whole disk has been performed. This has been done for many lines. Since line irradiances derived from full-Sun rasters provide the best opportunities for radiometric inter-comparisons, we present in Table 10.1 a selection of such observations treated with the latest SUMER calibration routine (`epoch_9`), normalized to 1 AU (astronomical unit). Typical relative standard uncertainties are less than 20 % for most of the emission lines, but 30 % for C IV. Note that the agreement with SOLSTICE in Section 10.3.2 was much better than these wide margins, indicating that the SUMER uncertainties, in particular at long wavelengths, are probably too conservative.

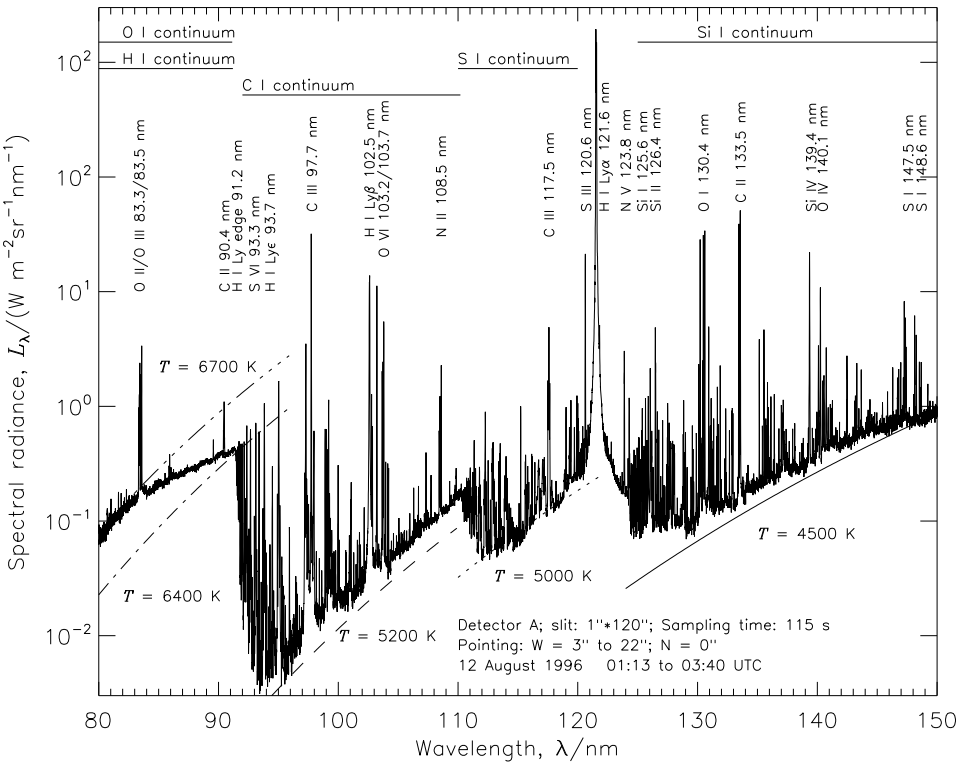

Figure 10.3: SUMER radiance spectrum of a quiet-Sun region in first order of diffraction (second-order spectral lines have been removed manually). Prominent lines and continua are identified. Some black-body radiation levels are shown to provide an estimate of the radiation temperatures of the continua. A SUMER spectral resolution element in first order corresponds to 7 μm on the scale of this diagram.

It should be mentioned that the latest calibration yields a relative SOLSTICE/SUMER agreement for C IV at 154.8 nm within 4 %.

All full-disk images were taken with the slit # 2 ($1'' \times 300''$) and most of them on detector A. These images allow us to determine the limb brightening of the corresponding emission lines, and also to separate the irradiance into contributions from quiet-Sun areas, coronal holes or active regions [*Wilhelm et al.*, 1998]. In the case of C III, missing parts of the disk have been restored with average disk values up to the photospheric limb. In previously calculated and published SUMER values [*Wilhelm et al.*, 1998, 1999b, 2000b] some of the line radiances seem to have been underestimated. This could be due to an attempt to obtain a *pure* image in a spectral line. New, detailed studies of the profiles led to the results listed in Table 10.1. For this refinement of the evaluation, gain and deadtime corrections were applied as indicated. For the He I line, a relative correction of about 9 % is now performed based on the actual detector counting rates. This is different from the earlier evaluations mentioned and explains the higher value obtained. The Ne VIII line has

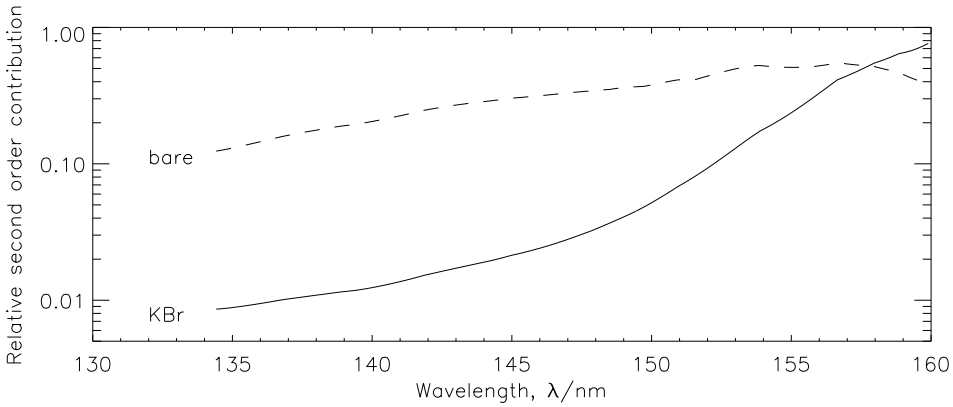

Figure 10.4: Fractional contribution of the H I Lyman continuum to the sum of the first- and second-order continuum at long wavelengths as observed on both photocathodes in reference spectra obtained with both detectors on 12 November 2001.

been observed in second order of diffraction, where it is hopelessly blended with weak Si I lines in first order, whose relative contributions, however, amount only to a few percent.

With the exception of O V, which was integrated on board, all other results are well within the declared uncertainty margins of the earlier results. We have thus studied the O V 63.0 nm line in greater detail using radiance data from inter-calibration runs, reference spectra and other quiet-Sun observations in 1996 together with measured centre-to-limb variations (limb-brightening factor of 3.7), and find an estimate for the average line irradiance in photons of 1.15×10^{13} s^{-1}m^{-2} with a relative standard uncertainty of 20 %. This value agrees with irradiances obtained from the full-Sun data within the uncertainty margins. An average of 1.37×10^{13} s^{-1}m^{-2} was obtained from observations in the years 1997 to 2000. There was no systematic difference between observations on the KBr photocathode and the bare MCP indicating that the second order O V line is not blended by any prominent first-order line.

During a 360° roll manœuvre of SOHO on 20 March 1997, the SUMER slit was set to cross the solar limb and then moved around the disk with the spacecraft rotation. Together with coordinated quiet-Sun radiance measurements, irradiance values for many emission lines could be estimated with a minimum of assumptions [*Dammasch et al.*, 1999b; *Schühle*, 2000c]. Taking the N V line at 123.8 nm as an example, the result in photons was $E(\mathrm{N\,V}) = 7.60 \times 10^{12}$ s^{-1}m^{-2} with a relative standard uncertainty of 25 %.

An overview of irradiance measurements and estimates obtained with SUMER is shown in Figure 10.5. Also included is an O V photon irradiance estimate at 1.84×10^{13} s^{-1}m^{-2} obtained during the same roll manœuvre. This value is more than a factor of 1.3 higher than the full-Sun irradiance in 1996. Inspection of the corresponding centre-to-limb variations showed significant enhancements at or near the limb in 1997 caused by small active regions. In assessing the consistency with other O V irradiance measurements, it must be taken into account that the method of estimating the irradiance from the roll data introduces considerable additional uncertainties. Estimates for thirty-three other emission lines are available from this roll as well.

Table 10.1: Observing parameters and irradiance results of complete solar images in the C III, Ne VIII, C IV, and He I emission lines on detector A with high spatial and the full SUMER spectral resolution. The O V window was spectrally integrated (i) over 50 pixels on board of SOHO, but corrected for Si I blends and continuum contributions (combined relative correction: 37 %).

Spectral line	C III	Ne VIII	C IV	He I	O V
Wavelength, λ/nm	97.7	77.0[a]	154.8	58.4[a]	63.0[a]
Temperature, T_e/kK	70	630	100	20	230
Exposure time, t_s/s	7.25	7.50	15.00	7.00	2.00
Angular step width, $\Delta s/''$	1.13	1.88	1.88	1.50	3.00
Photocathode	bare	bare	KBr	bare	KBr
Spectral window in pixel	25	25	50	25	50(i)
Date in 1996	28 Jan	02 Feb	04 Feb	02 Mar	14 Jun
Solar radius from Earth[b], $R_\odot/''$	974.5	973.9	973.6	968.3	944.8
Start time in UTC	22:40	02:05	02:06	23:22	11:46
Duration in h:min	25:27	16:03	31:34	27:24	3:44
$F_{10.7}/(10^{-22}$ W m^{-2} Hz$^{-1})$	71.8	74.2	71.4	69.0	69.8
Counting rate[c], $N_c/(10^6$ s$^{-1})$	691.7	18.55	13.78	34.24	114.1
Line irradiance at 1 AU					
$E/(\mu$W m$^{-2})$	131	7.78	83.8	34.6	41.4
in photons, $E/(10^{12}$ s^{-1}m$^{-2})$	64.5	3.01	65.3	10.2	13.1
Relative gain correction, c_g/%	35.6	1.5	1.6	5.0	10.0
Relative deadtime correction, c_d/%	11.8	0.5	0.4	4.3	6.1
Relative standard uncertainty, u_r/%	18	16	30	16	19

[a] Observed in second order of diffraction.
[b] Seen from SOHO the radius is larger by a factor of 1.01.
[c] If the full Sun were to be seen by the detector.

Another roll manœuvre was performed on 14 and 15 November 2001. SUMER was operated in a mode similar to that in 1997. Quick-look data confirmed that good observations have been obtained, but they could not be evaluated in time for this report.

Without considering the test period between 24 September and 6 October 1996 mentioned above and the resulting additional correction, the S VI and H I irradiances would be too low by a factor of 1.18, which would introduce a discontinuity much larger than the variations before that date suggest. A detailed study of the dependence of the responsivity of detector B on the gain settings (level of the high voltage) showed that half of this correction can be understood as a consequence of the specific test configuration. The remaining portion of the reduction could not be explained, but is well within the uncertainty margin anyway.

The correction can be applied by setting the keywords `test` and `detb` in `radiometry.pro`. It is shown in Figure 10.1(d) by the "Interim scale". Any evaluation of observations in the above time interval performed without the keyword `test` has to be corrected accordingly.

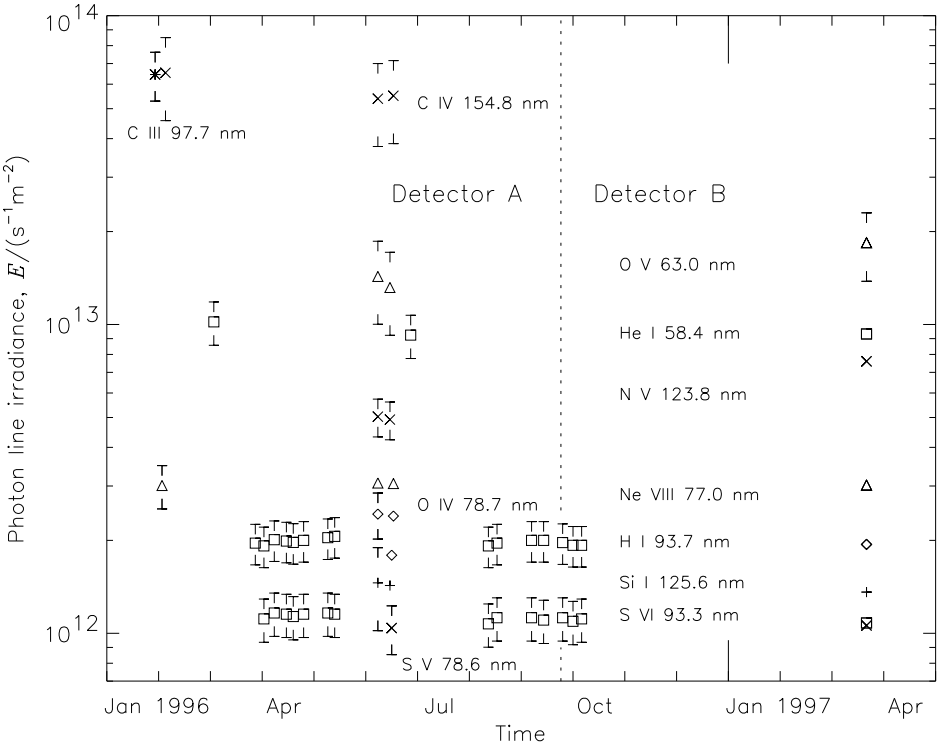

Figure 10.5: Solar irradiance observations in VUV emission lines with SUMER in 1996 and 1997. Detector B was used after 23 September 1996. Not all uncertainty margins are shown in the interest of clarity. Spectral lines with wavelengths shortward of 79 nm have been observed in second order.

10.5 Conclusions

SUMER data can be obtained for further investigations from the public domain of the SOHO archive (`http://soho.nascom.nasa.gov/data/catalogues/main.html`) or the SUMER Image Database (`http://www.linmpi.mpg.de/english/projekte/sumer/FILE/SumerEntryPage.html`).

Both SOHO and SUMER are still operational, albeit the latter with reduced performance capabilities, in particular concerning spatial rasters and the remaining count potential of the detectors. The responsivity curves in Figure 10.1 present the status before and after the SOHO attitude loss. The radiometric calibration of SUMER data requires the application of the programme `radiometry.pro`, of which the latest and official version is that contained in the software tree of Solarsoft at any given time. The December 2001 and February 2002 issues (`epoch_8` and `epoch_9`) contain two slightly-different versions according to their evaluation (`separate` or `joint`) except for the bare MCP in second order. We recommend the use of the joint alternative, when available, as it provides the best consistency between detectors A and B. However, in the interest of a complete change history of the independently-calibrated detectors the sequence of responsivity curves is also

continued in the old format, and, as mentioned in Section 10.3.3, the separate evaluation should be used for detector B between 75 nm and 88 nm.

Any modifications have been and will be announced to the user community, and are also documented in the comments accompanying the programme. An update of the history of the responsivity functions between October 1999 and December 2001 has been presented in Figure 10.2. With the help of epoch keywords, all past calibration stages can be recovered. Other keywords control the specific responsivity function to be applied. Programmes for deadtime corrections (`deadtime_corr.pro`) and the reversal of local gain depressions (`local_gain_corr.pro`) are also available for observations with high counting rates.

Given the calibration activities with SUMER outlined above, we have achieved a relative standard uncertainty of 15 % to 20 % in the wavelength range from 53 nm to 124 nm for high-resolution measurements in the spatial and spectral regimes. This is better than we could have anticipated in the planning phase of SOHO and SUMER. This success of the SUMER calibration, and of SOHO in general, will also be an important benchmark for future missions.

Acknowledgements

SUMER is financially supported by DLR, CNES, NASA and the ESA PRODEX programme (Swiss contribution). We thank C.D. Pike and the referee, R.A. Harrison, for many valuable comments and suggestions.

Bibliography

BIPM (Bureau International des Poids et Mesures), Le Système International d'Unités (SI) and The International System of Units, 7th ed., Sèvres, France, 1998.

Bohlin, R.C., Harris, A.W., Holm, A.V., and Gry, C., The ultraviolet calibration of the Hubble Space Telescope. IV - Absolute IUE fluxes of Hubble Space Telescope standard stars, *Astrophys. J. Suppl. Ser.* **73**, 413–439, 1990.

Brekke, P., and Kjeldseth-Moe, O., New radiometric values of the solar ultraviolet continuum radiation from 1500 to 1700 Å, *Astrophys. J.* **413**, L55–L58, 1994.

Dammasch, I.E., Wilhelm, K., Curdt, W., and Hassler, D.M., The Ne VIII (λ770) resonance line: Solar wavelengths determined by SUMER on SOHO, *Astron. Astrophys.* **346**, 285–294, 1999a.

Dammasch, I.E., Wilhelm, K., Curdt, W., and Schühle, U., Solar ultraviolet irradiance and radiance observations by SUMER on SOHO, *ESA SP*-**448**, 1165–1170, 1999b.

Domingo, V., Fleck, B., and Poland, A.I., The SOHO mission: An overview, *Sol. Phys.* **162**, 1–37, 1995.

Doschek, E.E., Laming, J.M., Doschek, G.A., Feldman, U., and Wilhelm, K., A comparison of measurements of solar extreme-ultraviolet spectral line intensities emitted by C, N, O, and S ions with theoretical calculations, *Astrophys. J.* **518**, 909–917, 1999.

Harrison, R.A., Sawyer, E.C., Carter, M.K., Cruise, A.M., Cutler, R.M., Fludra, A., Hayes, R.W., Kent, B.J., Lang, J., Parker, D.J., Payne, J., Pike, C.D., Peskett, S.C., Richards, A.G., Culhane, J.L., Norman, K., Breeveld, A.A., Breeveld, E.R., Al Janabi, K.F., McCalden, A.J., Parkinson, J.H., Self, D.G., Thomas, P.D., Poland, A.I., Thomas, R.J.,

Thompson, W.T., Kjeldseth-Moe, O., Brekke, P., Karud, J., Maltby, P., Aschenbach, B., Bräuninger, H., Kühne, M., Hollandt, J., Siegmund, O.H.W., Huber, M.C.E., Gabriel, A.H., Mason, H.E., and Bromage, B.J.I., The Coronal Diagnostic Spectrometer for the Solar and Heliospheric Observatory, *Sol. Phys.* **162**, 233–290, 1995.

Hollandt, J., Kühne, M., and Huber, M.C.E., Radiometric calibration of solar space telescopes - The development of a vacuum-ultraviolet transfer source standard, *ESA Bulletin* **69**, 1992.

Hollandt, J., Huber, M.C.E., and Kühne, M., Hollow cathode transfer standards for the radiometric calibration of VUV telescopes of the Solar and Heliospheric Observatory (SOHO), *Metrologia* **30**, 381–388, 1993.

Hollandt, J., Schühle, U., Paustian, W., Curdt, W., Kühne, M., Wende, B., and Wilhelm, K., Radiometric calibration of the telescope and ultraviolet spectrometer SUMER on SOHO, *Appl. Opt.* **35**, 5125–5133, 1996a.

Hollandt, J., Kühne, M., Huber, M.C.E., and Wende, B., Source standards for the radiometric calibration of astronomical telescopes in the VUV spectral range, *Astron. Astrophys. Suppl. Ser.* **115**, 561–572, 1996b.

Hollandt, J., Schühle, U., Curdt, W., Dammasch, I.E., Lemaire, P., and Wilhelm, K., Solar radiometry with the telescope and vacuum-ultraviolet spectrometer SUMER on the Solar and Heliospheric Observatory (SOHO), *Metrologia* **35**, 671–675, 1998.

Landi, E., Feldman, U., and Dere, K.P., CHIANTI – An atomic database for emission lines. Paper V: Comparison with an isothermal spectrum observed with SUMER, *Astrophys. J. Suppl.*, in press, 2002.

Lemaire, P., SUMER stellar observations to monitor responsivity variations, this volume, 2002.

Lemaire, P., Wilhelm, K., Curdt, W., Schühle, U., Marsch, E., Poland, A.I., Jordan, S.D., Thomas, R.J., Hassler, D.M., Vial, J.-C., Kühne, M., Huber, M.C.E., Siegmund, O.H.W., Gabriel, A., Timothy, J.G., and Grewing, M., First results of the SUMER telescope and spectrometer on SOHO. II. Imagery and data management, *Sol. Phys.* **170**, 105–122, 1997.

Nichols, J.S., and Linsky, J.L., The final archive and recalibration of the International Ultraviolet Explorer (IUE) satellite, *Astron. J.* **111**, 517–536, 1996.

Pauluhn, A., Rüedi, I., Solanki, S.K., Lang, J., Pike, C.D., Schühle, U., Thompson, W.T., Hollandt, J., and Huber, M.C.E., Intercalibration of SUMER and CDS on SOHO. I. SUMER detector A and CDS NIS, *Appl. Opt.* **38**, 7035–7046, 1999.

Pauluhn, A., Solanki, S.K., Schühle, U., Wilhelm, K., Lang, J., Thompson, W.T., Rüedi, I., Hollandt, J., and Huber, M.C.E., Comparison of quiet-Sun radiances measured by SUMER and CDS on SOHO, *Space Sci. Rev.* **97**, 63–66, 2001a.

Pauluhn, A., Rüedi, I., Solanki, S.K., Schühle, U., Wilhelm, K., Lang, J., Thompson, W.T., Hollandt, J., and Huber, M.C.E., Intercalibration of SUMER and CDS on SOHO. II. SUMER detectors A and B and CDS NIS, *Appl. Opt.* **40**, 6292–6300, 2001b.

Rottman, G.J., Woods, T.N., and Sparn, T.P., Solar-Stellar Irradiance Comparison Experiment 1. 1. Instrument design and operation, *J. Geophys. Res.* **98**, 10667–10677, 1993.

Samain, D., Bonnet, R.M., Gayet, R., and Lizambert, C., Stigmatic spectra of the Sun between 1200 Å and 2100 Å, *Astron. Astrophys.* **39**, 71–81, 1975.

Schühle, U., The cleanliness control program for SUMER/SOHO, In: UV and X-Ray Spectroscopy of Astrophysical and Laboratory Plasmas, *Proc. 10th International Colloquium*, (eds. E.H. Silver and S.M. Kahn), Cambridge University Press, 373–382, 1993.

Schühle, U., The SUMER instrument on SOHO: Design, performance predictions, and calibration aspects, *Proc. SPIE* **2283**, 47–52, 1994.

Schühle, U., Brekke, P., Curdt, W., Hollandt, J., Lemaire, P., and Wilhelm, K., Radiometric calibration tracking of the vacuum-ultraviolet spectrometer SUMER during the first year of the SOHO mission, *Appl. Opt.* **37**, 2646–2652, 1998.

Schühle, U., Curdt, W., Hollandt, J., Feldman, U., Lemaire, P., and Wilhelm, K., Radiometric calibration of the vacuum-ultraviolet spectrograph SUMER on the SOHO spacecraft with the B detector, *Appl. Opt.* **39**, 418–425, 2000a.

Schühle, U., Hollandt, J., Pauluhn, A., and Wilhelm, K., Mid-term radiance variation of far-ultraviolet emission lines from quiet-Sun areas, *ESA SP*-**463**, 427–430, 2000b.

Schühle, U., Wilhelm, K., Hollandt, J., Lemaire, P., and Pauluhn, A., Radiance variations of the quiet Sun at far-ultraviolet wavelengths, *Astron. Astrophys.* **354**, L71–L74, 2000c.

Schühle, U., Pauluhn, A., Hollandt, J., Lemaire, P., and Wilhelm, K., Radiance variations of vacuum-ultraviolet emission lines of the quiet Sun observed with SUMER on SOHO, *Phys. Chem. Earth (C)* **25**, 429–432, 2000d.

Thomas, R., 20:20 vision; SOHO cleanliness, this volume, 2002.

Wilhelm, K., Curdt, W., Marsch, E., Schühle, U., Lemaire, P., Gabriel, A.H., Vial, J.-C., Grewing, M., Huber, M.C.E., Jordan, S.D., Poland, A.I., Thomas, R.J., Kühne, M., Timothy, J.G., Hassler, D.M., and Siegmund, O.H.W., SUMER – Solar Ultraviolet Measurements of Emitted Radiation, *Sol. Phys.* **162**, 189–231, 1995.

Wilhelm, K., Lemaire, P., Curdt, W., Schühle, U., Marsch, E., Poland, A.I., Jordan, S.D., Thomas, R.J., Hassler, D.M., Huber, M.C.E., Vial, J.-C., Kühne, M., Siegmund, O.H.W., Gabriel, A., Timothy, J.G., Grewing, M., Feldman, U., Hollandt, J., and Brekke, P., First results of the SUMER telescope and spectrometer – Solar Ultraviolet Measurements of Emitted Radiation – on SOHO. I. Spectra and spectroradiometry, *Sol. Phys.* **170**, 75–104, 1997a.

Wilhelm, K., Lemaire, P., Feldman, U., Hollandt, J., Schühle, U., and Curdt, W., Radiometric calibration of SUMER: Refinement of the laboratory results under operational conditions on SOHO, *Appl. Opt.* **36**, 6416–6422, 1997b.

Wilhelm, K., Lemaire, P., Dammasch, I.E., Hollandt, J., Schühle, U., Curdt, W., Kucera, T., Hassler, D.M., and Huber, M.C.E., Solar irradiances and radiances of UV and EUV lines during the minimum of the sunspot activity in 1996, *Astron. Astrophys.* **334**, 685–702, 1998.

Wilhelm, K., Woods, T.N., Schühle, U., Curdt, W., Lemaire, P., and Rottman, G.J., The solar ultraviolet spectrum from 1200 Å to 1560 Å: A radiometric comparison between SUMER/SOHO and SOLSTICE/UARS, *Astron. Astrophys.* **352**, 321–326, 1999a.

Wilhelm, K., Lemaire, P., Dammasch, I.E., Hollandt, J., Schühle, U., Curdt, W., Kucera, T., Hassler, D.M., and Huber, M.C.E., Solar irradiances of UV and EUV lines during the minimum of the sunspot activity in 1996, *Adv. Space Res.* **24**, 229–232, 1999b.

Wilhelm, K., Schühle, U., Curdt, W., Dammasch, I.E., Hollandt, J., Lemaire, P., and Huber, M.C.E., Solar spectroradiometry with the telescope and spectrograph SUMER on the Solar and Heliospheric Observatory SOHO, *Metrologia* **37**, 393–398, 2000a.

Wilhelm, K., Lemaire, P., Dammasch, I.E., Hollandt, J., Schühle, U., Curdt, W., Kucera, T., Hassler, D.M., and Huber, M.C.E., Solar irradiances of ultraviolet emission lines measured during the minimum of sunspot activity in 1996 and 1997, *Phys. Chem. Earth (C)* **25**, 389–392, 2000b.

— 11 —

UV Radiometric Calibration of UVCS

LARRY D. GARDNER, PETER L. SMITH, JOHN L. KOHL,
NIGEL ATKINS, ANGELA CIARAVELLA, MARI PAZ MIRALLES,
ALEXANDER PANASYUK, JOHN C. RAYMOND,
LEONARD STRACHAN, JR., RAID M. SULEIMAN

Harvard-Smithsonian Center for Astrophysics, Cambridge, MA, USA

MARCO ROMOLI

Dip. di Astronomia e Scienza dello Spazio, Università di Firenze, Firenze, Italy

SILVANO FINESCHI

Osservatorio Astronomico di Torino, Pino Torinese, Italy

The Ultraviolet Coronagraph Spectrometer (UVCS) was characterized and radiometrically calibrated in the laboratory as a system at the Harvard-Smithsonian Center for Astrophysics in June of 1995. Component level calibrations of optical components and detectors were also performed. After launch, an in-flight calibration activity was carried out that extended the laboratory calibration, compared UVCS measurements of stars to those of other instruments and monitored the radiometric stability of UVCS through repeated measurements of stars that are believed to have nearly constant ultraviolet irradiance. In-flight measurements have, in general, confirmed the laboratory radiometric calibration. Comparisons to Spartan 201 observations of the same coronal structures agree within 10 %. The system responsivity, although it has changed somewhat during the six years of operation, is well behaved and characterizable. This paper describes the UVCS calibration and its results.

11.1 Introduction

In this paper we describe the radiometric calibration of UVCS and the current state of knowledge regarding its responsivity. This paper does not describe the extensive characterization of the instrument mechanisms and non-radiometric system properties that have been achieved through both laboratory and in-flight procedures. For example, the characterization of the variable slit widths is not presented even though this information is an integral part of the spectral radiance calibration. Similarly, the characterization of the pointing of the telescope mirrors is not described nor are the determinations of the wavelength scales and grating rotations. The laboratory characterization of the internal occulter position, which determines the limiting aperture for observations at selected heliographic heights, is not described, but the determination of the vignetting function, which depends on both the internal occulter position and variations of reflectances and grating efficiencies across the surface of the optical components, is described. Another important aspect of the

UVCS characterization is the stray light determination, which is a consideration for all UVCS observations. The stray light depends on the heliographic height of an observation. It can be determined by observing spectral lines of low charge state ions that do not exist in significant amounts in the corona. Comparisons of such measurements to laboratory stray light measurements yield consistent results. Calibration files containing all of this information as well as the radiometric calibration itself are included in the UVCS Data Analysis Software, which is available through the SOHO Archive and elsewhere. An important aspect of the in-flight calibration activity has been the monitoring of the detector gain stability. The gain of the microchannel plate (MCP) z-stack in the crossed-delay-line (XDL) detectors [*Siegmund et al.*, 1994] of UVCS degrades with accumulated photon dose on the photosensitive areas of the first MCP. This effect is believed to be a result of wear to the final MCP in the stack. In-flight measurements have been used to track the changes in gain across the detector surface and increase high voltage as necessary to ensure that the detected quantum efficiency remains constant to within ± 5 %.

The UVCS radiometric calibration is based on the pre-launch system level calibration, component calibrations and in-flight calibrations. The calibration of the O VI channel presented herein, including specified changes, is applicable for the entire mission. The calibration of the Ly-α channel is applicable through 3 September 1997 when the detector high voltage for that channel was lowered to reduce the current, and certain regions of the detector became unreliable. The system level laboratory calibration could only be done at one position of the internal occulter (i.e., the aperture used for observations at 2.7 solar radii). The in-flight calibration together with the component calibrations were used to extend the system calibration to all instrument apertures that have been used during the mission (i.e., those for every heliographic height observed). In-flight intercalibrations to UVCS/Spartan 201 and SUMER were accomplished using co-registered observations of the Sun during the mission. In addition, periodic measurements of stars, which are believed to have relatively constant UV spectral irradiances, have been used to determine the consistency of the UVCS calibration and that of Voyager, the International Ultraviolet Explorer (IUE) and Far Ultraviolet Spectroscopic Explorer (FUSE) spacecraft. Periodic measurements of the same stars have been used to indicate the stability of the UVCS responsivity over a six year period.

In-flight observations were also used to compare the laboratory radiometric calibrations of UVCS's two UV channels at overlapping wavelengths near 121.6 nm. A small difference was discovered. As a result, the calibrations of both channels were shifted so as to bring them into agreement with each other.

11.2 Instrument Description

The UVCS (see Figure11.1), a system of three externally and internally occulted telescopes feeding two ultraviolet spectrographic channels and one visible light polarimetric channel, has been described previously [*Kohl et al.*, 1995]. Light from the solar disk enters the UVCS aperture and is absorbed in a light trap mounted near the rear of the instrument. One edge of the aperture is a linear serrated blade that forms the edge of the external occulter; each UV telescope mirror resides in the shadow behind that occulter. Rays from the solar disk, diffracted by the external occulter, which would otherwise be specularly reflected by the telescope mirrors into the spectrograph, are intercepted by the internal

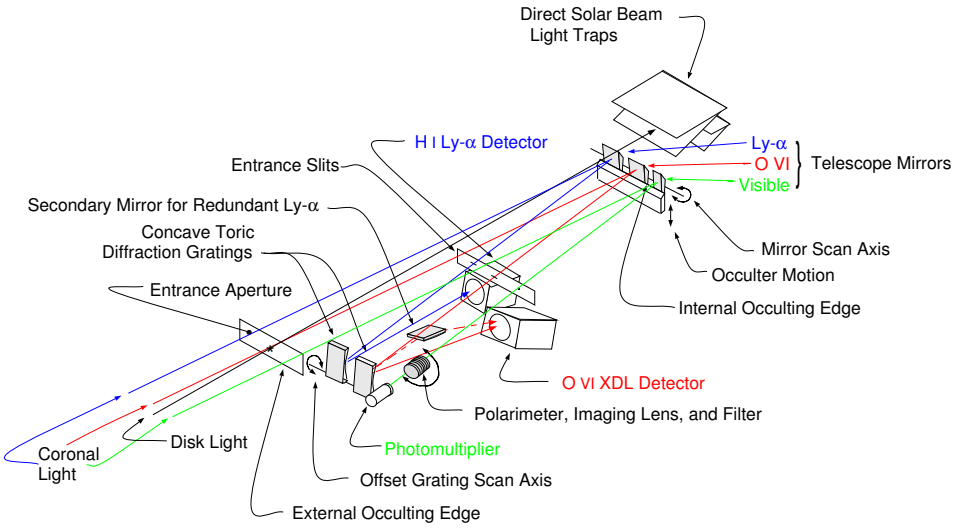

Figure 11.1: Schematic of the UVCS optical system.

occulter which can move perpendicularly to the external occulter edge. The selected position of the internal occulter depends on the heliocentric height observed. In this way the limiting aperture of UVCS for any given observation is determined by the position of the internal occulter. The UV telescope optical surfaces themselves are chemical vapor deposited (CVD) silicon carbide on silicon carbide substrates. The mirrors have a spherical figure with 750 mm focal lengths. Both UV spectrographic channels are normal incidence Rowland circle designs. Both have adjustable entrance slits. The diffraction gratings are toric in figure [*Huber et al.*, 1988] with 750 mm major radii of curvature and are held in independently adjustable Johnson-Onaka style mechanisms. The detector systems are microchannel plate based with XDL anodes. The grating ranges and rulings are chosen so as to center the H I Ly-α line (121.6 nm) in one channel and the O VI doublet 103.2 and 103.7 nm in the other. Inside the O VI channel there is an auxiliary mirror that is strategically placed to divert a band of light which includes the H I Ly-α wavelength toward the O VI detector when the O VI grating is rotated to a specific range of angles. In this way a "redundancy" has been created for the portion of the spectrum containing H I Ly α.

The instantaneous field of view of UVCS is a variable width slice of the corona approximately $40'$ long (i.e., in the direction that is tangent to the disk). The width of the slice (i.e., in the radial direction) is given by the ratio of the spectrometer slit width to telescope focal length and so is selectable between about $1''$ and $1.4'$. The images recorded by the XDL detectors display spatial imaging information along the slit length and spectral information in the direction of the width. The UVCS can be rolled about the sun-center axis by approximately 350 degrees, and the telescope mirrors can be rotated from 1.2 to 10 $R_\odot$. UVCS can also change its normally sun-centered pointing by $\pm 35'$. In this way UVCS can observe radial heights from –1 to 12 $R_\odot$.

11.3 Cleanliness

Cleanliness was an issue of major concern during the fabrication, integration, and testing of UVCS. Its stray light performance is sensitive to light scattering by particulate contamination, and its optical efficiencies are affected by molecular contamination photopolymerized on its optical surfaces. While the former is routinely controlled by carrying out the work on the instrument in suitable conventional cleanrooms, the latter requires attention to all manner of details ranging from choices of construction materials to appropriate filtration through activated carbon of the air circulated in the aforementioned cleanrooms. For UVCS the cleanliness program was laid out in appropriate process control documents that specified a total allowable quantity of chemical and particulate surface contamination, procedures for cleaning parts allowable solvents and materials, etc. Since the structure of UVCS was constructed of graphite fiber reinforced epoxy (GFRE), which is sensitive to the absorption of moisture, it was also essential to control humidity and to keep the instrument purged with dry gas whenever it was not actively being assembled or tested. A rigorous program was set up to monitor the contaminant levels, including moisture absorption, throughout all stages of construction, integration, and testing in order to verify compliance with the control documents and to be able to take corrective action before levels approach the allowable limits. The program was reasonably successful overall, and certainly none of its rigor should be relaxed for any future instrument. However with the benefit of hindsight, some changes would be made, i.e., the allowance of additional time for optical testing and component change-out as necessary, and the addition of doors and active pumping to the detectors to prevent deterioration of the photocathodes. For further details of the UVCS cleanliness program, see *Schühle et al.* [2002].

11.4 Laboratory Measurements of Instrument Properties

The UVCS system level tests were carried out in laboratories at the Harvard-Smithsonian Center for Astrophysics in June of 1995. A description of that work was published in 1996 [*Gardner et al.,* 1996] and only will be summarized here. Owing to the design of the internal occulter mechanism, the UVCS system level calibrations were limited to one optical aperture – the one used for measurements at a heliocentric height of 2.7 $R_\odot$ and corresponding to the internal occulter's launch-locked position.

The count rate C of the UVCS response to a source of spectral radiance $I(\lambda)$ is:

$$C = (w_s h_s w_m h_m)/f^2 \int I(\lambda)\varepsilon(\lambda)\mathrm{d}\lambda, \tag{11.1}$$

where w_s is the slit width, h_s is the slit height, w_m is the unvignetted mirror width, h_m is the mirror height and f is the telescope focal length. The system responsivity is given by:

$$\varepsilon(\lambda) = R_t(\lambda, x_t, y_t) E_g(\lambda, x_g, y_g) E_d(\lambda, x_d, y_d), \tag{11.2}$$

where $R_t(\lambda, x_t, y_t)$ is the mirror reflectance, $E_g(\lambda, x_g, y_g)$ is the grating efficiency including the coating and $E_d(\lambda, x_d, y_d)$ is the detected quantum efficiency of the detector system. All three of these quantities depend on wavelength and can vary over their respective surfaces. Hence, Equation (11.1) describes the count rate for a particular region of the aperture and a particular pixel.

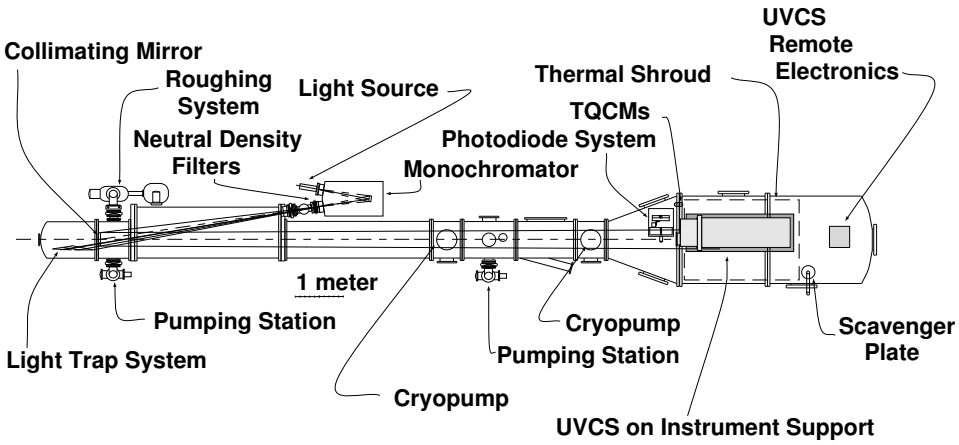

Figure 11.2: The arrangement for the UVCS system level calibration and characterization. This primary vacuum chamber and its peripheral units included the light sources, predispersing monochromator, the collimating mirror, standard photodiodes and instrument support. All of these units were equipped with mechanisms that facilitated remote control of the in-vacuum devices.

The effective area $A_{\rm eff}$ for a particular wavelength $\lambda_{\rm i}$ is given by

$$A_{\rm eff} = (w_{\rm m} h_{\rm m}) \varepsilon(\lambda_{\rm i}), \tag{11.3}$$

where an average value over the aperture is used for $R_{\rm t}$ and $E_{\rm g}$, and a reference area on the detector is used for $E_{\rm d}$. Equations (11.1) and (11.3) are applicable to the primary Ly-α and direct O VI channels but not to the redundant Ly-α path, which contains an additional optic inside the spectrometer. See Section 11.5.3.1.

The general arrangement for the UVCS radiometric calibration is shown in Figure 11.2. Radiation from a gas discharge light source was predispersed using a 1 meter radius monochromator with a 1200 line-per-mm grating. A single bright atomic line was focused onto its exit slit. The light passing through the slit (and through insertable filters of known density) was collimated by a 4.6 m focal length, f/10 mirror. The mirror was remotely adjustable from outside the vacuum and so the light could be directed toward the UVCS, which was mounted on a support that could be remotely translated and pivoted. The collimating mirror and the position of UVCS were adjusted so that the line radiation entered through the UVCS instrument aperture and onto its telescope mirrors completely filling the portion of the mirrors that was not covered by UVCS's internal occulter. That 11 mm wide portion of the mirrors, which is the one used for observations at 2.7 solar radii from sun-center, was the only part of the aperture that could be calibrated during the system level calibration. The UVCS radiometric response was measured against secondary photodiode (cesium telluride and aluminum oxide) standards from the National Institute of Standards and Technology (NIST). The NIST photodiodes resided on x-y translation stages located immediately in front of the UVCS and could be inserted anywhere within the collimated beam. The portion of the light striking each of the telescope mirrors was measured by scanning the appropriate photodiode over the portion of the beam illuminating the mirror. The

Table 11.1: Laboratory measured UV radiometric system responsivities. The relative standard uncertainty in the numbers presented is 16 %.

Wavelength /	System Responsivities		
nm	Ly-α channel	O VI channel	redundant Ly-α path
102.6		0.0033	
104.8		0.0030	
116.5	0.0022		
112.6	0.0020		
123.6	0.0021		0.0010
253.7**	$< 3\times10^{-9}$		

** With instrument configured to detect H I 121.6 nm.

intensity was uniform to within $\pm$ 10 %. The $\approx$1 mm wide exit slit of the predisperser was imaged onto each UVCS slit by a combination of the collimating mirror and the respective UVCS telescope mirror with demagnification by a factor of six. Each slit could be set large enough to pass the entire light bundle, which was passed on towards the respective grating where it was dispersed and focused onto an XDL detector. The count rates registered on the detectors (adjusted by the filters' densities) were compared directly to the output of the NIST photodiodes, thereby giving the system responsivity. Measurements were made for both UV channels at several wavelengths within their respective ranges.

A total relative standard uncertainty of 16 % for each of the radiometric measurements is computed as a quadature sum of the relative standard uncertainties in the calibration of the reference diode (10 %), the uniformity over the telescope aperture of the incident radiation (10 %), the variation of the incident light intensity during a measurement (5 %), and various miscellaneous uncertainties (5 % total) such as the calibration of the current measuring devices, areas of apertures, etc. The results obtained are reproduced in Table 11.1.

Since the laboratory system calibration could be accomplished at only one aperture, the determination of the behavior of the system responsivity of UVCS as a function of aperture was not carried out until after launch. To support in-flight measurements (presented in Section 11.5 of this paper), a laboratory study of the behavior of the efficiency of the UVCS gratings as a function of illuminated aperture was carried out using replicas made from the same masters as the flight gratings. A description of those measurements is published in *Gardner et al.* [2000]. The results are reproduced in Figure 11.3. Because of schedule constraints during the laboratory testing period, complete measurements of the variations of the instrument's responsivities over the full active areas of the detector systems, i.e., the flatfield-calibrations, could not be made. However, representative portions of the detectors were studied with the plan of confirming and extending the measurements in flight.

The laboratory calibration did not include system level measurements of the O VI channel second order responsivity. Estimates of responsivities at second order have been made using measurements of components and taking into account degradation observed in the detector systems.

Based on measurements of the individual components and/or replicas of the individual components, the responsivity at 104.8 nm should be the product of the reflectivity of

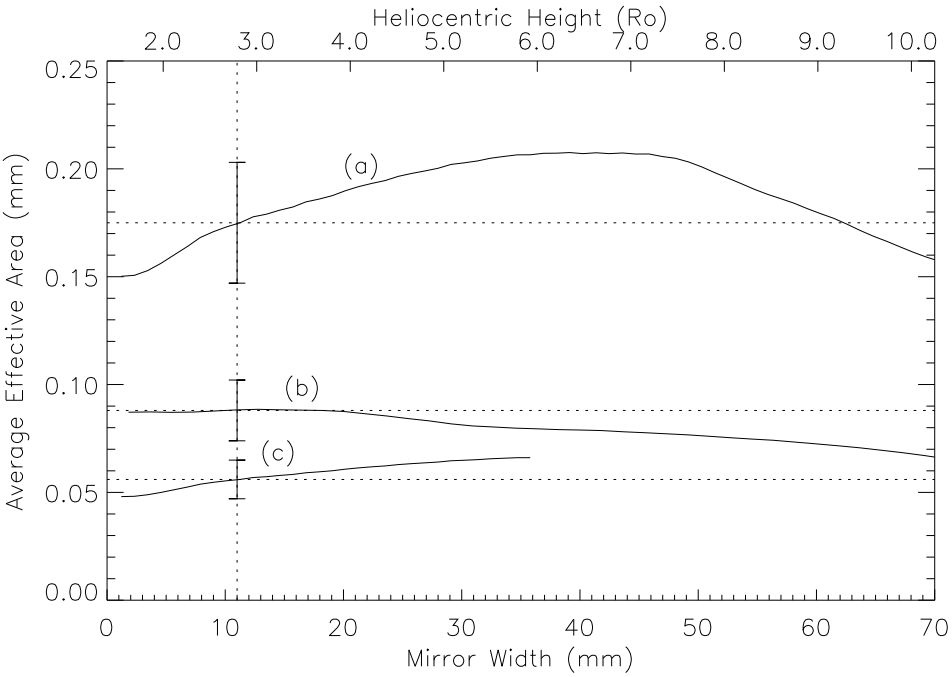

Figure 11.3: Behavior of the UVCS channels as a function of unvignetted width. Curves (a), (b), and (c) show the effective area averaged over the width of the aperture as functions of the mirror width for the O VI Ly-α, and redundant Ly-α channels, respectively, as determined from the laboratory measurements. The error bars denote the standard uncertainty in each curve and are plotted at the launch-locked aperture value of 11 mm. The horizontal dotted lines are provided as an aid to the eye.

the SiC-coated telescope mirror (46 %) [*Osantowski et al.*, 1992], the grating reflectivity (18 %), the groove efficiency averaged over the "standard aperture" of 11 mm width (49 %), and the detected quantum efficiency of the KBr-coated XDL detector (18 %) [*O.H.W. Siegmund, personal communication*, 1995; *Kohl et al.*, 1995]. However, the product of these numbers is 0.73 %, which is 2.1 times the measured system value. A similar analysis has been carried out for H I Ly-α 121.6 nm, which in the redundant Ly-α path of the O VI channel includes a reflection at an 85 degree angle of incidence (75 % efficient) off the MgF_2/Al coated auxiliary mirror. Here the loss factor is 3.2. Given the nature of the optical components and the environmental conditions experienced by UVCS, we believe the loss in responsivity at both wavelengths is consistent with damage to the KBr coating of the detector from exposure to water vapor (i.e., humidity). A reasonable way to model the loss in responsivity is to take a weighted linear combination of the quantum efficiencies of bare microchannel plates (from the same lot as UVCS) [*Siegmund et al.*, 1995] and of the assumed undegraded KBr coated microchannel plate (i.e., that of the actual UVCS detector) as measured at the component level [*Kohl et al.*, 1995]. It happens that 73 % "bare" plus 27 % KBr provide the observed degradation at both 104.8 and 121.6 nm.

To obtain a responsivity of the UVCS in second order at He I 58.4 nm, we first modify the efficiency of the XDL detector using the coefficients deduced above and the undegraded efficiencies for 58.4 nm. The overall detector efficiency at 58.4 nm is then reduced from 27 % to 12 %. Multiplying by the component efficiencies at 58.4 nm (telescope mirror, 27 %; average grating efficiency for the first 11 mm, 4.6 %; redundant mirror reflectivity, 70 %) provides a system level responsivity of about 0.10 % for the standard aperture.

An alternative method of estimating the responsivity at 58.4 nm can be made based on the performance of a "life-test" KBr coated detector. *Jelinsky et al.* [1996] report responsivity measurements that have been periodically made for 67 months. The detector, which was stored in dry nitrogen between laboratory air exposures at the time of measurement updates, has shown a 30 % loss of responsivity at 58.4 nm, a 21 % loss at 104.8 nm, and a loss of 36 % at 121.6 nm over the 67 months. Admittedly the environment experienced by the UVCS detectors has been very different from that experienced by the "life-test" unit. Indeed, the latter has likely been better controlled and the environment more benign than that experienced by UVCS during integration and testing. Nevertheless, if one assumes that the UVCS O VI detector has degraded in the same relative proportions as the life-test detector, then the degradation at 58.4 nm can be related to the observed degradations at 104.8 nm and 121.6 nm. Thus, comparing to 104.8 nm, one obtains a degradation given by the ratio of the test detector's degradation at 58.4 nm to that at 104.8 nm (0.30/0.21) times the observed degradation of the UVCS detector at 104.8 nm. The resulting UVCS system level responsivity at 58.4 nm is 0.061 %. Comparing to 121.6 nm, one obtains a degradation given by the ratio of the test detector's degradation at 58.4 nm to that at 121.6 nm (0.30/0.36), times the observed degradation of the UVCS detector at 121.6 nm. The resulting UVCS average system responsivity at 58.4 nm is 0.052 %.

Lacking better information, we choose to algebraically average the three values (0.10 %, 0.061 % and 0.052 %) to obtain a best estimate of 0.071 %. The relative standard uncertainty is estimated to be 50 % of this number. This value reflects the confidence in the methods used and is deliberately chosen to encompass all three values.

11.5 In-flight Radiometric Measurements

In-flight performance has been determined and monitored using specially designed observations of three source types: (1) stars, (2) the solar disk, and (3) the corona at heliocentric heights in the ranges 1.5 to 5.0 $R_\odot$.

11.5.1 Observations of Stars

Observations have been made by UVCS of about 15 stars that pass within 12 $R_\odot$ of sun-center. Voyager, IUE, and FUSE, among others, have made spectral irradiance measurements of one or more of the same stars in spectral ranges overlapping those of UVCS. A typical UVCS measurement consists of a "passage" of the star's image across the UVCS slits. Depending on the details of the trajectory of the star in the sky, the configuration of the UVCS roll and mirror angle can be set such that the angle of the passage relative to the UVCS slit edge is any angle between zero (i.e., perfectly aligned with the long dimension of the slit) and 90 degrees (i.e., at right angles to the long dimension of the slit). The slits

are set sufficiently wide and the exposure time is sufficiently short that the entire image of the star passes through the slits for several exposures. Multiple exposures and multiple passages are summed to improve the statistics for the less bright stars.

11.5.1.1 Responsivity Changes with Time from Star Observations

The stars that have been observed by UVCS are within its field of view typically for four to five days once per year. Several of the brightest stars have been observed each year of the mission. Some of these observations are suitable for the purpose of monitoring the UVCS radiometric calibration in so far as the stars observed (typically B-stars) have more or less constant emission in the UV. An example of such a set of observations from the O VI channel for the star δ Sco, a binary star system, is presented in Figure 11.4. It has been observed by UVCS with the same or nearly the same instrument configuration in November of every year since SOHO was launched. Figure 11.4(a) shows the spectra observed in 1996, 1999, and 2001. The data were all taken for an approximately 49 mm aperture and therefore are only marginally sensitive to any changes in the responsivity of the first few mm of the mirror. A portion of the spectrum on the left of the figure has contributions from the redundant path. Figure 11.4(b) shows integrals of the spectra from 100 nm to 140 nm (which includes an undetermined portion of "redundant" spectrum) plotted against the year in which each was taken. The data are consistent with a constant behavior of the UVCS radiometric response and the variability of this particular star system within about $\pm$10 %. However the plot suggests a trend toward a lower responsivity: a loss of about 2 % per year. Since the trend could be due to a variation in the UV output of this particular star system, which was observed to produce outbursts in the visible portion of the spectrum during the recent periastron passage [*Miroshnichenko et al.*, 2001], we have examined other data searching for possible response losses, particularly at small apertures.

Like δ Sco, the star ρ Leo has also been observed each year of the mission. The instrument configuration was in general not identical year to year. However, there has been sufficient "overlap" in the observations to provide insight into possible responsivity variations at small apertures. Partial data sets also exist for some other stars as well. In general, there exist a few measurements by other instruments made in this wavelength range for some of these stars. Shown in Figure 11.5 is a plot of the deduced responsivities. Each plotted point is the total count rate observed in a 1 nm band centered on the wavelength noted in the legend divided by the aperture width used for the measurement and then appropriately scaled. The wavelength bands chosen had negligible contributions from the redundant path. The error bars shown are typical of the standard uncertainty in each measurement. The solid black curve is the result of the laboratory component level measurements with the absolute scale set by the laboratory system level calibration at 2.7 $R_\odot$. The 1997 observations of ρ Leo at 101.0 nm were carried out at three apertures. They are normalized to the laboratory curve at the largest aperture and provide confidence that the shape of the laboratory curve is correct for the early part of the mission. In 1996 and 1999 measurements at 106.7 nm of ρ Leo were made at the same aperture of 35 mm. The ρ-Leo data from 1999 are actually a series of observations made at a number of different occulter values. The scale of the 1999 data was fixed by assuming a constant irradiance for ρ Leo and using the ratios of count rates observed in 1996 and 1999 for the same aperture. One can readily see that the responsivity at small apertures falls significantly and systemati-

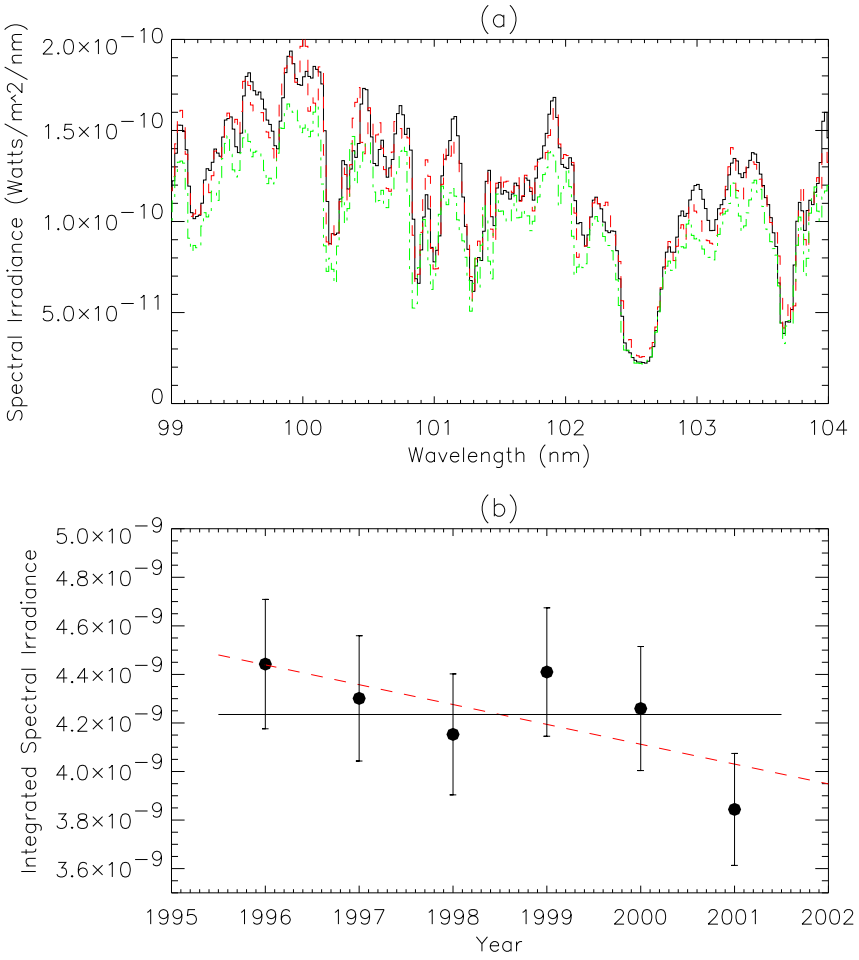

Figure 11.4: Yearly measurements of the short wavelength spectrum of δ Sco. (a) is an over-plot of O VI channel measurements from 1996, 1999, and 2001. The left-most portion of the measured spectrum, in each case, has redundant path contributions. (b) shows a time history of the integral of each measured spectrum from 100 nm to 104 nm. The measurements are constant within 10 %. However, the best fit to the data is a line with a small decreasing trend of 2 % per year. The error bars represent the standard uncertainties including those attributable to the flatfields.

cally below the laboratory plot. At the "standard aperture" of 11 mm, the responsivity for August of 1999 is 80 % of the laboratory value.

In December of 1999 observations were made of θ Oph at 111.1 nm as a function of the aperture. They are also shown in Figure 11.5. UVCS observations do not exist for θ Oph in 1996 or 1997, and consequently the scale cannot be set in the same way as it was for ρ Leo. However the data in 1999 include observations made at relatively large apertures. From the δ-Sco observations (see Figure 11.4) it was concluded that for large apertures

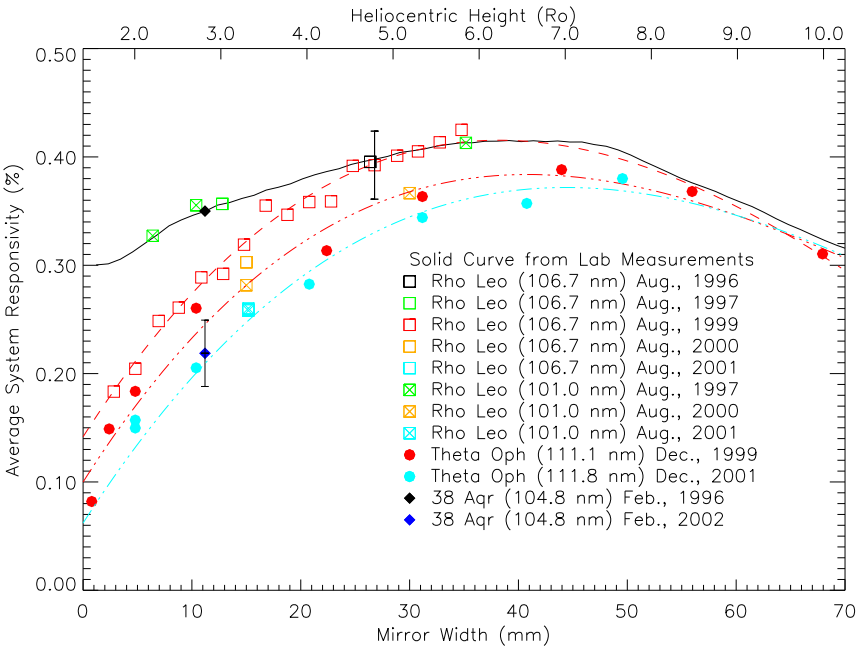

Figure 11.5: Aperture averaged measurements of the system responsivity determined from observations of stars. The identification of the various points is noted in the legend on the plot. The data from 1996 and 1997 are normalized to the laboratory values, which have the same relative variation with mirror width. The later data are put on a common scale through ratios of count rates observed at the same aperture values and the same wavelength for the same star. To connect different stars and thereby extend trends into later years, the relative scales are established using the demonstrated conclusion that the aperture averaged responsivity at apertures beyond 49 mm has changed very little in time. Implicit is the assumption that the irradiances of the stars are nearly constant in time. The smooth color curves, red-dashed, red-dash-dot, and blue-dash-dot, are third degree polynomial fits to the 1999 ρ-Leo, 1999 θ-Oph, and 2001 θ-Oph data, respectively. All three fits are constrained by the two highest aperture points of the 1999 θ-Oph data set.

there is no more than about 6 % degradation from November 1996, until November 1999. The scale of the 1999 θ-Oph data point at 44 mm aperture has therefore been adjusted to 6 % below the laboratory curve. The values at smaller apertures follow the same shape as the 1999 ρ-Leo curve within the uncertainties. The values at larger apertures follow the laboratory curve quite well.

In December of 2001 additional aperture scan observations were made of θ Oph at 111.8 nm. Although the data for the two years were taken at slightly different grating angles, they can be accurately put on the same scale, assuming the irradiance of the star is constant in time, using the data at the common apertures of 4.80 mm and 10.39 mm. At such small apertures the part of the spectrum containing redundant path contributions becomes less. One can then compare the data sets at the slightly different wavelength of 110.2 nm, thereby obtaining ratios of 0.82 and 0.79 at the apertures of 4.80 mm and

10.39 mm, respectively. The 2001 scan has been plotted at 80 % of the scale of the 1999 data. Note that the 2001 point at a 49 mm aperture falls very near the laboratory curve. Note also that measurement in 2001 of ρ Leo at a 15 mm aperture, which is scaled to a corresponding 1996 measurement, falls on a smooth interpolation between points on the 2001 θ-Oph scan.

There exists one other small set of data that ties recent behavior of the responsivity at small apertures to much earlier times. That data comes from observations of 38 Aquarii, a rather dim star in relation to the ones discussed above. The first measurements took place in February 1996, with an aperture of 11 mm. In February 2001, and again in February 2002, observations were repeated with the same instrument configuration as in 1996. The count rates observed in 2001 and 2002 have the same numerical value. The standard uncertainty is at the 10 % level. When the 1996 datum is normalized to the laboratory value, the 2002 point falls almost exactly on the December 2001, θ-Oph curve.

In summary, it is clear that the UVCS O VI channel *has* lost responsivity over the mission. The loss is limited to the part of the aperture used for observations at low heliocentric heights. The loss is greatest at the edge and tends to become less as the aperture is opened. The data are consistent with the yearly trend noted for large apertures in the δ Sco observations. The data are insufficiently accurate to determine exactly when the degradation began to occur, although there is some evidence that the responsivity in 1997 was about the same as in 1996. Clear evidence exists for degradation by August of 1999. The loss rate at the standard aperture of 11 mm is about 7.5 % per year beginning in 1997, i.e, the responsivity is at 62 % of the value at launch in 2002.

11.5.1.2 Absolute Stellar Spectroradiometry

Spectra of ρ Leo from the Ly-α channel are shown in Figure 11.6 together with spectra observed by IUE in April of 1980 [MAST Multimission Archive at Space Telescope, file SWP08650]. The UVCS measurements were made in August of 1996 at an aperture width of 26 mm. Assuming the Ly-α channel responsivity behavior in time parallels that of the O VI channel, there should be no degradation from the laboratory values. The UVCS data have been averaged so as to match the spectral resolution of the IUE data set. Coronal emission features (e.g., H I Ly-α 121.6 nm and Fe XII 124.2 nm) and stray light in the raw UVCS spectrum have been removed from the UVCS data. The spectral irradiance measured by UVCS is on average about 1.3 times larger than that found by IUE, nominally at the edge of one standard uncertainty of the comparison. ρ Leo has also been observed by SUMER [*Lemaire*, 2002]. Intercomparisons of UVCS and SUMER using those observations as well as observations of the star α Leo are in process at this writing.

A comparison of UVCS O VI channel observations of the star τ Tau to observations by Voyager [*Holberg et al.*, 1982; *J.B. Holberg, personal communication*, 1992] is presented in Figure 11.7. The measurement was made in June, 2001, at a UVCS mirror aperture of 35 mm. The UVCS responsivity has been adjusted downward by 10 % in accordance with the curves shown in Figure 11.5. The resolution of the UVCS data has been reduced to match the 1 nm resolution of Voyager. The two spectra match on average to within about 15 %, well within the UVCS uncertainty. UVCS has also observed Feige 110, a white dwarf star that is used as a calibration reference for FUSE [*Moos et al.*, 2000; *Sahnow et al.*, 2000]. The star has very weak UV emission as compared to the "hot" stars mentioned above. The integral of the spectrum between 102.6 nm and 103.7 nm measured by UVCS

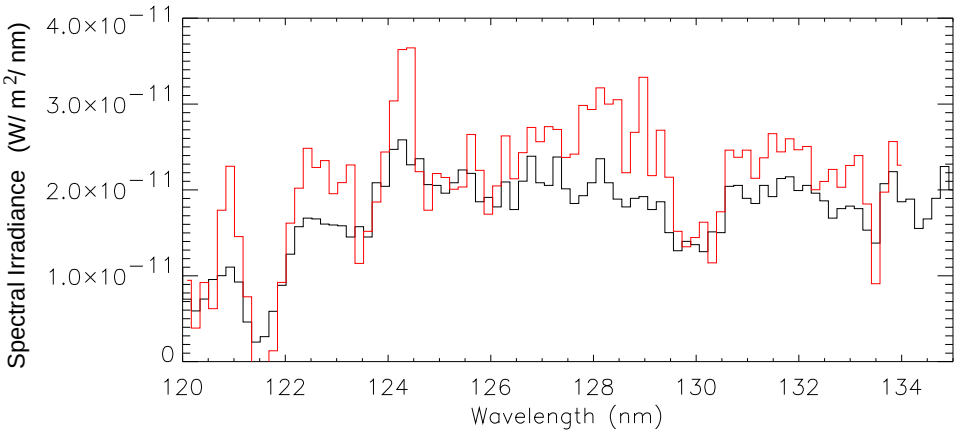

Figure 11.6: UVCS comparison to IUE. The solid dark line is a spectrum taken by IUE of the star ρ Leo. The red line is the UVCS observation of the same star. Coronal emission lines have been removed from the UVCS data. The UVCS data have been averaged to match the 0.17 nm resolution of this particular IUE data set.

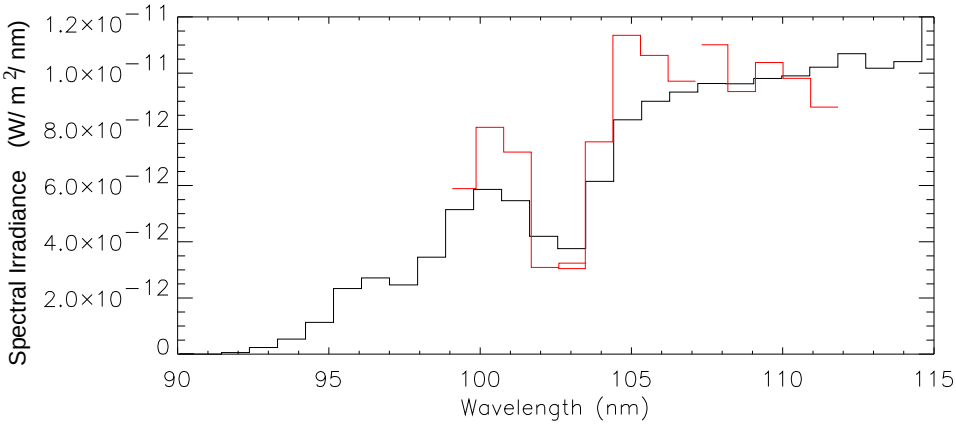

Figure 11.7: UVCS comparison to Voyager. The dark solid line is a spectrum taken by Voyager 1 of the star τ Tau in August 1992. The red line is the UVCS observation of the same star in June 2001. The UVCS data have been averaged to match the 1 nm resolution of Voyager and adjusted to reflect an 8 % loss of responsivity at the 35 mm aperture used for the observation. See Figure 11.5.

is less than 15 % below that observed by FUSE. The root mean square combined relative uncertainty is 25 %.

UVCS observations of ζ Tau, a hot supergiant star, have been used to develop a technique for separating the overlapping "redundant" (long wavelength) spectrum from the direct (short wavelength) spectrum in the UVCS O VI channel. A paper that describes the details of the method is in preparation [*B. Valcu, personal communication*, 2002].

Table 11.2: Comparison of UVCS and SUMER from ICAL_01 measurements in 1996 and 1997. Photon radiance given in units of 10^{12} s^{-1} cm^{-2} sr^{-1}.

	photon radiance		
Date	UVCS	SUMER	% Difference
96.09.30	3.64	4.66	–12 %
96.10.07	3.52	3.79	–3.7 %
96.11.04	3.64	5.49	–20 %
97.01.30	3.98	4.37	–4.7 %
97.03.14	3.98	3.78	+2.6 %
97.05.16	3.41	4.82	–17 %

11.5.2 Disk Observations

The first UVCS disk observations were carried out on 31 March 1996. Measurements of the Ly-α radiance were made at a number of positions on the disk in both the Ly-α and O VI channels. Only the first 0.8 mm of the telescope mirrors have ever been exposed to direct disk light. The UVCS neutral density filters, which attenuate Ly-α by a factor of ≈ 1000, were inserted to prevent saturation of the detectors.

Inter-calibration with SUMER has been carried out using co-registered and nearly simultaneous observations with both instruments of the N V line at 123.7 nm in 1996 and 1997. These observations were conducted as part of the SOHO Inter-Calibration (ICAL_01) Joint Observation Plan. The data from both instruments are listed in Table 11.2. The UVCS values are on average 18 % lower than those of SUMER. The relative standard uncertainties are 25 % (including counting statistics) in the UVCS values, and a similar value for SUMER. The combined relative uncertainty is thus 35 %, and all of the six data points are inside this value. All of the observations were carried out in 1996 and 1997, and no time-related trend to the differences is evident.

11.5.3 Coronal Observations

11.5.3.1 UVCS Independent Observations

One of the early tasks in-flight was the determination of the UVCS system responsivity as a function of unvignetted aperture (i.e., internal occulter location). The behavior of the primary Ly-α and O VI channels is relatively straight forward to determine; that of the redundant Ly-α path is not. The first such measurements were carried out in March of 1996. The telescopes were pointed to a height of about 2.5 $R_\odot$ in a coronal streamer. Observations of the H I Ly-α line and the O VI lines were then measured in all channels as the occulter was progressively changed from about 9 mm to zero width. The relative changes in intensity are consistent with the laboratory results from the replica grating discussed in Section 11.4.

At heliocentric heights above approximately 6 $R_\odot$ the light detected by UVCS is dominated by the weak H I Ly-α emission of the interplanetary medium. The interplanetary hydrogen gas is expected to be "cold" gas: i.e., its temperature should be about 8000 K [*Clark et al.*, 1995]. The photon emission is weak, about 3×10^{7} s^{-1} cm^{-2} sr^{-1}. We have

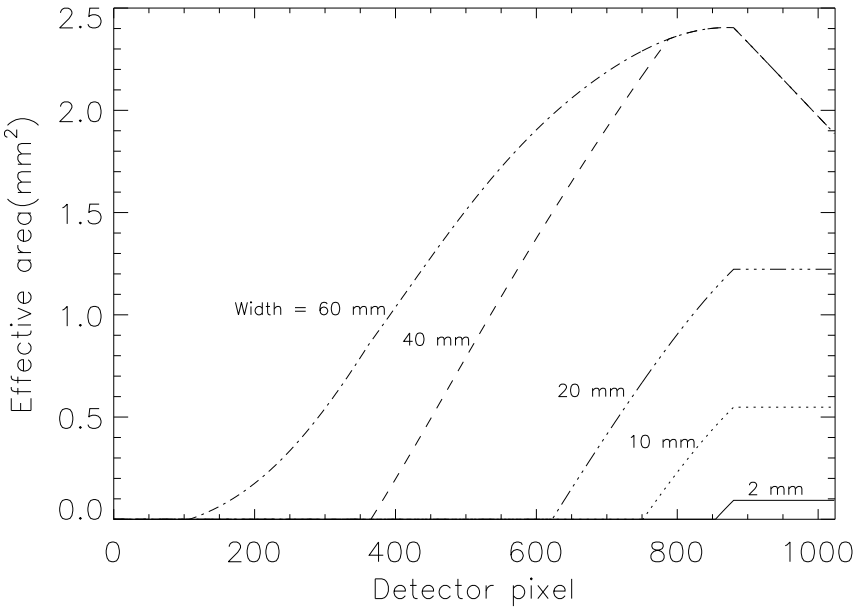

Figure 11.8: Effective area for the redundant path. The effective area is dependent on the actual unvignetted width of the telescope mirror and the vignetting by the redundant path auxiliary mirror. Shown are plots of the effective area for several example mirror widths.

used this emission to characterize the relative behavior of the responsivity as a function of aperture at large apertures for both the primary Ly-α channel and the redundant Ly-α path in the O VI channel.

The effective area of the redundant path in the O VI channel is a function of both the grating angle and the unvignetted telescope mirror aperture width. This is because the auxiliary mirror in the redundant path can be filled, over-filled, under-filled or completely missed by particular wavelengths depending on the unvignetted telescope aperture and grating angles. Its complete vignetting behavior has been mapped out using combinations of coronal measurements like those mentioned above at different grating angles in combination with the results of ray traces. The behavior, which includes the combination of the actual telescope mirror unvignetted aperture, the laboratory measured grating aperture non-uniformities, and the geometrical effects of the auxiliary mirror, is presented in Figure 11.8. The function has been incorporated into the UVCS Data Analysis Software.

After the recovery of SOHO from its mission interruption in 1998, the coronal aperture scan measurement was repeated with some additions, which allowed an extension of the results to higher aperture. For example, the method was to set the mirror to 3 $R_\odot$, take measurements as the occulter was closed to a position corresponding to about 2 $R_\odot$, then move the mirror to 2.5 $R_\odot$, and continue closing the occulter. Measurements for apertures up to about 4.5 $R_\odot$ were possible in this manner. Above 4.5 $R_\odot$ the emission is too weak to reliably obtain a scan. Such measurements have been repeated several times since the beginning of 2000 as an attempt to monitor changes in the *shape* of the system responsivity function. Since the corona is fundamentally variable, it is difficult to put the scans on a

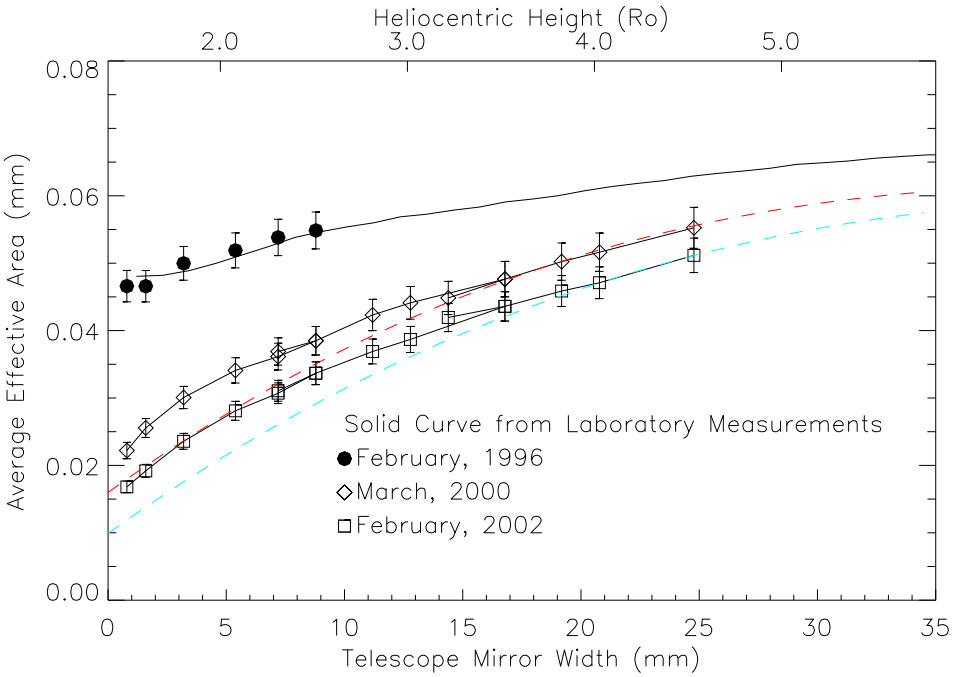

Figure 11.9: Average effective area of the redundant Ly-α path as a function of aperture width setting. Plotted is the maximum average effective area of the redundant path at 121.6 nm for the years 1996, 2000, and 2002. The colored dashed curves are appropriately scaled from Figure 11.5.

common absolute scale. In Figure 11.8 we have normalized the 1996 scan to the laboratory result, and the 1999 and 2002 scans to the corresponding curves obtained from observing stars (see Figure 11.5). The curves indicate a reduction in overall system responsivity of the redundant Ly-α path with time. However it appears that the reduction is less than that for the direct O VI channel. A more definitive conclusion awaits a better normalization for these data.

11.5.3.2 Intercalibration with Spartan 201

The Spartan 201 spacecraft, a Space Shuttle deployed and retrieved satellite, is comprised of the Ultraviolet Coronal Spectrometer (UVCS/Spartan) and the White Light Coronagraph (WLC/Spartan). UVCS/Spartan views a single spatial element at a time, has less spatial resolution than UVCS/SOHO and observes primarily the Ly-α spectral line. Its basic telescope design is similar to that of UVCS/SOHO. It has made measurements of the solar corona at H I Ly α on four two-day long flights, the first three occurring in 1993, 1994, and 1995, before SOHO was launched. The last flight occurred on 1 to 3 November 1998, shortly after SOHO was recommissioned after the mission interruption. UVCS/Spartan was radiometrically calibrated in the laboratory before and after each of its flights. Co-temporal and co-spatial observations of H I Ly α were made in streamers

and coronal holes with both UVCS/Spartan and UVCS/SOHO. After accounting for the responsivity decrease to 75 % of the UVCS/SOHO pre-launch value, the two instruments show agreement within 10 %. If the UVCS/Spartan and UVCS/SOHO calibrations are completely independent, then the uncertainty analysis indicates an expected relative standard uncertainty of 25 %.

11.5.4 Detector Flatfield Measurements

The pixel to pixel variation in the UVCS responsivity has been measured in-flight for large portions of the detectors. The initial measurements and subsequent monitoring utilized a combination of star observations and grating scans. The star observations are used to determine the variations in the direction that is perpendicular to dispersion and grating scans of solar spectral lines are used to determine the variations in the dispersion direction.

The approach for the star observations consists of orienting UVCS and setting each mirror so that a bright star is imaged in the center of each slit's narrow dimension and tracks down its long dimension. Exposures are repeatedly made. The star's spectrum is thus mapped from the "top" to the "bottom" of the detectors. Because of telemetry rate limitations, only a small portion of the spectrum at high resolution can be transmitted to the ground. Four bright UV stars (ζ Tau, α Vir, δ Sco, and θ Oph) have been used in this way. The spatial flatfield calibration can be extended to other portions of the detectors in the spectral direction using grating scans of line radiation (e.g., Ly α) from the corona or disk light diffracted from the external occulter. Additional information about the technique can be found in *Cosmo et al.* [2000].

The procedure is repeated periodically in order to track changes in the detectors' gain with photon dose. The high voltage applied to the microchannel plates is increased to restore the gain before the efficiency of the detector has fallen by more than 5 %.

Flatfield measurements have been made both in the laboratory prior to launch and in-flight. The pixel to pixel variation for the Ly-α detector is $\pm$10 % and the variation for the O VI detector is about $\pm$5 %. Given the magnitude of other uncertainties involved in UVCS radiometry, it is recommended that for essentially all analyses, the user not attempt to correct the data for flatfield variations, but instead adopt the above uncertainties. This is particular appropriate because of the uncertainties introduced by detector degradation as described above. Each detector has a few obvious defects where the detection efficiency approaches zero. Data from such regions should not be used.

11.6 Summary and Conclusions

Pre-flight laboratory measurements were made of the key UVCS/SOHO performance parameters such as spectral resolutions, radiometric responsivities, stray light levels, and flatfield variations over a limited portion of the fields. Measurements made in-flight have, in general, confirmed those laboratory measurements. Because the laboratory system radiometric calibration was only done for one particular limiting aperture (i.e., the one used for observations at 2.7 solar radii), a combination of laboratory component calibrations and in-flight observations were used to extend the calibration to all apertures used during

the mission. Over the six years of operation, the responsivity has decreased in a characterizable fashion for portions of the aperture. The UVCS first order radiometric calibration is in agreement with calibrations of UVCS/Spartan 201, SUMER, IUE, Voyager, and FUSE. Its accuracy is at a relative standard uncertainty of 20 % to 22 % depending on the year and the observed height. The second order radiometric calibration of UVCS is based on an analysis of laboratory component calibrations and modeled detector photocathode degradation. It is known only to an estimated relative standard uncertainty of 50 %.

Acknowledgements

This work is supported by NASA under grant NAG-510093 to the Smithsonian Astrophysical Observatory, by the Italian Space Agency, and by the PRODEX programme of ESA (Swiss contribution).

Bibliography

Clarke, J.T., Lallement, R., Bertaux, J.-L., and Quémerais, E., HST/GHRS observations of the interplanetary medium downwind and in the inner solar system, *Astrophys. J.* **448**, 893, 1995.

Cosmo, M.L., Smith, P.L., Atkins, N., Suleiman, R.M., Gardner, L.D., and Kohl, J.L., Flatfield of UVCS detectors for early part of SOHO mission, *Proc. SPIE* **3764**, 161, 1999.

Gardner, L.D., Kohl, J.L., Daigneau, P.S., Dennis, E.F., Fineschi, S., Michels, J., Nystrom, G.U., Panasyuk, A., Raymond, J.C., Reisenfeld, D.J., Smith, P.L., Strachan, L., Suleiman, R., Noci, G.C., Romoli, M., Ciaravella, A., Modigliani, A., Huber, M.C.E., Antonucci, E., Benna, C., Giordano, S., Tondello, G., Nicolosi, P., Naletto, G., Pernechele, C., Spadaro, D., Siegmund, O.H.W., Allegra, A., Carosso, P.A., and Jhabvala, M.D., Stray light, radiometric, and spectral characterization of UVCS/SOHO: laboratory calibration and flight performance, *Proc. SPIE* **2831**, 2, 1996.

Gardner, L.D., Atkins, N., Fineschi, S., Smith, P.L., Kohl, J.L., Maccari, L., and Romoli, M., Efficiency variations of UVCS/SOHO based on laboratory measurements of replica gratings, *Proc. SPIE* **4139**, 362, 2000.

Holberg, J.B., Forrester, W.T., Shemansky, D.E., and Barry, D.C., Voyager absolute far-ultraviolet spectrophotometry of hot stars, *Astrophys. J.* **257**, 656, 1982.

Huber, M.C.E, Timothy, J.G., Lemaitre, J.S., Tondello, G., Jannitti, E., and Scarin, P., Imaging extreme ultraviolet spectrometer employing a single toric diffraction grating: the initial evaluation, *Appl. Opt.* **27**, 3503, 1988.

Jelinsky, S.R., Siegmund, O.H.W., and Mir, J.A., Progress in soft-X-ray and UV photocathodes, *Proc. SPIE* **2808**, 617, 1996.

Kohl, J.L., Esser, R., Gardner, L.D., Habbal, S., Daigneau, P.S., Dennis, E.F., Nystrom, G.U., Panasyuk, A., Raymond, J.C., Smith, P.L., Strachan, L., van Ballegooijen, A.A., Noci, G., Fineschi, S., Romoli, M., Ciaravella, A., Modigliani, A., Huber, M.C.E., Antonucci, E., Benna, C., Giordano, S., Tondello, G., Nicolosi, P., Naletto, G., Pernechele, C., Spadaro, D., Poletto, G., Livi, S., Geiss, J., Timothy, J.G., Gloeckler, G., Allegra, A., Basile, G., Brusa, R., Wood, B., Siegmund, O.H.W., Fowler, W., Fisher, R., and

Jhabvala, M., The Ultraviolet Coronagraph Spectrometer for the Solar and Heliospheric Observatory, *Sol. Phys.* **162**, 313, 1995.

Lemaire, P., SUMER stellar observations to monitor responsivity variations, this volume, 2002.

MAST Multimission Archive at Space Telescope, file SWP08650 (ρ Leo).

Mirishnichenko, A.S., Fabregat, J., Bjorkman, K.S., Knauth, D.C., Morrison, N.D., Tarasov, A.E., Reig, P., Negueruela, I., and Blay, P., Spectroscopic observations of the δ Scorpii binary during its recent periastron passage, *Astron. Astrophys.* **377**, 485, 2001.

Moos, H.W., Cash, W.C., Cowie, L.L., Davidsen, A.F., Dupree, A.K., Feldman, P.D., Friedman, S.D., Green, J.C., Green, R.F., Gry, C., Hutchings, J.B., Jenkins, E.B., Linsky, J.L., Malina, R.F., Michalitsianos, A.G., Savage, B.D., Shull, J.M., Siegmund, O.H.W., Snow, T.P., Sonneborn, G., Vidal-Madjar, A., Willis, A.J., Woodgate, B.E., York, D.G., Ake, T.B., Andersson, B.-G., Andrews, J.P., Barkhouser, R.H., Bianchi, L., Blair, W.P., Brownsberger, K.R., Cha, A.N., Chayer, P., Conard, S.J., Fullerton, A.W., Gaines, G.A., Grange, R., Gummin, M.A., Hebrard, G., Kriss, G.A., Kruk, J.W., Mark, D., McCarthy, D.K., Morbey, C.L., Murowinski, R., Murphy, E.M., Oegerle, W.R., Ohl, R.G., Oliveira, C., Osterman, S.N., Sahnow, D.J., Saisse, M., Sembach, K.R., Weaver, H.A., Welsh, B.Y., Wilkinson, E., and Zheng, W., Overview of the Far Ultraviolet Spectroscopic Explorer mission, *Astrophys. J.* **538**, L1, 2000.

Osantowski, J.F., Keski-Kuha, R.A.M., Herzig, H., Toft, A.R., Gum, J.S., and Fleetwood, C.M., Optical coating technology for the EUV, *Adv. Space Res.* **11**, 185, 1991.

Sahnow, D.J., Moos, H.W., Ake, T.B., Andersen, J., Andersson, B.-G., Andre, M., Artis, D., Berman, A.F., Blair, W.P., Brownsberger, K.R., Calvani, H.M., Chayer, P., Conard, S.J., Feldman, P.D., Friedman, S.D., Fullerton, A.W., Gaines, G.A., Gawne, W.C., Green, J.C., Gummin, M.A., Jennings, T.B., Joyce, J.B., Kaiser, M.E., Kruk, J.W., Lindler, D.J., Massa, D., Murphy, E.M., Oegerle, W.R., Ohl, R.G., Roberts, B.A., Romelfanger, M.L., Roth, K.C., Sankrit, R., Sembach, K.R., Shelton, R.L., Siegmund, O.H.W., Silva, C.J., Sonneborn, G., Vaclavik, S.R., Weaver, H.A., and Wilkinson, E., On-orbit performance of the Far Ultraviolet Spectroscopic Explorer satellite, *Astrophys. J.* **538**, L7, 2000.

Siegmund, O.H.W., Stock, J.M., Marsh, D.R., Gummin, M.A., Raffanti, R., Hull, J., Gaines, G.A., Welsh, B.Y., Donakowski, B., Jelinsky, P.N., Sasseen, T., Tom, J.L., Higgins, B., Magoncelli, T., Hamilton, J.W., Battel, S.J., Poland, A.I., Jhabvala, M.D., Sizemore, K., and Shannon, J., Delay-line detectors for the UVCS and SUMER instruments on the SOHO Satellite, *Proc. SPIE* **2280**, 89, 1994.

Siegmund, O.H.W., Gummin, M.A., Sasseen, T., Jelinsky, P., Gaines, G.A., Hull, J., Stock, J.M., Edgar, M., Welsh, B., Jelinsky, S., and Vallerga, J., Microchannel plates for the UVCS and SUMER instruments on the SOHO satellite, *Proc. SPIE* **2518**, 344, 1995.

Schühle, U., Thomas, R., Kent, B.J., Clette, F., Defise, J.-M., Delaboudinière, J.-P., Fröhlich, C., Gardner, L.D., Hochedez, J.-F., Kohl, J.L., and Moses, J.D., Summary of cleanliness discussion: Where was the SOHO cleanliness programme really effective?, this volume, 2002.

— 12 —

In-flight Calibration of the UVCS White Light Channel

MARCO ROMOLI
Dip. di Astronomia e Scienza dello Spazio, Università di Firenze, Firenze, Italy

RICHARD A. FRAZIN, JOHN L. KOHL,
LARRY D. GARDNER, STEVEN R. CRANMER
Harvard-Smithsonian Center for Astrophysics, Cambridge, MA, USA

KEVIN REARDON
Dip. di Astronomia e Scienza dello Spazio, Università di Firenze, Firenze, Italy

SILVANO FINESCHI
Osservatorio Astronomico di Torino, Pino Torinese, Italy

The UVCS White Light Channel (WLC) is designed to measure the linearly polarized radiance (pB) of the corona, in the wavelength band from 450 nm to 600 nm, in order to derive one of the fundamental parameters of the solar corona: the electron density. This paper gives a thorough description of the in-flight radiometric calibration of the WLC, which uses the star α Leo and the planet Jupiter as transfer standards and is based on calibrations of ground-based instruments. The method for computing the polarized radiance from the measurements is also described, together with the stray light and polarization characterizations obtained from dedicated, in-flight measurements.

12.1 Instrument Description

The UVCS/WLC is discussed extensively in *Romoli* [1992], *Romoli et al.* [1993], and *Kohl et al.* [1995]. The UVCS/WLC is designed to measure the linearly polarized radiance of the corona in the band from 450 nm to 600 nm. Figure 12.1 is a schematic diagram of the UVCS/WLC telescope layout. Like the UV channels, the WLC is an internally- and externally-occulted coronagraph. The primary mirror focuses the coronal light onto the entrance pinhole. This pinhole corresponds to a 14″ by 14″ patch of sky. Figure 12.2 is a schematic diagram of the part of the WLC that lies beyond the entrance pinhole. The light diverges from the pinhole and first passes through a rotating, half-wave retarder plate (HWRP), which rotates the plane of linear polarization. Next, the light passes through a fixed linear polarizer, which allows only the component with the electric field vector oscillating in a specific direction to pass through. The amount of light transmitted depends on the angle between the plane of polarization of the incident light and the transmission axis of the polarizer. Choosing three different rotation angles of the HWRP allows one to

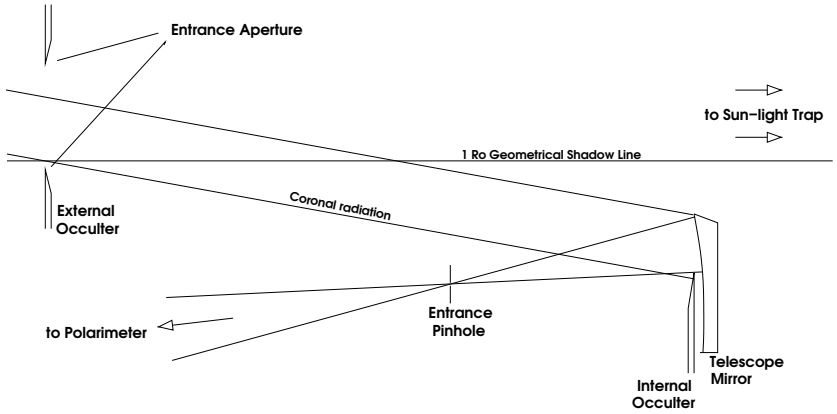

Figure 12.1: Schematic diagram of the UVCS/WLC telescope layout (not to scale).

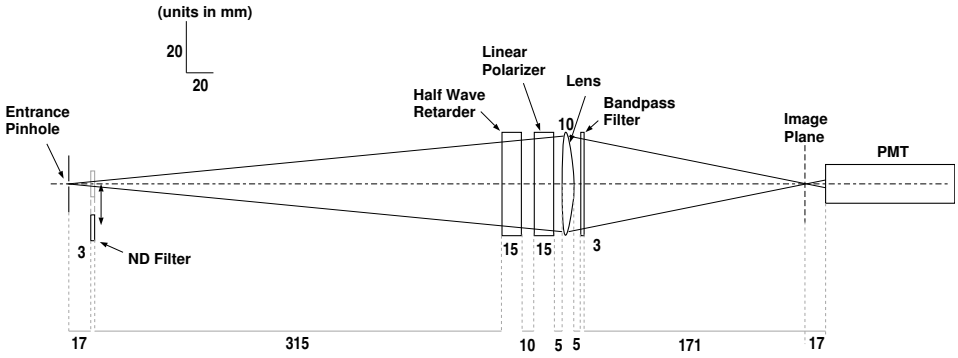

Figure 12.2: Schematic diagram of the UVCS/WLC polarimeter. Taken from *Kohl et al.* [1995].

determine the Stokes I, Q and U components, which is the linear polarization (see Section 12.2). After passing through the polarizer the light goes through a spherical lens and a bandpass filter (450 nm to 600 nm). The spherical lens forms an image of the pinhole just in front of the detector and the bandpass filter controls the spectral properties of the light. Since the linear polarizer is fixed, the light that passes through the lens and the bandpass filter and hits the detector is always 100 % linearly polarized in the same way, regardless of the observation. This makes the characterization of the optical system simpler. The detector is a photomultiplier tube (PMT) designed to work in photon counting mode.

12.2 Polarization Measurement

The polarization state of partially polarized light is most readily described by the vector of Stokes parameters, $\boldsymbol{s} = [s_I, s_Q, s_U, s_V]^T$, where ^{T} denotes the transpose operator.

Although *Collett* [1993] describes this elementary material in detail, we review it here. The Stokes vector $\boldsymbol{s} = [s_I, s_Q, s_U, s_V]^T$ has units of photon spectral radiance such as $\mathrm{cm}^{-2}\ \mathrm{s}^{-1}\ \mathrm{sr}^{-1}\ \mathrm{nm}^{-1}$. The I component is the total spectral radiance of the light including the polarized and unpolarized components. If the light is completely polarized $s_I = \sqrt{s_Q^2 + s_U^2 + s_V^2}$, and if the light is partially polarized $s_I > \sqrt{s_Q^2 + s_U^2 + s_V^2}$. For a given coordinate system, the Q component corresponds to horizontal (parallel to the x-axis) linear polarization if $s_Q > 0$ and vertical linear polarization if $s_Q < 0$. The U component corresponds to $+45°$ linear polarization if $s_U > 0$, and $-45°$ linear polarization if $s_U < 0$. The V component corresponds to right-circular polarization if $s_V > 0$ and left-circular polarization if $s_V < 0$. The angle of the plane linear polarization ψ is given by the relation $\tan 2\psi = s_U/s_Q$. Light that is elliptically polarized may have nonzero values for all four components of the Stokes vector.

The light from the solar disk Thompson scatters off the free electrons in the corona, and this scattered light is partially polarized [*Collett*, 1993] with the electric field vector of the polarized component oscillating tangentially to the solar disk. Given an appropriate coordinate system, the Stokes vector of the light that the corona emits is given by $[s_I, s_Q, 0, 0]^T$, where $s_Q > 0$. s_I and s_Q are related to the distribution of electron density along the line-of-sight (see, e.g., *Altschuler* [1979]). Thus, s_Q is the spectral radiance of the polarized portion of the coronal light. Dust makes a contribution to s_I but not s_Q, at least not within about 5 $R_\odot$ [*Billings*, 1966].

12.2.1 Polarization Computation

In this section we use the radiometric calibration and the polarization properties of the HWRP and the polarizer to calculate the first three components of the resulting Stokes vector $\boldsymbol{s} = [s_I, s_Q, s_U, s_V]^T$ for a source of arbitrary polarization. As we will see, the UVCS/WLC does not respond to the V component of the Stokes vector.

The effects of polarizing components in an optical system can be described using Mueller matrices. The Mueller matrices for retarder plates and polarizers as a function of rotation angle may be found in *Collett* [1993]. We will take the x-axis to be parallel to the occulter edge. The Mueller matrix for a HWRP with the fast axis rotated by an angle α relative to the x-axis is $\boldsymbol{M}_R(\alpha) = \boldsymbol{R}(-2\alpha)\boldsymbol{M}_R(0)\boldsymbol{R}(2\alpha)$, where $\boldsymbol{R}$ and $\boldsymbol{M}_R(0)$ are the Mueller matrices for rotation and a HWRP at $\alpha = 0$, respectively. The angle α in the $\boldsymbol{R}$ matrix is multiplied by two because the rotated Stokes vector, which is an intensity vector, is the product of the rotated electric-field vector and its complex conjugate. We have

$$\boldsymbol{M}_R(\alpha) = \begin{pmatrix} 1 & 0 & 0 & 0 \\ 0 & \cos 4\alpha & \sin 4\alpha & 0 \\ 0 & \sin 4\alpha & -\cos 4\alpha & 0 \\ 0 & 0 & 0 & -1 \end{pmatrix} \tag{12.1}$$

where the overall responsivity factor is set to unity (see below).

The Mueller matrix for an ideal polarizer with a fast axis at an angle β to the x direction is given by $\boldsymbol{M}_P(\beta) = \boldsymbol{R}(-2\beta)\boldsymbol{M}_P(0)\boldsymbol{R}(2\beta)$, where $\boldsymbol{R}$ and $\boldsymbol{M}_P(0)$ are the Mueller matrices for rotation and a linear polarizer at $\beta = 0$, respectively. Again, the angle β in

the $\boldsymbol{R}$ matrix is multiplied by two because the Stokes vector is a vector of intensities, not fields. We have

$$\boldsymbol{M}_P(\beta) = \frac{1}{2}\begin{pmatrix} 1 & \cos 2\beta & \sin 2\beta & 0 \\ \cos 2\beta & \cos^2 2\beta & \cos 2\beta \sin 2\beta & 0 \\ \sin 2\beta & \cos 2\beta \sin 2\beta & \sin^2 2\beta & 0 \\ 0 & 0 & 0 & 0 \end{pmatrix} \tag{12.2}$$

where the overall responsivity factor is set to unity (see below).

The Stokes vector describing the light after it passes through the HWRP and the polarizer is given by $\boldsymbol{s}' = \boldsymbol{M}_P(\beta)\boldsymbol{M}_R(\alpha)\boldsymbol{s} = \boldsymbol{M}(\alpha, \beta)\boldsymbol{s}$. The matrix product is:

$$\boldsymbol{M}(\alpha, \beta) = \frac{1}{2}\begin{pmatrix} 1 & \cos(4\alpha - 2\beta) & \sin(4\alpha - 2\beta) & 0 \\ \cos(2\beta) & \cos(2\beta)\cos(4\alpha - 2\beta) & \cos(2\beta)\sin(4\alpha - 2\beta) & 0 \\ \sin(2\beta) & \sin(2\beta)\cos(4\alpha - 2\beta) & \sin(2\beta)\sin(4\alpha - 2\beta) & 0 \\ 0 & 0 & 0 & 0 \end{pmatrix} \tag{12.3}$$

The value of the polarized spectral radiance s_Q (of which the linearly polarized coronal light is a part) is determined by measuring the count-rates at three rotation angles of the HWRP, α_1, α_2 and α_3. Since the PMT detector signal corresponds to the first element of $\boldsymbol{s}' = \boldsymbol{M}(\alpha, \beta)\boldsymbol{s}$, only the top row of Equation (12.3) is of consequence for our purposes. For a given position α of the HWRP, the count-rate per nanometer at wavelength λ_0 measured by the detector is

$$N_{\lambda_0}(\alpha) = \frac{1}{2}C\left(s_I + \cos(4\alpha - 2\beta)s_Q + \sin(4\alpha - 2\beta)s_U\right)/B_\odot(\lambda_0) \tag{12.4}$$

where $B_\odot(\lambda_0)$ is the spectral radiance of the center of the solar disk, and C, which has units s^{-1}, is a scaling factor. C depends on the responsivity, the geometry and the spectral response of the instrument and is described in Section 12.2.3.

12.2.2 WLC Polarization Characterization

Equation (12.4) must be an accurate representation of the observation process if the polarized radiance measurements made by the UVCS/WLC are to be meaningful. Equation (12.4) predicts that the count-rate due to an unpolarized source will not vary with the HWRP angle. Rasters of ρ Leo (done in August 2000) were made at three different HWRP angles. The resulting measurement shows (2 ± 2) % polarization. Since the UVCS/WLC typically measures 0.5 % to 9 % polarized signals, this test was not conclusive. However, later (16 June 2001) measurements of Jupiter show less than 0.5 % polarization.

A report of the tests performed on the flight polarimeter is given in *Pernechele et al.* [1997]. Nearly fully polarized visible light was focused on the entrance pinhole, and the count-rate on the flight PMT was read as the angle of the HWRP was varied.

Ignoring wavelength dependence, efficiencies and geometrical factors, the Stokes vector for a fully linearly polarized signal traveling along the z direction and with the electric field making an angle γ with the x axis is $\boldsymbol{s} = I[1, \cos 2\gamma, \sin 2\gamma, 0]^T$, where I is the total spectral radiance of the beam. Using this Stokes vector in Equation (12.3) to calculate the radiant flux at the PMT gives

$$\hat{R}_F = \frac{1}{2}I_0\,[1 + \cos(4\alpha - 2\beta - 2\gamma)] \tag{12.5}$$

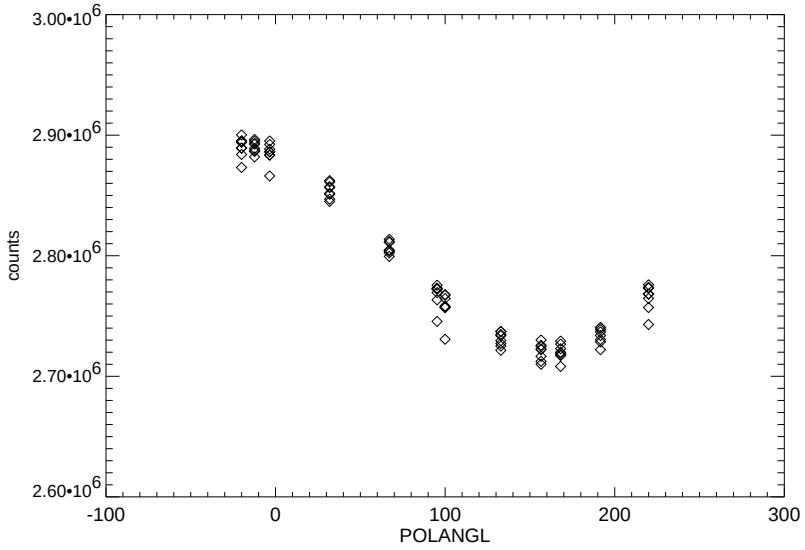

Figure 12.3: In-flight modulation curve. This figure shows the number of PMT counts versus the UVCS Data Analysis Software (DAS) variable POLANGL $= 4\alpha - 2\beta$ (in deg). This curve was retraced several times and the vertical scatter is caused by time variation of the corona. The data were taken between 19:02 h and 21:15 h on 18 April 1998 at 2.0 $R_\odot$ with 60 s exposures.

Equation (12.5) is called the *modulation curve*. This modulation curve describes the results of the white-light laboratory tests of *Romoli and Fineschi* [1993] to a high degree of accuracy. In-flight measurements of the modulation curve using the polarized light of the corona have also been made. An example of such a curve is given in Figure 12.3. In this case Equation (12.5) needs an additional constant term to account for the unpolarized fraction of the light.

In addition, *Frazin* [2002] performed laboratory tests on a replica of the UVCS/WLC polarimeter to verify its characteristics. All tests indicate that the instrument performs as intended.

12.2.3 WLC Radiometric Factor

The scaling factor, C, contains the radiometric factor that will be derived through the in-flight radiometric calibration. The number of counts per second detected by the PMT per unit wavelength, N_λ, according to Equation (12.4), is

$$\begin{aligned} N_\lambda(r,\alpha) &= R_T \frac{w_p h_p h_m w_m(r)}{f^2} T_L T_P T_F(\lambda)\eta(\lambda) \\ &\quad \times \frac{s_I(\lambda) + s_Q(\lambda)\cos 2\theta + s_U(\lambda)\sin 2\theta}{2} \end{aligned} \tag{12.6}$$

where we have put

$$2\theta = 4\alpha - 2\beta \tag{12.7}$$

and where w_p and h_p are the width and the height of the pinhole (both 50 μm), h_m is the telescope mirror height (3 cm), $w_m(r)$ is the exposed telescope mirror width, f is the mirror focal length (75 cm), R_T is the mirror reflectance, T_L is the lens transmittance and T_P is the polarizer transmittance[1]. $w_m(r)$ in centimeters is given by $0.792r - 0.951 - w_o$ [*Kohl et al.*, 1995], where r is the mirror angle in units of $R_\odot$ (969.6″, as seen from the average SOHO-Sun distance) and w_o is the amount of over-occultation by the internal occulter, 0.15 cm for most observations. The bandpass window spans the wavelength range from 450 nm to 600 nm. The bandpass filter has transmittance $T_F(\lambda)$, and the detected quantum responsivity of the detector system is given by $\eta(\lambda)$. $T_F(\lambda)$ and $\eta(\lambda)$ were measured on the flight units. Plots of $T_F(\lambda)$ and $\eta(\lambda)$ (normalized to unity at 546 nm) are shown in Figure 12.7.

We assume that the spectral distribution of the coronal radiation is the solar Fraunhofer spectrum radiation [*Kurucz et al.*, 1984] convolved with a Gaussian representing a Maxwellian electron velocity distribution corresponding to 10^6 K. Although the F-corona (which shows the Fraunhofer features as they appear on the Sun) and K-corona have different spectra, they differ only by convolution with a function representing the thermal distribution of electron velocities. Since we are integrating the spectrum over a bandpass of ≈150 nm, the convolution is of negligible consequence. Henceforth we ignore the distinctions between the F- and K-corona spectra.

The Stokes vector $\boldsymbol{s}(\lambda, r)$ can be written as $\boldsymbol{s}(\lambda, r) = B_\odot(\lambda)\boldsymbol{S}(r)$, where $B_\odot(\lambda)$ is the photospheric photon spectral radiance at Sun center (in units of cm^{-2} sr^{-1} s^{-1} nm^{-1}).[2]

The above assumption makes $\boldsymbol{S}(r)$ wavelength independent. The total count-rate is determined by integrating over the wavelength as follows:

$$N(r,\alpha) = R_T \frac{w_p h_p h_m w_m(r)}{f^2} T_L T_P \left[\int_0^\infty T_F(\lambda)\eta(\lambda)B_\odot(\lambda)\,\mathrm{d}\lambda\right] \frac{I + Q\cos 2\theta + U\sin 2\theta}{2} \tag{12.8}$$

where we have assumed that T_L, T_P and R_T vary slowly with wavelength over the optical band. We define ϵ to be the value of the responsivity at $\lambda_0 = 546$ nm:

$$\epsilon \equiv \frac{1}{2} R_T\, T_P\, T_L\, T_F(\lambda_0)\, \eta(\lambda_0)\ . \tag{12.9}$$

Using Equations (12.8), (12.7), and (12.9) the total count-rate is:

$$N(r,\alpha) = 2\mathrm{K} w_m(r) \frac{I + Q\cos 2\theta + U\sin 2\theta}{2} \tag{12.10}$$

where

$$\mathrm{K} = \epsilon \frac{w_p h_p h_m}{f^2} B_\odot(\lambda_0) \left[\int_0^\infty \frac{T_F(\lambda)}{T_F(\lambda_0)} \frac{\eta(\lambda)}{\eta(\lambda_0)} \frac{B_\odot(\lambda)}{B_\odot(\lambda_0)} \mathrm{d}\lambda\right] \tag{12.11}$$

[1]Here, the transmittance, T_P, is defined relative to the intensity of a radiation beam which is 100 % linearly polarized along the fast axis. Thus, the transmittance T_P can be ideally 1. This definition requires the dividing factor, 2, in the polarizer Mueller matrix.

[2]Henceforth, we always take $\boldsymbol{S} = [I, Q, U]^T$ to be the Stokes vector in units of photospheric photon spectral radiance at Sun center.

Table 12.1: Radiometric responsivity measurements.

method	responsivity
α Leo	(1.16 ± 0.12) %
Jupiter 1997	(1.33 ± 0.13) %
Jupiter 2001	(1.38 ± 0.13) %
mean of α Leo and Jupiter 2001	(1.27 ± 0.09) %

In the following sections, the parameters ϵ and K will be called the radiometric responsivity and the WLC radiometric calibration factor, respectively. K is the factor that is used in the UVCS Data Analysis Software (DAS) with the variable name `WLC.VLD.FACTOR`.

It is clear from Equation (12.10) that the factor C in Equation (12.4) is given by the expression:

$$C = 2\mathrm{K}w_m(r) \tag{12.12}$$

12.3 WLC Radiometric Calibrations

The overall radiometric calibration of the UVCS/WLC is still in progress. This section describes the in-flight radiometric calibration, which is based on observations of the star α Leo and the planet Jupiter. We stress that these are not direct calibrations, rather they use celestial objects as transfer standards and are based on calibrations of ground-based instruments.

Table 12.1 gives a summary of the various in-flight radiometric calibration measurements. All values are in agreement to within the stated standard uncertainties.

For the purposes of the inter-comparison work presented elsewhere in this volume [*Frazin et al.*, 2002], we adopt the average of the α-Leo and Jupiter 2001 calibrations. Because the pointing scheme was better for the Jupiter 2001 observations, we adopt the Jupiter 2001 calibration as the best value and regard the 1997 result as a confirmation. Thus, the 1997 Jupiter result is not included in the average. The uncertainty associated with the 1997 pointing scheme is not included in Table 12.1.

12.3.1 α-Leo Radiometric Calibration

In August 1998, as part of the UVCS calibration program, we made radiometric measurements of the star α Leo, a B7V star. The α-Leo radiometric calibration is based on literature values of the star's magnitude in the Johnson V band and the catalog of normalized stellar spectra compiled by *Breger* [1976]. Breger's spectra were measured with narrow-band filters. This should be adequate because the library of stellar spectra presented by *Jacoby et al.* [1984] shows that B7V stellar spectra are quite smooth between 400 nm and 650 nm, except for an absorption feature at 486 nm that has a full-width at half-maximum of about 2.3 nm. We used Breger's catalog to determine the shape of the spectra and the V magnitudes from the literature for the normalization. The mean of V magnitudes in the SIMBAD database is 1.36 mag. Accordingly, we calculate the α-Leo

photon spectral irradiance at $\lambda_0 = 546$ nm to be $F_{\lambda_0} = 2.91 \times 10^3$ cm^{-2} s^{-1} nm^{-1}. We use the symbol F_λ to represent the irradiance at other wavelengths.

We define $H_{\text{total}}(\lambda)$ to be the radiant flux reflected by the mirror. That is,

$$H_{\text{total}}(\lambda) = F_\lambda \, h_m w_m(r) \, R_T \tag{12.13}$$

where $h_m w_m(r)$ is the exposed mirror area in cm^2, and R_T is the telescope mirror reflectance. $H_{\text{total}}(\lambda)$ has units s^{-1} nm^{-1}. The star image in the plane of the pinhole (image plane) is smeared by the telescope optics. We represent this smeared image by the function $\hat{H}(\lambda; x, y)$, where x and y are coordinates in the pinhole plane. The y-axis is defined to be parallel to the internal occulter blade and UV slits (see Figure 12.1). $\hat{H}(\lambda; x, y)$ has units s^{-1} cm^{-2} nm^{-1} and satisfies the relation

$$H_{\text{total}}(\lambda) = \int\int \hat{H}(\lambda; x, y)\, \mathrm{d}x\mathrm{d}y \tag{12.14}$$

If the pinhole is centered at coordinates (x', y') in the pinhole plane, the number of photons per nanometer going through it is given by the expression:

$$H_p(\lambda, x', y') \equiv \int\int \hat{H}(\lambda; x, y)\Pi(\frac{x' - x}{l}, \frac{y' - y}{l})\, \mathrm{d}x\mathrm{d}y \tag{12.15}$$

where $\Pi(x, y)$ is the two-dimensional rectangle function (in each dimension it is unity from -1/2 to 1/2 and zero elsewhere) and l is the width of the (square) pinhole (0.005 cm or 13.76″). The rectangle function $\Pi(x'/l, y'/l)$ represents the square pinhole. H_p has units s^{-1} nm^{-1}. The measured count-rate is proportional to H_p. The rectangle function itself has an area of l^2. Thus, by the properties of the convolution integral in Equation (12.15) and Equation (12.14), we have the relation

$$H_{\text{total}}(\lambda) = \frac{1}{l^2}\int\int H_p(\lambda, x, y)\, \mathrm{d}x\mathrm{d}y \tag{12.16}$$

Since the star is unpolarized, the measured count-rate in units of s^{-1} is given by

$$C_r = \frac{1}{2} T_L T_P \int H_p(\lambda, x, y) T_F(\lambda) \eta(\lambda) \mathrm{d}\lambda \tag{12.17}$$

Integrating Equation (12.17) over x and y and using Equations (12.9), (12.13) and (12.16) yields

$$\frac{1}{l^2}\int\int C_r \mathrm{d}x\mathrm{d}y = \frac{1}{2} R_T h_m w_m(r) T_L T_P \int F_\lambda T_F(\lambda) \eta(\lambda) \mathrm{d}\lambda \tag{12.18}$$

$$= \epsilon h_m w_m(r) F_{\lambda_0} \int \frac{F_\lambda}{F_{\lambda_0}} \frac{T_F(\lambda)}{T_F(\lambda_0)} \frac{\eta(\lambda)}{\eta(\lambda_0)} \mathrm{d}\lambda \tag{12.19}$$

where ϵ is the radiometric responsivity. Equation (12.18) is similar in form to Equation (12.8). Due to the spectral differences between α Leo and the Sun, it is not useful to incorporate the calibration factor K as in Equation (12.10), although it may be calculated via Equation (12.11) once ϵ is known.

The goal of the α-Leo observation was to determine the responsivity ϵ by making a measurement of the left-hand-side integral in Equation (12.19).

From the perspective of the SOHO spacecraft, stars travel at constant velocity of about $v \approx 0.04\,''\,\mathrm{s}^{-1}$, or 1.45×10^{-5} cm s^{-1} in the pinhole plane. For the α-Leo observation, the star trajectory was inclined to the x-axis by 11°. Since $\cos(11°) \approx 0.9816$, this effect is negligible, and for the purpose of this discussion we will assume that the star trajectory is parallel to the x-axis. The observation consisted of eighteen passes. Before each pass the instrument was pointed so that the pinhole was ahead of the star and was not moved until the entire star image had passed by the pinhole. For each pass, the pinhole was placed so that the star's path was at a different value of the y-coordinate, relative to the pinhole. The value of y was determined from the spatial position of the star's UV signature in the O IV channel. Thus, we may consider the count-rate C_r in Equation (12.17) to be a function of time and y. We will use the notation $C_r(t, y)$ to symbolize this. Using the same proportionality factors as in Equation (12.17), we have the relationship:

$$C_r(t, y) \;\propto\; H_p\,(\lambda; x - v(t - t_0), y) \tag{12.20}$$

where t_0 is chosen so that the maximum count-rate occurs at $t = 0$. Figure 12.4 is an example that shows the time-variation of the count-rate during one pass. The example in the Figure is the first pass, which happened to be near $y = 0$, the center of the pinhole. Integrating $C_r(t, y)$ over time, we may define the quantity

$$\hat{C_r}(y) \equiv \int C_r(t, y)\, v\mathrm{d}t \tag{12.21}$$

$\hat{C_r}(y)$ has units of cm s^{-1}. Numerically integrating the count-rate in each pass gives a measurement of $\hat{C_r}(y)$. We will call $\hat{C_r}(y)$ the *integrated count-rate (ICR)*. $\hat{C_r}(y)$ is related to the responsivity ϵ via Equation (12.19) as follows:

$$\frac{1}{l^2}\int \hat{C_r}(y)\,\mathrm{d}y \;=\; \frac{1}{l^2}\int\int C_r \mathrm{d}x\mathrm{d}y \tag{12.22}$$

The result of the measument is $\epsilon = (1.16 \pm 0.12)$ %. The uncertainty analysis is discussed below.

12.3.2 α-Leo Uncertainty Analysis

The uncertainty in the α-Leo calibration is dominated by the uncertainty in the integration over the y-axis in Equation (12.22). Figure 12.5 shows the results of numerically integrating all of the passes according to Equation (12.21). The statistical uncertainties are negligibly small in the vertical direction because the data from which the integrals in Equation (12.21) were evaluated included millions of counts. The more significant uncertainty is in the y position of each pass, which was determined by fitting a Gaussian to the signal measured in the O VI channel. Each UV signal contained on the order of 2×10^4 counts. The statistical uncertainty in determining the centroid of the Gaussian was much smaller than the overall uncertainty inherent in this procedure. Only the variation of the error in the determination of the individual values of y is important since an overall shift will not affect the integral in the left-hand-side of Equation (12.22). A significant uncertainty is introduced by the fact that the UV spatial image of the star had a full-width at half-maximum of about 25″ while the spatial binning (3 pixels) was 21″, and because the spatial image of the star is not a Gaussian, as was assumed by the fitting procedure (rather,

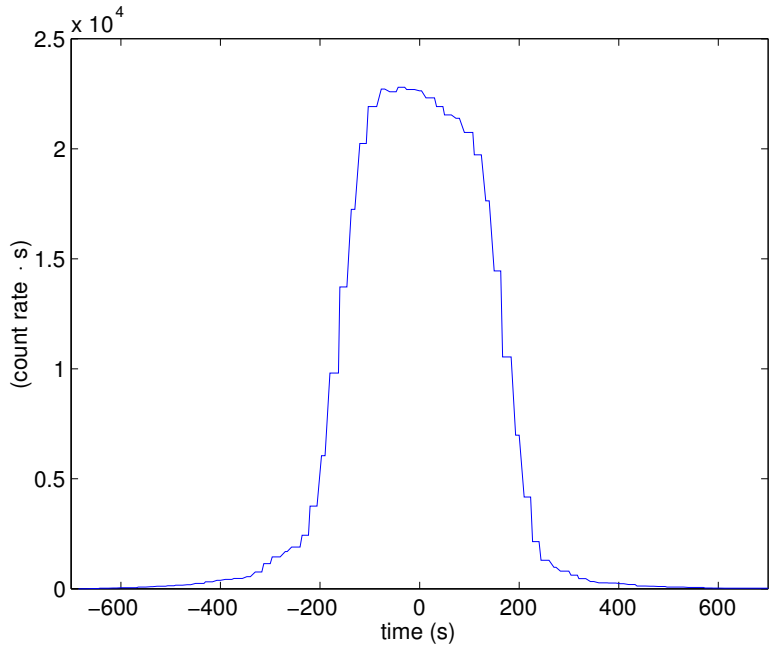

Figure 12.4: The count-rate as a function of time for the first α-Leo pass by the pinhole. The data set consists of a series of such passes.

it is a point spread function that is not accurately known). We can estimate this uncertainty as one-third of a spatial bin, or $7''$. We consider it to be roughly equivalent to a coverage factor $k = 2$ uncertainty. This $7''$ uncertainty is indicated as horizontal error bars in Figure 12.5.

Although we used spline interpolation of the data points in Figure 12.5 to estimate the left-hand-side integral in Equation (12.22), we chose to model this spatial profile as a sum of two Gaussians for the purposes of the uncertainty analyses of both α Leo and Jupiter, and for computations of the Jupiter broadening function discussed later. The two-Gaussian model can describe the data well, except for two points on the far left of Figure 12.5. We propagated the $7''$ uncertainty through a perturbation analysis in order to determine its effect on the parameters of the two Gaussian model. The result is that the sum of the areas of the two Gaussians has an uncertainty of 20 %. We consider this 20 % uncertainty to be coverage factor $k = 2$ since it is a direct result of the coverage factor $k = 2$ spatial uncertainty discussed above. Therefore, we take the standard uncertainty to be 10 %. The same perturbation analysis allowed us to determine the broadest and narrowest (coverage factor $k = 2$) profiles that are consistent with the data in Figure 12.5; they are shown by the dotted and dashed curves, respectively. These curves will be used later in Section 12.3.4.5 for the uncertainty analysis in the Jupiter calibration.

The SIMBAD data base shows fourteen V-magnitude measurements of α Leo spanning the years 1952 through 1986. The standard deviation of these measurements is 0.02 mag or 2 %. *Breger* [1976] has nine independent spectrophotometric scans of F_λ. The standard

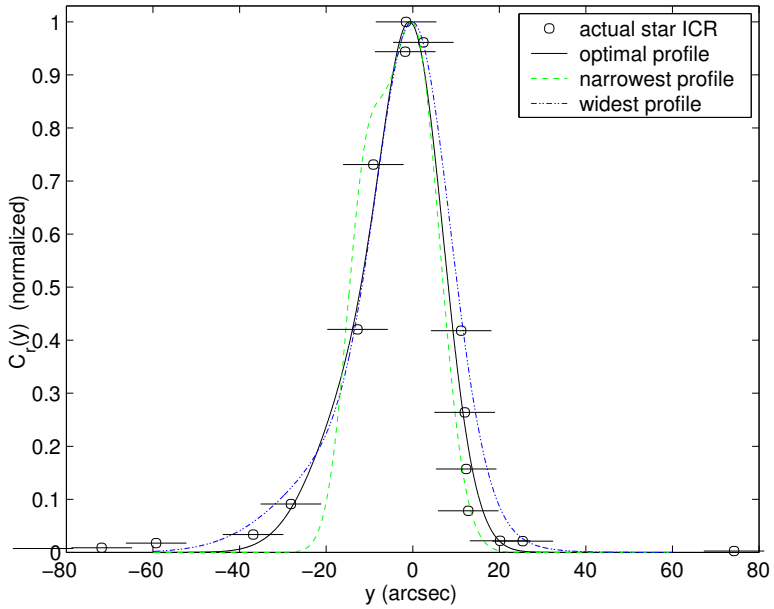

Figure 12.5: The α-Leo integrated count-rate (ICR) along the UV slit (circles) and three point spread function curves to describe it. The $7''$ (coverage factor $k = 2$) uncertainty on the determination of y for each pass is indicated by the horizontal error bars. The solid curve is the optimal one used to calculate the broadening factor in Section 12.3.4.4. The dotted and dashed curves are the broadest and narrowest functions that the data can justify at the coverage factor $k = 2$ uncertainty level (see text).

deviation of these normalized spectra is about 0.01 mag between 450 nm and 600 nm. Adding these in quadrature, we find that the determination of F_{λ_0} implies an uncertainty of 2 %.

The uncertainty due to counting statistics in the integrated count rates is negligible. Since the exposed mirror width $w_m(r)$ was 2.56 cm, and the uncertainty in the location of the internal occulter is on the order of 0.01 cm, this effect is also negligible. The curve $T_F(\lambda)$ was measured in the laboratory on several occasions, to within a few percent. $\eta(\lambda)$ was measured on the flight unit by Ball Aerospace. The $\eta(\lambda)$ measurement agrees with the curve given by the manufacturer. Since the measured responsivity ϵ includes the values of T_F and η at λ_0, any errors in the values of these curves at λ_0 will introduce no uncertainty, although errors in the shapes of these curves can do so. As Figure 12.7 shows, $T_F(\lambda)$ and $\eta(\lambda)$ are smooth curves, so the integral of their normalized product, as is called for in Equation (12.19), does not introduce significant uncertainty. Table 12.2 summarizes this uncertainty analysis.

Table 12.2: Summary of uncertainties for the α-Leo radiometric calibration: see Equation (12.29).

Item	Relative standard uncertainty (%)
positional uncertainty	10
stellar photometry	2
occulter position	0.5
$\int \cdots d\lambda$	≈ 0
Poisson statistics	≈ 0
quadrature sum	10

12.3.3 ρ-Leo Consistency Check

In August 1998, as part of the UVCS calibration program, we made radiometric measurements of the star ρ Leo. According to *Breger* [1976] and the SIMBAD data base, the ρ-Leo flux at 546 nm is 9.9 % that of α Leo and its $F_\lambda / F_{\lambda_0}$ curve is nearly identical in the UVCS/WLC band. This observation differs from that of α Leo described above only in that the star is a factor of about ten fainter in the visible and that not enough passes were done to make a measurement of $\int\int C_r \, dx dy$. Thus, instead of attempting to integrate something akin to the data in Figure 12.5, we multiplied the ρ-Leo integrated count-rates by ten and plotted them with the α-Leo data in Figure 12.6. Since these two data sets fall on the same curve, we take the ρ-Leo measurements as a confirmation of the validity of the α-Leo result.

12.3.4 Jupiter 2001 Radiometric Calibration

The Jupiter radiometric calibration is based on Jupiter observations taken in June 2001. This calibration accounts for both the spectral properties of Jupiter and the broad point spread function of the WLC. On 16 June 2001 Jupiter was at opposition and the angle between the Sun and Jupiter was only about 1.75° or 6 $R_\odot$, thus UVCS observed, essentially, the entire solar illuminated surface of Jupiter.

12.3.4.1 Jupiter Spectral Radiance Computation

The projected solar spectral photon irradiance hitting a surface element of Jupiter is given by the expression

$$F_{\text{in}}(\lambda) \;=\; B_\odot(\lambda) \frac{4}{5} \frac{\pi R_\odot^2}{d^2} \cos\varphi \tag{12.23}$$

where $B_\odot$ is the solar disk-center spectral radiance, d is the Sun-Jupiter distance, and φ is the angle between the normal to Jupiter's surface and the rays coming from the center of the solar disk. The factor 4/5 accounts for solar limb-darkening and the cosine factor accounts for the projection effect. Since the incoming spectral irradiance times the albedo is equal to the outgoing spectral irradiance we have

$$F_{\text{out}}(\lambda) \;=\; a(\lambda) F_{\text{in}}(\lambda) \tag{12.24}$$

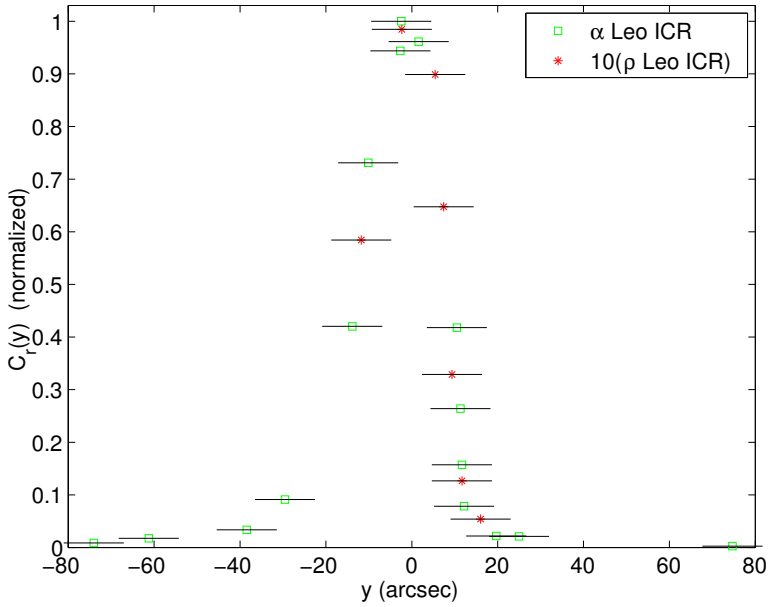

Figure 12.6: The α-Leo (squares) and ρ-Leo (asterisks) integrated count-rates along the UV slit. The ρ-Leo data have been multiplied by ten, according to the expected flux difference. Except for the factor of ten, both data sets have been normalized as in Figure 12.5. The horizontal error bars represent coverage factor $k = 2$ uncertainties. This is a confirmation of the α-Leo calibration because it gives no reason to believe that a complete data set on ρ Leo would give an inconsistent result.

where $a(\lambda)$ is the Bond albedo [*Allen*, 1976].

The relationship between F_{out} and the spectral radiance $I_J(\lambda)$ is determined by the angular distribution of the radiation. We assume that the radiance is not a function of angle [*Tejfel et al.*, 1994; *N. Chanover, personal communication*, 2001], that is $I_J(\lambda;\theta,\phi) = I_J(\lambda)$. Then we have the relation

$$F_{\text{out}}(\lambda) = \int_0^{2\pi}\int_0^{\pi/2} I_J(\lambda)\cos\theta\,\sin\theta\,\mathrm{d}\theta\mathrm{d}\phi = \pi I_J(\lambda) \tag{12.25}$$

Thus, from Equations (12.23), (12.24) and (12.25) we have the following Equation

$$I_J(\lambda) = B_\odot(\lambda)a(\lambda)\frac{4}{5}\frac{R_\odot^2}{d^2}\cos\varphi \tag{12.26}$$

12.3.4.2 Relationship Between Spectral Radiance and the Photomultiplier Count-rate

The count-rate N (in units of s^{-1}) measured by the detector for unpolarized light of photon spectral radiance I (in units of $cm^{-2}\ s^{-1}\ nm^{-1}\ sr^{-1}$) can be derived from Equation (12.6), and is given by the Equation

$$N \;=\; R_T\ T_P\ T_L\ \frac{1}{2}\ \frac{w_p h_p h_m w_m(r)}{f^2} \int I(\lambda)\ T_F(\lambda)\ \eta(\lambda)\ \mathrm{d}\lambda \tag{12.27}$$

Since Jupiter is essentially unpolarized, the HWRP has no effect and the linear polarizer cuts the intensity in half. Therefore we have placed a factor of one-half in Equation (12.27) instead of using the polarimeter Mueller matrix. Figure 12.7 is a plot of the wavelength-dependent detected quantum responsivity, the bandpass transmittance, the Sun-center spectral radiance and the reflected Jupiter spectrum [*Karkoschka*, 1994]: all normalized to unity at 546 nm. Using Equations (12.27) and (12.9), the relationship between the detector count-rate and the Jupiter radiance is

$$N_{\mathrm{Jupiter}} \;=\; 2\epsilon b \frac{w_p h_p h_m w_m(r)}{f^2} \left(\int \frac{T_F(\lambda)}{T_F(\lambda_0)} \frac{\eta(\lambda)}{\eta(\lambda_0)} \frac{I_J(\lambda)}{I_J(\lambda_0)}\, \mathrm{d}\lambda \right) \frac{I_J(\lambda_0)}{2} \tag{12.28}$$

where $\lambda_0 \;=\; 546$ nm and b is an instrument broadening factor, which is the fractional reduction in the apparent center radiance due to instrument blur. The evaluation of b for Jupiter is discussed below. Note that the integral in Equation (12.28) has units of wavelength.

12.3.4.3 Calibration Factor Computation

Using Equations (12.11) and (12.26), Equation (12.28) can be rewritten:

$$N_{\mathrm{Jupiter}} \;=\; b\mathrm{K} w_m(r) \left(\frac{\int \frac{T_F(\lambda)}{T_F(\lambda_0)} \frac{\eta(\lambda)}{\eta(\lambda_0)} \frac{I_J(\lambda)}{I_J(\lambda_0)}\, \mathrm{d}\lambda}{\int \frac{T_F(\lambda)}{T_F(\lambda_0)} \frac{\eta(\lambda)}{\eta(\lambda_0)} \frac{B_\odot(\lambda)}{B_\odot(\lambda_0)}\, \mathrm{d}\lambda} \right) a(\lambda_0) \frac{4}{5} \frac{R_\odot^2}{d^2} \cos\varphi \tag{12.29}$$

remembering that $\lambda_0 \;=\; 546$ nm; $w(r)$ is the exposed mirror width in centimeters, and K is the radiometric calibration factor defined in Section 12.2.3.

We may now use the Jupiter count-rates and Equation (12.29) to determine the value of K. The maximum Jupiter count-rate on 16 June 2001 was $1.59 \times 10^5\ s^{-1}$, the mirror width was $w_m(r) \;=\; 2.56$ cm, the ratio of the wavelength integrals is (150.5 nm)/(156 nm) = 0.965, a(546 nm) $\;=\;$ 0.493 [*Karkoschka*, 1994], $R_\odot \;=\; 6.96 \times 10^5$ km, and at that time the Sun-Jupiter distance was 7.630×10^8 km. Since the observation was essentially "straight on," we have $\cos\varphi \;\approx\; 1.0$. The value of b is shown below to be 0.72. Using these values in Equation (12.29), we find that

$$\mathrm{K} \;=\; 2.76 \pm 0.50 \;\times 10^{11}\ \mathrm{cm}^{-1}\ \mathrm{s}^{-1} \tag{12.30}$$

This calibration factor corresponds to a radiometric responsivity of $\epsilon \;=\; (1.38 \pm 0.13)\%$. The uncertainty analysis is discussed in Section 12.3.4.5.

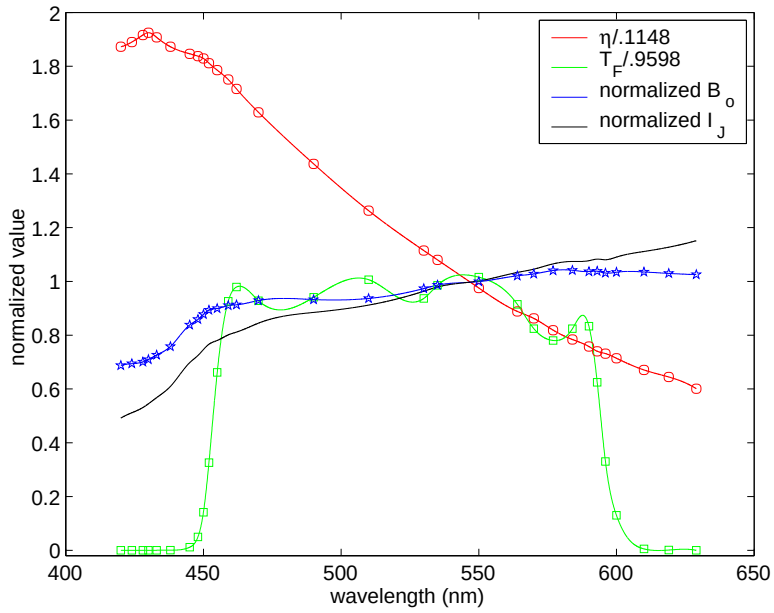

Figure 12.7: Radiometric calibration curves. Shown are the UVCS/WLC bandpass filter transmittance, the solar mean spectral radiance, the reflected Jupiter spectral radiance and the detected quantum responsivity: all normalized to unity at 546 nm.

12.3.4.4 Evaluation of the Broadening Factor *b*

The UVCS/WLC telescope mirror has out-of-focus and optical aberrations that strongly affect the observations of objects that are less than about $1'$ in size. These aberrations blur the image over the pinhole so that a significant fraction of the object's light will not pass through the pinhole. Jupiter is an extended object and its angular diameter, as viewed from Earth on the observation date, is about $30''$. This substantially lessens the broadening effect (compared to stars). We determined the broadening function with observations of the star α Leo by allowing it to drift past the pinhole as described in Section 12.3.1.

To calculate the one-dimensional (1D) broadening factor and its uncertainty, we convolved the Jupiter image, given by Equation (12.26), with the profiles shown in Figure 12.5 (see Section 12.3.2). The optimal 1D broadening factor (0.77) was calculated using the solid curve. The dotted and dashed curves in that figure lead to a (coverage factor $k = 2$) 9 % relative uncertainty in this factor.

Figure 12.8 shows the effect of the convolution. The dashed curve is the ideal Jupiter image, the solid curve is the optimal profile (same as the solid curve in Figure 12.5), and the dotted curve is the result of the convolution. The convolution reduced the (normalized) peak of the Jupiter image from 1.0 to 0.77 for the case of the optimal 1D profile.

The two-dimensional (2D) point broadening function was approximated by

$$p(u, v) \;=\; p_1(u)\,p_2(v) \tag{12.31}$$

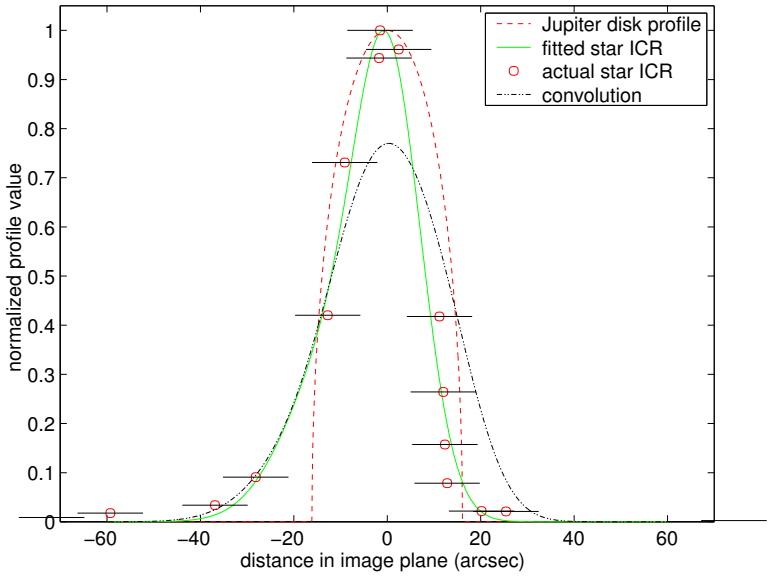

Figure 12.8: Illustration of Jupiter broadening parallel to the UV slit. The dashed curve is the Jupiter image, the solid curve is the optimal profile, and the dotted curve is the result of the convolution. Also shown in circles is the α-Leo integrated count-rate (ICR). The profiles of the Jupiter disk and α Leo have been normalized to the same peak value of unity.

where $p_1(u)$ and $p_2(v)$ are broadening functions parallel and perpendicular to the UV slit, respectively. $p_1(u)$ is shown in Figure 12.5. $p_2(v)$ was chosen to match one of the scans of α Leo as its image passed through the center of the white-light pixel and is shown in Figure 12.9. Figure 12.9 shows that the data are well-matched by convolving the 14″ width of the pinhole with a Gaussian optical spread function. The lower panel shows $p_2(v)$ and the pinhole and Gaussian functions that comprise it. The width of the Gaussian was varied to find a best fit to the data in the upper panel of Figure 12.9.

Comparison of Figures 12.9 and 12.5 shows that $p_2(v)$ is much narrower than $p_1(u)$. Thus, we expect the result of the 2D broadening calculation to be not much different than that of the 1D broadening calculation. Furthermore since $p_2(v)$ is narrower than $p_1(u)$ and is better constrained by the data, we can expect the uncertainty in the 2D broadening to be dominated by the uncertainty in the 1D broadening described above. Convolving $p(u, v)$ from Equation (12.31) with a 2D Jupiter image calculated from Equation (12.26) gives a 2D broadening factor of $b = 0.72$. Since Equation (12.31) is separable, the relative uncertainty in the broadening effect is still determined by the broadest and narrowest curves in Figure 12.5 and is 9 % (coverage factor $k = 2$).

12.3.4.5 Jupiter Uncertainty Analysis

The uncertainty analysis of the calibration factor K is based on Equation (12.29). The uncertainty in K is dominated by the uncertainties in the broadening factor b and the albedo

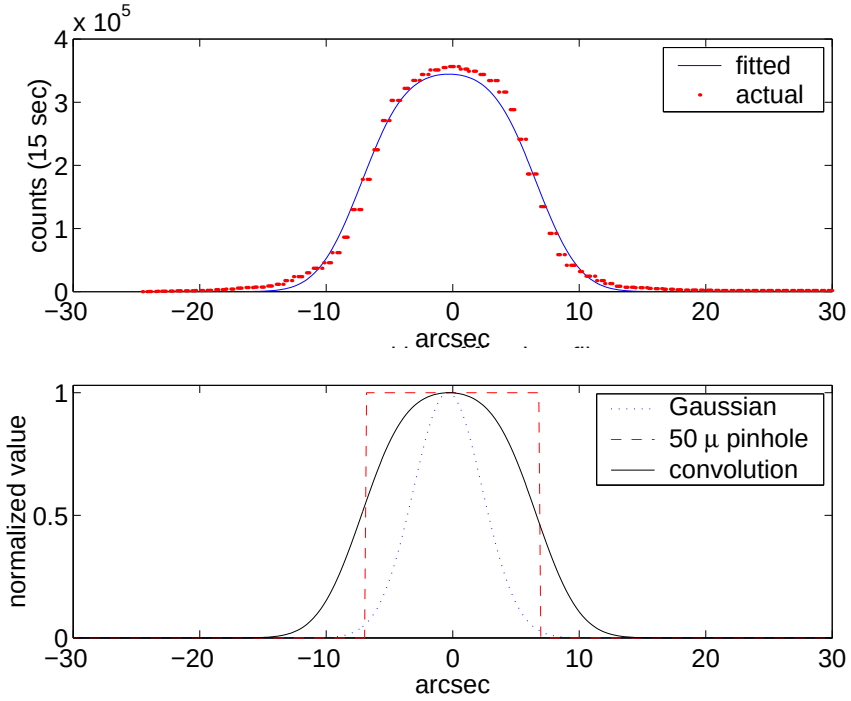

Figure 12.9: Illustration of the α-Leo image perpendicular to the UV slit length. The data in the upper panel were taken as the star passed through the center of the white-light pixel. The lower panel shows the best-fit (the width of the Gaussian was allowed to vary) composition of the fitted (solid) curve in the upper panel. The solid curves in both panels are identical.

a. The uncertainty in b has been discussed above. Since the 9 % relative uncertainty in b is based on a coverage factor $k = 2$ uncertainty in the spatial position of the α-Leo UV signature shown in Figure 12.5, it should also be considered roughly equivalent to a coverage factor $k = 2$ uncertainty. We will take the relative standard uncertainty to be 5 %.

Axel [1972] has compiled albedo measurements from a number of different authors, although only three measurements are within the UVCS/WLC bandpass. These albedo measurements range from 89 % to 102 % of values given by *Karkoschka* [1994]. The standard deviation of the four data sets (including Karkoschka's) is 7 %. We have adopted this value as the standard uncertainty in Jupiter's albedo. Including Karkoschka's 4 % relative standard radiometric uncertainty in quadrature, we take the overall relative standard uncertainty in Jupiter's albedo to be 8 %.

Since N_{Jupiter} was 1.59×10^5 s^{-1} and the exposure time was 15 s, the uncertainty due to Poisson statistics is negligible. Since the exposed mirror width $w_m(r)$ was 25.6 mm, and the uncertainty in the location of the internal occulter is on the order of 0.1 mm, the associated uncertainty is also negligible. The ratio of the wavelength integrals would be unity, except for the slight difference between curves $I_J(\lambda)/I_J(\lambda_0)$ and $B_\odot(\lambda)/B_\odot(\lambda_0)$,

Table 12.3: Summary of uncertainties for the Jupiter radiometric calibration: see Equation (12.29).

Parameter symbol	Parameter name	Relative standard uncertainty (%)
b	broadening parameter	5
$a(\lambda_0)$	albedo	8
$\cos\varphi$	radiation angle	2
$w_m(r)$	exposed mirror width	0.4
$N_{\text{Jupiter}}\times(15\text{ s})$	number of counts	0.065
$\int\cdots/\int\cdots$	ratio of integrals	≈ 0
$R_\odot$	solar radius	≈ 0
d	Sun-Jupiter distance	≈ 0
σ	Poisson statistics	≈ 0
quadrature sum		9.4

which are shown in Figure 12.7. Since these curves are so similar, the uncertainty in the ratio of integrals is negligible when compared to the uncertainty in the broadening factor or the albedo. For the 2001 Jupiter observations, the uncertainty in φ may be estimated by comparing the maximum count-rates in the five Jupiter passes and fitting them to a cosine curve. The result is $\varphi < 12^\circ$ for the central pass. Since $\cos(12^\circ) \approx 0.978$, this uncertainty is also negligible. The solar radius $R_\odot$ is known to three or four digits (see, e.g., *Allen* [1976]) and the Sun-Jupiter distance d can be calculated to several kilometers or less. This uncertainty analysis is summarized in Table 12.3.

12.3.5 Jupiter 1997 Radiometric Calibration

The Jupiter 1997 observation was almost identical to the 2001 observation described above, and has been described in detail by *Cranmer* [2001]. The only important difference between the two observations is the way in which the instrument was pointed. Since the pointing calibration had not yet been fully established and Jupiter's position relative to the Sun not precisely calculated for the 1997 observation, the UVCS/WLC was repointed after every exposure in an effort to put the WLC over the center of the planet. The result was a series of exposures randomly clustered around the planet. A histogram of the resulting intensities shows a clear cut-off at a maximum intensity. We have assumed that this cut-off intensity corresponds to the WLC being pointed near the center of the disk. In contrast, the Jupiter 2001 observations were carefully rastered in a way such that the observation plan ensured that the WLC was pointed at the center of the planet at some time. Since the 2001 pointing scheme was better, we use the 2001 observations to determine our best value of the Jupiter calibration and use the 1997 observation as a confirmation.

For the 1997 Jupiter observations, all of the analysis given above for the 2001 observations carries over exactly. The result is $\epsilon = (1.33 \pm 0.13)\,\%$.

12.4 A Model of the Stray Light in the WLC

In Section 12.2.1 we described the procedure for computing the first three components of the Stokes vector of the light that enters the pinhole, $\boldsymbol{s}$. This light has two components, one, $\boldsymbol{s}_c$, is coronal in origin and the other, $\boldsymbol{s}_i$, is instrumental in origin. Thus, $\boldsymbol{s} = \boldsymbol{s}_c + \boldsymbol{s}_i$. In this section we describe a model of $\boldsymbol{s}_i$, so that $\boldsymbol{s}_c$ may be determined from observations of the corona.

Romoli and Reardon [2000] performed an extensive analysis of the stray-light in the WLC. The fact that the photomultiplier gave a count-rate consistent with the dark-rate when the internal occulter completely covered the mirror indicates that all of the stray-light in the WLC comes from the mirror or its edge, and not from the internal occulter surface. While the mirror-edge may scatter light from the sunlight trap, the mirror surface is only illuminated by light from the corona and light from the solar disk that has been diffracted by the external occulter. In order to determine the contribution of diffracted light to the signal, it was first necessary to measure the Stokes vector of the distribution of diffracted light across the mirror surface. This was done by pulling back the internal occulter, which allows the specularly reflected ray of the diffraction pattern to enter the pinhole, and taking polarization measurements. The Stokes vector of the resulting diffraction pattern, as a function of position along the mirror surface x is denoted by $[D(x),\ q(x)D(x),\ u(x)D(x)]^T$.

Romoli and Reardon [2000] modeled the measured Stokes parameters as:

$$\begin{aligned} I &= \frac{I_e}{w_m(r)} + I_c(r) + \frac{A_I}{w_m(r)} \int_0^{w_m(r)} D(x)\phi(x,r)\,\mathrm{d}x \\ Q &= \frac{Q_e}{w_m(r)} + Q_c(r) + \frac{A_Q}{w_m(r)} \int_0^{w_m(r)} q(x)D(x)\phi(x,r)\,\mathrm{d}x \\ U &= \frac{U_e}{w_m(r)} + \frac{A_U}{w_m(r)} \int_0^{w_m(r)} u(x)D(x)\phi(x,r)\,\mathrm{d}x \end{aligned} \tag{12.32}$$

where r is the mirror angle; $w_m(r)$ is the exposed mirror width; I_e/w_m, Q_e/w_m and U_e/w_m are the Stokes parameters of the contribution from the mirror edge; I_c, and Q_c are the Stokes parameters of the contribution from the corona (U_c is assumed to be zero, using the proper reference system), A_I, A_Q and A_U are the coefficients of non-specular scattering for the three Stokes components, and $\phi(x,r)$ is the non-specular scattering function. The parameters w_m and r are fixed by the observations and all of the other parameters are determined by the curve-fits to specially designed observations. *Romoli and Reardon* [2000] examined several options for the scattering profile $\phi(x,r)$. Based on goodness-of-fit, they chose $\phi(x,r)$ to be a Lorentzian to the power of two.

Without entering the details of the special observations that were used to determine the values of the model parameters, the model is capable of determining the stray-light contribution at every height between 1.7 $R_\odot$ and 5 $R_\odot$ and for any position of the internal occulter. The stray-light correction term is computed, for the known exposed mirror width $w_m(r)$, from

$$Q_{\mathrm{corr}} = \frac{Q_e}{w_m(r)} + \frac{A_Q}{w_m(r)} \int_0^{w_m(r)} q(x)D(x)\phi(x,r)\,\mathrm{d}x \tag{12.33}$$

and subtracted from the measured Stokes Q.

Table 12.4: Results of stray-light model. $Q_{\rm corr}$ is the number that needs to subtracted from the observed polarized radiance when nominal (1.5 mm) occulting is used. $\Delta Q_{\rm corr}$ is the uncertainty in this quantity. These numbers are in units of Sun-center spectral radiance and assume the Jupiter 2001 radiometric calibration.

Height ($R_\odot$)	$Q_{\rm corr}$	$\Delta Q_{\rm corr}$
1.74	0.6×10^{-8}	0.2×10^{-8}
1.84	0.1×10^{-8}	0.0×10^{-8}
1.94	0.7×10^{-9}	0.3×10^{-9}
2.04	0.4×10^{-9}	0.1×10^{-9}
2.29	0.7×10^{-10}	0.4×10^{-10}
2.54	0.3×10^{-10}	0.4×10^{-10}
3.00	0.4×10^{-10}	0.2×10^{-10}
3.54	0.2×10^{-10}	0.1×10^{-10}
4.00	0.2×10^{-10}	0.1×10^{-10}
4.54	0.2×10^{-10}	0.1×10^{-10}
4.84	0.2×10^{-10}	0.1×10^{-10}

This model has been used to calculate a value of the Stokes Q parameter that should be subtracted from coronal measurements with nominal (1.5 mm) occulting. Table 12.4 gives the stray-light correction term as a function of height.

12.5 Conclusion

We have discussed the in-flight radiometric calibration, the polarization calibration and the stray-light calibration of the UVCS White Light Channel. The in-flight radiometric calibration is based on measurements of Jupiter performed in June 2001 and of α Leo obtained in 1997. The Jupiter 2001 measurement was confirmed by a previous measurement of Jupiter in 1997 and the α-Leo measurement was confirmed by a measurement of ρ Leo. The Jupiter 2001 and α-Leo measurements agree to within the stated uncertainties.

Acknowledgements

This work is supported by NASA under grant NAG5-10093 to the Smithsonian Astrophysical Observatory, by the Italian Space Agency, and by the Prodex programme of ESA (Swiss contribution).

Bibliography

Allen, C.W., Astrophysical Quantities, London, Athlone, 1976.

Altschuler, M.D., in Image Reconstruction from Projections: Implementation and Applications, edited by G.T. Herman, New York, Springer-Verlag, 1979.

Axel, L., Inhomogeneous models of the atmosphere of Jupiter, *Astrophys. J.* **173**, 451, 1972.

Billings, D.E., A Guide to the Solar Corona, New York, Academic Press, 1966.

Breger, M., Catalog of spectrophotometric scans of stars, *Astrophys. J. Suppl.* **32**, 7, 1976.

Collett, E., Polarized Light: fundamentals and applications, New York, Marcel Drekker Inc., 1993.

Cranmer, S.R., unpublished technical report, 2001.

Frazin, R.A., PhD Thesis, University of Illinois, Department of Astronomy, 2002.

Frazin, R.A., Romoli, M., Kohl, J.L., Gardner, L.D., Wang, D., Howard, R.A., and Kucera, T.A., White Light inter-calibrations of UVCS, LASCO and Spartan 201/WLC, this volume, 2002.

Jacoby, G.H., Hunter, D.A., and Christian, C.A., A library of stellar spectra, *Astrophys. J. Suppl.* **56**, 257, 1984.

Karkoschka, E., Spectrophotometry of the Jovian planets and Titan at 300- to 1000-nm Wavelength: The methane spectrum, *Icarus* **111**, 174, 1994.

Kohl, J.L., Esser, R., Gardner, L.D., Habbal, S., Daigneau, P.S., Dennis, E.F., Nystrom, G.U., Panasyuk, A., Raymond, J.C., Smith, P.L., Strachan, L., van Ballegooijen, A.A., Noci, G., Fineschi, S., Romoli, M., Ciaravella, A., Modigliani, A., Huber, M.C.E., Antonucci, E., Benna, C., Giordano, S., Tondello, G., Nicolosi, P., Naletto, G., Pernechele, C., Spadaro, D., Poletto, G., Livi, S., von der Lühe, O., Geiss, J., Timothy, J.G., Gloeckler, G., Allegra, A., Basile, G., Brusa, R., Wood, B., Siegmund, O.H.W., Fowler, W., Fisher, R., and Jhabvala, M., The Ultraviolet Coronagraph Spectrometer for the Solar and Heliospheric Observatory, *Sol. Phys.* **162**, 313, 1995.

Kurucz, R.L., Furenlid, I., Brault, J., and Testerman, L., Solar flux atlas from 296 to 1300 nm, NSO Atlas No.1, 1984.

Pernechele, C., Naletto, G., Nicolosi, P., Tondello, G., Fineschi, S., Romoli, M., Noci, G., Spadaro, D., and Kohl, J., Optical performances of the Ultraviolet Coronagraph Spectrometer of the Solar Heliospheric Observatory, *Appl. Opt.* **36**, 4, 813, 1997.

Romoli, M., PhD Thesis, The UVCS/SOHO coronagraph polarimeter, University of Florence, Department of Astronomy and Space Science, 1992.

Romoli, M., and Fineschi, S., unpublished technical report, 1993.

Romoli, M., Weiser, H., Gardner, L.D., and Kohl, J.L., Stray-light suppression in a reflecting white-light coronagraph, *Appl. Opt.* **32**, 3559, 1993.

Romoli, M., and Reardon, K., unpublished technical report, 2000.

Tejfel, T.G., Tejfel, V.G., Vdovichenko, V.D., Sinyaeva, N.V., Mosina, S.A., Gajsina, W.N., Kharitonova, G.A., Aksenov, A.N., Spectrophotometry of zonal cloud structure variations on Jupiter, *J. Geophys. Res.* **99**, 8411, 1994.

— 13 —

Radiometric Calibration of the SWAN Instrument

ERIC QUÉMERAIS, JEAN-LOUP BERTAUX
Service d'Aéronomie du CNRS
Verrières le Buisson, France

We discuss the radiometric calibration at H I Lyman α of the two SWAN sensors placed on the +Z and –Z sides of the SOHO spacecraft. Each unit has a detector with a 5×5 pixel array. The calibration includes flat-field and high-voltage setting corrections, as well as a cross-calibration and the determination of temporal variations of the responsivities. The calibration obtained by comparison with GHRS/HST interplanetary measurements in 1996 is extrapolated to the whole period of the SOHO mission. Calibration over the full wavelength range of the instrument (110 nm to 190 nm) is also discussed.

13.1 Introduction

The SWAN instrument is an H I Lyman-α photometer designed to study the interplanetary UV background. It consists of two sensor units of identical design (designated SU+Z, north ecliptic, and SU–Z, south ecliptic) put on opposite sides of the SOHO spacecraft. The detectors are multi-anode Micro Channel Plate (MCP) detector tubes from Hamamatsu.

The optical layout of the SWAN instrument is detailed in *Bertaux et al.* [1995]. Both sensors are equipped with an orienting periscope composed of two toroidal mirrors. The instantaneous field of view of each sensor unit is $5^\circ \times 5^\circ$ spread on 5×5 pixels, and a total field of view equal to half of the sky can be covered by use of stepper motors.

For each sensor, the mechanical entrance pupil is followed by the two toroidal mirrors of the orienting periscope. The light is then focused on the detectors through a hydrogen cell.

The aim of this paper is to describe how an in-flight radiometric UV calibration of the SWAN sensors can be obtained. This includes the determination of responsivity changes between 1996 and 2002 – work, that is still ongoing.

13.2 High-voltage and Flat-field Corrections

The high-voltage (HV) settings of the MCP have been used to increase or decrease the gain of the detectors according to the brightness of the source. Two HV levels (one for each sensor) have been defined as reference settings. They correspond to the values most often used: digital level 120 for SU+Z and digital level 140 for SU–Z. At regular time intervals, we have compared the counting rates obtained for the same source at different

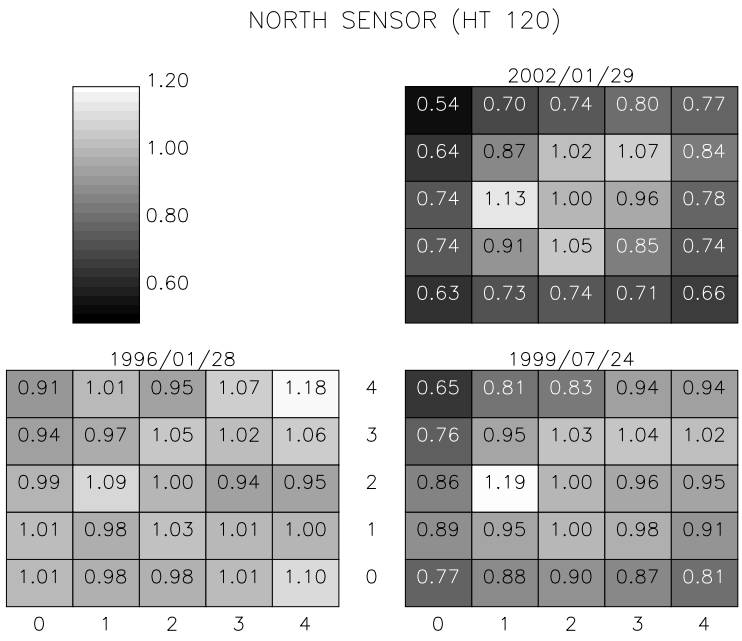

Figure 13.1: The SU+Z flat-field (FF) correction array at three different times of the SOHO mission. The values correspond to the reference HV setting of the sensor. We suspect that during the SOHO mission interruption of 1998 sunlight hit the pixels directly and caused a severe degradation, thus requiring a change of the flat-field correction values.

HV settings. The results of this procedure made it possible to convert the counting rate for any HV setting to the corresponding rate for the reference HV setting. Thus it is only necessary to define the calibration factor for the reference HV settings.

The detector pixels have different responsivities and degrade differently with time. We determine the responsivity ratios of the different pixels each week. To relate the resulting tables of responsivity ratios over time, we use the responsivity of the central pixel of the array as a reference. Figure 13.1 shows the value of the flat-field correction for the reference HV setting of SU+Z over the course of the mission. If all pixels had the same responsivity, the squares would all have the same shade of grey. After the SOHO mission interruption in 1998, the flat-field correction of the SU+Z sensor has changed dramatically; the contrast was enhanced. A similar study (not shown) has been performed for the SU–Z sensor.

Using the information described above, the SWAN sensor calibration is performed by determining the reference calibration factor for each sensor.

13.3 Variation of the Calibration Factor with Time

The reference responsivity of both sensors has changed with time. The SU+Z sensor suffered a strong deterioration during the mission interruption of 1998. A second degra-

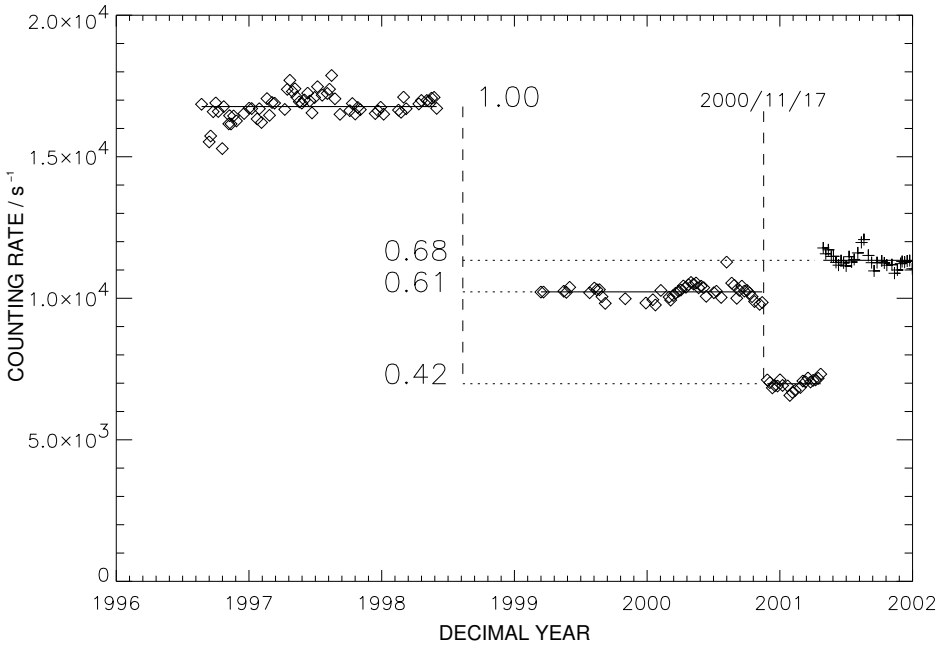

Figure 13.2: Time dependence of the reference counting rate observed for star HR 5191 seen by SU+Z (north ecliptic). The responsivity of the sensor is more or less constant except for two abrupt jumps. The first one (from 1.00 to 0.61) is due to the SOHO loss of attitude and subsequent mission interruption in 1998. The second jump (from 0.61 to 0.42) was caused by an operator error. Moreover, in mid-2001, the reference HV setting was increased to improve the statistics of the measurement (change from 0.42 to 0.68).

dation happened in November 2001, when the sensor was pointed by mistake towards the spacecraft for a long period of time. Solar light reflected from the spacecraft caused huge counting rates which degraded the responsivity of the sensor. The degradation of SU–Z is smoother. We find that, since the mission's recovery in October 1998, the relative annual decrease of the responsivity of the south sensor has been roughly 10 %.

The variations are determined by following the evolution of the counting rate obtained while observing the same star every week. Figure 13.2 shows the numerical results for a bright UV star seen by SU+Z. A similar result was obtained for the south sensor.

Figure 13.3 shows the ratio of the counting rates obtained from the two sensors when they looked at the same area of the sky at approximately the same time. The rates have been normalized to the HV reference settings and the abrupt degradations seen for SU+Z (Figure 13.2) have been corrected. What remains shows the rather rapid relative loss of responsivity of SU–Z (almost 60 % in six years). The rate of decrease became steeper after the SOHO recovery. Since we find that between the abrupt changes the north sensor is constant, we deduce that this curve shows the relative degradation of sensor SU–Z since the beginning of the mission for a constant high-voltage setting.

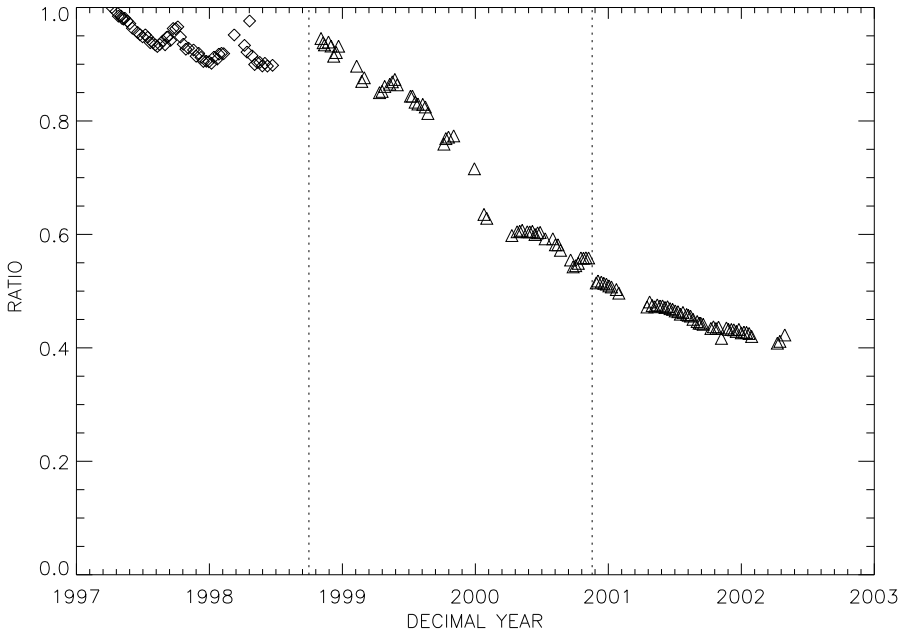

Figure 13.3: SU–Z/SU+Z, the ratio of the south sensor counting rates relative to those of the north sensor as a function of time. The values were obtained by comparing overlapping areas in the field of view of both sensors. The ratios are computed for reference HV settings (HV+Z=120, HV–Z=140) and include the corrections described above, and are normalized to 1 at the beginning of 1997. The curve actually represents the loss of responsivity of the south sensor for a constant HV setting.

13.4 Comparison with the Hubble Space Telescope

A first estimate of the responsivity at Lyman α for the two SWAN sensors was obtained in 1996 through a comparison with interplanetary UV background data obtained by the Goddard High Resolution Spectrometer aboard the Hubble Space Telescope (GHRS/HST) [*Clarke et al.*, 1998].

Let us denote with N_{p} the counting rate of a pixel that is viewing a region of the sky with a photon radiance of $\frac{10^6}{4\pi}$ s^{-1} cm^{-2} sr^{-1}. This corresponds to a photon flux density of 1 R.[1] We then get

- N_{p}^{+}(HV=120; 1996; 1 R) $= (1.17 \pm 0.11)$ s^{-1}
- N_{p}^{-}(HV=140; 1996; 1 R) $= (0.57 \pm 0.06)$ s^{-1}

From these values and taking into account the degradation observed for both sensors, we can deduce the value for the north sensor in early 2002 as

[1] A photon flux density (emittance) of one rayleigh (R) is defined as 10^6 s^{-1} cm^{-2} emitted isotropically [*Hunten et al.*, 1956].

- N_{p}^{+}(HV=120; 2002; 1 R) = 0.57 s^{-1}

The reduction factor used here (equal to 0.49) takes into account changes of the HV settings and the abrupt losses of responsivity. For the same date, the south responsivity ratio to its original value is equal to 0.43. This is deduced from Figure 13.3. We find that

- N_{p}^{-}(HV=140; 2002; 1 R) = 0.24 s^{-1}

13.5 SWAN Responsivity for Stars and for an Extended Source

The counting rate per pixel, N_{p}, for an extended monochromatic source with a photon radiance, L_{p}, in a spectral line at wavelength λ (i.e., H I Ly-α) is

$$N_{\mathrm{p}} = L_{\mathrm{p}}\ A\ \Omega\ T_{m1}(\lambda)\ T_{m2}(\lambda)\ T_c(\lambda)\ q(\lambda)\ \rho_c \tag{13.1}$$

where A is the area of the entrance pupil, Ω is the field of view, $T_{m1}(\lambda)$ and $T_{m2}(\lambda)$ are the reflectivities of the two mirrors (at H I Ly-α about 77 % each), $T_c(\lambda)$ is the transmission of the hydrogen cell with MgF_2 lenses (about 20 % at H I Ly-α), $q(\lambda)$ is the quantum efficiency of the photocathode (about 9 % at H I Ly-α), and ρ_c is the counting efficiency, which is independent of wavelength.

In our case we have $A = 5.72\ \mathrm{cm}^2$ and $\Omega = 3.05 \times 10^{-4}$ sr ($1^\circ \times 1^\circ$ field of view) Pulses created by photo-electrons on the photocathode may have a level smaller than the fixed threshold of the PAD (Pulse Amplifier Discriminator associated to each pixel). The level of a pulse may be increased by increasing the high voltage on the MCP. However, it was found in flight that the level of high voltage could not be set as high as desired because of frequent trip-off, for an unknown reason. (On the ground, the HV never tripped, even at the maximum level of HV). Therefore, the value of ρ_c is not precisely known; it is variable with the HV level and from one pixel to the next, which significantly contributes to the PRNU (Pixel-to-pixel Response Non Uniformity).

The quantity $\eta(\lambda) = T_{m1}(\lambda)\ T_{m2}(\lambda)\ T_c(\lambda)\ q(\lambda)\ \rho_c$ is called the spectral responsivity. It can be used both for a monochromatic extended source

$$N_{\mathrm{p}} = \eta(\lambda)\ A\ \Omega\ L_{\mathrm{p}} \tag{13.2}$$

and for the prediction of the counting rate, N^*, when observing a point source. A star with a spectral photon irradiance of E_λ would yield

$$N^* = A \int_\lambda \eta(\lambda) E_\lambda \mathrm{d}\lambda \tag{13.3}$$

Ground calibrations were performed by recording the response of SWAN to synchrotron radiation through a monochromator with a fixed exit slit isolating a narrow wavelength interval $\Delta\lambda$. Figure 13.4 shows the counting rate, C_λ, of the SWAN sensor as a function of monochromator wavelength. The short-wavelength cut-off is due to MgF_2 transmission, while the long-wavelength cut-off is due to the solar-blind CsI photocathode of the SWAN detectors. Let us first assume that the output spectral radiant flux, Φ_λ, from the monochromator is constant, then this curve may be used for the radiometric calibration

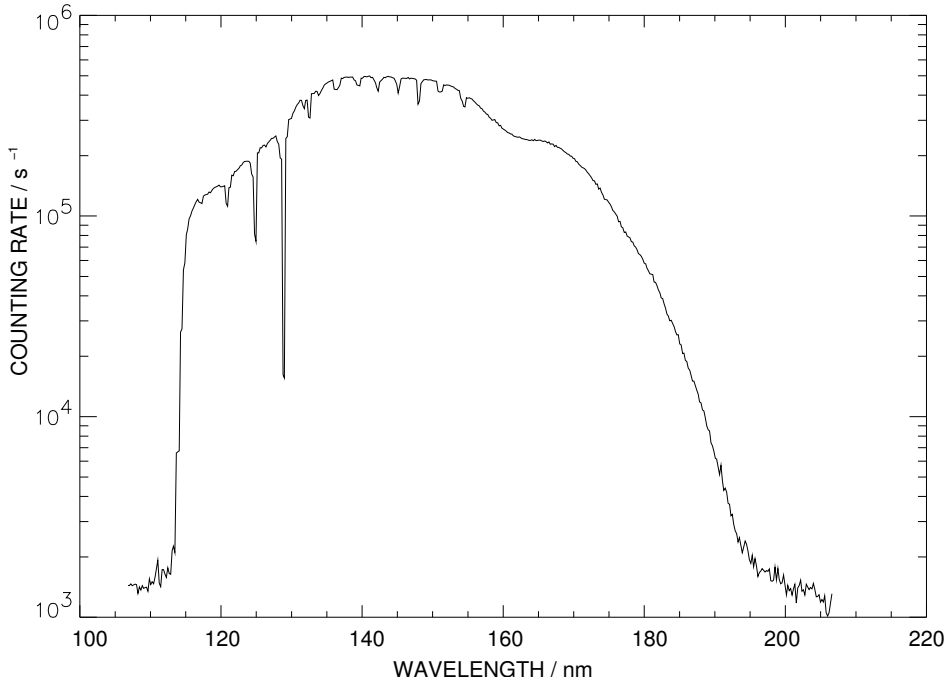

Figure 13.4: The counting rate, C_λ, of the SWAN sensor as a function of monochromator wavelength during a calibration run with synchrotron radiation. Strong and narrow absorption features are due to the (unwanted) presence of HCl in the H_2 absorption cell, a result of the reaction of H atoms with the AgCl that is used to seal the MgF_2 lenses to the glass through silver plates.

of SWAN together with observations of stars whose spectral irradiances, E_λ, are known from IUE or from the SOLSTICE experiment on UARS [*G. Rottmann, personal communication*, 1998], and the observed counting rates, $N_{\rm mes}$. It then follows with constant k (representing a wavelength-independent synchrotron radiation) that

$$\eta(\lambda) = \frac{C_\lambda}{k} = \frac{C_\lambda\ N_{\rm mes}}{k\ N^*} = \frac{N_{\rm mes}\ C_\lambda}{A \int E_\lambda C_\lambda {\rm d}\lambda} \tag{13.4}$$

However, the synchrotron radiation entering the monochromator is probably not constant, but varies smoothly with wavelength. By observing several stars with different spectral shapes (stellar types O, B, A), one can describe the synchrotron radiation flux with a linear function (or a function of higher order) and determine by a least-squares fit the coefficients of the polynomial describing Φ_λ. This work is still in progress (as of August 2002), and will lead to a better representation of $\eta(\lambda)$.

Bibliography

Bertaux, J.-L., Kyrölä, E., Quémerais, E., Pellinen, R., Lallement, R., Schmidt, W., Berthé, M., Dimarellis, E., Goutail, J.P., Taulemesse, C., Bernard, C., Leppelmeier, G., Summanen, T., Hannula, H., Huomo, H., Kehlä, V., Korpela, S., Leppälä, K., Strömmer, E., Torsti, J., Viherkanto, K., Hochedez, J.F., Chretiennot, G., Peyroux, R., and Holzer, T., SWAN: A study of Solar Wind Anisotropies on SOHO with Lyman alpha sky mapping, *Sol. Phys.* **162**, 403–439, 1995.

Clarke, J.T., Lallement, R., Bertaux, J.-L., Fahr, H., Quémerais, E., and Scherer, H., HST/GHRS observations of the velocity structure of interplanetary hydrogen, *Astrophys. J.* **499**, 482–488, 1998.

Hunten, D.M., Roach, F.E., and Chamberlain, J.W., A photometric unit for the airglow and aurora, *J. Atmos. Terr. Phys.* **8**, 345–346, 1956.

III. Intercalibration

— 14 —

Comparison of CDS Irradiance Measurements with SEM and EIT

WILLIAM T. THOMPSON
L3 Communications Analytics Corporation
NASA Goddard Space Flight Center
Greenbelt, MD, USA

DONALD R. MCMULLIN
University of Southern California
Space Sciences Center
Los Angeles, CA, USA

JEFFREY S. NEWMARK
Naval Research Laboratory
Washington, DC, USA

Observations of the solar irradiance have been made with the CDS Normal Incidence Spectrometer in the ranges 30.8 nm to 38.1 nm and 51.3 to 63.3 nm, on a semi-regular basis since March 1997. Also observed are the He II and Si XI lines at 30.4 nm in second order. We have used these observations to estimate the signal that SEM would see on those dates. In order to fill in the wavelengths below 30.0 nm, a DEM curve is generated from the CDS observations. Comparisons are also made with the EIT measurements for the same dates. Both pre-loss-of-attitude and post-recovery data are considered.

14.1 Introduction

We report here on intercomparisons between EUV irradiance measurements made by three instruments aboard the Solar and Heliospheric Observatory (SOHO): the Coronal Diagnostic Spectrometer (CDS) [*Harrison et al.*, 1995], the Solar EUV Monitor (SEM) [*Hovestadt et al.*, 1995], and the Extreme-ultraviolet Imaging Telescope (EIT) [*Delaboudinière et al.*, 1995]. Each of these instruments has different characteristics. For CDS to measure irradiance, a special observing program must be run to return the irradiance spectrum in the wavelength ranges 30.8 nm to 38.1 nm and 51.3 nm to 63.3 nm. Because this observing program takes thirteen hours to complete, CDS only measures the irradiance on a semi-regular basis, usually monthly. SEM, on the other hand, continuously monitors the irradiance, but does not have sufficient spectral resolution to separate out individual emission lines. Instead, the integrated flux from 26 nm to 34 nm is returned. Using a Differential Emission Measure (DEM) analysis [*Cook et al.*, 1999, 2002], EIT is able to derive a spectrum several times a day from its synoptic full-Sun observations in four bandpasses centered on 17.1 nm, 19.5 nm, 28.4 nm, and 30.4 nm. A DEM map is an individual DEM curve for each pixel in the field of view, which reproduces the intensities in the four EIT channels for that pixel and covers the temperature range from 0.8 MK to 2.5 MK. Using these maps one can model individual lines (e.g., He II 30.4 nm) or an instrumental bandpass (e.g., SEM 26 nm to 34 nm) to produce absolutely calibrated intensities. This DEM

modeling tool is used to calculate absolutely calibrated, solar EUV-irradiances over the SOHO mission lifetime [*Newmark et al.*, 2002].

In order to intercompare these three instruments, the results from CDS and EIT are integrated over the 26 nm to 34 nm bandpass for comparison with SEM. Since CDS does not observe this entire bandpass, the unobserved part of the spectrum is simulated based on a DEM analysis of the CDS data. For EIT, the entire bandpass is simulated from a separate DEM analysis.

When contact was temporarily lost with the SOHO spacecraft during 1998, changes occurred in the CDS instrument. In making the comparison of CDS with SEM and EIT, we will first concentrate on the period prior to the loss-of-contact, and then look at what changes are necessary for the period following the recovery.

14.2 The CDS Measurements

The CDS full-Sun irradiance observing program is described in *Brekke et al.* [2000] and in *Thompson and Brekke* [2000]. A series of 69 individual rasters is used to cover the entire Sun, returning the complete ranges of the two bands of the CDS Normal Incidence Spectrometer (NIS) from 30.8 nm to 38.1 nm (NIS-1) and 51.3 nm to 63.3 nm (NIS-2). The full observing sequence takes approximately 13.5 hours to complete.

Before the irradiance spectra can be analysed, corrections are applied for the aging of the detector [*Thompson*, 2000b]. An absolute calibration curve is then applied to the data, based on two sounding-rocket underflights in 1997 [*Brekke et al.*, 2000; *Thomas et al.*, 1999; *Thomas*, 2002]. These calibration steps are well-established for the period leading up to the loss-of-contact with the spacecraft in 1998. Later, we will discuss what modifications are required for the period after the recovery of the spacecraft.

Off-band scattering from the two gratings prevents us from measuring any continuum component to the spectrum. However in the NIS wavelength-bands, the spectrum can be completely characterized as a series of distinct emission lines. The next step in the CDS analysis is to fit each of these emission lines. For the period before loss-of-contact, these lines are fitted with Gaussian profiles.

CDS/NIS does not observe the entire SEM bandpass of 26 nm to 34 nm. In order to derive a complete spectrum in this bandpass from the CDS data, three separate components are required:

- The CDS first-order spectrum from 30.8 nm to 34.0 nm.
- The CDS second-order measurements of He II 30.38 nm, and Si XI 30.33 nm.
- A simulated spectrum from 26 nm to 30 nm, based on a DEM analysis of the CDS data.

Table 14.1 lists the lines in the CDS spectrum that were used for DEM analysis. The (full-Sun) intensities from these lines were fed into a DEM analysis tool written using the CHIANTI package [*Dere et al.*, 1997]. Ionization rates were based on *Arnaud and Raymond* [1992], and abundances were based on the *Meyer* [1985] coronal values, as they are delivered with the CHIANTI package. The pressure was kept constant at $n_e T = 10^{15}$ cm^{-3} K. A typical DEM derived from CDS data is shown in Figure 14.1,

Table 14.1: Lines observed by CDS used to derive full-Sun DEM curves as in Figure 14.1.

Wavelength / nm	Identification
31.18	Mg VIII
31.37	Mg VIII
31.50	Mg VIII
32.70	Fe XV
33.28	Al X
33.42	Fe XIV
34.11	Fe XI
34.57	Fe X
35.27	Fe XI
36.08	Fe XVI
36.81	Mg IX
36.92	Fe XI
37.41	O III
52.58	O III
54.11	Ne IV
54.21	Ne IV
54.39	Ne IV
55.00	Al XI
55.43	O IV
56.98	Ne V
57.22	Ne V
59.96	O III
60.84	O IV
62.50	Mg X
62.97	O V

and a typical spectrum, with both measured and DEM-derived components, is shown in Figure 14.2.

To estimate the sensitivity to the pressure chosen in the analysis, we performed our calculations at three different pressures $n_e T$: (10^{14}, 10^{15}, and 10^{16}) cm^{-3} K. When combined with the actual CDS observations above 30 nm, the resulting integrated irradiances between 26 nm to 34 nm were the same to within 1 %. We also made runs with different ionization rate and abundance files, to estimate the sensitivity to these assumptions. The results were the same to within 2 %.

14.3 Comparison of CDS with SEM and EIT

The measurements in each of the SEM first-order detectors can be summarized as

$$S = \sum I_\lambda Q_\lambda$$

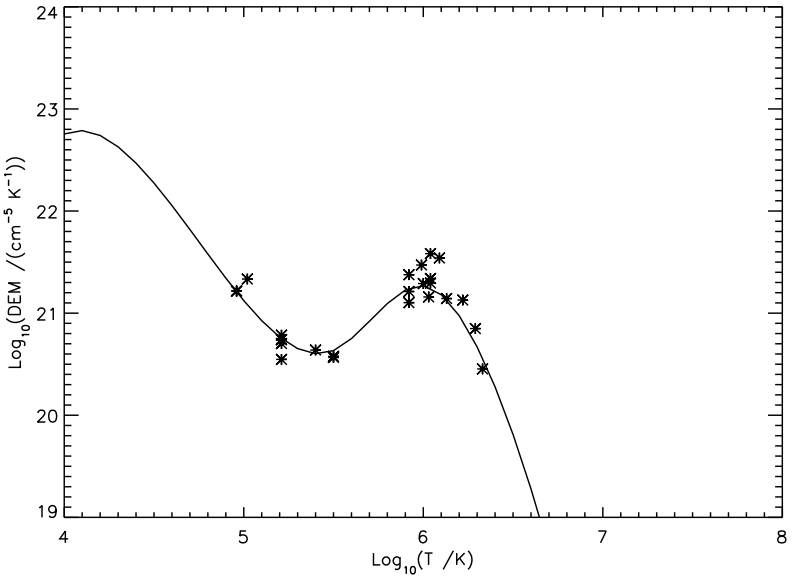

Figure 14.1: Typical DEM curve derived from CDS data.

where I_λ is the intensity of each of the spectral lines (or wavelength bins) contributing to the total, and Q_λ represents all the instrumental factors. In order to convert the raw signals S into physical values, one must know how the spectrum varies as a function of wavelength. To this end, the SEM team has adopted a standard reference spectrum (SOLERS22), with reference intensities R_λ. The irradiance F can then be estimated as

$$F \approx \sum I_\lambda Q_\lambda \left(\frac{\sum R_\lambda}{\sum R_\lambda Q_\lambda} \right) = \frac{S}{\langle Q \rangle}$$

A more complete description of the SEM data-reduction process is described in *Judge et al.* [1999].

In the standard SEM analysis, the reference spectrum R_λ is the same for all dates. This provides a uniform interpretation. However, in the real Sun, the different lines I_λ change independently of each other with the solar cycle. When the spectra based on CDS or EIT data are used as the reference spectra, the SEM values drop by ≈ 15 % to 20 % over the period before loss-of-contact, bringing them into better agreement with the CDS values, as demonstrated in Figure 14.3. When the CDS or EIT data are used as reference spectra, not only do the SEM values come down, but they come down by approximately the same amount, which demonstrates that CDS and EIT both agree on the distribution of energy over the spectral bandpass, even if their absolute calibrations may not be quite the same.

Figure 14.4 shows the ratio of the CDS and EIT data to the SEM results. When compared against the unmodified SEM signal, the CDS/SEM ratio holds fairly steady at ≈ 80 %. When the solar spectrum inferred from CDS is used as the reference spectrum, then the ratio increases to ≈ 90 %, showing better agreement. However, this does emphasize a slight slope with time, possibly indicating an unmodeled decline in the CDS instru-

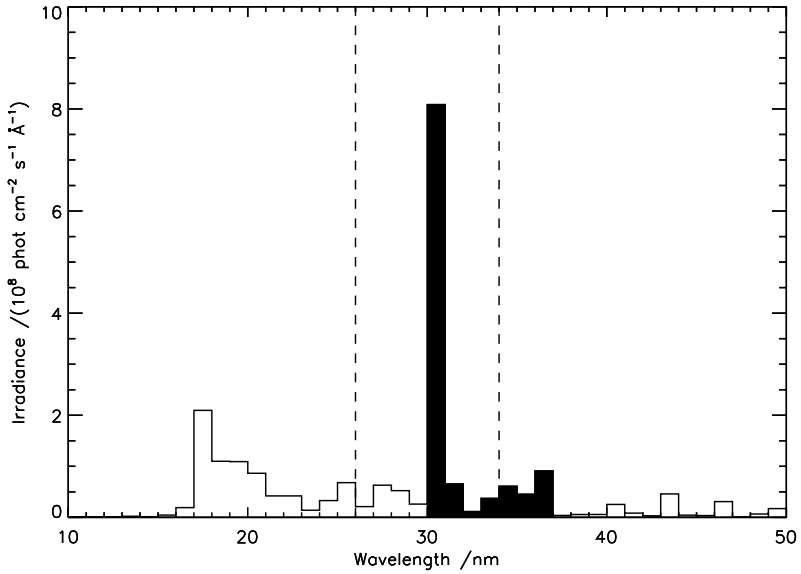

Figure 14.2: A typical CDS spectrum, combining an observed component (black) and a DEM derived component (white). The vertical dashed lines represent the limits of the SEM bandpass. The tallest bin, between 30 nm and 31 nm, is observed in second-order in the NIS long wavelength channel.

ment response. Another possible explanation, concerning the DEM analysis of the CDS data, will be discussed in Section 14.5. The EIT data, on the other hand, are consistently above the SEM values. Like CDS, the EIT/SEM ratio also shows an initial downward slope, but then levels off.

14.4 Changes to the Post-recovery CDS Data

After the SOHO spacecraft was recovered following the temporary loss-of-contact in the summer of 1998, it quickly became evident that changes had occurred in the CDS instrument. Slight changes had occurred in the positions of the two spectral ranges on the detector, which in general meant that lines were now being exposed onto fresher areas of the detector. There also appeared to be some general reduction (≈ 20 %) of the burn-in pattern. One of the most significant changes, though, was in the instrumental line profile. Before the loss of contact, the spectral lines were well fitted with Gaussian profiles. After recovery, this was no longer true. It was found that the post-recovery line profiles were

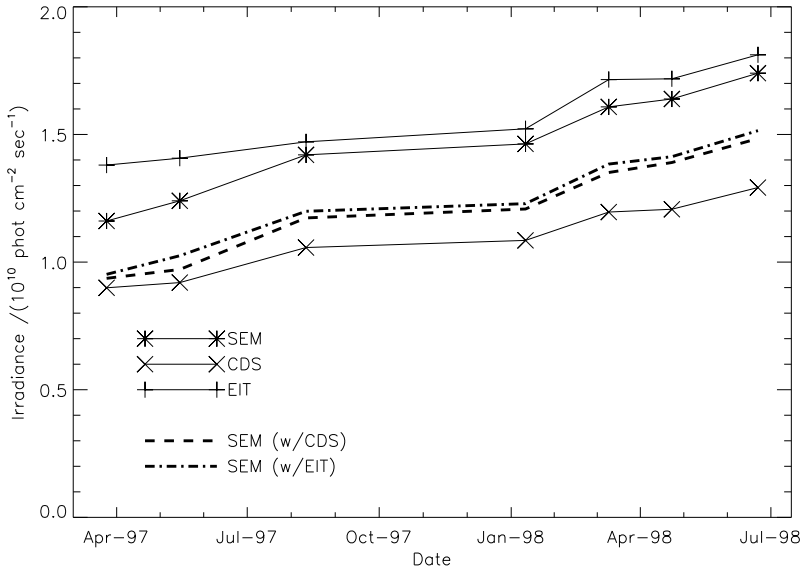

Figure 14.3: The solid lines represent 26 nm to 34 nm irradiances from SEM (*), CDS ($\times$), and EIT (+), where the SEM data is based on the SOLERS22 reference spectrum. The relative standard uncertainties on the respective data sets are SEM: 10 %, EIT: 15 %, and CDS: 25 %. Also shown is the modified SEM signal using the spectral observations of CDS (dash) and EIT (dot-dash) as the reference spectrum.

best fitted with a combination of a Gaussian for the core of the line, plus a term describing the broadened wings:

$$B(\lambda) = A_0 \left[(1-\alpha) \exp\left[-\frac{1}{2} \left(\frac{\lambda - \lambda_0}{\sigma} \right)^2 \right] + \frac{\alpha}{\left(\frac{\lambda - \lambda_0}{2\sigma\sqrt{2\ln(2)}} \right)^2 + 1} \right]$$

where α can have different values for the red ($\lambda > \lambda_0$) and blue ($\lambda < \lambda_0$) wings. The adopted values of α were:

$\alpha = 0.8$	NIS-1
$\alpha = 0.317$	NIS-2, $\lambda > \lambda_0$
$\alpha = 0.0884$	NIS-2, $\lambda < \lambda_0$

Since the He II and Si XI lines at 30.4 nm appear in second order in the NIS-2 channel, the asymmetric values of α for that channel are used for those lines.

The current version of the CDS data-analysis software applies the same absolute calibration for the post-recovery data that it does for the pre-loss data. Looking at long-term trends in the quiet-Sun, disk-center radiances, it appears that this assumption holds true for the first-order, long-wavelength channel. However, adjustments are needed for the short-wavelength channel, and for the second-order lines in the long-wavelength channel. For this study, adjustment factors were adopted for the post-recovery data shown in Table 14.2.

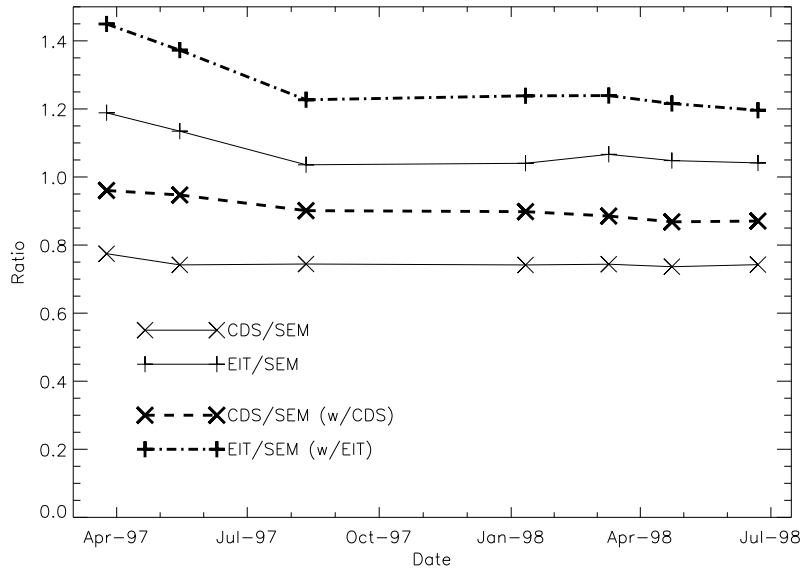

Figure 14.4: The solid lines represent the ratio of the CDS ($\times$) and EIT (+) irradiance measurements to the unmodified SEM irradiance based on the SOLERS22 reference spectrum (i.e., to the * symbols in Figure 14.3). The lines with dash and dot-dash patterns represent the ratios to the modified SEM signal using each instrument's measured spectrum as the reference spectrum (i.e., to the lines with the same patterns in Figure 14.3). These lines are drawn bold, to emphasize that they are the more relevant comparisons.

The results of Figures 14.3 and 14.4 are extended to the post-recovery period in Figures 14.5 and 14.6, respectively. Figure 14.5 shows that there is a basic overall consistency between the CDS, SEM, and EIT irradiance measurements: they increase and decrease together.

On the other hand, two artifacts in the CDS data are evident from Figure 14.6. First, there is a jump of $\approx$20 % in the CDS/SEM ratio in the period immediately following recovery, when the unmodified SEM data are used, based on the SOLERS22 spectrum. A more realistic comparison is to use the CDS spectra in the SEM data reduction, which decreases the jump to $\approx$ 10 %. This may represent a recovery from some unmodeled loss

Table 14.2: Adjustment factors applied to the post-recovery CDS data.

Channel	Factor
NIS-1	1.447
NIS-2, 1^{st} order	1
NIS-2, 2^{nd} order	1.167

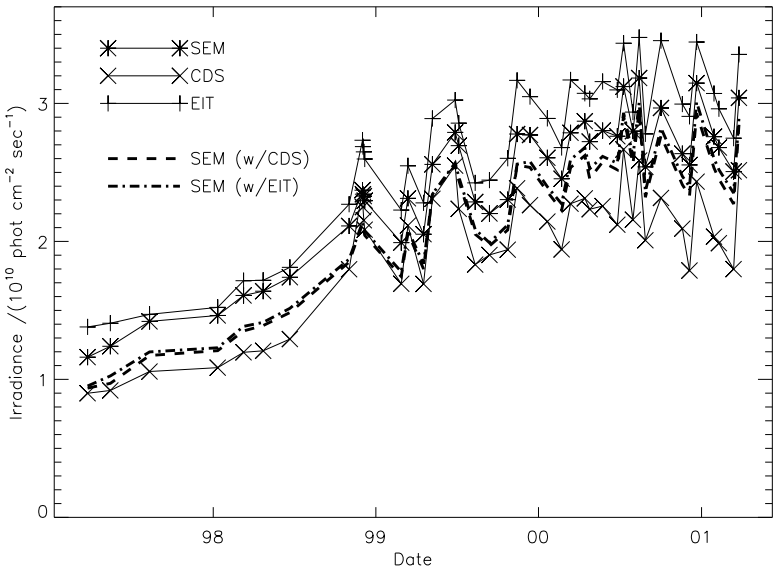

Figure 14.5: Extension of Figure 14.3 to the post-recovery period.

in the CDS instrument response, during the out-of-contact period. Or, it may mean that the adjustment factors in Table 14.2 for the post-recovery data are over-estimated. After contact was restored, there is again a slow, but steady, decline in the CDS/SEM ratio with time, which may indicate an unmodeled loss in the CDS instrument response (but see also Section 14.5). The post-recovery EIT behavior is consistent with the pre-loss-of-attitude behavior.

As the solar cycle progresses from minimum to maximum, the standard SEM values based on the SOLERS22 spectrum approach those based on either the CDS or EIT spectral observations. This is because the CDS and EIT spectra look more like the SOLERS22 spectrum when the Sun is more active.

There may be slight differences in the bandpasses between the two SEM first-order channels [*Judge et al.*, 1998]. This is due to the measured alignment of the SEM and the corresponding uncertainty of these measurements. The net result of this is that each first-order channel may be observing a slightly different bandpass and will therefore produce a slightly different count-rate for minor changes in the solar spectral distribution. Figure 14.7 shows the difference in the observed raw counts in the two SEM channels, compared against what the CDS and EIT instruments predict should be seen in these channels. Up until SOHO's loss-of-attitude, both CDS and EIT predict that the signal in channel three should be rising more quickly than channel one as the solar activity rises, while the measured difference shows little change with the solar cycle. This may indicate that the actual bandpasses for the two SEM channels are slightly different than the modeled bandpasses. After recovery, the CDS predictions level off, matching the SEM observations, while the EIT predictions continue to rise.

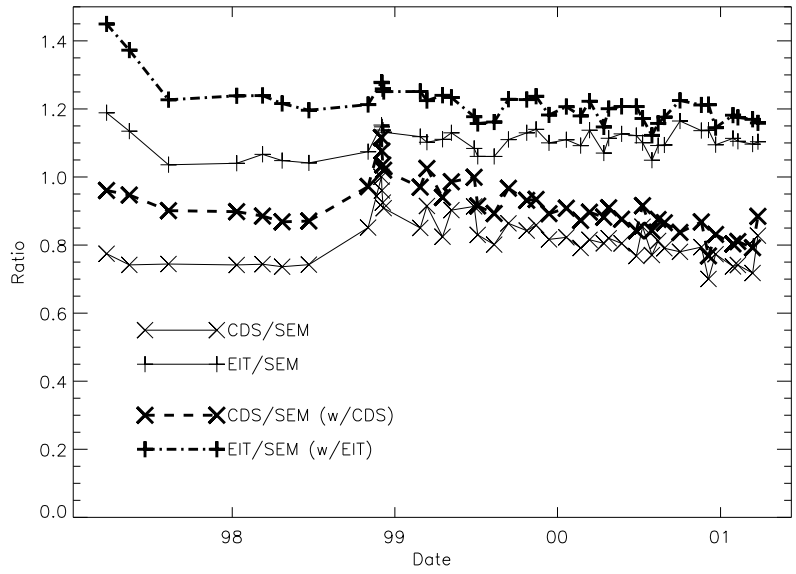

Figure 14.6: Extension of Figure 14.4 to the post-recovery period.

14.5 Behavior of Different CDS Components

Since the CDS spectrum over the SEM bandpass is built up of three distinct components, one important question is whether or not these components, or just a single component, can explain the artifacts in Figure 14.6. The single most important component is from the two second-order lines of He II and Si XI at 30.4 nm. Figure 14.8 shows the relative contribution of these two lines to the total SEM bandpass, based on both the CDS and EIT spectra. One can see that there is both agreement and disagreement between the two instruments over the importance of the two 30.4 nm lines to the SEM bandpass. Both agree that in 1997, when the Sun was near solar minimum, the radiation at 30.4 nm makes up about 80 % of the total SEM bandpass. As the solar cycle progresses, this drops to only about 55 % to 60 % by the year 2000. However, CDS consistently measures a somewhat bigger contribution from 30.4 nm, and this difference is larger after the out-of-contact period than before. This could be because the CDS second-order calibration after the loss-of-attitude is slightly overestimated, which could also explain the slight jump in the CDS/SEM ratio at that time.

Another way to look at the difference between the CDS and EIT data is to plot how much of the difference is due to the second-order CDS measurements at 30.4 nm, how much from the first-order spectrum longward of 31 nm, and how much from the DEM-derived spectrum shortward of 30 nm. These are shown in Figure 14.9. Up until the SOHO loss-of-attitude in the summer of 1998, the principal difference is in the bin containing the strong He II 30.4 nm line. However, as the solar cycle progresses, the component below 30 nm becomes more important. Detailed examination shows that most of this difference is in the Fe XV 28.4 nm line. Since this is one of the bandpasses directly observed by EIT,

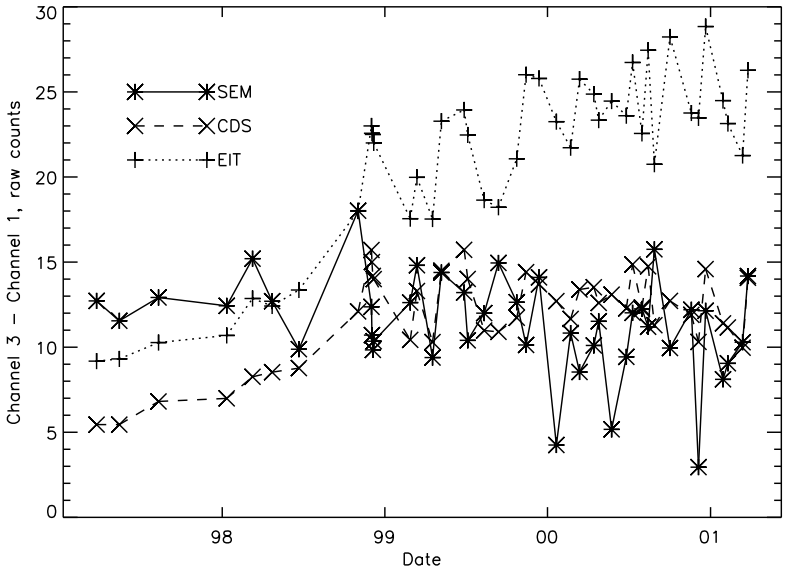

Figure 14.7: The solid curve shows the measured difference in raw counts between SEM channels 3 and 1. Also shown are the projected differences based on the CDS (dashed) and EIT (dotted) data.

it would appear that the DEM analysis of the CDS data being used here is failing to model correctly the brightness at 28.4 nm. Looking at Figure 14.1, this can be explained by the fitted curve not exactly reproducing the sharp cutoff at the highest temperatures.

If the synthetic spectra used to fill in the unobserved part of the SEM bandpass is underestimated, then this could explain several features in the disagreement between CDS and either SEM or EIT. First of all, it would substantially help explain why CDS consistently measures lower values than either of the other two instruments. Figure 14.9 also shows that most of the slow decline in the CDS/SEM ratio after the SOHO recovery can be attributed to the synthetic spectrum component.

14.6 Conclusions

The CDS, EIT, and SEM instruments all have good agreement of their measured irradiances within their combined uncertainties. When the spectral shapes from either CDS or EIT are used in the processing of the SEM raw data, the agreement between CDS and SEM improves, but is worse between EIT and SEM. The effect of the CDS and EIT spectral shapes on the SEM analysis is about the same.

The synthetic spectrum, used to fill in the part of the SEM bandpass not observed by CDS, has significantly less Fe XV 28.4 nm emission than is found in the EIT data. This is attributed to a lack of resolution in the fitted DEM. This under-prediction at 28.4 nm goes a long way towards explaining why the CDS integrated irradiance values between 26 nm

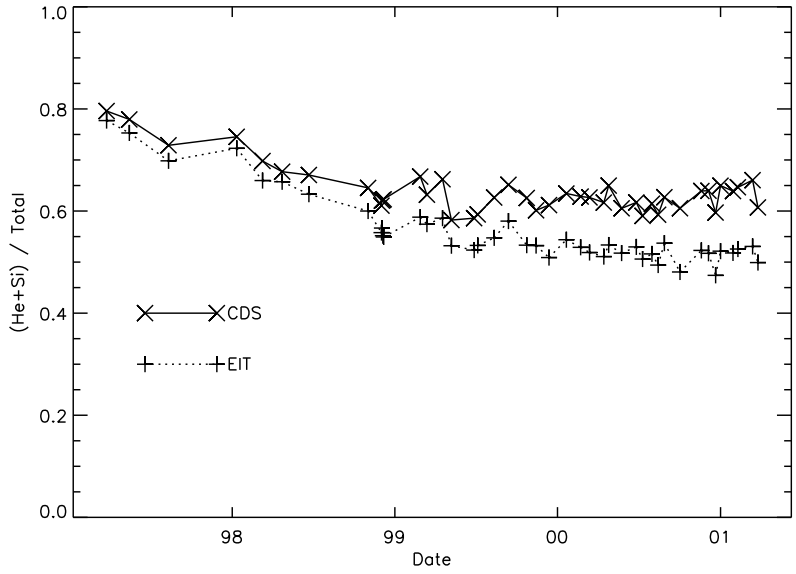

Figure 14.8: The relative importance of the He II and Si XI lines at 30.4 nm to the total SEM bandpass, based on CDS (solid) and EIT (dotted) spectra.

to 34 nm are lower then either SEM or EIT, and why the CDS/SEM ratio shows a slight decline with time. It should be emphasized that the disagreement between CDS and EIT at 28.4 nm is not a problem with their relative calibrations, since CDS does not observe in this part of the spectrum.

Immediately after the recovery of the SOHO spacecraft in late 1998, the CDS/SEM ratio shows a slight ≈ 10 % jump, which may mean that the 1.167 adjustment factor for second-order, 30.4 nm, post-recovery data may be overestimated.

The CDS and EIT spectra both predict count-rates in the two SEM channels whose difference behaves differently than the actual, observed difference, for the selected days in this study. Initially, as the solar activity increases, this predicted difference slowly increases, while the observed difference varies little over the solar cycle. The CDS predicted difference eventually levels off, matching the observed behavior, while the EIT prediction continues to rise. If the 28.4 nm component of the CDS spectrum were not underestimated, the CDS prediction might better match that of EIT. This inconsistency between the CDS and EIT predictions and the SEM observations may indicate that the actual bandpasses for the two SEM channels are slightly different than the modeled bandpasses. This is an area of future study regarding the alignment of the SEM and is not expected to change the results of SEM irradiance values beyond the stated uncertainty.

The relative importance of 30.4 nm (He+Si) to the total SEM bandpass gradually decreases from 80 % early in the mission to either 60 % as measured by CDS, or 50 % as measured by EIT. As the solar activity increases, the effect of the observed CDS and EIT spectra on the SEM measurements approaches that of the assumed SOLERS22 spectrum.

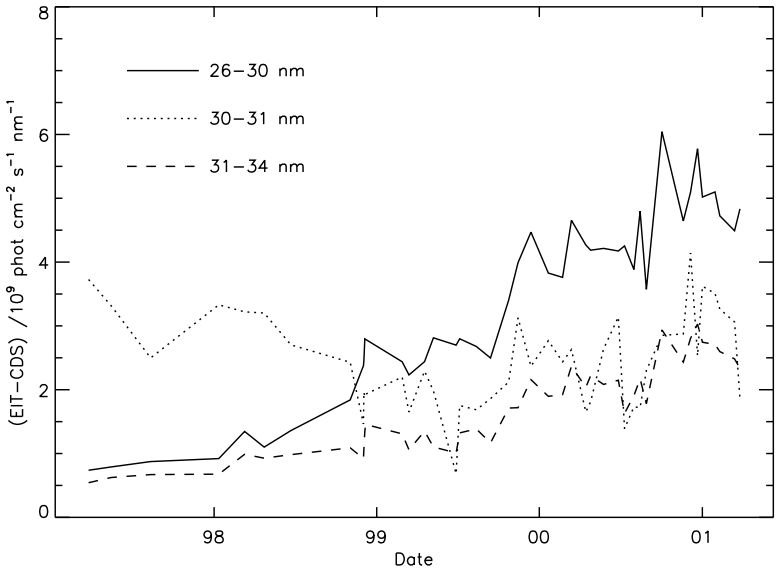

Figure 14.9: The difference between the CDS and EIT irradiances, split into three spectral ranges according to how they were derived from CDS data. The range 26 nm to 34 nm was not measured by CDS, but was derived via a DEM analysis.

Acknowledgements

Author JSN received support from NRL, the Office of Naval Research and NASA grant NDPRS-92385.

Bibliography

Arnaud, M., and Raymond, J., Iron ionization and recombination rates and ionization equilibrium, Astrophys. J. **398**, 394–406, 1992.

Brekke, P., Thompson,W.T., Woods, T.N., and Eparvier, F.G., The EUV solar irradiance spectrum observed with the Coronal Diagnostic Spectrometer (CDS) on SOHO, *Astrophys. J.* **536**, 959–970, 2000.

Cook, J.W., Newmark, J.S., and Moses, J.D., *in* Coronal Thermal Structure from a Differential Emission Measure Map, *Proc. 8th SOHO Workshop*, Paris, France, ESA SP-446, 1999.

Cook, J.W., Newmark, J.S., and Moses, J.D., Coronal differential emission measure maps derived from SOHO EIT, *Astrophys. J.*, in prep., 2002.

Delaboudinière, J.-P., Artzner, G.E., Brunaud, J., Gabriel, A.H., Hochedez, J.F., Millier, F., Song, X.Y., Au, B., Dere, K.P., Howard, R.A., Kreplin, R., Michels, D.J., Moses, J.D., Defise, J.M., Jamar, C., Rochus, P., Chauvineau, J.P., Marioge, J.P., Catura, R.C., Lemen, J.R., Shing, L., Stern, R.A., Gurman, J.B., Neupert, W.M., Maucherat, A.,

Clette, F., Cugnon, P., and van Dessel, E.L., EIT: Extreme-ultraviolet Imaging Telescope for the SOHO mission, *Sol. Phys.* **162**, 291–312, 1995.

Dere, K.P., Landi, E., Mason, H.E., Monsignori Fossi, B.C., and Young, P.R., CHIANTI–An Atomic Database For Emission Lines, *Astron. Astrophys. Supp.* **125**, 149–173, 1997.

Harrison, R.A., Sawyer, E.C., Carter, M.K., Cruise, A.M., Cutler, R.M., Fludra, A., Haynes, R.W., Kent, B.J., Lang, J., Parker, D.J., Payne, J., Pike, C.D., Peskett, S.C., Richards, A.G., Culhane, J.L., Norman, K., Breeveld, A.A., Breeveld, E.R., Al Janabi, K.F., McCalden, A.J., Parkinson, J.H., Self, D.G., Thomas, P.D., Poland, A.I., Thomas, R.J., Thompson, W.T., Kjeldseth-Moe, O., Brekke, P., Karud, J., Maltby, P., Aschenbach, B., Bräuninger, H., Kühne, M., Hollandt, J., Siegmund, O.H.W., Huber, M.C.E., Gabriel, A.H., Mason, H.E., Bromage, B.J.I., The Coronal Diagnostic Spectrometer for the Solar and Heliospheric Observatory, *Sol. Phys.* **162**, 233–290, 1995.

Hovestadt, D., Hilchenbach, M., Bürgi, A., Klecker, B., Laeverenz, P., Scholer, M., Grünwaldt, H., Axford, W.I., Livi, S., Marsch, E., Wilken, B., Winterhoff, H.P., Ipavich, F.M., Bedini, P., Coplan, M.A., Galvin, A.B., Gloeckler, G., Bochsler, P., Balsiger, H., Fischer, J., Geiss, J., Kallenbach, R., Wurz, P., Reiche, K.U., Gliem, F., Judge, D.L., Ogawa, H.S., Hsieh, K.C., Möbius, E., Lee, M.A., Managadze, G.G., Verigin, M.I., and Neugebauer, M., CELIAS - Charge, element, and isotope analysis system for SOHO, *Sol. Phys.* **162**, 441–481, 1995.

Judge, D.L., McMullin, D.R., Ogawa, H.S., Hovestadt, D., Klecker, B., Hilchenbach, M., Möbius, E., Canfield, L.R., Vest, R.E., Watts, R., Tarrio, C., and Kühne, M., First solar EUV irradiances obtained from SOHO by the CELIAS/SEM, *Sol. Phys.* **177**, 161–173, 1998.

Judge, D.L., McMullin, D.R., and Ogawa, H.S., Absolute Solar 30.4 nm flux from sounding rocket observations during the solar cycle 23 minimum, *J. Geophys. Res.* **104** A12, 28321–28324, 1999.

Meyer, J.-P., The baseline composition of solar energetic particles, *Astrophys. J. Supp.* **57,** 151–171, 1985.

Newmark, J.S., Cook, J.W., and McMullin, D.R., Solar model EUV and He II irradiances from SOHO EIT derived DEM maps, *Astrophys. J.*, in prep., 2002.

Thomas, R.J., Davila, J.M., Thompson, W.T., Kent, B.J., and Hollandt, J., The SERTS-97 cross-calibration of CDS and EIT on SOHO, *Bull. Am. Astro. Soc.* **31**, 850, 1999.

Thomas, R.J., Underflight calibration of SOHO CDS by SERTS-97, this volume, 2002.

Thompson, W.T., and Brekke, P., EUV Full-Sun imaged spectral atlas using the SOHO Coronal Diagnostic Spectrometer, *Sol. Phys.* **195**, 45–74, 2000.

Thompson, W.T., Differential scrubbing of an intensified CCD camera aboard the SOHO Coronal Diagnostic Spectrometer, *Optical Engineering* **39**, 2651–2659, 2000.

— 15 —

Underflight Calibration of SOHO CDS by SERTS-97

ROGER J. THOMAS
Laboratory for Astronomy and Solar Physics
NASA Goddard Space Flight Center
Greenbelt, MD, USA

Flights of the SERTS sounding rocket were made in 1997, 1999, and 2000 to provide updated radiometric and wavelength calibrations for several experiments on the SOHO mission. Just before or after each of these flights, end-to-end radiometric calibrations of the rocket payload were carried out using an EUV transfer standard light-source specially re-calibrated against the primary standard of BESSY I. These measurements established the absolute SERTS responsivity within a relative uncertainty of 17 % over its bandpass of 30 nm to 36 nm. During the flights, SERTS and SOHO CDS observed the same solar locations, as demonstrated by subsequent data co-registration with simultaneous SOHO EIT images, allowing the SERTS calibrations to be directly applied to both CDS and EIT. Following is a brief summary of the SERTS-97 radiometric calibration and the underflight cross-calibration that it provided for the CDS NIS channels at a time shortly before SOHO's temporary loss of pointing control.

15.1 Introduction

The Solar EUV Research Telescope and Spectrograph (SERTS) developed by the Goddard Space Flight Center (GSFC) is a rocket instrument that obtains imaged high-resolution spectra of individual solar features to study the Sun's corona and upper transition region. Flights in 1997, 1999, and 2000 also provided radiometric and wavelength calibrations for several experiments on the SOHO mission. For that purpose, end-to-end radiometric calibrations of SERTS were carried out just before or after each flight in the same facility that had been used to characterize the SOHO CDS experiment at Rutherford Appleton Laboratory (RAL) [*Lang et al.*, 2000, 2002], and using the same EUV light source specially re-calibrated against the primary EUV radiation standard of BESSY I. These measurements can establish the absolute SERTS responsivity within a relative standard uncertainty of 25 % or better at 12 wavelengths covering its bandpass of 30 nm to 36 nm. Post-flight wavelength calibrations were done at GSFC using laboratory standard lines of He II and Ne II. Each SERTS payload also carried an EUV solar flux monitor kindly provided by the University of Southern California (USC) [*McMullin et al.*, 2002]; its readings were used to validate calculations of atmospheric EUV transmission over the rocket's trajectory, and to provide an updated calibration for SOHO CELIAS. During each flight, SERTS and CDS observed the same solar locations, as demonstrated by subsequent data

Table 15.1: Radiant power and photon flux of the EUV transfer-standard source. Results are mean values of all calibration periods.

Emission Lines / nm	Integration Range / nm	Spectrum	Radiant Power / pW	Photon Flux / s^{-1}	Rel. Std. Uncert.
30.11	29.95-30.25	Ne III	10.4	1.58×10^6	7 %
30.38	29.90-30.90	He II	319.0	4.88×10^7	7 %
30.48/30.55	30.35-30.65	?	6.71	1.03×10^6	7 %
30.86	30.75-31.00	Ne III	4.10	6.37×10^5	7 %
31.31-31.39	31.20-31.55	Ne III	12.4	1.96×10^6	7 %
31.95/32.00	31.80-32.15	?	11.6	1.87×10^6	7 %
32.46/32.54	32.35-32.57	Ne II	4.34	7.10×10^5	7 %
32.65-32.81	32.57-32.82	Ne II	38.4	6.36×10^6	7 %
33.01-33.15	32.82-33.35	Ne II	21.3	3.53×10^6	7 %
35.22-35.39	35.00-35.40	Ne II	17.7	3.17×10^6	7 %
35.50-35.75	35.40-35.85	Ne II	59.3	1.06×10^7	7 %
36.14/36.25	35.95-36.45	Ne II	43.0	7.84×10^6	7 %

co-registration with simultaneous SOHO EIT images, allowing the SERTS calibrations to be directly applied to both CDS and EIT. Following is a brief summary of the SERTS-97 radiometric calibration and the underflight cross-calibration that it provided for the CDS NIS-1 and NIS-2 channels, a few months before SOHO's loss of pointing control in 1998.

15.2 Calibration Source – EUV Transfer Standard

To support SOHO, the Physikalisch-Technische Bundesanstalt (PTB) developed a special EUV radiometric transfer standard, based on a hollow-cathode lamp combined with collimating optics [*Hollandt et al.*, 2002]. Different gasses can be fed through the hollow cathode to provide radiation from a wide variety of emission lines. Controls for the operating conditions of the lamp ensure that its output is stable and repeatable. The lamp's exit aperture is a 0.6 mm-diameter pinhole positioned at the focal point of an inverted grazing-incidence Wolter Type-II telescope, which had been made by GSFC for the SERTS program, then donated to PTB. A collimated beam emerges from the telescope, and is limited to a diameter of 5 mm by a final aperture. The entire device is mounted on a table that can be moved and tilted in a controlled manner.

This source was characterized by PTB against the BESSY I electron storage ring, a primary radiometric standard, and used to carry out the pre-launch calibrations of the SOHO CDS experiment. In 1995, the source was again specially re-characterized directly against BESSY I for the SERTS project over the spectral bandpass of 26 nm to 38 nm. These later measurements demonstrated that the source showed no systematic degradation over the several-year period involved, and that its absolute radiant power at each wavelength could be established to within a relative standard uncertainty of 7 %. Table 15.1 lists the final results of all such BESSY runs with the transfer source for the wavelengths used to calibrate the SERTS instrument, at 11 sets of lines between 30 nm to 36 nm by using neon, and at 30.38 nm by using helium. Further details of this source and its calibration are given by *Hollandt et al.* [2002].

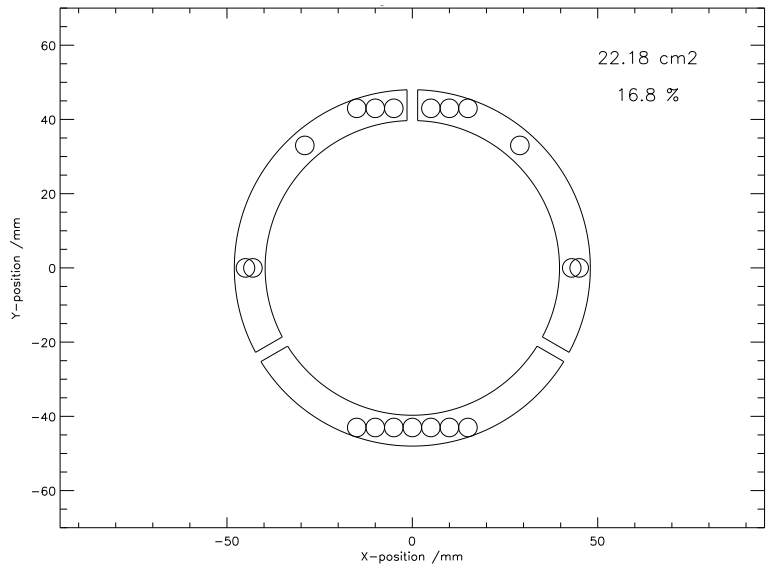

Figure 15.1: The entrance aperture of the SERTS-97 instrument. Smaller circles show the areas illuminated by the narrow beam of the EUV calibration source.

15.3 SERTS-97 Radiometric Calibration

In September 1997, the SERTS rocket payload was shipped to RAL and installed in the same vacuum chamber that had been used to carry out the pre-launch calibrations of the SOHO CDS instrument. The calibration source described above was then attached and aligned to the SERTS optical axis by means of a red laser shining through the source optics. This laser was adjusted to retro-reflect from the SERTS reference mirror, and its position was set to illuminate a specific target point on the SERTS telescope aperture. In that orientation, a spotting telescope attached to the source table was locked into position sighting a corresponding target point on a map of the SERTS aperture that was attached to the side of the rocket payload. In addition, an auto-collimator, also attached to the source, was locked into position viewing the reflection from a large flat mirror that was fixed to the other side of the SERTS instrument. These both looked through window ports in the vacuum chamber's door, so that the relative position and tilt between the source and instrument could always be controlled during the calibration runs. Flexible bellows in the vacuum pipe connecting the source to the vacuum chamber permitted the needed motions and tilts. In order to assure that all source radiation reached the detector, the slit of the SERTS spectrometer was removed. The entrance aperture of the SERTS-97 instrument is an annulus with inner and outer radii of 39.70 mm and 48.01 mm, and with three spider-arms each 2.87 mm wide. Various parts of the aperture are illuminated by translating the narrow source-beam relative to the payload. Horizontal translation is accomplished by a motorized table inside the vacuum chamber on which the payload is mounted, while vertical translation is done by jacking the source-table up and down. A total of nineteen

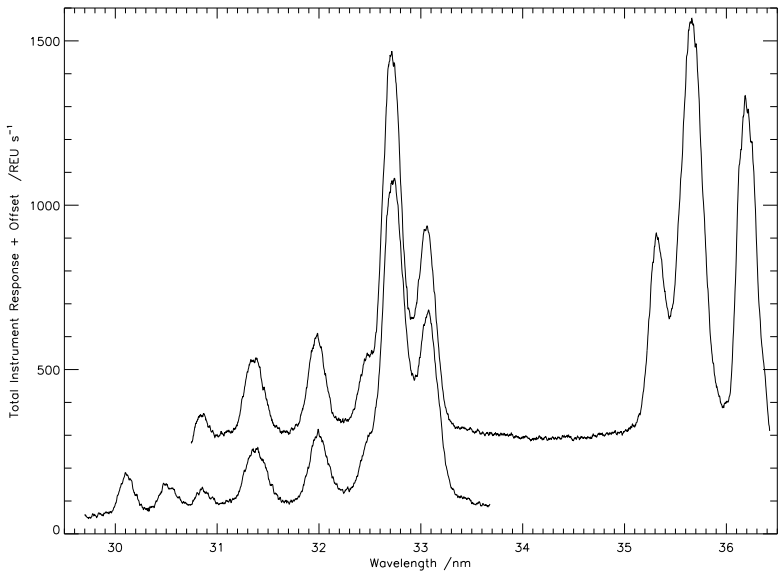

Figure 15.2: Representative results of spatially summed responses to neon. Two different tilts of the source were required in order to cover the full wavelength range when using that gas.

locations within the instrument aperture were covered with the 5 mm-diameter beam in this way, representing 16.8 % of its full area (Figure 15.1).

SERTS-97 used an intensified CCD detector with a 3072×2048 array of 9-micron pixels[1], cooled to -20 °C. For each entrance aperture location, this detector recorded a spectrally dispersed image of the 0.6 mm source pinhole in the various emission lines being emitted. Since all of the useful neon lines could not fit onto the detector in one image, two different tilts of the source were required in order to cover the full wavelength range when using that gas. Representative results of spatially summed responses to neon are shown in Figure 15.2, in which the eleven measured spectral features can be seen. Although some of these features appear blended, their separate contributions can be reliably determined by fitting multiple Gaussians to the overall profiles. Several routine adjustments are applied to all of the recorded data, including dark image subtraction, de-biasing, non-linearity correction, flat-fielding, median filtering, and then spatial summing. The non-linearity correction is determined by comparing data that differ only by exposure time, and is used to convert the raw recorded Data Numbers (DN) to Relative Exposure Units (REU). The total response rate in REU/s at each wavelength is then found by Gaussian fits to all 99 of the corrected calibration images, taken on ten days during the full run of three weeks. Since a given wavelength feature was recorded multiple times, the values of those readings were averaged for each entrance aperture position measured, and then averaged again over all aperture positions to simulate full-aperture illumination.

[1] 1 micron = 1 μm = 10^{-6}m

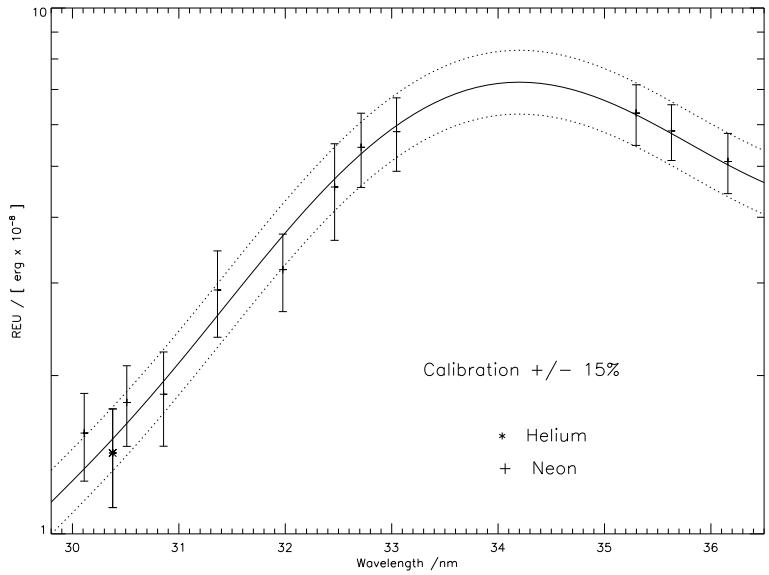

Figure 15.3: SERTS-97 absolute end-to-end response in Relative Exposure Units (REU) per erg as a function of wavelength. Error bars show the total range of values measured from the different sub-aperture positions.

The final calibration is shown in Figure 15.3, which gives the measured SERTS-97 absolute end-to-end response in units of REU/erg as a function of wavelength. The peaked shape of the curve is mainly due to the multilayer coating on the spectrograph grating, which was applied to enhance its EUV efficiency. Error bars reflect the total range of values measured from the various entrance aperture positions. The solid line is a Gaussian plus slope, which represents the measurements to well within the 15 % uncertainty limits shown. This response curve giving Resp/Srce is then used with the following relationships

$$\begin{aligned} \text{Cal} &= \text{Srce} \times (\text{K/PScl})^2 \,/\, \text{Area} \,/\, \text{Resp} \\ \text{Lobe Calibration} &= \text{Cal} \,/\, \text{Pix}^2 \\ \text{Slit Calibration} &= \text{Cal} \,/\, \text{Pix} \,/\, \text{Slit} \end{aligned}$$

and with the various geometric values given in Table 15.2 to determine the appropriate calibration factors for SERTS observations made either with its narrow slit or with its wide lobe. In the table, Slit is the width of the spectrometer's narrow slit, and Area refers to the instrument's entrance aperture; both were measured with an accurate travelling microscope. Pix is the detector pixel size, taken from manufacturer's specifications. PScl is the spatial Plate Scale of the instrument, which was determined by cross-correlations of SERTS lobe data against simultaneous EIT images, both at 30.4 nm [*W.T. Thompson, personal communication*, 1999]. This was done in units of SOHO-arcsec/SERTS-pixel, and so requires conversion by the factors of 1.00282 1AU-arcsec/SOHO-arcsec, and of 9 μm/SERTS-pixel. Finally, K is just the number of arcsec per radian. The resulting relative standard uncertainty of Cal (which has units of erg cm^{-2} sr^{-1} REU^{-1} μm^2) is 17 %.

Table 15.2: SERTS-97 calibration conversion.

Calibration Factors		Units	Rel. Std. Uncert.
Resp	Resp(λ)	REU / s	15.0 %
Srce	Srce(λ)	erg / s	7.0 %
Slit	21.5	μm	2.0 %
Area	22.18	cm^2	1.0 %
PScl	0.7869 / 9 $\times$ 1.00282	$''$/ μm	0.2 %
Pix	9.0	μm	0.0 %
K	180 $\times$ 60 $\times$ 60 / π	$''$/ rad	0.0 %

15.4 CDS Underflight Calibration

On 18 November 1997 at 1935 UT, the calibrated SERTS payload was launched from White Sands Missile Range, New Mexico, and made imaged spectral observations of active region NOAA 8108 on the solar disk at heliographic coordinates N21E18. Starting a few hours before this flight and ending a few hours after it, the CDS instrument on SOHO observed the same solar target with spectral coverage that included the SERTS bandpass. Cross-correlations of the resulting images at He II 30.4 nm with the full-disk image from SOHO EIT allowed all three to be spatially co-registered to within 1.8$''$. The alignment was verified by comparing spatial distributions of the highly variable Fe XVI 33.5 nm emission measured by both SERTS and CDS, which showed excellent relative agreement. A 30$''$ area along the SERTS slit was not used in the cross-calibration because a small sub-flare there caused too much time variability. However, on the remaining area of overlap between the CDS raster-field and the SERTS slit (190$''$), all consecutive observations agree within 2 %.

In addition to the standard data-reduction procedures mentioned in the previous Section, two other corrections were applied to the SERTS flight data. The first was an adjustment for atmospheric extinction at rocket altitudes, which was computed using radar measurements of the flight trajectory and the MSIS-86 model of the Earth's neutral thermosphere [*Hedin*, 1987]. SERTS-97 carried a full-disk EUV monitor provided by USC, whose measurements showed that atmospheric extinction is indeed well-fitted by the MSIS model used, and in any case is less than 10 % for all but two of the SERTS exposures. The second correction was to reduce instrumental line-profile distortions by applying two iterations of LUCY, a SolarSoft IDL routine based on image restoration methods described by *Richardson* [1972] and by *Lucy* [1974]. Pre-flight laboratory images were used to provide the instrumental point-spread function for that correction. The CDS measurements were likewise treated with their standard data-reduction routines, except that no radiometric factors were applied so that they were left in raw units of detector photon-events.

Both SERTS and CDS data were then spatially averaged over their area of overlap, excluding the sub-flare, giving the spectral curves shown in Figure 15.4. Here the SERTS measurements are in absolute units, while the CDS data have been scaled to match; both have arbitrary offsets to show the curves more clearly. All line intensities were found by Gaussian fits relative to the local background. Those indicated by vertical bars were strong and clean enough to be used in the cross-calibration. Since the CDS spectral resolution is

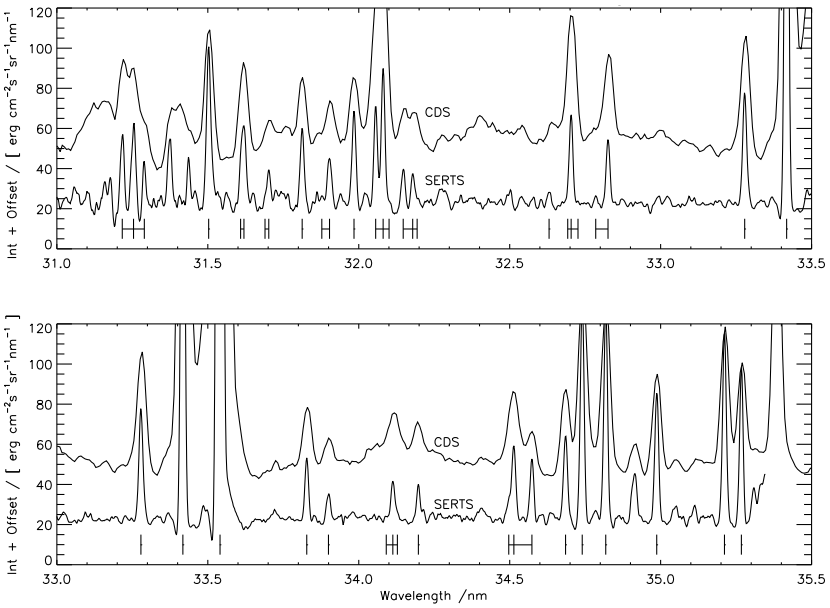

Figure 15.4: Comparison of SERTS and CDS NIS-1 spectral measurements made on 18 November 1997, spatially averaged over the same areas of the solar disk. The 26 spectral features used in the NIS-1 cross-calibration are indicated.

somewhat poorer than that of SERTS, a number of lines had to be grouped in the comparison, but this still allowed valid cross-calibrations at a total of 26 wavelengths in the CDS NIS-1 channel, and another two (second spectral-order) wavelengths in CDS NIS-2.

The final results are summarized in Figure 15.5. The error bars here represent line-fitting uncertainties only, and do not include the effect of uncertainty in the SERTS absolute calibration. The Figure includes an additional point at 36.8 nm from the Woods-97 rocket flight [*Brekke et al.*, 2000], which seems to agree well with an extension of the SERTS results. The polynomial fit (solid line) matches nearly every point to within 15 %, as indicated by the close dotted lines on either side. This curve has been implemented in SolarSoft as the current CDS NIS-1 calibration, through the following relationships:

Response = poly(Wave, Coef)
Coef = [–1.88868822, 0.166374198, –0.00490782871, 4.86757761e-05]

where poly is the IDL-library routine for evaluating polynomial functions. The listed values of Coef give the CDS NIS-1 conversion factor, Response, in units of photon events per (erg cm^{-2} sr^{-1}) when the variable wavelengths, Wave, are input in units of nm. Also shown is the previous calibration curve used for CDS NIS-1 [*Landi et al.*, 1997], as well as the original curve from pre-launch measurements, demonstrating the significant improvement provided by the SERTS-97 underflight re-calibration of the CDS experiment.

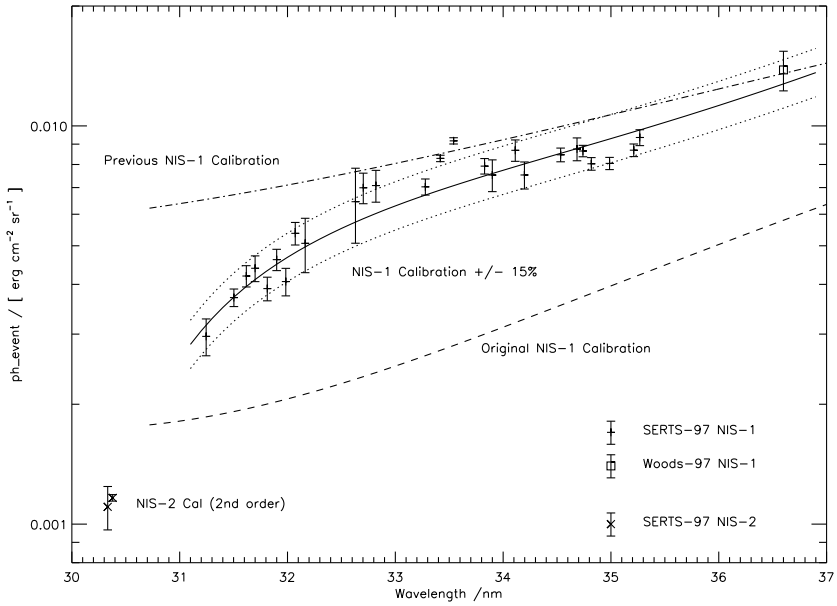

Figure 15.5: The ratio of CDS intensities in detector photon-event units to those measured by SERTS-97 in absolute units. Two points at 30.3 and 30.4 nm are for the second spectral order of NIS-2; all others are for first-order NIS-1. See the text for explanations of the various curves.

Acknowledgements

The PTB transfer source was developed under the leadership of Michael Kühne, while its characterization at BESSY I and operation at RAL were primarily done by Jörg Hollandt. SERTS calibrations at RAL depended on the tireless efforts of Barry Kent, and on the constant support of Richard Harrison. Much of the SERTS software, as well as CDS cross-calibration operations and data reduction, were carried out by William Thompson. The SERTS rocket project, initiated by Werner Neupert, has been led over the past twelve years by Joseph Davila. Heartfelt thanks are extended to Jim Lang, William Thompson, and especially to Anuschka Pauluhn for their many helpful suggestions and patient editing of the present manuscript. This work is funded by NASA RTOPs 370-18-37 and 344-17-38.

Bibliography

Brekke, P., Thompson, W.T., Woods, T.N., and Eparvier, F.G., The extreme-ultraviolet solar irradiance spectrum observed with the Coronal Diagnostic Spectrometer (CDS) on SOHO, *Astrophys. J.* **536**, 959–970, 2000.

Hedin, A.E., MSIS-86 Thermospheric Model, *J. Geophys. Res.* **92**, 4649–4662, 1987.

Hollandt, J., Kühne, M., Huber, M.C.E., and Wende, B., Source standards for radiometric calibration of astronomical telescopes in the VUV spectral range traceable to the primary standard BESSY, this volume, 2002.

Landi, E., Landini, M., Pike, C.D., and Mason, H.E., SOHO CDS-NIS in-flight intensity calibration using a plasma diagnostic method, *Sol. Phys.* **175**, 553–570, 1997.

Lang, J., Kent, B.J., Breeveld, A.A, Breeveld, E.R., Bromage, B.J.I., Hollandt, J., Payne, J., Pike, C.D., and Thompson, W.T., The laboratory calibration of the SOHO Coronal Diagnostic Spectrometer, *J. Opt. A: Pure Appl. Opt.* **2**, 88–106, 2000.

Lang, J., Thompson, W.T., Pike, C.D., Kent, B.J., and Foley, C.R., The calibration of the Coronal Diagnostic Spectrometer, this volume, 2002.

Lucy, L.B., An iterative technique for the rectification of observed distributions, *Astronom. J.* **79**, 745–754, 1974.

McMullin, D.R., Judge, D.L., Hilchenbach, M., Ipavich, F., Bochsler, P., and Bürgi, A., In-flight comparisons of solar EUV irradiance measurements provided by the CELIAS/SEM on SOHO, this volume, 2002.

Richardson, W.H., Bayesian-based iterative method of image restoration, *J. Opt. Soc. Am.* **62**, 55–59, 1972.

— 16 —

Intercalibration of CDS and SUMER

ANUSCHKA PAULUHN
International Space Science Institute
Bern, Switzerland

JAMES LANG
Rutherford Appleton Laboratory
Chilton, Didcot, Oxfordshire, UK

UDO SCHÜHLE, SAMI K. SOLANKI, KLAUS WILHELM
Max-Planck-Institut für Aeronomie
Katlenburg-Lindau, Germany

WILLIAM T. THOMPSON
L3 Communications Analytics Corporation
NASA Goddard Space Flight Center
Greenbelt, MD, USA

C. DAVID PIKE
Rutherford Appleton Laboratory
Chilton, Didcot, Oxfordshire, UK

ISABELLE RÜEDI
Physikalisch Meteorologisches Observatorium
World Radiation Center
Davos, Switzerland

JÖRG HOLLANDT
Physikalisch-Technische Bundesanstalt
Berlin, Germany

MARTIN C.E. HUBER
International Space Science Institute
Bern, Switzerland

Simultaneous observations of the same solar features with different instruments provide a way to compare radiometric calibrations and detect changes in responsivity with time of EUV instruments in space within the combined uncertainties of the individual instruments. Here we present the intercalibration of the SUMER (Solar Ultraviolet Measurements of Emitted Radiation) instrument (detectors A and B) and the two CDS (Coronal Diagnostic Spectrometer) instruments, the Normal Incidence Spectrometer (NIS) and the Grazing Incidence Spectrometer (GIS) on the Solar and Heliospheric Observatory (SOHO). This work describes the results of the Joint Observing Programme Intercal_01 and presents quiet-Sun comparisons from March 1996 up to February 2001, which represents the complete set of all available Intercal_01 measurements. Recent calibration updates of both instruments are employed, and the results indicate a very good correlation and agreement of the measured radiances within the combined uncertainties.

16.1 Introduction

During several measurement campaigns, two or more of the EUV instruments on SOHO observe nearly simultaneously to investigate common targets on the Sun. Some

of these Joint Observing Programmes (JOPs) are dedicated to intercomparisons of the radiometric calibrations of the instruments in orbit. The radiometric intercalibration between the extreme- and far-ultraviolet spectrometers CDS and SUMER has been introduced in previous papers [*Pauluhn et al.*, 1999, 2001]. Here we report on a comparison of measurements of the SUMER instrument and the Normal Incidence Spectrometer (NIS) as well as the Grazing Incidence Spectrometer (GIS) of CDS using the most recent calibrations (see also *Wilhelm et al.* [2002] and *Lang et al.* [2002]). SUMER is a stigmatic, normal-incidence telescope and spectrometer using two superposed orders of diffraction to cover the wavelength range from 46.5 nm to 161.0 nm. Two identical detectors (A and B) can be used for observations in their common wavelength-range below 147 nm. The CDS instrument is a double spectrometer, combining the wide wavelength-range of a grazing-incidence device and the stigmatic-imaging performance of a normal-incidence instrument to cover the wavelength range from 15.0 nm to 78.5 nm. Both the NIS and the GIS are fed simultaneously through a common slit by a grazing-incidence telescope.

SOHO's intercalibration JOP Intercal_01 includes the simultaneous observation, by SUMER and CDS-NIS, of quiet areas near Sun centre in the chromospheric line He I 58.4 nm and the two coronal lines Mg X at 60.9 nm and 62.4 nm as well as, by SUMER and CDS-GIS, in the 77.0 nm Ne VIII line. Later, the O V line at 63.0 nm was also included in the SUMER and CDS-NIS comparisons. The two latter lines (O V and Ne VIII) represent ion formation temperatures of approximately 2.5×10^5 K and 6×10^5 K, respectively, and thus belong to the transition region or the low corona and both exhibit a strong variability.

After a description of the data reduction (Section 16.2), we compare the average, absolute radiances of SUMER and CDS-NIS for the entire period of the intercalibration observing programme (Section 16.3), from March 1996 until the loss of the SOHO spacecraft in July 1998, as well as the post-recovery data until February 2001. Next (Section 16.4), we present the results of the comparison between SUMER and CDS-GIS. A summary of the results and conclusions is given in Section 16.5 .

16.2 Data Reduction

16.2.1 The SUMER Data

Since the data reduction applied to the SUMER data in this study has been performed as described by *Pauluhn et al.* [2001], the only differences being the radiometric calibration factors, we restrict ourselves to a brief summary. For a general description of the SUMER instrument and its data we refer to *Wilhelm et al.* [1995]. SUMER's telescope mirror can be stepped in multiples of single steps of $0.38''$ to move the solar image across the spectrometer's entrance slit. The slit with angular dimensions of $1'' \times 300''$ is imaged by the spectrograph on the detectors with a resolution of about $1''$ per pixel in the spatial direction and 4.4 pm per spectral pixel in first order. An area of $60'' \times 300''$ was registered by a raster scan of the telescope with a step size of $0.76''$ in the east-west direction. After November 1996, raster scanning (in normal-current mode) was stopped and the scans were (apart from a few dedicated measurements) limited to the drift of the solar surface across the slit caused by solar rotation. Thus the area sampled by solar rotation was $3.5'' \times 300''$. Each raster was registered for 21 min 20 s, being composed of 80 exposures of 16 seconds each. The data obtained after November 1996 are therefore strongly oversampled in the

spatial direction. In spite of this we use all 80 exposures when determining the average radiance in the field of view noting that this significantly dampens the effect of temporal variability of the line emission. The SUMER data were corrected for the flat-field, the geometric distortion, and for detector electronics effects such as dead-time and local gain-depression. The radiances have been calculated as integrals of Gaussian functions fitted to the line profiles. These Gaussians have been determined by least-squares fits of single or multiple Gaussian functions and a linear background (representing the contribution of the continuum) to the observed spectra at every spatial position. Only the area under the Gaussian, representing the main spectral line, is considered. From March 1996 to August 1996 SUMER used its detector A; from September 1996 until June 1998 SUMER used its detector B, and following the loss and recovery of the spacecraft, from November 1998 to July 2000, SUMER alternately used both detectors. The post-recovery data have been corrected for the detector responsivity-loss following *Schühle et al.* [2000], using the factors 1.36 for 58.4 nm, 1.40 for 60.9 nm, 1.30 for 62.4 and 63.0 nm, and 1.60 for 77.0 nm after employing the SUMER SolarSoft programme `radiometry.pro` with the keyword `/before`. The relative standard uncertainty for SUMER's radiometric calibration is 20 % before loss-of-attitude and 36 % post-recovery [*Pauluhn et al.*, 2001; *Wilhelm et al.*, 2002].

16.2.2 The CDS Data

In CDS, fully described by *Harrison et al.* [1995], a Wolter-Schwarzschild-II type grazing-incidence telescope focuses the solar image at the entrance slit of a dual spectrometer via a scan mirror. Two apertures before, and light stops after the telescope define the optical paths illuminating the spectrometers. The field of view of the telescope covers $4'$ by $4'$.

16.2.2.1 CDS-NIS

The stigmatic NIS has two toroidal, concave gratings with different ruling densities, which are mounted side-by-side and slightly tilted. They disperse two different wavelength-bands one above the other on to the same detector. The first wavelength-band (NIS-1) ranges from 30.8 nm to 38.1 nm, and the second band (NIS-2) from 51.3 nm to 63.3 nm. The spectral pixel size of the CDS-NIS ranges from 7.0 pm at 31.0 nm to 11.8 pm at 63.3 nm. The data of JOP Intercal_01 reported here have been measured on NIS-2 using a slit of angular dimensions $4'' \times 240''$. Images are made by spatial rastering (moving the slit perpendicular to its long axis) in steps of $4''$, thus producing $60'' \times 240''$ images, consisting of arrays of 15 (horizontal) by 143 (vertical) spatial pixels. The size of the spatial pixel along the slit corresponds to $1.68''$. The exposure time at each location was 80 s, resulting in a total accumulation time of 20 min for one raster. The main steps of the CDS data reduction consisted of corrections for burn-in and flat-fielding. The images corresponding to the total line radiation were obtained by integrating a Gaussian fit in exactly the same way as with the SUMER data. For the CDS-NIS spectrometer the post-recovery line profiles exhibit wings of different strength on each side of each spectral line. This change is attributed to the prolonged heating causing an irreversible distortion in the instrument. Special fitting routines have been developed to account for the changed profiles [*Thompson*, 1999]. The relative standard uncertainties for the radiometric calibration of CDS are 20 % for the He I line and 30 % for the Mg X lines [*Pauluhn et al.*, 2001; *Lang et al.*, 2002].

16.2.2.2 CDS-GIS

In the GIS, radiation from the slit illuminates a spherical grating which is set at grazing incidence. Dispersed radiation from the grating is incident on to four separate one-dimensional detectors placed at fixed positions around the Rowland circle (GIS-1: 15.1 nm to 22.1 nm, GIS-2: 25.6 nm to 33.8 nm, GIS-3: 39.3 nm to 49.3 nm, and GIS-4: 65.6 nm to 78.5 nm). For a description of the GIS and its detectors, see *Breeveld et al.* [1992] and *Breeveld* [1996]. Focussing of the radiation only occurs along the direction of dispersion. The image of the slit is astigmatic. Spatial information of the solar image formed at the entrance slit is obtained by using square "pinhole" slits, and by moving both the scan mirror, for east-west solar motion, and the slit, for north-south solar motion. In this way the required pattern (or raster) across the image can be constructed. For the present observations a $4'' \times 4''$ slit was used to give a $32'' \times 32''$ raster. Each of the 64 observations lasted 20 s, yielding an observation time of 23 min 22 s including telemetry overheads. The GIS detector data need correcting for fixed pattern and ghost effects, electronics dead-time, background, burn-in and flat-field. A thorough description of the GIS and its data reduction procedure is given in the CDS Software Notes 54 to 56 [*Bentley*, 1999; *Breeveld*, 2000a, b]. Additionally, a recently calculated correction for burn-in effects [*C. R. Foley, personal communication*, 2002] has been employed. The magnitude of the ghost correction was estimated for one observational raster (64 spatial positions). The fitting was done for the data with and without the ghost correction. For the 59 available fits of this observation, the average relative correction was (15 ± 2) %, noting that the typical fit uncertainty was about 10 % [*Pauluhn et al.*, 2002]. The relative standard uncertainty in the radiometric laboratory calibration of GIS is 30 % [*Lang et al.*, 2000].

16.3 Comparison of the Radiances of SUMER and CDS-NIS

For the CDS-SUMER intercomparison we have to distinguish three periods with different conditions. In Phase I (March 1996 to August 1996), we can compare quasi-simultaneous measurements of overlapping areas on the Sun. In Phase II (September 1996 to June 1998), only averages of the total radiances in the areas scanned can be compared. This is also the case for the majority of the post-recovery measurements (Phase III, November 1998 to February 2001). Also, for most of the time (Phases II and III) the CDS instrument scanned a much larger portion of the Sun. Consequently it observed different features from SUMER and so, potentially, could record different radiances. Another source of uncertainty is the fact that, as the solar activity maximum approaches, it becomes more and more difficult to find truly quiet-Sun areas. An overview of the various temporal and spatial scales of solar variability is given by *Solanki* [2002].

16.3.1 Long-term Comparison of the Averaged Radiances

Figures 16.1 to 16.3 display the time series of all available radiances averaged over the rasters made by the two instruments as part of the Intercal_01 campaign. The three different phases of the intercalibration campaign are separated by vertical lines. Figure 16.1a shows the averaged radiances of all available measurements of Intercal_01 in He I 58.4 nm.

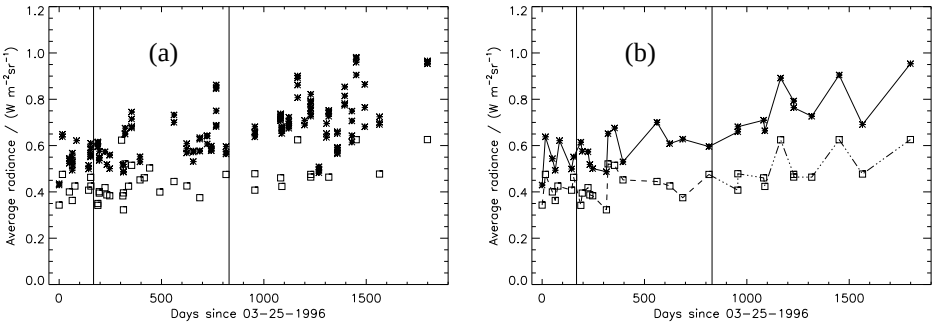

Figure 16.1: Spatially averaged radiances in He I 58.4 nm measured with CDS (stars) and SUMER (squares). The three phases of the intercalibration record (SUMER detector A, SUMER detector B, post-recovery) are separated by vertical lines. a) All available data. b) Simultaneous measurements of SUMER and CDS.

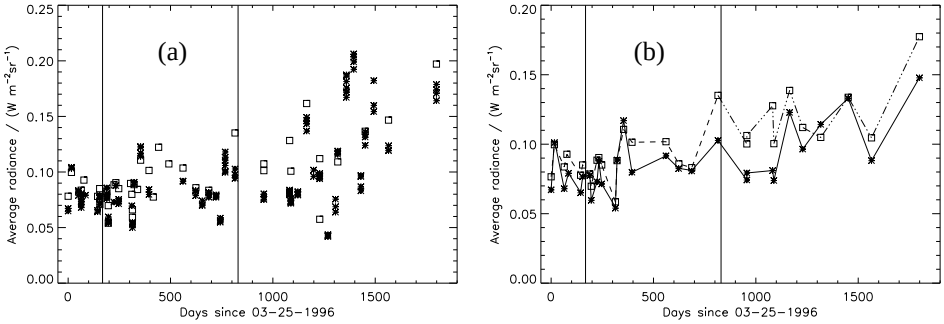

Figure 16.2: Radiances in Mg X 60.9 nm, see Figure 16.1 for details.

Figure 16.1b shows the same data, but is restricted to the truly simultaneous measurements by both instruments. To keep the influence of the inhomogeneity and intrinsic variability of the solar radiation at a minimum, only these data are used in the comparisons between the two instruments. In Figures 16.2 and 16.3 the same quantities are depicted for the Mg X 60.9 nm line and the Mg X 62.4 nm line, respectively. The measurements of day 1165 (June 1999) and day 1565 (July 2000) were made away from disk-centre and extrapolated to disk-centre values, according to the centre-to-limb variation described by *Wilhelm et al.* [2000]. The variability increases significantly during Phase III, especially in the coronal lines. The data recorded on days 1165 (June 1999) and 1451 (March 2000), as well as the latest measurements (February 2001), probably contain parts of active regions. Finally, Figure 16.4 gives the ratios of the averaged radiances SUMER/CDS. The ratio of SUMER/CDS varies mainly within the range of ± 20 % of its arithmetic mean over the entire time-period.

16.3.2 Correlation of the Time Series

In order to find out whether the time-variability of the signals is solar or instrumental, we calculate the correlation between the two time series of nearly simultaneous measure-

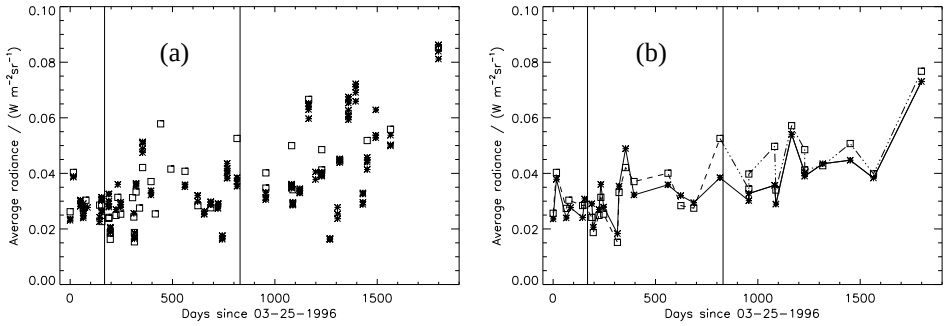

Figure 16.3: Radiances in Mg X 62.4 nm, see Figure 16.1 for details.

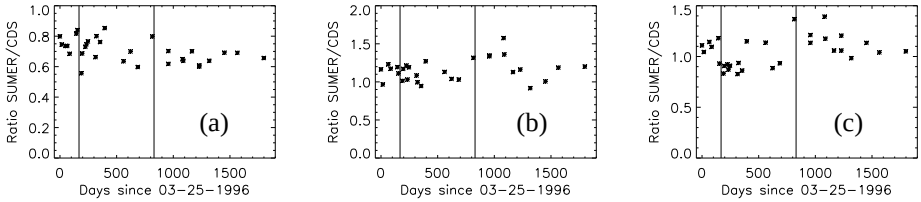

Figure 16.4: Ratios of the averages of the radiances of SUMER relative to CDS. a) He I 58.4 nm, b) Mg X 60.9 nm, and c) Mg X 62.4 nm.

ments. A high correlation indicates that the variability is solar rather than instrumental. For the He I 58.4 nm line, the correlation of the time series of the CDS and SUMER simultaneously-measured radiances (averaged over the corresponding rasters) amounts to 84 %, 57 %, and 94 % for the three phases. The correlations for the Mg X 60.9 nm line are 94 %, 84 %, and 87 %, while for Mg X 62.4 nm they are 92 %, 84 %, and 97 %. During the measurements of Phase I, raster scans over an area of $60'' \times 300''$ (SUMER, detector A) and $60'' \times 240''$ (CDS) were made and the common field of view was determined for the comparison. During Phase II, when SUMER's detector B was used, and later, the conditions for a comparison were not as good as before because SUMER's field of view was restricted to an area of about $3.5'' \times 300''$. This explains the lower correlation of the two time series over this period. Especially in the He I line, which shows the network very clearly, the correlation of the SUMER and CDS averaged radiances drops significantly during the second half of Phase II. In the post-recovery Phase III, SUMER was also not scanning most of the time, apart from two days when its scanning mechanism was operated in a high-current mode. Although in Phase III the conditions of both instruments have changed considerably, the correlation of the two instruments remains surprisingly high. This may have to do with the fact that the Sun was most active during this phase and the solar variability, due to a general increase in magnetic flux even in the quiet Sun, is the largest. The correlation between the two time series (corrected as described earlier) for the *entire* period of intercalibration measurements (Phases I to III) amounts to 85 %, 90 %, and 94 % for He I 58.4 nm, Mg X 60.9 nm, and Mg X 62.4 nm, respectively. In Table 16.1 the average relative differences $\langle \mathrm{CDS}_{\mathrm{phase_i}}\text{-}\mathrm{SUMER}_{\mathrm{phase_i}} \rangle / \langle \mathrm{CDS} \rangle_{\mathrm{phase_i}}$ of the three time-periods are given. In

Table 16.1: Average relative differences between the CDS and SUMER time series ⟨CDS-SUM⟩/⟨CDS⟩ (in %).

wave-length / nm	Mar96–Aug96 (I)	Sep96–Jun98 (II)	Nov98–Feb01 (III)	
			individual facts.	SUM factor 1.45
58.4	23 ± 5	28 ± 9	34 ± 5	30 ± 5
60.9	-13 ± 8	-12 ± 11	-19 ± 19	-23 ± 19
62.4	-7 ± 9	0 ± 16	-11 ± 11	-24 ± 11
63.0	–	–	-17 ± 19	-31 ± 19

the Mg X lines and in the O V line the uncertainty of this average difference is rather large. In the last column of Table 16.1 the relative differences as obtained using SUMER's average post-recovery correction-factor (implemented in the SUMER SolarSoft programme `radiometry.pro`) are given.

Note that apart from including one additional measurement (data of 26 February 2001) we used an updated and improved calibration for CDS as well as for SUMER, and therefore the results differ from the earlier ones described in *Pauluhn et al.* [2001], although the data analysis is exactly the same. It is also noticeable that, using the new calibrations, SUMER measures higher radiances in all lines apart from He I. In the He I line at 58.4 nm, CDS measures 30 % higher radiances than SUMER. For the O V line at 63.0 nm only post-recovery measurements were available within the intercalibration data set. All radiance values of both instruments fall well within the range of their combined uncertainties.

16.4 Comparison of the Radiances of SUMER and CDS-GIS

16.4.1 Long-term Comparison of the Averaged Radiances

Figure 16.5 displays the time series of all available radiances averaged over the rasters made by the two instruments as part of the Intercal_01 campaign. The vertical lines indicate the time of the spacecraft loss-of-attitude. Figure 16.5a depicts all available averaged radiances of the CDS-GIS and SUMER measurements, Figure 16.5b shows the quasi-simultaneous averaged radiances. Whereas the SUMER data are available from March 1996, the earliest data of the CDS-GIS are from May 1996.

For the period before the SOHO accident the CDS-GIS measures (63 ± 10) % higher radiances than SUMER (average relative differences). This offset changes slightly post-recovery, when it reduces to approximately (54 ± 11) %. The average ratio of the GIS to the SUMER average radiances amounts to 2.6 ± 0.9 before loss and 2.1 ± 0.7 afterwards. The difference between the pre- and post-accident ratios can have various reasons. Firstly, it can be a purely statistical effect (note the relative standard uncertainties of 35 % in the weighted averages of the ratios), for instance induced by the selection of the data points, that is, the sampling of the intercalibration measurements. Secondly, the SUMER post-recovery correction factor at 77.0 nm (1.60) could be too high. Using the averaged correction factor of 1.45, which is also employed in `radiometry.pro` the average post-

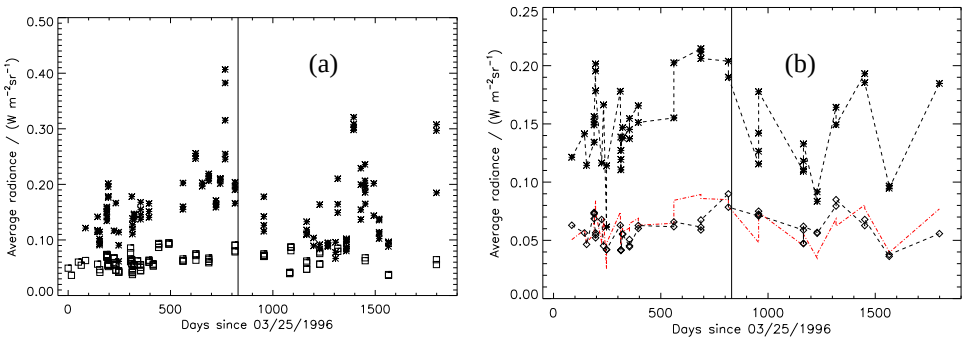

Figure 16.5: Spatially averaged radiances in Ne VIII 77.0 nm measured with CDS (stars) and SUMER (squares). The vertical lines indicate the date of the loss-of-contact with the SOHO spacecraft. a) All available data. b) Simultaneous measurements of SUMER and CDS. The red line shows the CDS data divided by a factor 2.6.

recovery ratio of GIS and SUMER is 2.4. Assuming that the GIS responsivity has not changed due to the SOHO accident, a factor of 1.3 for the SUMER post-recovery correction would give a consistent offset for the GIS and SUMER measurements at 77.0 nm before and after the SOHO loss-of-attitude. Another possibility for a different offset before and after the loss-of-attitude would be a slight systematic change of the GIS responsivity after loss-of-attitude, which is, due to the strong variability in this line, hard to detect. It is rather probable that the result is influenced by a combination of these effects.

The large variability of the line intensity on short time-scales is clearly visible in the time series. Even images registered shortly after each other (from twenty minutes to some hours) show differences in their averages of up to 40 % in CDS-GIS, and up to 20 % in SUMER. This difference in temporal variability is most likely due to the temporal and spatial differences in the raster scanning of both instruments [*Pauluhn et al.*, 2002]. Successively restricting the SUMER image to smaller sizes showed that, for a SUMER image size reduced by a factor of approximately 4.5, both variabilities are in close agreement.

16.4.2 Correlation of the Time Series

The correlation of the time series of the CDS-GIS and SUMER nearly simultaneously measured averaged radiances in the Ne VIII line amounts to 0.49 before the SOHO accident. Afterwards, it amounts to 0.65 if the last and temporally slightly isolated data of 26 February 2001 are omitted, and 0.53 if these last data are included. For the pre-accident measurements, when SUMER provided raster-scans for the intercalibration, the correlation increases substantially when reducing the SUMER area by a factor of 4 to 6, i.e., restricting the SUMER image to nearly GIS-size.

16.4.3 Revision of the GIS Radiometric Calibration

Revising the CDS-GIS responsivity to make GIS and SUMER intercalibration results agree sufficiently within their combined uncertainties for the period before SOHO's loss-of-attitude means increasing the GIS responsivity at 77.0 nm by 2.6 ± 0.9. This is consistent with the change of a factor 1.9 at 73.2 nm suggested in *Del Zanna et al.* [2001]. In fact,

re-normalising their result to allow for the recent CDS responsivity correction (Version 3 to Version 4 of the CDS calibration), the factor becomes 2.2 [cf., *Lang et al.*, 2002].

Note that for both, CDS NIS-1 and GIS, the alignment of the laboratory calibration source was difficult to establish and that a factor greater than suggested here was applied to the NIS-1 responsivity [*Brekke et al.*, 2000; *Lang et al.*, 2002]. The increase of the GIS efficiency thus gives consistent results noting that the relative standard uncertainty of the GIS radiometric calibration (computed from the combined uncertainties of the GIS data processing, burn-in, the weighted ratios, and the SUMER calibration) is then estimated to be 40 % at 77.0 nm and (considering the uncertainty of the laboratory calibration for the wavelength dependence) 45 % at other wavelengths.

16.4.4 Statistical Distribution of the Time series

The different resolutions, fields of view, and sampling techniques of both instruments make it difficult to compare their performances directly. We therefore employ a statistical approach and, after considering the average radiances, now investigate the distributions of the intensity values measured by the two instruments. To study the temporal evolution of the shape of the histograms of the radiances, we divided each data set into four subsets of the radiances for four successive time periods (see Figure 16.6). For better comparison of the results from the two instruments, we also rescaled the histograms by dividing all radiance values by the corresponding mean radiances. Although the sample sizes are much smaller for the GIS data, apart from the expected resolution-induced differences (see *Pauluhn et al.* [2000] and below), the distributions agree relatively well.

The best fits to the radiance histograms are lognormal functions. With x being the radiance, μ the mean, σ the standard deviation defining a width w as $w = \sqrt{2}\sigma$, and N_0 a normalization or strength factor, a lognormal distribution is characterized by a probability density $\rho(x) = \frac{N_0}{x} \exp(-\frac{(\ln(x)-\mu)^2}{2\sigma^2})$. The GIS histograms tend to be narrower and more peaked, which may be related to the lower spatial-resolution of the GIS. Next we test whether this assumption is correct. For this purpose we derive a relation between the spatial resolution of an intensity image and the parameters of the lognormal fits by successively reducing the SUMER resolution (by binning in both spatial directions). For this purpose, we restricted ourselves to SUMER raster images, in order to start from the nominal resolution of around $1''$. The SUMER scans used were mainly taken from June to August 1996 (10 scans) and one scan from November 1999. The changes of the width and peak height of the lognormal fit functions with resolution of the SUMER data are shown in Figure 16.7. The dashed line shows a least-squares fit to the curve, and the dotted lines give the uncertainty margin. The CDS-GIS images selected for the comparison were taken in the periods from June 1996 to the end of 1997 and files from October to December 1999 (to have better statistics). All in all, the 53 CDS files, of 8×8 pixels, do not reach the sample statistics of SUMER with 11 files of 80×300 pixels. The lognormal parameters deduced from the CDS-GIS (with a spatial resolution about 20 times coarser than SUMER's) have been included as diamonds in Figure 16.7. They fall well within the expected range. Hence, differences between the distributions obtained from the two instruments are mainly due to differences in spatial resolution.

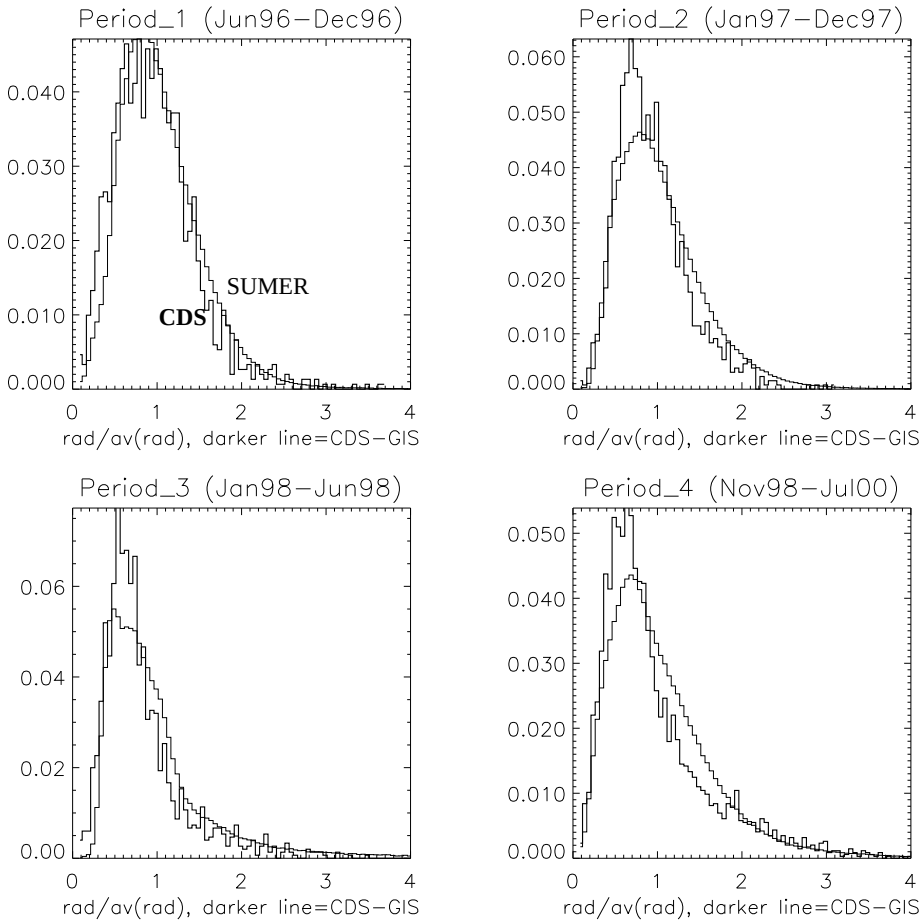

Figure 16.6: Histograms, computed as relative frequencies, of all SUMER and CDS-GIS radiance values for four different time periods (given at the top of each frame), normalized and scaled to a mean value of 1.0 for better comparison.

16.5 Summary and Conclusions

The intercalibration between CDS and SUMER is re-assessed, using the most recent available instrument calibrations. The earlier results regarding the stability of the CDS and SUMER instruments, even after loss and recovery of the spacecraft, are confirmed. However, some relatively large discrepancies could be reduced, and for SUMER and CDS NIS, the radiance values lie within the range of their combined uncertainties. In the He I line at 58.4 nm, the CDS instrument measures on average 30 % higher values than SUMER. In all the other lines studied, SUMER measured radiances which are higher than those given by CDS.

SUMER and CDS GIS can be compared in the Ne VIII line at 77.0 nm, which CDS measures on the GIS-4 detector. The average ratio of GIS-4 to SUMER radiances is 2.6

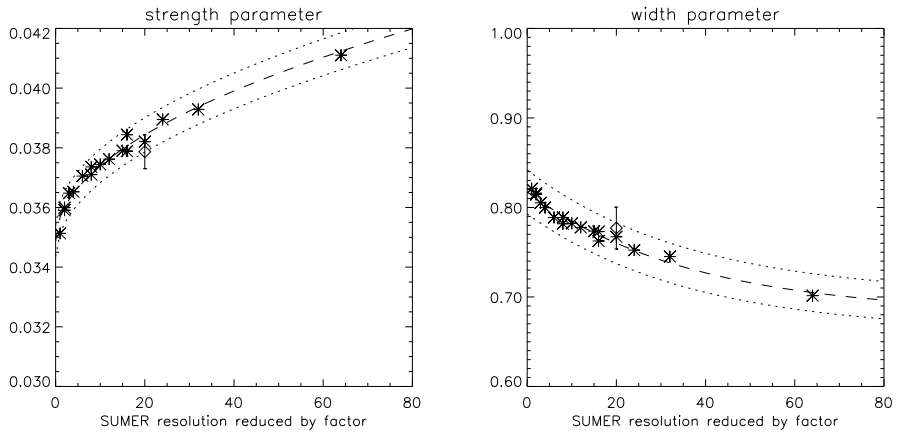

Figure 16.7: Variation of the parameters of the lognormal distribution with the SUMER resolution. Shown are also a least-squares fit to the data and the uncertainty margins. The corresponding parameters of the CDS-GIS distribution are indicated by the diamonds. In order to start with SUMER's full resolution, this comparison only used a subset of SUMER and CDS data: those in which SUMER was scanning.

for the data before loss-of-attitude and 2.1 afterwards. A corresponding change in CDS-GIS responsivity is suggested in *Pauluhn et al.* [2002].

In general, the radiometric, in-orbit comparison shows that the ratio between the responsivities of the two instruments remained constant with time until the SOHO accident. It has to be noted that the post-recovery radiance values are affected by larger uncertainties than those in the initial comparison, and that this period of the comparison is also subject to increased solar activity. Variations in solar radiance (due to long-term changes in the solar output or to residual solar activity in what were thought, at the time of the observations, to be quiet solar regions) clearly dominate over instrumental changes. The degradations in responsivity, which have plagued earlier solar space-telescopes after exposure to solar irradiation in space, are still absent from these two instruments on the SOHO mission after nearly five years in space.

Even after the loss and recovery of the spacecraft, when the instruments had been exposed to extreme temperature conditions, the radiometric calibration of both instruments could be maintained, although with a higher uncertainty.

Acknowledgements

SOHO is a project of international cooperation between ESA and NASA. CDS was built and is operated by a consortium led by the Rutherford Appleton Laboratory and including the Mullard Space Science Laboratory, the NASA Goddard Space Flight Center, the Max-Planck-Institute for Extraterrestrial Physics, Garching and Oslo University. The SUMER project is financially supported by Deutsches Zentrum für Luft- und Raumfahrt (DLR), the Centre National d'Etudes Spatiales (CNES), the National Aeronautics and Space Administration (NASA), and the ESA PRODEX programme (Swiss contribution). We thank C. R. Foley for providing the GIS burn-in time series. A. P. wants to

thank the Institute of Technology Transfer (INTEC) of the HTA Bern and especially U. Künzler for the management of the PRODEX project. The Institute of Astronomy of the ETH Zürich is thanked for support and hospitality during most of the project work.

Bibliography

Bentley, R.D., CDS-GIS instrument guide, CDS Software Note 54, vers. 1, 1999.

Breeveld, A.A., Edgar, M.L, Smith, A., Lapington, J.S., and Thomas, P.D., A SPAN MCP detector for the Coronal Diagnostic Spectrometer, *Rev. Sci. Inst.* **63**, 1, 1992.

Breeveld, A.A., Ultraviolet detectors for solar observations on the SOHO spacecraft, University of London Ph.D. Thesis, 1996.

Breeveld, E.R., GIS software user manual, CDS Software Note 55, vers. 4, 2000.

Breeveld, E.R., GIS calibration details, CDS Software Note 56, vers. 1, 2000.

Brekke, P., Thompson,W.T., Woods, T.N., and Eparvier, F.G., The extreme-ultraviolet solar irradiance spectrum observed with the Coronal Diagnostic Spectrometer (CDS) on SOHO, *Astrophys. J.* **536**, 959–970, 2000.

Del Zanna, G., Bromage, B.J.I., Landi, E., and Landini, M., Solar EUV spectroscopic observations with SOHO/CDS. I. An in-flight calibration study, *Astron. Astrophys.* **379**, 708–734, 2001.

Harrison, R.A., Sawyer, E.C., Carter, M.K., Cruise, A.M., Cutler, R.M., Fludra, A., Haynes, R.W., Kent, B.J., Lang, J., Parker, D.J., Payne, J., Pike, C.D., Peskett, S.C., Richards, A.G., Culhane, J.L., Norman, K., Breeveld, A.A. Breeveld, E.R., Al Janabi, K.F., McCalden, A.J., Parkinson, J.H., Self, D.G., Thomas, P.D., Poland, A.I., Thomas, R.J., Thompson, W.T., Kjeldseth-Moe, O., Brekke, P., Karud, J., Maltby, P., Aschenbach, B., Bräuninger, H., Kühne, M., Hollandt, J., Siegmund, O.H.W., Huber, M.C.E., Gabriel, A.H., Mason, H.E., and Bromage, B.J.I., The Coronal Diagnostic Spectrometer for the Solar and Heliospheric Observatory, *Sol. Phys.* **162**, 233–290, 1995.

Lang, J., Kent, B.J., Breeveld, A.A, Breeveld, E.R., Bromage, B.J.I., Hollandt, J., Payne, J., Pike, C.D., and Thompson, W.T., The laboratory calibration of the SOHO Coronal Diagnostic Spectrometer, *J. Opt. A: Pure Appl. Opt.* **2**, 88–106, 2000.

Lang, J., Thompson, W.T., Pike, C.D., Kent, B.J., and Foley, C.R., The radiometric calibration of the Coronal Diagnostic Spectrometer, this volume, 2002.

Pauluhn, A., Rüedi, I., Solanki, S.K., Lang, J., Pike, C.D., Schühle, U., Thompson, W.T., Hollandt, J., and Huber, M.C.E., Intercalibration of SUMER and CDS on SOHO. I. SUMER detector A and CDS NIS, *Appl. Opt.* **38**, 7035–7046, 1999.

Pauluhn, A., Solanki, S.K., Rüedi, I., Landi, E., and Schühle, U., Statistics of quiet Sun extreme ultraviolet intensities, *Astron. Astrophys.* **362**, 737–745, 2000.

Pauluhn, A., Rüedi, I., Solanki, S.K., Schühle, U., Wilhelm, K., Lang, J., Thompson, W.T., Hollandt, J., and Huber, M.C.E., Intercalibration of SUMER and CDS on SOHO. II. SUMER A and B detectors and CDS NIS, *Appl. Opt.* **40**, 6292–6300, 2001.

Pauluhn, A., Lang, J., Breeveld, E.R., Solanki, S.K., and Schühle, U., Intercalibration of SUMER and CDS on SOHO. III. SUMER and CDS GIS, *Appl. Opt.*, in press, 2002.

Schühle, U., Hollandt, J., Pauluhn, A., and Wilhelm, K., Mid-term radiance variations of far-ultraviolet emission lines from quiet-Sun areas, ESA SP-463, 427–430, 2000.

Solanki, S.K., Solar variability, this volume, 2002.

Thompson, W.T., Post-recovery broadened line profiles, CDS Software Note No. 53, 1999.

Wilhelm, K., Curdt, W., Marsch, E., Schühle, U., Lemaire, P., Gabriel, A., Vial, J.-C., Grewing, M., Huber, M.C.E., Jordan, S.D., Poland, A.I., Thomas, R.J., Kühne, M., Timothy, J.G., Hassler, D.M., and Siegmund, O.H.W., SUMER-Solar Ultraviolet Measurements of Emitted Radiation, *Sol. Phys.* **162**, 189–231, 1995.

Wilhelm, K., Lemaire, P., Dammasch, I.E., Hollandt, J., Schühle, U., Curdt, W., Kucera, T., Hassler, D.M., and Huber, M.C.E., Solar irradiances of ultraviolet emission lines measured during the minimum of sunspot activity in 1996 and 1997, *Phys. Chem. Earth* (C) **25**, 5-6, 389–392, 2000.

Wilhelm, K., Schühle, U., Curdt, W., Dammasch, I.E., Hollandt, J., Lemaire, P., and Huber, M.C.E., Solar vacuum-ultraviolet radiometry with SUMER, this volume, 2002.

— 17 —

White Light Inter-calibrations of UVCS, LASCO-C2 and Spartan 201/WLC

RICHARD A. FRAZIN
Harvard-Smithsonian Center for Astrophysics, Cambridge, MA, USA

MARCO ROMOLI
Dip. di Astronomia e Scienza dello Spazio
Università di Firenze, Firenze, Italy

JOHN L. KOHL, LARRY D. GARDNER
Harvard-Smithsonian Center for Astrophysics, Cambridge, MA, USA

DENNIS WANG, RUSSELL A. HOWARD
E.O. Hulburt Center for Space Research
Naval Research Laboratory, Washington, DC, USA

THERESE A. KUCERA
NASA Goddard Space Flight Center, Greenbelt, MD, USA

This paper describes comparisons among white light polarized radiances (pB) as measured by the Ultraviolet Coronagraph Spectrometer White Light Channel (UVCS/WLC), the Large Angle and Spectrometric Coronagraph Experiment C2 instrument (LASCO-C2) and the Spartan 201 White Light Coronagraph (Spartan 201/WLC). UVCS/WLC and LASCO-C2 are generally in agreement, although there are some systematic trends and discrepancies that still require explanation. UVCS/WLC and Spartan 201/WLC agree to within the measurement uncertainties. Spartan 201/WLC and LASCO-C2 are not directly compared to each other in this paper.

17.1 Introduction

The UVCS White Light Channel (UVCS/WLC; *Kohl et al.* [1995]), the Large Angle and Spectrometric Coronagraph Experiment C2 instrument (LASCO-C2; *Brueckner et al.* [1995]), and the Spartan 201 White Light Coronagraph (Spartan 201/WLC; *Fisher and Guhathakurta* [1994]) all measure the polarized radiance (pB) of the solar corona. In this paper we present a systematic comparison of their pB measurements. A paper that describes the calibration of Spartan 201/WLC and a direct inter-comparison of LASCO-C2 and the Spartan 201/WLC is in preparation [*T.A. Kucera, personal communication*, 2002].

Although the UVCS/WLC calibration is still in progress, for the purposes of this paper we adopt the in-flight calibration that is described in *Romoli et al.* [2002], which also gives

a brief summary of the UVCS/WLC and its characteristics. A description of the LASCO-C2 calibration is in preparation [*R.A. Howard, personal communication*, 2002].

17.2 Observations

We present two types of comparisons of UVCS/WLC and LASCO-C2. The first type is based on special observations that were designed specifically for the purpose of intercalibration. The second type of comparison is based on synoptic observations, which are part of the daily observation program of both UVCS and LASCO. The UVCS synoptic program is described by *Panasyuk* [1999]. The UVCS/WLC to LASCO-C2 comparisons based on special observations were made at a larger range of heights, have better spatial co-registration (at least in the cases when the star ρ Leo was used as a pointing marker, see below), have smaller time differences between the UVCS/WLC and LASCO-C2 exposures, and allow more time for the UVCS mirror mechanism to settle (see below). However, the comparison based on synoptic observations is valuable because it has many more data points (about 17 000 UVCS/WLC pBs), which have been taken in the same systematic way throughout the mission. Unlike the special observations, the UVCS/WLC synoptic data set includes observations of coronal holes. We also present a comparison of UVCS/WLC and Spartan 201/WLC, which required special observations on the part of UVCS.

The special observations for the UVCS/WLC to LASCO-C2 comparisons were taken in August and September 1996, during the ρ-Leo solar crossings of August 1999 and 2000, and in early April 2000. The special observations for the UVCS/WLC to Spartan comparison were taken during the STS-95 John Glenn shuttle mission in early November 1998. The observations used for synoptic comparisons come from the years 1996 through 2000.

All of the LASCO-C2 data used for the comparisons presented here were multiplied by 0.8 in order to renormalize them to Sun-center radiance (as opposed to mean-Sun). This operation was not required for the Spartan 201 data because they were already normalized to the Sun-center value.

Any externally occulted coronagraph is subject to vignetting, that is, the effective aperture of the instrument is a function of position in the field of view. Since the UVCS/WLC instrument has a linear occulter and the optics are believed to be uniform, the vignetting function is proportional to the exposed mirror area ($h_m w_m(r)$ in *Romoli et al.* [2002]). LASCO-C2 and Spartan 201 have circular occulters and their vignetting functions are much more complicated.

The LASCO-C2 vignetting function is derived from laboratory measurements and from observing the irradiances of stars passing through the field of view. The vignetting function is 1.0 at the edge of the field (about 6 $R_\odot$), and approaches 0.0 near 2.3 $R_\odot$. From 2.5 to 4.0 $R_\odot$ the vignetting function goes from 0.1 to 0.45 [*D. Wang, personal communication*, 2001].

All of the UVCS/WLC pB values were corrected for stray light, as described in *Romoli et al.* [2002]. The stray light correction is not necessarily just a matter of subtracting a background because the background may be *negative*. The coronal pB (in the appropriate coordinate system) is equal to the Q-component of the Stokes vector and is positive. The Q-component of the stray light signal may be positive or negative. The analysis of *Romoli*

et al. [2002] shows that for the UVCS/WLC, the stray light contribution to Q is positive and table 4 in *Romoli et al.* [2002] gives the values that must be subtracted.

Since the UVCS/WLC selects different position angles in the corona by rotating about an axis, the occulting geometry and instrumental stray light are nearly independent of position angle. There is a slight variation of the occulting geometry due to the fact that the roll ring is not perfectly circular [*Frazin*, 2002]. This causes pointing changes on the order of 15″, which have been taken into account in the UVCS Data Analysis Software (DAS). This pointing correction was included in the inter-comparison work presented here.

The roll offset described above changes the alignment between the occulting system and the Sun. Both the observations taken in the spring of 2000, in which the pointing stages were used to compensate for the roll offset, and the stray light analysis used in *Romoli et al.* [2002] show that these small variations do not affect the stray light correction.

All of the UVCS/WLC pB measurements, both special and synoptic, have been corrected for a mirror mechanism nonlinearity and an electronic mirror-grating cross-talk effect, both of which affect the pointing. The mirror-grating cross-talk effect has been discussed in detail by *Fineschi et al.* [1997]. The calibration of the mirror mechanism nonlinearity was done with UV observations of the star ρ Leo [*Frazin*, 2002]. This calibration accounted for the SOHO-Earth parallax, which is necessary because the SOHO-Earth vector affects the position of the star relative to the Sun. Such pointing considerations are important because the UVCS/WLC is a 1-pixel instrument with a projected image of 14″ by 14″. The UVCS pointing analysis shows that the position of the WLC pixel can be located within a standard uncertainty of 20″.

The UVCS special observations taken during the ρ-Leo solar crossings of 1999 and 2000 did not rely on the pointing analysis because they used the star as a pointing marker (in fact, these observations are the basis of the UVCS pointing analysis). In these cases the pointing of the UVCS instrument was determined from the star's UV signature in the O VI channel, the alignment of which to the WLC is known. The UVCS/WLC was not pointed at the star; it made measurements of the corona. The UVCS/WLC radiometric measurements of ρ Leo described in *Romoli et al.* [2002] come from a separate set of observations.

The UVCS mirror mechanism has a temperature sensitivity that can affect the pointing. About an hour is required for the mechanism to reach equilibrium. This effect sometimes manifests after large changes in the roll angle, which can cause a rearrangement of the temperature gradients in the instrument. Care has been taken to ensure that this effect does not have any important consequences for pB measurement. Exposures taken at the three rotation angles of the half-wave retarder plate (HWRP) must measure the emission from the same spatial location of the corona. Since the UVCS special observations, except for those used in the Spartan 201 comparison, involved spending enough time at one roll angle for the mechanism to settle, the mechanism settling causes no problems. Most of the UVCS/WLC special observations used for the Spartan 201 comparison also allowed sufficient time to reach equilibrium. Those with short exposure times (60 s, 180 s per pB cycle) sometimes allowed less time for settling. All of the measurements taken with short exposures show very little evidence of problems associated with mechanism settling (which manifests as jitter in time series plots). Thus, we do not expect any effects due to settling in these data.

The original synoptic observation plan was designed before the mirror settling problem was discovered. The synoptic plan was changed in March 1999 to address this concern.

The new synoptic plan has a shorter pB sequence (i.e., a set of exposures using three HWRP orientations) and takes several sequences at each height. Comparisons of the pB values from the old and new synoptic plans show no differences for heights above 2.0 $R_\odot$. Furthermore, comparisons of the pBs from the old synoptic sequences to observations at the same height and roll angle with sufficient settling time show no clear differences, either. Analysis has shown that the settling time for the pB sequences in the original synoptic plan was short enough to eliminate the settling problem.

The comparisons presented here suffer, by varying degrees, from a lack of temporal co-registration between observations of the instruments involved. The corona varies on all temporal scales [e.g., *Solanki*, 2002] and it is difficult to characterize this variation. There is no doubt that some of the scatter in the comparison plots is due to a lack of simultaneity. The UVCS/WLC to LASCO-C2 comparisons based on synoptic observations are simultaneous to within 12 hours or less; the data with larger time differences were not used. The UVCS/WLC to LASCO-C2 comparisons of special observations have much better temporal co-registration due to efforts made to coordinate LASCO-C2 and UVCS. These efforts involved taking extra pB sequences on the part of LASCO-C2. For the 1996 comparison, the time differences are 5 hours or less. For the 1999 ρ-Leo passage, three of the data points (i.e., sets of joint pB observations at common spatial locations and times) have time differences of about 2, 2, and 3 hours. The other 8 have differences of about an hour or less. For the 2000 ρ-Leo comparison, two of the data points have time differences of about 11 and 7 hours. The other five have time differences of 3 hours or less. For the Spring 2000 comparison, efforts were made to take LASCO-C2 pB sequences both before and after the UVCS/WLC pB sequences, "sandwiching" the UVCS/WLC pBs within a 2 hour time span. This was successful for 7 of the 8 data points. In the other case, there is a LASCO-C2 observation about 3 hours before the UVCS/WLC pB and another about 24 hours later. For the UVCS/WLC to Spartan comparison, the time differences vary between 14 and 0 hours, with 6 (the squares in Figure 17.6) of the 19 data points having time differences of 2 hours or less.

17.3 Uncertainty Analyses

Below we present four types of measured quantities. These are UVCS/WLC pBs, LASCO-C2 pBs, ratios of (UVCS/WLC pB)/(LASCO-C2 pB), and ratios of (UVCS/WLC pB)/(Spartan 201 pB). In this section we quantify the uncertainties in each. All uncertainties are treated statistically as random sign errors and stated for approximately the standard uncertainty level (i.e., 68 % confidence).

17.3.1 UVCS/WLC pB Uncertainty

A major contributor to the uncertainty in UVCS/WLC pBs is the 7 % radiometric uncertainty in the in-flight calibration, described in *Romoli et al.* [2002]. The accuracy of the polarimetry has also been discussed there and we associate no significant uncertainty with this aspect of the measurement.

Correcting for stray light introduces uncertainty into the UVCS/WLC pB measurements. The fractional uncertainty is given by $\delta Q_s/(Q_m - Q_s)$, where Q_m is the measured pB before stray light correction, Q_s is the value of the stray light correction that needs to

be subtracted, and δQ_s is the uncertainty in the stray light correction. The values of Q_s and δQ_s as a function of radius are given in table 4 in *Romoli et al.* [2002]. For both the UVCS/WLC to LASCO-C2 and the UVCS/WLC to Spartan comparisons based on special observations (i.e., those shown in Figures 17.1 and 17.6), this uncertainty was calculated individually for each data point and is reflected in the error bars. However, in order to give the reader an understanding of the size of these corrections, we take the time to discuss some averages.

Above 2 $R_\odot$, the mean of $\delta Q_s/Q_s$ from table 4 in *Romoli et al.* [2002] is 0.57 and the standard deviation is 0.13. The median of $Q_s/(Q_m - Q_s)$ for the UVCS/WLC data used in Figure 17.1 (which contains 30 data points) is 0.13; the mean is 0.19, and the standard deviation is 0.15. By multiplying $\langle \delta Q_s/Q_s \rangle$ ($\langle\ \rangle$ indicates that the mean is to be taken) by the median of the $Q_s/(Q_m - Q_s)$ distribution, we get a measure of the size of the uncertainty in the UVCS/WLC correction. Thus, we have $0.57 \times 0.13 \approx 0.07$, and the median relative standard uncertainty is about 7 %. The uncertainty due to the UVCS/WLC stray light correction in observations used for the UVCS/WLC to Spartan comparison is highly variable. The maximum value of $0.57 \times Q_s/(Q_m - Q_s)$ (recalling that $< \delta Q_s/Q_s >= 0.57$, as discussed above) is 0.76 (the next highest are 0.35 and 0.21), the minimum is 0.01, the median is 0.04, the mean is 0.12, and the standard deviation is 0.19. Thus, we take the median relative standard uncertainty due to instrument stray light for the UVCS/WLC to Spartan pB comparison to be 4 %.

The uncertainty due to the stray light correction was similarly calculated for the synoptic observations. At position angles of 0° and 180° at 2.6 $R_\odot$ the average relative standard uncertainty due to the stray light correction is 6 % and the standard deviation is 1 %. At position angles of 90° and 270° at 2.7 $R_\odot$ the average relative standard uncertainty is 2 % and the standard deviation is 1 %, and at 3.0 $R_\odot$ the average is 5 % and the standard deviation is 2 %.

The uncertainty in the UVCS/WLC vignetting is determined by the standard uncertainty in the location of the internal occulter, which is 0.1 mm. At the lowest height used in this paper, about 1.6 $R_\odot$, the exposed mirror width is about 1.6 mm, giving a relative standard uncertainty of 6.25 %. At 2.1 $R_\odot$, the exposed mirror width is about 5.6 mm, giving a relative standard uncertainty of 1.8 %, and it is even smaller at larger heights. The 1.6 $R_\odot$ measurement is only used for the Spartan 201 comparison, and 6 % is negligible compared to the 20 % Spartan 201 radiometric relative standard uncertainty. We have shown that it is negligible compared to other uncertainties and we will not consider it further.

This analysis is summarized in Table 17.1.

17.3.2 LASCO-C2 pB Uncertainty

The LASCO-C2 radiometric calibration is based on measurements of stars that drift through the field of view. The residuals have a standard deviation of about 3 %, and we take this to be the radiometric relative standard uncertainty. The LASCO-C2 CCD flat-field has been determined by closing the door in front of the telescope and taking images of the door diffuser. The result is that the flat-field is uniform to within 2 % [*D. Wang, personal communication*, 2001].

The amount of polarized stray light in LASCO-C2 is difficult to determine and work in this area is still in progress. However, since the C2 and C3 coronagraphs agree in their

Table 17.1: Summary of relative standard uncertainties in UVCS/WLC pB measurements. Angles refer to the position angle which is measured counter-clockwise from the projection of solar north.

source	resulting uncertainty in pB
radiometry	7 %
stray light (special obs., LASCO-C2 comparison (2.4 – 5.0 $R_\odot$), median)	7 %
stray light (special obs., Spartan comparison (1.7 – 4.3 $R_\odot$), median)	4 %
stray light (synoptic obs., 0° *and* 180°, 2.6$R_\odot$, mean)	6 %
stray light (synoptic obs., 90° *and* 270°, 2.7$R_\odot$, mean)	2 %
stray light (synoptic obs., 90° *and* 270°, 3.0$R_\odot$, mean)	5 %
quadrature sum (special obs., LASCO-C2 comparison (2.4 - 5.0 $R_\odot$), median)	10 %
quadrature sum (special obs., Spartan comparison (1.7 - 4.3 $R_\odot$), median)	8 %
quadrature sum (synoptic obs., 0° *and* 180°, 2.6$R_\odot$, mean)	9 %
quadrature sum (synoptic obs., 90° *and* 270°, 2.7$R_\odot$, mean)	7 %
quadrature sum (synoptic obs., 90° *and* 270°, 3.0$R_\odot$, mean)	9 %

Table 17.2: Summary of relative standard uncertainties in LASCO-C2 pB measurements.

source	resulting uncertainty in pB
radiometry	3 %
flat-field	2 %
vignetting (above 2.9 $R_\odot$)	8 %
vignetting (below 2.9 $R_\odot$)	30 %
quadrature sum (above 2.9 $R_\odot$)	9 %
quadrature sum (below 2.9 $R_\odot$)	30 %

overlap region (above 4 $R_\odot$), in both coronal holes and streamers, and C3 has a much larger occulting disk, it may be that C2 stray light is not a significant issue for the comparisons reported here.

The accuracy of the LASCO-C2 vignetting function has been tested by watching the star ρ Leo pass through the field of view. The corrected irradiance of the star is flat to about 8 % from 2.9 to 6 $R_\odot$. Inside of 2.9 $R_\odot$ the vignetting function needs improvement, with the star 30 % dimmer than expected at the edge of the occulter near 2.5 solar radii. Since the star track is just one line through the field of view the problem of correcting the entire field of view remains [*D. Wang, personal communication*, 2001].

For lack of a better procedure, we assign an 8 % vignetting relative standard uncertainty to the LASCO-C2 pBs above 2.9 $R_\odot$, and 30 % below.

This analysis is summarized in Table 17.2.

17.3.3 UVCS/WLC to LASCO-C2 pB Ratio Uncertainty

The uncertainty in the UVCS/WLC to LASCO-C2 pB ratio is a combination of the uncertainties described in the previous two sections plus additional uncertainties due to

Table 17.3: Summary of relative standard uncertainties in the UVCS/WLC to LASCO-C2 pB ratios. Angles refer to the position angle which is measured counter-clockwise from the projection of solar north. No uncertainty due to temporal co-registration has been included in the quadrature sums (see text).

source	resulting uncertainty in pB
UVCS/WLC radiometry	7 %
UVCS/WLC stray light (special obs., LASCO-C2 comparison (2.4 – 5.0 $R_\odot$), median)	7 %
UVCS/WLC stray light (synoptic obs., 0° *and* 180°, 2.6 $R_\odot$, mean)	6 %
UVCS/WLC stray light (synoptic obs., 90° *and* 270°, 2.7 $R_\odot$, mean)	2 %
UVCS/WLC stray light (synoptic obs., 90° *and* 270°, 3.0 $R_\odot$, mean)	5 %
LASCO-C2 radiometry	3 %
LASCO-C2 flat-field	2 %
LASCO-C2 vignetting (above 2.9 $R_\odot$)	8 %
LASCO-C2 vignetting (below 2.9 $R_\odot$)	30 %
spatial co-registration	5.5 %
quadrature sum (below 2.9 $R_\odot$)	32 %
quadrature sum (above 2.9 $R_\odot$, non-coronal hole)	15 %

inaccurate spatial and temporal co-registration. Since we have no way to estimate the uncertainty due to inaccurate temporal co-registration, we do not attempt to do so. There is no doubt that some of the scatter in the UVCS/WLC to LASCO-C2 pB ratio plots is due to a lack of simultaneity, however this should not produce any systematic trends.

The uncertainty due to inexact spatial co-registration is more readily analyzed. The LASCO-C2 pixel position standard uncertainty is on the order of $10''$ and the standard uncertainty in the UVCS pointing analysis is about $20''$. In order to evaluate the importance of this pointing uncertainty we found the LASCO-C2 pB pixel that matched our best determination of the position of the UVCS/WLC and looked at the values in the surrounding $1'$ by $1'$ (3 pixel by 3 pixel) box of the LASCO-C2 pB image. We took the standard deviation of these 9 pB values divided by their mean value as the relative standard uncertainty due to co-registration. We repeated this procedure 10 times at heights ranging from 2.6 to 4.0 $R_\odot$. The mean of the 10 values is 0.055 and the standard deviation is 0.0285 due to co-registration; thus we take the relative standard uncertainty in the UVCS/WLC to LASCO-C2 pB ratio to be (5.5 ± 2.9) %.

This analysis is summarized in Table 17.3.

17.3.4 UVCS/WLC to Spartan 201 pB Ratio Uncertainty

The Spartan 201 relative standard uncertainty in radiometry is reported to be 20 % [*T.A. Kucera, personal communication*, 2002], and this dominates the uncertainty in the comparison to UVCS/WLC. The Spartan 201 stray light uncertainty is still in progress, but 10 % is probably an upper limit because the dynamic range of the Spartan 201 pB data used to produce Figure 17.6 is about 10 at 1.7 $R_\odot$. Since the Spartan 201 images can be co-registered with those of LASCO-C2 to a high degree of accuracy, we use the spatial co-registration relative standard uncertainty of 5.5 % given in the previous section. Since we have no way to estimate the uncertainty due to inaccurate temporal co-registration, we

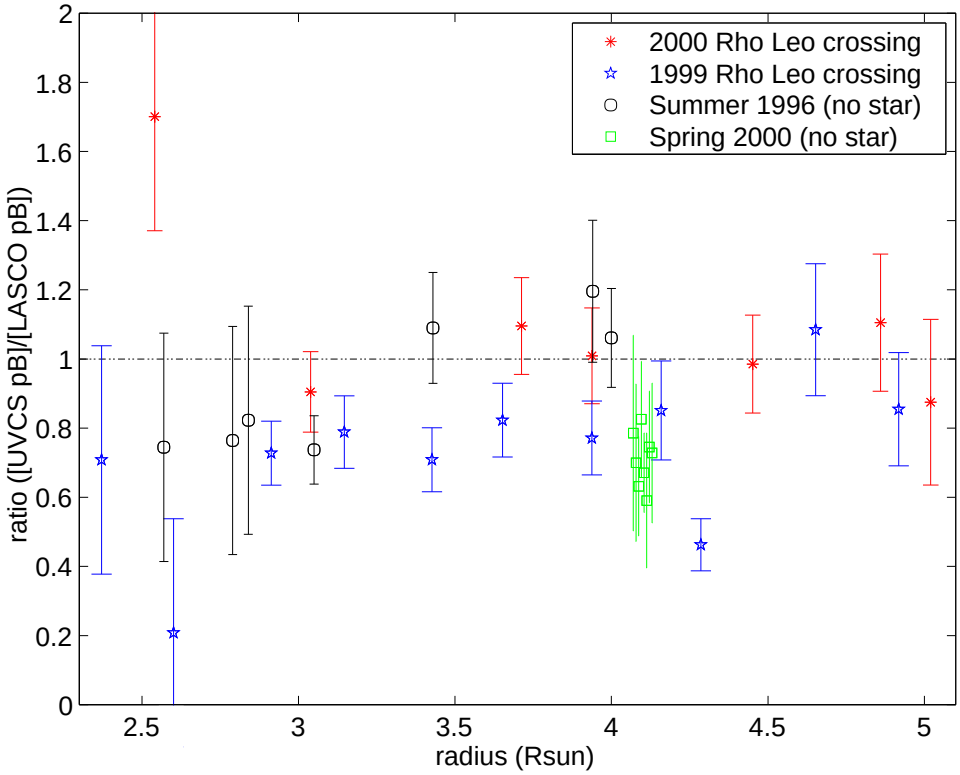

Figure 17.1: Four comparisons of the UVCS/WLC to LASCO-C2 pB ratio. See text for details.

do not attempt to do so. There is no doubt that some of the scatter in Figure 17.6 is due to a lack of simultaneity, however this should not produce any systematic trends. This analysis is summarized in Table 17.4.

17.4 Results

17.4.1 UVCS/WLC and LASCO-C2: Special Observations

Figure 17.1 shows the results of the UVCS/WLC and LASCO-C2 comparison based on special observations. It consists of four different data sets. The error bars represent the 17 % and 33 % relative standard uncertainties from Table 17.3. The four different data sets depicted in Figure 17.1 are as follows:

1. The black circles represent data taken on 20 August and 1 September 1996. The ratios range from about 0.65 to 1.2.

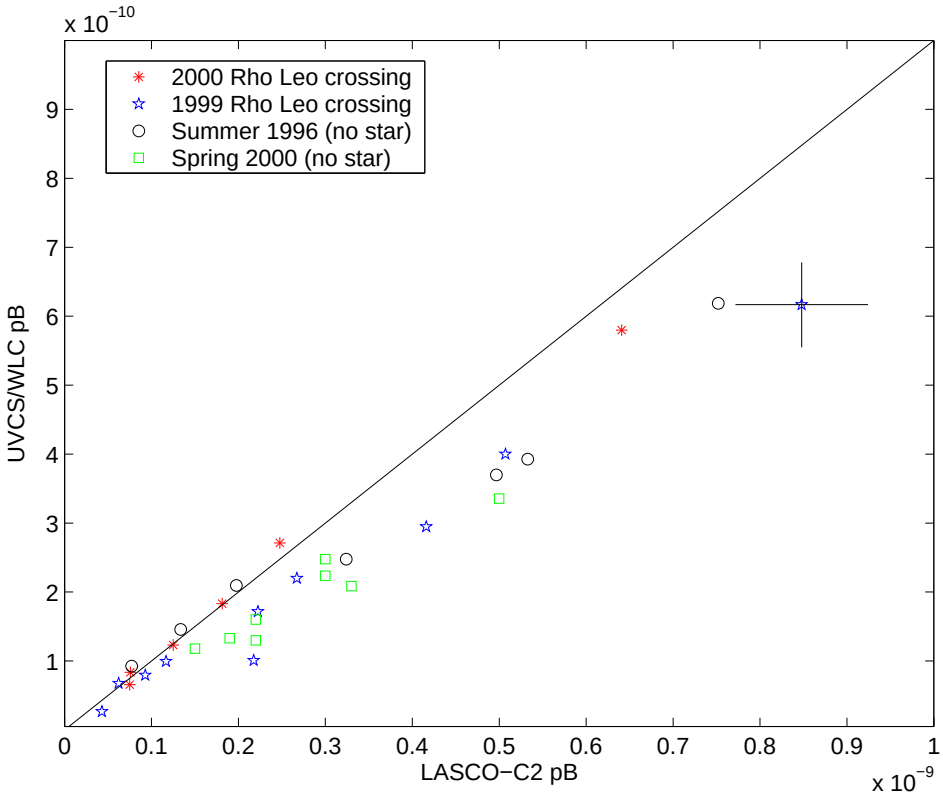

Figure 17.2: Scatter plot corresponding to the four comparisons in Figure 17.1. The error bars shown are representative of the sample. An uncertainty analysis is given in the text. Several outliers from Figure 17.1 are not shown here.

2. The blue pentagrams represent data taken at the time of the ρ-Leo crossing in August 1999. ρ Leo was used as a pointing marker to aid in co-registration. Except for three outliers, the ratio is between 0.65 and 0.85.

3. The red asterisks represent data taken during the ρ-Leo crossing in August and September 2000. Again, ρ Leo was used as a pointing marker. Except for one outlier, the ratios vary from about 0.85 to 1.1, and are all larger than the 1999 ρ-Leo ratios.

4. The green squares represent data taken in April 2000 at 4.15 $R_{\odot}$ (spread out for display). These ratios cluster around 0.7 and vary from about 0.55 to 0.8.

The median of all the ratios in Figure 17.1 is 0.79, the mean is 0.84 and the standard deviation is 0.25.

Figure 17.2 is a plot of LASCO-C2 pB versus UVCS/WLC pB corresponding to the data points in Figure 17.1, except that three of the 34 points are missing. These three points

Table 17.4: Summary of relative standard uncertainties in the UVCS/WLC to Spartan 201 pB ratios. No uncertainty in temporal co-registration has been included in the quadrature sum (see text).

source	resulting uncertainty in pB ratio
UVCS/WLC radiometry	7 %
UVCS/WLC stray light (median)	4 %
Spartan 201 radiometry	20 %
spatial co-registration	5.5 %
quadrature sum (median)	22 %

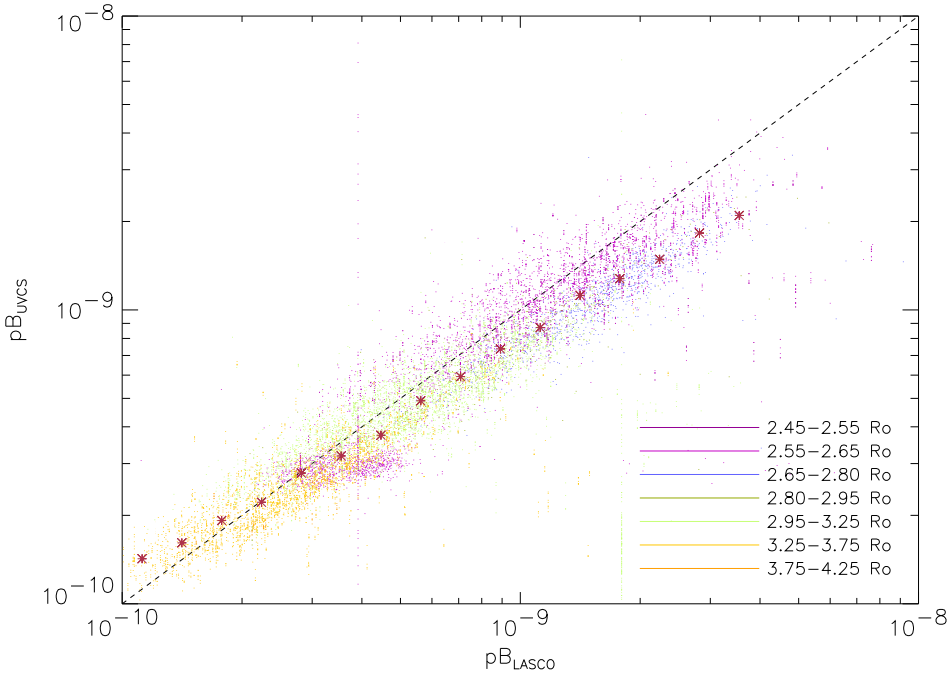

Figure 17.3: Scatter plot for all synoptic data. The LASCO-C2 pB is plotted on the x-axis and the UVCS/WLC pB is plotted on the y-axis. Different colors are used for data taken at different heights. The asterisks represent the median of the distribution.

are the outliers in Figure 17.1 and have not been included in order to have a smaller scale of the display. Error bars are only given for one of the data points. The relative standard uncertainties in both the UVCS/WLC and LASCO-C2 measurements are representative of the sample. For more details on the uncertainties see Section 17.3.

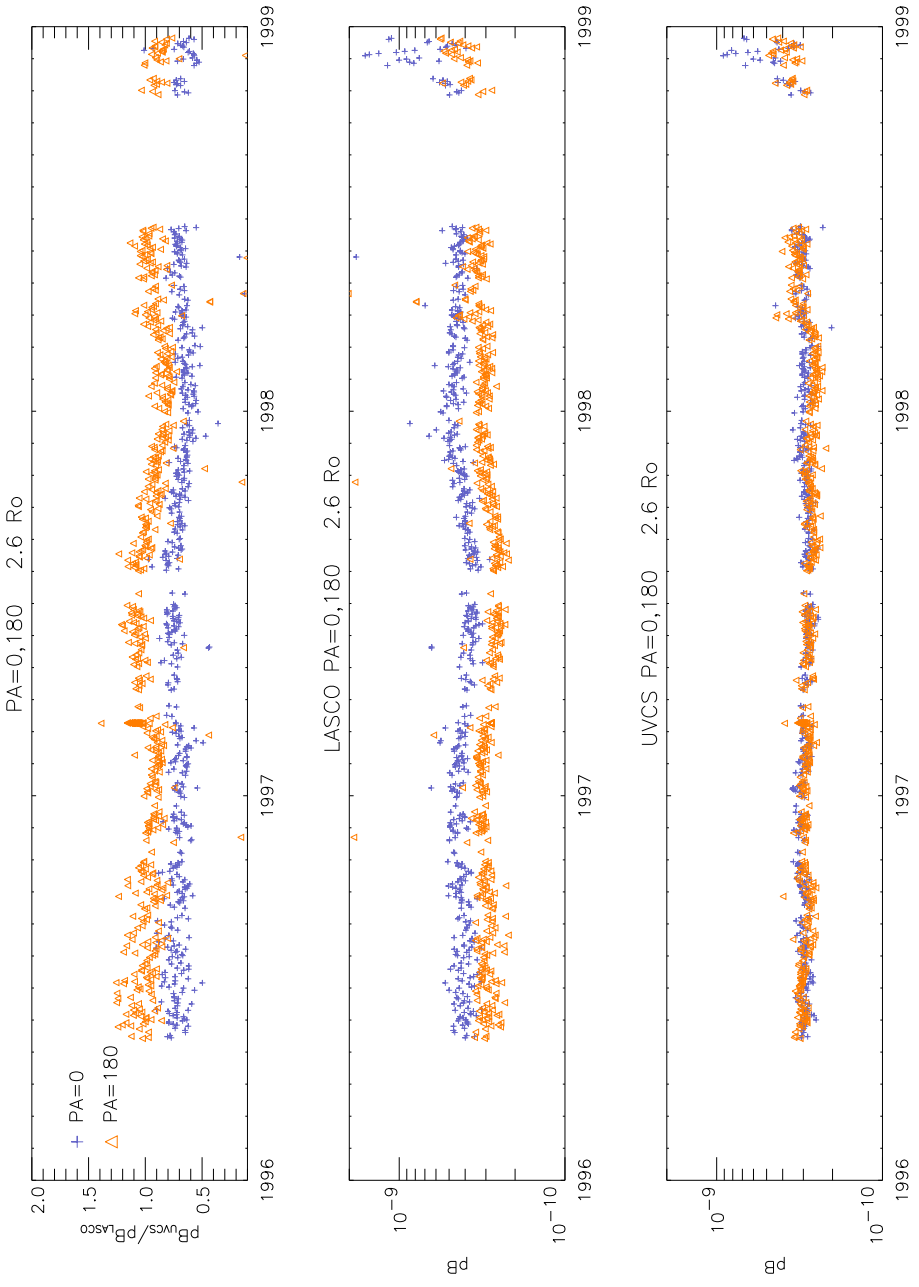

Figure 17.4: Time behavior plots of the coronal hole pBs, taken at position angles of 0 ° and 180° and at a height of 2.6 $R_{\odot}$. The top panel shows the pB ratio (UVCS/WLC to LASCO-C2), the middle panel shows the LASCO-C2 pBs, and the bottom panel shows the UVCS/WLC pBs. The orange triangles and blue crosses represent position angles of 0 ° and 180°, respectively. Note the systematic difference between the north and south coronal hole pBs as seen by LASCO-C2.

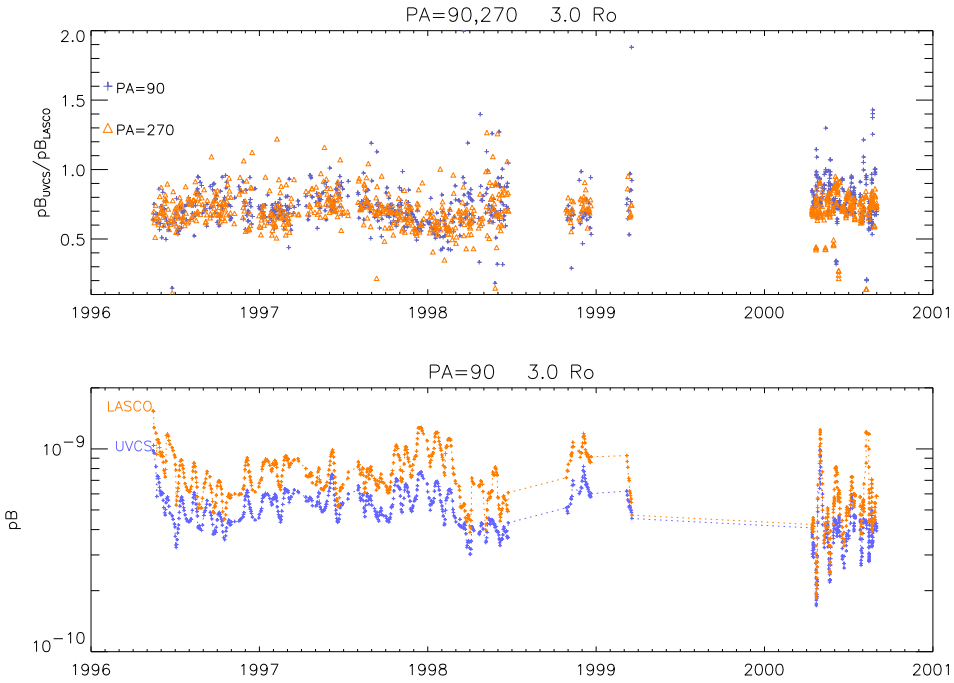

Figure 17.5: Time behavior plots of the equatorial pBs, taken at position angles of 90 ° and 270° and at a height of 3.0 $R_{\odot}$. The top panel shows the pB ratio (UVCS/WLC to LASCO-C2) and the bottom panel shows the individual UVCS/WLC and LASCO-C2 pBs.

17.4.2 UVCS/WLC and LASCO-C2: Synoptic Observations

Figure 17.3 is a plot of LASCO-C2 pB versus UVCS/WLC pB for the selected synoptic data. The asterisks represent the median of the distribution. As the figure shows, the median value of the UVCS/WLC to LASCO-C2 pB ratio decreases with signal strength.

Figures 17.4 and 17.5 illustrate the time behavior of LASCO-C2 and UVCS/WLC pB measurements. Figure 17.4 shows that the UVCS/WLC measurements in both the north and south coronal holes are more constant in time than the LASCO-C2 measurements. It is also interesting and puzzling to note that while the UVCS/WLC pB measurements in the north and south coronal holes are about equal, the LASCO-C2 measurements show a clear and systematic difference. Figure 17.5 is a similar plot, but made for the equatorial regions. There is not much evidence of any difference in the pB ratio above the east and west limbs.

17.4.3 UVCS/WLC and Spartan 201: Special Observations

Figure 17.6 shows the ratio of the UVCS/WLC pB to that of Spartan 201 during the STS-95 John Glenn Space Shuttle mission in November 1998. These data points show a ra-

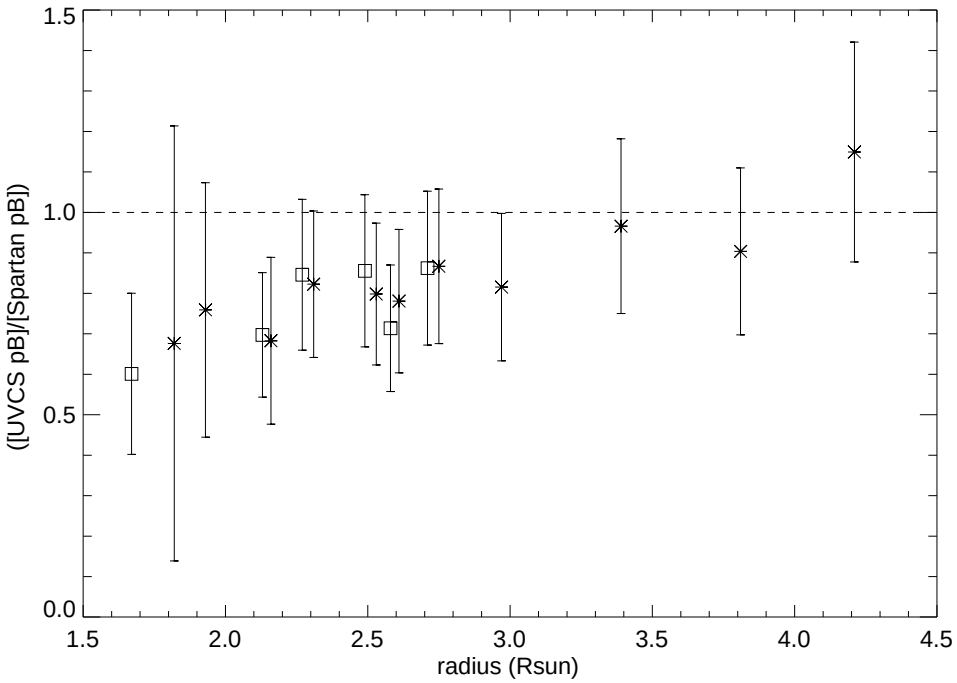

Figure 17.6: Ratio of the UVCS/WLC to the Spartan 201 White Light Coronagraph pBs for observations taken during the STS-95 John Glenn shuttle mission in November 1998. The data points represented by the squares have a stronger signal and better simultaneity than those represented by the asterisks.

tio of about 0.8 at most heights. The data points with larger ratios (some of the asterisks), have poor simultaneity and weaker signals. The squares have much better simultaneity, larger signals and less UVCS/WLC stray light uncertainty. The median of the ratios denoted by the asterisks is 0.81, the mean is 0.83 and the standard deviation is 0.13. The median of the ratios denoted by the squares is 0.85, the mean is 0.76 and the standard deviation is 0.10.

17.5 Discussion

As was mentioned above, the median of all the ratios in Figure 17.1 is 0.79, the mean is 0.83 and the standard deviation is 0.25. The median relative standard uncertainty in the individual ratios is 33 % for heights below 2.9 $R_{\odot}$ and 15 % for heights above 2.9 $R_{\odot}$ (see Table 17.3). The difference of the mean pB values of the UVCS/WLC and LASCO-C2 when approximately co-registered is about 20 %. This difference can be explained by the described sources of uncertainty.

The asterisks in Figure 17.3 mark the median of the scatter distribution, and they show that the median value of the UVCS/WLC to LASCO-C2 pB ratio decreases with signal

strength. The low ratios at high pB (typically found at low heights) could be explained by a systematic shift introduced by errors in the LASCO-C2 vignetting function at low heights where the correction is large. The high ratio at low pB (typically found at large heights) could be explained by incorrect stray light subtraction on the part of either or both instruments, or by the radiometric uncertainty being exceeded by the LASCO-C2 vignetting correction at low heights.

Figure 17.4 shows another curious trend: LASCO-C2 sees a difference in the coronal polarized radiance between the north and south coronal holes but UVCS/WLC does not. It is very difficult to explain this behavior in terms of the UVCS/WLC instrument, since it is a single pixel instrument that rotates about an axis to look at different position angles. This design makes the UVCS/WLC occulting geometry and stray light properties independent of position angle, as is described in Section 17.2.

Two possibilities that might explain the difference in polar pB values come to mind:

- LASCO-C2 has more polarized stray light in the north than in the south near 2.6 $R_\odot$, which was the only height at positions angles of 0° and 180° used for this comparison.
- The C2 vignetting function, which can be a function of position angle as well as radius [*Brueckner et al.*, 1995], is in fact different for position angles of 0° and 180° at 2.6 $R_\odot$, and different from the current calibration values.

Of the two possibilities considered, the second is not unlikely because the vignetting correction is quite large for 2.6 $R_\odot$.

Figure 17.6 shows that the UVCS/WLC pBs are generally in agreement with those of Spartan 201, within the uncertainties. The median of all of the ratios in the figure is 0.81.

Acknowledgements

The authors thank Mari Paz Miralles for helping with the UVCS pointing calculations. This work is supported by NASA under grant NAG5-10093 to the Smithsonian Astrophysical Observatory, by the Italian Space Agency, and by the PRODEX programme of ESA (Swiss contribution).

Bibliography

Brueckner, G.E., Howard, R.A., Koomen, M.J., Korendyke, C.M., Michels, D.J., Moses, J.D., Socker, D.G., Dere, K.P., Lamy, P.L., Llebaria, A., Bout, M.V., Schwenn, R., Simnett, G.M., Bedford, D.K., Eyles, C.J., The Large Angle Spectroscopic Coronagraph (LASCO), *Sol. Phys.* **162**, 357, 1995.

Fineschi, S., O'Neal, R., and Modigliani, A., unpublished technical report, 1997.

Fisher, R.R., and Guhathakurta, M., SPARTAN 201 White Light Coronagraph Experiment, *Space Sci. Rev.* **70**, 267, 1994.

Frazin, R.A., PhD Thesis, University of Illinois, Department of Astronomy, 2002.

Kohl, J.L., Esser, R., Gardner, L.D., Habbal, S., Daigneau, P.S., Dennis, E.F., Nystrom, G.U., Panasyuk, A., Raymond, J.C., Smith, P.L., Strachan, L., van Ballegooijen, A.A., Noci, G., Fineschi, S., Romoli, M., Ciaravella, A., Modigliani, A., Huber, M.C.E., Antonucci, E., Benna, C., Giordano, S., Tondello, G., Nicolosi, P., Naletto, G., Pernechele,

C., Spadaro, D., Poletto, G., Livi, S., von der Lühe, O., Geiss, J., Timothy, J.G., Gloeckler, G., Allegra, A., Basile, G., Brusa, R., Wood, B., Siegmund, O.H.W., Fowler, W., Fisher, R., and Jhabvala, M., The Ultraviolet Coronagraph Spectrometer for the Solar and Heliospheric Observatory, *Sol. Phys.* **162**, 313, 1995.

Panasyuk, A.V., Three dimensional reconstruction of UV emissivities in the solar corona using the Ultraviolet Coronagraph Spectrometer data from Whole Sun Month, *J. Geophys. Rev.* **104**, 972, 1999.

Romoli, M., Frazin, R.A., Kohl, J.L., Gardner, L.D., Cranmer, S.R., Reardon, K., and Fineschi, S., In-flight calibration of the UVCS White Light Channel, this volume, 2002.

Solanki, S.K., Solar variability, this volume, 2002.

— 18 —

SUMER Stellar Observations to Monitor Responsivity Variations

PHILIPPE LEMAIRE
Institut d'Astrophysique Spatiale, Unité Mixte CNRS-Université Université de Paris XI, Orsay, France

Regular observations of α Leo have been performed by SUMER in order to track responsivity variations in the 95 nm to 160 nm range. Degradation in responsivity ranging from about 2 % to 5 % at 150 nm and 20 % at 100 nm have been demonstrated for the SUMER optical paths using both A and B detectors between 1996 and 1999. Later, between 1999 and 2001, with the optical path using the A detector, the 100 nm responsivity loss is about 20 %, while that at 150 nm is insignificant.

18.1 Introduction

Reference stars have for several decades been used for in-flight stellar radiance calibration of space instrumentation, for example the Orbiting Astronomical Observatory (OAO-2) [*Bless et al.*, 1976], the International Ultraviolet Explorer (IUE) [*Bohlin et al.*, 1980; *Nichols and Linsky*, 1996] and the Hubble Space Telescope (HST) [*Bohlin et al.*, 1990; *Bohlin*, 1996]. Recently the in-flight irradiance calibration of the solar instrumentation SOLSTICE on the Upper Atmosphere Research Satellite (UARS) was also performed using a set of reference stars [*Woods et al.*, 1993].

The selected stars must be inside the field of view of the instrument and provide enough signal to be well above the possible instrumental scattered light resulting from the nearby solar radiation. While these two conditions are easy to fulfill for a large set of stars with the $4^\circ \times 4^\circ$ SOLSTICE field of view, which can be selected anywhere in the entire celestial sphere, or with the $10^\circ \times 10^\circ$ UVCS field of view centered on the Sun (see the paper in this volume, *Gardner et al.* [2002]), only very few stars are bright enough to be used in the $1^\circ \times 1^\circ$ Sun-centered SUMER field of view [*Wilhelm et al.*, 1995].

Among the stars used by the three experiments α Leo is a very bright B7 V star in the vicinity of the ecliptic plane that was nearly aligned with the Sun on 23 August 1999, within the SUMER/SOHO field of view. From nearly 30 years of observations, the α-Leo flux is stable in the visible and in the FUV down to 120 nm, see, e.g., observations of the TD-1 satellite [*Jamar et al.*, 1976], OAO-2 [*Code and Meade*, 1979] and the Astronomical Netherlands Satellite (ANS) [*Wesselius et al.*, 1982]. In SUMER, the α-Leo star flux is used as the absolute in-flight reference in the 120 nm to 160 nm range. The stability of the α-Leo flux, used in this paper, also provides a good reference for the long-term evolution of the SUMER responsivity in the 95 nm to 160 nm wavelength range and a reference to compare the relative photometric responsivity of the two SUMER optical paths, using A

and B detectors, in the same spectral range. Hereafter the SUMER common optical paths (the telescope, the collimator and the scan mirrors, and the grating [*Wilhelm et al.*, 1995]) with A and B detectors will be referred to as A and B channels, respectively.

After a short description of the star observations, we report and discuss the results obtained on the responsivity variation of SUMER since the launch, and the responsivity ratio between the two detectors in the 95 nm to 160 nm wavelength range.

18.2 Star Observations

The description of the SUMER spectrometer is given in *Wilhelm et al.* [1995]. On 23 August 1999 the star α Leo crossed the solar meridian at about +1700″ from disk-centre. In 1996, the star was drifting across the 4″×300″ and the whole detector A spectral image (1024 pixel or about 4.4 nm) was binned by 20 pixels (0.086 nm) and sent through the telemetry in few selected wavelength positions. In 1997 with detector B, in 1999 with detector A and B, and 2001 with detector A, the star was drifting across a 300″ diameter hole and, during the drift, a wavelength scan of the entire 95 nm to 160 nm wavelength range was performed. This hole was used during ground tests, it is aligned with, and on the same support as, the 4″×300″, 1″×300″ and 0.3″×300″ slits.

The main correction applied to the data is the subtraction of the scattered light given by the telescope mirror fully illuminated by the Sun. The star trace on the detector is a line along the spectral direction that can be easily corrected for the scattered light measured on each side along the spatial direction. Knowing the drift rate of the star across the 300″ spectrometer entrance hole, its location is defined, the incidence angle on the grating is slightly modified and the corresponding wavelength offset can be computed and corrected for each exposure.

Table 18.1: Days during which high voltage was applied to A or B detectors.

	A detector		B detector	
period / d	on / d	duty cycle / %	on / d	duty cycle / %
1996-01-22 to 1996-09-24 (248)	243	98.0	2	0.8
1996-09-24 to 1996-12-31 (99)	0	0.0	87	87.9
1997-01-01 to 1997-08-31 (243)	1	0.4	211	86.8
1997-09-01 to 1997-12-31 (122)	0	0.0	61	50.0
1998-01-01 to 1998-06-22 (173)	2	1.1	60	34.7
attitude loss				
1998-10-05 to 1998-12-31 (88)	2	2.3	23	26.1
1999-01-01 to 1999-08-31 (243)	24	9.9	104	42.8
1999-09-01 to 1999-12-31 (122)	36	29.5	0	0.0
2000-01-01 to 2000-08-31 (244)	48	19.7	2	0.8
2000-09-01 to 2000-12-31 (122)	77	63.1	2	1.6
2001-01-01 to 2001-08-31 (243)	70	28.8	0	0.0
Total..... (1947)	503	25.8	550	28.2

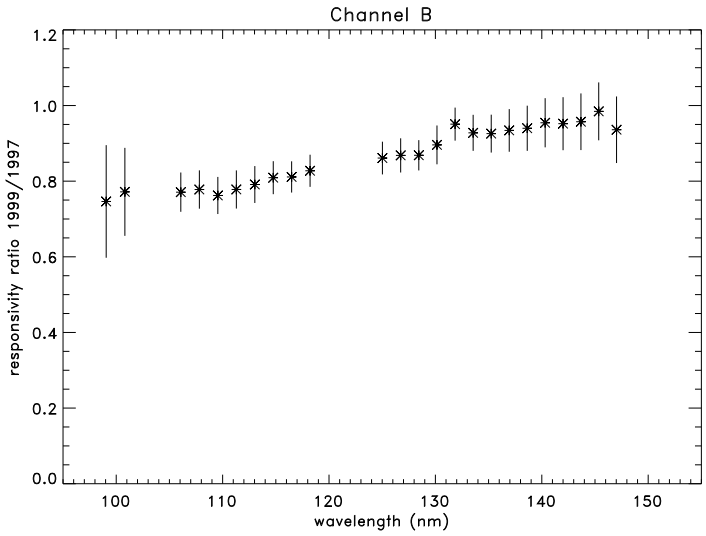

Figure 18.1: Responsivity variation of the B channel between 1997 and 1999 established from α-Leo observations on 23 August 1999. The standard uncertainties (1-σ) are plotted.

18.3 Responsivity Variation

The A detector was mainly used from the beginning of SUMER operations, from 22 January 1996 to 24 September 1996 (B was on briefly in January 1996). From 24 September to August 1999 the B detector was selected (except for a few tests on A). Detector A has currently been the only one in use, see Table 18.1.

18.3.1 Responsivity Variation of the B Channel

From α-Leo observations made with the B channel in 1997 and in 1999 (before and after the 1998 SOHO attitude loss), the measured responsivity variation is displayed on Figure 18.1.

The relative standard uncertainties noted in this figure and in the following are deduced from the detector count statistics averaged over about 1 nm, with a correction from the scattered light contribution. A small systematic relative uncertainty of about 5 % might possibly be due to a shift of the pulse height distribution of the detector resulting from a low high-voltage applied on the microchannel plate (MCP).

18.3.2 Responsivity Variation of the A Channel

Similar observations done with the A channel show the responsivity variations between the 1999 and 2001 observations, and the 1996 and 2001 observations (see Figure 18.2).

From Figure 18.1 and Figure 18.2 it appears that:

- A significant loss of responsivity occurred between 1999 and 1997; the loss is greater at shorter wavelengths than at long wavelengths.

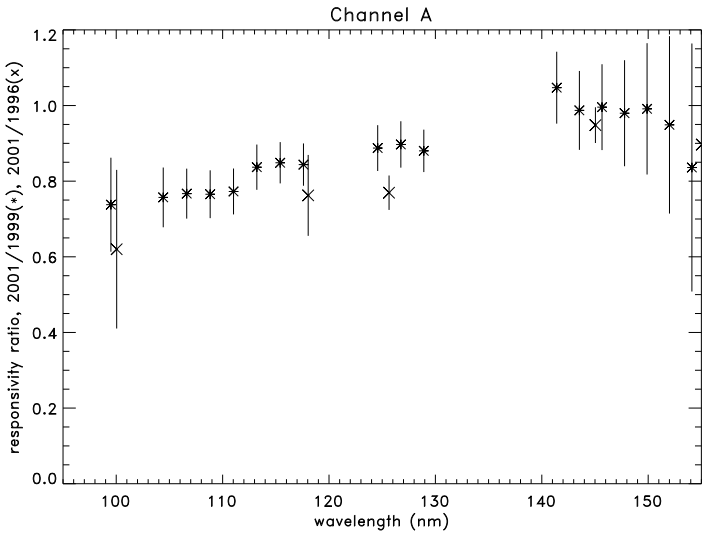

Figure 18.2: Responsivity variation of the A channel between 2001, 1999 and 1996 established from α-Leo observations on 23 August 1999. The standard uncertainties are plotted.

- The short wavelength range is still loosing responsivity between 1999 and 2001.

The similar shapes of the curves in Figure 18.1 and Figure 18.2 imply that most of the responsivity loss comes from the optical path common to channels A and B. Since no significant responsivity loss was detected before the SOHO attitude loss, a contamination of the optics during the SOHO attitude loss (SUMER temperature was estimated at -80 °C) is suspected of producing this responsivity loss. A simultaneous change of the A and B detectors photocathode responsivity in the KBr and bare MCP parts seems excluded; no significant modification of the KBr-to-bare responsivity ratio has been detected.

18.4 A and B Channels Responsivity Ratio

The observation of α Leo was performed on 23 August 1999, with A and B detectors, one after the other. The derived responsivity ratio is shown in Figure 18.3.

The ratio B/A increases with wavelength (within the 95 nm to 150 nm spectral range). The result is in good agreement with the measurements made during the ground calibration before the SOHO launch ([*Wilhelm et al.*, 1995], Figure 7). So, it seems that there is no variation of A and B channels relative responsivity with time.

18.5 Conclusion

The regular observation of bright stars within the field of view provides a powerful technique to monitor the responsivity variation of the solar SUMER ultraviolet spectrometer.

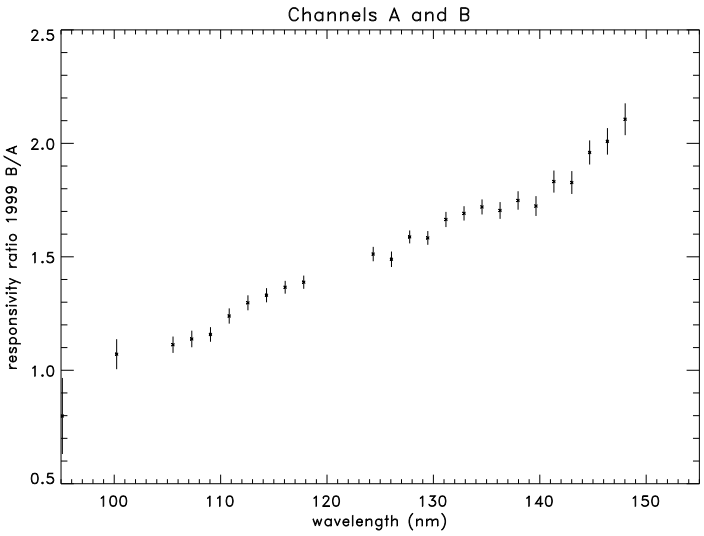

Figure 18.3: Responsivity ratio of the B and A channels in 1999 established from α-Leo observations on 23 August 1999. The standard uncertainties are plotted.

Several results have been obtained:

- The responsivity degradation of the spectrometer with A or B detector between the observations performed before and after the SOHO attitude loss indicates a loss of optical reflectivity. The loss could be due to optics contamination.
- The responsivity loss is still increasing, mainly at short wavelengths.
- The responsivity ratio of the A and B detectors after the SOHO attitude loss is very similar to the measurements performed before the SOHO launch. The two detectors have a similar time variation.

Acknowledgements

The SUMER project is financially supported by DLR, CNES, NASA and the ESA PRODEX programme (Swiss contribution). SOHO is a project of international cooperation between the European Space Agency (ESA) and the National Aeronautics and Space Administration (NASA). The discussions with the SUMER and UVCS teams and the contribution of John Raymond who provided the star path in SOHO coordinates have contributed to the success of the observations. I want to thank the referee for his detailed critical reading which helped to improve the paper.

Bibliography

Bless, R.C., Code, A.D., and Fairchild, E.T., Ultraviolet photometry from the Orbiting Astronomical Observatory. XXI. Absolute energy distribution of stars in the ultraviolet, *Astrophys. J.* **203**, 410, 1976.

Bohlin, R.C., Spectrophotometric standards from the far-UV to the near-IR on the white dwarf flux scale, *Astron. J.* **111**, 1743, 1996.

Bohlin, R.C., Harris, A.W., Holm, A.V., and Gry, C., The ultraviolet calibration of the Hubble Space Telescope. IV. Absolute IUE fluxes of Hubble Space Telescope Standard Stars, *Astrophys. J. Suppl. Ser.* **73**, 413, 1990.

Bohlin, R.C., Holm, A.V., Savage, B.D., Snijders, M.A.J., and Sparks, W.M., Photometric Calibration of the International Ultraviolet Explorer (IUE), *Astron. Astrophys.* **85**, 1, 1980.

Code, A.D., and Meade, M.R., Ultraviolet photometry from the Orbiting Astronomical Observatory. XXXII. An atlas of utraviolet stellar spectra, *Astrophys. J. Suppl. Ser.* **39**, 195, 1979.

Gardner, L.D., Smith, P.L., Kohl, J.L., Atkins, N., Ciaravella, A., Miralles, M.P., Panasyuk, A., Strachan Jr., L., Suleiman, R.M., UV Radiometric Calibration of UVCS, this volume, 2002.

Jamar, C., Macau-Hercot, D., Monfis, A., Thompson, G.I., Houziaux, L., and Wilson, R., Ultraviolet bright-star spectrophotometric catalogue. A compilation of absolute photometric data obtained with the Sky Survey Telescope (S2/68) on the European Astronomical Satellite TD-1, *ESA SR-27*, 1976.

Nichols, J.S., and Linsky, J.L., The final archive and recalibration of the International Ultraviolet Explorer (IUE) satellite, *Astronom. J.* **111**, 517, 1996.

Wesselius, P.R., van Duinen, R.J., de Jonge, A.R.W., Aalders, J.W.G., Luinge, W., and Wildeman, J., ANS Ultraviolet Photometry, Catalogue of Point Source, *Astron. Astrophys. Suppl. Ser.* **49**, 427, 1982.

Wilhelm, K., Curdt, W., Marsch, E., Schühle, U., Lemaire, P., Gabriel, A., Vial, J.-C., Grewing, M., Huber, M.C.E., Jordan, S.D., Poland, A.I., Thomas, R.J., Kühne, M., Timothy, J.G., Hassler, D.M., and Siegmund, O.H.W., SUMER – Solar Ultraviolet Measurements of Emitted Radiation, *Sol. Phys.* **162**, 189, 1995.

Woods, T.N., Rottman, G.J., and Ucker, G.J., Solar-Stellar Irradiance Comparison Experiment 1. 2. Instrument Calibrations, *J. Geophys. Res.* **98** (D6), 10 679, 1993.

IV. Atomic Physics

— 19 —

The CHIANTI Atomic Database and Instrument Calibration: a Symbiosis

HELEN E. MASON, GIULIO DEL ZANNA
Department of Applied Mathematics and Theoretical Physics
University of Cambridge, Cambridge, UK

KENNETH P. DERE, ENRICO LANDI
Naval Research Laboratory
Washington, DC, USA

MASSIMO LANDINI
Dipartimento di Astronomia e Scienza dello Spazio
Università di Firenze, Firenze, Italy

PETER R. YOUNG
Harvard-Smithsonian Center for Astrophysics
Cambridge, MA, USA
now at Rutherford Appleton Laboratory
Chilton, Didcot, Oxfordshire, UK

The CHIANTI atomic database comprises a comprehensive, accurate and up-to-date database of atomic parameters, necessary for emission-line spectroscopy. The suite of user-friendly software allows plasma diagnostics to be carried out. Since its release in 1996, CHIANTI has become a standard resource for the analysis of solar spectra. Accurate atomic data can provide the foundation for in-flight instrument calibrations. Conversely, an accurate instrument calibration can provide a check on atomic parameters. The internal consistency of spectral-line intensities can be used to highlight specific anomalies. In this paper, we illustrate how CHIANTI has been used to validate the calibration of solar EUV instruments: SOHO-CDS, -SUMER, -EIT and SERTS. In addition, we show how anomalous spectral-line intensities indicate the need for more accurate atomic calculations.

19.1 Introduction

Spectroscopic diagnostics using UV, EUV and X-ray line intensities are a fundamental tool for the measurement of physical parameters of solar and stellar atmospheres, such as the electron density, temperature, plasma emission measure and chemical composition. See *Mason and Monsignori Fossi* [1994] for a comprehensive review. These diagnostics require a large amount of accurate atomic data, including energy levels, radiative transition probabilities and collisional excitation rates. The CHIANTI project [*Dere et al.* 1997,

2001, *Landi et al.* 1999, *Young et al.* 2002] aims to provide the solar and astrophysics communities with these atomic data. CHIANTI is applicable to a range of physical conditions pertinent to optically-thin plasmas in collisional ionization equilibrium. In addition, theoretical spectral-line emissivities can be used to check instrument calibrations. The accuracy of both the diagnostics and calibration results depends critically on the reliability of the atomic data used.

The accuracy of theoretical calculations can best be assessed from a direct comparison with measurements in well-controlled laboratory experiments. Unfortunately, conditions that exist in astrophysical plasmas are difficult to reproduce in the laboratory. As a result, only a small amount of the atomic data in the CHIANTI database has been verified in this way. Consequently, most of the conclusions regarding the plasma properties of the solar corona that are reported in the literature are based on comparisons between observations and ab initio calculations.

As part of the CHIANTI project, systematic comparisons have been carried out between CHIANTI emissivities and high-resolution solar spectra. The CHIANTI atomic database provides an important check on the calibration of the spectra and the broad-band filters. The method of deriving the relative radiometric calibration of solar instruments using intensity ratios of density- and temperature-insensitive lines was first proposed by *Neupert and Kastner* [1983]. CHIANTI emissivities for a number of ions, formed at different temperatures, have also been used to deduce a differential emission measure distribution for the emitting plasma. Where discrepancies between CHIANTI and measured line-intensities do exist, they point out potential mis-identifications, new identifications, line blending, possible calibration problems, data reduction errors or cases where atomic data need to be improved.

The first studies compared CHIANTI and the Solar EUV Rocket Telescope and Spectrograph (SERTS) observations [*Thomas and Neupert*, 1994] in the 17 nm to 45 nm spectral range. These studies are discussed in Section 19.2. The Coronal Diagnostic Spectrometer (CDS) on board the Solar and Heliospheric Observatory (SOHO) observes many emission lines from a large number of highly-ionised ions of the most abundant elements, covering a large range of temperatures. CDS, therefore, provides an excellent opportunity for a detailed diagnostic study of the transition-region and coronal plasma. The large number of emission lines covering an extensive wavelength range also allows an in-flight calibration to be obtained by comparison of observed and CHIANTI emissivities. A short overview of the work carried out with CDS using CHIANTI is given in Section 19.3.1. Details of the CDS in-flight calibration using CHIANTI are given in a separate paper by *Del Zanna* [2002] and a detailed paper by *Del Zanna et al.* [2001a]. A comparison has recently been made of CHIANTI emissivities with the Solar Ultraviolet Measurements of Emitted Radiation (SUMER) observations of the quiet solar corona in the 50 nm to 160 nm spectral range. Details of these results are given in Section 19.3.2. CHIANTI has also been used in the calibration and analysis of observations from the EUV Imaging Telescope (EIT) on SOHO (see Section 19.3.3). CHIANTI has been used to check which spectral lines contribute to the various EIT channels for different solar regions having different characteristic temperatures. This type of study is important for all imaging instruments: for example Yohkoh SXT (Soft X-ray Telescope) and TRACE (Transition Region And Coronal Explorer).

Following a workshop on atomic data requirements for SOHO [*Lang*, 1994], an international collaboration known as the Iron Project [*Hummer et al.*, 1993] was established

with the aim of carrying out systematic, electron-scattering calculations for ions of astronomical interest, using the best available methods. In particular, members of the Iron Project have concentrated on the sequence of iron ions prevalent in the corona. The inclusion of these new, high-accuracy atomic data in CHIANTI is crucial to the successful analysis of solar spectra. Examples of Iron Project results and comparisons with solar observations are given in Section 19.4.

19.2 SERTS

A description of the SERTS instrument is given by *Neupert et al.* [1992]. A spectrum of an active region obtained in the first rocket flight in 1989 (SERTS-89) was published by *Thomas and Neupert* [1994]. The SERTS-89 instrument covered the 23.5 nm to 45.0 nm wavelength region in first order and 17.0 nm to 22.5 nm in second order. The spectrum is composed of optically-allowed transitions from ions formed in the 5×10^4 K to 4×10^6 K temperature range, encompassing the upper chromosphere, the transition region and the corona.

Emission-line intensities from the SERTS-89 observations have been compared with CHIANTI (Version 1) emissivities by *Young et al.* [1998]. In general, excellent agreement was found. However, at the longest wavelengths (42 nm to 45 nm), the observed intensities were found to be systematically low. The use of density-insensitive ratios and branching ratios led *Young et al.* [1998] to suggest a correction to the SERTS-89 intensity calibration for wavelengths greater than 40 nm. This demonstrates the enormous potential of the CHIANTI database as a means for checking the instrumental intensity calibration.

The version of SERTS flown in 1995 (SERTS-95) incorporated a multilayer-coated diffraction grating that enhanced the instrumental sensitivity in the second-order waveband. This gives rise to sharply-peaked response functions, which are more difficult to calibrate reliably. *Brosius et al.* [1998a] present active-region and quiet-Sun spectra derived from SERTS-95 observations. The relative radiometric calibration was derived by means of density- and temperature-insensitive line-intensity ratios [*Brosius et al.*, 1998b], using CHIANTI.

19.3 SOHO

19.3.1 CDS

CDS comprises two spectrometers: the Normal Incidence Spectrometer (NIS) and the Grazing Incidence Spectrometer (GIS). The NIS detector observes two spectral ranges (NIS-1: 30.8 nm to 38.1 nm and NIS-2: 51.3 nm to 63.3 nm), with stigmatic optics. The GIS has four detectors (GIS-1: 15.1 nm to 22.1 nm, GIS-2: 25.6 nm to 33.8 nm, GIS-3: 39.3 nm to 49.3 nm and GIS-4: 65.6 nm to 78.5 nm). CDS studies allow the simultaneous extraction of both spatial and spectral information, thus enabling quantitative, spectroscopic-diagnostic analyses to be carried out. Initial results from the CDS instrument are given in *Harrison et al.* [1997]. The CHIANTI database and software was originally integrated into the CDS software package by C.D. Pike. Figure 19.1 shows a comparison of a CDS spectrum with a CHIANTI spectrum. The plots are based on the results of the active-region analysis published in *Landi and Landini* [1998]. The synthetic spectrum is

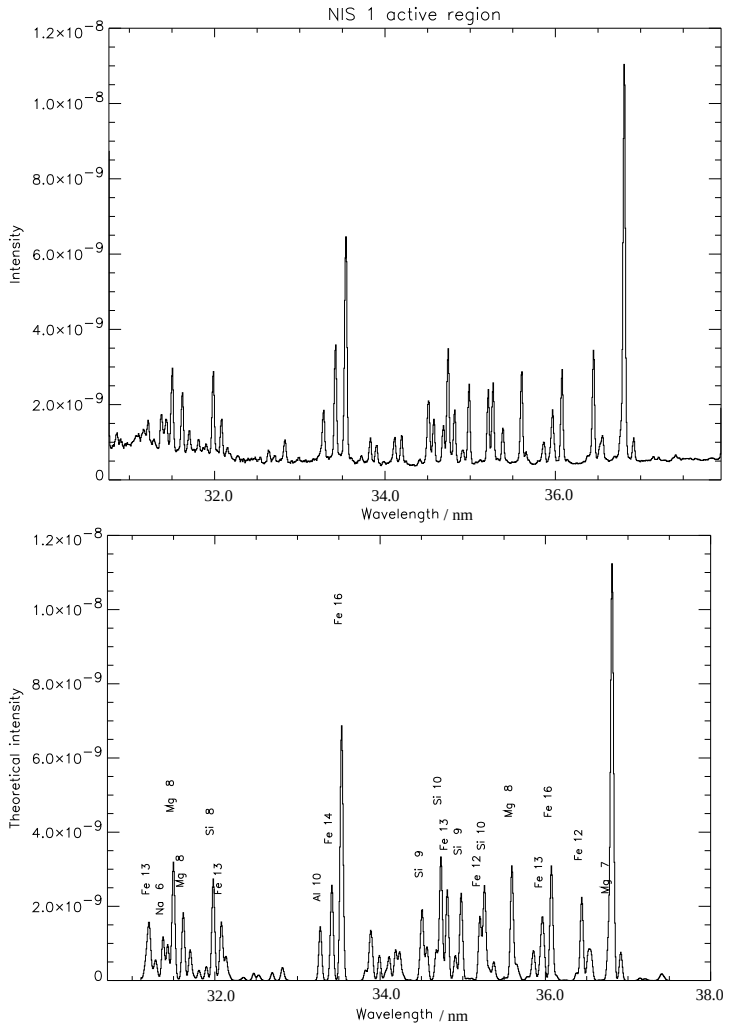

Figure 19.1: Synthetic spectrum for an active-region dataset, taken from *Landi and Landini* [1998]. Top: CDS NIS-1 observed spectrum, and bottom: CHIANTI synthetic spectrum. The intensity units are erg cm^{-2} s^{-1} $arcsec^{-2}$.

calculated using a coronal chemical composition and the DEM curves and density reported in that paper. It shows the excellent degree of accuracy and completeness of the CHIANTI database. The apparent continuum emission in the CDS spectrum is instrumental in origin. The spectroscopic diagnostic capabilities of CDS are presented in *Mason et al.* [1997, 1999]. These require a reliable CDS calibration. In particular, the study of elemental abundances is a field of intense interest [*Mason and Bochsler*, 1999]. For example, *Young and Mason* [1997] investigated the relative elemental abundance of magnesium to neon in an active region. High electron-densities and photospheric abundances were found, which could possibly be related to emergent flux. In contrast, the footpoints of larger coronal

structures show coronal abundances. These results depend critically on the CDS calibration, in particular between the two wavelengh ranges of NIS-1 and NIS-2. *Fletcher et al.* [2001] have pursued this topic and find indications that transition-region brightenings and elemental abundance variations could be closely related to changes in magnetic topology. A strong warning is given by *Del Zanna et al.* [2002] and *Gianetti et al.* [2000] that limitations of the calibration, the analysis method and the atomic data can all lead to serious errors in elemental-abundance determinations. It is best, whenever possible, to use both NIS and GIS observations for such studies.

Many Joint Observing Programmes (JOPs) have been carried out with SOHO. For example, *Gibson et al.* [2002] monitored the structure and evolution of an active region by combining SOHO, TRACE, Yohkoh and ground-based observations. These multi-instrument campaigns require careful co-alignment and an accurate cross-calibration of different instruments.

An evaluation of CHIANTI data for the CDS NIS coronal lines has been carried out by *Landi et al.* [2002]. They chose a set of off-disk observations which were found to be almost isothermal over several hours. They found very good agreement between the electron temperature and density measured from spectral-line intensity ratios and those values derived from an emission measure analysis. Overall, good agreement was found between different ions and different isoelectronic sequences. Some blends are indicated and individual cases of discrepancies between the CDS observations and CHIANTI suggest there is a requirement for improved atomic data.

19.3.2 SUMER

The SUMER spectrometer on board SOHO covers the 50 nm to 160 nm spectral range and offers a unique opportunity to check CHIANTI predictions for emission lines in this rich wavelength range. In general, these lines are either optically-allowed lines due to low-ionization stages formed in the 2×10^4 K to 3×10^5 K temperature range (typical of the solar chromosphere and transition region) or optically-forbidden and intercombination lines formed in the solar corona at $T > 3 \times 10^5$ K. When the SUMER field-of-view is on the disk, the lower-temperature lines dominate the spectrum; when SUMER observes plasma beyond the solar disk, the lower-temperature lines, to a large extent, disappear and the hotter lines become most prominent.

Landi et al. [2002] compared the CHIANTI emissivities with an off-disk coronal spectrum observed at distances from the limb between 1.03 and 1.045 solar radii, in quiet conditions. By so doing, they limited their investigation to ions having maximum fractional abundances in the temperature range 3×10^5 K $< T_e < 3 \times 10^6$ K. The choice of such a region had the advantage that the emitting plasma was nearly isothermal. The emission measure technique allowed a simultaneous measurement of both the electron temperature and the emission measure of the emitting plasma. An example of the emission measure technique is given in Figure 19.2, where lines from nitrogen-like ions are used. The place where the curves cross gives the derived temperature and emission measure values. Excellent agreement was found between the temperature measured for all coronal lines in the dataset and the *Feldman et al.* [1999] value for the same observations. The intensity calibration of the SUMER instrument and the elemental abundance adopted for the study were confirmed, and several blends were identified. A few areas of disagreement were found, where the problems were probably due to inaccuracies of atomic physics or

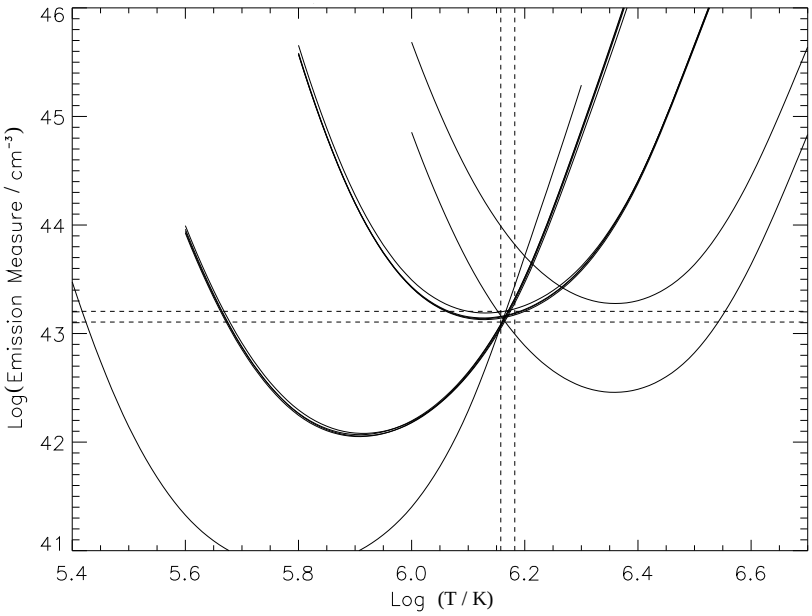

Figure 19.2: Example of the emission measure analysis (on isothermal plasmas) applied to SUMER line intensities. The curves displayed are the $\frac{I_{obs}}{G(T)}$ functions of Al VII, Si VIII, S X and Ar XII lines, where I_{obs} is the observed intensity and $G(T)$ is the contribution function of each line calculated using CHIANTI. The crossing region, marked by the dashed lines, indicates the value of the plasma emission measure and temperature. The line missing the common crossing region clearly indicates the presence of a blend or of some atomic physics problems.

to unidentified blending. By simultaneously comparing lines of many different ions, the emission-measure technique allowed the problems in individual transitions along the entire isoelectronic sequence to be tracked, thus enabling a discrimination between blending problems and real atomic physics inaccuracies.

Overall, the CHIANTI database has been very successful in reproducing the SUMER coronal spectrum. Future studies will be devoted to the cooler part of the spectrum, by comparing CHIANTI emissivities with on-disk observations of quiet Sun from SUMER.

19.3.3 EIT Plasma Response

The EIT instrument has been designed to be sensitive to the solar spectrum in four narrow wavelength-bands. These wavelength bands have been chosen to correspond to four strong lines that are produced in four distinct, narrow temperature-regimes. The wavelength bands are listed in Table 19.1. In order to understand the response of the EIT to coronal and transition-region plasmas at various temperatures, it is necessary to have a model of the solar spectrum at the wavelengths where EIT is sensitive. The CHIANTI database and spectral code provide an accurate and comprehensive model spectrum for calculating the EIT plasma response. They provide good predictions of the strong primary

Table 19.1: EIT Wavelength Bands.

Wavelength	Dominant Ion	Characteristic Temperature
17.1 nm	Fe IX, X	9×10^5 K
19.5 nm	Fe XII	1.3×10^6 K
28.4 nm	Fe XV	2×10^6 K
30.4 nm	He II	8×10^4 K

lines in the EIT passbands as well as the weaker lines and the continuum. These various components can be significant contributors at temperatures outside the contribution function of the principal lines.

The primary calibration of the EIT spectral response is based on measurements, taken at the Orsay synchrotron, with flight components of the EIT. This work has been reported by *Dere et al.* [2000]. An integration of the solar spectrum using the CHIANTI database is shown in Figure 19.3. These calculations are based on the instrument response function given in *Dere et al.* [2000]. The three curves refer to three positions of the EIT filter wheel. The solar variability model of *Warren, Mariska and Lean* [1998] suggests that the CHIANTI models can underestimate the intensities of He II 25.6 nm and 30.4 nm by factors of two and six respectively. However, they do seem to reproduce correctly the He I intensities, although this may just be fortuitous. *Newmark* [2001] has reanalysed the EIT preflight calibration data and found that the second-order mirror reflectivities of the He II 30.4 nm channel should provide a non-negligible reflectivity at wavelengths just longward of 17 nm. To produce the response curves included in the EIT calibration software, Newmark has included this change to the He II 30.4 nm bandpass as well as extending the wings of the EIT response functions. The helium line intensities were calculated with CHIANTI using standard active-region and quiet-Sun differential emission measures from OSO-6 observations. It is assumed that collisional excitation is dominant and that the line is optically thin.

Del Zanna et al. [2002] have made a direct comparison of CDS-GIS and EIT. Plumes were found to exhibit a quasi-isothermal distribution, which peaks at a lower temperature ($T = 7$ to 8×10^5 K) than the surrounding coronal-hole region. Elemental abundances in the plumes exhibit only a small departure from photospheric values. A comparison was made with the broad-band images of EIT, showing that, in the plume, the low temperature Fe VIII emission is the dominant contribution to the 'Fe XII 19.5 nm' EIT filter.

The 17.1 nm and 19.5 nm EIT filters have been used by various authors to deduce that plumes are about 30 % cooler than the surrounding coronal-hole regions. In order to confirm this result, a comparison was made between the GIS scans and the EIT 17.1 nm and 19.5 nm images. A direct comparison is possible because GIS spectrally resolves the emission lines observed by the EIT filters. The observed and calibrated GIS spectra were multiplied by the EIT effective-areas [*Dere et al.*, 2000], to simulate the EIT observed bandpasses. GIS spectra of the three regions were chosen as representative of plume, coronal-hole and quiet-Sun areas. These spectra were multiplied by the EIT filter response. The three spectra of the various solar features show how different lines, formed at a range of temperatures, contribute to the emission seen by the EIT. The transmission

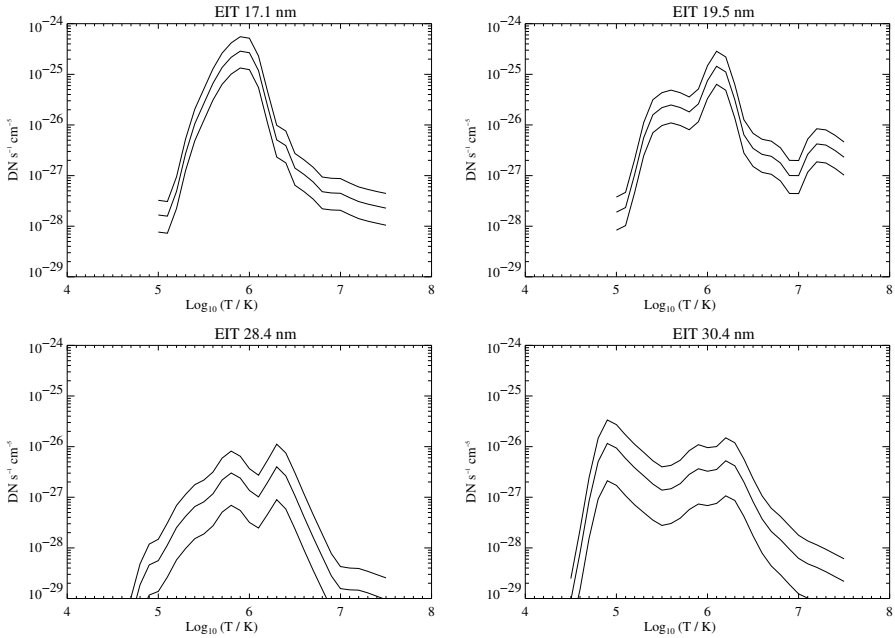

Figure 19.3: An integration of the solar spectrum obtained with the CHIANTI database based on the EIT response function given in *Dere et al.* [2000], with DN s $^{-1}$ per unit emission measure plotted as a function of electron temperature for each of the four EIT channels. DN is simply the 'digital number' output by the instrument electronics. The CHIANTI spectrum was derived using the *Mazzotta et al.* [1998] ionization equilibria and the coronal abundances of *Feldman and Laming* [2000].

of the EIT 17.1 nm filter can be regarded as almost isothermal with contributions mainly from Fe IX and Fe X for all three solar regions. In the EIT 19.5 nm filter, the situation is quite different, as Figure 19.4 shows. In the quiet-Sun spectrum the main contribution is from Fe XII lines, mixed with some Fe X, Fe XI and Fe XIII emission. However, in the coronal-hole and plume spectra, the cooler lines (Fe VIII, Fe X, Fe XI) become increasingly dominant in comparison to the Fe XII lines. This shows that it is incorrect to assume that the observed emission in the EIT 19.5 nm filter is predominantly from Fe XII, and explains why plumes are visible in the EIT 19.5 nm images. Since the lines observed in the EIT 19.5 nm filter are formed over such a wide range of temperatures, it is dangerous to use this filter for temperature diagnostics.

19.4 The Iron Project: Fe IX, Fe XII and Fe XIV

The comparisons of CHIANTI with SERTS and SOHO observations highlighted some inconsistencies, which indicated the need for better atomic data. The iron ions are particularly difficult to represent with an accurate atomic model. Some examples are presented here of new calculations from within the Iron Project for Fe IX, Fe XII and Fe XIV.

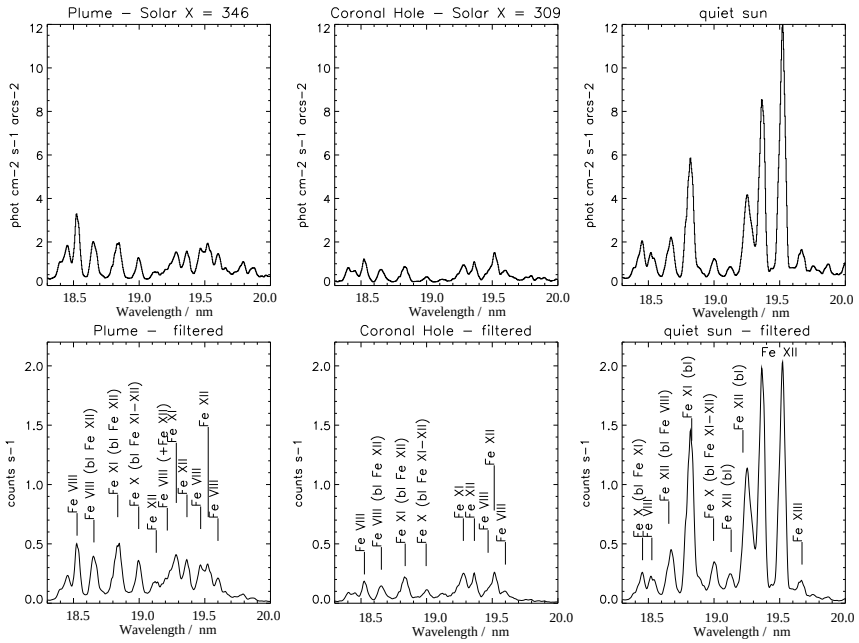

Figure 19.4: Top: GIS-1 spectra of plume, coronal hole and quiet sun. Details of the parameters used in CHIANTI to produce these spectra are given in *Del Zanna et al.* [2002]. Bottom: same as above, but multiplied by the EIT 19.5 nm filter response.

Fe XIV is one of the most important diagnostic ions in the solar corona. Transitions within Fe XIV give rise to spectral lines in the visible (green line, 530.3 nm) and extreme-ultraviolet wavelength ranges. *Storey et al.* [1996, 2000] calculated new atomic data for Fe XIV. The electron-scattering calculation was more sophisticated than any previous work on this ion. Significant differences with earlier work were found in the excitation rates for many transitions. A comparison was made between predicted line-intensity ratios and those observed in solar-coronal spectra, including those from SERTS-89 and CDS. Several long-standing inconsistencies between the theoretical and observed intensity ratios, as detailed by *Young et al.* [1998], were resolved by these new atomic data.

Recent analyses of SERTS-89 data have been carried out for Fe IX by *Storey and Zeippen* [2001]. They have shown that their new atomic data lead to significant changes in line-intensity ratios. These new data resolve some major inconsistencies between the observed and theoretical Fe IX spectra.

Fe XII also plays a key role in diagnostic studies because of its wealth of strong spectroscopic lines covering a wide wavelength-range in the UV and EUV spectral regions, spanning several instruments on SOHO. A new set of atomic data for Fe XII was calculated by *Binello et al.* [1998a, 1998b]. In *Binello et al.* [2001] a comparison is made between the theoretical line intensities and solar observations for a range of plasma densities and temperatures. The SERTS-89 and SERTS-95 observations of quiet Sun and solar active-regions provided a useful means of testing the quality of the atomic data. For the Fe XII density-insensitive ratios, they found generally good agreement between theoreti-

cal and observed ratios. However, the electron densities derived from the Fe XII spectral lines for SERTS-89 and SERTS-95 show persistently greater densities than those from other ions formed at similar temperatures. This highlights a serious discrepancy. Further improvements to the atomic model may help to resolve this problem for this troublesome and complex ion.

19.5 Conclusions

Imaging instruments can provide high spatial and time resolution observations. They have clearly demonstrated that the solar atmosphere contains dynamic, filamentary structures. Spectroscopic instruments provide good diagnostic capabilities for plasma parameters. Both imaging and spectroscopic instruments require accurate calibrations to obtain reliable scientific results. In-flight calibrations can and have been performed for solar instruments using high quality atomic data. The CHIANTI package (atomic database and supporting software) has contributed significantly to this effort. It is freely available and is now widely used by the solar-physics community.

Acknowledgements

The work of E. Landi was supported by a grant from NASA's Applied Informations System Research Program (AISRP). HEM and GDZ acknowledge financial support from PPARC. SOHO is a project of international collaboration between ESA and NASA.

Bibliography

Binello, A.M., Landi, E., Mason, H.E., Storey, P.J. and Brosius, J.W., A comparison between theoretical and solar Fe XII UV line intensity ratios, *Astron. Astrophys.* **370**, 1071, 2001.

Binello, A.M., Mason, H.E., and Storey, P.J., Atomic data for the Iron Project: Electron impact excitation of optically allowed and intercombination transitions in transitions in Fe XII, *Astrophys. J. Suppl.* **127**, 545, 1998a.

Binello, A.M., Mason, H.E., and Storey, P.J., Atomic data for the Iron Project: Electron impact excitation of fine structure transitions in the ground configuration of Fe XII, *Astrophys. J. Suppl. Ser.* **131**, 153, 1998b.

Brosius, J.W., Davila, J.M., and Thomas, R.J., Solar active region and quiet-Sun extreme-ultraviolet spectra from SERTS-95, *Astrophys. J. Suppl. Ser.* **119**, 255, 1998a.

Brosius, J.W., Davila, J.M., and Thomas, R.J., Calibration of the SERTS-95 spectrograph from iron line intensity ratios, *Astrophys. J.* **497**, L113, 1998b.

Del Zanna, G., Bromage, B.J.I., Landi, E., and Landini, M., Solar EUV spectroscopic observations with the SOHO/CDS instrument. I - An in-flight calibration study, *Astron. Astrophys.* **379**, 708, 2001a.

Del Zanna, G., Bromage B.J.I., and Mason, H.E, Elemental abundances of the low corona as derived from SOHO/CDS observations, Proc. of the Joint SOHO-ACE Workshop 2001 on Solar and Galactic Composition, (March 6 - 9, 2001), Bern, Switzerland, AIP Conf. Proc. **598**, 59, 2001b.

Del Zanna, G., Bromage, B.J.I., and Mason, H.E., SOHO CDS observations of polar plumes, *Astron. Astrophys.* submitted, 2002.

Dere, K.P., Landi, E., Mason, H.E., Monsignori Fossi, B.C., and Young, P.R., CHIANTI – A database for EUV emission lines. Paper I: Wavelengths greater than 50 Å, *Astrophys. J. Suppl. Ser.* **125**, 149, 1997.

Dere, K.P., Landi, E., Young, P.R., and Del Zanna, G., CHIANTI – An atomic database for emission lines. Paper IV: Extension to X-ray wavelengths, *Astrophys. J. Suppl. Ser.* **134**, 331, 2001.

Dere, K.P., Moses, J.D., Delaboudinière, J.-P., Brunaud, J., Carabetian, C., Hochedez, J.F., Song, X.Y., Catura, R.C., Clette, F., and Defise, J.M., The preflight photometric calibration of the Extreme-ultraviolet Imaging Telescope EIT, *Sol. Phys.* **195**, 13, 2000.

Feldman, U., Doschek, G.A., Schühle, U., and Wilhelm, K., Properties of quiet-Sun coronal plasmas at distances of 1.03 to 1.50 solar radii along the solar equatorial plane, *Astrophys. J.* **518**, 500, 1999.

Feldman, U., and Laming, J.M., Element abundances in the upper atmospheres of the Sun and stars: Update of observational results, *Physica Scripta* **61**, 222, 2000.

Fletcher, L, Lopez Fuentes, M.C., Mandrini, C.H., Schmieder, B., Démoulin, P., Mason, H.E., Young, P.R., and Nitta, N., A relationship between transition region brightenings, abundances, and magnetic topology, *Sol. Phys.* **203**, 255, 2001.

Gianetti, D., Landi, E., and Landini, M., The effect of different ion fraction datasets on plasma diagnostics, *Astron. Astrophys.* **360**, 1148, 2000.

Gibson, S.E., Fletcher, L., Del Zanna, G., Pike, C.D., Mason, H.E., Mandrini, C.H., Démoulin, P., Gilbert, H., Burkepile, J., Holzer, T., Alexander, D., Liu, Y., Nitta, N., Qui, J., Schmieder, B., and Thompson, B.J., The structure and evolution of a sigmoidal active region, *Astrophys. J.* in press, 2002.

Harrison, R.A., Fludra, A., Pike, C.D., Payne, J., Thompson, W.T., Poland, A.I., Breeveld, E.R., Breeveld, A.A., Culhane, J.L., Kjeldseth-Moe, O., Huber, M.C.E., and Aschenbach, B., High resolution observations of the extreme ultraviolet Sun, *Sol. Phys.* **170**, 123, 1997.

Hummer, D.G., Berrington, K.A., Eissner, W., Pradhan, A.K., Saraph, H.E., and Tully, J.A., Iron Project: Goals and methods, *Astron. Astrophys.* **279**, 298, 1993.

Landi, E., Feldman, U., and Dere, K.P., CHIANTI – An atomic database for emission lines. Paper V: Comparison with an isothermal spectrum observed with SUMER, *Astrophys. J.* , in press, 2002.

Landi, E., and Landini, M., Temperature and density diagnostics of quiet Sun and active regions observed with CDS NIS, *Astron. Astrophys.* **340**, 265, 1998.

Landi, E., Landini, M., Dere, K.P., Young, P.R., and Mason, H.E., CHIANTI – A database for EUV emission lines. Paper III: Continuum radiation and extension of the ion database, *Astrophys. J. Suppl. Ser.* **135**, 339, 1999.

Lang, J. (Editor), *Atomic Data and Nuclear Data Tables* **57**, 1994.

Mason, H.E., and Bochsler, P., Compostion and elemental abundance variations in the solar atmosphere and solar wind, *Space Sci. Rev.* **87**, 105, 1999.

Mason, H.E., Landi, E., Pike, C.D., and Young, P.R., Electron density and temperature structure of a limb active region observed by SOHO-CDS, *Sol. Phys.* **189**, 129, 1999.

Mason, H.E., and Monsignori Fossi, B.C., Spectroscopic diagnostics in the VUV for solar and stellar plasmas, *Astron. Astrophys. Rev.* **6**, 123, 1994.

Mason, H.E., Young, P.R., Pike, C.D., Harrison, R.A., Fludra, A., Bromage, B.J.I., and Del Zanna, G., Application of spectroscopic diagnostics to early observations with the SOHO Coronal Diagnostic Spectrometer, *Sol. Phys.* **170**, 143, 1997.

Mazzotta, P., Mazzitelli, G., Colafrancesco, S., and Vittorio, N., Ionization balance for optically thin plasmas: Rate coefficients for all atoms and ions of the elements H to Ni, *Astrophys. J. Suppl. Ser.* **133**, 403, 1998.

Neupert, W.M., Epstein, G.L., Thomas, R.J., and Thompson, W.T., An EUV imaging spectrograph for high-resolution observations of the solar corona, *Sol. Phys.* **137**, 87, 1992.

Neupert, W.M., and Kastner, S.O., A spectroscopic method for calibration of solar extreme ultraviolet instrumentation, *Astron. Astrophys.* **128**, 181, 1983.

Newmark, J.S., http://umbra.nascom.nasa.gov/eit/eit_guide/chap6.html, 2001.

Storey, P.J., Mason, H.E., and Saraph, H.E., Atomic data from the IRON project; Electron impact excitation for the Fe XIV fine-structure transition $^2P^o_{1/2}$–$^2P^o_{3/2}$, *Astron. Astrophys.* **309**, 677, 1996.

Storey, P.J., Mason, H.E., and Young, P.R., Electron impact excitation of the Fe XIV EUV transitions, *Astron. Astrophys. Suppl.* **141**, 285, 2000.

Storey, P.J., and Zeippen, C.J., Coronal Fe IX line intensities and electron density diagnostics, *Mon. Not. R. Astr. Soc.* **324**, L7–L10, 2001.

Thomas, R.J., and Neupert, W., Extreme ultraviolet spectrum of a solar active region from SERTS, *Astrophys. J. Suppl. Ser.* **91**, 461, 1994.

Warren, H.P., Mariska, J.T., and Lean, J., A new reference spectrum for the EUV irradiance of the quiet Sun 1. Emission measure formulation, *J. Geophys. Res.* **103**, 12077, 1998.

Young, P.R., Landi, E., and Thomas, R.J., CHIANTI: An atomic database for EUV emission lines. Paper II: Comparison with the SERTS-89 active region spectrum, *Astron. Astrophys.* **329**, 291, 1998.

Young, P.R., and Mason, H.E., The Mg/Ne abundance ratio in a recently emerged flux region observed by CDS, *Sol. Phys.* **175**, 523, 1997.

Young, P.R., Del Zanna, G., Landi, E., Dere, K.P., Mason, H.E., and Landini, M., CHIANTI – An atomic database for emission lines. Paper VI: Proton rates and other improvements, *Astrophys. J. Suppl.*, submitted, 2002.

— 20 —

The Use of Atomic Data for the In-flight Calibration of the CDS Spectrometers

GIULIO DEL ZANNA
Department of Applied Mathematics and Theoretical Physics
University of Cambridge, Cambridge UK

I describe a general method that has been used for the in-flight cross-calibration of the CDS spectrometers. This method relies on accurate atomic data and uses the Sun as a 'calibration' source. It was successfully applied in the past to calibrate other EUV spectrometers. The results show significant differences from the laboratory calibration, good agreement with the calibrations based on two rocket-flights flown in 1997 and excellent stability of the CDS instrument during the same year. It is suggested that this method be used to monitor the in-flight calibration of future EUV spectrometers.

20.1 Introduction

Plasma parameters such as densities, temperatures and element abundances of the solar transition-region and corona can now be determined with a good accuracy, using extreme-ultraviolet (EUV) spectrometers such as CDS and SUMER on board SOHO. However, any uncertainty in the intensity calibration affects the determination of these parameters, particularly when the emission lines are not close in wavelength or are seen in different detectors. The intensity calibration of the instruments is, therefore, a fundamental requirement for any scientific use of EUV spectra.

The CDS instrument observes the solar corona with two spectrometers, the Normal Incidence Spectrometer (NIS) and the Grazing Incidence Spectrometer (GIS). A description of the complete CDS instrument can be found in *Harrison et al.* [1995]. The CDS instrument is particularly complex to calibrate: it covers a wide wavelength range (15 nm to 78 nm) with five detectors giving six wavebands with second-order lines identified in three of them. Ground measurements of the CDS calibration [*Lang et al.*, 2000] suffered various uncertainties or limitations, and methods to check the in-flight calibration were needed. *Del Zanna* [1999] and *Del Zanna et al.* [2001] presented a comprehensive study, providing the first complete in-flight inter-calibration of all nine CDS channels. The in-flight calibration has been achieved with the use of a calibration method which compares observations with the most up-to-date atomic data provided by the CHIANTI database: see *Dere et al.* [1997]. Excellent agreement was found with the results of the two independent calibrations based on rocket-borne instruments flown in 1997 [*Brekke et al.*, 2000; *Thomas et al.*, 1999], thus showing the validity of the method adopted. On the other hand, significant differences remained with some of the ground calibration results. In particular, the NIS-1 and all the GIS responsivities in first-order were found to be underestimated, in

the ground calibration, by factors of about two. The cross-calibration of the CDS channels was found to be stable during 1997.

20.2 A Calibration Method Based on Atomic Data

In the absence of a suitable on board calibration source, the only possibility is to use the solar emission as a 'calibration' source. The calibration process consists of four steps. The first step is the selection of the most suitable set of observations where the effects of solar variability are negligible. This is extremely important for all cases of cross-calibration between channels that do not observe simultaneously, as is the case of the GI and NI spectrometers. Solar rotation, spatial overlapping and temporal variability, are all issues. In particular, the high variability in all the transition-region lines, predominantly located at the supergranular network boundaries, makes most non-simultaneous observations unusable. The second step is the direct cross-calibration between spectrally-overlapping regions, when they are present, as in the case of CDS.

The third step is the selection of the most suitable 'calibration' lines to be used. The idea is to choose only those groups of calibration lines whose ratios are independent of the observed source. The first ratios to examine are branching ratios (ratios of lines that share a common upper-level). These intensity-ratios depend only on the radiative transition probabilities, and are generally known with 10 % accuracy. Next, ratios of density-insensitive lines are considered, by comparing observed and calculated values. A differential emission measure (DEM) analysis must be performed to assess blending and to take into account any temperature effects in temperature-sensitive calibration line-ratios. It is important to check that each line ratio is indeed constant both temporally and spatially. This can be done by observing different regions on the Sun. Also, one must check if there are any opacity effects. The procedure is then to apply the comparison to all the available ions. When agreement is found between the results obtained by the use of many lines of different ions, the relative calibration between the various channels is obtained.

For each pair of lines of the same ion, the responsivity ratio was derived from the observed and theoretical radiance-ratio. For each ratio, once one responsivity value was fixed, then the other is obtained directly. Figure 20.1 shows the CDS absolute responsivities derived from various line-ratios by fixing the value of one reference line for each ion. The responsivities of the reference lines were chosen in order to fit a continuous, smooth curve for each channel. The uncertainties in the ratios have been calculated by taking the uncertainties in the line intensities and adding 10 % to account for unknown uncertainties of the calculated atomic physics values. These uncertainties, therefore, do not include all possible systematic errors and should be considered as lower estimates. However, the results obtained from different observations (superimposed on Figure 20.1) show a small scatter, well within the estimated uncertainties, which gives confidence in the results.

Note that if only density- and temperature-insensitive ratios are used, the results are independent of the adopted densities, the ionization equilibrium or the temperature distribution of the source. Also note that uncertainties in the atomic data are difficult to estimate, but typically are 10 % to 30 %. The key issue is to identify all the calibration ratios that have shown excellent agreement (say within 10 %) between previous solar observations and predictions based on atomic theory. There is no reason why the calibration ratios ob-

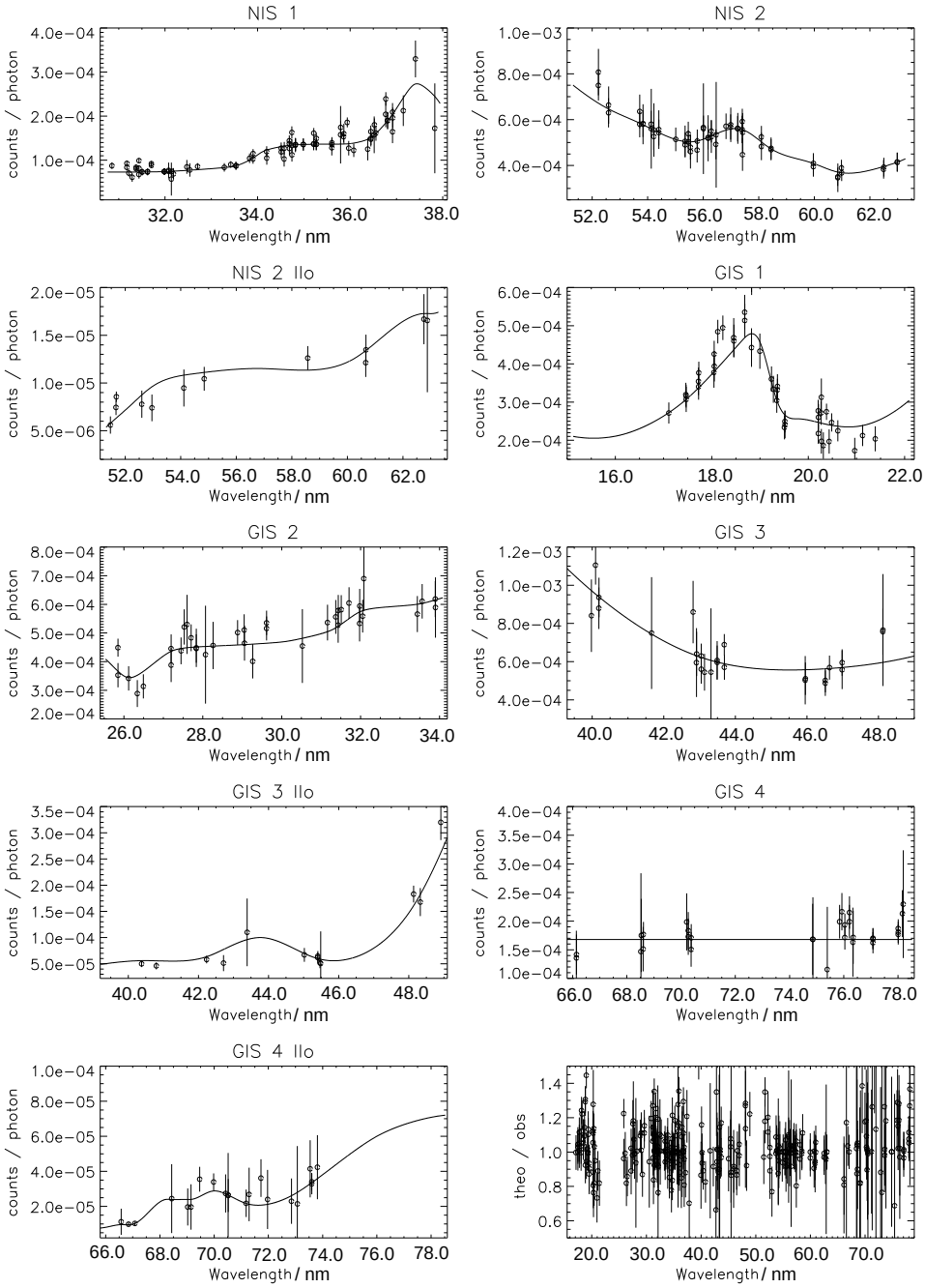

Figure 20.1: The CDS NIS and GIS responsivities (solid lines), first and second order, as derived from pre-loss-of-attitude observations. The responsivities derived from all the line-ratios used are superimposed. The bottom-right plot shows the ratio of the theoretical to the observed line-intensities for all the lines used.

served by different EUV instruments should differ, if the same atomic data are used and the instruments are well-calibrated against primary standards.

This method has already been applied a few times in the past. *Neupert and Kastner* [1983] used this method for an in-flight calibration of the OSO V and OSO VII EUV spectrometers, in the 15 nm to 40 nm range. Recently, the method was successfully applied by *Brosius et al.* [1998a, b] to calibrate the Solar EUV Rocket Telescope and Spectrometer observations in 1995 (SERTS-95), using averaged active-region and quiet-Sun spectra and CHIANTI (version 1.01, except for Fe XIV). The same method was also applied by *Young et al.* [1998] to check the calibration of the SERTS-89 active-region spectrum [*Thomas and Neupert*, 1994].

In order to make full use of this diagnostic method for calibration purposes, given the uncertainties in the atomic data and the observed intensities, it is essential to use as many lines emitted by the same ion as possible. It is also important to use as many ions as possible, in order to reduce the possibility that incorrect atomic data for a single ion would affect the results.

The fourth step is to choose, for each calibration line, the most appropriate observations. This is not trivial. It is useful to observe different solar regions (e.g., on-disc and off-limb spectra, as well as quiet-Sun and active regions) in order to assess line identifications (in particular the absence of blending) and the constancy of the calibration ratios. Also, one should select observations where the plasma has uniform density and is isothermal. This reduces any effects that inhomogeneities can have on the line ratios and allows the use of lines that are not strictly temperature- and density-insensitive.

It is recommended that, in the absence of any more direct techniques, future EUV spectrometers observe a sufficient number of 'calibration' lines which can be used to constrain the relative calibration of the spectral region(s) observed. Possibly, these 'calibration' lines should be formed in the corona, rather than in the transition region.

20.3 The CDS In-flight Calibration

In the case of CDS, the intercalibration studies that have been routinely run since the beginning of the mission are not sufficient to obtain a comprehensive calibration of all the CDS channels, since they were designed for another purpose and only few spectral lines were observed. Moreover, only a few reliable calibration line-ratios are observed in each spectrometer. The worst case is represented by the NIS; there is no good line-ratio that can be used for an accurate cross-calibration between NIS-1 and NIS-2. The in-flight cross-calibration of the NIS channels, therefore, requires that NIS and GIS observations are considered together. *Del Zanna et al.* [2001] described the full-wavelength GIS and NIS near-simultaneous observing sequences that have been designed and performed for the purpose of monitoring the CDS in-flight responsivity.

A large number of line-ratios useful for the CDS calibration has been identified and described in *Del Zanna* [1999] and *Del Zanna et al.* [2001]. In most cases, agreement with previous findings based on CHIANTI predictions and SERTS observations [*Young et al.*, 1998; *Del Zanna*, 1999; *Brosius et al.*, 1998b] has been found, although many more cases have been highlighted. Only a few examples are given below.

Among the brightest lines in the CDS spectra are the doublets, whose radiance-ratio in the optically-thin, collisional case equals two. Unfortunately, in most cases the doublets,

when observed by CDS, are blended with other lines. In the case of the Fe XVI (NIS-1, 33.54 nm and 36.0 nm lines), the line at 33.54 nm is blended, not only with a Mg VIII line, but also with an Fe XII [*Del Zanna*, 1999]. The Al XI, Ca X and Mg X doublets are also blended, but this time with transition-region lines. The doublets are free of blending only in off-limb spectra, where they become the strongest NIS-2 lines.

Transition-region (cool) lines are crucial for a relative calibration of the NIS-1 and NIS-2 channels. Most of the NIS-1 lines are coronal lines, but most of those observed by NIS-2 are formed in the transition region. So these two channels can only be cross-calibrated by use of GIS spectra, which record both transition-region and coronal lines.

The helium lines are a special case that deserves mention. Although the physics of the formation of the helium lines is still not understood [see, e.g., *Andretta and Jones*, 1997], the helium lines are extremely useful for calibration purposes. In fact, they are the brightest lines in the solar EUV spectrum, and their radiance ratios are exceptionally constant, independent of the part of the solar atmosphere observed. This remarkable (yet unexplained) characteristic of the helium lines is described in *Del Zanna et al.* [2001] but was already noted by *Andretta and Jones* [1997] using Skylab data [*Vernazza and Reeves*, 1978]: the lines of the He I series present constant radiance ratios against the 58.435 nm resonance line. The same applies to the ratio of the He I/He II resonance lines, which is also constant, independent of the solar region observed. For our use, the Skylab data of *Vernazza and Reeves* [1978] presented two serious problems. One problem was the low spectral resolution, which led to most of the helium lines being blended. Another problem was the uncertainty of the calibration, especially at shorter wavelengths, where the He II 30.378 nm resonance line is. Unfortunately, no accurate measurements of absolutely-calibrated He I and He II line intensities have been found in the literature, and the only set of well-calibrated values are indeed those reported in *Vernazza and Reeves* [1978], which in turn rely on a laboratory calibration and rocket flights. The CDS instrument, for the first time, overcomes these two problems. All the lines are well-separated. For example, the He II 30.378 nm line is well separated from the Si XI 30.33 nm resonance line. *Del Zanna* [1999] has analysed a large number of NIS-2 observations, and has confirmed that the He I line-ratios are indeed constant in the quiet Sun and coronal holes. The same applies to the He I/He II resonance-line ratio, with an average value measured by CDS of about 0.07. The CDS in-flight calibration found by *Del Zanna et al.* [2001] gives excellent agreement with the Skylab data for the He I 53.7/58.4 nm and He I/He II ratios, thus independently confirming the Skylab in-flight calibration. The results for the He I 53.7/58.4 nm ratio are also in excellent agreement with the rocket-flight results of *Brekke et al.* [2000], although not with the laboratory calibration.

20.4 Conclusions

I have reviewed some of the findings of *Del Zanna et al.* [2001] that can be of general use for the in-flight calibration of future EUV spectrometers such as those that will be flown on board Solar-B. Given the characteristics of the current EUV instruments, and the experience gained in the case of CDS, it is suggested that the calibration performed on the ground be reviewed and monitored with an in-flight calibration such as the one presented here. Long-term variations of the absolute calibration should still be checked against rocket flights which are calibrated on the ground against primary standards before and after the flight.

Acknowledgements

I would like to thank the CDS team (and in particular R. Harrison, C. D. Pike, W. Thompson, and J. Lang) for their support in the planning and operation of the instrument and for useful comments; also R.J. Thomas for stimulating discussions and H. E. Mason for continuous support and suggestions. Support from PPARC (UK) is acknowledged.

Bibliography

Andretta, V., and Jones, H.P., On the role of the solar corona and transition region in the excitation of the spectrum of neutral helium, *Astrophys. J.* **489**, 375, 1997.

Brekke, P., Thompson, W.T., Woods, T.N., and Eparvier, F.G., The extreme-ultraviolet solar irradiance spectrum observed with the Coronal Diagnostic Spectrometer (CDS) on SOHO, *Astrophys. J.* **536**, 959, 2000.

Brosius, J.W., Davila, J.M., and Thomas, R.J., Calibration of the SERTS-95 spectrograph from iron line intensity ratios, *Astrophys. J. Letters* **497**, L113, 1998.

Brosius, J.W., Davila, J.M., and Thomas, R.J., Solar active regions and quiet-sun extreme-ultraviolet spectra form SERTS-95, *Astrophys. J. Suppl. Ser.* **119**, 255, 1998.

Del Zanna, G., Extreme ultraviolet spectroscopy of the solar corona, PhD Thesis, University of Central Lancashire, 1999.

Del Zanna, G., Bromage, B.J.I., Landi, E., and Landini, M., Solar EUV spectroscopic observations with SOHO/CDS. I. An in-flight calibration study, *Astron. Astrophys.* **379**, 708, 2001.

Dere, K.P., Landi, E., Mason, H.E., Monsignori Fossi, B.C., and Young, P.R., CHIANTI: An atomic database for emission lines, *Astron. Astrophys. Suppl. Ser.* **125**, 149, 1997.

Harrison, R.A., Sawyer, E.C., Carter, M.K., Cruise, A.M., Cutler, R.M., Fludra, A., Haynes, R.W., Kent, B.J., Lang, J., Parker, D.J., Payne, J., Pike, C.D., Peskett, S.C., Richards, A.G., Culhane, J.L., Norman, K., Breeveld, A.A., Breeveld, E.R., Al Janabi, K.F., McCalden, A.J., Parkinson, J.H., Self, D.G., Thomas, P.D., Poland, A.I., Thomas, R.J., Thompson, W.T., Kjeldseth-Moe, O., Brekke, P., Karud, J., Maltby, P., Aschenbach, B., Bräuninger, H., Kühne, M., Hollandt, J., Siegmund, O.H.W., Huber, M.C.E., Gabriel, A.H., Mason, H.E., and Bromage, B.J.I., The Coronal Diagnostic Spectrometer for the Solar and Heliospheric Observatory, *Sol. Phys.* **162**, 233–290, 1995.

Lang, J., Kent, B.J., Breeveld, A.A, Breeveld, E.R., Bromage, B.J.I., Hollandt, J., Payne, J., Pike, C.D., and Thompson, W.T., The laboratory calibration of the SOHO Coronal Diagnostic Spectrometer, *J. Opt. A: Pure Appl. Opt.* **2**, 88–106, 2000.

Neupert, W.M., and Kastner, S.O., A spectroscopic method for calibration of solar extreme ultraviolet instrumentation, *Astron. Astrophys.* **128**, 181, 1983.

Thomas, R.J., and Neupert, W.M., Extreme ultraviolet spectrum of a solar active region from SERTS, *Astrophys. J. Suppl. Ser.* **91**, 461, 1994.

Thomas, R.J., Davila, J.M., Thompson, W.T., Kent, B.J., and Hollandt, J., The SERTS-97 cross-calibration of CDS and EIT on SOHO, *Bull. Am. Astron. Soc.* **31**, 850, 1999.

Vernazza, J.E., and Reeves, E.M., Extreme ultraviolet composite spectra of representative solar features, *Astrophys. J. Suppl. Ser.* **37**, 485, 1978.

Young, P.R., Landi, E., and Thomas R.J., CHIANTI: An atomic database for emission lines. II. Comparison with the SERTS-89 active region spectrum, *Astron. Astrophys.* **329**, 291, 1998.

V. Working Group Reports

— 21 —

Summary of Cleanliness Discussion: Where was the SOHO Cleanliness Programme Really Effective?

UDO SCHÜHLE
Max-Planck-Institut für Aeronomie
Katlenburg-Lindau, Germany

RON THOMAS
former ESA/ESTEC, Noordwijk, The Netherlands
private Whiteoaks, Monkmead Lane, West Chiltington, UK

BARRY J. KENT
Rutherford Appleton Laboratory
Chilton, Didcot, Oxfordshire, UK

FRÉDÉRIC CLETTE
Observatoire Royal de Belgique
Bruxelles, Belgium

JEAN-MARC DEFISE
Centre Spatial de Liège
Angleur-Liège, Belgium

JEAN-PIERRE DELABOUDINIÈRE
Institut d'Astrophysique Spatiale
Orsay, France

CLAUS FRÖHLICH
Physikalisch Meteorologisches Observatorium
World Radiation Center
Davos, Switzerland

LARRY D. GARDNER, JOHN L. KOHL
Harvard-Smithsonian Center for Astrophysics
Cambridge, MA, USA

JEAN-FRANÇOIS HOCHEDEZ
Observatoire Royal de Belgique
Bruxelles, Belgium

J. DANIEL MOSES
Naval Research Laboratory
Washington, DC, USA

The working group on cleanliness has been formed to recapitulate for each instrument the measures taken during the SOHO cleanliness programme and their effects. U. Schühle, together with B. Kent and R. Thomas, has collected the individual instruments' input to a catalogue of questions reviewing their efforts and experience. Thus, an open and straightforward discussion of the cleanliness issues for the individual instruments is presented. The actions during design and assembly as well as experience in-flight are summarized and commented with hindsight. Special emphasis has been given to the phase of extreme conditions during SOHO's loss-of-attitude.

21.1 Introduction

The somewhat provocative question in the title of this report did generate discussion and promoted input from the experimenters of all SOHO instruments represented at the Workshops.

The cleanliness programme within the SOHO project was a common effort of ESA and the SOHO experimenters. The goal was to ensure stable radiometric performance of the spacecraft and, in particular, of all instruments during the SOHO mission. Thus, cleanliness requirements had to be defined for instruments and spacecraft (the latter mostly based on the requirements set by the instruments), and, since each experiment on SOHO was sensitive to contamination in a different way, it was necessary to define cleanliness requirements for the individual instruments. This resulted in a "Cleanliness Control Plan" that governed all activities related to cleanliness and contamination.

The performance of the instruments during scientific operation proves that the cleanliness effort was effective, and, by tracking changes in responsivity over the mission duration, it can now be shown quantitatively how effective it was.

During its discussions, the Cleanliness Working Group (whose composition was identical with the authors of this report) tried to collect the experimenters' experience in reducing – and, as it turned out, nearly eliminating – degradation of the radiometric performance by cleanliness control. The experiment and spacecraft representatives were invited to "tell their story" about the specific measures for contamination control that later were successful in reducing radiometric degradation. The period of SOHO's loss-of-attitude has, however, affected some of the experiments, and the inferred degradation mechanisms were included in our discussions.

For the benefit of future space missions, and as a means to gather as much information as possible from all parties involved, the PIs of the relevant experiments have been asked to state

- where their instrument cleanliness programme was most effective,
- which design features they had used to improve cleanliness,
- how they had derived and implemented their cleanliness requirements, and
- how they had monitored and verified cleanliness.

21.2 Cleanliness Measures, as Viewed by Experimenters

The following is a compilation of the various responses received. We are reproducing them here without modification in order to provide proof of all the information available.

21.2.1 CDS

A) Where was the cleanliness programme really effective?

Instrument design features

Instrument design is central to contamination control.

- The optics bench was configured as a complete metal enclosure containing only metal support structures and optical components – with two well-considered exceptions.
- The entrance apertures to the telescope and thence the rest of the optics were controlled by doors, to prevent ingress of contaminants during ground assembly and in-flight thruster firings.
- The only mechanism that required lubrication inside the optical bench was the slit-scan mechanism lead screw which used a burnished dry lead film.
- The scan-mirror drive could be operated outside the optical bench and was driven through a labyrinth seal. Flexibility was provided by unlubricated flexural pivots.
- All electronics were outside the optical bench. The grazing-incidence spectrometer detector pre-amplifiers and high-voltage units accessed the detectors via sealed feedthroughs.
- Purge systems used during assembly and spacecraft integration used clean, dry gas delivered to the cleanest volumes first.
- Quartz crystal microbalances (QCM) at ambient temperature were installed to monitor deposition on optics.
- Vent ports were fitted with labyrinth seals.
- A sacrificial dust-cover, fabricated from Kapton, was used during spacecraft integration, and was removed during red tag item removal.

Were cleanliness requirements defined for the instrument sub-assemblies, optics, detectors?

- Each element of the optical chain had a contamination budget which defined allowed levels of molecular and particulate contamination at designated phases of the programme (integration, post-delivery and end-of-life).
- In addition, each type of system (for example electronic, structure, mechanism, cable) and each material (for example Al alloy, elastomer, electronics board) had a designated cleaning procedure which included a vacuum bake with a required final partial-pressure limit for organics.

What were the bases for these definitions?

- Optical modelling was used to estimate the contamination that resulted in a 10 % loss in performance. This was used as the end-of-life budget for molecular contamination. However, these programmes had to be used with caution as they were based on the rather unrealistic case of modelling with smooth, uniform layers of contaminant for which the refractive index was known. For hydrocarbons the refractive index values (n and k) for carbon and polythene were used.
- Molecular transport calculations using ESABASE software were carried out to supplement optical modelling, and to indicate potential problem areas.

- The allowable reduction in performance due to particulates was determined on scientific grounds, such as loss of throughput due to absorption, loss of contrast due to scattering. This resulted in a budget for surface obscuration by particles for each optical element. The time required to meet such surface cleanliness levels in a cleanroom of a given class was given by a series of curves calculated by U. Schühle (see report of the SUMER group) and these curves were used to define procedure times and cleanroom conditions.

What measures were taken to satisfy these requirements?

- All materials used in any part of the CDS instrument were subjected to a screening process which included an outgassing measurement.
- All components were precision cleaned by use of a procedure developed in-house which had been verified using X-ray photo-electron spectroscopy (XPS).
- Component cleaning included a vacuum bake at pressures of ≈ 100 μPa for at least eight hours at a temperature appropriate for that component (e.g., 60 °C for electronics and 100 °C for structural components made out of Al alloy).
- Following the vacuum bake, parts were transferred to heat-sealed clean bags and then opened only in a clean assembly area.
- CDS was assembled in a Class 100 cleanroom, which had been independently verified by the CDS science team.
- The number of staff members in the cleanrooms was controlled based on experience gathered during build of the engineering model (EM). Cleanroom clothing, especially gloves, were verified to be adequate.
- The CDS team was given frequent briefings on the importance of cleanliness.

How were these measures verified?

- The cleanrooms were monitored for particulates by facility staff and independently by CDS contamination control staff.
- Particulate fall out (PFO) plates were used to monitor the cleanroom environment and the surfaces of the instrument. PFO plates were monitored weekly and monthly.
- Vacuum chambers were monitored with high-sensitivity (10 pPa) residual gas analysers and gold-on-glass witness mirrors which were inspected by XPS measurements.
- The cleanroom environment was monitored with aluminium-on-glass witness mirrors which were inspected by infrared reflectance spectrometry.
- All facilities for vibration, thermal vacuum and calibration were subject to a cleanliness audit immediately prior to and during CDS tests.
- The complete instrument was thoroughly inspected using an ultraviolet lamp (black light) and a bright, white-light source.

B) Would you make any changes with respect to cleanliness control for a future similar instrument?

In general the control procedures taken on CDS worked well. The engineering model was a useful test of these and some things were changed as a result of that experience. So a potential change is that the very large overhead associated with contamination control early in the programme needs to be recognized.

C) Would you look for changes at spacecraft level for a SOHO II? If so, which?

This also worked well; the formation of the Contamination Control Board, in particular, provided a spacecraft-wide view of contamination. It is our impression that the spacecraft contractor was not aware of the importance of contamination control as early as the experiments; once they were aware, this was reasonably well-controlled.

D) How was the stability of calibration affected by contamination?

CDS responsivity remained constant until the loss-of-attitude after almost three years of operation. This indicates that none of the optical surfaces was compromised by contamination effects. The on-board QCM's in the NI and GI spectrometers indicated an integrated contaminant load of up to 10 ng cm^{-2} and 50 ng cm^{-2}, respectively, until this time.

E) Evidence for performance changes in flight with explanation:

Until the loss-of-attitude at the end of 1998 there was no change in CDS operating parameters. However, following the recovery from attitude loss, during which CDS was exposed to temperatures in excess of 100 °C for up to three months, some changes have been observed.

The QCM in the normal-incidence spectrometer (NIS) saw a post-recovery contaminant load of ≈ 120 ng cm^{-2} and the QCM in the grazing-incidence spectrometer (GIS) recorded ≈ 440 ng cm^{-2} after recovery. The responsivity of the normal-incidence spectrometer channel 1 (NIS-1) (short wavelength) had decreased by a factor of 1.45 (to be confirmed). The wavelength range of NIS-1 had shifted to longer wavelengths by about 0.05 nm. The responsivity of NIS-2 in first order remained unchanged. The responsivity of NIS-2 in second order, however, had decreased by 15 % (to be confirmed). The NIS-1 spectral-line shapes, which, prior to the accidental loss-of-attitude, were essentially Gaussian profiles now have large, extended wings.

These changes are consistent with a layer of contamination deposited on the NIS gratings as recorded by the QCM. The wavelength shift in NIS-1 is believed to be due to a small mechanical shift in the grating.

21.2.2 EIT/LASCO

A) Where was the cleanliness programme really effective?

Instrument design features

The main design features which addressed the cleanliness issues were:

- The selection of proper materials (all-metal structure, mechanisms and coatings).

- The isolation of the camera electronics in a separate enclosure, outside the optical section, which, itself, was designed as a vacuum tank for the protection of filters during SOHO launch.
- The inclusion of venting ports. However, due to the requirements of an airtight enclosure, there was limited venting at the back of the instrument, in particular in the camera section.
- A front door, which was airtight (EIT was put under internal vacuum during the integration and launch phases).

Were cleanliness requirements defined for the instrument sub-assemblies, optics, detectors?

For the EIT experiment, the molecular contamination was the prime concern. Indeed, the cooled CCD sensor is acting as a very efficient trap for contaminants. Any ice or organic deposit on the detector absorbs EUV radiation very efficiently, leading to a long-term degradation of the instrument efficiency and thus making any in-flight radiometric calibration difficult to achieve.

What were the bases for these definitions?

The cleanliness requirements used for EIT are given hereafter:

Particle fall-out

The total allowed particle fall out for the EIT instrument was equal to an obscuration (surface coverage) factor of 8×10^{-4}. This total amount was distributed as follows:

- environmental tests (on-ground): 2×10^{-4},
- assembly and integration: 1×10^{-4},
- optics manufacturing and mounting: 1×10^{-4},
- tests at spacecraft level: 1×10^{-4},
- launch phase: 3×10^{-4},

Airborne contamination

When the door was open and the instrument exposed to air contamination, the instrument was held in cleanroom Class 300 (FED-STD-209D).

Molecular contamination

EIT's components, CCD Camera and computer were built and handled to the same cleanliness specifications as LASCO. The maximum allowed molecular contamination before launch was a thickness of 2.5 nm of any type of contaminant on filters, mirrors and detector. This corresponds to a maximum level of 250 ng cm $^{-2}$ of any type of contaminant. Detailed specifications are given in Table 21.1.

What measures were taken to satisfy these requirements?

Coatings and materials have been chosen in accordance with the above requirements. All tests and calibrations were carried out in Class 100 cleanroom environment. The contamination was monitored during the entire period of integration of the experiment by use of a witness mirror which was fixed on the internal side of the front door of the telescope.

Table 21.1: EIT/LASCO contamination control specifications per MIL-STD-1246B (in nm).

Component	Assembly	Integration	Pre-launch	On-orbit	End of Life
CCD	2.5	2.5	2.5	5.0	5.0
Internal Surfaces	5.0	5.0	5.0	10.0	10.0
External Surfaces	20.0	20.0	20.0	20.0	20.0

Once on the spacecraft, EIT was kept permanently under vacuum to protect its internal filters during the launch. This prevented any additional contamination until SOHO was in space. Information about the calibration and test setups can be found in *Delaboudinière et al.* [1995], *Song* [1995], and *Defise* [1999].

How were these measures verified?

Besides the analysis of the witness mirror, the EIT approach was based on the stringent control of material selection and of cleanliness procedures.

B) Would you make any changes with respect to cleanliness control for a future similar instrument?

- Based on the experience with EIT (see below), carefully considered requirements should be introduced to ensure that instruments are kept sealed long enough after launch so that proper outgassing of the spacecraft is achieved.

- Regarding the instrument design itself, it is highly probable that contaminants would have been driven off much more rapidly without the confinement in the camera section. Adequate escape paths should be included in future designs, either between the different instrument sections or towards the outside.

C) Would you look for changes at spacecraft level for a SOHO II? If so, which?

No.

D) How was the stability of calibration affected by contamination?

A steady decrease of the overall instrument responsivity started as soon as the instrument door was opened in space, with the CCD sensor operated at its nominal temperature (-68 °C), in January 1996. Subsequent CCD bakeouts restored the responsivity only in part. Starting in the summer of 1996, a non-uniform degradation of the sensor was detected. The degradation pattern formed a negative image of the average Sun, suggesting that it was due to the accumulated dose of EUV radiation at the focal plane. Those effects affected strongly the in-flight calibration and flat-field determination.

E) Evidence for performance changes in flight with explanation:

The current understanding of the processes affecting the EIT response is as follows:

- Two components contribute to the degradation: internal charge-collection efficiency losses (CCE) in the CCD sensor and absorption of EUV radiation by deposited contaminants. The first effect is independent of contamination issues.

- Both above mechanisms had similar importance before the spring of 1998, but the CCE effect seems to account for all further degradation afterwards.

- EUV flat-field images obtained in March to April 1996, before the first CCD bake-out, show the distinctive patterns of ice crystals. This provides additional support to the general hypothesis that a thick ice layer, well above the 5-nm specification, was deposited on the CCD chip right after launch. This might be associated with the premature opening of the EIT launch lock.

- Although the bulk of the contamination can be identified as water ice, part of the degradation might be due to organic contaminants which polymerized on the detector under the action of EUV radiation. This deposit cannot be driven off efficiently by subsequent bakeouts.

- In the first part of the mission, even short one-hour bakeouts produced a strong recovery which was followed by a quick decay of the responsivity. After mid-98, bakeouts have a much more limited effect. A slow and steady decay is then observed.

- The above behaviour suggests that contaminants were trapped inside the camera section, because this volume was largely closed, with few paths for particles to escape through the optical section of the telescope (Al filter on front of the CCD, two small vents, optically obstructed, to avoid stray light). Therefore, during bakeouts, contaminants were driven off but remained in the immediate vicinity of the CCD, and they then quickly re-deposited on the cold CCD sensor surface.

- We surmise that trapped contaminants have been entirely released out in 1998 due to enhanced internal heating of the telescope. The cause is still unclear: sudden increase of the pinhole area in the front Al filters, allowing more visible light to enter the telescope tube, or the abnormal heating associated with SOHO's loss-of-attitude.

21.2.3 SUMER

A) Where was the cleanliness programme really effective?

Instrument design features

Most effective was a design for cleanliness. Many features of the instrument design have been implemented for cleanliness reasons. Below is a list of these design features and the reasons for their implementation (in parentheses):

- Clean metal optical housing (i.e., no organic composite material in optical compartments).

- Aperture door to close/open the optical compartment (to reduce ingress from outside).

- A window, which blocked UV, as part of the aperture door (to keep the primary mirror at highest temperature by insolation).
- Solar wind deflector plates (with high voltage applied to deflect solar wind away from the telescope mirror).
- Use of ultra-high vacuum components/materials inside optical housing (high-T materials).
- Avoid organic material inside optical compartments (to minimize potential outgassing).
- Keep primary mirror at highest temperature by solar illumination (to reduce deposition on sensitive surfaces).
- Dry lubrication on MoS_2 basis for all mechanisms (inorganic lubrication, no outgassing).
- Use flexural metal pivots instead of bearings where possible (no lubrication needed).
- Keep electronic components outside optical compartments to keep organic materials away from optics. For example, detectors were sealed around their front faces to keep their rear-sides isolated from the optics.
- Large venting ports for all subsections of the optical compartments (for efficient venting).
- Plasma and straylight barriers at venting ports (to avoid ions getting inside spectrometer).
- Purging of optical compartments at all times (to overpressurise and clean away offgassing species).
- Spring-loaded aperture door (as venting port, but loaded to keep overpressure).

Were cleanliness requirements defined for the instrument, sub-assemblies, optics, detectors?

Cleanliness requirements were defined and were applicable for all flight hardware. Contamination modelling calculations resulted in different requirements for optics, detectors, and other sub-assemblies. All cleanliness requirements have been calculated by modelling the degradation due to all possible types of contamination and degradation effects that could be expected during exposure to solar EUV irradiance and solar-wind particles, self-contamination by dust particles and outgassing organic condensables, as well as effects of a combination of these.

What were the bases for these definitions?

The basis for the determination of a cleanliness requirement was the acceptable performance degradation throughout the entire mission that was caused by all possible contamination sources. A loss of 15 % of the reflectivity of each mirror was set as a limit of acceptable performance loss. This would result in about 50 % overall loss of responsivity, and determined the level of molecular contamination inside the optical compartment. The obscuration effect by particles on each mirror was not considered to be of driving

importance, because the effect of scattering was more stringent: the scientific objectives of SUMER required that the scattered intensity from the telescope mirror must be below 1×10^{-5} at an angle of $2'$.

With respect to calibration stability, molecular contamination was regarded as the major concern. Normal-incidence mirrors are more affected than grazing-incidence mirrors. A normal-incidence grating is also affected the most by a contaminating layer, because not only is the reflectivity degrading but so too is the diffraction efficiency. Mirrors were identified as the most sensitive surfaces of the SUMER instrument. To derive the amount of contamination that could be tolerated, it was assumed that any organic material of sufficient thickness on a mirror would lead to an attenuation of the reflected beam. Also taken into account was the fact that the effect of organic contaminants may be dramatically enhanced when the surface is exposed to solar ultraviolet radiation when photo-chemical reactions lead to polymerization of deposited material. Some time ago this was identified as the prime degradation process of optical instruments in space which are exposed to solar UV radiation.

To confirm quantitatively theoretical model predictions, experimental studies have been performed by contaminating mirror samples in vacuum while monitoring the amount of contamination and intermittent measurements of the reflectivity. As a result, a tolerable contamination layer of 60 ng cm^{-2} (of material with a uniform density of 1 g cm^{-3}) was specified to stay within the budget set by the requirements mentioned above.

In addition, irradiation by solar wind particles (protons and α particles) may contribute to the polymerization process, although at a much smaller rate, since their flux is much smaller than the UV flux. However, the radiation damage due to this particle bombardment, which was investigated in an experimental simulation, led to a visible alteration of the surface, presumably associated with a roughening of the surface profile with degrading effects on the scattering properties of the mirror. Thus it was concluded that for SUMER a solar-wind deflector was needed.

With regard to particulate contamination, a theoretical calculation was made to study the amount of obscuration and scatter caused by accumulated dust particles on the telescope mirror. The level of cleanliness of a surface is characterized by a particle size distribution according to MIL-STD-1246B. Our calculation, therefore, modelled the effect of opaque, spherical particles with a size-distribution given by MIL-STD-1246B and giving rise to an angular scattering distribution derived by Fraunhofer diffraction theory. The number of particles larger than a given size can be plotted as a function of this cleanliness level. This is shown in Figure 21.1.

The angular distribution of radiation scattered by Fraunhofer diffraction was calculated with the given particle size distribution. At very small angles, any particle size contributes to the scattering and, as a result, the scattering level is approximately given by the obscuration factor. Thus, from Figure 21.2, the cleanliness level which must be achieved for a given straylight specification can be derived.

In order to comply with the requirements given above, the surface cleanliness level of the optical compartment of the instrument was specified. All surfaces inside the SUMER instrument had to be compliant with a cleanliness Level 200 (according to MIL-STD-1246B). Under the assumption of a dust settlement function in cleanrooms (a result of empirical studies in cleanrooms found by *Buch and Barsch* [1987]), the exposure time of mirrors in cleanrooms could be calculated for different air-cleanliness classes. The result

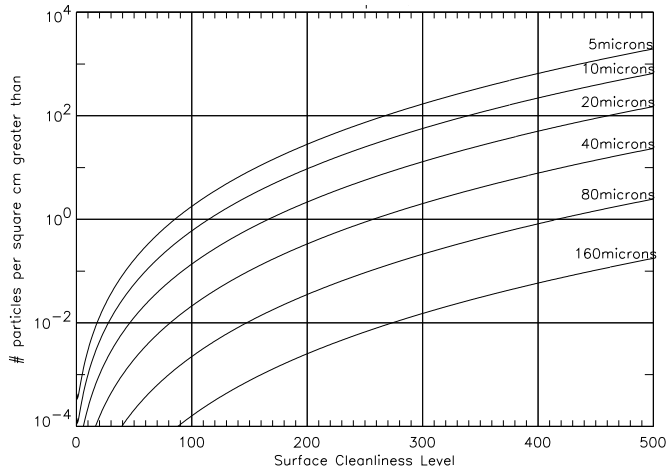

Figure 21.1: Number of particles equal to or larger than a given size versus Surface Cleanliness Levels of MIL-STD-1246B.

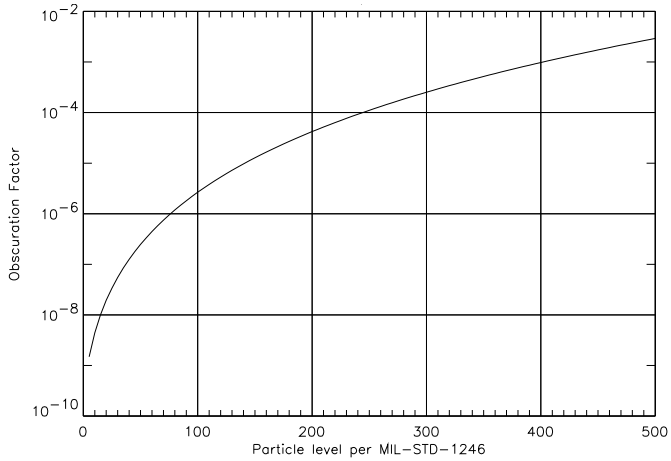

Figure 21.2: The obscuration factor versus Surface Cleanliness Level. The area is obscured by the particle distribution of MIL-STD-1246B.

is shown in Figure 21.3 for cleanroom classes between Class 10 and Class 100 000. It can be used to help decide which class of cleanroom is needed for the project.

What measures were taken to satisfy these requirements?

To stay within the contamination budget, which was extremely tight for those surfaces of the instrument that are inside the optical compartment, strict rules for the flight hardware had to be implemented. Measures implemented to maintain cleanliness were:

- Material and component selection: materials that are high-vacuum compatible, or stable at high temperatures, were preferred; no plasticizers were allowed.

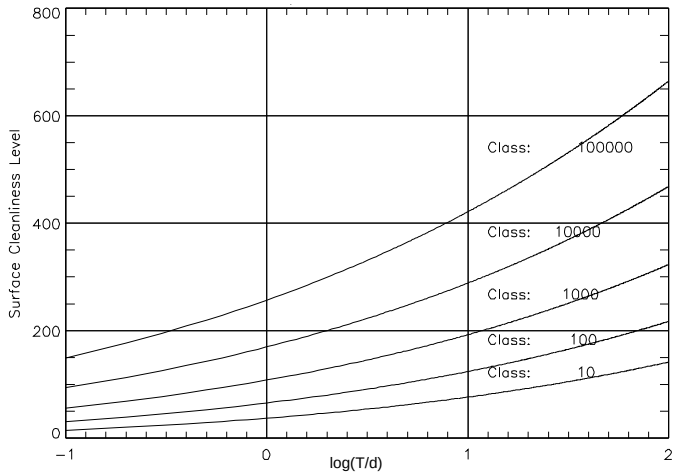

Figure 21.3: Surface Cleanliness Level (of MIL-STD-1246B) versus time of exposure in laminar flow cleanrooms of Classes 10 to 100 000 (FED-STD-209D).

- Outgassing tests of all components that contained organic parts: components had been subjected to detailed outgassing tests at increasing temperatures, including chemical identification of outgassing species. If the component was found to be acceptable, the conditioning procedure (bake-out temperature and time) was derived from this test.
- Precision cleaning of all flight hardware: cleaning procedures have been written for different types of hardware according to their compatibility with cleaning solvents.
- Vacuum baking and purging cleaning of all parts and components after cleaning: after they had been cleaned, all components were placed in a vacuum oven with an oil-free roughing pump (membrane pump) and purged with dry, clean gaseous nitrogen during the baking process. This turned out to be more effective than high-vacuum baking.
- Cleanroom facility (Class 100): the time of exposure of optical parts in the cleanroom during integration and alignment tests made the use of a Class 100 cleanroom a requirement. Such a cleanroom was used for the integration of all flight hardware components.
- Charcoal-filtered cleanroom air: the air circulation system of the cleanroom was equipped with charcoal filters to avoid organic contaminants in the cleanroom air.
- Oil-free pumping systems for test and calibration systems: all vacuum systems had oil-free pumps.
- Packaging in clean bags: hardware was always packed in cleanroom bags for storage.
- Purging of the instrument whenever possible with dry N_2 (Grade 5.0, corresponding to a relative purity of 99.999 %).

How were these measures verified?

A variety of control and verification methods had to be used:

- Particle counters in all cleanroom areas.
- Inspection with bright UV lamp and white-light spot beam. The UV black light lamp was very useful for detecting fluorescing dust. Flakes or chips of metal, which do not fluoresce under UV light, were detected by use of a bright white-light spot under grazing incidence.
- Microscopic inspection of incoming or cleaned hardware. A UV black light was used for visual inspection and detection of dust particles on surfaces.
- PFO monitor plates used as witness plates in cleanrooms/benches. The surface coverage of the monitor plates can be evaluated by a PFO-meter.
- Use of witness mirrors and verification by IR analysis.
- QCM monitors were used in vacuum test chambers.
- Verification of surface cleanliness level by particle counts using tape-lift-sampling (according to ASTM E 1216). The number of particles larger than a given size was counted under a microscope and compared to the chart in Figure 21.1.

B) Would you make any changes with respect to cleanliness control for a future similar instrument?

- Given the loss of responsivity experienced during the loss-of-attitude of SOHO (see point "E" below), there is no reason to relax the cleanliness requirements or descope any of the efforts.
- Intensify control and verification of material selection process.

C) Would you look for changes at spacecraft level for a SOHO II? If so, which?

For a PI-payload type of mission, intensify common material selection and screening. Make rough vacuum baking with dry pumps and purging mandatory for cleaning hardware.

D) How was stability of calibration affected by contamination?

The calibration turned out to be remarkably stable during the nominal mission time. There was no effect of contamination until a redistribution of contaminants occurred due to temperature excursions during SOHO's loss-of-attitude.

E) Evidence for performance changes in flight with explanation:

During the operation of the instrument in space, no degradation due to contamination could be detected, thus proving the effectiveness of the cleanliness efforts. After SOHO's loss-of-attitude, however, a loss of responsivity was found. We assume that the loss in spectral responsivity was as indicated in Table 21.2

Table 21.2: Relative responsivity loss after SOHO's loss-of-attitude, measured at several wavelengths:

He I 58.4 nm	26 %
Mg X 60.9/62.4 nm	28 %
N V 123.8 nm	39 %
Ne VIII 77.0 nm	34 %
H I Ly continuum 88.0 nm	29 %

These relative responsivity changes are thought to be due to residual contamination present inside the instrument; contamination apparently had been collected on cooler surfaces of the instrument structure during the preceding years. Following the loss of SOHO's attitude, the telescope mirror was the coldest surface, since it was not illuminated, while its radiator faced cold space. As a result, during this time, contaminants might have been driven off any surface that was heated while the Sun was hitting the spacecraft sideways, and these were probably collected on the cold mirror.

21.2.4 SEM

A) Where was the cleanliness programme really effective?

Instrument design features

The instrument was designed so that all electronics were completely separated from the spectrometer. Specifically, the electronics was located immediately under the optical bench in an enclosed box which could slowly vent to space but not toward the optical bench. Further, a shutter was kept in front of the solar-viewing aperture for several days so that the instrument could outgas without sunlight polymerizing any hydrocarbons that might have condensed on the thin-film filters in the optical train prior to spacecraft commissioning in flight.

Were cleanliness requirements defined for the instrument sub-assemblies, optics, detectors?

Cleanliness requirements were limited to storage of the instrument optical components in a dry-nitrogen atmosphere when they were not in use.

What were the bases for these definitions? What measures were taken to satisfy these requirements?

During calibration, all vacuum systems were oil free and during fabrication only clean benches and filtered, air-conditioned laboratories were utilized. The basis for the modest requirements was our previous experience in sounding-rocket missions where a comparison of pre-flight and post-flight calibration consistently showed insignificant changes in instrument responsitivity when the above procedures were followed. (With hindsight, the evidence gained from rocket flights may not have been entirely valid for the circumstances of a long-term spacecraft mission.)

How were these measures verified?

The programme manager verified that the above procedures were followed. No further checks were implemented until underflight calibration rockets were flown following the launch and commissioning of SOHO.

B) Would you make any changes with respect to cleanliness control for a future similar instrument?

No.

C) Would you look for changes at spacecraft level for a SOHO II? If so, which?

We do not believe we could practically improve our contamination control without the installation of a Class 100 clean room at the University of Southern California. The result would probably be of marginal value.

D) How was the stability of calibration affected by contamination?

It seems most likely that spacecraft outgassing has been the source of our observed (minor) degradation of instrument responsivity.

E) Evidence for performance changes in flight with explanation:

The changes in responsivity of the SOHO SEM instrument are consistent with the deposition of a contamination layer equivalent to the absorption of a total of 15.0 nm of carbon on our optical elements (aluminium thin-film filters) since the time our instrument was delivered for integration on the spacecraft until now (1 October 2001). This is rather little integral contamination since 1995, but its effect must be accounted for and the responsivity must be corrected accordingly, so that we can measure the absolute solar irradiance with an accuracy of 10 %. The sounding-rocket underflights have been necessary to continue to ensure this accuracy. The contaminant deposition rate has now slowed significantly, as has the change in instrument responsivity. Lower outgassing of the spacecraft and/or our instrument would evidently be helpful in reducing, or perhaps eliminating, noticeable contamination-induced responsivity changes. This assumes that the spacecraft test-chambers were not the source of apparent contaminant-driven responsivity changes.

21.2.5 UVCS

A) Where was the cleanliness programme really effective?

Instrument design features

The cleanliness programme was laid out in appropriate process-control documents that specified a total allowable quantity of chemical and particulate surface contamination, procedures for the cleaning of parts, allowable solvents and materials. The cleanliness requirements on UVCS were as follows:

- For the interior of the UVCS housing and all items internal to housing, non-volatile residue was to be < 100 ng cm^{-2} and particle count was to be $< 8 \times 10^4$ m^{-2} for sizes > 5 μm.

- For the exterior of UVCS housing and all items external to the housing, non-volatile residue was to be < 250 ng cm^{-2} and particle count was to be $< 9 \times 10^5$m^{-2} for sizes > 5 μm.

What were the bases for these definitions?

For our optics, the requirements were based on the allowable and expected UV absorption through, and UV induced polymerization of, the adsorbed layers. In addition, the particulate levels were controlled to a low level to minimize scatter of direct sunlight impinging on optical surfaces (e.g., the sunlight trap) within the instrument. For other surfaces it was based on models of outgassing, migration of material to the optical surfaces and subsequent photo-polymerization.

Certain components, such as detectors and the structure itself, required special attention. The UVCS structure was made of Graphite Fiber Reinforced Epoxy (GFRE), which had a non-negligible coefficient of moisture expansion. Thus it had to be kept very dry through a rigorous purging programme. A specification for total allowable moisture absorption and appropriate test and measurement procedures were developed. The detectors' photocathodes, which also are sensitive to moisture, were open to the ambient environment. Attempts at a continuous dry-nitrogen purge for them were made.

What measures were taken to satisfy these requirements? How were these measures verified?

To control particulate contamination, cleanrooms of Class 10 000 and cleanbenches of Class 100 within cleanrooms were used for all assembly work. The cleanroom air-handling systems typically used prefilters containing activated charcoal to remove hydrocarbons from the circulating air and thereby limit the deposition of volatile hydrocarbons. To minimize water absorption and moisture-induced degradation, humidity was controlled, and purging programmes were instituted as appropriate.

Special attention was paid to materials selection: only those with low or no outgassing characteristics were used whenever possible. In cases where there were no low- or zero-outgassing substitutes available, the quantities were limited and/or the material was enclosed or encapsulated to prevent or limit the outgassing. Attention was paid to design details. For example, no enclosed (and therefore uncleanable) volumes or voids were allowed in the UVCS structural elements. In addition, electronic subassemblies, which typically run "warm" and outgas plasticizers, were vented to the exterior of the UVCS instrument, away from optical surfaces.

Laboratory tests were carried out on the GFRE material. Samples of the material were heated and located in proximity to optical surfaces that were simultaneously illuminated with intense UV radiation. The UV reflectance of those optics was measured in situ as a function of exposure time to determine if the GFRE was emitting UV-absorbing material that was collecting on the (room temperature) optical surface. No change in UV reflectance of the test optics was found for tests of the material used for UVCS. Special care was taken with lubricants: in some assemblies (for example in cavities containing optical components) none was allowed. In other cases, only those that had very low vapour-pressures and did not contain silicone were allowed.

To drive off volatiles, cables and other parts were vacuum baked before installation. The instrument structure was vacuum baked several times primarily to drive out absorbed water, but this was effective in removal of other volatiles as well. The instrument was purged with dry nitrogen gas whenever it was not actively being assembled, tested, or

aligned. Frequent measurements were carried out of particle and molecular deposition onto witness plates that "traveled" with the instrument.

"Washes" of some subassemblies could be directly carried out. The rinses were then analyzed both to determine quantities of residue, both volatile and non-volatile, and, using infrared absorption techniques, to determine its identity. Temperature-controlled quartz-crystal microbalances (TQCMs) together with analysis of material deposited onto traps cooled by liquid nitrogen were used during vacuum exposures of component parts and the entire instrument to measure outgassing rates. The identity of the material deposited onto the traps was determined using infrared-absorption measurements. Reflectance measurements in the vacuum UV were carried out on the flight components themselves late in the programme.

Based on the findings, it was decided to replace the optical elements just before final assembly. The replacement occurred approximately ten months before launch. Finally, the instrument was allowed to outgas in flight for one month prior to solar-UV exposure. The idea was to allow absorbed moisture and other volatiles to escape to space before UV polymerization was possible.

B) Would you make any changes with respect to cleanliness control for a future similar instrument?

UV detectors would have doors and be actively pumped prior to launch. There would be time scheduled for changeout of optics immediately prior to final delivery.

The cleanliness control programme was generally successful. Consequently no part of it can be easily identified as "excessive" or "unnecessary".

C) Would you look for changes at spacecraft level for a SOHO II? If so, which?

Final delivery of instruments should be as close to launch as is possible. Optical components or subassemblies could then be changed out as necessary.

D) How was the stability of calibration affected by contamination?

The UVCS end-to-end calibrations were done in June of 1995. Based on component measurements as compared to end-to-end response, there was loss of quantum efficiency of a factor of two for the UVCS O-VI detector and a factor of four for the UVCS Ly-α detector. Purging of the open UV detectors was therefore only marginally successful.

In flight we have carried out observations of a number of stars and compared our intensity measurements, based on the June 1995 calibration, to those of other instruments on other spacecraft. In general, agreement within the estimated uncertainties has consistently been found. Many of these observations have been repeated on a yearly basis from the beginning of the mission. No changes have been observed. In addition we have compared co-temporal and co-spatial observations of the corona to those made by Spartan 201. Again, agreement within the uncertainty has been found.

Using the internal occulter to control the vignetting of the aperture, we have also carried out measurements of the response of UVCS as a function of unvignetted aperture. Again, except for perhaps the first 1 mm of mirror at its edge, no discernible changes in response have been found during the mission, or compared to component-level testing.

E) Evidence for performance changes in flight with explanation:

As mentioned above, repeated observations of the same stars (both before and after the accidental attitude loss), have been carried out. In general we have not seen discernible changes in UVCS response to those stars. Observation of interplanetary hydrogen Ly-α emission as a function of unvignetted aperture indicates no measurable change during the mission even though the mission-integrated light exposure to the mirrors has been very non-uniform (as is required by the coronagraphic occulting system). We therefore believe that the performance of UVCS is stable and essentially unchanged since its end-to-end test in 1995.

21.2.6 VIRGO

A) Where was the cleanliness programme really effective?

The approach of VIRGO was a pragmatic one, no verification but stringent control of measures:

- Very stringent requirements for materials selection.
- Degassing of all manufactured parts before assembly into sub-units or the experiment in vacuum at temperatures between 60 °C and 120 °C (depending on material, parts, etc.).
- Assembly of printed circuits in clean benches (before cleaning and degassing).
- Assembly of all sub-units and the experiment in a Class 50 000 cleanroom with charcoal filters (hydrocarbons rather than dust were the important issue).
- After assembly, purging with grade 6 N_2 (implying a relative purity of 99.9999 %) with lowest available amount of hydrocarbons.
- When leaving the cleanroom, purging was always maintained (during tests with the Sun and transportation to environmental tests, Assembly, Integration and Verification (AIV) etc.).
- Flooding at the end of the vacuum tests was always performed through the purging line.

B) Would you make any changes with respect to cleanliness control for a future similar instrument?

No.

C) Would you look for changes at spacecraft level for a SOHO II? If so, which?

No.

D) How was the stability of calibration affected by contamination?

Very much so. Compared to the EURECA (EUropean REtrievable CArrier) mission the Solar Photometer (SPM) degraded much less (the observed loss of responsivity after five years is still much less than on EURECA after nine months in space).

E) Evidence for performance changes in flight with explanation:

The loss of attitude influenced the radiometers in a way which is still not completely understood. However it is not an issue of cleanliness.

21.3 Comments on the Measures Taken for the Individual Instruments

21.3.1 CDS

Here the critically clean hardware was mounted inside the instrument's optical bench, with actuators mounted outside, and coupled to an internal movable mirror or slit by flexible couplings. The optical bench was purged with dry gas until launch to minimize ingress of contaminants. The shutter function was provided by a pair of doors mounted on the front face of the instrument exterior.

21.3.2 EIT

The evacuated telescope was a good choice for this experiment. External contamination thus was no threat to performance after assembly (apart from periods when the door had to be opened for functional testing). The low pressure was also imposed by the need to minimize stresses on the thin-film filters during launch.

The moderate vacuum was, however, a nuisance at spacecraft level, particularly once the spacecraft was integrated with the launcher. Also, the vacuum was not quite good enough to remove all effects of moisture on the detector performance.

A bad feature for cleanliness was the necessity for two actuators to drive filter wheels inside the telescope volume, because the windings and lubricants of the actuators are a likely source of molecular contamination. The CCD detector was moreover the coldest item within the telescope and the history of operations shows that periodic warming to $+30$ °C was necessary to restore performance. A higher bake-out temperature might have been beneficial.

21.3.3 LASCO

This instrument was less sensitive to molecular contamination since it was designed for visible light. This allowed the three telescopes to contain mechanisms with low risk of polymerising deposited outgassing beyond the first optical element since that blocked UV. The front surface of that element obviously was exposed to the full solar spectrum but was itself protected by the shutter door while outgassing materials on the Sun-facing side were limited in number and could be carefully selected. Continuous purging was applied.

21.3.4 MDI

As in LASCO, the first window of MDI limited transmission of short wavelengths (in fact to a 5-nm bandpass in red light) and, like CDS, MDI had an internal optical bench although this was mainly for thermal control. These measures limited the sensitivity to molecular contamination almost entirely to the front face of the entrance window and to the cold CCD.

21.3.5 SEM

SEM did suffer some performance loss as if acquiring a carbon deposit. This instrument was a late addition to SOHO's payload and was fitted in a non-ideal location looking along the surface of a thermal blanket with a poor view of space and so was warmer than is usual.

21.3.6 SUMER

SUMER elected to have two optical compartments. The first accommodates a primary mirror in full sunlight which as a consequence is quite hot (at 80 °C). The second contains a grating and two detectors, but these have low levels of illumination since there is a slit between the two compartments. The entrance door of the instrument has a window that transmits sufficient visible and infrared light to ensure that the primary mirror is at the highest temperature found in the instrument.

21.4 Concluding Remarks

In trying to eliminate the degradation of the radiometric responsivity of the SOHO instruments, a suitable design was paramount. The main measures taken by the larger (EUV) instruments were:

- Ensuring that optics were well separated from potential contamination sources,
- a careful selection of materials,

and before proceeding with the assembly:

- Vacuum baking of relevant items with monitoring of the outgassed products.

Instrument designers also attempted to budget for contamination effects though this is difficult to do with much confidence for the VUV, given the limited knowledge of the character of the deposited materials. This was a particularly delicate problem when the detector had an open (exposed) photocathode whose photo-electron emission could be modified by the deposition of extraneous materials.

More detrimental to the stability of calibration is the effect of scrubbing of the channel plates in the open detectors of SUMER and CDS. This makes continuous compensation for gain degradation necessary. Only with regular calibration comparison measurements (JOP Intercal_01) was this possible. For the SUMER detectors, the gain degradation led to untimely blindness because not enough high voltage was available from the electrical power

supply unit to compensate for all the decrease in gain. In future missions, such inherent instability of the channel plate detectors can only be avoided if channel plate detector heads are scrubbed under vacuum and kept sealed under vacuum by a cover which can be opened for calibration and mission deployment. Such a cover mechanism was originally planned for one of the SUMER detectors but fell victim to schedule constraints.

Venting of a detector compartment to a less critical one carries the risk that venting flows might reverse under some circumstances. This is avoided most easily by providing a positive purge gas flow from the optical compartment. An overpressure in the optical compartment can be supported, as it was done in SUMER, by sealing the detectors around the rim of their front faces.

CDS and SUMER stress that cleanliness control must be considered early in the programme and must be adequately funded. Materials selection can consume much test time before selection can be confirmed. A common test programme might be valuable even before instrument phase B commences. This is supported by the answers to the question about spacecraft improvements.

With the exception of the consequences of the period when attitude control was lost and large temperature excursions occurred in most experiments, the radiometric responsivity of the SOHO instruments was essentially stable in flight. The measures taken to maintain a clean spacecraft and clean instruments have been very successful.

Acknowledgements

The authors are grateful to M.C.E. Huber and C.D. Pike for useful suggestions and editorial support.

Bibliography

Buch, J.D., and Barsch, M.K., Analysis of particulate contamination buildup on surfaces, *Proc. SPIE* **777**, 43–54, 1987.

Defise, J.-M., Analyse des performances instrumentales du télescope spatial EIT, PhD Thesis, Univ. de Liège, 1999.

Delaboudinière, J.-P., Artzner, G.E., Brunaud, J., Gabriel, A.H., Hochedez, J.F., Millier, F., Song, X.Y., Au, B., Dere, K.P., Howard, R.A., Kreplin, R., Michels, D.J., Moses, J.D., Defise, J.M., Jamar, C., Rochus, P., Chauvineau, J.P., Marioge, J.P., Catura, R.C., Lemen, J.R., Shing, L., Stern, R.A., Gurman, J.B., Neupert, W.M., Maucherat, A., Clette, F., Cugnon, P., and van Dessel, E.L., EIT: Extreme-ultraviolet Imaging Telescope for the SOHO mission, *Sol. Phys.* **162**, 291–312, 1995.

Song, X.Y., Caractérisation et étalonnage radiométrique du télescope solaire EIT à l'aide du rayonnement synchrotron (entre 10 et 100 nm), PhD Thesis, Univ. Paris-Sud, IAS, Orsay, 1995.

— 22 —

CDS and SUMER Intercalibration Working Group Report

ANUSCHKA PAULUHN
International Space Science Institute
Bern, Switzerland

JAMES LANG
Rutherford Appleton Laboratory
Chilton, Didcot, Oxfordshire, UK

UDO SCHÜHLE, KLAUS WILHELM
Max-Planck-Institut für Aeronomie
Katlenburg-Lindau, Germany

C. DAVID PIKE
Rutherford Appleton Laboratory
Chilton, Didcot, Oxfordshire, UK

PHILIPPE LEMAIRE
Institut d'Astrophysique Spatiale
Unité Mixte CNRS-Université
Université de Paris XI, Orsay, France

WILLIAM T. THOMPSON
L3 Communications Analytics Corporation
NASA Goddard Space Flight Center
Greenbelt, MD, USA

GIULIO DEL ZANNA, HELEN E. MASON
Department of Applied Mathematics and Theoretical Physics
University of Cambridge, Cambridge, UK

TOM N. WOODS, RYAN KEENAN
Laboratory for Atmospheric and Space Physics
University of Colorado, Boulder, CO, USA

J. LEN CULHANE, CARL R. FOLEY
Mullard Space Science Laboratory, University College London
Holmbury St Mary, Surrey, UK

JÖRG HOLLANDT
Physikalisch-Technische Bundesanstalt
Berlin, Germany

ISABELLE RÜEDI
Physikalisch Meteorologisches Observatorium
World Radiation Center
Davos, Switzerland

MARTIN C.E. HUBER
International Space Science Institute
Bern, Switzerland

ROGER J. THOMAS
NASA Goddard Space Flight Center
Greenbelt, MD, USA

During the entire SOHO mission the performance of both the CDS and SUMER instruments has been well monitored, and additionally their intercalibration programme has been realised thoroughly. Therefore, special emphasis has been set on the discussion and refinement of the results of the CDS-SUMER intercomparison. During the workshops, and beyond in several individual teams, known problems and questions were brought forth, new ideas were discussed, corresponding action items were formulated and their results evaluated. The following gives a short summary of the main elements of the group's work.

22.1 Introduction

The aim of the CDS-SUMER splinter group is to identify and discuss questions and future work to complete the intercalibration between the two instruments. Intercalibration between CDS NIS-2 and SUMER detectors A and B based on the Intercal_01 measurements has been published in *Pauluhn et al.* [2001]. Among the topics and questions discussed in the working group were

- possible instrumental effects, especially for He I where the discrepancy between the instruments was largest,
- intensity dependent effects,
- variability of He I with the solar cycle,
- CDS wide slit burn-in correction,
- cross-check of the CDS GIS-4 calibration by comparison with SUMER at 77.0 nm,
- responsivity changes after SOHO's loss of attitude.

22.2 Instrumental and Data Processing Effects

In order to check that the CDS data had been correctly processed, taking into account the most recent flatfield corrections, all CDS Intercal_01 data were reprocessed independently. No significant differences were detected apart from the last data point which had been burn-in corrected twice. This lead to a downward correction of the corresponding CDS intensities bringing it into better agreement with SUMER.

Although the wide slit burn-in correction to the flatfield procedure had been correctly implemented for the Intercal comparisons with SUMER, this effect had not been taken into account for the comparisons of irradiance in the work of *Brekke et al.* [2000] which was used to determine the CDS responsivity calibration. Application of this correction has resulted in a new CDS NIS calibration (Version 4). At 58.4 nm this increased the CDS responsivity by 15 %, bringing the measurements into better agreement with SUMER. (The responsivity increase for the other wavelengths was smaller and amounted to 12 %, 7 %, and 4 % at 60.9 nm, 62.4 nm, and 63.0 nm, respectively.) Table 22.1 shows the comparisons of the measurements as published in *Pauluhn et al.* [2001] and as obtained implementing the above corrections. The relative differences of CDS and SUMER for the post-recovery period (last two columns of Table 22.1) have been calculated using the

Table 22.1: Average relative differences between the CDS and SUMER time series (CDS-SUM)/CDS (in %). Shown are the values as obtained with the old calibration (CDS Version 3 and SUMER `epoch_7`) and the newest calibration (CDS Version 4 and SUMER `epoch_9`), old $\Longrightarrow$**new.**

wave-length / nm	Mar96–Aug96 (I)	Sep96–Jun98 (II)	Nov98–Jul00 (III) SUM corr. wl dep.	Nov98–Jul00 (III) SUM factor 1.45
58.4	33 $\Longrightarrow$ **23** $\pm$5	38 $\Longrightarrow$ **28** $\pm$9	43 $\Longrightarrow$ **33** $\pm$5	39$\Longrightarrow$ **28** $\pm$5
60.9	7 $\Longrightarrow$**–13** $\pm$8	2 $\Longrightarrow$**–12** $\pm$11	0 $\Longrightarrow$**–19** $\pm$18	–7 $\Longrightarrow$**–22** $\pm$18
62.4	16 $\Longrightarrow$ **–7** $\pm$9	9 $\Longrightarrow$ **0** $\pm$16	5 $\Longrightarrow$**–11** $\pm$12	–6 $\Longrightarrow$**–24** $\pm$11
63.0	–	–	–4 $\Longrightarrow$**–17** $\pm$19	–15 $\Longrightarrow$**–30** $\pm$19

individual wavelength dependent correction factors (as given in *Schühle et al.* [2001]) as well as the average correction factor over all wavelengths resulting in an average loss of efficiency of 31 % for the SUMER detector (as used in `radiometry.pro`).

Effects of blending from unidentified lines were discussed, particularly in relation to the O V line at 63.0 nm. For SUMER, this could most probably be excluded after repeated inspection of the line spectra and as measurements made on the different detector parts (bare and KBr) had indicated before.

22.3 Intensity Dependent Effects

To search for intensity dependent effects, the highest and lowest 20 % of each image taken in Intercal_01 have been compared separately. The difference between CDS and SUMER intensity measurements was found to be greater in the lower intensities by about 10 to 15 %. Degrading the SUMER images to CDS resolution (see *Pauluhn et al.* [1999]) explained the differences.

22.4 Variability of He I with the Solar Cycle

One possible calibration technique for tracking the degradation of the SOHO instruments is the observation of quiet Sun regions on a regular basis because it has been thought that the quiet Sun radiance could have a constant value, independent of the 11-year solar cycle activity. However, *Schühle et al.* [2001] report for the SUMER quiet Sun calibrations that the quiet Sun radiances appear to have significant 11-year solar cycle variability. They show for the quiet Sun observations during the SOHO mission that the coronal and transition region emissions have about a factor of two increase at solar maximum and that the chromospheric emissions have less variability. Are these SUMER quiet Sun variations real quiet Sun variations, could instrument artifacts affect the measured quiet Sun variations, or could active network be contaminating the region considered to be quiet Sun? *Schühle et al.* [2001] studied the effects of instrument degradation and conclude that the quiet Sun variations, measured at several different wavelengths, are not likely to be related to any known instrument artifacts.

To study any possible contribution of active network to the quiet Sun measurements in the Intercal_01 data, EIT 30.4 nm images at the corresponding raster image positions were

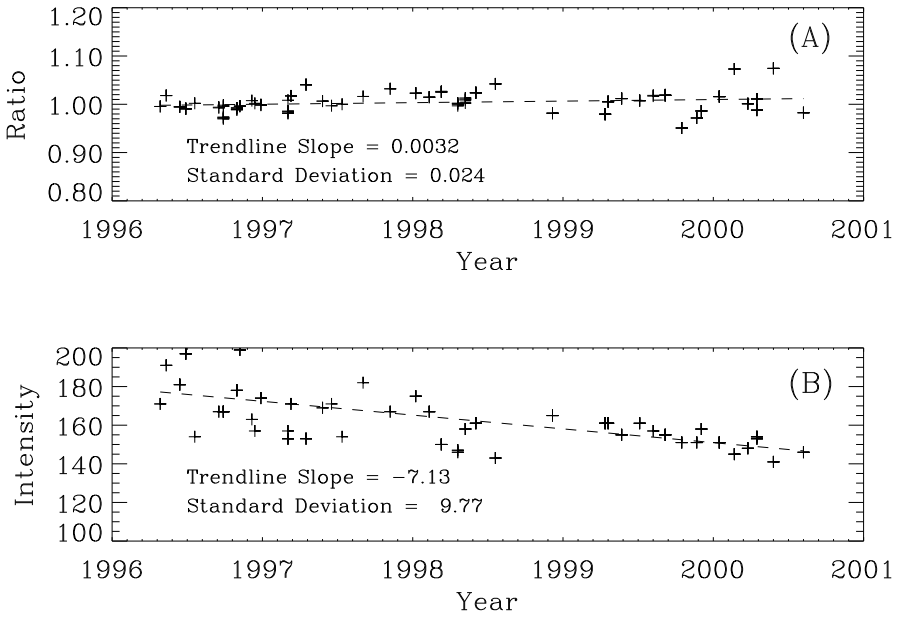

Figure 22.1: The intensity ratios in panel A, which are relative to the assumed quiet Sun intensity, are derived from the EIT 30.4 nm images at the location of the the SUMER-CDS ICAL_01 slit areas. The flat trend of this ratio indicates that the SUMER-CDS ICAL_01 slit areas were indeed located over quiet Sun regions. The assumed quiet Sun intensity, as shown in panel B, is the peak of the intensity histogram from the EIT 30.4 nm images. The trend of the quiet Sun intensity includes effects of EIT instrument degradation and any true quiet Sun intensity changes; however, the instrument degradation is the dominant trend.

studied. *Worden et al.* [1999] show that the EIT 30.4 nm images have a high contrast for the active network. The EIT full-disk images, typically one per day was selected for this study, are first rotated to the time of the calibration measurements, using the EIT image obtained closest to the CDS and SUMER observations. Then the EIT image intensity histogram is analyzed to determine the quiet Sun relative intensity, which is assumed to be the peak in the intensity histogram. Finally, the region over the Intercal_01 areas in the EIT image is averaged and compared to the quiet Sun relative intensity. The ratio of the intensity over the Intercal_01 region to the quiet Sun intensity is essentially unity throughout the SOHO mission, with standard deviation of only 2 % (see Figure 22.1). This indicates that the joint observations have a very minor contamination of active network.

22.5 CDS Wide Slit Burn-in Correction

The CDS flatfield correction for the wide slit burn-in is based on the long-term behavior of the He I 58.4 nm line at disk center. The central raster from the daily synoptic observation is processed to produce a daily average value. To avoid active latitudes, only the central 2′ of the slit height are used. Without a correction for the wide slit burn-in, the long term behavior of these daily average values is a slow decline. As the solar cycle advances, the distribution of values splits into two populations. One population continues the slow, steady decline. The second population consists of a much broader distribution of values representing areas of more active Sun. This second group always lies above the first group, never below. The wide slit burn-in correction is chosen to flatten the first distribution, i.e. the statistically quieter areas rotating through disk center. The corresponding O V 63.0 nm daily average values are used to cross-check the procedure.

22.6 Cross-check of the CDS GIS-4 Calibration by Comparison with SUMER

Following recent checks of the performance of the GIS detector, burn-in (often also called long-term gain-depression) effects were found. This reduces the detector countrates and yields a correction of about 15 % in mid 1997 and of nearly 40 % at the end of 2001 at 77.0 nm. Comparing the CDS GIS-4 and the SUMER measurements at 77.0 nm, an average increase of the GIS efficiency by a factor of 2.6 gives consistent results [*Pauluhn et al.*, 2002].

22.7 Responsivity Changes after SOHO's Loss of Attitude

SUMER's responsivity changed as described in *Pauluhn et al.* [2001] and *Wilhelm et al.* [2002], the CDS NIS-2 instrument showed no change of responsivity after SOHO's attitude loss [*Lang et al.*, 2002]. The NIS-1 and NIS-2 second order, as well as the GIS change are under investigation.

Bibliography

Brekke, P., Thompson, W.T., Woods, T.N., and Eparvier, F.G., The EUV solar irradiance spectrum observed with the Coronal Diagnostic Spectrometer (CDS) on SOHO, *Astrophys. J.* **536**, 959–970, 2000.

Lang, J., Thompson, W.T., Pike, C.D., Kent, B.J., and Foley, C.R., The radiometric calibration of the Coronal Diagnostic Spectrometer, this volume, 2002.

Pauluhn, A., Rüedi, I., Solanki, S.K., Lang, J., Pike, C.D., Schühle, U., Thompson, W.T., Hollandt, J., and Huber, M.C.E., Intercalibration of SUMER and CDS on SOHO. I. SUMER detector A and CDS NIS, *Appl. Opt.* **38**, 7035–7046, 1999.

Pauluhn, A., Rüedi, I., Solanki, S.K., Schühle, U., Wilhelm, K., Lang, J., Thompson, W.T., Hollandt, J., and Huber, M.C.E., Intercalibration of SUMER and CDS on SOHO. II. SUMER A and B detectors and CDS NIS, *Appl. Opt.* **40**, 6292–6300, 2001.

Pauluhn, A., Lang, J., Schühle, U., Solanki, S.K., Wilhelm, K., Thompson, W.T., Pike, C.D., Rüedi, I., Hollandt, J., and Huber, M.C.E., Intercalibration of SUMER and CDS, this volume, 2002.

Schühle, U., Wilhelm, K., Hollandt, J., Lemaire, P., and Pauluhn, A., Radiance variations of the quiet Sun at far-ultraviolet wavelengths, *Astron. Astrophys.* **354**, L71–L74, 2000.

Wilhelm, K., Schühle, U., Curdt, W., Dammasch, I.E., Hollandt, J., Lemaire, P., and Huber, M.C.E., Solar vacuum-ultraviolet radiometry with SUMER, this volume, 2002.

Worden, J., Woods, T.N, Neupert, W.M., and Delaboudinière, J.P., Evolution of chromospheric structures: How chromospheric structures contribute to the solar He II 30.4 nanometer irradiance and variability, *Astrophys. J.* **511**, 965–975, 1999.

— 23 —

Irradiance Working Group Report

DONALD R. MCMULLIN
University of Southern California, Space Sciences Center
Los Angeles, California, USA

TOM N. WOODS
Laboratory for Atmospheric and Space Physics,
University of Colorado, Boulder, CO, USA

INGOLF E. DAMMASCH, KLAUS WILHELM
Max-Planck-Institut für Aeronomie
Katlenburg-Lindau, Germany

DARRELL L. JUDGE
University of Southern California, Space Sciences Center
Los Angeles, California, USA

PHILIPPE LEMAIRE
Institut d'Astrophysique Spatiale,
Universite de Paris XI, Orsay, France

JEFFREY S. NEWMARK
Naval Research Laboratory
Washington, DC, USA

WILLIAM T. THOMPSON
L3 Communications Analytics Corporation
NASA GSFC, Greenbelt, MD, USA

W. KENT TOBISKA
Space Environment Technologies
Pacific Palisades, California, USA

The aim of the Irradiance Working Group for the SOHO Inter-Calibration Workshop was to validate the SOHO Vacuum Ultraviolet (VUV) instrument calibrations by inter-comparing full-disk irradiance results obtained with SOHO EUV instruments and, where possible, compare results with instruments external to SOHO. For many of the instruments, full-disk irradiance measurements are not the primary objective of instrument design. As such, almost all instruments required atypical observing modes in order for their data to be compared with observations from other instruments. While different instruments on SOHO provide irradiance measurements in a variety of spectral regions, comparisons were possible in overlapping wavelength bands. All comparisons are normalized to their 1 AU values. A general description of how irradiance measurements are compiled for each instrument and a summary of the comparisons are provided in this report. The irradiance measurements from SOHO are available for VUV wavelengths from 1 nm to 154.8 nm.

23.1 Introduction

The SOHO payload contains a complement of instrumentation to provide high spectral and spatial resolution of EUV radiation from the solar disk and corona, and to measure the absolute flux of the electromagnetic radiation covering the wavelength range from the EUV through the visual radiation region. Originally, the SOHO instruments that were to provide measurements of the solar irradiance, that is the radiation integrated over the full-disk of the Sun, were SUMER, CDS, UVCS, EIT, VIRGO, and to an extent, SWAN. Due to the nature of observations and science objectives of VIRGO and SWAN, these instruments were not considered by the working group which limited the inter-comparisons to direct solar irradiance observations in the EUV region. Measuring the absolute solar irradiance in the EUV regime can be difficult as this region is known to be highly variable and detectors tend to degrade (for various reasons). As such, the SOHO Science Working Team recognized from the beginning that potential drift in responsivity of optical instrumentation over the duration of the SOHO mission was of particular concern. An in-flight validation was necessary of the calibrations performed on the ground long before the mission. A dedicated SOHO Inter-Calibration Working Group was installed early in the project to initiate programs to cross-calibrate the instruments, and to monitor their performance in flight.

Since no calibration sources are on board, the Sun must be used as a common target for inter-comparisons. Comparisons of the solar radiances measured by different, but overlapping, channels of the same instrument, different instruments on SOHO, and other external instruments have proven to be important techniques for the validation of the SOHO measurements. When comparing solar radiances measured by different instruments, it is important to view the same surface feature or features on the Sun at the same time because the activity on the Sun is very dynamic over all timescales [e.g., *Solanki*, 2002]. Observations of the quiet-Sun network, even those taken at different times and different locations, can also provide useful comparisons, once proper corrections are included. In any case, corrections must first account for the different spatial and spectral resolutions of the instruments; otherwise, the variations across a surface feature and effects of spectral band width will more likely dominate the differences in a comparison than the differences related to the pre-flight calibrations. Another approach to validate the SOHO measurements is to perform comparisons of the full-disk solar irradiance. Such comparisons require a special operating mode for high spatial resolution spectrometers since they must scan their slit over the full disk, which is typically accomplished over several hours. For these solar irradiances, there is often a sacrifice of spatial resolution and/or spectral resolution in order to limit the experiment time and the telemetry downlink data-volume.

Inter-Calibration Joint Observing Programs (ICAL-JOPs) were designed to facilitate the inter-calibration of various instruments. ICAL-JOPs used common target areas on the Sun or in the corona, and/or used the irradiance of the full-Sun for comparisons at the common wavelength bands. While the observations of common areas on the Sun are performed regularly, the full-Sun irradiance observations have unfortunately not been scheduled for inter-calibration purposes, except for rare occasions of calibration rocket underflight campaigns. The comparison of instrument responsivities by irradiance measurements thus relies on data obtained on those occasions where the full-Sun irradiance was measured by the multiple instruments at or near the same time. On request of the SOHO Inter-Calibration Working Group (SICWG) at the 5th SOHO Science Working Team (SWT) meeting at

ESTEC in November 1990 the following recommendation to the scientific community in general was issued by the SOHO SWT Executive Meeting.

> *"The SOHO Prime Scientific Objectives would benefit from EUV relative and absolute radiometric calibration updates for certain SOHO experiments (CDS, SUMER, EIT, UVCS, SWAN and CELIAS). A secondary benefit would be for absolute radiometric measurements of EUV solar irradiance for aeronomy. The SOHO SWT will recommend the most appropriate instrumentation and/or supporting missions."*

To address this objective, a Solar EUV Monitor (SEM) was added to the SOHO suite of EUV instruments, hosted by the original SOHO/CELIAS instrument. The basic premise for inter-calibration was that the inclusion of an independent solar EUV monitor to continuously measure the total EUV flux on board SOHO would make the Sun itself available as a transfer standard for irradiance inter-comparisons at any time of the mission.

23.2 Applications of Calibrated Irradiance Data

Besides the usefulness of calibrated irradiance data for inter-comparisons and calibration validation, absolute solar irradiance data have applications in basic scientific research and recently in commercial applications. While it is not the intent of this paper to comprehensively cover all aspects of irradiance applications, a few examples are provided so the reader may better understand the importance of accurately calibrated solar irradiance data.

The solar spectral irradiance in the VUV is an important source of energy for aeronomic processes throughout the solar system. The solar VUV photons are absorbed in planetary and cometary atmospheres, as well as throughout the heliosphere, via photodissociation of molecules, photoionization of molecules and atoms, and photoexcitation including resonance scattering (e.g., see *Chamberlain* [1978]). Additionally, the Sun, a main sequence G2 V star, is the only star which can be observed without interstellar absorption, and thus provides an excellent stellar source for comparison of theory with data.

The VUV radiation, which photoionizes the neutral atmospheric constituents, participates in the formation of the ionosphere. The photoelectrons created in this process interact further with the neutrals, leading to further excitation, dissociation, and ionization. The kinetic energy of the fragments produced in the absorption processes drives the atmospheric heating. The absorption of the solar UV also initiates many atmospheric chemical cycles, such as the chemistry of water vapor, ozone, and nitric oxide in the Earth's atmosphere (e.g., see *Brasseur and Solomon* [1986]).

As a specific example, the chemistry cycle of ozone in the Earth's stratosphere consists of the creation of ozone via the photodissociation of molecular oxygen followed by the combination of the atomic oxygen with molecular oxygen, followed by the destruction of ozone via direct photodissociation. All atmospheric processes are wavelength dependent and are expected to be as variable as the intrinsic wavelength dependent solar variability. Therefore, accurate measurements of the solar UV spectral irradiance, along with an understanding of the solar physics which produces its variability, are important for detailed studies of the Sun and its interactions with solar system objects.

Calibrated solar irradiances from SOHO and other spacecraft are incorporated into empirical models and have made significant improvements to the accuracy of those mod-

els. SOHO SEM data, for example, have been incorporated into the SOLAR2000 model [*Tobiska et al.*, 2000] and have improved the average of correlation coefficients across the EUV spectrum from 0.83 nm to 0.97 nm between versions 1.05 and 1.16 of that model. Improved solar irradiances are used in operational atmospheric density models for satellite drag. They are also used in ionospheric models to produce electron density profiles for HF radio signal propagation and total electron content (TEC) for GPS signal uncertainties.

23.3 Irradiance Measurements

The SOHO solar irradiance measurements are obtained from the SEM, CDS, EIT, and SUMER instruments and they are summarized in this section. In addition, the irradiance observations from instruments external to SOHO are briefly described here.

23.3.1 SEM Solar Irradiances

The CELIAS/SEM instrument aboard SOHO continuously monitors the EUV solar irradiance in an 8 nm wavelength band centered at 30.4 nm (first order), and in a broad wavelength band between 0.1 and 50 nm (central order) [*Judge et al.*, 1998]. The SEM has been operating continuously throughout the SOHO mission providing irradiance measurements in its two band passes with a time cadence of 15 s. For comparisons with other SOHO instruments, SEM 15 s observations are averaged over the observing period of the instrument with which its data are being compared. In the case of CDS and EIT intercomparisons, the SEM values used were daily averages. The relative standard uncertainty in absolute flux for each channel is approximately 10 % [*McMullin et al.*, 2002]. The data show evidence of persistent solar EUV/soft X-ray active regions throughout this solar cycle, which appear in the data base as both 27-d and short-term (minutes to hours) solar EUV irradiance variations.

23.3.2 CDS Solar Irradiances

The CDS irradiance measurements are described in a separate report [*Thompson et al.*, 2002]. Since CDS has a small field of view, continuous monitoring of the full solar disk irradiance is not possible. Instead, special irradiance measurements, where the CDS slit is stepped over the entire solar disk, have been made on an approximately monthly basis since March 1997. Most recently, this has been increased to about once every two weeks. Each observation takes more than thirteen hours to complete. The full spectral range of the CDS Normal Incidence Spectrometer (NIS) is observed, so that the irradiance in each emission line can be extracted by fitting the line shape. The relative standard uncertainty in the CDS absolute calibration ranges from 15 % to 25 %, depending on the wavelength observed. When the uncertainties in the flatfield corrections are included, this rises to values of 20 % to 30 %. Along with the irradiance values, low resolution images of the Sun can be obtained at the stronger solar lines.

23.3.3 EIT Solar Irradiances

The Extreme-ultraviolet Imaging Telescope (EIT) on SOHO provides wide-field images of the corona and transition region with 2.6″ pixels at up to 1.4 solar radii. The telescope uses two normal-incidence, multilayer-coated optic mirrors to define four spectral bandpasses. The response is selected to peak on emission lines produced either in the transition region (He II 30.4 nm), quiet corona (Fe IX/X 17.1 nm and Fe XII 19.5 nm), or hotter corona (Fe XV 28.4 nm). Full-Sun images in each of these bandpasses have been obtained daily over the SOHO mission thus far, except for brief periods and SOHO attitude losses. Broadband irradiances that are useful for examining trends over the solar cycle are determined by simple summing of all pixels in these images. A method [*Cook et al.*, 1999] has been developed to construct differential emission measure (DEM) maps, using EIT images from the four channels, over the temperature range log T/K = 4.6 to 6.5. A DEM map is an individual DEM curve for each pixel in the field of view, which reproduces the intensities in the four EIT channels for that pixel. Using these maps one can model individual lines (e.g., He II 30.4 nm) or an instrumental bandpass (e.g., SEM 26 nm to 34 nm) to produce absolutely calibrated intensities. This DEM modelling tool has been used to calculate full-disk, absolutely calibrated, EUV irradiances over the SOHO mission thus far [*Newmark et al.*, 2002].

23.3.4 SUMER Solar Irradiances

SUMER irradiance measurements have been performed by integrating raster scan images of the full solar disk at certain wavelengths of strong solar lines. These scans were only performed while the telescope raster mechanism was still fully operational, that is, before October 1996. Irradiance estimates in many lines in the SUMER wavelength range were also obtained during SOHO roll manœuvres. In order to acquire the irradiance of the Sun, the spectrograph entrance slit of $1'' \times 300''$ was scanned in east-west (and reverse) direction in a way that the solar disk was covered in eight overlapping swaths. One such measurement takes several hours. The irradiance at each wavelength was determined by integrating the intensity in the line after subtraction of continuum background signal for scans with full spectral information.

23.4 Comparison Results

The results from the irradiance comparisons are broken down into three sections: solar EUV comparisons between CDS, EIT, SEM, and SUMER on SOHO, solar EUV comparisons between the SOHO instruments and three EUV rocket experiments, and solar VUV comparisons between SOHO SUMER and UARS SOLSTICE. With irradiance comparisons, the corrections for different spectral resolution are important and have been incorporated in the comparisons of the measurements from different instruments. The comparison of solar irradiances between the SOHO UV instruments and instruments external to SOHO is the focus of this paper.

23.4.1 Solar Irradiance Inter-comparisons on SOHO

Between SOHO instruments, EUV irradiance values were compared in two distinct groups. The first was between CDS, SEM and EIT which identified an overlapping region where EUV irradiance comparisons between all three instruments could be made. The second comparison group was between CDS and SUMER at specific VUV lines.

23.4.2 CDS-SEM-EIT Comparisons

Thompson et al. [2002] describe the comparison of the CDS irradiance measurements with those from SEM and EIT. The individual spectral lines observed by CDS are combined to reconstruct the SEM bandpass of 26 nm to 34 nm. The part of the SEM bandpass not observed by CDS is simulated through a DEM analysis of the CDS spectrum. The CDS 26 nm to 34 nm irradiances are approximately 5 % to 15 % lower than those derived from the SEM measurements, when the CDS or EIT spectral shapes are taken into account. Also, the CDS irradiances are 5 % to 30 % lower than the EIT values. The irradiances from all three instruments agree within their uncertainties. CDS and EIT are in good agreement over how much of the SEM signal is due to the He II and Si XI lines at 30.4 nm.

23.4.3 CDS-SUMER Comparisons

CDS/SUMER irradiance comparisons were performed in 1996, during solar minimum. SUMER observed the irradiance in the He I 58.4 nm line on 2 March, and the O V 63 nm line on 14 June, which are compared to CDS observations on 24 April and 12 June, respectively. The CDS observations are not the normal irradiance measurements, but full-Sun images in a few selected lines. The on-board compression of these data summed over the line profile, so special software was developed to apply the appropriate calibrations to these data. However, these observations overlap with the regular irradiance observations which started up the following year, when the two CDS observation sets are consistent to within a few percent for these two bright lines. The CDS and SUMER irradiances for He I 58.4 nm agree with each other to within 10 %, with the CDS irradiance slightly higher than the SUMER value. However, CDS observes an irradiance for the O V 63 nm that is about 35 % lower than that measured by SUMER. This is just consistent within the combined uncertainties of the two measurements. More information on these comparisons can be found in *Wilhelm* [2002] and *Wilhelm et al.* [2002].

23.4.4 SOHO Solar Irradiance Comparisons with Other Instruments

Throughout the SOHO mission there have been simultaneous irradiance measurements made by other instruments that can be used for comparisons. The SOLar STellar Irradiance Comparison Experiment (SOLSTICE) aboard the Upper Atmosphere Research Satellite (UARS) has been making daily measurements of the solar UV irradiance since October 1992 [*Rottman et al.*, 1993; *Woods et al.*, 1993]. The SOLSTICE instrument is designed to measure the solar UV irradiance from 119 nm to 420 nm with 0.1 nm to 0.2 nm spectral resolution. The pre-flight calibrations for SOLSTICE are primarily based on the direct calibrations at the NIST SURF, and the in-flight calibrations are based on stable (main

Table 23.1: Solar UV Irradiance Comparisons for SOHO instruments.

Event	Date	Wavelength / nm	Photon Irrad. / (s^{-1} m^{-2})	Instrument
LASP Rocket	15 May 1997	26 – 34	1.24×10^{14}	SOHO SEM
			1.03×10^{14}	LASP Rocket EGS
LASP Rocket	2 Nov 1998	26 – 34	1.27×10^{14}	SOHO SEM
			0.93×10^{14}	LASP Rocket XPS
SUMER Cal	Jun 1996	N V 123.8	5.67×10^{12}	SOHO SUMER
			6.59×10^{12}	UARS SOLSTICE
SUMER Cal	Feb and Jun 1996	C IV 154.8	6.02×10^{13}	SOHO SUMER
			6.79×10^{13}	UARS SOLSTICE

sequence, early-type O, B) stars using the same optical elements used for the solar measurements. The total measurement accuracy of the SOLSTICE solar irradiances is 3 % to 5 %, which has been validated by several other solar UV irradiance measurements [*Woods et al.*, 1996].

The high accuracy of the UARS SOLSTICE solar UV irradiances [*Woods et al.*, 1996] is useful for validating the SOHO SUMER measurements. The comparison of the solar UV irradiance measurements from SOHO SUMER in 1996 to the UARS SOLSTICE, as listed in Table 23.1, shows deviations less than 14 %, which are well within the combined uncertainties of the two instruments [*Wilhelm et al.*, 1999]. *Wilhelm et al.* [1999] present the comparisons of the N V 123.8 nm and C IV 154.8 nm irradiances obtained in February and June 1996. An important aspect of these comparisons is the correction of the line blends, especially for the SOLSTICE instrument, which has a lower spectral resolution of about 0.1 nm versus the SUMER resolution of about 4 pm. The comparisons of the N V and C IV irradiances indicate that the SUMER measurements are lower than the UARS SOLSTICE measurements by 14 % and 11 %, respectively. These irradiance comparisons, along with a SUMER radiance comparison from 120 nm to 156 nm, suggest that the SUMER results could be too low by 10 % to 15 % [*Wilhelm et al.*, 1999].

During the SOHO mission, there have been two measurements of the solar extreme ultraviolet irradiance by sounding rocket instruments from the Laboratory for Atmospheric and Space Physics (LASP) at the University of Colorado (CU). These LASP rocket measurements were made on 15 May 1997 and 2 November 1998 using two EUV irradiance instruments built as prototype instruments for the Solar EUV Experiment (SEE) for the NASA Thermosphere Ionosphere Mesosphere Energetics Dynamics (TIMED) satellite [*Woods et al.*, 1998]. One of these instruments is the EUV Grating Spectrograph (EGS). The EGS instrument is a normal-incidence, Rowland-circle grating spectrograph with a 64×1024 CODACON detector. The EGS is designed to measure the solar EUV irradiance from 25 nm to 195 nm with a spectral resolution of 0.17 nm per detector anode. The EGS is calibrated directly at the NIST SURF and has a total measurement accuracy of about 10 %. The other instrument is the XUV Photometer System (XPS), and it is a set of twelve Si photodiodes with thin-film coatings to measure the solar X-ray ultraviolet (XUV) irradiance from 1 nm to 35 nm with each diode having a bandpass of about 7 nm. Some of these photometers are calibrated at NIST SURF, and some are calibrated at PTB BESSY,

and the total measurement accuracy ranges from 7 % to 30 %. The other instruments on the LASP rocket payload are described by *Woods et al.* [1994].

The LASP rocket measurements of the solar EUV irradiance, with an accuracy of about 10 %, are useful for SOHO instrument validation. In the case of the SOHO CDS instrument, the May 1997 rocket measurement is used to adjust the calibration for the CDS NIS [*Brekke et al.*, 2000]. This comparison between EGS and CDS NIS showed that the original CDS irradiance values were about a factor of two higher than the rocket results. Because other pre-flight calibration analysis showed that the CDS NIS responsivity should be higher, *Brekke et al.* [2000] report the new CDS NIS responsivity corrections based on the comparison to the LASP rocket measurement, and these corrections have been adopted by the CDS project. In the case of the SOHO SEM instrument, the comparison to the 15 May 1997 rocket measurement, as listed in Table 23.1, indicates that the SEM 26 nm to 34 nm photon irradiance (1.24×10^{14} s^{-1} m^{-2}) is 20 % higher than the LASP rocket EGS measurement. The uncertainty of the LASP rocket EGS measurements at 30 nm is about 30 %; this larger uncertainty is related to lower responsivity near 30 nm for both the rocket EGS and XPS instruments. With the SEM uncertainty of 10 %, this comparison between SEM and the LASP rocket measurement is within their uncertainties. A similar result, as indicated in Table 23.1, is found for the comparison of SEM and the LASP rocket XPS measurement on 2 November 1998; that is, the SEM 26 nm to 34 nm irradiance value is larger than the rocket measurement.

23.5 Conclusions

Through the course of examining the SOHO data available, as presented in this report, it is clear that the solar spectral irradiances from SOHO VUV instruments, with few exceptions, are in good agreement with each other and with irradiance measurements external to SOHO within their instrument uncertainties. One conclusion of the SOHO Inter-Calibration Irradiance Working Group is that the calibrations used in the production of solar irradiance values for the SOHO instruments have been validated to within the combined uncertainties of the instruments. It should also be noted that this report is not meant to replace the detailed calibration papers and reports that have been produced for the individual instruments, and the reader is encouraged to review the referenced works in this report for additional information. Another conclusion of this working group is that the SOHO irradiance measurements provide accurate, significantly new results of the solar VUV irradiance, especially important in the EUV region where very few irradiance measurements exist.

Acknowledgements

Author JSN received support from NRL, the Office of Naval Research and NASA grant NDPRS-92385.

Bibliography

Brasseur, G., and Solomon, S., Aeronomy of the Middle Atmosphere: Chemistry and Physics of the Stratosphere and Mesosphere, Dordrecht, Boston, 1986.

Brekke, P., Thompson, W.T., Woods, T.N., and Eparvier, F.G., The extreme-ultraviolet solar irradiance spectrum observed with the Coronal Diagnostic Spectrometer (CDS) on SOHO, *Astrophys. J.* **536**, 959–970, 2000.

Chamberlain, J.W., Theory of Planetary Atmospheres: An Introduction to Their Physics and Chemistry, Academic Press, New York, 1978.

Cook, J.W., Newmark, J.S., and Moses, J.D., Coronal thermal structure from a differential emission measure map, *Proc. 8^{th} SOHO Workshop*, Paris, France, ESA SP-446, 1999.

Judge, D.L., McMullin, D.R., Ogawa, H.S., Hovestadt, D., Klecker, B., Hilchenbach, M., Möbius, E., Canfield, L.R., Vest, R.E., Watts, R., Tarrio, C., and Kühne, M., First solar EUV irradiances obtained from SOHO by the CELIAS/SEM, *Sol. Phys.* **177**, 161, 1998.

McMullin, D.R., Judge, D., Hilchenbach, M., Ipavich, F., Bochsler, P., Bürgi, A., In-flight comparisons of solar EUV irradiance measurements provided by the CELIAS/SEM on SOHO, this volume, 2002.

Newmark, J.S., Cook, J.W., McMullin, D.R., Solar EUV variability as measured by SOHO EIT, in preparation, 2002.

Rottman, G.J., Woods, T.N., and Sparn, T.P., Solar Stellar Irradiance Comparison Experiment I: 1 Instrument design and operation, *J. Geophys. Res.* **98**, 10667–10677, 1993.

Solanki, S.K., Solar variability, this volume, 2002.

Tobiska, W.K., Woods, T., Eparvier, F., Viereck, R., Floyd, L., Bouwer, D., Rottman, G., and White, O.R., The SOLAR2000 empirical solar irradiance model and forecast tool, *J. Atmos. Solar Terr. Phys.* **62**, 1233, 2000.

Thompson, W.T., McMullin, D.R., and Newmark, J.S., Comparison of CDS irradiance measurements with SEM and EIT, this volume, 2002.

Wilhelm, K., Woods, T.N., Schühle, U., Curdt, W., Lemaire, P., and Rottman, G.J., The solar ultraviolet spectrum from 1200 Å to 1560 Å: A radiometric comparison between SUMER/SOHO and SOLSTICE/UARS, *Astron. Astrophys.* **352**, 321–326, 1999.

Wilhelm, K., Calibration and inter-calibration of SOHO's vacuum-ultraviolet instrumentation, this volume, 2002.

Wilhelm, K., Schühle, U., Curdt, W., Dammasch, I.E., Hollandt, J., Lemaire, P., and Huber, M.C.E., Solar Vacuum-Ultraviolet Radiometry with SUMER, this volume, 2002.

Woods, T.N., Rottman, G.J., and Ucker, G., Solar Stellar Irradiance Comparison Experiment I: 2 Instrument calibration, *J. Geophys. Res.* **98**, 10679–10694, 1993.

Woods, T.N., Rottman, G.J., Bailey, S., and Solomon, S.C., Vacuum-ultraviolet instrumentation for solar irradiance and thermospheric airglow, *Optical Eng.* **33**, 438, 1994.

Woods, T.N., Prinz, D.K., London, J., Rottman, G.J., Crane, P.C., Cebula, R.P., Hilsenrath, E., Brueckner, G.E., Andrews, M.D., White, O.R., VanHoosier, M.E., Floyd, L.E., Herring, L.C., Knapp, B.G., Pankratz, C.K., and Reiser, P.A., Validation of the UARS solar ultraviolet irradiances: Comparison with the ATLAS 1 and 2 measurements, *J. Geophys. Res.* **101**, 9541–9569, 1996.

Woods, T.N., Eparvier, F.G., Bailey, S.M., Solomon, S.C., Rottman, G.J., Lawrence, G.M., Roble, R.G., White, O.R., Lean, J., and Tobiska, W.K., TIMED Solar EUV Experiment, *Proc. SPIE* **3442**, 180–191, 1998.

VI. Outlook

— 24 —

The EUV Imaging Spectrometer and its Role in the Solar-B Mission

J. LEN CULHANE
Mullard Space Science Laboratory, University College London
Holmbury St Mary, Surrey, UK

GEORGE A. DOSCHEK
Naval Research Laboratory
Washington, DC, USA

TETSUYA WATANABE
National Astronomical Observatory of Japan
Mitaka, Tokyo 181, Japan

JAMES LANG
Rutherford Appleton Laboratory
Chilton, Didcot, Oxfordshire, UK

Given the importance of the SOHO EUV instrument calibration techniques for the Japan/US/UK Solar-B mission, the nature of Solar-B is briefly described and the three scientific instruments on board the spacecraft are discussed. The EUV Imaging Spectrometer (EIS) instrument is described in some detail since it is anticipated that the SOHO calibration techniques will have direct application to the absolute calibration of EIS. The key scientific aims of Solar-B are presented.

24.1 Introduction

The radiometric intercalibration of the SOHO instruments is discussed extensively in this book. The lessons learned regarding the methods for absolute calibration of Extreme-UltraViolet (EUV) spectrometers in particular, have important applications for future solar physics missions. One of these is the Japanese/US/UK Solar-B mission that is being built with the support of the three agencies, ISAS, NASA and PPARC. Solar-B has at its heart a large diffraction-limited Solar Optical Telescope (SOT) of 0.5 m aperture with its associated Focal Plane Package (FPP) of instruments. There are in addition two further instruments: the X-ray Telescope (XRT) and the EIS which are designed to provide complementary information about the solar atmosphere. They study the connections between the emerging magnetic field which originates below the photosphere and the processes and structures that characterise the Sun's outer atmosphere: chromosphere, transition region and corona.

Here the nature of Solar-B, its operation and the instruments are briefly discussed and the Solar-B scientific aims and anticipated outcomes are summarized. We describe the EIS instrument in somewhat greater depth; the methods for its calibration are presented in detail by *Lang et al.* [2002a].

Figure 24.1: Schematic view of the Solar-B spacecraft. The locations of the scientific instruments described in the text (SOT, FPP, XRT, EIS) are indicated. The SOT forms the main body of the spacecraft with the service module located beneath. The deployed solar arrays (SAP) are also indicated.

24.2 Solar-B and its Instruments

The Solar-B spacecraft, which is being built and will be launched by Japan's Institute of Space and Astronautical Science (ISAS) in August 2005, is illustrated in Figure 24.1. The satellite will be in a polar Sun-synchronous orbit with inclination 97.9 degrees, altitude 600 km and a nominal lifetime in orbit of three years. Solar-B is a follow-on to the highly successful Japan/US/UK Yohkoh (Solar-A) collaboration. On this occasion, ISAS will provide the spacecraft, the launch vehicle (ISAS MV), and major elements of the scientific instruments. The spacecraft is being developed by Mitsubishi Electric Corporation (MELCO) under contract to ISAS. It points continuously at the Sun for periods of eight months using a three-axis stabilisation system. Full-Sun illumination is interspersed with periods of four months that include short eclipses of up to 20 minutes duration. Solar-B has a total mass of ≈ 900 kg and its two solar arrays develop a power output of 500 W at end-of-life. Data are stored in a 3 Gbit solid state mass memory and transmitted to ground stations during 10 minute passes at a rate of 5 Mbit/s over both S- and X-band links. The spacecraft pointing system has a 3σ stability of $\approx 0.6''$ for a 2 s period or $1.1''$ in 20 s.

As shown in Figure 24.1, the spacecraft will accommodate three major instruments: a 0.5 m Solar Optical Telescope (SOT) with its associated Focal Plane Package (FPP), an X-ray Telescope (XRT) and an EUV Imaging Spectrometer (EIS).

This coordinated set of optical, X-ray and EUV instruments will investigate the interaction between the Sun's photospheric velocity and magnetic fields (SOT/FPP) and its

extended atmosphere: chromosphere and corona (XRT/EIS). The anticipated outcome will be an improved understanding of the mechanisms by which solar magnetic flux emerges through the Sun's surface and how the constant interaction of these flux elements controls the behaviour and variability of the Sun's extended atmosphere. We note that the dynamic behaviour of the high atmosphere in turn exerts a crucial influence on the near-Earth environment.

24.2.1 Solar Optical Telescope and its Focal Plane Package (SOT/FPP)

The 0.5 m optical telescope feeds radiation to a suite of instruments (FPP) which are designed to observe the photosphere in visible radiation with a pixel size of 0.05″ to 0.08″ or 35 km to 60 km and to measure velocity and vector magnetic fields using a combination of narrow and broad-band filter imagers and a spectropolarimeter.

The telescope will be diffraction limited at 660 nm and provide imaging from 388 nm to 660 nm with a resolution of 150 km on the Sun. The field of view of $> 200'' \times 100''$ is designed to capture an entire active region and significant portions of the surrounding quiet network. An image stabilization system will operate to $< 0.02''$ to remove spacecraft jitter over a frequency range of 2 Hz to 20 Hz. The tip/tilt mirror is linked to a correlation tracker which employs a fast readout 50×50 pixel CCD for image stabilization. The complex FPP is illustrated schematically in Figure 24.2. Radiation passes through a rotating waveplate for polarization modulation before any oblique reflections occur.

Radiation is fed in parallel to these analyzer/detector systems:

I. Narrow-band tuneable birefringent filter with ≈ 0.01 nm bandwidth which provides imaging and vector magnetograph capability and operates in the wavelength range 517 nm to 657 nm.

II. Broad-band filter imager, operating in the range 388 nm and 670 nm, which uses interference filters with passbands of between 0.3 nm and 1.0 nm for short exposures and high image-quality.

III. Spectro-polarimeter which obtains dual-line dual-polarization spectra (Fe I 630.1 nm / 630.2 nm) for high precision Stokes polarimetry. The spectral range is 0.2 nm with a resolution of ≈ 0.0025 nm.

I and **II** above have a common focal plane and share a detector – a back-illuminated Marconi Applied Technologies CCD with 2048×4096 pixels of 0.053″ and frame transfer operation.

The three instruments will thus produce broad and narrow-band filter images, Dopplergrams and both longitudinal and vector magnetic field measurements. The accuracy of magnetic field measurement will be ≈ 1 G to 5 G for longitudinal field and 30 G to 50 G for transverse field with a typical measurement time of ≈ 5 minutes.

The SOT/FPP science goals include studies of:

I. *Magnetic Flux Transport*

Observe how magnetic flux emerges, disperses and disappears from the solar surface, including weak intranetwork fields ($B < 400$ G), determine whether magnetic field is generated in or near the surface, i.e., by fast dynamo action.

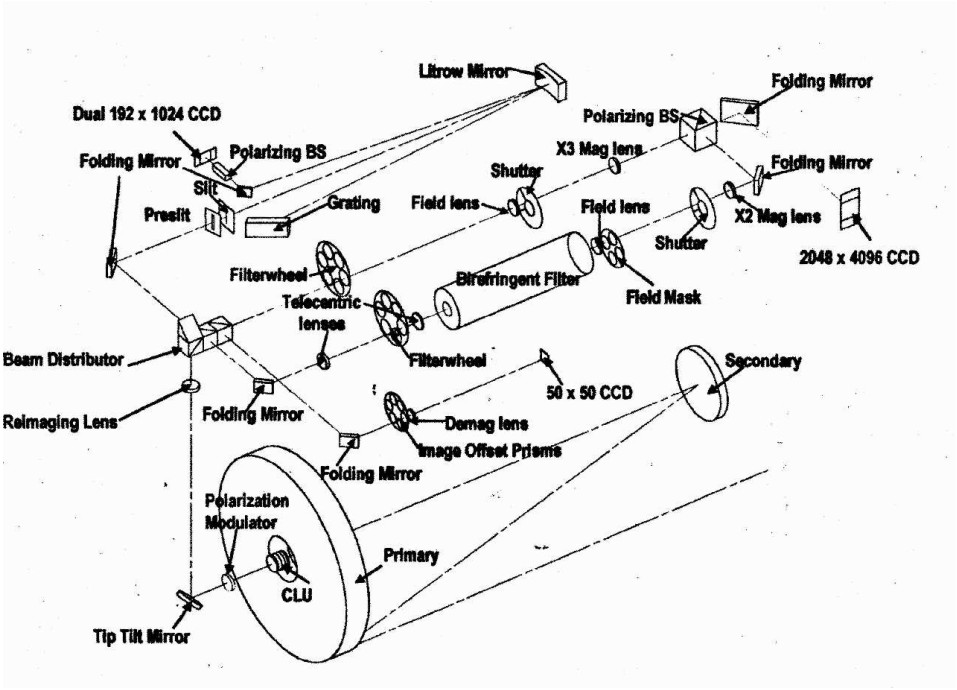

Figure 24.2: Schematic diagram of the Solar-B Solar Optical Telescope and its associated Focal Plane Package. Radiation from the 0.5 m telescope is distributed to three different instruments through a polarization modulator and with a tip-tilt mirror used for image stabilisation. Details are given in the text.

II. *Scales of Convection*
Investigate the relationship of the granulation, mesogranulation, and supergranulation.
III. *Sunspots and Active Regions*
Measure the vector magnetic field of sunspots and plage areas, observe the formation, dynamics and decay of entire active regions.
IV. *Upper Atmospheric Connections*
Determine the consequences of the configuration of the surface magnetic field for the structure and dynamics of the outer atmosphere.
V. *Solar Cycle Evolution*
Measure the effect of active regions on the solar cycle irradiance modulation.

24.2.2 Grazing Incidence X-ray Telescope (XRT)

The grazing incidence XRT is similar in construction and operation to the instrument flown on the Yohkoh spacecraft [*Tsuneta et al.*, 1991]. It is designed to image the coronal plasma on scales ranging from elementary bright points to those of extended coronal streamers. It also has sufficient dynamic range which, coupled with exposure control, will allow it to accommodate both low surface brightness structures and solar flares. Its per-

formance has been enhanced over that of the Yohkoh instrument in a number of areas. The XRT will respond to plasma temperature over a broader range than was possible with Yohkoh due to a somewhat different choice of filters. The instrument operates in the wavelength range 0.2 nm to 6.0 nm. Radiation is incident on a Wolter type I telescope with two reflections to form an image that is registered on a Marconi Applied Technologies back-illuminated CCD with 2048 $\times$ 2048 pixels of 1″ (13.5 μm) dimension. The system is illustrated schematically in Figure 24.3. The image scale is 1″ per pixel which is a factor 2.5 better than that of the Yohkoh telescope. With a field of view of 35′, the whole Sun is visible when the spacecraft is pointed close to disc centre. However the system can be operated to acquire full or partial-frame images with a corresponding improvement in exposure cadence to a minimum value of 2 s. Individual exposure times can be in the range 4 ms to 10 s. The chosen filters allow plasma to be sampled in the temperature range 0.5 MK to 20.0 MK.

As was the case for Yohkoh, a small, centrally mounted and accurately co-aligned optical telescope provides visible images in the wavelength range (430 $\pm$ 10) nm. Use of a shutter system allows these images to be registered on the same CCD as is used to obtain X-ray images. This in turn allows accurate co-alignment of the X-ray image data with the observations being undertaken by the other two instruments.

In scientific terms, the X-ray telescope will enable a similar range of scientific studies to those undertaken by the Soft X-ray Telescope instrument on Yohkoh though with extensions arising from the enhanced angular resolution and enlarged temperature coverage. However, like the EUV spectrometer which is discussed in the next section, the Solar-B philosophy involves the careful use of both instruments in conjunction with the photospheric measurements by the SOT/FPP to elucidate the connections between the dynamic magnetic and velocity fields in the photosphere and the behaviour of the Sun's extended atmosphere.

24.2.3 Extreme Ultra-violet Imaging Spectrometer (EIS)

The EIS records solar EUV spectra that contain information on the dynamics, velocity, temperature, and density of the emitting plasma. This instrument represents the next stage of development in this area following on from the continuing successful operation of the SOHO Coronal Diagnostic Spectrometer (CDS; *Harrison et al.* [1995]) whose calibration is discussed in detail elsewhere in this volume [*Lang et al.*, 2002b]. It responds in two bands in the range of $\approx$ 15 nm to 30 nm with an approximately ten times higher effective aperture than that of the SOHO CDS. The enhanced throughput is achieved by i) employing multilayer-coated optics, ii) restricting the wavelength ranges covered, iii) employing fewer reflections and iv) detecting the photons in back-thinned CCDs with high quantum efficiencies of $\approx$ 80 % at the EUV wavelengths of interest. Spectra are obtained with good spatial resolution and can be observed at many locations within an entire solar structure. The emission lines in particular are registered with sufficient time resolution to permit a determination of the plasma dynamics and temperature as a function of position within solar flare and active region loops. Use of a selectable 40″ slot permits spectral images to be accurately related in position to the images obtained by the Solar-B white light and X-ray telescopes. Thus EIS is the first solar spectrometer operating below 30 nm that is capable of obtaining high spectral resolution data with both good spatial and temporal resolution.

a)

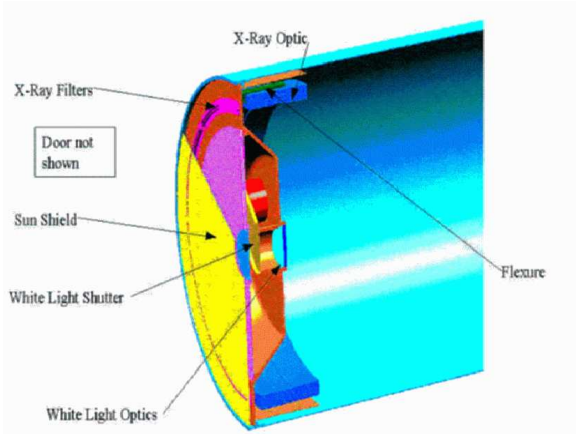

b)

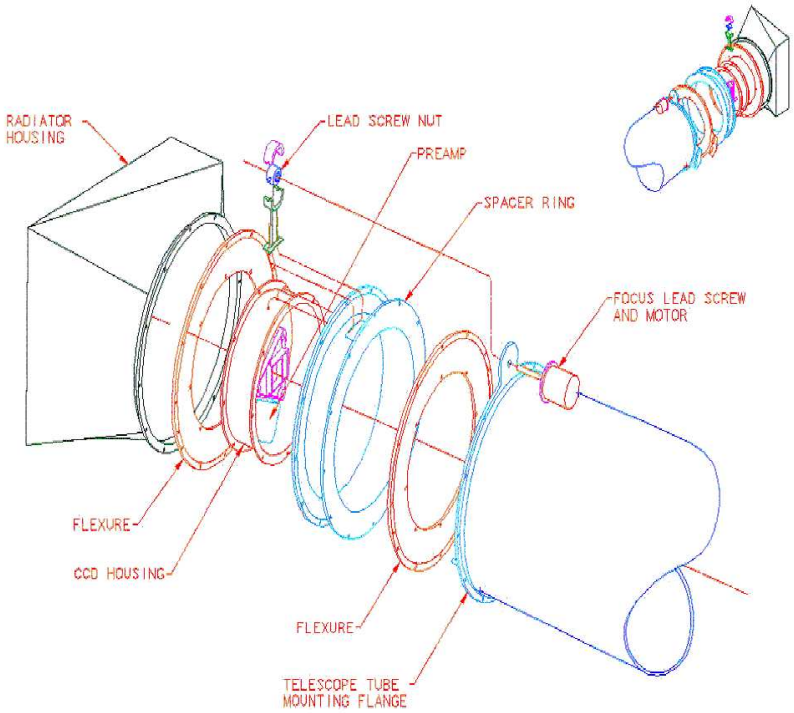

Figure 24.3: Schematic diagram of the SOT. a) Front of the telescope assembly indicating the location of the two-element grazing reflector and its associated entrance filters. Location of the small on-axis white light telescope is also indicated. b) CCD assembly at the telescope focus including the focus adjust mechanism and the cooling radiator.

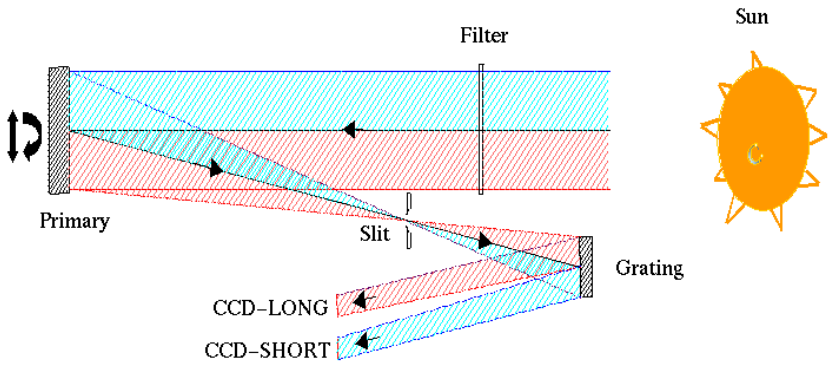

Figure 24.4: Schematic outline of the operation of the EIS instrument. Details are discussed in the text.

A simple schematic illustration of the EIS instrument is given in Figure 24.4. Solar radiation passes through a thin (≈ 150 nm) aluminium entrance filter that is required to reject visible light and thermal energy. Radiation is then collected by the primary mirror and focused through a slit mechanism and a second filter onto a grating. Diffracted radiation from two designated wavelength bands is finally registered on a pair of CCDs.

The instrument uses a stigmatic off-axis parabola as the primary mirror and thus can observe a slice of the Sun $\leq 8'$ high along the slit. In the dispersion plane, the parabola is scanned in $1''$ steps to enable the build-up of an image of $\approx 6'$ extent set by aberrations and by the range of the fine scanning mechanism. In addition there is a coarse motion which allows the mirror to be offset by $\approx 15'$.

A more detailed schematic diagram is given in Figure 24.5. The structure is fabricated from composite panels to ensure low mass and a very low thermal expansion coefficient. It has an overall length of 3.2 m with the other two dimensions being ≈ 0.5 m. Instrument mass, including the main electronic processing and power system which is mounted in the main body of the spacecraft, is ≈ 63 kg. Radiation enters from the right of the diagram and passes through the entrance filter which is contained in a vacuum housing and which will be maintained at ≈ 0.1 atm pressure[1] until the spacecraft has achieved orbit. This protects the very thin filter from acoustic loading during the launch phase. The primary mirror, of 150 mm aperture, has each half of its area coated with a different multilayer which is optimized for a specific wavelength range. Radiation then passes through a slit/slot mechanism with four positions (slits of $1''$ and $2''$ and slots of $40''$ and $250''$), a high speed shutter for exposure control and a redundant thin aluminium light-rejection filter. The toroidal grating, with a uniform ruling density of 4200 lines/mm and multilayer

[1] 1 atm = 101325 Pa

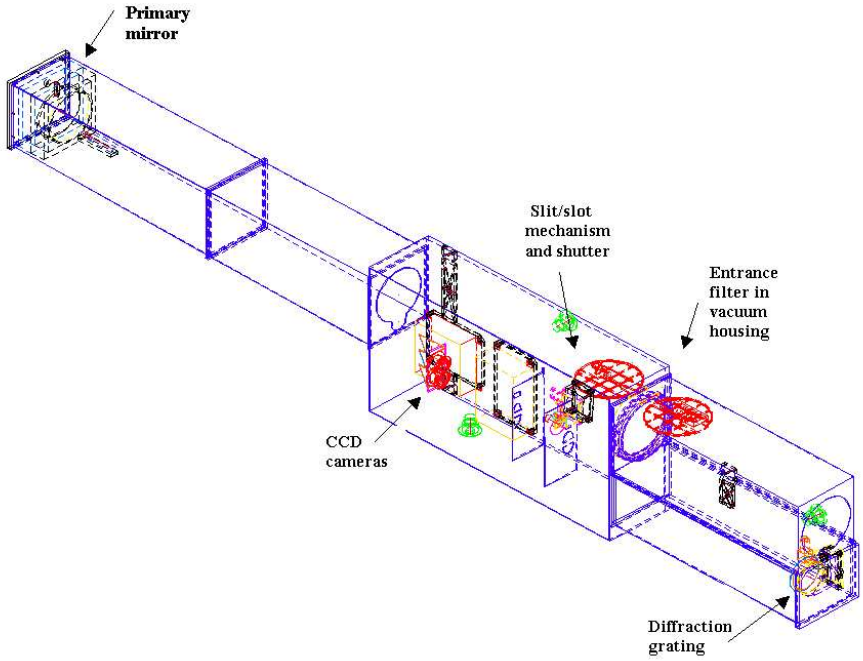

Figure 24.5: Schematic diagram of the EIS instrument showing the identity and location of the key subsystems.

coatings which match those of the mirror, is equipped with a focus mechanism for final in-orbit adjustment. Finally the two selected EUV wavelength bands are registered by two thinned back-illuminated CCDs of high quantum efficiency for the chosen wavelengths. These devices, again from Marconi Applied Technologies, have 2048 pixels (13.5 μm) along the dispersion direction with 1024 pixels along the slit.

The mirror and grating combination has a spatial resolution capability of 2″ while the plate scale is 1″ for each 13.5 μm CCD pixel. The multilayer coatings are optimised for two wavelength ranges namely 17 nm to 21 nm and 25 nm to 29 nm. These are discussed in greater detail in the paper on instrument calibration by *Lang et al.* [2002a] where the calculated reflectivity curves are presented. Emission lines from transition region (0.1 MK to 1.0 MK), coronal (1 MK to 3 MK) and solar flare (6 MK to 25 MK) plasmas are included. For data of signal-to-noise ratio > 10, the spectral resolution of 0.0022 nm allows the measurement of velocity from line centroid displacement with a precision of ± 3 km/s while non-thermal line width measurement will be to an accuracy of ± 20 km/s following subtraction of thermal Doppler and instrumental profiles. Under control of the shutter, exposure times can range from < 50 ms (suitable for solar flares) through 3 s to 10 s for strong active region lines up to 20 s to 30 s for quiet Sun emission.

24.3 Solar-B Mission Science

The principal scientific aims of the large SOT and its sophisticated FPP have already been listed in Section 24.2. These centre on the measurement of photospheric velocity and vector magnetic fields with spatial resolution of ≈ 150 km on the Sun's surface. Thus on some theoretical estimates, the mission will obtain for the first time quantitative measurements of the magnetic field on scales small enough to resolve the elemental flux tubes. Coupled with the photospheric plasma velocity measurements, it will become possible to study quantitatively the magnetic interactions that can be seen qualitatively in SOHO MDI data to result in the replacement of the magnetic flux above the photosphere on time scales of approximately two days. It is also planned to use the techniques of helioseismology to study the behaviour of the plasma below the surface of the photosphere in the convection zone.

Based on this new and detailed understanding of the magnetic and velocity fields on the surface, their role in controlling the Sun's upper atmosphere, chromosphere, transition region and corona, will be fully investigated by the simultaneous use of the other two instruments on the payload, namely the XRT and the EIS.

The overall aims of the Solar-B mission may therefore be summarized as follows:

I. Investigate the modes of energy transfer from the photosphere through the transition region to the corona. This will involve in particular the study of the causal relationship between coronal phenomena and the dynamics of photospheric magnetic fields and will require coordinated observations by all the Solar-B instruments.

II. Establish quantitatively the mechanism or mechanisms responsible for coronal heating. This should include the understanding of quiet Sun and active region heating since the possibility that they may involve different mechanisms remains open. Candidate mechanisms include magnetic reconnection, microflares and wave heating.

III. Determine the mechanisms responsible for a range of transient phenomena. These include small explosive events or nanoflares, eruptions including active region outflows, sudden prominence or coronal plasma disconnections, solar flares and coronal mass ejections. Here the focus will be on the triggering mechanisms, energy transport, mass motions and the role of both local and global magnetic field rearrangement.

IV. Study the modulation of the solar luminosity. While interest in this topic involves a timescale of several solar cycles, the Solar-B optical telescope is expected to be able to establish a detailed connection between magnetic field changes and luminosity variations for important structures in the solar atmosphere.

24.4 Conclusions

In this paper we have briefly described the Solar-B mission, its scientific aims and its instrumentation with special emphasis on the EIS. The outstanding feature of Solar-B clearly lies in its potential to address issues of flux emergence and plasma velocity in the photosphere with unprecedented spatial resolution and with long-term vector magneto-

graphic capability at high duty cycle using the SOT and its associated FPP. The availability of two further instruments (XRT and EIS) will allow observations undertaken in the photosphere to be related in a systematic manner – in both space and time, to the behaviour of the Sun's extended atmosphere and to important transient events (such as flares and coronal mass ejections) which may well have a significant influence for Earth's climate and the near-Earth space environment. The mission follows in the footsteps of the outstandingly successful Yohkoh with the same three agency partners involved, namely Japan's ISAS, the USA's NASA and the UK's PPARC. Absolute calibration of solar spectroscopic instruments is crucial for the eventual value of the acquired observational data. This paper, and the accompanying contribution on the detailed proposal for the calibration of the EIS instrument, describe how the teams involved in Solar-B are facing this important challenge.

Acknowledgements

The EIS instrument is built by an international consortium which includes groups in the UK (MSSL, Birmingham and RAL), in the USA (NRL, GSFC), in Japan (NAOJ) and in Norway (University of Oslo). Provision of the spacecraft, launch and operations by the Japanese Institute for Space and Astronautical Science is gratefully acknowledged. Support for the programme is provided by PPARC (UK), NASA (USA), Ministry of Education, Science and Culture (Japan) and the Norwegian Research Council.

Bibliography

Harrison, R.A., Sawyer, E.C., Carter, M.K., Cruise, A.M., Cutler, R.M., Fludra, A., Haynes, R.W., Kent, B.J., Lang, J., Parker, D.J., Payne, J., Pike, C.D., Peskett, S.C., Richards, A.G., Culhane, J.L., Norman, K., Breeveld, A.A., Breeveld, E.R., Al Janabi, K.F., McCalden, A.J., Parkinson, J.H., Self, D.G., Thomas, P.D., Poland, A.I., Thomas, R.J., Thompson, W.T., Kjeldseth-Moe, O., Brekke, P., Karud, J., Maltby, P., Aschenbach, B., Bräuninger, H., Kühne, M., Hollandt, J., Siegmund, O.H.W., Huber, M.C.E., Gabriel, A.H., Mason, H.E., and Bromage, B.J.I., The Coronal Diagnostic Spectrometer for the Solar and Heliospheric Observatory, *Sol. Phys.* **162**, 233–290, 1995.

Lang, J., Kent, B.J., and Seely, J.F., The proposed calibration of Solar-B EIS, this volume, 2002a.

Lang, J., Thompson, W.T., Pike, C.D., Kent, B.J., and Foley, C.R., The calibration of the Coronal Diagnostic Spectrometer, this volume, 2002b.

Tsuneta, S., Acton, L., Bruner, M., Lemen, J., Brown, W., Caravalho, R., Catura, R., Freeland, S., Jurcevich, B., and Owens, J., The soft X-ray telescope for the SOLAR-A mission, *Sol. Phys.* **136**, 37–67, 1991.

— 25 —

The Proposed Calibration of Solar-B EIS

JAMES LANG
Rutherford Appleton Laboratory
Chilton, Didcot, Oxfordshire, UK

BARRY J. KENT
Rutherford Appleton Laboratory
Chilton, Didcot, Oxfordshire, UK

JOHN F. SEELY
Naval Research Laboratory
Washington, DC, USA

The next Japanese solar mission, Solar-B, is due for launch in 2005. One of its three instruments is an Extreme-ultraviolet Imaging Spectrometer (EIS). In order fully to exploit the data obtained, a radiometric calibration is required. This paper describes the proposed laboratory calibration, which uses the same calibrated source and other equipment as in the calibration of the SOHO Coronal Diagnostic Spectrometer. Short overviews of EIS and its cleanliness programme and a brief account of the calibration source are given. Calculations of the efficiency of EIS are presented followed by sections detailing the proposed calibration and the calibration uncertainty budget. The in-flight calibration situation is discussed.

25.1 Introduction

The next Japanese solar mission, Solar-B, is due for launch in August 2005. It has a payload of three, coordinated instruments primarily to investigate the modes of energy transfer from the photosphere to the corona. An overview of the mission, its scientific aims and its three instruments is presented by *Culhane et al.* [2002] in the preceding paper. The Solar-B Extreme-ultraviolet Imaging Spectrometer (EIS) will provide emission spectra which will allow the dynamics, temperature and density of the solar plasma to be determined. As its name suggests, EIS operates in the extreme-ultraviolet (EUV) region of the spectrum. This is a difficult wavelength region for the provision of a radiometric calibration. Previously, the reported relative uncertainties of such satellite instrumentation were, for OSO IV a factor of two [*Reeves and Parkinson*, 1970], OSO VI 40 % to a factor of two [*Huber et al.*, 1973], Skylab S082A within 40 % for a line ratio [*Dere et al.*, 1979] and a factor two for a line intensity [*Dere*, 1982] and Skylab S055 35 % above 45 nm and a factor two below 45 nm and over most of the range covered in second order [*Reeves et al.*, 1977]. Most of these instruments exhibited a loss in responsivity when in orbit, and the references given describe how this was monitored. More recently, for the Coronal Diagnostic Spectrometer (CDS) on SOHO, *Lang et al.* [2000] reported a laboratory calibration in the 15.0 nm to 78.5 nm range with estimated standard uncertainties of around 30 %, and this has been maintained so far for five and a half years in space. The laboratory calibration proposed for EIS is based on that of CDS and is described in the present paper.

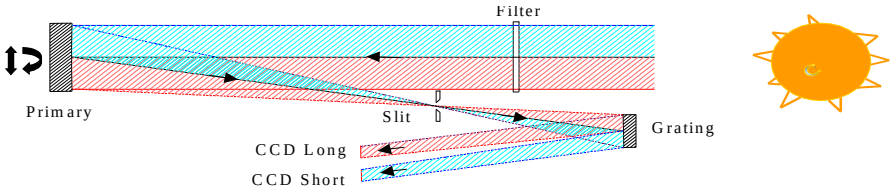

Figure 25.1: The EIS optical layout.

Following a brief description of EIS and the cleanliness programme being undertaken, an overview of the calibration source is given. Calculations of the EIS spectral efficiency are then presented. The proposed laboratory calibration is subsequently described, followed by sections on the uncertainties and the in-flight calibration situation.

25.2 Overview of EIS

To optimise its throughput, EIS was designed to have a minimum number of reflections. It consists of a telescope feeding a stigmatic spectrometer, as shown in Figure 25.1. The telescope, which is illuminated at normal incidence, is an off-axis parabola of 15 cm diameter clear aperture with a focal length of 1.934 m. The mirror is multilayer-coated to improve its EUV reflectivity, each half of the mirror having Mo/Si pairs tuned to give two wavebands, namely 18.0 nm to 20.4 nm and 25.0 nm to 29.0 nm. The mirror is articulated allowing motion in the solar E-W direction and has a fine pointing mechanism which gives a $\pm 3'$ image range with $\pm 0.5''$ accuracy and a coarse pointing mechanism giving a $\pm 15'$ image motion with an accuracy of $\pm 3''$. The fine pointing gives a rastering capability. The focal plane of the telescope is at the entrance slit of the normal-incidence spectrometer. One of four slits ($1''$, $2''$, $40''$ and $250''$ wide) can be chosen. The used length of the slits is $512''$ N-S on the Sun. The holographic, laminar, toroidal grating in the spectrometer has an average radius of 1.181 m and is ruled at 4200 lines/mm. The grating has a multilayer coating, which is matched to the primary mirror, and has a focus mechanism. The spectrometer is used in first order, giving a dispersion of 0.165 nm/mm and a magnification of 1.4. The radiation diffracted by the grating is focussed on to CCD detectors, one for each waveband. The CCDs are Marconi (formerly EEV) type 42-40, thinned and back-illuminated with 13.5 micron[1] pixels, 1024 (corresponding to $1024''$) along the slit by 2048 (i.e., 4.0 nm) in the spectral dispersion direction. Only 512 pixels (corresponding to $512''$) of the 1024 will be used, the extra being available to allow for any movements caused by the spacecraft launch. An aluminium entrance-filter of 150 nm thickness is provided to reject solar heat and visible radiation. Another similar filter is located in the spectrometer near the slit and the shutter. The shutter is used to control the CCD exposures, which may be from 10 ms to a few hundred seconds.

[1] 1 micron = 1 μm = 10^{-6} m

25.3 Cleanliness

The use of normal-incidence EUV optical components drives the contamination control requirements; on the other hand it is expected to ease some of the problems encountered in the radiometric calibration (cf., *Lang et al.* [2000]).

The basis of the approach for EIS is to build on the experience of the flight hardware groups from their involvement in various payloads in the SOHO programme. In particular, the EIS team are building on the work done for the CDS programme [*Harrison et al.*, 1995; *Kent et al.*, 1993, 1994] by tailoring the contamination control document and cleaning schedules to the Solar-B mission and including new cleaning schedules as appropriate, e.g., for the composite material used for the structure. The mechanical-thermal model is being made to the proposed flight-cleanliness standards to build confidence for the flight-model programme. Furthermore, as the same facilities and some of the same staff at the Rutherford Appleton Laboratory (RAL) are being used, the heritage of the CDS programme in the assembly, integration and verification of the instrument will be of direct benefit. For in-flight contamination monitoring, two quartz-crystal microbalances will be used, one placed near the entrance filter on the primary mirror side and the other adjacent to the detector.

25.4 The Calibration Source

To calibrate EIS, we plan to use again the standard source with which CDS [*Hollandt et al.*, 2002; *Lang et al.*, 2000] was calibrated and which has been used repeatedly as a standard for the calibration of the SERTS rocket payload [*Thomas*, 2002]. Briefly, the standard source is a secondary standard which has been radiometrically calibrated by PTB in Berlin by use of a primary standard, namely the BESSY I electron storage ring. It is planned to re-calibrate the source at BESSY II after the calibration of EIS is completed. An extremely stable, high-current, hollow-cathode, discharge lamp is used to provide the EUV line radiation. It emits unpolarised radiation from the buffer gas and sputtered cathode material (aluminium). Radiation from the 1 cm diameter hollow cathode is stopped down by a 0.6 mm diameter pinhole at the focus of a Wolter II telescope, which is used to provide the 5 mm diameter collimated output beam from the source.

25.5 Calculation of EIS Efficiency

As part of the optical design optimisation, the responsivity of EIS was calculated. The same calculations also allow estimates of the count rates expected in the calibration. In addition, it has been agreed that each optical element of EIS will have its efficiency, as a function of wavelength, measured independently at the Brookhaven synchrotron prior to delivery for assembly. Thus, when the calibration is being done, a model based on experimental measurements will be available. Comparisons of the model and the actual calibration will help to reduce systematic errors.

For the present model, we use the transmission of a 150 nm thick aluminium filter with an oxide layer of 15 nm thickness [*Seely*, 2000], as shown in Figure 25.2. We thus assume that the filters will age before launch to give a thickness of 15 nm of oxide. *K.P. Dere*

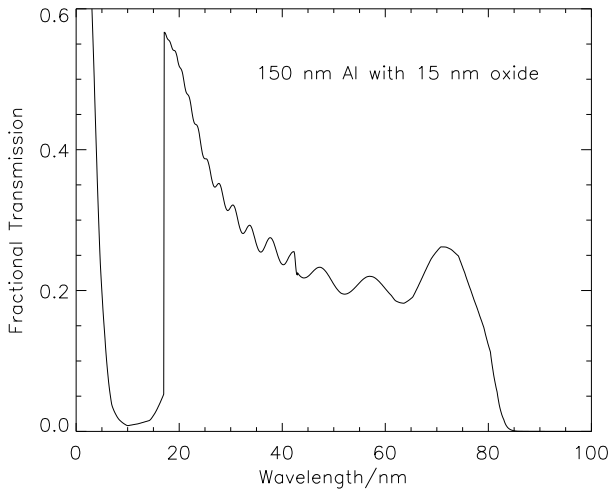

Figure 25.2: The transmission of an aluminium filter 150 nm thick with 15 nm oxide coating.

suggested [*personal communication*, 1999] that measurements of the filters on SOHO EIT support roughly an 8 nm buildup. With only 8 nm there would be an improvement of almost a factor of two in transmission in the long-wavelength band. Both filters are mounted on support meshes which have a transmittance of 85 %. The front filter has an additional support segment which transmits 80 % of the incident radiation. The multilayer coatings on the primary mirror and grating have calculated reflectivities [*Seely*, 2000] as given in Figure 25.3. Note that, in the calculation of the responsivity, the multilayer reflectivity enters twice, since both the primary mirror and grating are coated. The groove efficiency of the grating has been calculated by *Seely* [2000] as 35 % and the quantum efficiency of the CCD is taken as 80 % at all wavelengths in either waveband. These efficiencies, taken with the area of the primary mirror (88.4 cm^2) and a slit width of $1''$, allow the evaluation of the effective areas, i.e., the responsivity, as presented later.

25.6 The Laboratory Calibration of EIS

The source does not fill the EIS entrance aperture, so mapping of the aperture will be needed. The source will be moved vertically, EIS horizontally. One difficulty encountered when calibrating CDS was that for the shorter-wavelength channel of the Normal Incidence Spectrometer (NIS) and Grazing Incidence Spectrometer (GIS) the alignment of the source and CDS could not be checked, especially when doing the aperture scans. This is best done by viewing the image of the source on the EIS detector. The beam-spot at the focus of a reverse-illuminated, 212 cm focal-length telescope (as in the calibration source) is 0.60 mm, and so the EIS mirror of 193.4 cm focal length, will bring the beam to a 0.55 mm diameter spot. This implies a slit-width of at least $59''$. The largest slit will allow this check of the alignment to be made.

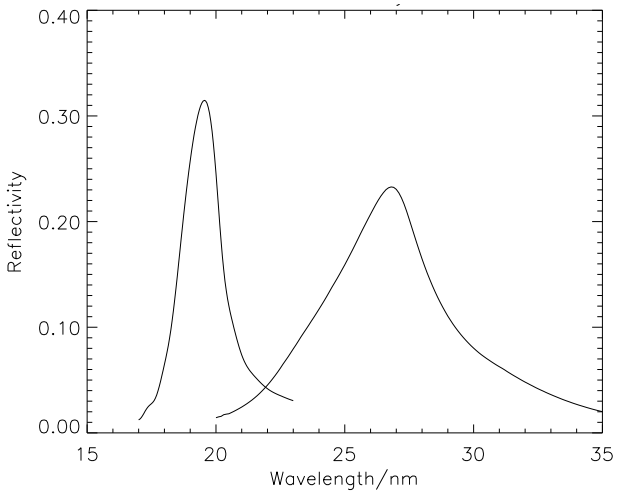

Figure 25.3: The reflectivity of the multilayer coatings: one centred at 19.5 nm the other at 27.0 nm.

Some of the lines proposed for the calibration were not in fact calibrated for the CDS work. However, because EIS must be delivered to a specified date and because BESSY I is no longer operational and the beam line needed at BESSY II is not yet operational, the necessary source calibration will be done after the EIS laboratory calibration.

25.6.1 The Long-wavelength Range (25.0 nm to 29.0 nm)

The calibration lines available are 25.1/.2 nm Ne III, 25.6 nm He II, 26.7/.8 nm Ne II and 28.3/.4 nm Ne III. The latter two lines were used for CDS and have calibrated intensities available. Using these and the EIS predicted efficiency, expected count-rates in the lines are around 1000 counts/s. Figure 25.4 shows the effective area for the long-wavelength channel and the distribution of the calibration lines as a function of wavelength. There is a sparse, but still reasonable, coverage with wavelength.

25.6.2 The Short-wavelength Range (17.0 nm to 21.0 nm)

The source spectrum as observed during the laboratory calibration of the CDS GIS is shown in Figure 25.5. Although the wavelength range of EIS was given above as 18.0 nm to 20.4 nm (the usable in-orbit range), the bandpass is in fact 17.0 nm to 21.0 nm. In the 17.0 nm to 18.0 nm wavelength range, the throughput is very low, and in the 20.4 nm to 21.0 nm range the solar lines are weak and thus the integration times for the Sun will mean that the spacecraft pointing-stability will compromise the performance of EIS. However, in the laboratory long, stable and repeatable exposures will be possible. In the full wavelength-range, the calibration lines available are 16.95 nm to 17.56 nm Al III, 18.0 nm to 18.2 nm Ne IV, 18.5 nm to 18.75 nm Ne IV, 19.4 nm to 19.5 nm Ne IV and 20.4 nm to 20.9 nm Ne IV. The first and last lines were used in the CDS calibration while the others were seen. Note that the shortest-wavelength line-complex straddles the aluminium edge at

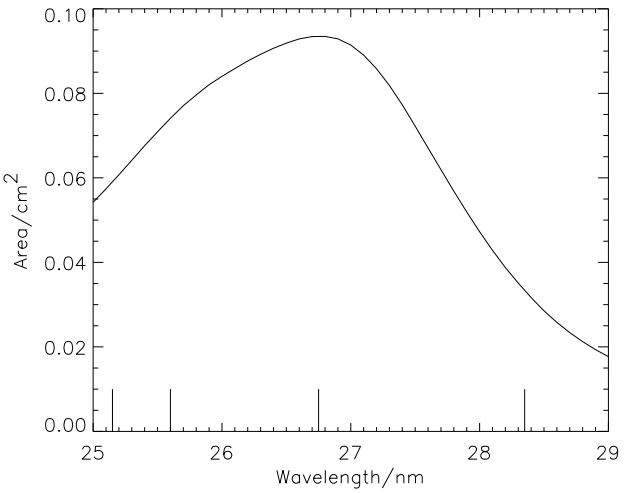

Figure 25.4: The long-wavelength channel effective area and the distribution of the available calibration lines as a function of wavelength.

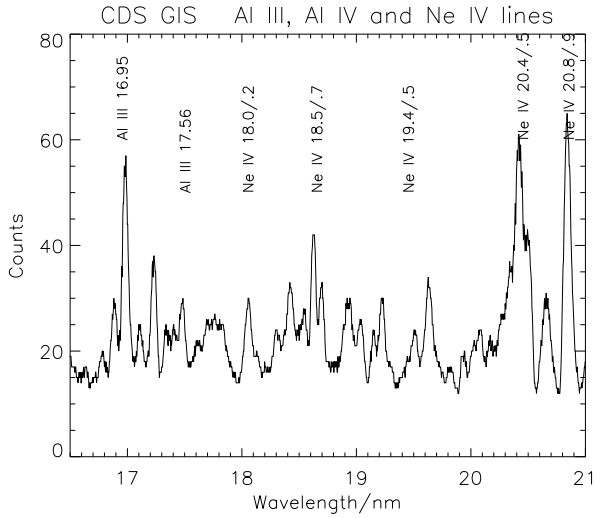

Figure 25.5: Calibration source spectrum taken in the laboratory using the CDS GIS. CDS has solar-blind detectors and thus does not have filters.

17.0 nm and will be measured with the aluminium filters in place. The source recalibration will also be done with a comparable aluminium filter. Figure 25.6 shows the effective area for the short-wavelength channel and the distribution of the calibration lines as a function of wavelength.

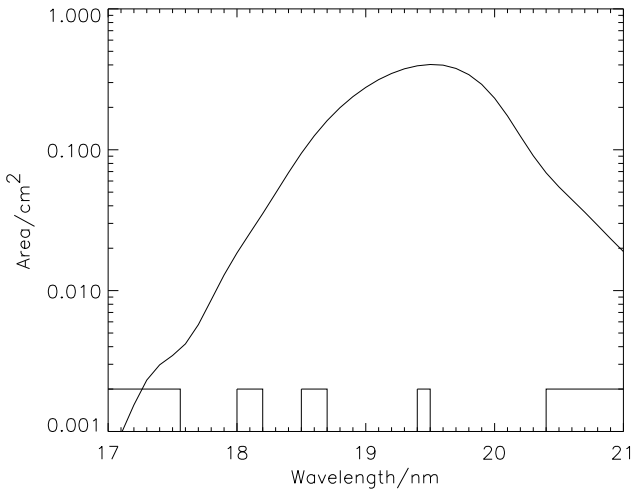

Figure 25.6: The short-wavelength channel effective area and the distribution of the available calibration lines as a function of wavelength.

The calibrated source lines used in the short-wavelength range are weaker than those in the long-wavelength range, particularly the shortest-wavelength line. In addition, the sensitivity of EIS falls more rapidly at the short-wavelength edge of the band. Thus the expected count rates in the calibration at 20.4 nm to 20.9 nm and 16.95 nm to 17.56 nm are 100 counts/s and 0.5 counts/s respectively. For the latter count rate, 3 % counting statistics will take about 40 minutes and to map the source beam over the entrance aperture at points 1 cm apart will take about 70 hours. Hopefully the schedule will allow time for good counting-statistics to be obtained.

25.7 Uncertainties

Care will be taken when doing the work to minimise uncertainties. Having a slit wide enough to check the alignment will be a good start. In addition, the availability of a model based on measurements of the individual optical components will allow checks for systematic errors. The standard uncertainty of the source calibration is 7 or 8 % depending on the line used, the standard uncertainties in the aperture-size measurement and the count-to-photon ratio should be around 15 % and 20 % respectively, giving a total, estimated, standard uncertainty of 26 %.

25.8 The In-flight Calibration Situation

A direct in-flight check on the calibration can be obtained by use of rocket underflights. As far as practicable, the same area of Sun will be observed simultaneously by the payload and EIS. It is proposed that the NASA-GSFC-EUNIS-rocket payload, which is under development [*Thomas and Davila*, 2001] will be used for this work. As presently envisaged,

the wavelength range of EUNIS will encompass the EIS short wavelength-band. The efficiencies of the individual optical elements of the payload will be measured at the NIST synchrotron, and the whole payload will be calibrated at RAL before and after launch, using the same equipment as for EIS.

25.9 Conclusions

The laboratory calibration of EIS will demonstrate that EIS performs to its specification. To do this, EIS has to be tested end-to-end by illuminating it with extreme-ultraviolet radiation. As well as a wavelength calibration, the work will provide an aperture determination, bandwidth check and counts-to-photon measurements as a function of wavelength. The laboratory calibration will benefit from the re-use of SOHO CDS calibration equipment and the expertise gained with it. Thus we expect to minimise the uncertainties.

Acknowledgements

John Mariska is thanked for supplying the computer program to calculate the effective areas. The EIS instrument is being built by an international consortium which includes UK groups (MSSL, Birmingham and RAL), US (NRL, GSFC), Japan (NAOJ) and Norway (University of Oslo). Provision of spacecraft, launch and operations by the Japanese Institute for Space and Astronautical Science is gratefully acknowledged. Support for the programme is provided by PPARC (UK), NASA (USA), Ministry of Education, Science and Culture (Japan) and the Norwegian Research Council.

Bibliography

Culhane, J.L., Doschek G.A., Watanabe, T., and Lang, J., The EUV Imaging Spectrometer and its role in the Solar-B mission, this volume, 2002.

Dere, K.P., Extreme ultraviolet spectra of solar active regions and their analysis, *Sol. Phys.* **77**, 77–93, 1982.

Dere, K.P., Mason, H.E., Widing, K.G., and Bhatia, A.K., XUV electron density diagnostics for solar flares, *Astrophys. J. Suppl. Ser.* **40**, 341–364, 1979.

Harrison, R.A., Sawyer, E.C., Carter, M.K., Cruise, A.M., Cutler, R.M., Fludra, A., Hayes, R.W., Kent, B.J., Lang, J., Parker, D.J., Payne, J., Pike, C.D., Peskett, S.C., Richards, A.G., Culhane, J.L., Norman, K., Breeveld, A.A., Breeveld, E.R., Al Janabi, K.F., McCalden, A.J., Parkinson, J.H., Self, D.G., Thomas, P.D., Poland, A.I., Thomas, R.J., Thompson, W.T., Kjeldseth-Moe, O., Brekke, P., Karud, J., Maltby, P., Aschenbach, B., Bräuninger, H., Kühne, M., Hollandt, J., Siegmund, O.H.W., Huber, M.C.E., Gabriel, A.H., Mason, H.E., and Bromage, B.J.I., The Coronal Diagnostic Spectrometer for the Solar and Heliospheric Observatory, *Sol. Phys.* **162**, 233–290, 1995.

Hollandt, J., Kühne, M., Huber, M.C.E., and Wende, B., Source standards for radiometric calibration of astronomical instruments in the VUV spectral range traceable to the primary standard BESSY, this volume, 2002.

Huber, M.C.E., Dupree, A.K., Goldberg, L., Noyes, R.W., Parkinson, W.H., Reeves, E.M., and Withbroe, G.L., The Harvard Experiment on OSO-6: Instrumentation, calibration, operation, and description of observations, *Astrophys. J.* **183**, 291–312, 1973.

Kent, B.J., Swinyard, B.M., and Hicks, D.H., Contamination effects on EUV optics in the space environment, *Proc. SPIE* **1945**, 348–360, 1993.

Kent, B.J., Swinyard, B.M., and Martin, E.L., Contamination control and material screening for the extreme ultraviolet Coronal Diagnostic Spectrometer on SOHO, *Proc. SPIE* **2210**, 474–484, 1994.

Lang, J., Kent, B.J., Breeveld, A.A., Breeveld, E.R., Bromage, B.J.I., Hollandt, J., Payne, J., Pike, C.D., and Thompson, W.T., The laboratory calibration of the SOHO Coronal Diagnostic Spectrometer, *J. Opt. A: Pure Appl. Opt.* **2**, 88–106, 2000.

Seely, J.F., Multilayer grating for the Extreme Ultraviolet Spectrometer (EIS), *Proc. SPIE* **4138**, 174–181, 2000.

Reeves, E.M., and Parkinson, W.H., Calibration changes in EUV solar satellite instruments, *Appl. Opt.* **9**, 1201–1208, 1970.

Reeves, E.M., Timothy, J.G., Huber, M.C.E., and Withbroe, G.L., Photometric calibration of the EUV spectroheliometer on ATM, *Appl. Opt.* **16**, 849–857, 1977.

Thomas, R.J., and Davila, J.M., EUNIS: A solar EUV normal incidence spectrometer, *Proc. SPIE* **4498**, 161–172, 2001.

Thomas, R.J., Underflight calibration of SOHO CDS by SERTS-97, this volume, 2002.

— 26 —

Future Solar Irradiance Observations from the NASA TIMED and SORCE Satellites

TOM N. WOODS, GARY J. ROTTMAN
Laboratory for Atmospheric and Space Physics
University of Colorado
Boulder, Colorado, USA

The NASA Thermosphere, Ionosphere, and Mesosphere Energetics and Dynamics (TIMED) mission and the NASA Earth Observing Systems' (EOS) SOlar Radiation and Climate Experiment (SORCE) mission will begin new observations of the solar spectral irradiance in August 2001 and August 2002, respectively. The Solar EUV Experiment (SEE) for the TIMED mission will measure the solar vacuum ultraviolet (VUV) spectral irradiance from 1 nm to 195 nm. The EOS SORCE satellite includes four instruments aboard to measure the total solar irradiance (TSI) and solar spectral irradiance from 115 nm to 2000 nm and 1 nm to 35 nm. Calibrations for these instruments use state-of-the-art techniques based primarily on the radiometric standards of electrical substitution radiometers (ESRs) and radiometric standards from the US National Institute of Standards and Technology (NIST). Therefore, these well-calibrated irradiances are useful for validation of other solar measurements, such as from several instruments aboard the SOHO satellite.

26.1 Science Background

The solar ultraviolet (UV) irradiance below 315 nm is the primary source of energy absorbed into the Earth's atmosphere. The altitudes where the solar radiation is absorbed are shown in Figure 26.1 as a function of wavelength. The basic thermal structure of the atmosphere is a result of the absorption of the solar radiation via photodissociation and photoionization of the neutral atmosphere. The solar UV radiation is also of utmost importance for studies of the atmospheric chemistry, such as for ozone. The solar far UV (FUV) radiation from 100 nm to 220 nm photodissociates molecular oxygen in the stratosphere and mesosphere, from which the atomic oxygen leads to the creation of ozone. At the same time, the solar middle UV (MUV) radiation from 200 nm to 310 nm is the primary loss mechanism for ozone through photodissociation of ozone in the stratosphere. The balance of these two reactions, along with other numerous, but minor, ozone chemical reactions, establishes the ozone layer with the peak ozone density in the stratosphere [*Chamberlain*, 1978; *Brasseur and Solomon*, 1986]. The solar UV irradiance and its variability are equally important for studies of the other planetary atmospheres, comets, and the heliosphere. The solar spectral irradiance, as shown in Figure 26.2, has the general characteristic of a continuum spectrum throughout, with many absorption features, both lines and absorption edges, and at the shorter wavelengths superposed with emission features. The visible and

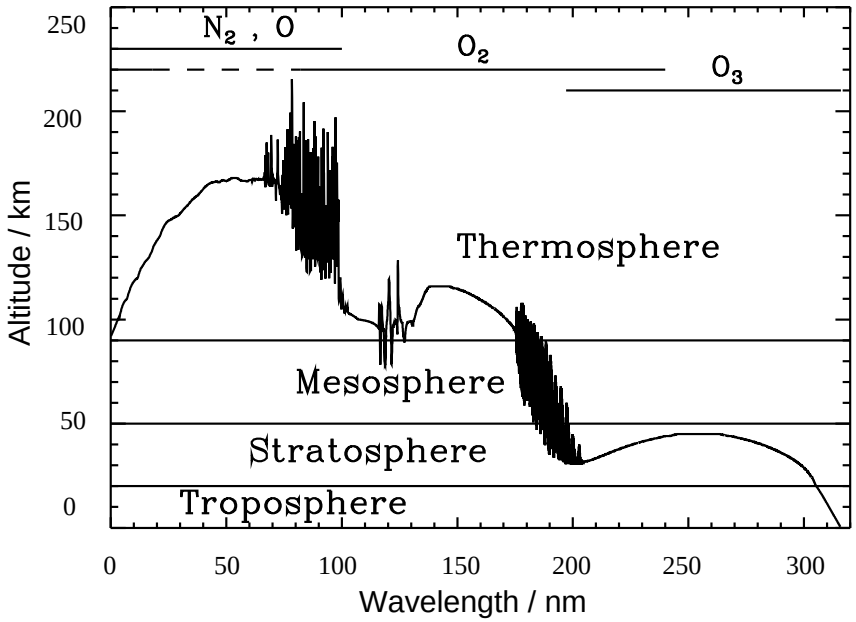

Figure 26.1: Absorption of the solar radiation in Earth's atmosphere. The altitude where optical depth is unity is shown for wavelengths below 320 nm. The atmospheric constituents primarily responsible for the absorption are shown at the top as a function of wavelength. Most of the solar radiation above 315 nm reaches the surface or is scattered by clouds and aerosols back into space.

near IR wavelengths originate low in the solar photosphere. Progressing toward the ultraviolet the emissions, in general, originate higher and higher in the solar atmosphere. Below 200 nm, the emissions are predominantly from the chromosphere along with several bright, high-temperature emissions originating from the transition region and corona. The current understanding of the variations of the solar irradiance is that the visible radiation varies less than one percent and that the shorter wavelength UV radiation can vary by a factor of two or more. The visible observations therefore require precision and accuracy that can only be achieved from space, and observations achieving suitable accuracy were not realized until 1979. Although the ultraviolet radiation from the Sun varies by much larger factors, its measurement also requires access to space because the radiation does not penetrate the atmosphere. Precise space measurements obtained during the past 20 years imply that TSI varies on the order of 0.1 % over the solar cycle, but with greater variations on a short-term basis. How the solar irradiance variations are distributed in wavelength is still poorly understood. The largest relative solar variations are factors of two or more at ultraviolet and shorter wavelengths, but the greater total energy available at visible and longer wavelengths makes their small variations potentially more important.

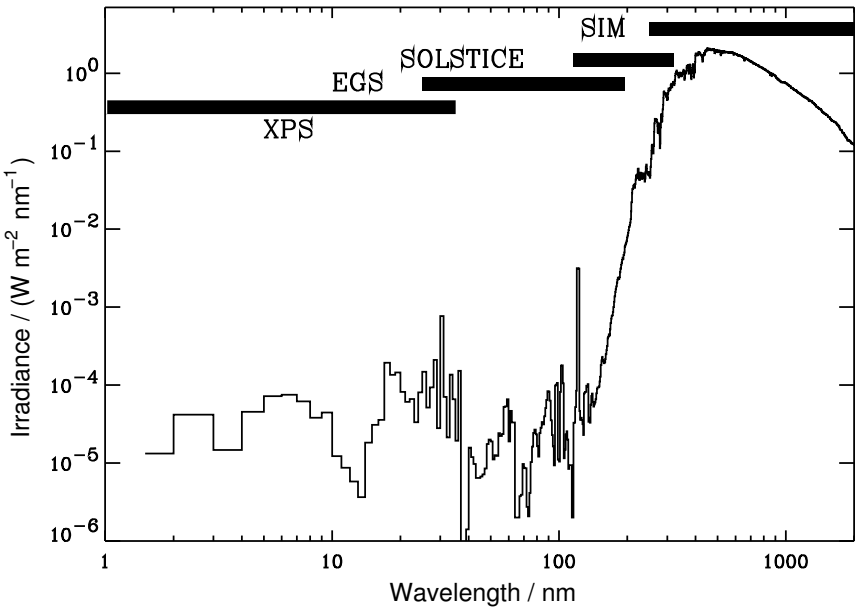

Figure 26.2: Solar irradiance spectrum from 1 nm to 2000 nm in 1 nm intervals. The solar UV irradiance is as much as six orders of magnitude dimmer than the visible irradiance. Horizontal bars indicate the spectral coverage of the SORCE and TIMED instruments as discussed in Section 26.2.

26.2 Instrumentation

The TIMED SEE includes two instruments to measure the solar VUV spectral irradiance from 1 nm to 195 nm. The EUV Grating Spectrograph (EGS) has a spectral range from 25 nm to 195 nm with a 0.4 nm spectral resolution and is derived from sounding rocket experiments [*Woods and Rottman*, 1990; *Woods et al.*, 1994]. The XUV Photometer System (XPS) includes nine silicon XUV photodiodes with thin film filters deposited directly on the photodiode. This XUV photometer set measures the solar irradiance from 1 nm to 35 nm with each filter having a spectral bandpass of about 5 nm. The original XPS concept was designed for the SORCE mission in the late 1980s and has already flown on sounding rocket experiments and the Student Nitric Oxide Explorer (SNOE: 1998 to present) [*Bailey et al.*, 2000]. The prototype SEE instruments have flown as sounding rocket experiments in 1997 and 1998, and these observations have provided validation for the measurements made by the SOHO CDS [*Brekke et al.*, 2000], EIT, SEM, and SUMER instruments. There are four solar irradiance instruments on the SORCE satellite. The Total Irradiance Monitor (TIM) instrument uses redundant bolometers to continue the precise measurements of TSI that began with the ERB instrument in 1979 and have continued to the present with the ACRIM and SOHO VIRGO measurements. The SOLar Stellar Irradiance Comparison Experiment (SOLSTICE), a pair of redundant grating spectrometers, will continue the solar UV spectral irradiance measurements between 120 nm and 300 nm, as currently obtained by the Upper Atmosphere Research Satellite (UARS). The UARS

Table 26.1: Characteristics of the TIMED and SORCE Solar Irradiance Instruments.

	SORCE	SORCE	SORCE	TIMED	BOTH
Property	TIM	SIM	SOLSTICE	EGS	XPS
Instrument Type	Cavity Bolometer	Prism Spectrometer	Grating Spectrometer	Grating Spectrograph	Filter Photometer
Wavelength Range / nm	All (TSI)	250–2000	115–320	25–195	1–35
Spectral Resolution / nm	N/A	0.5–34	0.1	0.4	5–10
Detectors	ESR	ESR Si Diodes InGaAs Diodes	PMT	64×1024 CODACON	Si Diodes
Field of View	4° cone	1.5°× 1.5°	1.5°× 1.5°	5°× 12°	12° TIMED 4° SORCE
Total Accuracy / %	0.01	0.05	5	10	20
Relative precision / (%/yr)	0.001	0.01	1	2	4

SOLSTICE measurements have been used to validate the SOHO SUMER measurements [*Wilhelm et al.*, 1999]. The Spectral Irradiance Monitor (SIM) is a new prism spectrometer designed to measure the solar spectral irradiance from 250 nm to 2000 nm with high precision and accuracy. The SORCE XPS is almost identical to the XPS on the TIMED SEE instrument, and it will measure the solar spectral irradiance from 1 nm to 35 nm, the most variable part of the solar spectrum. The spectral coverage of the SORCE instruments is not fully redundant, but each instrument slightly overlaps the spectral range of the adjacent instrument for purposes of data validation. The characteristics of the TIMED and SORCE solar irradiance instruments are listed in Table 26.1. A summary of each instrument follows, and more detailed descriptions are given in other instrument papers.

The TIM instrument on SORCE will measure the total solar irradiance (TSI) with a total accuracy (standard uncertainty) of 100 parts per million (ppm), where 1 ppm = 0.0001 %, and a relative precision (stability) of 10 ppm per year. The TIM incorporates four cavities (cones) as the bolometer detectors and adheres to the basic concepts of Electrical Substitution Radiometers (ESR). The TIM ESR has two identical cavities, each electrically heated, but only one illuminated with the light to be measured. In its normal operational mode, the TIM shutter is cycled 50 % open and 50 % closed every 100 seconds throughout the orbit. A phase-sensitive detection algorithm at the shutter fundamental frequency provides a major improvement in reducing the noise uncertainties by factors of 100 to 400 over the previous DC measurements. The pre-flight calibration for TIM relies on the National Institute of Standards and Technology (NIST) standards for volt and ohm and the measurement of the area of the TIM apertures at NIST. The in-flight calibration relies on using redundant channels weekly and a ground-based copy of TIM, which may fly annually as a Space Shuttle experiment. *Lawrence et al.* [2000a, 2000b] provide a more detailed description of the TIM instrument.

The SIM instrument on SORCE will measure the solar spectral irradiance in the 250 nm to 2000 nm range with a total accuracy of 500 ppm and a relative precision of 100 ppm per year. The SIM is a new instrument development using a prism as the single optical element

and an electrical substitution radiometer (ESR) as the primary detector. In addition, two Si photodiodes and an InGaAs photodiode are used for the UV, visible and IR portion of the spectrum, respectively. The photodiodes, having a faster response time than the ESR, are used for most of the spectral measurements, and the ESR, being an absolute detector, provides a calibration for the photodiodes at several discrete wavelengths. The pre-flight calibration for SIM relies on the NIST standards for volt and ohm for its reference ESR and laboratory measurements of the area of the SIM apertures and of the prism transmission. The SIM is designed as a dual-spectrometer to provide in-flight calibrations with the redundant channel on a weekly basis. Additionally, a periscope system couples the two spectrometers and is used with two additional photodiodes (Si and InGaAs) to obtain in-flight measurements of the prism transmission. *Harder et al.* [2000a, 2000b] provide a more detailed description of the SIM instrument.

The SOLSTICE instrument on SORCE will measure the solar spectral irradiance in the 115 nm to 320 nm range with a total accuracy of 5 % and a relative precision of 0.5 % per year. These accuracy and precision values are larger than the SIM values because today's UV calibrations standards are not as precise as those in the visible. Nevertheless, because the solar UV varies far more than the visible, SOLSTICE still exceeds the measurement requirement. This instrument is a modified Monk-Gillieson grating spectrometer with photomultiplier tube (PMT) detectors and is an improved version of the UARS SOLSTICE instrument [*Rottman et al.*, 1993; *Woods et al.*, 1993]. The unique design of the SOLSTICE spectrometer is that both the Sun and calibration stars can be observed with the same optics and detectors by changing only the entrance and exit slit sizes and integration time to accommodate the different intensity levels. The pre-flight calibration of SOLSTICE relies on the synchrotron source at the NIST Synchrotron Ultraviolet Radiation Facility (SURF-III). In addition to the in-flight calibration with about 20 stars, SOLSTICE has redundant (identical) spectrometers for use as backup and in-flight validation. *McClintock et al.* [2000] provide a more detailed description of the SORCE SOLSTICE instrument.

The EGS instrument on TIMED will measure the solar spectral irradiance in the 25 nm to 195 nm range with a total accuracy of 10 % and a relative precision of 2 % per year. The design for the EGS is a normal-incidence 1/4 m Rowland circle grating spectrograph with a 64 $\times$ 1024 CODACON detector [*McClintock et al.*, 1982]. The CODACON detector uses gold-coated microchannel plates (MCP) and coded anode electronics for its readout. The pre-flight calibration of EGS relies on the synchrotron source at the NIST SURF-III. The in-flight calibrations include weekly redundant channel measurements and additional calibrations using the prototype SEE instruments on annual sounding rocket flights. *Woods et al.* [1998] provide a more detailed description of the EGS instrument. The XPS instrument on both TIMED and SORCE will measure the solar spectral irradiance in the 1 nm to 35 nm range with a total accuracy of 20 % and a relative precision of 4 % per year.

The XPS is a package of nine silicon XUV photodiodes for measuring the XUV and EUV irradiance from 1 nm to 35 nm and at Ly α (121.6 nm). Each XUV photodiode has a thin-film filter to provide an approximately 7 nm spectral bandpass. These thin-film filters are deposited directly on the photodiode to avoid using delicate metal foils, which are difficult to handle, prone to develop pin holes, and degrade with time. The SORCE XPS is almost identical to the TIMED SEE XPS. The main differences are that some of the XUV filters on the silicon photodiodes were improved for the SORCE XPS and that some of the electronic components were upgraded to meet the requirements for the longer

SORCE mission. The pre-flight calibration of XPS relies on the synchrotron source at the PTB BESSY for the TIMED XPS and at the NIST SURF-III for the SORCE XPS. For in-flight calibration purposes, three of the nine XUV photometers are redundant and will be used weekly for tracking instrument degradation. *Woods et al.* [1998, 1999] provide a more detailed description of the XPS instrument.

26.3 Mission Summaries

The spacecraft for the TIMED mission is provided by the Johns Hopkins University Applied Physics Laboratory (JHU-APL). The TIMED satellite is a 3-axis stabilized satellite that maintains a nadir view for the three atmospheric instruments aboard. The SEE includes a one-axis gimbal table for pointing the EGS and XPS instruments towards the Sun for about three minutes per orbit. The TIMED mission was launched on a Delta II on 7 December 2001 into an orbit with a 630 km altitude and 74° inclination. The goal for the mission lifetime is two years. The spacecraft mission operations will be conducted at the JHU-APL Mission Operations Center (MOC). The TIMED SEE Payload Operations Center (POC), located at LASP in Boulder, Colorado, has full responsibility for operating the SEE instrument and for all science data production activities. The standard data product for the TIMED SEE measurements is the daily-averaged irradiances reported from 1 nm to 195 nm in 1 nm intervals.

The spacecraft for the SORCE mission is provided by Orbital Sciences Corporation (OSC). The SORCE satellite is a 3-axis stabilized satellite for pointing the instruments towards the Sun for the primary solar measurements for about 60 minutes per orbit, as well as for pointing towards stars for the SOLSTICE in-flight calibrations. The SORCE mission is scheduled for launch on a Pegasus XL in October 2002 into an orbit with a 645 km altitude and 40° inclination. The goal for the mission lifetime is six years. Mission operations, including both spacecraft and science operations, will be conducted at the SORCE Mission Operations Center (S-MOC), located at LASP in Boulder, Colorado. The SORCE Science Operations Center (S-SOC) in Boulder has full responsibility for all science data production activities. The standard data products for the SORCE measurements are the daily-averaged and 6-hour averaged irradiances reported for the total irradiance and a full spectrum from 1 nm to 2000 nm (excluding 35 nm to 115 nm) in 1 nm intervals below 300 nm and in intervals that vary from 1 nm to 34 nm above 300 nm.

There is a strong need to continue well-calibrated and long-term solar spectral irradiance measurements for current and future studies of the solar connection to the Earth's climate and atmosphere. In addition, these well-calibrated solar irradiance instruments can provide a validation for other solar UV measurements, such as from the SOHO satellite.

Bibliography

Bailey, S.M., Woods, T.N., Barth, C.A., Solomon, S.C., Canfield, L.R., and Korde, R., Measurements of the solar soft X-ray irradiance from the Student Nitric Oxide Explorer: First analysis and underflight calibrations, *J. Geophys. Res.* **105**, 27 179–27 193, 2000.

Brasseur, G., and Solomon, S., Aeronomy of the Middle Atmosphere: Chemistry and Physics of the Stratosphere and Mesosphere, Dordrecht, Boston, 1986.

Brekke, P., Thompson, W.T., Woods, T.N., and Eparvier, F.G., The extreme-ultraviolet solar irradiance spectrum observed with the Coronal Diagnostic Spectrometer (CDS) on SOHO, *Astrophys. J.* **536**, 959–970, 2000.

Chamberlain, J.W., Theory of Planetary Atmospheres: An Introduction to Their Physics and Chemistry, Academic Press, New York, 1978.

Harder, J., Lawrence, G., Rottman, G., and Woods, T., The Spectral Irradiance Monitor: SIM, *Metrologia* **37**, 415–418, 2000a.

Harder, J.W., Lawrence, G.M., Rottman, G.J., and Woods, T.N., Spectral Irradiance Monitor (SIM) for the SORCE mission, *Proc. SPIE* **4135**, 204–214, 2000b.

Lawrence, G., Rottman, G., Harder, J., and Woods, T., The solar Total Irradiance Monitor: TIM, *Metrologia* **37**, 407–410, 2000a.

Lawrence, G.M., Rottman, G.J., Kopp, G., Harder, J.W., McClintock, W.E., and Woods, T.N., Total Irradiance Monitor (TIM) for the EOS SORCE mission, *Proc. SPIE* **4135**, 215–224, 2000b.

McClintock, W.E., Barth, C.A., Steele, R.E., Lawrence, G.M., and Timothy, J.G., Rocket-borne instrument with a high-resolution microchannel plate detector for planetary UV spectroscopy, *Appl. Opt.* **21**, 3071, 1982.

McClintock, W.E., Rottman, G.J., and Woods, T.N., SOLar STellar Irradiance Comparison Experiment II (SOLSTICE II) for the NASA Earth Observing Systems Solar Radiation and Climate Experiment (SORCE) mission, *Proc. SPIE* **4135**, 225–234, 2000.

Rottman, G.J., Woods, T.N., and Sparn, T.P., Solar Stellar Irradiance Comparison Experiment I: 1 Instrument Design and Operation, *J. Geophys. Res.* **98**, 10667–10677, 1993.

Wilhelm, K., Woods, T.N., Schühle, U., Curdt, W., Lemaire, P., and Rottman, G.J., The solar ultraviolet spectrum from 1200 Å to 1560 Å: A radiometric comparison between SUMER/SOHO and SOLSTICE/UARS, *Astron. Astrophys.* **352**, 321–326, 1999.

Woods, T.N., and Rottman, G.J., Solar EUV irradiance derived from a sounding rocket experiment on 10 November 1988, *J. Geophys. Res.* **95**, 6227, 1990.

Woods, T.N., Rottman, G.J., and Ucker, G., Solar Stellar Irradiance Comparison Experiment I: 2 Instrument calibration, *J. Geophys. Res.* **98**, 10679–10694, 1993.

Woods, T.N., Rottman, G.J., Bailey, S., and Solomon, S.C., Vacuum-ultraviolet instrumentation for solar irradiance and thermospheric airglow, *Optical Eng.* **33**, 438, 1994.

Woods, T.N., Prinz, D.K., London, J., Rottman, G.J., Crane, P.C., Cebula, R.P., Hilsenrath, E., Brueckner, G.E., Andrews, M.D., White, O.R., VanHoosier, M.E., Floyd, L.E., Herring, L.C., Knapp, B.G., Pankratz, C.K., and Reiser, P.A., Validation of the UARS solar ultraviolet irradiances: Comparison with the ATLAS 1 and 2 measurements, *J. Geophys. Res.* **101**, 9541–9569, 1996.

Woods, T.N., Eparvier, F.G., Bailey, S.M., Solomon, S.C., Rottman, G.J., Lawrence, G.M., Roble, R.G., White, O.R., Lean, J., and Tobiska, W.K., TIMED Solar EUV Experiment, *Proc. SPIE* **3442**, 180–191, 1998.

Woods, T.N., Rodgers, E., Bailey, S.M., Eparvier, F.G., and Ucker, G., TIMED Solar EUV Experiment: Pre-flight calibration results for the XUV Photometer System, *Proc. SPIE* **3756**, 255–264, 1999.

— 27 —

The Solar Package on ISS: SOL-ACES

FRANK G. WIENHOLD, JOACHIM ANDERS, BOGDAN GALUSKA,
ULRICH KLOCKE, MANFRED KNOTHE, EUGEN NESKE,
WOLFGANG J. RIEDEL, GERHARD SCHMIDTKE,
RALF SINGLER, ULRICH ULMER, HELMUT WOLF

Fraunhofer Institute of Physical Measurement Technology
Freiburg, Germany

The "solar package" comprises the experiments SOLSPEC (UV/Vis to IR spectral range), SOVIM (total solar radiation) and SOL-ACES to be installed on a Coarse Pointing Device (CPD) of the International Space Station for a 1.5 year mission launched in 2003. The CPD allows for measuring periods of at least fifteen minutes per orbit totaling approximately 600 hours per year of solar observations. The Solar Auto Calibrating EUV/UV Spectrometers (SOL-ACES) are currently developed to measure the solar radiation (full disk) in the 17 nm to 220 nm spectral range with four grazing-incidence grating spectrometers. To obtain high radiometric accuracy of better than 10 %, a double ionization chamber is assigned to each of the spectrometers as a primary detector standard. Optical bandpass filters are mounted on a filter wheel to be placed at the entrance apertures of the spectrometers and ionization chambers and thereby will establish the radiometric link between these devices. The spectrometers are designed as scanning monochromators operating at fixed incidence angles. The deflected radiation is monitored by rotating an assembly containing a parabolic mirror, an exit slit and a channel electron multiplier around the grating center. The optical length of the ionization chamber of 0.5 m is divided into two identical electrode sections. In addition, the transmitted radiation is measured by a silicon diode detector located at the end of the absorption path. Detector and electrode signals are recorded as a function of the gas pressure in the chamber, which is increased from zero to a few hectopascal during a single measurement. These data permit the absolute quantification of the radiant solar flux in the wavelength interval transmitted by the bandpass filter and the correction for secondary effects, such as ionization caused by photoelectrons. With these measurements the spectrometer efficiencies at the filter bandpass wavelengths can be recalibrated as required during the mission.

27.1 Introduction

The primary scientific goal of the Solar Package is the accurate determination of the total solar irradiance and the impact of its variation on the Earth's climate. The Solar Package consists of three instruments to be installed on the International Space Station (ISS) during the early utilization period. The mission is planned to begin in early 2003 and to last for at least 1.5 years.

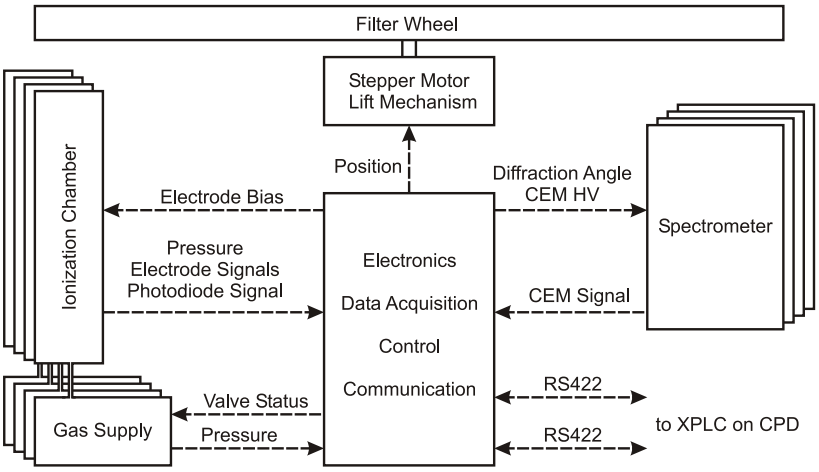

Figure 27.1: Overview of the functional components of SOL-ACES.

Three instruments on a common pointing platform (Coarse Pointing Device, CPD) will be located on the wake starboard Express Pallet Adapter of the ISS outbound zenith Express Pallet. The CPD is designed to provide a minimum of 600 solar observation hours per year with at least fifteen minutes of continuous solar observation during an ISS orbit.

The instruments of the Solar Package are a total solar irradiance radiometer (SOVIM) supplied by the World Radiation Center, Davos, Switzerland and two full-disk solar spectrophotometers. The SOLSPEC spectrophotometer, developed at the Sevice d'Aeronomie of the CNRS, Paris (France), covers the spectral range from the UV (180 nm) to the infrared (3000 nm). SOLSPEC is complemented in the 17 nm to 220 nm spectral range by the Solar Auto-Calibrating EUV/UV Spectrometers (SOL-ACES).

SOL-ACES aims to provide spectral measurements of the solar EUV/UV irradiance with a radiometric accuracy of better than 10 % using ionization chambers as radiometric detector standards. The data obtained will be used to study physical processes of the solar atmosphere during the period of solar cycle 23, and to quantify impact and forcing of the solar EUV/UV radiation on the Earth's upper atmosphere, providing input for thermosphere-ionosphere modeling. In this context the data will be used to improve solar EUV/UV emission models and to derive EUV/UV indices for different applications [*Schmidtke*, 1976]. This will be supported by semi-empirical modeling of solar active regions. Another topic is the investigation of solar-stellar relations. During its mission period SOL-ACES will also offer the possibility of intercalibrating the solar EUV/UV spectrometers, which have no in-orbit calibration capabilities based on radiometric detector standards. This paper describes the setup and functional principle of SOL-ACES, which is currently under development at the Institute of Physical Measurement Technology in Freiburg, Germany.

Table 27.1: Optical properties, wavelength ranges and wavelength resolution of the spectrometers.

Spectrometer	Grating, rules/mm	Incidence Angle / °	Scan Angle / °	Wavelength Range / nm	Wavelength Resol. / nm
1	3600	84	69 – 53	16.9 – 54.4	0.3
2	2400	84	69 – 53	25.4 – 81.6	0.4
3	1800	83	68 – 46	36.6 – 151.8	0.6
4	1200	83	68 – 46	54.5 – 227.7	0.9

27.2 Instrument Description

The dimensions of the SOL-ACES instrument are 24 cm×28 cm×60 cm with a total mass of 23 kg. The setup of the main components is shown in Figure 27.1. The spectral measurement of the solar irradiance is performed by four grating spectrometers. To account for efficiency changes during the spectrometers' lifetime caused by the interaction of the high-energy solar radiation with the optical surfaces, four ionization chambers serving as radiometric detector standards are assigned individually to each of the spectrometers. The gas supply system of a single ionization chamber allows a well-controlled pressurization of the chamber with a gas whose ionization level is selected to match the corresponding wavelength range of the spectrometer. To relate the ionization chamber measurement to the spectrometer efficiency, up to eleven optical bandpass filters mounted on a filter wheel are used. By rotating the wheel, each filter can be located at the spectrometer entrance aperture or moved to the entrance window position of the ionization chamber. The filter wheel also seals the chamber. The electronic unit controls the components' mechanisms and acquires the related data. It is linked to the External Payload Computer of the CPD by two serial RS 422 lines for instrument control and data transmission.

27.2.1 Spectrometers

The grating spectrometers operate as scanning monochromators. The setup of the optical components and the optical geometry, as indicated in Figure 27.2, is identical for all four spectrometers. To cover different wavelength ranges, gratings with adequate grating constants are used. With the grating positioned at a fixed angle of incidence (83 ° or 84°) the dispersed radiation is focused through the spectrometer exit slit by a parabolic mirror and collected by a channel electron multiplier (CEM) operated in a pulse-counting mode. The width of the exit slit is adapted to the wavelength resolution defined by the field-of-view of the solar disk.

The parabolic mirror, the exit slit and the CEM are mounted on a subassembly. It is rotated around the grating center thereby focusing radiation of different dispersion angles through the exit slit onto the CEM. By this arrangement the incident angles for the optical surfaces remain constant during the scan resulting in a smooth dependence of spectrometer efficiency on wavelength. Grazing incidence is also used for the parabolic mirror, resulting in low angular variation of the incidence angle over the mirror aperture (75 ° to 80°),

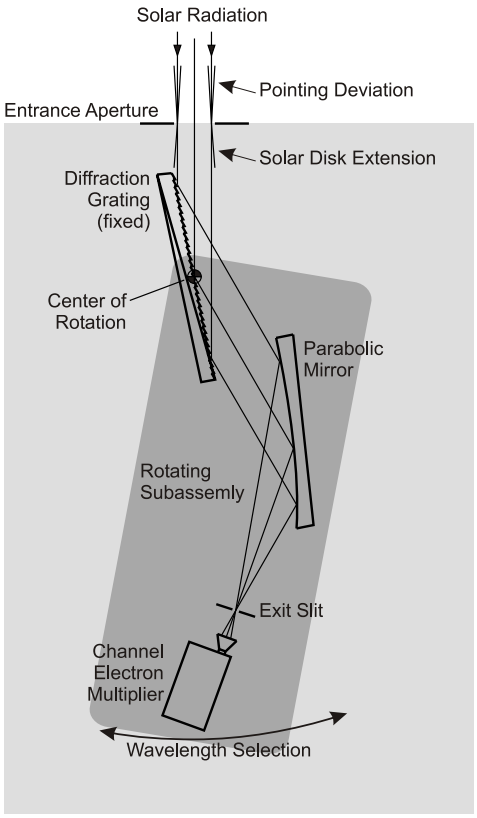

Figure 27.2: Spectrometer optical components and geometry.

high mirror reflectivity, and low reflectivity variation with wavelength. In addition to the field-of-view of the solar disk (32′) the optical geometry has to tolerate the possible misalignment of 18′ induced by the pointing device. These constraints lead to the layout of the four spectrometers summarized in Table 27.1.

27.2.2 Ionization Chambers

The ionization chambers of 0.5 m total length contain two successive electrode sections of identical geometry and a silicon detector at the lower end, as indicated in Figure 27.3. The signal of this detector permits a consistency check with the measured ion currents. The gas supply system of each chamber is designed to pressurize in two steps, a slow pressure increase from vacuum to approximately 10^{-2} hPa during the first 90 s followed by a faster increase to 1 hPa during the next 9 s. The electrons generated by photoionization of the gas are collected on the inner surface of a cylindrical anode (30 mm in diameter), while the slow ions are driven to the cathode by the bias potential (−30 V) of the low-field ion chamber [*Samson and Haddad*, 1974]. Transimpedance amplifiers convert the cathode current into a voltage signal.

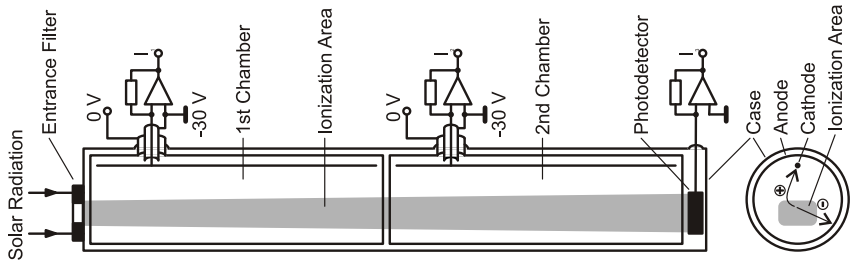

Figure 27.3: Scheme of the ionization chambers.

During the phase of the slow pressure increase, the chamber is operated in the optically-thin mode with an absorption of less than 25 % over the full length. Pressure and geometry are the same in the two electrode sections to ensure equal quantum efficiency. Thereby both the incident irradiance and the quantum efficiency can be deduced at any pressure from the two ion-current signals, eliminating the influences of gas impurities, ion loss (recombination) or additional ion generation (secondary ionization by photoelectrons) in this phase of the measurement [*Samson*, 1967].

While the pressure increases to 1 hPa, the ionization chamber is operated in the saturated mode, increasing the absorption to more than 99.9 %. Then the deviation of the ion signal pressure dependence from the saturation plateau is used to identify pressure dependent secondary effects. The "true" ion current, which would be present in the absence of these effects, is obtained by extrapolation of the saturation signal to zero pressure [*Carlson et al.*, 1984]. At the end of the measurement the chamber is vented to ambient vacuum conditions by lifting the filter wheel.

27.2.3 In-orbit Calibration

The filter bandpass regions define calibration intervals in the spectrometers' wavelength ranges. Due to the smooth efficiency characteristic of the spectrometers with respect to wavelength, efficiency curves can be established by interpolating between the calibration intervals.

A calibration cycle proceeds as follows. Two successive spectrometer scans are recorded without and with the filter at the entrance aperture. The absolute filter transmittance is determined from the ratio of the spectra to monitor changes in the filter characteristic that may be caused by exposure to the radiation. Immediately after the spectrometer scans, the absolute solar flux in the filter bandpass region is measured using the ionization chamber. The time required by this sequence is less than ten minutes; in general the solar irradiance can be assumed to be constant during this period. The ionization chamber measurement and the integrated data of the spectrometer covering the filter bandpass range define the spectrometer efficiency at this calibration interval.

The sequence is repeated for different filters in successive orbits to obtain the spectrometer calibration in the complete SOL-ACES wavelength region. Both the spectrometer scan and the ionization chamber measurements are performed in less than three minutes each. The orbital solar pointing time of fifteen minutes offered by the CPD allows five such elementary measurements. For solar observations five spectrometer scans are made with

aperture open. In calibration mode a filter is placed in the aperture for the fourth spectrometer scan,and the ionization chamber measurement terminates the sequence. Calibration cycles are scheduled twice per week in the first month of the mission, once per week in the following five months, and once in two weeks for the final year.

27.3 Summary

A solar EUV/UV spectrometer system is currently being developed to be flown as part of the Solar Package on the ISS during the early utilization period in 2003 and 2004. Four grazing-incidence grating spectrometers cover the wavelength range from 17 nm to 220 nm integrated over the solar disk. The instrument is equipped with a unique in-orbit calibration capability using sets of optical bandpass filters in conjunction with double-ionization chambers as radiometric standards. Owing to the in-orbit calibration a radiometric accuracy of better than 10 % is expected for the whole mission period.

Bibliography

Carlson, R.W., Ogawa, H.S., Philips, E., and Judge, D.L., Absolute measurement of the extreme UV solar flux, *Appl. Opt.* **23**, 2327–2332, 1984.

Samson, J.A.R., Techniques of Vacuum Ultraviolet Spectroscopy, Wiley, New York, 1967.

Samson, J.A.R., and Haddad, G.N., Absolute photon flux measurement in the vacuum ultraviolet, *J. Opt. Soc. Am.* **64**, 47–54, 1974.

Schmidtke, G., EUV indices for solar-terrestrial relations, *Geophys. Res. Lett.* **3**, 573–576, 1976.

— 28 —

The Solar Orbiter Mission and Design Recommendations

UDO SCHÜHLE
Max-Planck-Institut für Aeronomie
Katlenburg-Lindau, Germany

RON THOMAS
former ESA/ESTEC, Noordwijk, The Netherlands
private Whiteoaks, Monkmead Lane, West Chiltington, UK

JEAN-FRANÇOIS HOCHEDEZ
Royal Observatory of Belgium
Bruxelles, Belgium

A short overview is given of the Solar Orbiter mission. First, the key scientific aims of the mission are briefly described. As the mission profile has consequences on the design of the payload instruments and their calibration, the mission design is described. Possible implications and problems for the cleanliness and the calibration stability of the instruments are outlined. Some solutions are discussed.

28.1 Introduction

As one of ESA's future solar missions, the Solar Orbiter was selected in October 2000. It is planned to be launched around 2011. Similar to SOHO, its payload will consist of a suite of instruments to investigate the Sun and the heliosphere. It is thus appropriate to consider here if any lessons learned from SOHO could be usefully transferred to Solar Orbiter. We take an excerpt from the "Solar Orbiter Assessment Study Report" [*ESA*, 2000] in order to give an overview of the mission perspectives, the prospective payload and the mission orbit all of which have specific implications for the cleanliness and stability of calibration of the instruments. We review some of the cleanliness procedures adopted for the SOHO project which may be applicable to the Solar Orbiter.

28.2 Solar Orbiter Scientific Aims

The Sun's atmosphere and the heliosphere represent uniquely accessible domains of space, where fundamental physical processes common to solar, astrophysical and laboratory plasmas can be studied in detail and under conditions impossible to reproduce on Earth or to study from astronomical distances. With the results from missions such as Helios, Ulysses, Yohkoh, SOHO, ACE, and TRACE we have advanced enormously our

understanding of the Sun, its corona, the associated solar wind and the three-dimensional heliosphere. After these missions, we have reached the point where further in-situ measurements, now much closer to the Sun, together with high-resolution imaging and spectroscopy from a near-Sun and out-of-ecliptic perspective, promise to bring about new insights and perhaps major breakthroughs in our understanding of solar and heliospheric physics. The Solar Orbiter will, through a novel orbital design and innovative instrumentation, provide the required measurements and observations, and will, for the first time, explore the uncharted, innermost regions of our solar system. It will study the Sun from close-up (45 solar radii, or 0.21 AU), fly by the Sun and examine the solar surface and the space above from a co-rotating vantage point. It will provide images of the Sun's polar regions from heliographic latitudes as high as $38°$. The near-Sun interplanetary measurements, together with simultaneous remote-sensing observations of the Sun, will permit us to disentangle spatial and temporal variations at the solar surface, the corona and inner heliosphere. They will allow us to understand the characteristics of the solar wind and energetic particles in close linkage with the plasma conditions in their source regions on the Sun. By approaching as close as 45 solar radii, the Solar Orbiter will view the solar atmosphere with unprecedented spatial resolution (35 km pixel size, equivalent to $0.05''$ from Earth). Over extended periods of time the Solar Orbiter will deliver images and data of the polar regions and the side of the Sun not visible from the Earth at that time. The scientific goals of the Solar Orbiter mission can be summarized as follows. It will determine, in-situ, the properties and dynamics of plasma, fields and particles in the near-Sun heliosphere. It will investigate the fine-scale structure and dynamics of the Sun's magnetized atmosphere, using close-up, high-resolution remote sensing. Using the solar co-rotation passes, it will identify the links between activity on the Sun's surface and the resulting evolution of the corona and inner heliosphere. Finally, it will observe and fully characterize the Sun's polar regions and equatorial corona from high latitudes. The Solar Orbiter will achieve its wide-ranging aims from a specially-designed orbital trajectory and using a suite of sophisticated instruments.

28.3 Mission Profile and Spacecraft Design

The Solar Orbiter scientific requirements define a mission profile in terms of orbital parameters, launch windows, payload mass, etc., that is the driver for the spacecraft design. The required final orbit is characterized by a perihelion distance as close as possible to the Sun with a high orbital inclination with respect to the solar equator. To achieve such a trajectory, a long transfer-period is required and low-thrust solar electric propulsion (SEP) will be used. In addition, several swing-bys at Venus are necessary to make use of planetary gravity assists. The projection of the orbit on the equatorial plane is shown in Figure 28.1. The mission profile is composed of three phases:

1. The cruise phase, which starts at spacecraft separation from the launcher and ends at the start of scientific operations (some science may be performed during the cruise phase).
2. The nominal mission phase, during which the main scientific mission is performed.
3. The extended mission phase, when further gravity assist manoeuvres will allow higher-inclination observations.

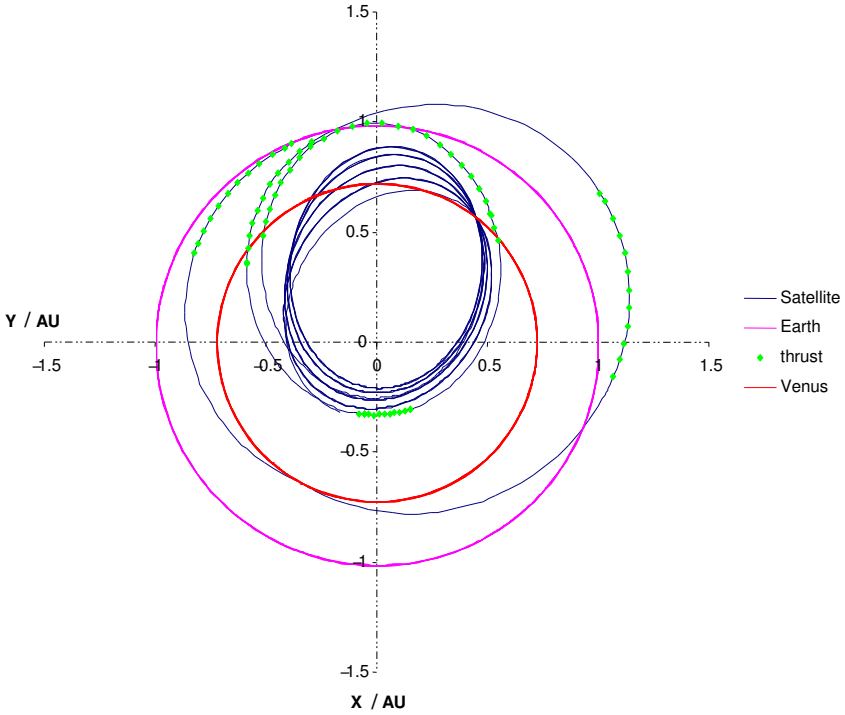

Figure 28.1: X-Y-plane projection of the Solar Orbiter trajectory.

During the cruise phase (0 to 1.86 years) there are SEP-thrust phases, with durations ranging from 6 to 105 days, and Venus swing-bys driving the semi-major axis changes and the inclination increase. During the nominal mission (1.86 to 4.74 years, duration: 2.88 years), the orbit is typically of order 150 days, taking the spacecraft from about 0.2 AU to 0.9 AU. There are two Venus swing-bys in this 7-orbit phase taking the orbital inclination to over 30°. During the extended mission (4.74 to 7.02 years, duration: 2.28 years), there are two further Venus swing-bys over six orbits which provide a continued increase in the orbital inclination. The important orbital parameters (perihelion distance and heliographic latitude) are shown in Figures 28.2 and 28.3. The orbit assures a close distance to the Sun relatively early during the mission, while a high, scientifically satisfactory, heliographic latitude is achieved towards the final phase of the mission. The celestial coordinates of the Sun, Venus and Earth yield a launch window of three weeks in every nineteen months. Figure 28.4 shows the overall configuration of the Solar Orbiter spacecraft during scientific observations. The spacecraft body has a cross-section of 1.6 m (Y) $\times$ 1.2 m (Z) and its length is 3.0 m (X). The $+X$ side, which faces the Sun ($\pm 30°$), is covered by a thermal shield shadowing the spacecraft body. In order to minimize the energy input from the Sun, the cross-section of the spacecraft in the Y, Z plane has been minimized.
The spacecraft is of modular design, with a Service Module (SVM) and a Payload Module (PLM). The $\pm Y$ sides of the PLM accommodate the cruise solar arrays (two wings, three panels per wing) and the top-shield radiators. The optical instruments are right beneath

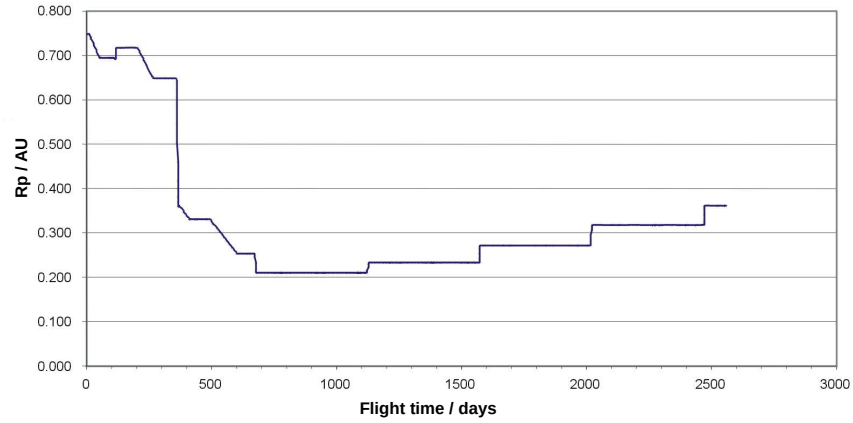

Figure 28.2: Distance of perihelion of each orbital path.

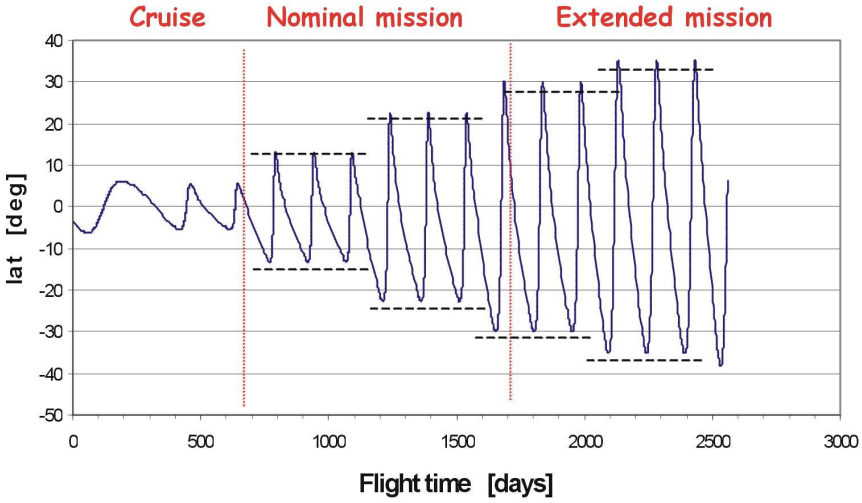

Figure 28.3: Spacecraft solar latitude with respect to the equator.

the top shield and are pointed in the $+X$ direction. They are isostatically attached to the central cylinder and may be cooled by radiators to cold space on the $\pm Z$ sides. The instruments' electronic boxes are mainly mounted on the bottom panel of the PLM. The SVM accommodates the orbit solar panels and the solar electric propulsion equipment radiators on the $\pm Y$ panels. The high gain antenna (HGA) and the thrusters are attached to the $+Z$ panel. In order to cope with different attitudes and distances from the Sun, both solar arrays incorporate a one-degree-of-freedom (1-DOF) driving mechanism. The cruise solar array can be jettisoned. The HGA mast (2 m long) is mounted on a 2-DOF mechanism and ensures coverage throughout the mission. The spacecraft is 3-axis stabilized and always Sun pointed (X-axis), except during SEP firing. The Sun-pointing face of the Solar

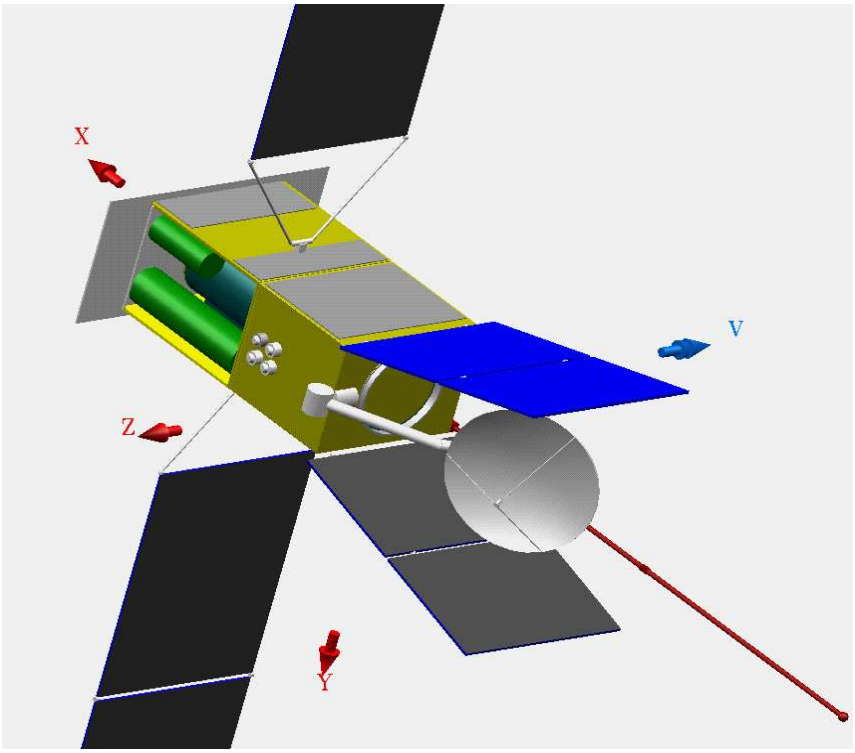

Figure 28.4: Configuration of the Solar Orbiter.

Orbiter is as small as is possible in order to minimize the thermal input from the Sun. The remaining spacecraft surfaces will carry radiators. The extreme environments encountered by the spacecraft throughout the whole mission drive the thermal design of the Solar Orbiter. At one extreme, the spacecraft is orbiting the Sun at distances as close as 0.21 AU. At the other extreme, the spacecraft is as far as 1.21 AU from the Sun. Another important factor is the electrical propulsion that intermittently generates a considerable amount of heat inside the spacecraft. Therefore the thermal design has to accommodate a wide range of heat load levels and locations. The basic design concept consists of shading as much as possible every part of the spacecraft from the Sun at the closest approach to the Sun and during the ion-thruster firings in the cruise phase. To this aim, a sunshield has been included at the $+X$ side of the spacecraft. It extends on the $\pm Z$ sides to make sure that the spacecraft is shadowed even when the $+X$ axis is offset by as much as 10° from the Sun. (The $\pm Z$ offset of 10° occurs during the SPT firing at the closest approach to the Sun (0.33 AU) during the cruise phase.)

28.4 The Strawman Payload

The payload must be state-of-the-art, withstand the considerable thermal load at 45 solar radii, comply with the general requirements of a low-mass, compact and integrated

Table 28.1: In-situ heliospheric instrumentation.

Name	Acronym	Measurement	Specifications	Mass / kg	Size / (cm×cm×cm)
Solar Wind Plasma Analyser	SWA	Thermal ions and electrons	0 to 30 keV/Q; 0 to 10 keV	6	20 × 20 × 20
Radio and Plasma Wave Analyser	RPW	AC electric and magnetic fields	μV/m to V/m; 0.1 nT to μT	10	15 × 20 × 30 (electronics box)
Radio Sounding	CRS	Wind density and velocity	X-band; Ka-band	(USO 200g)	5 × 5 × 5
Magnetometer	MAG	DC magnetic field	to 500 Hz	1	10 × 10 × 10
Energetic Particle Detector	EPD	Solar and cosmic-ray particles	Ions and Electrons 0.01 to 10 MeV	4	10 × 20 × 20
Dust Detector	DUD	Interplanetary dust particles	Mass (g): 10^{-16} to 10^{-6}	1	10 × 10 × 10
Neutral Particle Detector	NPD	Neutral hydrogen and atoms	0.6 to 100 keV	1	10 × 10 × 20
Neutron detector	NED	Solar neutrons	e > 1 MeV	2	10 × 10 × 10

design, make use of on-board data compression/storage and require a modest data transmission rate. The selected payload, which meets the solar and heliospheric science objectives of the mission, encompasses two instrument packages: in-situ heliospheric instruments and remote-sensing instruments. The design of these instrument packages builds upon heritage of the previous Helios, Yohkoh, SOHO, Ulysses, WIND, ACE and TRACE missions.

28.4.1 In-situ Heliospheric Instruments

The in-situ instruments on Solar Orbiter constitute a package of sensors suited to a comprehensive study of the solar-wind plasma, its constituents, motions, and energetic processes. Additional instrumentation is included for the detection of neutral atoms, neutrons, circumsolar and interplanetary dust, solar radio emission and local magnetic fields. A list of the in-situ instruments with their main specifications is given in Table 28.1.

28.4.2 Remote-sensing Solar Instruments

An integrated ensemble of high-resolution remote sensing instruments is proposed for the Solar Orbiter: an EUV full-Sun and high-resolution imager, a high-resolution EUV spectrometer covering selected emission lines from the chromosphere to the corona, a high-resolution visible-light telescope and magnetograph, an EUV and visible-light coronagraph and a radiometer. Table 28.2 lists the instruments of the remote-sensing package and their main specifications.

All the disk-observing instruments will resolve small-scale dynamical processes in the solar atmosphere. The combination of instruments proposed provides a complete set of

Table 28.2: Remote-sensing instrumentation.

Name	Acronym	Measurement	Specifications	Mass / kg	Size / (cm×cm×cm)
Visible-light Imager and Magnetograph	VIM	High-res. disk imaging and polarimetry	Fe 630 line	26	30 × 40 × 120
EUV Imager and Spectrometer	EUS	Imaging and diagnostics of TR and corona	EUV emission lines	22	30 × 15 × 140
EUV Imager	EXI	Corona imaging	He and Fe Ion lines	36	40 × 40 × 250
Ultraviolet and Visible Light Coronagraph	UVC	Imaging and diagnostics of the corona	Coated mirror coronagraph	17	20 × 20 × 50
Radiometer	RAD	Solar constant	Visible light	4	11 × 11 × 22

multi-wavelength measurements required to understand the Sun's magnetized atmosphere from below the photosphere up into the extended corona.

28.5 Implications and Constraints for the Payload

Technical challenges to the instruments of the Solar Orbiter payload are mainly imposed by the mission design. We see four major causes for potential technical problems:

1. The varying orbital distance to the Sun results in a thermally-variable and thus difficult environment.
2. The close approach to the Sun causes severe technical problems because of the increased radiation flux.
3. Limited communication with the spacecraft requires autonomous operation and storage of large data volumes.
4. The mass resources are limited, yet high-resolution instrumentation requires additional thermal hardware (to cope with the thermal environment mentioned under point 1).

Resolution of these problems must be achieved while aiming at stability of the spacecraft and, as a result, stability of calibration.

28.5.1 What Can Be Learned from SOHO? Recommendations for Solar Orbiter

The stability of the calibration of SOHO's optical and UV instruments is a result of the cleanliness program imposed on instruments and spacecraft. Among others, the material selection and design features were the main contributors to success: see the "Summary of Cleanliness Discussion" in this volume [*Schühle et al.*, 2002]. Although in most cases it is

not possible to remove all actuators from the optically critical volumes, the materials used for these actuators can be critically screened and space-conditioned and separated from the components of the control electronics. SEM's degradation, though small, underlines the importance of the correct location of instrument apertures with respect to other spacecraft hardware. Also within individual instrument enclosures, proper hardware placement is of importance. For instance, where a rotating shutter is used close to a cooled CCD with provision for periodic warm up, provision must be made to ensure that the shutter sector used for this latter phase differs from that normally used during observations.

It is surprising that the design of the Solar Orbiter spacecraft as described in the reference did not build more on the SOHO experience. A good feature of the latter was the PLM box structure supporting the instruments on five sides, with a sunshield over the upper end protecting the top-mounted instruments and the PLM structure from excessive solar heating. The space between the upper end of the structure and that shield was closed by thermal blankets and vented at a controlled location away from any instrument aperture. All instrument thermal blankets were designed to eject outgassed products to the $-X$ direction (or outboard where that was impossible).

Solar Orbiter presently has a cylindrical structure with the optical instruments mounted on its surface under the shield, but apparently with their front faces coincident with that of the shield. The non-optical instruments are mounted on the forward face of the cylinder. It seems that any outgassing from these latter instruments, the structure and the hot shield may have an easy path to the optical instrument apertures. We would suggest that the sunshield be located, say, 30 cm ahead of the optical instrument aperture plane and the top end of the structure, which should be closed at $+X$ and positively vented near $-X$. The space between each optical instrument and the shield should have a structure to deflect outgassing from the central instruments to the sides of the optical apertures; this structure need not be more substantial than a membrane (kapton, if thermal considerations are acceptable). If each optical instrument has an external door, then the actuator should be mounted outboard of the aperture. The instrument could carry the outgassing shield mentioned in this paragraph mounted on the two inboard sides. Outgassing from the $-X$ side of the sunshield will depend on material selection, which needs attention. However, taking account of the long time between launch and first observations should do much to clean up the shield.

The mission profile shows periods when the internal instruments' heaters could be powered to "bake-out" optics before observations, there being ample power available when the SEP is not operating. Figure 28.5 shows the possible temperature evolution for the shield, based on tables 7-1 and 17-1 and figure 11-3 of the reference. Notice that real-time data telemetry and commanding are not possible during periods when the Sun-spacecraft distance is less than 0.5 AU. Ideally, in this bake-out phase, venting of the products to space should be enhanced. The entrance aperture is not suitable for this as its area is small and, in molecular flow path terms, it will be far from the baked detector. A large, baffled vent offering a flow rate of 1000 l s^{-1}, or even a venting door close to the baked optics, should be considered. Some of the remote sensing instruments have large primary mirrors in full Sun. This means they will face heat input of 952 W m^{-2} at aphelion (1.2 AU) to 34 kW m^{-2} at perihelion (0.2 AU) and will be radiatively cooled for the hot case. The large temperature excursion in flight is going to be a severe test of the mountings and interfaces between the mirrors and the metal supports and perhaps of the thermal stability of the mirrors themselves. Compensation for the thermal excursions cannot be accomplished by

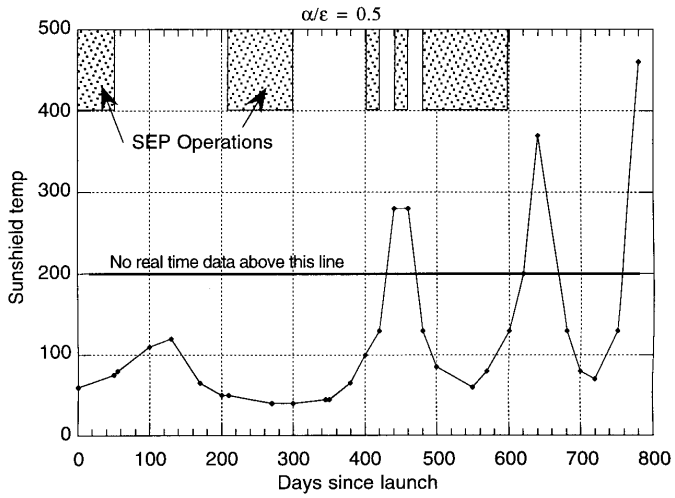

Figure 28.5: Possible temperature evolution for the shield. Also shown are periods (example 600 to 620 days) when internal instruments' heaters could be powered to "bake out" optics before observations, there being ample power available when the SEP is not operating.

heater power. Concepts for variable heat transfer from telescopes to radiators are needed, for example regulated heat pipes. Heat-rejection filters (different for EUV than for visible), which reduce heat input to instruments but are stable to radiation, could also limit the ultraviolet bandpass inside the instrument, resulting in reduced contamination sensitivity. In the same way, selective mirror coatings, reflecting only the wanted part of the solar spectrum while transmitting most of the unused spectrum into a heat sink, would separate the heat and ultraviolet radiation from mirrors further down in the optical path and from the focal planes. Offpointing in cruise phases can be as much as 30° at 1 AU and 10° at the closest SEP operation with some risk of asymmetric heating of the instrument bodies. Such excursions are similar to those experienced by SOHO during the loss-of-attitude, which resulted in redistribution of contaminants inside instruments. In the case of SUMER this resulted in a loss of responsivity of 31 % (on the average), which otherwise would have not experienced any degradation. Thus a clean internal design is not sufficient under these circumstances. A large venting area without UV illumination, preferably with instrument heating, can reduce this degradation effect.

One solution to reduce the large difference in heat input between open and closed aperture doors is to use SUMER-type doors which transmit visible light (ideally longer than 300 nm) at all times and so remove the transient thermal effects from the exposures. Yet the offpointing problem remains, as does the variation of input between aphelion and perihelion in most operational orbits, assuming that the primary mirror is cooled by a radiator that can dump the entire heat load irrespective of the orbit position. The volumes of the instruments are large and naturally fall into two or more separated compartments, the largest containing the primary and secondary mirrors and being difficult to keep clean while the other(s) can be more easily isolated from the spacecraft, with purging possible on the ground. Large instruments could fold their optical paths and thus shorten and stiffen

their optical benches. This would reduce the thermal-control problems and, as a bonus, assist in minimizing the mass. For EUV instruments, however, there is a high price to pay in throughput for each reflection, which might not be acceptable for any resolving instrument measuring radiances.

Dry-gas purging is difficult to guarantee on a continuous basis at spacecraft level, but we would recommend that provision be made for this. Purging should be foreseen as a weekly operation for, say, one hour and on exit from thermal vacuum tests or other tests resulting in cold detectors. This applies to most optical instruments, and we expect that more frequent or even continuous purging may be necessary for some detector types.

The instruments of the Solar Orbiter should be expected to have a high duty cycle in order to catch small scale dymamic processes, but one of the most serious bottlenecks of the mission will indeed be the limited telemetry. On the other hand, one cannot afford to undersample or even miss interesting events. This concern can be resolved by having the capacity to autonomously trigger on pre-determined categories of phenomena. This implies taking a number of observations that will not be down-linked. This solution also demands advanced processing on board. Assuming that stored data will normally be read out on a first-in, first-out basis, it might prove useful to apply on-board intelligence to tag some data for earliest possible read-out.

The stability of the instrument responsivities, and particularly of the focal plane flat-fields, must be monitored carefully if it is to be maintained. For instruments imaging the full solar disk, the diameter will indeed vary throughout the orbit, resulting in a variable exposure and thus in a less deterministic evolution of the exposure and potential degradation of the detector. The latter effects should therefore be minimized by new technological developments for focal-plane arrays (see "New Detector Concepts" in this volume [*Hochedez et al.*, 2002]). Simultaneously, the instruments should explore means for recalibration (calibration lamps, assessment of the mirror changes).

The Solar Orbiter mission profile makes the operational conditions much more variable, making stability of calibration a very important issue. The stability that was possible on a mission like SOHO may not be achievable. However, we are optimistic that in spite of the severe thermal problems to be faced, but given the success of SOHO, Solar Orbiter will not present undue cleanliness problems.

Acknowledgements

We thank E. Marsch (of the Max-Planck-Institut für Aeronomie) for his contributions to this description of the Solar Orbiter mission.

Bibliography

ESA, Solar Orbiter – A high-resolution mission to the Sun and inner heliophere, Assessment Study Report, SCI(2000) 6, 2000.

Hochedez, J.-F., Schühle, U., and Lemaire, P., New detector concepts, this volume, 2002.

Schühle, U., Thomas, R., Kent, B.J., Clette, F., Defise, J.-M., Delaboudinière, J.-P., Fröhlich, C., Gardner, L.D., Hochedez, J.-F., Kohl, J.L., and Moses, J.D., Summary of cleanliness discussion: Where was the SOHO cleanliness programme really effective? this volume, 2002.

— 29 —

New UV Detector Concepts

JEAN-FRANÇOIS HOCHEDEZ
Royal Observatory of Belgium
Bruxelles, Belgium

UDO SCHÜHLE
Max-Planck-Institut für Aeronomie
Katlenburg-Lindau, Germany

PHILIPPE LEMAIRE
Institut d'Astrophysique Spatiale
Orsay, France

BOLD (Blind to the Optical Light Detectors) is an international initiative dedicated to the development of novel imaging detectors for UV solar observations. It relies on the properties of wide-bandgap semiconductor materials (in particular diamond and Al-Ga-nitrides). This investigation is proposed in view of the Solar Orbiter UV instruments, for which the expected benefits of the new sensors, visible blindness and radiation hardness, will be highly valuable. Despite various advances in the technology of imaging detectors over the last few decades, the present UV imagers based on silicon CCDs or microchannel plates exhibit limitations which are inherent to their actual material and technology. Yet the utmost spatial resolution, fast temporal cadence, sensitivity, and photometric accuracy will all be decisive for forthcoming solar space missions. The advent of imagers made of large wide-bandgap semiconductors would surmount many present weaknesses. This would open up new scientific prospects and, by simplifying their design, would even make the instruments cheaper. As for the Solar Orbiter, the aspiration for wide-bandgap semiconductor-based UV detectors is still more desirable because the spacecraft will approach the Sun where heat and radiation fluxes are high. We describe the motivations leading to such new developments, and present a programme to achieve revolutionary flight cameras within the Solar Orbiter schedule.

29.1 Motivations

Current solar atmospheric studies show that the need for improved UV observations is paramount.

Practically, the observational data can be obtained by emphasizing apparently independent attributes: temporal, spectral, spatial resolutions, signal-to-noise ratio, field of view, etc. Scientific investigations benefit from all of these aspects. However, they are coupled by the physical processes to be observed. For example, smaller phenomena usually have less brightness, and evolve faster. This implies that the quests for high resolution, cadence and sensitivity are fundamentally indivisible, and the goal would be to maximize all of them consistently. These features unfortunately conflict from the instrumental perspective, putting constraints on the design and operation of the optical system and the focal plane instrumentation.

In the imaging instrument case, let us consider a small area, A_{Sun}, *at* the Sun with a homogeneous photon radiance L ($\mathrm{m}^{-2}\,\mathrm{s}^{-1}\,\mathrm{sr}^{-1}$) in the direction of one particular pixel P of the instrument. The focal length is implicitly adjusted to have A_{Sun} match this pixel. Ω_{eff} will denote the *effective* solid angle of the whole telescope as seen from A_{Sun}, i.e. $\Omega_{\mathrm{eff}} = A_{\mathrm{eff}}\, d^{-2}$, with A_{eff} being the effective area of the instrument, and d the Sun-telescope distance. The responsivity, ϵ, and the telescope aperture, A_{aper}, are embedded into A_{eff}. The number of photons, S, detected in the considered pixel P then is:

$$S = L\, A_{\mathrm{Sun}}\, T_{\mathrm{ExposureTime}}\, \Omega_{\mathrm{eff}} \tag{29.1}$$

Due to the Poisson statistics, the SNR (signal-to-noise ratio) is always smaller than $S/\sqrt{S} = \sqrt{S}$. Hence,

$$\frac{SNR^2}{A_{\mathrm{Sun}}\, T_{\mathrm{ExposureTime}}} \leq \frac{L\, A_{\mathrm{eff}}}{d^2} \tag{29.2}$$

Equation (29.2) relates the concrete values of an observation, on the left-hand side, to other conditions, on the right-hand side. This formulation stresses the mutual limitations of the spatial resolution, temporal cadence, and SNR. The left-hand side can be seen as a specification for a future instrument. It is restricted by external premises controlled by the Sun (L), the hardware design (A_{eff}), or the mission orbit (d). Under these circumstances, the operation of a given instrument may also carry out trade-offs between the cadence, limited by $T_{\mathrm{ExposureTime}}$, the spatial resolution, which is adjustable by binning, and the signal-to-noise ratio, which ought to be kept at a significant level.

With fixed focal length and pixel size, solar structures will be resolved at much smaller spatial scales by going closer to the Sun. However, the signal observed by one resolving element (pixel) will not change. The *angular* resolution of instruments presently flown on space missions is of the order of 1″. For Solar Orbiter [*Marsch et al.*, 2000; *Fleck et al.*, 2000] elements of 0.5″ or better are expected. Thus one anticipates spatial resolving elements of 75 km at the Sun from 0.21 AU for the EUV spectrograph (EUS) and 35 km for the EUV imager (EXI). This corresponds to an area at the Sun of more than a factor 100 smaller than achieved by SUMER or TRACE. But the typical time constants then are much shorter, because structures evolve faster at these scales. By extrapolating the relationship between the areas and durations of quiet-Sun brightenings [*Berghmans et al.*, 1998], such events should last less than 100 ms, whereas typical exposure times of current instruments are in the 10 s range; another factor of 1000 would be needed to sample the intensity curves with 10 ms intervals. Assuming the contrast will be the same, which is not guaranteed due to line-of-sight effects, the radiation collected by one pixel (at 0.5 ″) will be comparable to TRACE. Fortunately, the radiance L may happen to be locally higher than the spatially-averaged radiance seen in current measurements, which would result from the improved resolution associated with the low filling factor of magnetic structures suggested by present observations. But it is very apparent that the effective area of the instruments has to be maximized. It is the purpose of BOLD to increase, as much as possible, the effective area of the UV instruments by using innovative imagers [*Hochedez et al.*, 2000, 2001a,b, 2002; *E. Monroy et al., J.L. Pau et al., personal communications*, 2002].

Due to the large temperature range of the solar atmosphere, the wavelength region of coronal observations includes the UV spectrum, from the XUV to the NUV. It is technologically a difficult range as far as the optics and sensors are concerned. The performance

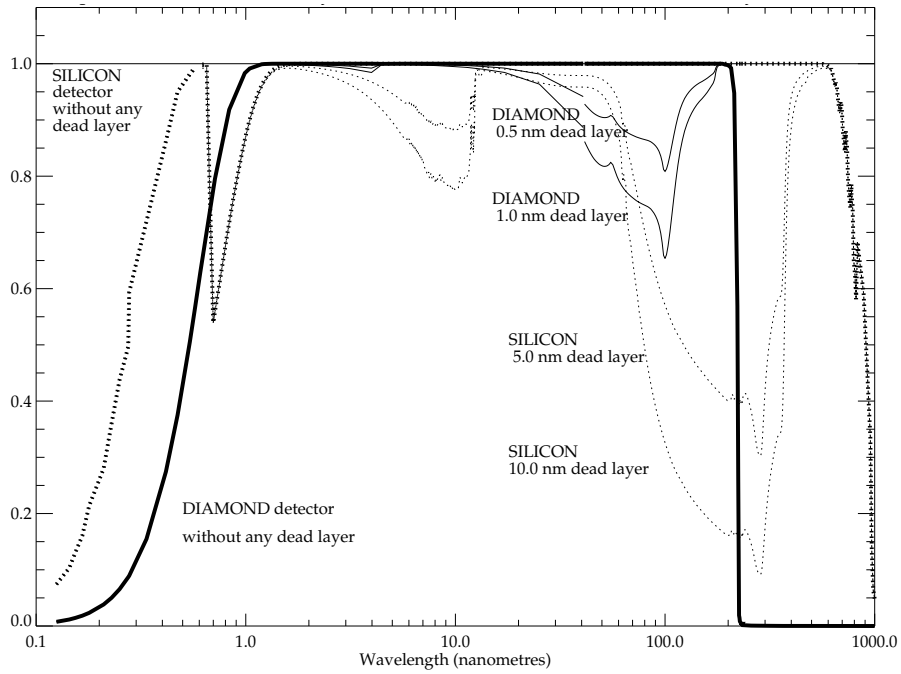

Figure 29.1: A Comparison of QE between Silicon and Diamond detectors estimated by a simple dead-layer model. The plain curves correspond to diamond; the dotted curves to silicon. The thick lines show the modeled QE with no dead layer. In all instances, the depletion layer is 10 μm thick.

of ultraviolet detectors has improved over the last few decades in different respects, and astrophysical instrumentation has taken advantage of that, and developed accordingly. Large, sensitive silicon CCDs and microchannel plates contributed significantly to the achievements of recent solar missions, such as SOHO [e.g., *Thompson*, 1999], Yohkoh, TRACE and others. But the properties of the focal plane units are still the limiting factors in the performance of modern telescopes. Present UV imagers exhibit shortcomings which are difficult to overcome within their technology. CCD-based detectors suffer from several drawbacks.

- The penetration depth of the photons in the silicon determines a pan-chromatic sensitivity that is deleterious when observing a bright visible source such as the Sun (Figure 29.1). One, therefore, adds filters in the optical design which block the undesired visible light, but, which then, regrettably, attenuate the throughput in the ultraviolet.

- Cooling must be implemented to reduce the dark current and to prevent degradation from ionizing radiation. This is a challenging and costly concern in space missions.

- Additionally, the cooled detector turns into a cold trap for contaminants, which stick to the sensitive surface. As a result, bake-out resources are needed to frequently

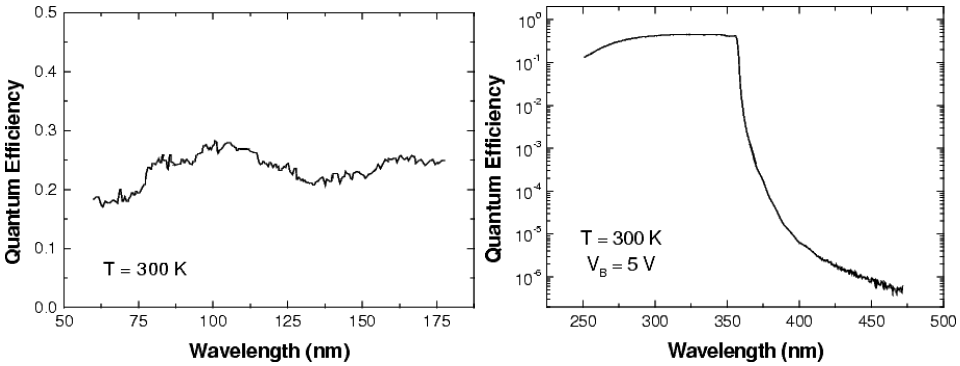

Figure 29.2: Spectral response of GaN MSM photodetectors in the vacuum-UV range (Left), and in the visible and near-UV range (Right). After *E. Monroy et al. and O. Hainaut et al., personal communications* [2002].

drive off the volatile condensable material from the detector surface. Organic contaminants (including hydrocarbons), furthermore, have longer residence times on the cold surface, and they polymerize under the UV signal, which degrades the detector operations irreversibly.

- The ionizing radiation of the space environment leads to pollution of images with "cosmic-ray hits" (points and streaks) that are hard to disentangle from the solar signal.
- The surface and interfaces can charge under particle or UV doses. This deteriorates the charge collection efficiency (CCE), and hence the stability and spatial homogeneity of the quantum efficiency (QE) [*Defise et al.*, 1997]. The applicability of the pre-launch calibration is thereafter compromised. Moreover, the ensuing degradations reduce the sensitivity of the focal plane, i.e., they jeopardize the lifetime of the instrument.

In the VUV range, microchannel plate intensifiers have to be used because no imaging devices presently exist that are intrinsically sensitive in this wavelength range. They still need pixel sensors for position encoding, which may be CCDs, incorporating thereby some of the previous problems, or anode arrays that sense the position of the incident photon by centroiding the electron cloud produced by the channel plate, and converting it into a pixel array. The latter avoids the drawbacks of CCDs, is inherently less sensitive to cosmic rays, and needs no cooling. But microchannel plates have major additional drawbacks.

- They need high voltage for amplification.
- Due to scrubbing, their gain reduces continuously during usage. This makes the calibration difficult to maintain. The high voltage must be increased to compensate for scrubbing.
- Their resolution is limited by the pore size to about 10 μm.
- Their count-rate capability is limited due to gain saturation.

- The image is distorted in two ways: due to alignment errors of the fibres, and due to inhomogeneity of the electric field between the channel plate and the anode.

New detector devices based on wide-bandgap semiconductors (diamond or aluminium-gallium-nitrides) can overcome many of the restrictions listed above [*Goldberg*, 1999; *Mainwood*, 2000]. Like the CCDs in the past they will open new opportunities in the development of solar telescopes, coronagraphs, and spectrometers of higher capabilities. They will be more cost-effective than previous detectors by sparing the development and the weight of cooling hardware, radiative shields and bake-out resources. Below, several of the relevant benefits which make them promising UV imaging sensors.

- The wide bandgap allows the detector to operate at ambient or even higher temperatures.

  1. Cooling hardware is no longer needed.
  2. The contamination is reduced.
  3. Heating resources for bake-out are not needed.
  4. *Materials can be selected with such large bandgaps that they are insensitive to the most intense part of the solar spectrum, which makes the detectors "solar-blind", yet still sensitive in the ultraviolet.* (See Figure 29.2.) As the filters rejecting the visible spectrum also reduce the heat input to the instrument, they usually cannot be suppressed altogether, but they would not be necessary for optical reasons anymore. Nevertheless, whether one is kept or not, the associated loss of effective area will be significantly reduced.

- The compact crystal network of, for example, diamond, provides better radiation-hardness; the smaller atomic numbers offer a smaller cross-section to damaging radiation, and fewer artefacts due to cosmic-rays.

- The absence of an oxide layer will improve the QE, its uniformity (flatfield) and its stability.

- Thanks to a greater resistance to electrical breakdown, the field strength can be higher, and the pixel can potentially be in the sub-micrometer range: an order of magnitude smaller than present, silicon-based detectors.

- Due to higher carrier velocities, the detector is fast, thereby reducing read-out overheads and the need for a shutter.

- In particular, the new detectors are directly sensitive to the VUV, which avoids entirely all the drawbacks related to microchannel plate intensifiers.

29.2 The BOLD Project

29.2.1 Specifications

More than six UV imagers are anticipated in the Solar Orbiter assessment study report. The format requirements are similar (arrays from 2k by 2k, to 4k by 4k pixels), but

the wavelengths differ, ranging from 4 nm to 150 nm. The limited telemetry rate of deep space missions makes partial read-out (windowing) and random pixel access necessary to reduce the readout overheads. Read-out on the chip, developed for active pixel sensors (APS-CMOS technology), is also compatible with the current concepts for BOLD sensors, and will be demonstrated during the feasibility phase. In addition to the large imaging arrays baselined above, simpler UV detectors, of one or a few pixels, will also be included as total irradiance or technological monitors. They would benefit from wide-bandgap semiconductor-based technologies too.

29.2.2 Programme

Diamond and aluminium-gallium-nitride materials are currently under investigation. They have the most promising properties with respect to our goals. The plan aiming at novel flight detectors must take into account several factors; in particular:

- The final devices must optimize their set of parameters: wavelength range, pixel array size. Their superiority to alternative technologies will be demonstrated in view of the science required of each instrument.
- The final devices must be ready in time: fully adapted, tested, selected, space-qualified and calibrated well in advance of integration.

To achieve this, strategic lines have been worked out:

1. The project aims to provide large, solar-blind, UV-sensitive cameras within the schedule of the Solar Orbiter: prototype demonstrated five years before launch.
2. All Solar Orbiter UV instruments are addressed.
3. Progress will be via a set of transitional objectives. The key solutions are demonstrated separately first.
4. Comprehensive tests evaluate diamond and nitride devices of comparable architectures.
5. The methodology traces all devices through all relevant experiments.
6. The tests extend from the XUV to the visible covering the range of anticipated benefits. Appropriate facilities are available: synchrotron (XUV to VUV), lasers and lamps (VUV-visible).
7. Hybrid devices, which may combine the merits of the APS-CMOS and BOLD concepts, are foreseen.
8. Empirical and theoretical modelling are key components to control the expected feedback from the experiments to the fabrication process.

Another important ingredient to success comes from an appropriate organization and a policy of rapid disclosure of the measurements through modern communications media (`http://bold.oma.be`) and publications.

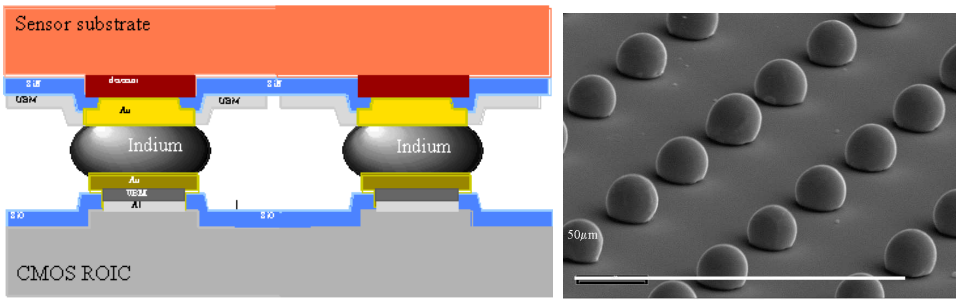

Figure 29.3: Left : Schematic view of a hybrid structure interfacing a wide-bandgap semiconductor membrane with an APS-CMOS sensor via indium bumps by way of the flip-chip technology. Right : Photograph of 7 μm electroplated indium bumps on 10 μm pitch (under development, density of bumps: 10^6 cm^{-2}). Courtesy of IMEC, Leuven.

Hybrid structures have been designed (Figure 29.3). The indium-bumps technology and the flip-chip integration allow interfacing of the sensitive membrane with standard CMOS circuitry. Special read-out electronics can be included for example for random access to subarrays, which takes full advantage of the APS concepts and preserves most BOLD features. Amorphous membranes could also be appropriate for such hybridization. All selected solutions encompass the required objectives of solar-blindness, better quantum efficiency, stability and uniformity of response, radiation-hardness, fast read-out, random pixel access and contamination reduction. The manufactured devices will be radiometrically characterized with synchrotron beam lines, laser sources and monochromated UV lamps in several European facilities. Nitride and diamond imagers will be systematically intercompared and will be judged against competing technologies so as to drive the development process and the final selection of flight hardware. The main focus will be on assessing the detectors' radiation-hardness, UV efficiency, solar-blindness and ageing robustness, in addition to testing their fundamental functions.

Acknowledgements

The authors are indebted to the many colleagues from diverse fields that contributed the crucial ingredients of this project. In addition to the authors, the main co-proposers are : J. Alvarez (Laboratoire de Génie Electrique de Paris (LGEP), Gif, France), D. F. Auret (University of Pretoria, South Africa), M.-C. Castex (Laboratoire de Physique des Lasers, Villetanneuse, France), A. Deneuville (Laboratoire d'Etudes des Propriétés Electroniques des Solides (LEPES), Grenoble, France), J.-M. Defise (Centre Spatial de Liège, Université de Liège, Angleur, Belgium), P. Dhez (Laboratoire pour l'Utilisation du Rayonnement Electromagnétique (LURE), Orsay, France), B. Fleck (ESA), O. Hainaut (Institut d'Astrophysique Spatiale and LURE, Orsay, France), M. Idir (LURE, Orsay, France), J.-P. Kleider (LGEP, Gif, France), J. Manca (Institute for Materials Research (IMO), Diepenbeek, Belgium), E. Monroy (CEA, Grenoble, France), P. Muret (LEPES, Grenoble, France), E. Muñoz (Departamento. de Ingeniería Electrónica, UPM, Madrid, Spain), M. Nesladek (Institute for Materials Research, Diepenbeek, Belgium), F. Omnes (Centre de Recherche sur l'Hétéro-Epitaxie et ses Applications, Valbonne, France), E. Pace (XUV Lab, University of Firenze, Italy) J. L. Pau (DIE/UPM, Madrid, Spain), V. Ralchenko (General Physics Institute of the Russian Academy of Sciences, Moscow, Russia), J. Roggen (IMEC, Leuven, Belgium), M. Schreck (IPLE, Augsburg, Ger-

many), C. Van Hoof (IMEC, Leuven, Belgium), M. Vanecek (Institute of Physics, Czech Academy of Sciences, Prague, Czechia).

The authors thank the referee for his careful reviewing of the paper.

Bibliography

Berghmans, D., Clette, F., and Moses, D., Quiet Sun EUV transient brightenings and turbulence. A panoramic view by EIT on board SOHO, *Astron. Astrophys.* **336**, 1039, 1998.

Defise, J., Clette, F., Moses, J.D., and Hochedez, J.-F., In-orbit diagnostics of EIT EUV CCD radiation-induced aging, *Proc. SPIE* **3114**, 598, 1997.

Fleck, B., Marsch, E., Schwenn, R., Antonucci, E., Bochsler, P., Bougeret, J.-L., Harrison, R.A., Marsden, R., Vial, J.-C., Solar Orbiter – A high-resolution mission to the Sun and inner heliosphere, AAS/Solar Physics Division Meeting, 32, 0296, 2000.

Goldberg, Y.A., Semiconductor near-ultraviolet photoelectronics, *Semicond. Sci. Technol.* **14**, R41–R60, 1999.

Hochedez, J.-F., Verwichte, E., Bergonzo, P., Guizard, B., Mer, C., Tromson, D., Sacchi, M., Dhez, P., Hainaut, O., Lemaire, P., Vial, J.-C., Future diamond UV imagers for solar physics, *Physica Status Solidi Applied Research* **181**, 141, 2000.

Hochedez, J.-F., Bergonzo, P., Castex, M.-C., Dhez, P., Hainaut, O., Sacchi, M., Alvarez, J., Boyer, H., Deneuville, A., Gibart, P., Guizard, B., Kleider, J.-P., Lemaire, P., Mer, C., Monroy, E., Muñoz, E., Muret, P., Omnes, F., Pau, J.L., Ralchenko, V., Tromson, D., Verwichte, E., and Vial, J.-C., Diamond UV detectors for future solar physics missions, *Diamond and Related Materials* **10/3-7**, 669–676, 2001.

Hochedez, J.-F., Lemaire, P., Pace, E., Schühle, U., and Verwichte, E., Wide bandgap EUV and VUV imagers for the Solar Orbiter, SP-493, in proceedings of Solar Encounter, The First Solar Orbiter Workshop, Puerto de la Cruz, Tenerife, Spain, 14-18 May 2001.

Hochedez, J.-F., Alvarez, J., Auret, F.D., Bergonzo, P., Castex, M.-C., Deneuville, A., Defise, J.M., Fleck, B., Gibart, P., Goodman, S.A., Hainaut, O., Kleider, J.-P., Lemaire, P., Manca, J., Monroy, E., Muñoz, E., Muret, P., Nesladec, M., Omnes, F., Pace, E., Pau, J.L., Ralchenko, V., Roggen, J., Schühle, U., Van Hoof, C., Recent progresses of the BOLD investigation towards UV detectors for the ESA Solar Orbiter, *Diamond and Related Materials*, in press, 2002.

Mainwood, A., Recent developments of diamond detectors for particles and UV radiation, *Semicond. Sci. Technol.* **15**, R55–R63, 2000.

Marsch, E., Antonucci, E., Bochsler, P., Bougeret, J.-L., Fleck, B., Harrison, R., Marsden, R., Schwenn, R., and Vial, J.-C., Solar Orbiter, a high-resolution mission to the Sun and inner heliosphere, IAU Symposium 203, 565, 2001.

Thompson, W.T., UV detectors aboard SOHO, *Proc. SPIE* **3764**, 196, 1999.

Glossary

SOHO's Instruments

CDS Coronal Diagnostic Spectrometer

CELIAS Charge, ELement and Isotope Analysis System

COSTEP COmprehensive SupraThermal and Energetic Particle analyzer

EIT Extreme ultraviolet Imaging Telescope

ERNE Energetic and Relativistic Nuclei and Electron experiment

LASCO Large Angle and Spectrometric COronagraph

MDI Michelson Doppler Imager

SEM Solar Extreme ultraviolet Monitor

SUMER Solar Ultraviolet Measurements of Emitted Radiation

SWAN Solar Wind ANisotropies

UVCS UltraViolet Coronagraph Spectrometer

VIRGO Variability of solar IRradiance and Gravity Oscillations

Other Instruments / Spacecraft

ACE Advanced Composition Explorer

EGS EUV Grating Spectrograph

FUSE Far-Ultraviolet Spectroscopic Explorer

SERTS Solar EUV Research Telescope and Spectrograph

HRTS High Resolution Telescope and Spectrograph (on HST)

HST Hubble Space Telescope

ISS International Space Station

IUE International Ultraviolet Explorer

Pioneer Series of spacecraft for study of the interplanetary and outer solar system

SNOE Student Nitric Oxide Explorer

SOLSTICE SOLar-Stellar Irradiance Comparison Experiment (on UARS)

SORCE SOlar Radiation and Climate Experiment

SPARTAN 201 Shuttle-launched and -retrieved satellite missions for coronal studies

SUSIM Solar Ultraviolet Spectral Irradiance Monitor (on UARS)

TIMED Thermosphere, Ionosphere, Mesosphere, Energetics and Dynamics mission

TRACE Transition Region And Coronal Explorer

UARS Upper Atmosphere Research Satellite

Ulysses Spacecraft for the study of the heliosphere, out-of-ecliptic orbit, passing over the solar poles

Voyager Twin spacecraft mission, studying the outer solar system

WIND Spacecraft for magnetospheric and ionospheric studies

Yohkoh Japanese for “sunbeam”, satellite that carried instruments for X-rays and gamma rays

Institutions

ESA European Space Agency

NASA National Aeronautics and Space Agency (US)

ISAS Institute of Space and Astronautical Science (Japan)

BIPM Bureau International des Poids et Mesures

NIST National Institute of Standards and Technology (US)

PTB Physikalisch-Technische Bundesanstalt (Germany)

Other

SICWG SOHO Inter-Calibration Working Group

Cal-SO Rocket underflights for SOHO cross-calibration

Wavelength Bands

Nomenclatures for wavelength bands are often rather arbitrary, not unambiguous, and certainly not consistent from author to author. The vacuum-ultraviolet (VUV) spectral region, for example, is often subdivided into a far ultraviolet (FUV) and an extreme ultraviolet (EUV) range. A possible and rather common classification is the following:

Name (Abbreviation)	Nominal Range
X-rays	0.1 nm – 10 nm (0.1 keV – 10 keV)
soft X-rays	0.3 nm – 10 nm (0.1 keV – 3 keV)
vacuum UV (VUV)	$<$ 200 nm
ultraviolet (UV)	$<$ 450 nm
visible	450 nm – 750 nm
near infrared (NIR)	750 nm – 2.5 μm
far infrared (FIR)	2.5 μm – 100 μm
sub-millimetre (sub-mm)	100 μm – 1 mm

Authors' Addresses

Joachim Anders
Fraunhofer Institute of
Physical Measurement Technology
Heidenhofstraße 8
79110 Freiburg, Germany
email: joachim.anders@ipm.fhg.de

Nigel Atkins
Harvard-Smithsonian Center for
Astrophysics
Cambridge, MA 02138, USA
email: natkins@cfa.harvard.edu

Frédéric Auchère
Universities Space Research Association
NASA GSFC
Greenbelt, MD 20771, USA
email: auchere@filament.nascom.nasa.gov

Jean-Loup Bertaux
Service d'Aéronomie du CNRS
BP 3, 91371, Verrières le Buisson, France
email: bertaux@aerov.jussieu.fr

Peter Bochsler
Physikalisches Institut der Universität Bern
Sidlerstrasse 5
3012 Bern, Switzerland
email: peter.bochsler@soho.unibe.ch

Alfred Bürgi
Physikalisches Institut der Universität Bern
Sidlerstrasse 5
3012 Bern, Switzerland
email: alfred.buergi@arias.ch

Angela Ciaravella
Harvard-Smithsonian Center for
Astrophysics
Cambridge, MA 02138, USA
email: aciaravella@cfa.harvard.edu

Frédéric Clette
Observatoire Royal de Belgique
Avenue Circulaire, 3
1180 Bruxelles, Belgium
email: fred@oma.be

Steven R. Cranmer
Harvard-Smithsonian Center for
Astrophysics
Cambridge, MA 02138, USA
email: scranmer@cfa.harvard.edu

J. Len Culhane
Mullard Space Science Laboratory
University College London
Holmbury St Mary, Dorking, Surrey, UK
email: jlc@mssl.ucl.ac.uk

Werner Curdt
Max-Planck-Institut für Aeronomie
Max-Planck-Straße 2
37191 Katlenburg-Lindau, Germany
email: curdt@linmpi.mpg.de

Ingolf E. Dammasch
Max-Planck-Institut für Aeronomie
Max-Planck-Straße 2
37191 Katlenburg-Lindau, Germany
email: dammasch@linmpi.mpg.de

Jean-Marc Defise
Centre Spatial de Liège
4031 Angleur-Liège, Belgium
email: jmdefise@ulg.ac.be

Jean-Pierre Delaboudinière
Institut d'Astrophysique Spatiale
91405 Orsay, France
email: boudine@ias.fr

Giulio Del Zanna
Department of Applied Mathematics and
Theoretical Physics
University of Cambridge, Cambridge, UK
email: g.del-zanna@damtp.cam.ac.uk

Kenneth P. Dere
Naval Research Laboratory
4555 Overlook Ave., SW
Washington, DC 20375, USA
email: dere@halcyon.nrl.navy.mil

George A. Doschek
Naval Research Laboratory
4555 Overlook Ave., SW
Washington, DC 20375, USA
email: gdoschek@ssd5.nrl.navy.mil

Silvano Fineschi
Osservatorio Astronomico di Torino
10025 Pino Torinese, Italy
email: finesci@arcetri.astro.it

Carl R. Foley
Mullard Space Science Laboratory
University College London
Holmbury St Mary, Dorking, Surrey, UK
email: caf@mssl.ucl.ac.uk

Richard A. Frazin
Harvard-Smithsonian Center for Astrophysics
Cambridge, MA 02138, USA
email: rfrazin@cfa.harvard.edu

Claus Fröhlich
Physikalisch Meteorologisches Observatorium / World Radiation Center
Dorfstrasse 33
7260 Davos Dorf, Switzerland
email: cfrohlich@pmodwrc.ch

Bogdan Galuska
Fraunhofer Institute of Physical Measurement Technology
Heidenhofstraße 8
79110 Freiburg, Germany
email: bogdan.galuska@ipm.fhg.de

Larry D. Gardner
Harvard-Smithsonian Center for Astrophysics
Cambridge, MA 02138, USA
email: gardner@cfa.harvard.edu

Martin Hilchenbach
Max-Planck-Institut für Aeronomie
Max-Planck-Straße 2
37191 Katlenburg-Lindau, Germany
email: hilchenbach@linmpi.mpg.de

Jean-François Hochedez
Observatoire Royal de Belgique
Avenue Circulaire, 3
1180 Bruxelles, Belgium
email: hochedez@oma.be

Jörg Hollandt
Physikalisch-Technische Bundesanstalt
Abbestraße 2-12
10587 Berlin, Germany
email: joerg.hollandt@ptb.de

Russell A. Howard
Naval Research Laboratory
4555 Overlook Ave., SW
Washington, DC 20375, USA
email: howard@nrl.navy.mil

Martin C.E. Huber
International Space Science Institute
Hallerstrasse 6
3012 Bern, Switzerland
email: mceh@bluewin.ch

Fred Ipavich
Department of Physics and Astronomy and IPST, University of Maryland
College Park, MD, USA
email: ipavich@umtof.umd.edu

Darrell L. Judge
University of Southern California
University Park, SHS-274
Los Angeles, California, USA
email: judge@usc.edu

Ryan Keenan
Laboratory for Atmospheric and Space Physics
University of Colorado
1234 Innovation Drive
Boulder, CO, USA
email: ryan.keenan@lasp.colorado.edu

Barry J. Kent
Rutherford Appleton Laboratory
Chilton, Didcot, Oxfordshire
OX11 0QX, UK
email: b.j.kent@rl.ac.uk

Ulrich Klocke
Fraunhofer Institute of Physical Measurement Technology
Heidenhofstraße 8
79110 Freiburg, Germany
email: ulrich.klocke@ipm.fhg.de

Manfred Knothe
Fraunhofer Institute of Physical Measurement Technology
Heidenhofstraße 8
79110 Freiburg, Germany
email: manfred.knothe@ipm.fhg.de

John L. Kohl
Harvard-Smithsonian Center for Astrophysics
Cambridge, MA 02138, USA
email: jkohl@cfa.harvard.edu

Therese A. Kucera
NASA Goddard Space Flight Center
Code 682
Greenbelt, MD 20771, USA
email: terese.kucera@gsfc.nasa.gov

Michael Kühne
Physikalisch-Technische Bundesanstalt
Abbestraße 2-12
10587 Berlin, Germany
email: michael.kuehne@ptb.de

Enrico Landi
Naval Research Laboratory
4555 Overlook Ave., SW
Washington, DC 20375, USA
email: enrico.landi@nrl.navy.mil

Massimo Landini
Dip. di Astronomia e Scienza dello Spazio
Università di Firenze
Largo Enrico Fermi 2
50125 Firenze, Italy
email: landini@arcetri.astro.it

James Lang
Rutherford Appleton Laboratory
Chilton, Didcot, Oxfordshire
OX11 0QX, UK
email: j.lang@rl.ac.uk

Philippe Lemaire
Institut d'Astrophysique Spatiale
Unité Mixte, CNRS-Université
Université de Paris XI
91405 Orsay Cedex, France
email: lemaire@medoc-ias.u-psud.fr

Helen E. Mason
Department of Applied Mathematics and Theoretical Physics
University of Cambridge
Cambridge, UK
email: h.e.mason@damtp.cam.ac.uk

Donald R. McMullin
University of Southern California
University Park, SHS-274
Los Angeles, California, USA
email: mcmullin@usc.edu

Mari Paz Miralles
Harvard-Smithsonian Center for Astrophysics
Cambridge, MA 02138, USA
email: mmiralles@cfa.harvard.edu

J. Daniel Moses
Naval Research Laboratory
4555 Overlook Ave., SW
Washington, DC 20375, USA
email: moses@nrl.navy.mil

Eugen Neske
Fraunhofer Institute of Physical Measurement Technology
Heidenhofstraße 8
79110 Freiburg, Germany
email: eugen.neske@ipm.fhg.de

Jeffrey S. Newmark
Naval Research Laboratory
4555 Overlook Ave., SW
Washington, DC 20375, USA
email: newmark@midas.nrl.navy.mil

Alexander Panasyuk
Harvard-Smithsonian Center for Astrophysics
Cambridge, MA 02138, USA
email: apanasyuk@cfa.harvard.edu

Anuschka Pauluhn
International Space Science Institute
Hallerstrasse 6
3012 Bern, Switzerland
email: pauluhn@issi.unibe.ch

C. David Pike
Rutherford Appleton Laboratory
Chilton, Didcot, Oxfordshire
OX11 0QX, UK
email: c.d.pike@rl.ac.uk

Eric Quémerais
Service d'Aéronomie du CNRS
BP 3, 91371, Verrières le Buisson, France
email: eric.quemerais@aerov.jussieu.fr

John C. Raymond
Harvard-Smithsonian Center for Astrophysics
Cambridge, MA 02138, USA
email: jraymond@cfa.harvard.edu

Kevin Reardon
Dip. di Astronomia e Scienza dello Spazio
Università di Firenze
Largo Enrico Fermi 2
50125 Firenze, Italy
email: reardon@arcetri.astro.it

Wolfgang J. Riedel
Fraunhofer Institute of Physical Measurement Technology
Heidenhofstraße 8
79110 Freiburg, Germany
email: wolfgang.riedel@ipm.fhg.de

Marco Romoli
Dip. di Astronomia e Scienza dello Spazio
Università di Firenze
Largo Enrico Fermi 2
50125 Firenze, Italy
email: romoli@arcetri.astro.it

Gary J. Rottman
Laboratory for Atmospheric and
Space Physics
University of Colorado
1234 Innovation Drive
Boulder, CO, USA
email: gary.rottman@lasp.colorado.edu

Isabelle Rüedi
Physikalisch Meteorologisches
Observatorium / World Radiation Center
Dorfstrasse 33
7260 Davos Dorf, Switzerland
email: i.ruedi@pmodwrc.ch

Gerhard Schmidtke
Fraunhofer Institute of
Physical Measurement Technology
Heidenhofstraße 8
79110 Freiburg, Germany
email: gerhard.schmidtke@ipm.fhg.de

Udo Schühle
Max-Planck-Institut für Aeronomie
Max-Planck-Straße 2
37191 Katlenburg-Lindau, Germany
email: schuehle@linmpi.mpg.de

John F. Seely
Naval Research Laboratory
4555 Overlook Ave., SW
Washington, DC 20375, USA
email: john.seely@nrl.navy.mil

Ralf Singler
Fraunhofer Institute of
Physical Measurement Technology
Heidenhofstraße 8
79110 Freiburg, Germany
email: ralf.singler@ipm.fhg.de

Peter L. Smith
Harvard-Smithsonian Center for
Astrophysics
Cambridge, MA 02138, USA
email: plsmith@cfa.harvard.edu

Sami K. Solanki
Max-Planck-Institut für Aeronomie
Max-Planck-Straße 2
37191 Katlenburg-Lindau, Germany
email: solanki@linmpi.mpg.de

Rudolf von Steiger
International Space Science Institute
Hallerstrasse 6
3012 Bern, Switzerland
email: vonsteiger@issi.unibe.ch

Leonard Strachan, Jr.
Harvard-Smithsonian Center for
Astrophysics
Cambridge, MA 02138, USA
email: lstrachan@cfa.harvard.edu

Raid M. Suleiman
Harvard-Smithsonian Center for
Astrophysics
Cambridge, MA 02138, USA
email: rsuleiman@cfa.harvard.edu

Roger J. Thomas
NASA Goddard Space Flight Center
Code 682
Greenbelt, MD 20771, USA
email: Roger.J.Thomas@gsfc.nasa.gov

Ron Thomas
Whiteoaks, Monkmead Lane
West Chiltington, UK
email: rsethomas@compuserve.com

William T. Thompson
L3 Communications Analytics Corporation
NASA Goddard Space Flight Center GSFC
Greenbelt, MD 20771, USA
email: thompson@orpheus.nascom.nasa.gov

W. Kent Tobiska
Space Environment Technologies
Pacific Palisades, California, USA
email: ktobiska@spacenvironment.net

Ulrich Ulmer
Fraunhofer Institute of
Physical Measurement Technology
Heidenhofstraße 8
79110 Freiburg, Germany
email: ulrich.ulmer@ipm.fhg.de

Dennis Wang
Naval Research Laboratory
4555 Overlook Ave., SW
Washington, DC 20375, USA
email: wang@ares.nrl.navy.mil

Tetsuya Watanabe
National Astronomical Observatory of Japan
Mitaka, Tokyo 181, Japan
email: watanabe@solar.mtk.nao.ac.jp

Burkhard Wende
Physikalisch-Technische Bundesanstalt
Abbestraße 2-12
10587 Berlin, Germany
email: burkhard.wende@ptb.de

Frank G. Wienhold
Fraunhofer Institute of
Physical Measurement Technology
Heidenhofstraße 8
79110 Freiburg, Germany
email: frank.wienhold@ipm.fhg.de

Klaus Wilhelm
Max-Planck-Institut für Aeronomie
Max-Planck-Straße 2
37191 Katlenburg-Lindau, Germany
email: wilhelm@linmpi.mpg.de

Helmut Wolf
Fraunhofer Institute of
Physical Measurement Technology
Heidenhofstraße 8
79110 Freiburg, Germany
email: helmut.wolf@ipm.fhg.de

Tom N. Woods
Laboratory for Atmospheric and
Space Physics
University of Colorado
1234 Innovation Drive
Boulder, CO, USA
email: tom.woods@lasp.colorado.edu

Peter Wurz
Physikalisches Institut der Universität Bern
Sidlerstrasse 5
3012 Bern, Switzerland
email: peter.wurz@soho.unibe.ch

Peter R. Young
Rutherford Appleton Laboratory
Chilton, Didcot, Oxfordshire
OX11 0QX, UK
email: p.r.young@rl.ac.uk